

**Corrosion behavior of API X100 steel in near-neutral pH
bicarbonate environments: experimental and modelling studies**

by

IBRAHIM M. GADALA

B.A.Sc. *with distinction*, The University of British Columbia, 2010

M.A.Sc., The University of British Columbia, 2012

A THESIS SUBMITTED IN PARTIAL FULFILLMENT OF THE REQUIREMENTS
FOR THE DEGREE OF

DOCTOR OF PHILOSOPHY

in

THE FACULTY OF GRADUATE AND POSTDOCTORAL STUDIES

(Materials Engineering)

The University of British Columbia

(Vancouver)

April 2017

© Ibrahim M. Gadala, 2017

Abstract

API X100 is a new high-strength low-alloy steel which has garnered great interest from the pipeline industry due to the economic benefits it offers in terms of lower material, transportation, and fabrication costs. However, buried pipeline steels suffer from external corrosion and cracking, the mechanism of which in near-neutral pH environments is not yet fully understood. This dissertation presents and discusses the results of several electrochemical studies and numerical models conducted on X100 steel, contributing to a more complete understanding of the fundamental corrosion processes occurring in these environments. Improved simulation accuracy for corrosion rates and pipeline integrity is achieved. Applications of this research are strongest within the buried oil and gas transmission pipeline field, yet are extendable to other infrastructural and engineering applications such as utility piping systems and steel reinforcements of buried or concrete structures.

Results of this work elucidate the criticality of even minor pH variations within the near-neutral pH environment on the corrosion and passivation of X100. Conflicting impacts of $[\text{HCO}_3^-]$ versus $\% \text{CO}_2$ on corrosion rate are revealed, attributed to the gradual dominance of hydrogen evolution cathodic reactions involving HCO_3^- species at higher pH. A finer three region subdivision of the near-neutral pH range is proposed based on the dissolution, dissolution-adsorption, adsorption-diffusion, and diffusion-controlled behaviors which appear as pH, $[\text{HCO}_3^-]$, $[\text{Cl}^-]$, $[\text{SO}_4^{2-}]$, and temperatures are changed. Dynamic electrochemical impedance spectroscopy identifies the role of $\text{Cl}^-/\text{SO}_4^{2-}$ in increasing corrosion rate, decreasing pre-passive stage diffusion, and decreasing passive layer protection. Increased porosity of FeOOH tubercle structures formed in low dissolved $[\text{O}_2]$ environments augments diffusion therein, spurring the exclusive formation of Fe_2O_3 underneath instead of only Fe_3O_4 . Hydrogen diffusivity in X100 steel is found to be $4.4 \times 10^{-7} \text{ cm}^2/\text{s}$. During free corrosion, a diffusible hydrogen concentration of 1 atomic ppm is also measured in the alloy. Simulations in the Finite Element models developed

indicate ideal anode placements and applied voltages for an underground cathodic protection system. Additionally, the transient evolution of an external corrosion defect which reaches 3 mm deep within 3 years is visualized, wherein the pipeline's structural integrity is diminished by 8% of the intact pipeline strength.

Preface

The following journal articles, book chapter, and articles in the proceedings of professional conferences have been published from the research work presented in this dissertation. Professor Akram Alfantazi extensively helped with all aspects of the research work.

Peer-reviewed Journals and Book Chapter:

1. **I. M. Gadala**, M. Abdel Wahab, and A. Alfantazi, “Simulating the burst pressure of externally corroded underground gas transmission pipelines using a finite element corrosion model and stress analysis,” [under review].
2. **I. M. Gadala**, H. M. Ha, P. Rostron, and A. Alfantazi, “Formation and evolution of oxide/oxyhydroxide corrosion products on low-alloy steel during exposure to near-neutral pH solutions containing oxygen and nitrate,” *Corrosion*, vol. 73, no. 3, pp. 221-237, March 2017.
3. H. M. Ha, **I. M. Gadala**, and A. Alfantazi, “Hydrogen Evolution and Absorption in an API X100 Line Pipe Steel Exposed to Near-Neutral pH Solutions,” *Electrochimica Acta*, vol. 204, pp. 18-30, June 2016.
4. F. F. Eliyan, **I. M. Gadala**, H. M. Ha, and A. Alfantazi, “Pipeline Corrosion,” *ASTM Fuels and Lubricants Handbook: Technology, Properties, Performance, and Testing*, 2nd edition. PA: ASTM International, 2016.
5. **I. M. Gadala**, M. Abdel Wahab, and A. Alfantazi, “Numerical simulations of soil physicochemistry and aeration influences on the external corrosion and cathodic protection design of buried pipeline steels,” *Materials and Design*, vol. 97, pp. 287-299, May 2016.
6. **I. M. Gadala** and A. Alfantazi, “A study of X100 pipeline steel passivation in mildly alkaline bicarbonate solutions using Electrochemical Impedance Spectroscopy under potentiodynamic conditions and Mott-Schottky,” *Applied Surface Science*, vol. 357A, pp. 356-368, Dec 2015.
7. **I. M. Gadala** and A. Alfantazi, “Low Alloy X100 Pipeline Steel Corrosion and Passivation Behavior in Bicarbonate-Based Solutions of pH 6.7 to 8.9 with Groundwater Anions: An Electrochemical Study,” *Metallurgical and Materials Transactions A*, vol. 46, no. 7, pp. 3104–3116, April 2015.
8. **I. M. Gadala** and A. Alfantazi, “Electrochemical behavior of API-X100 pipeline steel in NS4, near-neutral, and mildly alkaline pH simulated soil solutions,” *Corrosion Science*, vol. 82, pp. 45–57, May 2014.

Peer-reviewed Conference Proceedings:

9. **I. M. Gadala** and A. Alfantazi, “Inhibitive effectiveness of hydrazine oxygen scavenger on low-alloy steel in near-neutral pH underground conditions,” *Proceedings of the ACA Corrosion and Prevention Conference*, November 13 – 16 (2016), Auckland, New Zealand.
10. **I. M. Gadala**, M. Abdel Wahab, and A. Alfantazi, “A finite element model of the external corrosion of buried pipeline steel under the combined influence of heat transfer, cathodic protection, and oxygen diffusion in surrounding soil,” *Proceedings of NACE CORROSION 2016*, March 6 – 11 (2016), Vancouver, Canada.
11. **I. M. Gadala**, A. Alfantazi, Z. Farhat, and A. M. A. Mohamed, “External corrosion of API-X100 pipeline steels in near-neutral pH soils of variable aeration and nitrate ion content,” *Proceedings of the 10th ASME RioPipeline*, September 22 – 24 (2015), Rio de Janeiro, Brazil.
12. **I. M. Gadala** and A. Alfantazi, “An Electrochemical Impedance Spectroscopy study of the corrosion of buried low-alloy steel infrastructure used in energy transportation and storage,” *Proceedings of the Energy & Materials Research Conference (EMR)*, February 25 – 27 (2015), Madrid, Spain.
13. **I. M. Gadala** and A. Alfantazi, “Bicarbonate, temperature, and pH influences on the passivation of API-X100 pipeline steel in simulated groundwater solutions,” *Proceedings of the 10th ASME International Pipeline Conference (IPC)*, September 29 – October 3 (2014), Calgary, Canada.

The following table identifies the specific publication(s) upon which each corresponding chapter of this dissertation is based:

Chapter number in dissertation	Publication number(s) from the list above
2	4
5	7, 8, and 13
6	6 and 12
7	2, 9, and 11
8	3
9	1, 5, and 10

Table of Contents

Abstract.....	ii
Preface.....	iv
Table of Contents.....	vi
List of Tables.....	ix
List of Figures.....	xii
List of Abbreviations.....	xxi
List of Chemical Formulae.....	xxiii
List of Symbols.....	xxv
Acknowledgements.....	xxx
Dedication.....	xxxi
1 Introduction.....	1
1.1 Impact of pipeline corrosion.....	2
1.2 Importance for Canada.....	3
1.3 High-Strength Low-Alloy steels.....	3
1.4 Environments causing external SCC.....	5
1.5 Motivation.....	8
2 Literature review.....	9
2.1 Ionic and pH influences on corrosion processes in anoxic soil environments .	10
2.2 Time-dependent corrosion product and surface effects in anoxic and oxic soil environments.....	15
2.3 Hydrogen evolution, absorption, and diffusion processes in steels exposed to simulated soil solutions.....	21
2.4 Numerical modelling of corrosion, CP, and pipeline structural integrity.....	27
2.4.1 Models and simulations of steel corrosion with CP and gas transport.....	27
2.4.2 Models of the residual strength and integrity of corroded pipelines.....	32
3 Objectives.....	36
3.1 Key technical objectives.....	37
4 Approach and methodology.....	38
4.1 Material and specimen preparation.....	38
4.1.1 Microstructural evaluation.....	39
4.1.2 Preparation of specimens.....	41
4.2 Test environments and methods.....	42
4.2.1 Standard NS4 solution and variants.....	42
4.2.2 Electrochemical test methods for corrosion and passivation processes.....	43
4.2.3 Electrochemical test method for hydrogen permeation and diffusion.....	46
4.2.4 Microscopy and chemical characterization methods.....	49

4.3	Modelling geometries and meshes.....	50
5	Electrochemical behavior of X100 pipeline steel in deaerated HCO_3^- solutions of near-neutral, mildly acidic, or mildly alkaline pH	54
5.1	OCP and LPR measurements.....	55
5.2	PDP testing and parameter variations based on E -pH.....	58
5.2.1	Passive and passive-like PDP responses.....	59
5.2.2	Anodic parameter relationships with E -pH.....	64
5.3	EIS tests at OCP in deaerated nn-pH conditions.....	74
5.3.1	Subdivision of electrochemical response based on pH range.....	83
5.4	Summary.....	83
6	Quantitative studies of the properties & growth of corrosion products on X100 steel in mildly alkaline deaerated HCO_3^- solutions using EIS and Mott-Schottky	85
6.1	Details of dynamic EIS, PSP, and Mott-Schottky test methods.....	87
6.2	Dynamic step-wise anodizing EIS test.....	89
6.2.1	Active corrosion at $E < E_{p1}$	89
6.2.2	Corrosion and passive-like behavior in the $E_{p1} < E < E_{p2}$ transition.....	94
6.2.3	Corrosion and passivation processes at $E > E_{p2}$	98
6.3	Protective and semiconductive properties of anodized FeCO_3	102
6.3.1	Current density decay and qualitative analysis of Bode $ Z $ results.....	102
6.3.2	Semiconductive properties analysis using Mott-Schottky.....	105
6.4	Summary.....	108
7	Extended immersion studies of the formation of oxide/oxyhydroxide corrosion products on X100 steel during exposure to nn-pH HCO_3^- solutions with O_2, N_2H_4, and/or NO_3^-	110
7.1	Test environments and experimental procedures.....	112
7.2	Short-term electrochemical tests at immersion times ≤ 1 h.....	115
7.2.1	OCP < 1 h.....	115
7.2.2	PDP at 1 h.....	119
7.3	Surface analysis following 24 h or 168 h immersions.....	126
7.4	Periodic electrochemical tests during 24 h immersions in 0 – 20 ppm $[\text{O}_2]$ and 0 – 0.015 M $[\text{NO}_3^-]$ conditions.....	134
7.4.1	OCP.....	134
7.4.2	EIS.....	138
7.4.3	LPR.....	146
7.5	Summary.....	149
8	Evaluation of hydrogen evolution, absorption, and diffusion in X100 steel exposed to nn-pH HCO_3^- solutions of various ion constituents and temperatures ..	151
8.1	Environments and hydrogen permeation conditions.....	152
8.1.1	Hydrogen permeation conditions.....	154
8.2	Results of OCP and cathodic polarization ($E < -1.2 \text{ V}_{\text{SCE}}$).....	155
8.2.1	Environmental effects on cathodic polarization results.....	156
8.2.2	Surface deposit effects on cathodic polarization results.....	160
8.3	Results of hydrogen permeation experiments.....	161

8.4	Discussion of OCP, cathodic PDP, and permeation results.....	165
8.4.1	Hydration of CO ₂ and [HCO ₃ ⁻ -CO ₃ ²⁻] in CO ₂ -H ₂ O system	165
8.4.2	HER on X100 at OCP and cathodic potentials	170
8.4.3	Hydrogen permeation in X100 exposed to nn-pH HCO ₃ ⁻ solutions.....	174
8.5	Summary	176
9	FEM of the external corrosion and structural integrity of buried pipelines under the influences of CP, gas diffusion, and environment physicochemistry	178
9.1	Modelling details: governing phenomena and equations.....	181
9.1.1	Heat transfer, CP, and O ₂ diffusion phenomena	181
9.1.2	Initial conditions and boundary conditions for governing phenomena	183
9.1.3	Reaction kinetics at exposed steel surface	185
9.2	Polarization experiments and equations for coupled simulations.....	189
9.2.1	Temperature- and O ₂ -dependent fittings for m-model.....	189
9.2.2	Temperature- and %CO ₂ -dependent fittings for mm-model	194
9.3	<i>E_{Fe}</i> , <i>C_{O2}</i> , and <i>i</i> simulation results from m-model	196
9.3.1	Temperature, ϕ , and <i>C_{O2}</i> contours	196
9.3.2	<i>E_{Fe}</i>	199
9.3.3	<i>i_{Fe}</i>	201
9.3.4	<i>C_{O2}</i> , <i>i_{O2}</i> , and <i>i_{H2}</i>	203
9.3.5	Practical CP design applications	206
9.4	ϕ evolution, defect growth, and stress analysis in mm-model	209
9.4.1	ϕ evolution within the disbondment.....	209
9.4.2	Growth of corrosion defect and implications on structural integrity	210
9.5	Model convergence through mesh sensitivity analysis.....	217
9.6	Summary	219
10	Conclusions.....	222
10.1	Key contributions and broad implications	222
10.2	Summary of important technical findings.....	226
10.3	Suggestions for future work.....	231
	References.....	233
	Appendices.....	253
	Appendix A: supplementary figures for chapter 5.....	253
	Appendix B: supplementary figures for chapter 6.....	260
	Appendix C: supplementary figures and tables for chapter 7.....	262
	Appendix D: supplementary tables and figures for chapter 8.....	269
	Appendix E: supplementary tables and figures for chapter 9.....	272

List of Tables

Table 1-1: Natural gas transmission pipeline incident summary by cause for 1/1/2002 - 12/31/2003, from US Department of Transportation’s Office of Pipeline Safety [4]	2
Table 1-2: Characteristics of nn-pH and high pH external SCC in pipelines – adapted from [13]– [15]	6
Table 4-1: Chemical composition and carbon equivalent (CE) of API X100 steel used in laboratory tests	39
Table 4-2: Maximum and minimum element size, maximum element growth rate, and resolution of curvature values for extra coarse to extra fine mesh resolutions, within the soil domain vs. at electrode/ground boundaries in Figure 4-4b.....	53
Table 5-1: EIS component values for NS4 solution at 25, 40, or 55 °C purged with 5% CO ₂ /95% N ₂ , or 100% CO ₂	77
Table 5-2: EIS component values for NS4 + 10x HCO ₃ ⁻ solution	80
Table 5-3: EIS component values for NS4 + 10x HCO ₃ ⁻ solutions with added Cl ⁻ and/or SO ₄ ²⁻ at 25 °C, purged with 5% CO ₂ /95% N ₂ (pH 7.6)	82
Table 6-1: Anodizing potentials (E_{an}) in each potential range for step-wise anodizing-EIS routine	87
Table 6-2: EIS component values for 0.1 M [HCO ₃ ⁻] solution with and without Cl ⁻ /SO ₄ ²⁻ at $E_{an} = -0.65 V_{SCE}$ (early active E region)	91
Table 6-3: EIS component values for 0.1 M [HCO ₃ ⁻] solution with and without Cl ⁻ /SO ₄ ²⁻ at $-0.5 V_{SCE}$ (late active potential region), and 0.1 M [HCO ₃ ⁻] solution without Cl ⁻ /SO ₄ ²⁻ at $-0.4 V_{SCE}$ (transition potential region)	93
Table 6-4: EIS component values for 0.1 M [HCO ₃ ⁻] solution with Cl ⁻ /SO ₄ ²⁻ at $-0.475 V_{SCE}$ (transition potential region)	97
Table 6-5: EIS component values for 0.1 M [HCO ₃ ⁻] solution with Cl ⁻ /SO ₄ ²⁻ at $-0.1 V_{SCE}$ (passive formation potential region) and $0.175 V_{SCE}$ (passive potential region), and without Cl ⁻ /SO ₄ ²⁻ at $-0.25 V_{SCE}$ (passive formation potential region) and $0.5 V_{SCE}$ (passive potential region)	100
Table 6-6: EIS component values for 0.1 M [HCO ₃ ⁻] solution without Cl ⁻ /SO ₄ ²⁻ at $1.1 V_{SCE}$ (transpassivation potential region)	101
Table 7-1: List of [O ₂] and [NO ₃ ⁻] combinations studied in this chapter, based on the reference NS4 electrolyte of AA*, with corresponding measured $C_{O_2,i}$, pH, and conductivities of solutions	113

Table 7-2: List of temperature and [N ₂ H ₄] combinations studied in short term corrosion inhibition tests of this chapter based on reference NS4 electrolyte of environment AA [*] , with corresponding measured $C_{O_2,i}$	114
Table 7-3: List of temperature and [N ₂ H ₄] combinations studied in extended 168 h immersion corrosion inhibition tests of this chapter based on environment AA [*] in Table 7-2, with corresponding measured $C_{O_2,i}$	114
Table 7-4: Values of E_{co1} and E_{co2} extracted from PDP plots of N ₂ H ₄ treated environments, with corresponding ranges of the low-current region.....	124
Table 7-5: Values of i_{a1} and i_{a2} extracted from PDP plots of N ₂ H ₄ treated environments, with corresponding i_{max} values in low i region and minimum percent decrease in i	125
Table 7-6: Comparison of R_p values from LPR with R_p^* or R_p^{**} from EIS component sums, in solutions with 0, 6, and 20 ppm O ₂ at 2, 8, 16, and 24 h immersion.....	147
Table 8-1: Approximate concentrations and % fractions of H ₂ CO ₃ , HCO ₃ ⁻ , and CO ₃ ²⁻ in the CO ₂ -H ₂ O system for a temperature of 20 °C and 1 atm CO ₂	168
Table 8-2: Summary of steady state permeation current densities and diffusible hydrogen concentrations in the X100 steel exposed to the NS4 solution under different charging conditions	175
Table 9-1a: Governing transport equations and related parameters in each module of the m-model [290]	181
Table 9-1b: Values or expressions for the thermal, electrical, and diffusion properties of the soil media in the m-model [290]	1812
Table 9-2: Overall formulations and reaction-specific equations governing reaction kinetics in the uncoupled m-model.....	187
Table 9-3: Regression fit equations and corrosion parameters governing reaction kinetics in the coupled simulations of the m-model, <u>extracted from polarization plots</u>	192
Table 9-4: List of OCP values for environments studied for mm-model, characterized by temperature, %CO ₂ concentration in deaerating purging gas, and pH.....	194
Table 9-5: C_1 and C_2 parameter results of regression fits for i_c evaluation (i_c as a function of $E_s(x)$, C_1 , and C_2)	194
Table 9-6: Comparison of P_b/P_{bi} ratio results obtained from {E-9.19} versus those from the shell element FEM of Figure 9-11, using corrosion defect values simulated from the corrosion module of the mm-model	217
Table C-1: Corrosion parameters obtained from Tafel extrapolation of deaerated PDP results of three NO ₃ ⁻ concentrations	263

Table C-2: Fitting results for linear and nonlinear regressions of final OCP values at 1 h and 24 h (Figure 7-1), valid for [O ₂] values between 0 and 20 ppm	266
Table C-3: EIS component values for deaerated 0.2 ppm O ₂ solution (pH 6.7, 0.005 M NO ₃ ⁻) at 2, 8, 16, and 24 h immersion	267
Table C-4: EIS component values for 5.8 ppm O ₂ solution (pH 7.7, 0.005 M NO ₃ ⁻) at 2, 8, 16, and 24 h immersion	267
Table C-5: EIS component values for 20.4 ppm O ₂ solution (pH 8.6, 0.005 M NO ₃ ⁻) at 2, 8, 16, and 24 h immersion	268
Table D-1: Test conditions and the measured natural pH of the test solutions in chapter 8	269
Table D-2: Some forms of Henry's law and values of Henry's constant for various gases in water at 298 K [277], [278]	271
Table E-1 (for mm-model): Maximum element size, minimum element size, and maximum element growth rate for coarse to fine mesh resolutions, within the electrolyte domain vs. at the exposed steel surface in Figure 4-5	272
Table E-2 (for m-model): Thermal conductivity and volumetric heat capacity parameters for the soil structure and ψ combinations simulated	272
Table E-3 (for mm-model): List of current, potential, current balance, reaction kinetics (<u>extracted from polarization plots</u>), and regression fit equations governing corrosion simulations, with corresponding numbers, details, and conditions.....	273
Table E-4 (for mm-model): Maximum radial depth (d_{defect_max}) and longitudinal length (l_{defect}) dimensions [mm] of corrosion defects at 1 and 3 year time stages for all temperatures (T_{wall}), applied potentials (E_{app}), and coating disbondment opening sizes (w) simulated	276
Table E-5: Mechanical properties of various grades of HSLA pipeline steels [152]	277

List of Figures

Figure 1-1: North American network of major liquid transmission pipelines [1]	1
Figure 1-2: Development flow chart of HSLA pipeline steels from 1965 to 2009 [8]	4
Figure 1-3: Three conditions necessary for pipeline SCC, with corresponding dependencies [13]	6
Figure 1-4: Areas of near-neutral pH SCC formation on external pipeline surfaces [13].....	7
Figure 2-1: The numerous environmental, material, and surface effects on metal corrosion in soil environments, ranging from the macroscale to the smaller surface level scale [34]	9
Figure 2-2: Schematic showing the effect of CO ₂ concentration on the environment's pH, and the resulting influence on aggressiveness (where t_e/t_{air} is the time to failure ratio in environment over that in air) [24].....	11
Figure 2-3: Potentiodynamic polarization in 0.1, 0.5, and 0.8 M HCO ₃ ⁻ solutions at 20 °C in (a) Cl ⁻ -free and (b) Cl ⁻ -containing conditions [56]	12
Figure 2-4: (a) Actual CP levels at different positions from opening mouth (OM) and different times; (b) pH distribution of the electrolyte inside the shielded disbondments at different positions from opening mouth, and different times [25]	13
Figure 2-5: (a) Surface morphology of CaCO ₃ layer formed on X70 surface after 40 h immersion in 5% CO ₂ NS4 solution at 22 °C; (b) i_{corr} map measured on X70 specimen covered with CaCO ₃ [41]	16
Figure 2-6: (a) E_{corr} (vs. SCE) of pretreated steel under anoxic conditions in nn-pH saline solutions, where square points show R_p values from LPR; (b) Schematic illustrating the film transition process within an acidified pore, assuming separation of anode (Fe dissolution) and cathode (HCO ₃ ⁻ discharge) [68]	17
Figure 2-7: Variation of embrittlement index (using % reduction in area) with potential for X100 steel [90].....	21
Figure 2-8: (a) Hydrogen permeation curves of X65 specimens (600-grit finish) at -1200 mV with and without calcium carbonate coatings (b) Hydrogen permeation current vs. applied cathodic potential [93].....	23
Figure 2-9: SEM morphologies of the cross-section of X100 specimen and the chemical composition obtained at the individual inclusions (a) an Al-enriched inclusion; (b) a Si-enriched inclusion [108].....	25
Figure 2-10: Steady-state H amount released from an X100 steel specimen as a function of the charging current density, where the C_H^* needed to initiate HIC is identified [108]	26

Figure 2-11: (a) Planar cross-section of buried tank and anode system modelled in [125], with meshing of the soil media; (b) Potential distribution at surface of tank for different anode positions (circle: bottom of pit, square: at half depth, triangle: critical potential)	28
Figure 2-12: (a) Schematic view of a cross-section of the internal CP system investigated in [130], where r_a is the wire anode radius, r_c is the hollow cylinder (cathode) radius, and d is the offset distance from the central axis (b) Steady-state potential measured at 180° in (a) as a function of d in electrolytes of different conductivities (triangle: 1% NaCl, square: 0.6% NaCl, diamond: 0.3% NaCl, and star: 0.15% NaCl).....	30
Figure 2-13: Comparisons between experiments, the linear fit (i.e. {E-2.7}), and predictions from DNV and B31G codes [146]	33
Figure 2-14: (a) Experimental and FEM CIC defect profiles; (b) 3D simulation results for 60% wall thickness CIC defect model, showing spatially-dependent σ_{VM} from a 5.59 MPa internal pressure [53]	35
Figure 4-1: Microstructure of API X100 steel sample etched with: (a) 2% nital, with corresponding differentiation of ferrite and bainite phases according to ASTM E562-08; and (b) LePera solution; (c) graphical representation of M-A phase identification using ImageJ analysis software	40
Figure 4-2: Schematic of experimental setup for electrochemical tests of corrosion and passivation [162]	44
Figure 4-3: Electrochemical H permeation and diffusion cell: (a) components and assembly (b) measuring apparatus and settings (with two potentiostat instruments or two channels of one multistat) [154].....	48
Figure 4-4: (a) 3D representation of buried pipeline with CP anodes (right), and axis of model cross-section (left); (b) 2D representation of model geometry and dimensions.....	51
Figure 4-5: 2D cross-section of pipeline in longitudinal plane with coating defect (zoomed section), dimensions, and mesh of trapped water region.....	53
Figure 5-1: Effect of HCO_3^- , purging environment, and temperature on solution pH.....	55
Figure 5-2: Open circuit potentials vs. pH in all solutions free of Cl^- and/or SO_4^{2-} additions (varying HCO_3^- , purging gas, and temperature).....	56
Figure 5-3: Corrosion activity vs. pH based on polarization resistance values of select data.....	58
Figure 5-4: PDP in 5% CO_2 /95% N_2 purged NS4 + 10x HCO_3^- at 25, 40, and 55 °C (pH 7.6, 7.9, and 8.1, respectively).....	60
Figure 5-5: PDP profiles in 100% CO_2 purged NS4 + 10x HCO_3^- at 25, 40, and 55 °C (pH 6.4, 6.6, and 6.7, respectively).....	62

Figure 5-6: PDP in 5% CO ₂ /95% N ₂ purged NS4 + 10x HCO ₃ ⁻ at 25 °C with various Cl ⁻ and/or SO ₄ ²⁻ ion content (pH 7.6 for all)	63
Figure 5-7: 1 mV/s PDP profiles of specimen in NS4 Cl ⁻ - and SO ₄ ²⁻ -containing solutions with 7.19 < pH < 8.85.....	65
Figure 5-8: Current density peaks E_{p1} and E_{p2} plotted vs. pH for Cl ⁻ - and SO ₄ ²⁻ -containing solutions at 1 mV/s and 0.5 mV/s, and Cl ⁻ - and SO ₄ ²⁻ -free solutions at 1 mV/s	66
Figure 5-9: Passive current density i_p plotted vs. pH for Cl ⁻ - and SO ₄ ²⁻ -containing solutions at 1 mV/s and 0.5 mV/s, and Cl ⁻ - and SO ₄ ²⁻ -free solutions at 1 mV/s.....	69
Figure 5-10: Potential difference ΔE plotted vs. pH for Cl ⁻ - and SO ₄ ²⁻ -containing solutions at 1 mV/s and 0.5 mV/s, and Cl ⁻ - and SO ₄ ²⁻ -free solutions at 1 mV/s.....	70
Figure 5-11: Breakdown or transpassivation potentials E_{bd1} and E_{bd2} plotted vs. pH for Cl ⁻ - and SO ₄ ²⁻ -containing solutions at 1 mV/s and 0.5 mV/s, and Cl ⁻ - and SO ₄ ²⁻ -free solutions at 1 mV/s	71
Figure 5-12: (a) SEM image (x150 magnification) of FeCO ₃ -Fe ₃ O ₄ /γ-Fe ₂ O ₃ discrete boundary: (zoom) x700 magnification of Fe ₃ O ₄ growth over FeCO ₃ crystals; (b) XRD pattern of a specimen removed from a PDP scan in pH 8.36 solution (top profile), and control sample with no corrosion product (bottom profile)	73
Figure 5-13: EIS for NS4 solution at 25, 40, and 55 °C purged with 5% CO ₂ /95% N ₂ (pH 6.7, 6.8, and 7.0, respectively) or 100% CO ₂ (pH 5.4, 5.5, and 5.6, respectively): (a) Nyquist impedance representation, (b) proposed EEC for 100% CO ₂ results	76
Figure 5-14: Proposed EEC for 5% CO ₂ /95% N ₂ purged NS4 solution at 25, 40, and 55 °C (pH 6.7, 6.8, and 7.0, respectively) and 100% CO ₂ purged NS4 + 10x HCO ₃ ⁻ solution (pH 6.4, 6.6, and 6.7, respectively)	77
Figure 5-15: NS4 + 10x HCO ₃ ⁻ solution at 25 °C purged with 100% N ₂ (pH 8.9), and at 25, 40, and 55 °C purged with 100% CO ₂ (pH 6.4, 6.6, and 6.7, respectively), and 5% CO ₂ /95% N ₂ (pH 7.6, 7.9, and 8.1, respectively) (a) Nyquist impedance representation for all cases, (b) enlarged Nyquist impedance representation for 5% CO ₂ /95% N ₂ and 100% CO ₂ purged cases	79
Figure 5-16: Proposed EEC for 5% CO ₂ /95% N ₂ purged NS4 + 10x HCO ₃ ⁻ at 25, 40, and 55 °C (pH 7.6, 7.9, and 8.1, respectively), and 100% N ₂ purged NS4 + 10x HCO ₃ ⁻ solution at 25°C (pH 8.9).....	80
Figure 5-17: Nyquist impedance representation plots for NS4 + 10x HCO ₃ ⁻ solutions with added Cl ⁻ and/or SO ₄ ²⁻ at 25 °C, purged with 5% CO ₂ /95% N ₂ (pH 7.6)	81

Figure 6-1: Comparative PDP plot for 0.1 M $[\text{HCO}_3^-]$ solution with and without NS4 $\text{Cl}^-/\text{SO}_4^{2-}$ scanned at 0.5 mV/s or 1 mV/s, labelled for potential regions of step-wise anodizing-EIS routine	88
Figure 6-2: Schematic of the two independent electrochemical test routines conducted in this chapter	89
Figure 6-3: Nyquist impedance representation in active corrosion region ($\text{OCP} < E \leq E_{pl}$)	90
Figure 6-4: (a) Nyquist impedance representation in transition and passive layer formation region ($E_{pl} < E \leq 0 \text{ V}_{\text{SCE}}$); (b) Proposed physical occurrences for EIS at $-0.4 \text{ V}_{\text{SCE}}$ in solution without NS4 $\text{Cl}^-/\text{SO}_4^{2-}$	95
Figure 6-5: (a) Nyquist impedance representation in passive and transpassive region ($E > 0 \text{ V}_{\text{SCE}}$); (b) Proposed corresponding physical occurrences for EIS at $-0.25 \text{ V}_{\text{SCE}}$, $-0.1 \text{ V}_{\text{SCE}}$, $0.5 \text{ V}_{\text{SCE}}$ and $0.175 \text{ V}_{\text{SCE}}$	99
Figure 6-6: (a) Proposed EEC and corresponding physical occurrences for EIS at $-0.25 \text{ V}_{\text{SCE}}$, $-0.1 \text{ V}_{\text{SCE}}$, $0.5 \text{ V}_{\text{SCE}}$ and $0.175 \text{ V}_{\text{SCE}}$; (b) Proposed EEC for EIS at $1.1 \text{ V}_{\text{SCE}}$ in solution without $\text{Cl}^-/\text{SO}_4^{2-}$	100
Figure 6-7: Current density decay profiles of specimen anodized at $0.5 \text{ V}_{\text{SCE}}$ in 0.1, 0.25, or 0.5 M NaHCO_3 at 25, 50, or 75 °C (pH 7.8 – 9.3).....	103
Figure 6-8: Bode $ Z $ profiles of specimen after 1 h PSP in at $0.5 \text{ V}_{\text{SCE}}$ in 0.1, 0.25, or 0.5 M NaHCO_3 at 25, 50, or 75 °C (pH 7.8 – 9.3)	104
Figure 6-9: Dependence of N_{d1} , N_{d2} , and E_{fb} of passive layer on $[\text{NaHCO}_3]$ (0.1, 0.25, or 0.5 M) and temperature (25, 50, or 75 °C)	106
Figure 6-10: Dependence of (δ_{sc}) with respect to E , $[\text{NaHCO}_3]$ (0.1, 0.25, or 0.5 M), pH, and temperature (25, 50, or 75 °C).....	108
Figure 7-1: Final OCPs reached after 1 h and 24 h immersion (separate tests) as a function of $[\text{O}_2]$, with nonlinear fit profiles overlaid	115
Figure 7-2: Influence of N_2H_4 treatment concentration on 1 h OCP values at 25 and 50 °C.....	118
Figure 7-3: PDP in 0 ppm, 6 ppm, and 20 ppm O_2 solutions with 0.015 M added NO_3^-	120
Figure 7-4: PDP in (a) 6 ppm O_2 solutions with 0, 0.005, and 0.015 M added NO_3^- , and (b) 20 ppm O_2 solutions with 0, 0.005, and 0.015 M added NO_3^-	121
Figure 7-5: PDP profiles of aerated environments at 25 and 50 °C, treated with N_2H_4	124
Figure 7-6: SEM images of steel specimen surface following immersion in solution containing 6.0 ppm O_2 (pH 7.8) and 0.015 M NO_3^- : (left) low magnification; (top-right) as imaged high magnification with <u>50 μm scale bar</u> ; and (bottom-right) high magnification with <u>50 μm scale bar</u> analyzed by color threshold.....	128

Figure 7-7: SEM images of steel specimen surface following immersion in 21.2 ppm O ₂ (pH 8.9) and 0.015 M NO ₃ ⁻ : (left) low magnification; (top-right) as imaged high magnification with <u>50 μm scale bar</u> ; and (bottom-right) high magnification with <u>50 μm scale bar</u> analyzed by color threshold	129
Figure 7-8: Ex-situ XPS spectra of specimen immersed in 6 ppm and 20 ppm O ₂ solutions free of NO ₃ ⁻	130
Figure 7-9: Ex-situ Raman spectra of specimen immersed in 6 ppm and 20 ppm O ₂ solutions free of NO ₃ ⁻	131
Figure 7-10: SEM images and corresponding ex-situ XRD spectra of X100 specimen surface following 168 h immersion in environments periodically treated with N ₂ H ₄ as described in Table 7-3: (a), (b) 25 °C; (c), (d) 50 °C.....	133
Figure 7-11: Full spectrum OCP transients Table 7-1 conditions during 24 h (same legend as Figure 1-C)	135
Figure 7-12: Nyquist impedance representation and fit profiles for deaerated solution containing 0.005 M NO ₃ ⁻ (0.2 ppm O ₂ , pH 6.6): (a) at 2, 4, 6, 8, 10, and 12 h immersion times, with proposed EEC; (b) at 14, 16, 18, 20, 22, and 24 h immersion times.....	139
Figure 7-13: Nyquist impedance representation and fit profiles for 5.8 ppm O ₂ solution (pH 7.7) containing 0.005 M NO ₃ ⁻ : (a) at 2, 4, 6, 8, 10, and 12 h immersion times, with proposed EEC; (b) at 14, 16, 18, 20, 22, and 24 h immersion times.....	140
Figure 7-14: Nyquist impedance representation and fit profiles for 5.8 ppm O ₂ solution (pH 7.7) containing 0.005 M NO ₃ ⁻ : (a) at 2, 4, 6, 8, 10, and 12 h immersion times, with proposed EEC; (b) at 14, 16, 18, 20, 22, and 24 h immersion times.....	144
Figure 7-15: Diagram illustrating the influence of Δ[O ₂] between: (1) 6 ppm O ₂ and (2) 20 ppm O ₂ conditions on the evolution mechanism of the Fe-oxyhydroxide tubercle and sub-tubercle Fe-oxide layer(s), where \widetilde{d}_p represents the average pore size in the tubercle	145
Figure 7-16: Polarization resistance (R_p) vs. immersion time, calculated from periodic LPR scans conducted in: (a) deaerated and 6 ppm O ₂ solutions containing 0, 0.005, or 0.015 M NO ₃ ⁻ ; (b) 20 ppm O ₂ solutions containing 0, 0.005, or 0.015 M NO ₃ ⁻	148
Figure 8-1: Open circuit potential of X100 steel in different test solutions of Table D-1 at 20 °C	155
Figure 8-2: Cathodic behavior of X100 steel in: (a) deaerated (100% N ₂) NS4 and modified NS4 solutions at 20 °C; (b) open air NS4 and modified NS4 solutions at 20 °C.....	157

Figure 8-3: Cathodic behavior of X100 steel in: (a) NS4 solution under different gas atmospheres; (b) NS4 solution under different gas atmospheres during constant potential holds at -0.8, -0.9 and -1.0 V_{SCE} 158

Figure 8-4: Cathodic polarization curves of X100 steel in: (a) 100% CO_2 NS4 solution at 20, 40, and 60 °C, natural pHs; (b) NS4 solution with adjusted pH at 20 °C..... 159

Figure 8-5: Characterization of the deposit on X100 steel held at -1.2 V_{SCE} in 100% CO_2 NS4 solution: (a) SEM photo after 1 h; (b) EDX/EDS spectrum of a particle formed 161

Figure 8-6: Permeation results for X100 steel exposed to 100% CO_2 NS4 solution (20 °C) at a hydrogen charging current density of -500 $\mu A/cm^2$: (a) permeation current transient; (b) determination of D_{eff} of the X100 steel from permeation current transient using {E-8.1}, where the slope of the $\log((i_{perm}-i_{bg}) \times t^{0.5})$ vs. $1/t$ plot is obtained by linear fitting..... 162

Figure 8-7: The current response in the H entry and exit sides (cathodic i_{charge} and anodic i_{perm} , respectively) during the permeation experiment in NS4 solution. The purging gas in the charging compartment is switched from 100% N_2 to 5% CO_2 to 100% CO_2 164

Figure 8-8: The current response at the H entry and exit sides during the permeation experiment in 100% CO_2 NS4 solution at 20 °C. The surface potential of the steel sample at the entry side is first switched from -0.85 to -1.15 V_{SCE} with 100 mV/step/4 h then is left at unpolarized (i.e. OCP) before the solution in the entry compartment is drained out to leave the sample open to air 165

Figure 8-9: Speciation diagram of the CO_2 - H_2O system calculated at 25 °C using Medusa software 167

Figure 8-10: Concentration of dissolved CO_2 and carbonate species in solution with respect to pH, with $pCO_2 = 1$ atm at: (a) 20 °C; (b) 40 °C; and (c) 60 °C..... 169

Figure 8-11: OCP of X100 steel in NS4 and modified NS4 solutions under different purging gas atmospheres at 20 °C 171

Figure 8-12: Cathodic polarization curves of scale-covered X100 steel in NS4 solution at 20 °C 174

Figure 9-1: Pipeline wall and initial (ambient) soil temperature fluctuations with respect to soil structure, depth, and time in m-model..... 184

Figure 9-2: (a) PDP profiles of X100 steel sample in deaerated and aerated NS4 solutions at 30 and 50 °C; (b) cathodic regime of PDP profiles (with regression fits) showing E - and temperature-dependent O_2 reduction and H evolution kinetics; and (c) LPR fitting results for X100 specimen immersed in NS4 with combinations of deaeration, aeration, and temperature 191

Figure 9-3: Contours of: (a) induced soil temperature [K (°C)] for peat with $\psi = 0.60$ at hottest conditions; (b) ϕ [V _{SCE}] for sand with $\psi = 0.60$ at hottest induced temperatures; and (c) CO ₂ [mol/m ³] for clay with $\psi = 0.20$ at hottest induced temperatures	198
Figure 9-4: E_{Fe} evaluated at $\theta = 0^\circ$ and $\theta = 90^\circ$ in minimum and maximum induced temperature profiles, different soil structures, and ψ using: (a) uncoupled governing equations; and (b) coupled governing equations	200
Figure 9-5: i_{Fe} evaluated at $\theta = 0^\circ$ and $\theta = 90^\circ$ in minimum and maximum induced temperature profiles, different soil structures, and ψ using: (a) uncoupled governing equations; and (b) coupled governing equations	202
Figure 9-6: (a) i_{O_2} and (b) i_{H_2} , evaluated at $\theta = 0^\circ$ and $\theta = 90^\circ$ in minimum and maximum induced temperature profiles, different soil structures, and ψ using coupled governing equations	205
Figure 9-7: Influence of CP design parameters on the model results for simulations at $T_{wall} = 323$ K, $\theta = 0^\circ$, and $\psi = 0.2$ or 0.3 : (a) E_{Fe} and i_{Fe} as a function of CP anode distance from exposed pipeline surface; and (b) i_{O_2} and i_{H_2} as a function of E_{app}	208
Figure 9-8: Timeline of corrosion defect growth into the exposed steel surface and ϕ evolution throughout the 150 week exposure, for $E_{app} = -1$ V _{SCE} , 1 mm coating disbondment opening, and $T_{wall} = 25$ °C	209
Figure 9-9: Length of corrosion defect (l_{defect}) [mm] along exposed steel surface and x -position of d_{defect_max} (maximum defect depth) [mm] reached during 0 – 150 weeks of exposure, for all E_{app} , coating disbondment opening, and T_{wall} values simulated: (a) $T_{wall} = 25$ °C, (b) $T_{wall} = 50$ °C	211
Figure 9-10: Maximum depth [mm] of corrosion defect (d_{defect_max}) below original steel surface from 0 – 150 weeks of exposure, for all E_{app} , coating disbondment opening, and T_{wall} values simulated: (a) $T_{wall} = 25$ °C, (b) $T_{wall} = 50$ °C	213
Figure 9-11: 3D representation of: (a) intact pipe FEM with shell elements; (b) corroded pipe section used to simulate structural integrity based on the defect dimensions resulting from the corrosion module	215
Figure 9-12: Convergence profiles for i_{O_2} and i_{H_2} results (at $T_{wall} = 323$ K, $\theta = 0^\circ$, and $\psi = 0.2$ or 0.3) using extra coarse to extra fine mesh resolutions in m-model	218
Figure A-1: PDP in 5% CO ₂ /95% N ₂ purged NS4 at 25, 40, and 55 °C (pH 6.7, 6.8, and 7.0, respectively)	253
Figure A-2: 100% CO ₂ purged NS4 at 25, 40, and 55 °C (pH 5.4, 5.5, and 5.6, respectively)..	253
Figure A-3: NS4 at 25 °C with 5% CO ₂ /95% N ₂ , 100% CO ₂ , and 100% N ₂ purging gas (pH 6.7, 5.4, and 8.9, respectively).....	254

Figure A-4: 5% CO ₂ /95% N ₂ purged NS4 at 25 °C with various Cl ⁻ and/or SO ₄ ²⁻ ion concentrations (pH 6.7)	254
Figure A-5: (top-left) E–pH diagram for Fe in water; (top-right) Simplified E–pH diagram for Fe in water indicating the domains of immunity, corrosion, and passivity, including the experimental passivation potential as a central dashed line; (bottom) E–pH diagram of Fe in water with the presence of chlorides, where GR1(Cl ⁻) is chloride green rust ([Fe ²⁺ ₃ Fe ³⁺ (HO ⁻) ₈] ⁺ · [Cl ⁻ · nH ₂ O] ⁻) [308].....	255
Figure A-6: E–pH diagram for the Fe–HCO ₃ ⁻ –CO ₃ ²⁻ –H ₂ O system at around 50 °C, where GR1 is carbonate green rust ([Fe ²⁺ ₄ Fe ³⁺ ₂ (HO ⁻) ₁₂] ²⁺ · [CO ₃ ²⁻ · 2H ₂ O] ²⁻) [186]	256
Figure A-7: Bode θ _{EIS} for NS4 solution at 25, 40, and 55 °C purged with 5% CO ₂ /95% N ₂ (pH 6.7, 6.8, and 7.0, respectively) or 100% CO ₂ (pH 5.4, 5.5, and 5.6, respectively).....	256
Figure A-8: Bode Z for NS4 solution at 25, 40, and 55 °C purged with 5% CO ₂ /95% N ₂ (pH 6.7, 6.8, and 7.0, respectively) or 100% CO ₂ (pH 5.4, 5.5, and 5.6, respectively).....	257
Figure A-9: Bode Z for NS4 + 10x HCO ₃ ⁻ solution at 25 °C purged with 100% N ₂ (pH 8.9), and at 25, 40, and 55 °C purged with 100% CO ₂ (pH 6.4, 6.6, and 6.7, respectively), and 5% CO ₂ /95% N ₂ (pH 7.6, 7.9, and 8.1, respectively)	257
Figure A-10: Enlarged Bode Z for NS4 + 10x HCO ₃ ⁻ solution at 25, 40, and 55 °C purged with 100% CO ₂ (pH 6.4, 6.6, and 6.7, respectively), and 5% CO ₂ /95% N ₂ (pH 7.6, 7.9, and 8.1, respectively)	258
Figure A-11: Bode θ _{EIS} for NS4 + 10x HCO ₃ ⁻ solution at 25 °C purged with 100% N ₂ (pH 8.9), and at 25, 40, and 55 °C purged with 100% CO ₂ (pH 6.4, 6.6, and 6.7, respectively), and 5% CO ₂ /95% N ₂ (pH 7.6, 7.9, and 8.1, respectively)	258
Figure A-12: Bode Z and θ _{EIS} plots for NS4 + 10x HCO ₃ ⁻ solutions with added Cl ⁻ and/or SO ₄ ²⁻ at 25 °C, purged with 5% CO ₂ /95% N ₂ (pH 7.6).....	259
Figure B-1: Solution [NaHCO ₃], pH, and temperature relationships of test conditions in chapter 6	260
Figure B-2: Z vs. frequency in the E > 0 V _{SCE} region (see Figure 6-5a for legend of star data points).....	260
Figure B-3: Mott-Schottky plots at 1 kHz between -0.5 V _{SCE} and 1 V _{SCE} after 1 h of anodizing in 0.5 M NaHCO ₃ at 25, 50, and 75 °C (pH 8.5, 8.9, and 9.3, respectively)	261
Figure B-4: Mott-Schottky plots at 1 kHz between -0.5 V _{SCE} and 1 V _{SCE} after 1 h of anodizing in 0.1, 0.25, or 0.5 M NaHCO ₃ at 75 °C (pH 8.8, 9.2, and 9.3, respectively).....	261
Figure C-1: Full spectrum OCP profiles showing stability approaching 1 h, in all conditions of Table 7-1.....	262

Figure C-2: OCP transients approaching 1 h of immersion in all test environments of Table 7-2	263
Figure C-3: PDP in 0 ppm, 6 ppm, and 20 ppm O ₂ in NO ₃ ⁻ -free solutions	264
Figure C-4: PDP in 0 ppm, 6 ppm, and 20 ppm O ₂ solutions with 0.005 M added NO ₃ ⁻	264
Figure C-5: SEM images of steel specimen surface following immersion in NS4 solution deaerated with 5% CO ₂ /95% N ₂ and containing 0.015 M NO ₃ ⁻ (0.1 ppm O ₂ , pH 6.7)	265
Figure C-6: Different corrosion product formations and steel substrate at the edge of the tubercle formed in solution containing 6.0 ppm O ₂ (pH 7.8) and 0.015 M NO ₃ ⁻	265
Figure C-7: Ex-situ XRD spectra of specimen immersed in 6 ppm and 20 ppm O ₂ solutions free of NO ₃ ⁻	266
Figure D-1: Cathodic polarization curves of X100 steel in 100% CO ₂ NS4 and modified NS4 solutions at 20 °C	269
Figure D-2: Cathodic polarization curves of X100 steel in: (a) 100% CO ₂ NaHCO ₃ -added NS4 solution at 20, 40, and 60 °C, natural pHs; (b) NaHCO ₃ -added NS4 solution with adjusted pH at 20 °C	270
Figure E-1 (for mm-model): Polarization profiles of X100 specimen immersed in different temperature and %CO ₂ environments, obtained through electrochemical corrosion experiments: (a) LPR fitting results at $E < OCP$; (b) cathodic regime of PDP results, with regression fits; and (c) anodic regime of PDP results.....	274
Figure E-2 (for m-model): C_{O_2} evaluated at $\theta = 0^\circ$ and $\theta = 90^\circ$ in minimum and maximum induced temperature profiles, different soil structures, and ψ using: (a) uncoupled governing equations; and (b) coupled governing equations	275
Figure E-3 (for mm-model): Convergence profiles of interfacial surface-electrolyte potential parameter (E_s) averaged over full length of exposed steel surface ($E_{s_average}$), for coarse, normal, and fine mesh resolutions	277

List of Abbreviations

2D	Two-dimension(al)
3D	Three-dimension(al)
API	American Petroleum Institute
appm	Atomic parts per million
ASME	American Society of Mechanical Engineers
BISO	Bilinear Isotropic Hardening
CE	Carbon Equivalent
CIC	Crack-in-Corrosion
CP	Cathodic Protection
CPE	Constant phase element
DNV	Det Norske Veritas
EDX/EDS	Energy-dispersive X-ray Spectroscopy
EEC	Electrochemical equivalent circuit
EIS	Electrochemical Impedance Spectroscopy
FEM	Finite Element Model(ling)/Method
HE	Hydrogen embrittlement
HER	Hydrogen evolution reactions
HIC	Hydrogen induced cracking
HSLA	High-strength low-alloy
ICP-MS	Inductively Coupled Plasma Mass Spectrometry
LPR	Linear Polarization Resistance
MA	Martensite-retained austenite
mm-model	Millimeter-scaled model
m-model	Meter-scaled model
mmpy	Millimeters per year
mpy	Milli-inches per year
NACE	National Association of Corrosion Engineers
nn-pH	Near-neutral pH
OCP	Open circuit potential
PCIM	Pipeline Corrosion Integrity Management
PDP	Potentiodynamic Polarization
PHMSA	Pipeline and Hazardous Materials Safety Administration
PSP	Potentiostatic Polarization
ppb	Parts per billion
ppm	Parts per million
SCC	Stress corrosion cracking
SCE	Saturated calomel electrode
SEM	Scanning Electron Microscope/Microscopy

SHE	Standard hydrogen electrode
SVET	Scanning Vibrating Electrode Technique
TDS	Total dissolved solids
US	United States
USD	United States Dollars
XPS	X-ray Photoelectron Spectroscopy
XRD	X-ray Diffraction

List of Chemical Formulae

Ag	Silver
Al	Aluminum
Ar	Argon
C	Carbon
C ₂ H ₆ O	Ethanol
C ₃ H ₆ O	Acetone
C ₆ H ₃ N ₃ O ₇	Picric Acid
Ca	Calcium
CaCl ₂	Calcium chloride, anhydrous
Cl ⁻	Chloride
CO ₂	Carbon dioxide
CO ₃ ²⁻	Carbonate
Cu/CuSO ₄	Copper/Copper-Sulfate
Fe(OH) ₂	Iron (II) hydroxide
Fe ²⁺	Ferrous
Fe ³⁺	Ferric
FeCO ₃	Iron (II) carbonate (siderite)
H	Elemental hydrogen
H ⁺	Hydrogen ion (proton)
H ₂	Diatomic hydrogen, gas
H ₂ CO ₃	Carbonic acid
HCO ₃ ⁻	Bicarbonate
HNO ₃	Nitric acid
KNO ₃	Potassium nitrate
Mg	Magnesium
MgSO ₄	Magnesium sulfate
MnS	Manganese sulfide
Na ₂ S ₂ O ₅	Sodium metabisulfite
Na ₂ SO ₄	Sodium sulfate
NaCl	Sodium chloride
NaHCO ₃	Sodium bicarbonate
NaOH	Sodium hydroxide
NO ₃ ⁻	Nitrate
N ₂	Diatomic nitrogen, gas
O	Elemental oxygen

O_2	Diatomic oxygen, gas
O^{2-}	Oxide
OH^-	Hydroxide
Pd	Palladium
S	Sulfur
S^{2-}	Sulfide
Si	Silicon
SiC	Silicon carbide
SO_4^{2-}	Sulfate

List of Symbols

a_m	Monolayer capacity
A_w	Atomic weight
C	Capacitance (general)
C_a	Adsorption capacitance (equivalent from corresponding CPE)
C_{ads}	Concentration of the adsorbed electroactive species/compound
C_{dl}	Double layer capacitance (equivalent from corresponding CPE)
C_{H^*}	Critical H concentration
$C_{H\sigma,T}$	Hydrogen concentration at a crack tip
C_{O_2}	Effective O ₂ diffusivity in soil
C_s	Subsurface H concentration at entry side of permeation specimen
C_{sc}	Space-charge layer capacitance
C_v	Volumetric heat capacity
D	Pipeline diameter in FEM
d_{defect}	Depth of corrosion defect in FEM
d_{defect_max}	Maximum corrosion defect depth in FEM
D_{eff}	Effective H diffusivity
D_{O_2}	Soil O ₂ concentration
E	Electrochemical potential of steel electrode
e^-	Electron charge (1.60×10^{-19} C)
E_{anode}	Equilibrium potential of the anode-soil half-cell in FEM
E_{app}	Applied voltage between pipeline and anode in FEM
E_{bd1}	First potential of sustained layer breakdown or transpassivation
E_{bd2}	Second potential of sustained layer breakdown or transpassivation
E_{bulk}	Trapped water electrolyte potential in bulk solution outside disbondment
E_c	Critical potential in C_{sc} vs. E plots
E_{co}	Potential of new anodic-cathodic reaction couple
E_{corr}	Corrosion potential
E_{eq}	Electrochemical equilibrium (reversible) potential
E_{fb}	Flat band potential

E_{Fe}	Potential difference at pipeline-soil interface in FEM
E_o	Overlap potential of two or more polarization curves
E_{p1}	First potential of sustained current density decrease
E_{p2}	Second potential of sustained current density decrease
$E_s(x)$	Potential difference at electrode-trapped water interface in FEM
E_{trans}	Transition potential
E_w	Withdrawal potential
h	Hour
i	Current density, general
I	Current, general
i_a	Net anodic current density
i_{bg}	Background permeation current density
i_c	Net cathodic current density
i_{charge}	Charging current density for hydrogen permeation
I_{corr}	Corrosion current
i_{corr}	Corrosion current density
i_{lim}	Limiting current density
i_{max}	Maximum current density (at/in a specific potential level/range)
in	Inch
i_{O2}	O ₂ reduction current density
i_p	Passive current density (lowest value if changing with potential)
i_{perm}	Permeation current density
i_{ss}	H permeation current density at steady state
$i_{th,CP}$	CP current density threshold (for HIC)
i_{total}	Total net current density in FEM simulations ($i_a - i_c$)
j	Imaginary number ($\sqrt{-1}$)
K	Boltzmann constant ($1.38 \times 10^{-23} \text{ m}^2 \text{ kg s}^{-2} \text{ K}^{-1}$)
K_{eq}^i	Adsorbate equilibrium constant
k_{IG}	Intrinsic Griffin toughness
km	Kilometers
ksi	Kilopound per square inch

K_{sp}	Solubility product
K_{th}	Threshold stress intensity factor
L	Coating disbondment length in FEM, or specimen thickness in H diffusion
l_{defect}	Length of corrosion defect in FEM
m	Meter
M	Molar concentration
mm	Millimeter
MPa	megapascal
mV	millivolts
n	Number of electrons in a reaction, or charge of an ion
n_a	Charge on dissolved cation from anodic oxidation (typically 2 for Fe)
N_d	Donor density of n-type semiconductors
n_i	Common valence of a specific element “i”
n_m	Surface phase capacity
Pa	Pascal
Q	Heat flux density
Q_a	Constant phase adsorption element
Q_{dl}	Constant phase double layer element
Q_f	Constant phase film element
Q_l	Charge flux
R	Gas constant
R_a	Adsorption resistance
R_{ct}	Charge transfer resistance
R_f	Film resistance
R_{O_2}	O ₂ depletion flux
R_p	Polarization resistance
R_p^*	Sums of EIS resistance component values
R_p^{**}	Sums of EIS resistance and diffusion component values ($R_p^* + W$)
R_{pore}	Pore resistance
R_{steel}	Penetration rate in the exposed steel in FEM
T	Temperature, general

t	Time (general), or pipeline wall thickness in FEM
t_b	Breakthrough time
t_{lag}	Time H permeation current reaches 63% of i_{ss}
T_{wall}	Pipeline wall temperature in FEM
V_H	Molar volume of hydrogen in steel
w	Coating disbondment width in FEM
W	Width of modelled soil section in FEM
W_A	Warburg constant
wt%	Percent mass fraction (aka weight %)
x_i^l	Molar fraction of adsorbate i ($\sum_{i=1}^k x_i^l = 1$)
Z	Impedance, general
Z_{CPE}	CPE impedance
Z_{im} of Z''	Impedance, imaginary component
Z_{re} of Z'	Impedance, real component
$ Z $	Impedance magnitude
α_{ads}	Adsorption constant in Hill-Langmuir isotherm
δ_{sc}	Thickness of space charge layer
Δ	Change or range in any specific parameter denoted in suffix (e.g. ΔO_2)
ε	Dielectric constant
ε_0	Permittivity of free space (8.85×10^{-12} F/m)
θ	Fractional coverage of adsorbate during adsorption, or pipeline circumferential angle (from 9 o'clock position) in FEM
θ_{ads}	Fractional coverage of the adsorbent surface
θ_{EIS}	Phase angle in EIS
λ	Thermal conductivity
ρ	Density, general
ρ_{Fe}	Density of Fe
σ	Electrical conductivity, general
σ_H	Crack-tip hydrostatic stress
σ_U	Ultimate tensile strength

σ_y	Yield stress (at an offset strain of 0.5%)
ν_{O_2}	Stoichiometric coefficient of O_2 in reduction reaction
ϕ	Soil potential in modelling studies
ϕ	Air porosity ratio in soil
ψ	Soil volumetric wetness
ω	Frequency of alternating current

Acknowledgements

First and foremost, I wish to sincerely thank my supervisor and mentor, Professor Akram Alfantazi, for his instrumental role in the completion of this work. It has truly been a privilege to work under his supervision and guidance. I appreciate his patience, generous financial support, wise judgement, and continual encouragement throughout my doctoral program.

Funding for the research presented in this thesis has mainly been provided through NPRP Grant 6-027-2-010 from the Qatar National Research Fund (a member of Qatar Foundation). Parts of this work have been conducted during an Erasmus Mundus exchange funded by the European Commission. These financial supports have been very beneficial and are greatly appreciated.

Special gratitude goes to all my colleagues in the Corrosion Group at UBC for their valuable friendship, scientific input, and positive influence, in particular: Hung Ha, Ibrahim Abushwashi, Masyam Mohammadi, Lokesh Choudhary, Wei Wang, Hamid Zebardast, Faysal Eliyan, Jing Liu, Michael Mahon, Marie Licausi, Victor Padilla, Shabnam Pournazari, and Davood Nakhaie. I also thank the members of the Materials Engineering staff at UBC for their help and patience during this work, in particular: Jacob Kabel, Michelle Tierney, Fiona Webster, Glenn Smith, Ross McLeod, and Mary Jansepar. I also sincerely appreciate the assistance of Hatim Jefri during the summer of 2014 through his Mitacs Globalink exchange from KSA. Special gratitude and thanks go to Professor Magd AbdelWahab for his supervision and guidance during my 6 month exchange at Ghent University in Belgium.

No words can describe how grateful I feel for the love and backing of all my family members. I am greatly indebted to them all, from my mother Omnia for her unconditional love and concern, my father, Professor Mohamed Gadala, for his wise advice and encouragement, to my beautiful sisters Marwa and Mariam for their affection, even when living abroad. I only wish I am as good a son and brother as they are parents and sisters.

لِعَائِلَتِي الْمُحِبَّةِ
To my loving family

1. Introduction

Pipelines are the most preferred method of transporting large volumes of crude oil, natural gas, and petroleum products over long distances. Compared to alternative methods of transportation such as by road or rail, pipelines are the safest and most efficient [1]. Yet, pipelines still suffer hundreds of ruptures and spills every year. Government estimates claim that large petroleum pipelines will experience a spill every 16 years for every 1000 km [2]. Based on the vast lengths of pipeline infrastructure currently in operation nationally and internationally, with over 100,000 km in Canada alone [3], this statistic is a serious concern for governments, operating companies, adjacent human communities, and regional ecosystems. Hence, ensuring the safety and integrity of pipelines in service and designing reliable future pipelines is undoubtedly of great importance to governments, energy companies, the general public, and the environment.

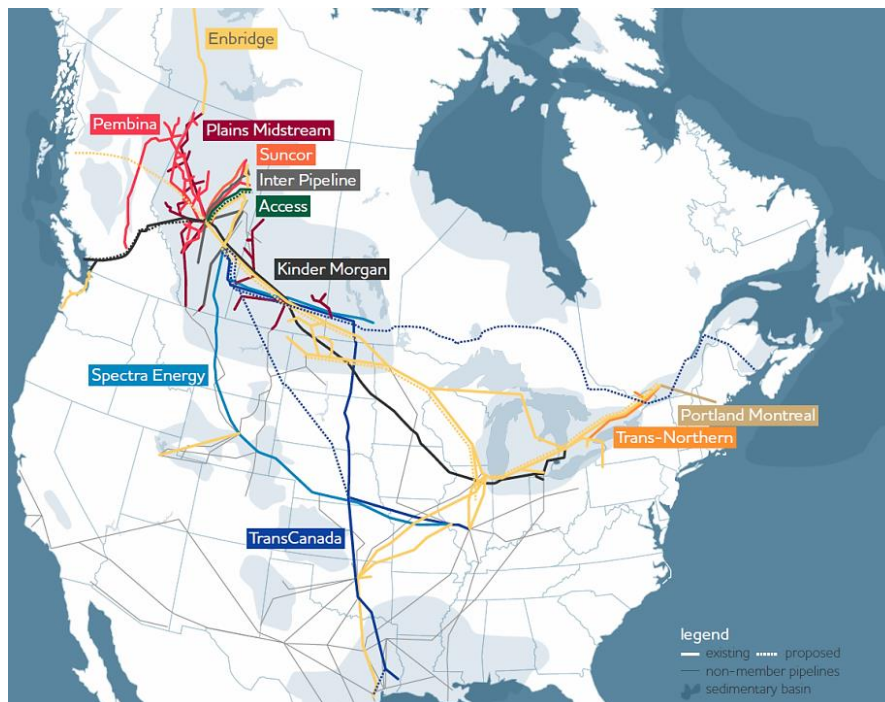


Figure 1-1: North American network of major liquid transmission pipelines [1]

1.1 Impact of pipeline corrosion

Of the many causes and contributors to pipeline failures, corrosion ranks as the most important. Statistics by the US Department of Transportation's Pipeline and Hazardous Materials Safety Administration [4] reveal that pipeline corrosion is, on average, the second leading cause of pipeline failure incidents. As seen in Table 1-1, in terms of the total damage caused by any single contributor to transmission pipeline failure, corrosion often takes the lead over other factors such as natural force damage, equipment failure, or excavation damage. Corrosion of pipelines therefore has a direct and strong effect on their life. Since corrosion is influenced by many different factors, the life of a pipeline is correspondingly a function of these factors, such as quality of construction, coatings, cathodic protection (CP) systems, nature of the transported product, physicochemical properties of the external environment, operating conditions, and maintenance methods.

Table 1-1: Natural gas transmission pipeline incident summary by cause for 1/1/2002 - 12/31/2003, from US Department of Transportation's Office of Pipeline Safety [4]

Reported Cause	Number of Incidents	% of Total Incidents	Property Damages	% of Total Damages	Fatalities	Injuries
Excavation Damage	32	17.8	\$4,583,379	6.9	2	3
Natural Force Damage	12	6.7	\$8,278,011	12.5	0	0
Other Outside Force Damage	16	8.9	\$4,688,717	7.1	0	3
Corrosion	46	25.6	\$24,273,051	36.6	0	0
Equipment	12	6.7	\$5,337,364	8.0	0	5
Materials	36	20.0	\$12,130,558	18.3	0	0
Operation	6	3.3	\$2,286,455	3.4	0	2
Other	20	11.1	\$4,773,647	7.2	0	0
Total	180		\$66,351,182		2	13

Pipeline corrosion and subsequent failure have an economic and environmental impact which can hardly be understated. Since the start of the 1990s, concerns regarding the threat of corrosion to pipeline integrity have been high due to the significant economic losses and undesirable environmental damage associated with pipeline failures. Historically, corrosion has been identified as a major cause of reportable pipeline incidents in North America [5] and the

main culprit behind a significant pipeline failure in the Gulf of Mexico costing \$1 billion (USD) [6]. Internal corrosion along the complete length of pipelines regularly results in costly maintenance programs. The corrosion-related cost to the transmission pipeline industry is approximately \$5.4 to \$8.6 billion annually, 52% of which is geared towards maintenance programs [4]. This is a large financial burden on pipeline operators and is sought to be minimized as much as possible through research and development.

1.2 Importance for Canada

Canadian companies in the pipeline industry such as TransCanada Ltd. and Enbridge Inc. are actively pursuing contracts for future pipeline projects. They strive to offer the best safety and integrity for these projects to reduce costs, protect the environment, and eliminate any human injury or loss of life associated with a failure. They are also keen on developing more efficient and reliable processes and methods for operating and maintaining their existing pipeline infrastructure. Based on the aforementioned historical data and statistics, advancements in the understanding of pipeline corrosion through research and the development of superior corrosion control methods are two sensible means of achieving these goals. Furthermore, scientific research and technological advancements enhancing pipeline safety can contribute greatly in building public confidence regarding the subject of oil and natural gas transportation. The opinion and confidence of the general public regarding the safety of oil and gas transportation is critical for the support and approval of associated projects. For the abovementioned reasons, research on pipeline corrosion is of paramount importance for oil and gas companies in general, and Canadian pipeline companies in specific.

1.3 High-Strength Low-Alloy steels

High-strength low-alloy (HSLA) steels are extensively utilized in pipeline construction for their desirable strength-to-weight ratios, a benefit which comes at only a modest price premium vs. conventional low-carbon steels [7]. The development of HSLA pipeline steels was

led by advancements in steel rolling processes, where thermo-mechanical (TM) rolling replaced hot rolling and normalizing as shown in Figure 1-2 [8]. Further enhancement of the overall process consisted of an accelerated cooling (AC) step succeeding the TM rolling, making it possible to produce the X80 grade under the American Petroleum Institute (API) classification according to minimum yield strength (80 ksi or 550 MPa).

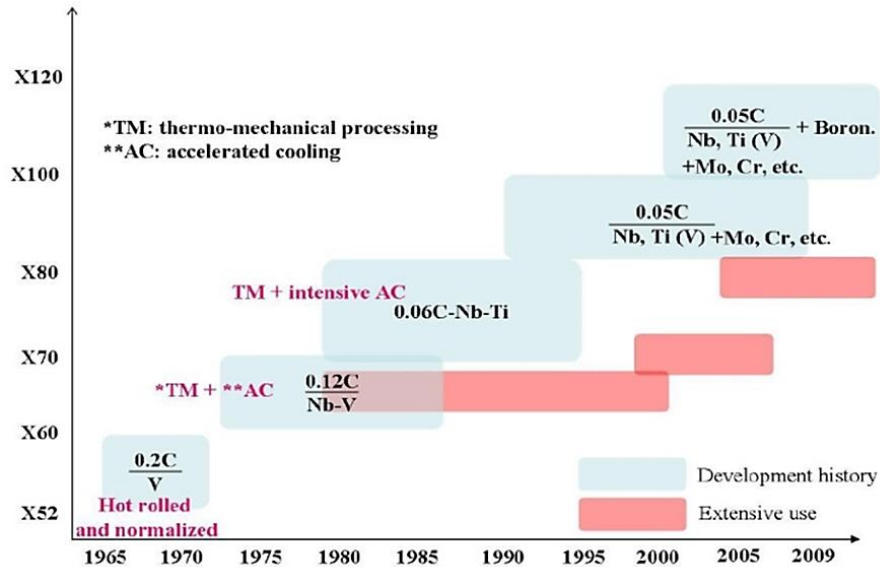


Figure 1-2: Development flow chart of HSLA pipeline steels from 1965 to 2009 [8]

Today, much of the existing global pipeline infrastructure uses API X70 (483 MPa) and API X80 steel grades. More recently, micro-alloying with molybdenum, copper, and nickel has further increased alloy strength. The resulting API X100 (690 MPa) steel grade has garnered great interest from industry, due to the economic benefits it offers in terms of lower material, transportation, and fabrication costs [9]. Successful installation of the highest grade pipeline steel available in the world today (API X120, 825 MPa) was recently achieved for the first time by TransCanada Ltd., and research on various performance aspects of this steel is currently ongoing [10], [11]. Higher strength steel grades directly improve cost efficiency by withstanding higher operating pressures and greater design throughputs without the need for increasing pipe wall thickness. However, susceptibility of steel to cracking often increases with strength, due to the

corresponding reduction in ductility and toughness. The extent of this adverse reciprocal relationship must be further understood and minimized to avoid failures of HSLA pipelines in service [12].

1.4 Environments causing external SCC

Stress corrosion cracking (SCC) is the cracking induced from the combined influence of tensile stress and a corrosive environment on a susceptible material. In SCC, cracks penetrate into the susceptible material while most of the remaining surface stays intact. SCC is therefore classified as a catastrophic form of corrosion, since the detection of these cracks can be very challenging and, even when detected, the extent of their damage on the structure is not easily foreseen. The tensile stress required for SCC may be in the form of the applied stress listed in Figure 1-3, or residual stress introduced from fabrication processes like welding and heat treatment.

The second SCC requirement, a corrosive environment, depends on the location of interest within the pipeline system. On the pipeline's internal surface, the corrosive environment is the internal media determined by product being transported and its physical/operational conditions such as viscosity and flow rate. This environment is always contact with the susceptible pipeline steel alloy, since internal surfaces are rarely coated. Externally, the corrosive environment for underground pipelines is the surrounding soil, which comes into contact with the susceptible material only at holidays and disbondments in the external coating. Samples of the environment gathered near locations where external SCC occurred on buried pipelines reveal that a carbonate (CO_3^{2-}) – bicarbonate (HCO_3^-) electrolyte is responsible for the chemical degradation of the steel. Properties of this potent environment such as temperature, pH, and dissolved CO_2 content significantly influence the resulting corrosion and SCC crack morphologies, as shown in Table 1-2. The third SCC requirement, a susceptible material, varies with properties such as composition, amount and size of inclusions, microstructure, and surface state. Even within the

narrow spectrum of HSLA pipeline steels (X70 – X120) researched in pipeline corrosion studies, there exists critical differences in material microstructure and inclusion content which change the corrosion behavior (see literature review of chapter 2).

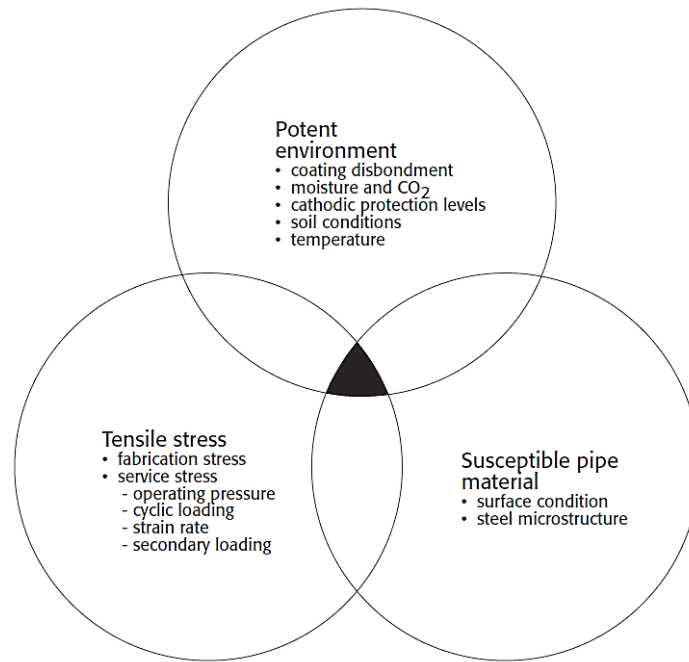


Figure 1-3: Three conditions necessary for pipeline SCC, with corresponding dependencies [13]

Table 1-2: Characteristics of nn-pH and high pH external SCC in pipelines – adapted from [13]–[15]

Factor	External SCC form	
	Near-neutral pH	High pH
Associated electrolyte	pH ~ 5 – 8.5 Dilute HCO ₃ ⁻ solution	pH > 9.3 Concentrated CO ₃ ²⁻ –HCO ₃ ⁻ solution
Location	<ul style="list-style-type: none"> • 65% between compressor station and 1st downstream block valve • 12% between 1st & 2nd valves • 5% between 2nd & 3rd valves • 18% downstream of third valve 	<ul style="list-style-type: none"> • Typically within 20 km downstream of compressor station • Number of failures falls markedly with increased distance from compressor and lower pipe temperature
Temperature	<ul style="list-style-type: none"> • No apparent correlation with temperature of pipe • Appear to occur in the colder climates where [CO₂] in groundwater is higher 	<ul style="list-style-type: none"> • Growth rate decreases exponentially with temperature decrease
Electrochemical potential	<ul style="list-style-type: none"> • At free corrosion potential • Cathodic protection largely ineffective at SCC sites 	<ul style="list-style-type: none"> • -600 to -750 mV (Cu/CuSO₄) • Cathodic protection is effective to achieve these potentials
Crack path and morphology	<ul style="list-style-type: none"> • Primarily transgranular (across the steel grains) • Wide cracks with evidence of substantial corrosion of crack side wall 	<ul style="list-style-type: none"> • Primarily intergranular (between the steel grains) • Narrow, tight cracks with no evidence of secondary corrosion of the crack wall

Two types of external SCC have been discovered on pipelines: near-neutral pH (nn-pH) SCC in the 5 – 8 range and high pH SCC in the 9 – 13 range. High pH is the classical form of SCC, occurring with effective CP in the -600 to -750 mV Cu/CuSO₄ range and the presence of a concentrated CO₃²⁻-HCO₃⁻ environment. The resulting cracking morphology is intergranular (IG), with decreasing growth rate at lower temperatures. High pH external SCC has been researched extensively [16]–[18]. There is general agreement regarding the mechanisms and controlling factors of this form of SCC, namely, anodic dissolution at grain boundaries and repeated rupture of passive films that form over the crack-tip. On the other hand, understanding of nn-pH SCC is more limited. In fact, to date, there is no precise mechanism identified to understand nn-pH SCC crack initiation and no predictive model developed to define the rate of crack growth [15], [19]. That being said, there is a considerable amount of evidence that anodic dissolution and hydrogen embrittlement play critical roles in the nn-pH SCC mechanism [20]–[23].

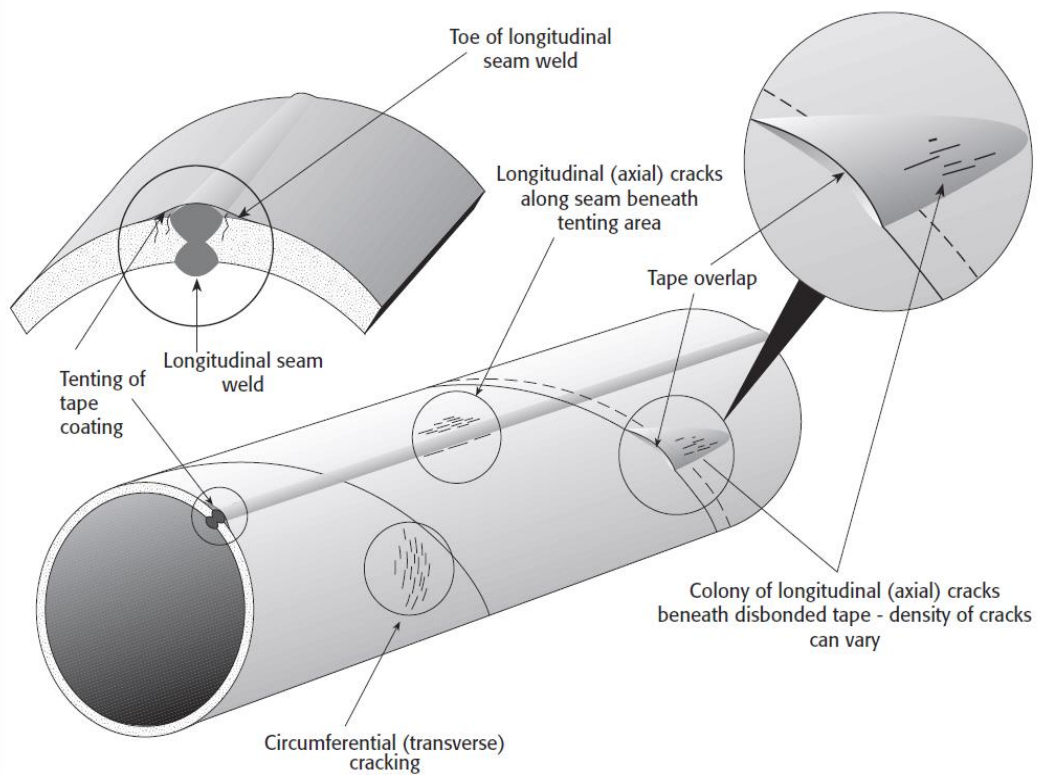


Figure 1-4: Areas of near-neutral pH SCC formation on external pipeline surfaces [13]

Near-neutral pH SCC was initially discovered in Canada in the mid-1980s, and occurs in a dilute 10^{-3} M HCO_3^- electrolyte containing dissolved CO_2 and other groundwater anions like chloride (Cl^-) and sulfate (SO_4^{2-}) [24]. This electrolyte has a low electrical conductivity, on the order of $1000 \mu\text{S}/\text{cm}$, and is typically found in the regions under disbonded coatings shown in Figure 1-4 [25]. The disbonded coating partially shields the CP from reaching exposed locations deep within these disbondments. Combined with the low conductivity of the electrolyte underneath, CP levels at these locations are insufficient, if not completely absent [26], [27]. The resulting cracking morphology from nn-pH SCC is transgranular, as revealed by the quasi-cleavage morphology, little branching, and significant lateral corrosion resulting in the destruction of the original crack faces [28].

1.5 Motivation

This dissertation focuses on the external corrosion of API X100 pipeline steel in aqueous environments of nn-pH between 5 and 9. The broad motivation behind this research is the advancement of a fundamental understanding and simulation capability of environmental, microstructural, and surface/interfacial influences on HSLA steel corrosion. The environmentally-assisted diminishment of structural integrity is directly linked to corrosion and hence is also studied. Applications of this research are strong within the buried transmission pipeline field; however, understanding corrosion behaviors of infrastructural steels in aqueous environments with nn-pH, low conductivity, and CP-deficient or CP-absent characteristics is of benefit in numerous other applications. This includes potable or tap water piping systems [29], closed-loop freshwater piping circuits [30], crevices [31], and buried or concrete-embedded reinforcements [32], [33].

2. Literature review¹

The corrosion behavior of HSLA steels depends on numerous environmental, material, and surface properties which range from the macroscale of the overall environment, such as the soil topology, to the smaller scale of the metal, corrosion product, and electrolyte interfaces as shown in Figure 2-1 [34]. In nn-pH buried environments specifically, aspects which affect HSLA steel corrosion include anion constituents, dissolved CO₂ and oxygen (O₂) content, pH, CP effectiveness, steel microstructure, and surface effects such as corrosion product growth and morphology [14], [35]–[38]. It is particularly important to understand the electrochemical processes that occur at the metal surface, including the development of anodic and cathodic sites and the rate of reactions at these sites. In addition, the mechanisms with which oxide or passive layers impact electrochemical corrosion activity through the control of specie diffusion to and from reaction sites is a critical area of further study [34], [39]–[41].

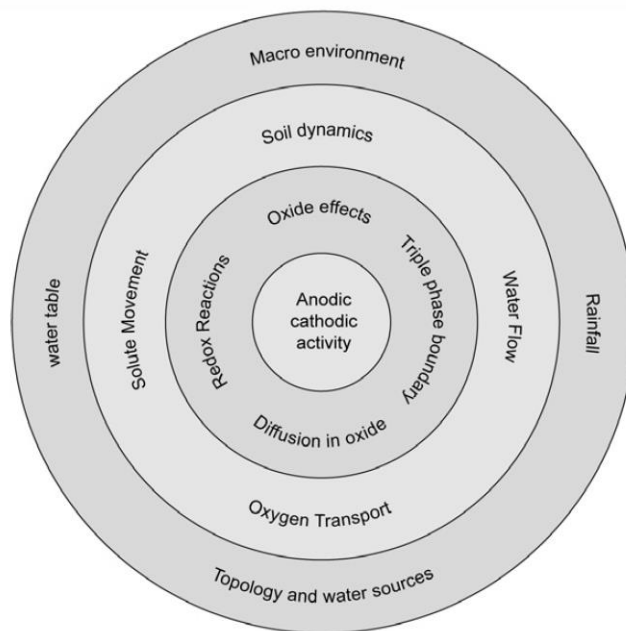


Figure 2-1: The numerous environmental, material, and surface effects on metal corrosion in soil environments, ranging from the macroscale to the smaller surface level scale [34]

¹ F. F. Eliyan, **I. M. Gadala**, H. M. Ha, and A. Alfantazi, “Pipeline Corrosion,” *ASTM Fuels and Lubricants Handbook: Technology, Properties, Performance, and Testing*, 2nd edition. PA: ASTM International, 2016.

The following is a review of previous studies on the external corrosion of ferrous metals in aqueous nn-pH environments which encompass the interrelated topics illustrated in Figure 2-1. Investigations of secondary processes such as hydrogen (H) ingress, diffusion, and embrittlement are also discussed due to their dependence on corrosion processes and their influence on pipeline integrity. Finally, previous works which present computer models and numerical simulations relevant to external pipeline corrosion and the structural integrity of corroded pipelined are reviewed.

2.1 Ionic and pH influences on corrosion processes in anoxic soil environments

The role of environmental influences such as ionic composition, pH, temperature, and CO₂/O₂ concentrations in the corrosion of buried pipelines is still of interest to researchers. A number of researchers have carried out electrochemical studies in laboratory settings simulating real service conditions [42]–[45]. There are also numerous articles in the literature on the behavior of metals in solutions simulating the various physicochemical conditions which arise in underground environments [46]–[48].

In a comparative investigation of 4 different soil types extracted from areas where nn-pH SCC was found on the TransCanada pipeline system, Chen et al. found that the majority of SCC-tested samples exhibit transgranular, cleavage, or quasi-cleavage morphology perpendicular to the loading axis [24]. It is suggested that the relative aggressiveness of a soil environment to SCC is determinable by the change in pH between CO₂-saturated and CO₂-free anoxic solutions. More aggressive soils exhibit a narrower range of pH, and higher levels of CO₂ reduce pH which increases corrosion leading up to SCC (Figure 2-2). Less aggressive soils hinder significant corrosion dissolution toward crack development, resulting in cracking at 45° to the loading axis of the tensile sample, with elongated ductile dimples. These deformation-induced cracks therefore occur on the plane of highest shear stress, prevailing over the brittle cracks forming perpendicular

to the loading axis. Increased corrosion leading to greater SCC susceptibility in environments of greater CO₂ concentration was also found by Fang et al. [49].

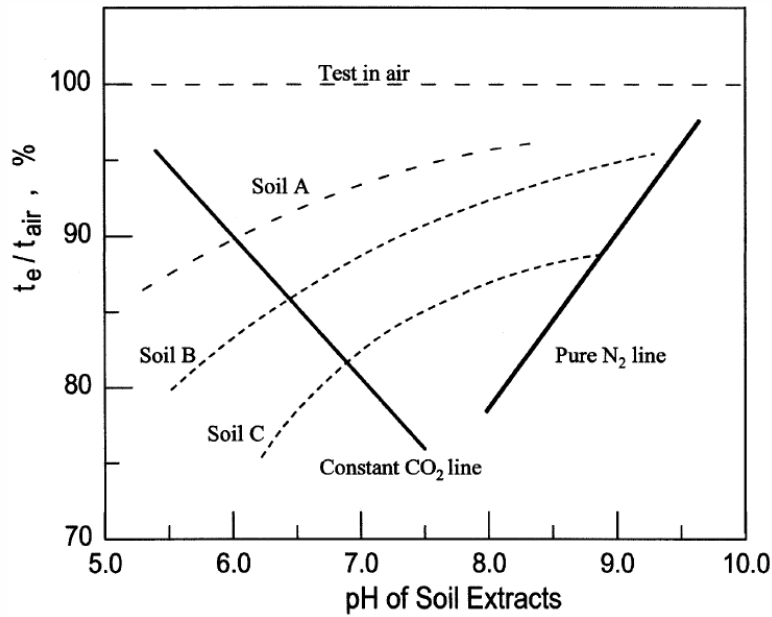


Figure 2-2: Schematic showing the effect of CO₂ concentration on the environment’s pH, and the resulting influence on aggressiveness (where t_e/t_{air} is the time to failure ratio in environment over that in air) [24]

In the nn-pH conditions of [24], varied levels of Cl⁻ activity appears to have a minor effect on SCC susceptibility. Slow strain rate tensile (SSRT) tests in standard NS4 and NOVA type simulated nn-pH solutions also reveal no significant effect for Cl⁻ at most potentials [50]; the composition of NS4 contains an order of magnitude greater Cl⁻ concentration than that of NOVA. Yet, Cl⁻ attack seems to be a function of pH as suggested by Liang et al. in [51], where it is found to be more severe at higher pH. Anodic dissolution at local sites on the metal surface due to Cl⁻ attack results in pitting, even in extracted soil solutions with a fairly alkaline pH of approximately 9. Likewise, in soil solutions with pH values notably more acidic to the nn-pH range (i.e. < 5), an increased ratio of Cl⁻ to other anions has also been reported to cause pitting [52]. Since SCC cracks initiate readily from the bottom of pits due to the stress concentrating effect of the metal loss at those locations [53], increased pitting results in higher SCC susceptibility. Three essential events occur at the bottom of pits: concentration of applied and/or

residual stresses [54], preferential electrochemical dissolution of the metal, and local acidification of the environment [55]. The established chronology between pitting and SCC necessitates that tests without stress are performed in material-environment combinations of interest. In other words, to understand corrosion behavior leading up to pitting and crack initiation, fundamental electrochemical studies under no load are needed.

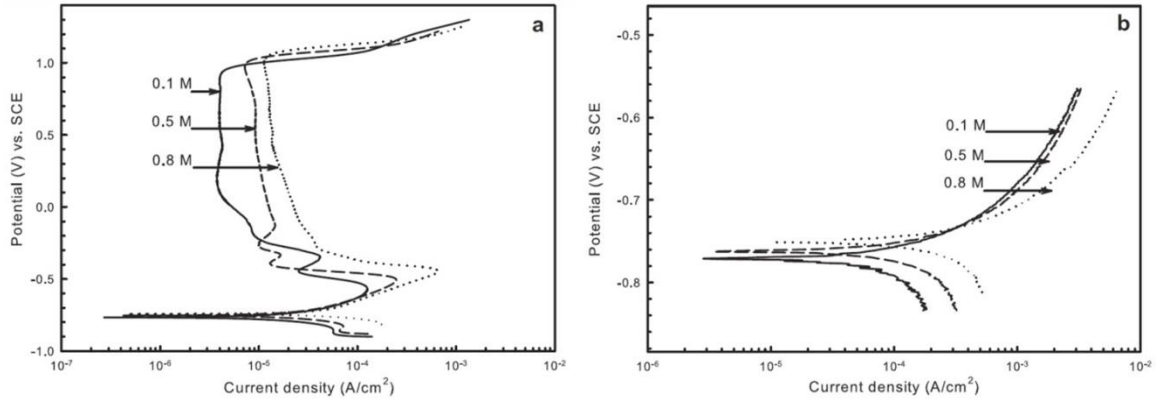


Figure 2-3: Potentiodynamic polarization in 0.1, 0.5, and 0.8 M HCO₃⁻ solutions at 20 °C in (a) Cl⁻-free and (b) Cl⁻-containing conditions [56]

Eliyan et al. evaluated the basic electrochemical behavior of X100 in relatively concentrated HCO₃⁻ solutions (0.1 – 0.8 M), and described clear enhancements in passive layer development driven by HCO₃⁻, and opposing Cl⁻ attack on passivation combined with augmentation of corrosion rate as seen in Figure 2-3. At open circuit potential (OCP) and using electrochemical impedance spectroscopy (EIS), the diffusion found in Cl⁻-free solutions is eliminated in Cl⁻-containing solutions, and adsorptive processes are manifested instead. At anodic sites, Cl⁻ accelerates anodic dissolution and ferrous (Fe²⁺) release from iron specimen, as discussed by Lorenz and Heusler in [57] and supported experimentally by Zhang et al. [58]. In similar characterizations of passive films formed on steel in HCO₃⁻ solutions using EIS, the suppression of diffusion processes with increased Cl⁻ concentrations was also found [59]. Evaluation of the semiconductive properties of these films using Mott-Schottky further reveals increases in passive film thickness in the absence of Cl⁻, attributed to lower donor densities of the

space-charge layer, the thickness of which (δ_{sc}) is found through {E-2.1} below. In this potential (E) dependent equation, ε is the dielectric constant of the passive film, ε_0 is the permittivity of free space, e is electron charge, N_d is the donor density (for n-type semiconductors only), E_{fb} is the flat band potential, k is the Boltzmann constant, and T is the temperature in Kelvin.

$$\delta_{sc} = \sqrt{\frac{2\varepsilon\varepsilon_0}{eN_d} \left(E - E_{fb} - \frac{kT}{e} \right)} \quad \{\text{E-2.1}\}$$

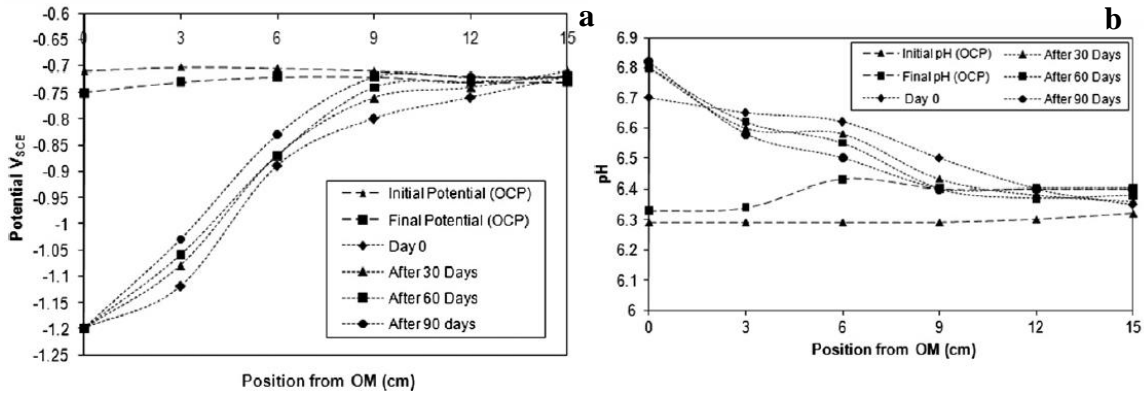
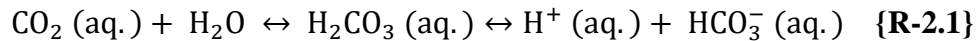


Figure 2-4: (a) Actual CP levels at different positions from opening mouth (OM) and different times; (b) pH distribution of the electrolyte inside the shielded disbondments at different positions from opening mouth, and different times [25]

The typical test setup of most nn-pH corrosion and SCC tests neglects the concentration-cell aspect of the corresponding environment under pipeline coating disbondments. Since the chemistry of the solution trapped in the disbondment is altered due to the effect of the gradient in CP [60], a tensile specimen exposed to a single pH and CP environment is not representative of the real conditions present in nn-pH corrosion and SCC. In a novel testing method designed by Eslami et al., large coating disbondments are simulated with a poly methyl methacrylate partial shield between the tensile specimen and the corrosive electrolyte [25]. CP is only applied at the opening (holiday) in the coating, and only enters the disbondment region through this opening due disbondment shielding. The distribution of pH and potential (vs. saturated calomel electrode, SCE), monitored periodically throughout the cell, clearly indicates the variable redox conditions within the disbondment (Figure 2-4). This results in corrosion rates and crack initiation severities

which follow a nonlinear relationship; between the opening mouth of the disbondment and the furthest point in the shielded disbondment crevice, the largest pit diameters and highest percentage of pit coverage are discovered. This is proportional not only to corrosion, but also to microcracks at the bottom of the pits and SCC severity. Thus, it is neither the region with full CP (at opening mouth) nor the region lacking any CP (at the crevice tip) which is most critical in terms of corrosion. This finding highlights the need for more investigations into the fundamental electrochemical processes occurring on steel surfaces with changes in pH *within* the nn-pH range, and likewise variations in CP near OCP.

Akin to electrolyte pH differences based on disbondment dimensions and exposure times, albeit still within the nn-pH range, ionic composition of the electrolyte is a variable which varies based on soil physicochemical properties. The ionic constituent differences between the standard simulative electrolytes of NS4 [61], NOVA [50], C1 [62], C2 [25], and others undoubtedly affect corrosion performances of HSLA steels exposed to them. In solutions adjusted to pH 3–7 and containing NaCl, CaCl₂, Na₂SO₄, MgSO₄, NaHCO₃ and KNO₃, weight loss and electrochemical experiments reveal that corresponding parameters, which included the corrosion current and potential (I_{corr} and E_{corr}), were strongly dependent on pH [63]; the greatest mass loss and I_{corr} occur at pH 3. This is a recurring result [42] which is corroborated by corrosion acceleration in acidic soil environments, such as those acidified from acid rain [47]. In nn-pH underground conditions, the only significant pH-altering electrolyte constituents are HCO₃⁻ and dissolved CO₂ concentrations, governed by the temperature-dependent carbonic acid (H₂CO₃) association and dissociation equilibrium of {R-2.1} [64], [65]:



In electrochemical tests carried out to study the effect of electrolyte composition, the aggressiveness of cations is reported to follow the order $\text{K}^+ > \text{Mg}^+ > \text{Ca}^{2+}$, whereas that of the anions follows the order $\text{SO}_4^{2-} > \text{HCO}_3^- > \text{NO}_3^-$ [48]. The differences in corrosion incurred by

these various ions were not dramatic, causing a modest increase in I_{corr} around OCP. In EIS tests conducted in these environments, the analysis of which consisted of a three-element electrochemical equivalent circuit (EEC), all anions decreased the charge transfer resistance (R_{ct}) [47], [48], [63]. Liu et al. argued that while the presence of K^+ decreased R_{ct} , Ca^{2+} and Mg^{2+} increased it [48]. In the work of Benmoussa et al., it was additionally found that the aggressiveness of solution increases with temperature, and contrariwise R_{ct} increases with time due to the development of a protective film.

Electrochemical tests conducted in the laboratory also reveal a relatively high correlation between polarization resistance (R_p) and mass loss in conditions relevant to buried pipelines [44], [45]. Furthermore, the mass transfer of O_2 plays a vital role in the kinetics of corrosion, where the entire process is limited by a combination of activation and diffusion control as postulated in [45]. Yet, it should be importantly noted that great difficulty exists in suitably accelerating corrosion in a laboratory environment, as resistivity values in the field do not match those in the laboratory; hence the electrochemical parameters derived from soil solution tests do not match field corrosivity tests [66]. The stimulating and interplaying effects of solution chemistry, notably pH and ionic composition, are sought to be understood through simulated soil environments. Yet, since solution chemistry is only one of many factors controlling corrosion in buried environments, this must be met with more comprehensive investigation of surface layer growth, diffusion, CP, and auxiliary effects present in reality. This is achievable through dedicated studies of time-dependent surface effects, as reviewed in section 2.2 below, H evolution and diffusion secondary processes, as reviewed in section 2.3, and numerical models of diffusion, CP, and corrosion processes in underground environments, as reviewed in section 2.4.

2.2 Time-dependent corrosion product and surface effects in anoxic and oxic soil environments

The early work of Scully and Brandy evaluated soil corrosion of buried steel pipe with linear polarization resistance (LPR) and EIS tests [46]. Corrosion rates calculated from these

electrochemical methods decrease with time of exposure. In a comparative study of internal and external corrosion of buried cast iron pipe, Sancy et al. found markedly lower corrosion rates on internal surfaces and notably different forms of impedance spectra [67]. On the inner surfaces, the metal behaved as a semi-infinite conducting porous electrode, where a CO_3^{2-} layer at pore edges limited the cathodic reaction to occurrence exclusively on the bottom of the pores. On external surfaces, mass-transfer limited behavior manifests akin to that seen in [45], where it is believed that the cathodic reaction is controlled by diffusion through the non-conducting porous layer. Figure 2-5a is an example of the porous nature of calcium carbonate (CaCO_3) corrosion product formed on X70 steel after 40 hour (h) immersion in 5% CO_2 NS4 solution at 22 °C, with the corresponding corrosion current density (i_{corr}) map showing a localized corrosion distribution dependent on the surface layer morphology [41]. The i_{corr} map shown is obtained using the Scanning Vibrating Electrode Technique (SVET) on a Scanning Electrochemical Microscope (SECM). In this technique, i_{corr} is proportional to the test solution conductivity, the vibrating amplitude (usually $\pm 30 \mu\text{m}$) of the scanning microelectrode, and the potential difference of this fine microelectrode (10 μm tip) between the peak and valley during its vibration normal to the surface of the specimen.

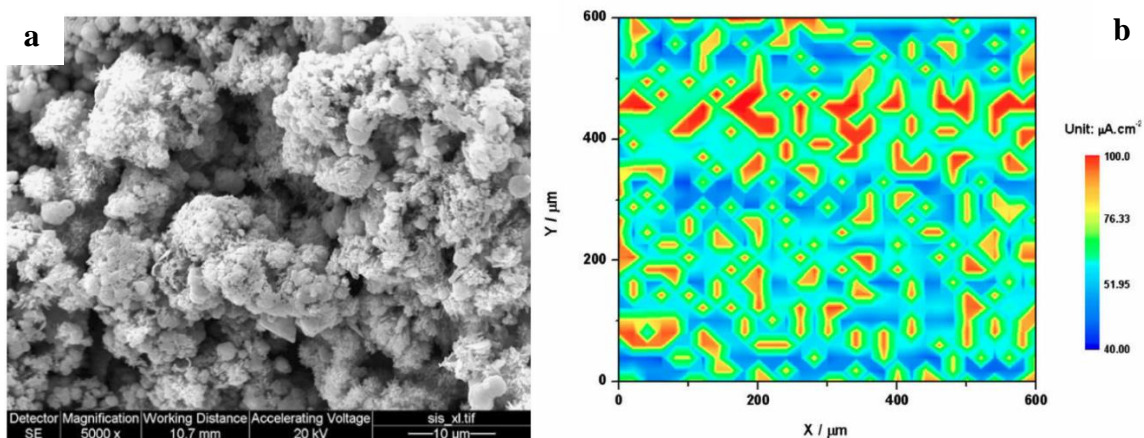


Figure 2-5: (a) Surface morphology of CaCO_3 layer formed on X70 surface after 40 h immersion in 5% CO_2 NS4 solution at 22 °C; (b) i_{corr} map measured on X70 specimen covered with CaCO_3 [41]

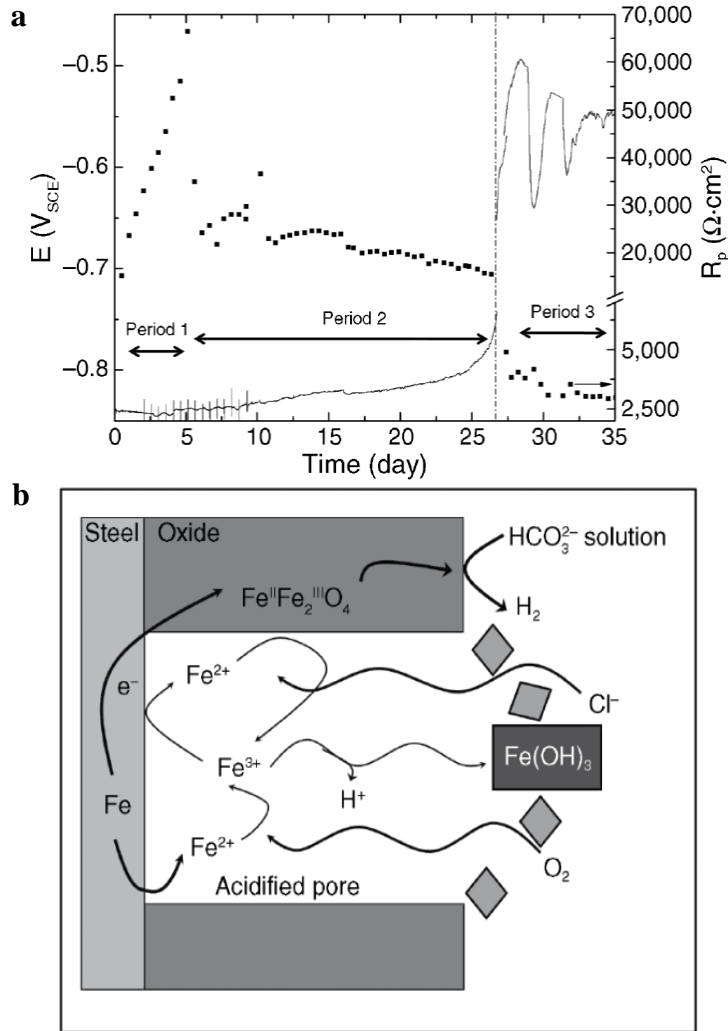


Figure 2-6: (a) E_{corr} (vs. SCE) of pretreated steel under anoxic conditions in nn-pH saline solutions, where square points show R_p values from LPR; (b) Schematic illustrating the film transition process within an acidified pore, assuming separation of anode (Fe dissolution) and cathode (HCO_3^- discharge) [68]

In CO_3^{2-} – HCO_3^- environments, a main corrosion product causing passivation is iron carbonate (siderite, FeCO_3), with a formation dependent on pH and HCO_3^- concentration according to {R-2.2} below [56], [67]. Not only do CO_3^{2-} – HCO_3^- concentrations have a significant effect on passive/oxide layer development as shown in [67], the development of this layer over time greatly affects ensuing corrosion processes. Electrochemical studies contribute to the understanding of this time-dependent process in ways not readily possible from field exposures, where cumulative corrosion rate is normally only measured at the end of tests.



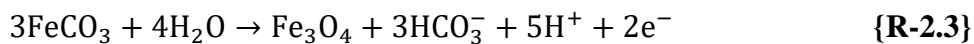
A common trend in the growth of passive/oxide layers on corroding steel is the decrease of I_{corr} with time, coupled with an increase in R_{ct} or R_p measured by EIS or LPR, respectively [34]. X60 steel exposed to a soil-simulating solution develops a corrosion layer which causes both an initial decrease in R_{ct} and a continuous increase in the double-layer capacitance modelled with a constant phase element (CPE) in the three-element EEC [43]. Yet decreasing overall corrosion can lead to localization of anodic activity and an increase in I_{corr} as shown by Aung and Tan [69]. This is backed by the findings of Norin and Vinka which suggest differences in the factors controlling local and general corrosion rates of buried carbon steel [70].

In a study of nominally anoxic corrosion of carbon steel in nn-pH saline environments, Sherar et al. identified an upsurge in corrosion rates corresponding to a sharp decrease in R_p (see Figure 2-6a) during periodic LPR tests on specimens pretreated with an initial FeCO_3 film [68]. It is postulated that a film transition process occurs within the acidified pore of iron oxide/oxyhydroxide formations developed during the 35 day exposure of these tests. The enhanced corrosion rate is suggested to be sustained by proton (H^+) reduction from HCO_3^- on Fe_3O_4 surfaces, while accelerated corrosion occurs primarily at anodic sites at the base of acidified faults within the film as shown in Figure 2-6b.

The potential decrease observed in Figure 2-6a on pretreated carbon steel resembles that which was reported by Qin et al. on a millscale-covered pipeline surface [71]. Millscale is a highly oxidized deposit ($\text{O}/\text{Fe} \approx 2.4$) containing iron oxidation products and aluminosilicate clay minerals commonly originating from furnace slag, and consisting of a dual-layer morphology. Whereas millscale-free specimens exhibit a constant OCP or E_{corr} during immersion, millscale-covered specimen exhibit potential decreases with time in three distinct stages. After a first relatively stable E_{corr} stage, potential falls rapidly in the second stage due to reductive oxide dissolution, wherein pore enlargement of the porous oxide morphology occurs. The resistance of

the pores (R_{pore}) in the EIS fit results falls markedly in this second stage of immersion, consistent with solution penetration into the pores of the millscale. Again, like in [68] the porous structure of the millscale augments the corrosion rate by separating the anodic and cathodic sites and keeping a high ratio of cathodic to anodic surface areas. The pores continue to enlarge with time and the establishment of a double-layer at the exposed metal becomes easier, corroborating the mechanism proposed by Linter and Burstein for pores in a $\text{Fe}(\text{OH})_2$ -containing film [64] and by Belmorke et al. in an electrolyte-penetrated paint film [43].

In O_2 -containing actual and simulated environments, HSLA steels often develop multi-component corrosion products including complexes of Fe^{2+} and/or ferric (Fe^{3+}) with hydroxide ($\text{Fe}(\text{OH})_2$), carbonate (FeCO_3), oxide (Fe_3O_4 and Fe_2O_3), and oxyhydroxide ($\gamma/\alpha\text{-FeOOH}$) [30], [42], [72]–[78]. Oxidation reactions of compounds found in these multi-layer corrosion products are viable at different O_2 concentrations, such as the oxidation of FeCO_3 in nominal O_2 conditions [79] versus that of $\text{Fe}(\text{OH})_2$ in the complete absence of O_2 [32], [80]. With increasing O_2 content, reddish/orange oxide/oxyhydroxide tubercle formations appear during excavation as speckles on the white FeCO_3 deposit [81]. Some suggest that this is the result of anoxic corrosion products air oxidizing during excavation and subsequent examination [82], whereas it could potentially be due to electrochemical reactions involving anoxic corrosion products, such as through {R-2.3} [73]. Furthermore, temperature plays a role in protective iron oxide formation; Nie et al. found that oxides form on metal surface at ambient temperatures but not at elevated temperatures at around 50 °C [45]. Conflicting causalities of corrosion product formations prompt more studies of corrosion and passivation steps in oxic environments, especially on new alloys like X100. O_2 concentrations are variable in practical situations not limited simply to soils, hence understanding the different O_2 -dependent viabilities of these reactions is important.



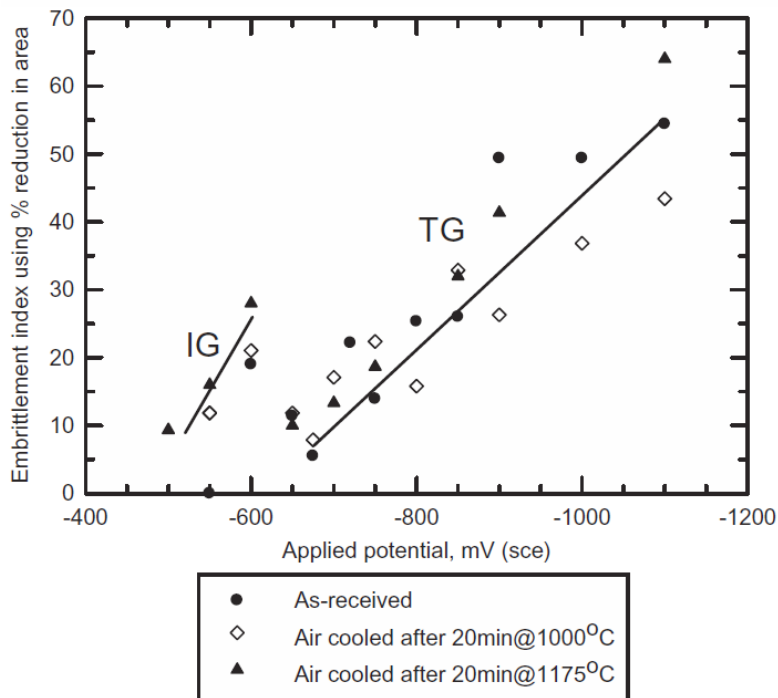
Underneath disbonded pipeline coatings, corroded surfaces not only affect the corrosion rate of the exposed steel, but also the rate of polarization achieved within the disbondment. The

effectiveness of CP in a highly insulating tape disbondment on a steel surface covered with γ -FeOOH and Fe₂O₃ was investigated by Perdomo et al. [83]. It was found that the rate at which the potential decreases in the disbondment in the corroded conditions is about half that of the bare steel condition (rate of decrease: bare steel > Fe₂O₃ > γ -FeOOH). In addition, OCPs for the rusted surfaces are more positive than the bare-steel condition. Low O₂ levels recorded from samples extracted from within the crevice are suggested to be due to the reduction of O₂ into OH⁻, a process which increases the acidity of the local solution with distance from the coating opening (the highest CP is found at the opening). This finding agrees with the periodic pH measurements of Eslami et al., shown previously in Figure 2-4b.

The anoxic local conditions at the coating opening mouth with the application of CP, and the corresponding increased alkalinity, are fundamental in reducing corrosion rates at exposed metal coordinates there. It appears from the findings presented in [83] that CP current does not need to flow directly to all coordinates of the exposed steel in a disbondment for protection to be realized. Since the ability of pits to remain active depends on the local composition and pH of the solution within the pit [55], the concentration cell effect with the disbondment has implications on pit initiation and growth. Concentrated solutions within the pit are often covered by the remaining passive oxide layer, which ruptures when the pit reaches a critical size [84]. Rupturing can also occur with applied stress and can be simulated through the forced electrode abrasion technique, with which Park et al. [52] identified increased pit repassivation on X65 pipeline steel in high pH solutions compared to low pH solutions. The sufficient passivity of the high pH conditions allows for selective dissolution at the grain boundaries, leading to intergranular SCC. In contrast, the pits in low pH conditions do not repassivate and manifest a pit-to-transgranular SCC mechanism.

2.3 Hydrogen evolution, absorption, and diffusion processes in steels exposed to simulated soil solutions

Hydrogen induced cracking (HIC) and hydrogen embrittlement (HE), resulting from the entry of atomic H into metals, are predominant forms of failures to which high-strength steels are susceptible [85], [86]. Transgranular SCC in underground pipelines is characterized by wide cracks with quasi-cleavage morphology and little branching [28], [87]–[89]. The crack sides often suffer significant lateral corrosion resulting in the destruction of the original crack faces.



increase in the susceptibility of steels to transgranular SCC at more cathodic potentials also supports the proposed HE mechanism, as shown by Mustapha et al. [90] (Figure 2-7) and in [92], [95], [96].

It is generally acknowledged that higher strength reduces steel resistance to HIC, as found in the work of Hardie et al. [86], where tensile specimens of X60, X80, and X100 steels are pre-charged with H through cathodic polarization in a sulphuric acid solution. H content in metals increases with charging time [98], but reaches what can be considered a saturation plateau after a certain time. For example, in [93] the H content in X65 steel is observed to increase linearly with charging time up to 800 minutes, remaining nearly constant thereafter (Figure 2-8). Upon loading, steel specimens typically experience significant loss in ductility, the degree of which increases with charging current density [86]. This is confirmed by [19], where the SCC susceptibility of steel in the simulated soil solution was found to have the same order as the subsurface H concentration (C_s). At a H pre-charging current density of 0.10 mA mm^{-2} , the degree of HE increased with steel strength [86], matching the findings of Capelle et al. [98] for X52, X70, and X100.

Electrochemical and corrosion studies of steels in nn-pH soil environments mainly focus on anodic processes [19], [97], [99]. The cathodic processes on steels, particularly the hydrogen evolution reactions (HER) which might play an important role in controlling transgranular SCC mechanisms in the nn-pH environment, are not thoroughly understood. This is because our understanding of the HER in CO_3^{2-} - HCO_3^- solution is mainly obtained from studies of internal corrosion of pipelines exposed to CO_2 solutions [36], [100]–[103], wherein corrosion environments usually contain a significant amount of dissolved salts (e.g. approximately 3% NaCl) and have a pH in the range of 4 to 5. These electrolytes are far more concentrated and more acidic than the corrosive electrolyte of soils surrounding pipelines at locations where transgranular SCC is found. Nevertheless, in these internal pipeline corrosion studies though, it was found that the presence of CO_2 increases the corrosion rate of corrosion of Fe by increasing

the rate of the HER [64], [100], [103]. Many researchers have suggested that the cathodic current is the sum of the currents for H^+ reduction and H_2CO_3 discharge, at least in nn-pH and alkaline environments. However, at higher pH the direct discharge of HCO_3^- becomes important at the corresponding E_{corr} of steels [104].

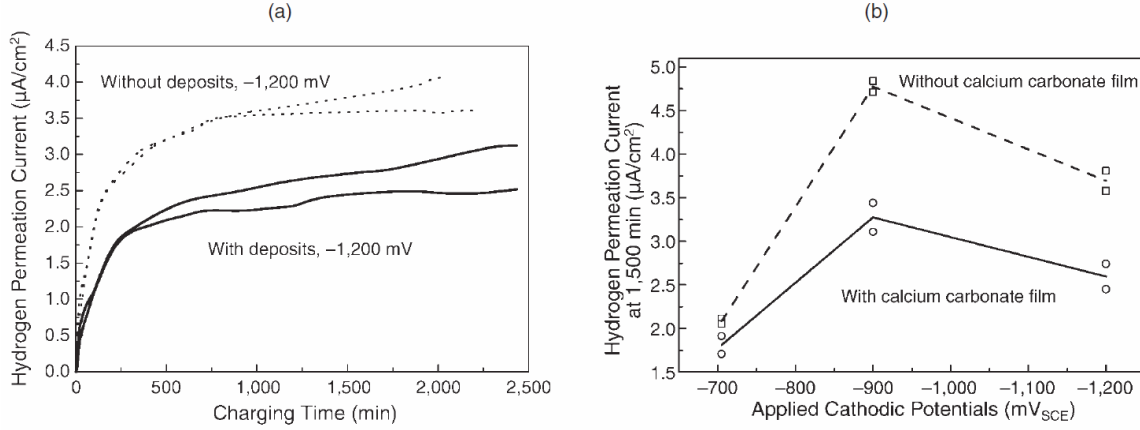


Figure 2-8: (a) Hydrogen permeation curves of X65 specimens (600-grit finish) at -1200 mV with and without calcium carbonate coatings (b) Hydrogen permeation current vs. applied cathodic potential [93]

Understanding the effects of parameters such as solution chemistry, aeration condition, CO_2 , pH, and temperature on the kinetics of the cathodic reactions, particularly HER on HSLA steels, is important in studies of the transgranular SCC mechanism in nn-pH soil environments surrounding buried pipelines. H generation kinetics on the steel surface will affect the amount of H absorbed into the material and subsequently assist SCC crack growth. Following ingress, H in steel reduces the threshold stress intensity (K_{th}) as shown in {E-2.2} below. This equation describes the dependence of K_{th} on C_s , where α , α'' , and β' are constants, k_{IG} is the intrinsic Griffith toughness for cleavage fracture without H, σ_{YS} is the yield strength of the material, and $C_{H\sigma,T}$ is the H concentration at the crack tip [105]. $C_{H\sigma,T}$ is proportional to C_s through {E-2.3}, where σ_H is the crack-tip hydrostatic stress, V_H is the molar volume of H in the steel, T is temperature, and R is the gas constant [106], [107]:

$$K_{th} = \frac{1}{\beta'} \exp \left[\frac{(k_{IG} - \alpha C_{H\sigma,T})}{\alpha'' \sigma_{YS}} \right] \quad \{\mathbf{E-2.2}\}$$

$$C_{H\sigma,T} = C_s \exp \left[\frac{\sigma_H V_H}{RT} \right] \quad \{\mathbf{E-2.3}\}$$

Recent studies on H damage manifestations in API X100 line pipe steels, including HIC under severe cathodic charging in both acidic and alkaline environments [104], [108], [109] and HE under different potential ranges in bicarbonate solutions [90], emphasize the need to understand the H generation, absorption, and transport kinetics in this modern HSLA material. Depending on HSLA steel grade, a critical H concentration (C_H^*) exists at which significant loss of local fracture resistance occurs. C_H^* decreases with increasing σ_{YS} and ultimate tensile strength (σ_U), approximately following an inverse quadratic relationship where C_H^* is proportional to $1/\sigma_U^2$ [98]. This decrease can be explained by dislocations being “more pinned” by the precipitates found in higher strength steels. In other reports, a CP current density threshold ($i_{th,CP}$) is identified instead of C_H^* in the steel, since this is more applicable for creating safe CP design standards. In a report on the precautions necessary to eliminate microcracking damage to plain carbon steels subject to CP, Cialone and Asaro indicate that CP currents should be restricted to below 0.06 mA mm⁻² [110], a value comparable to that reported by Hardie et al. in [90].

Steel alloy grade, strength, and heat treatment, in addition to specimen geometry, notches, defects, mode of H charging, and rate of loading upon charging are all factors which affect C_H^* and $i_{th,CP}$ [98], [104], [108], [111], [112]. Researchers have focused on the specific aspects of steel grade to better understand its influence on HIC/HE. The number, distribution, and types of inclusions in each steel alloy influence H uptake, diffusion, and HIC. Inclusions, especially oxides and carbides, serve as effective sites for HIC crack initiation [104], [108], [111]. Dong et al. observe that cracks initiate preferentially at aluminum oxide, titanium oxide, and ferric carbide inclusions in X100 steels [104]. This suggests that different types of inclusions are more detrimental than others, an observation ratified by the findings of Jin et al. where H-induced cracks initiated mainly at Aluminum (Al) and Silicon (Si) enriched oxide inclusions (Figure 2-9) in X100 specimens [108]. No cracks were associated with the elongated Magnesium Sulfide

(MnS) inclusions or the inclusions with a mixed composition including Calcium (Ca), Al, O, and Sulphur (S).

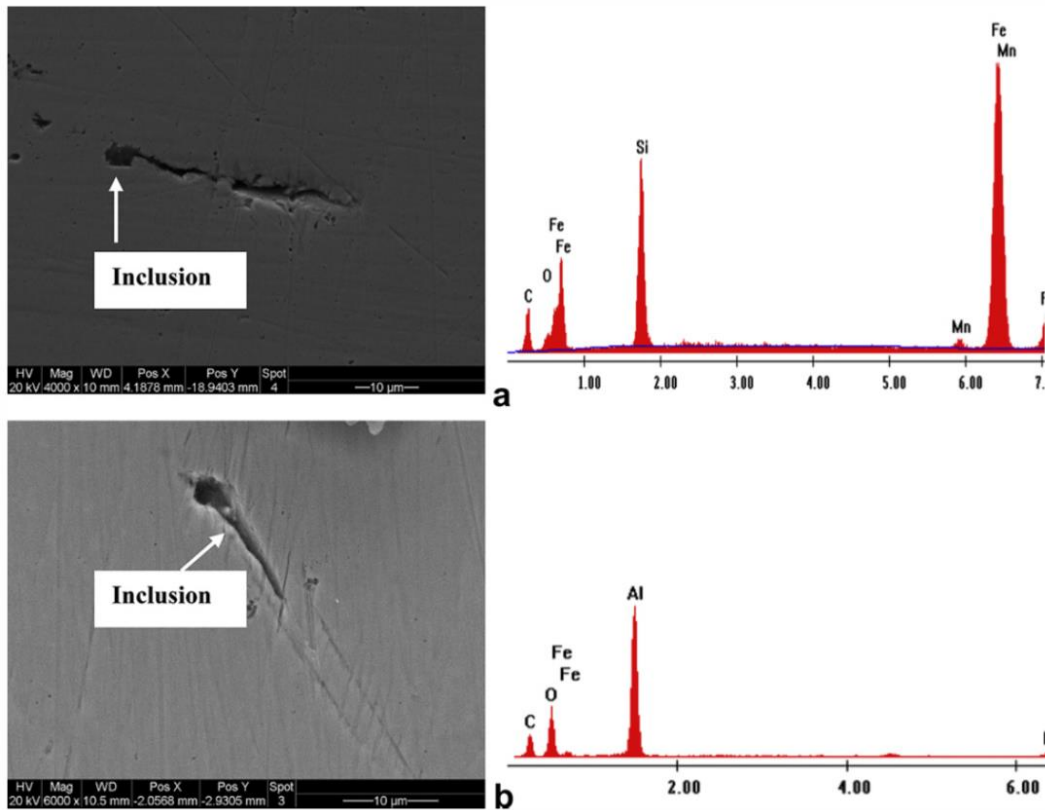


Figure 2-9: SEM morphologies of the cross-section of X100 specimen and the chemical composition obtained at the individual inclusions (a) an Al-enriched inclusion; (b) a Si-enriched inclusion [108]

Since steel alloy grade is only one of the factors affecting C_H^* or $i_{th,CP}$, even HSLA steels of the same grade can exhibit different sensitivities to H. This can be due to different heat treatments, where for instance H appears uninfluential on the ductility of as-received and spray-cooled X70 specimens, yet affects quenched and quenched-&-tempered specimens considerably [112]. Environmental and surface conditions of steels also play a large role in H-induced damage mechanisms. Corrosion product deposits on the steel greatly impede H ingress. Reduced H flux is typically measured on specimens with a corrosion product deposits such as $CaCO_3$, compared to those with bare surfaces [93]. Of the 3 steps controlling H permeation/ingress, namely {1} evolution of H through reduction, {2} H adsorption onto steel surface, and {3} H penetration into

the steel, H adsorption and penetration are greatly hindered by the presence of corrosion products [41], leading to improved resistance to SCC (shown for mill-scale covered vs. machined surfaces in [113]). It is well accepted that the HER of step {1} proceeds through three sub-steps [114]–[116]: {i} electrochemical reduction/evolution of H₂O (in nn-pH or alkaline solutions) or H⁺ (in acidic solutions), {ii} electrochemical recombination of evolved H, and {iii} chemical desorption of H. Even though H evolution is greatly enhanced on the typically porous corrosion products (e.g. Figure 2-5a) due to the increased effective area for the HER as shown in [41], the decelerated steps {2} and {3} on electrodes covered with corrosion products decreases C_s .

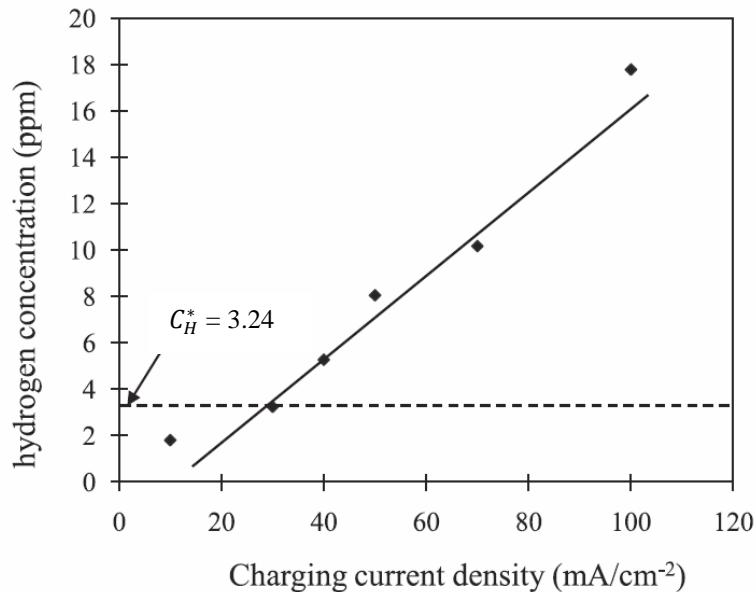


Figure 2-10: Steady-state H amount released from an X100 steel specimen as a function of the charging current density, where the C_H^* needed to initiate HIC is identified [108]

It is also well documented that the uptake of H is increased by increasing temperature [20], [117]. A comparison of HIC findings in [86], [110] versus those in [108] further verifies this; in the latter, HIC only occurs in the X100 sample after 20 hours of charging at $i_{th,CP} = 30$ mA cm⁻² (0.3 mA mm⁻²), corresponding to $C_H^* = 3.24$ parts per million (ppm) in Figure 2-10, found using the JIS Z3113 method [118], [119]. This value is 3 times that of [86], reported to be 0.10 mA mm⁻² for the same X100 alloy, and also around 3 times the $C_H^* \approx 1$ ppm found for X65 quenched and tempered specimen [120]. The difference in results is suggested here to be due to

dissimilar charging times between the reports and the 20 °C temperature difference during pre-charging.

With respect to mechanical property degradation, H absorption, desorption, specimen geometry, and C_H^* of a material are all interrelated. For example, even though resistance to H absorption is high for bare X100 steel in comparison to other HSLA grades, X100 still has relatively higher susceptibility to HE due to a lower C_H^* (inversely proportional to σ_U as mentioned earlier). Moreover, the H desorption behavior of the steel will dictate the speed of recovery of ductility after H ingress. Recovery to air-charged levels of ductility can fully materialize if specimens are left for several days at ambient temperature after charging [121]. This H desorption can be quantified to identify the H concentration decay profile, which normally reaches a steady-state concentration after 72 hours [93]. These findings from desorption tests suggest that the primary cause of HE is the H trapped in the steel microstructure and not the microcracks resulting from the H stressing trap locations and inclusions, since microcracks do not heal after desorption.

2.4 Numerical modelling of corrosion, CP, and pipeline structural integrity

2.4.1 Models and simulations of steel corrosion with CP and gas transport

Mitigation strategies for external pipeline corrosion revolve around two methods: CP and protective coatings [35], [122]. The corrosion of pipeline steel following coating failure is lessened by CP systems, but is heavily affected by physicochemical properties of the immediate surrounding soil as elaborated in section 2.1. In the bulk soil not immediately adjacent to a coating failure, physicochemical soil properties like soil moisture content, soil type, soil resistivity, soil pH, redox potential, and microbes in the soil are critical with regards to CP effectiveness [123], especially in sections between the CP anode and the pipeline [124]. These properties have influential impacts on gas diffusion and heat transfer phenomena. Complexities

arise from the compound dependence of electrical resistivity, gas diffusivity, or thermal conductivity parameters on one or more soil properties/conditions such as particle distribution, porosity, moisture, and temperature [42].

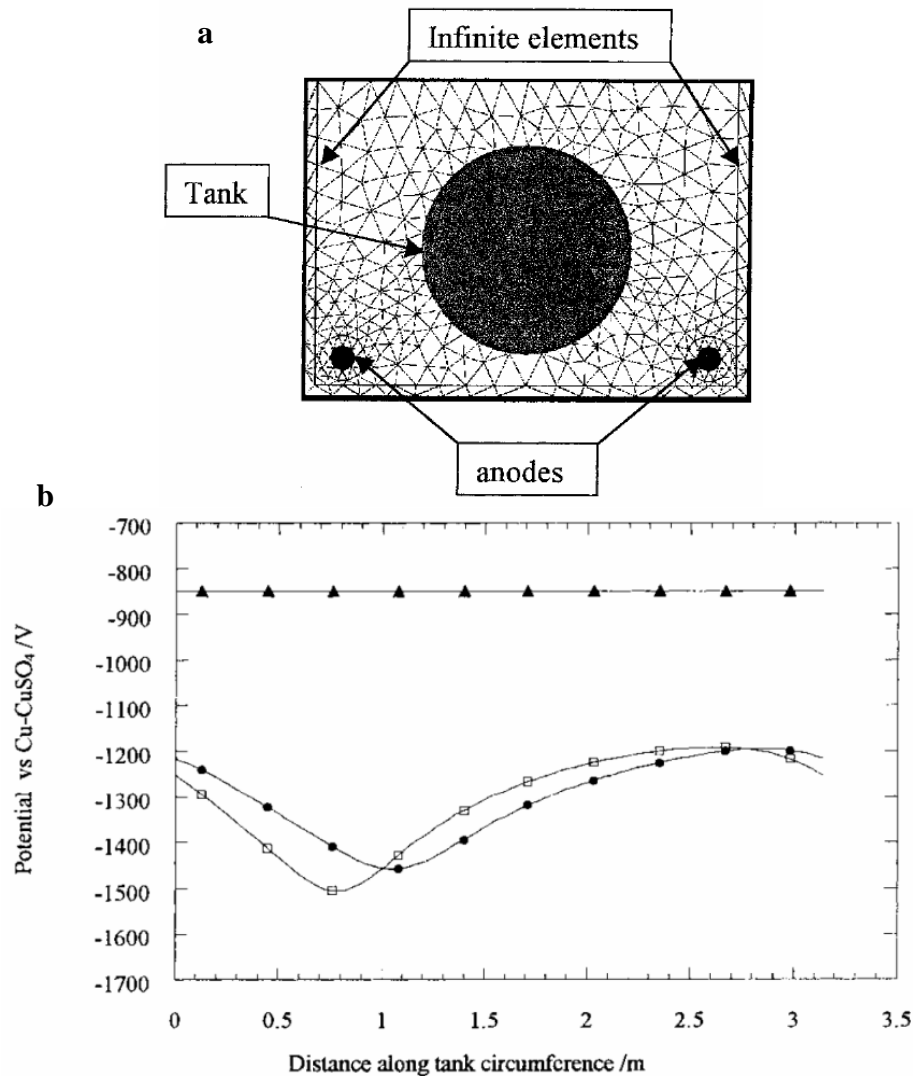


Figure 2-11: (a) Planar cross-section of buried tank and anode system modelled in [125], with meshing of the soil media; (b) Potential distribution at surface of tank for different anode positions (circle: bottom of pit, square: at half depth, triangle: critical potential)

Empirical correlations for predicting soil corrosivity often intentionally overlook certain soil parameters or conditions for simplicity. Booth et al. report in an early study that simply resistivity and redox potential are sufficient predictors of corrosivity (better than moisture content) [126], whereas more recently, Tomlinson and Woodward reveal that soil type and

structure are the determining factors regardless of other properties including the structure's position with respect to the water table [127]. Empirical limits separating corrosivity categories have been postulated, such as a minimum of 20 wt. % moisture content for the soil to be considered "non-aggressive" [126], or a soil resistivity of at least 1000 Ω -cm to avoid classification as "very corrosive" [128]. Empirical guidelines such as these simplify the complex reliance of gas transport, heat transfer, and ensuing reaction kinetics on many interdependent soil parameters, leading to erroneous predictions of corrosion rates and ultimately incorrect assessments of structural integrity. Modelling and numerical simulations can capture a larger spectrum of the fundamental processes occurring on cathodically protected pipelines with coating failures and provide more accurate data on unfavorable environmental conditions, perilous operating parameters, and critical corrosion locations on exposed surfaces [125], [129], [130].

In the work of Rabiou et al., a finite element model was used to compare the relative influence of coating quality, soil electric conductivity, and CP anode size, position, and type on the corrosion of buried steel tanks [125]. Although the soil's electrical conductivity played a leading role in consequent corrosion, in addition to parameters related to the CP system like the anode position as shown in Figure 2-11b, the model did not consider other important soil-related parameters such as water content. The work of Miltiadou and Wrobel incorporated the influence of the limiting current density of O_2 reduction with the electrolyte conductivity parameter, and used a semi-analytical solution of governing equations to compute the distribution of electrical potential within the electrolyte [129]. Yet, spatial and time dependent differences in electrolyte properties, specifically gas transport or electric conductivity, were not accounted for since the electrolyte considered was uniform and non-porous. Similarly, Martinez and Stern simulated the effectiveness of an impressed current CP system in a uniform and non-porous electrolyte media inside a cylindrical structure [130]. The wire anode running along the cylinder's length supplied the CP current to the internal surfaces through the conductive path provided by the electrolyte within (Figure 2-12a). The spatially-dependent potential of the internal surfaces was simulated

based on input parameters such as anode-cathode distance and electrolyte conductivity (Figure 2-12b). When compared to experimental results, the model estimated the cathode potential distribution with good accuracy, provided the experimental conditions resembled those presumed by the model.

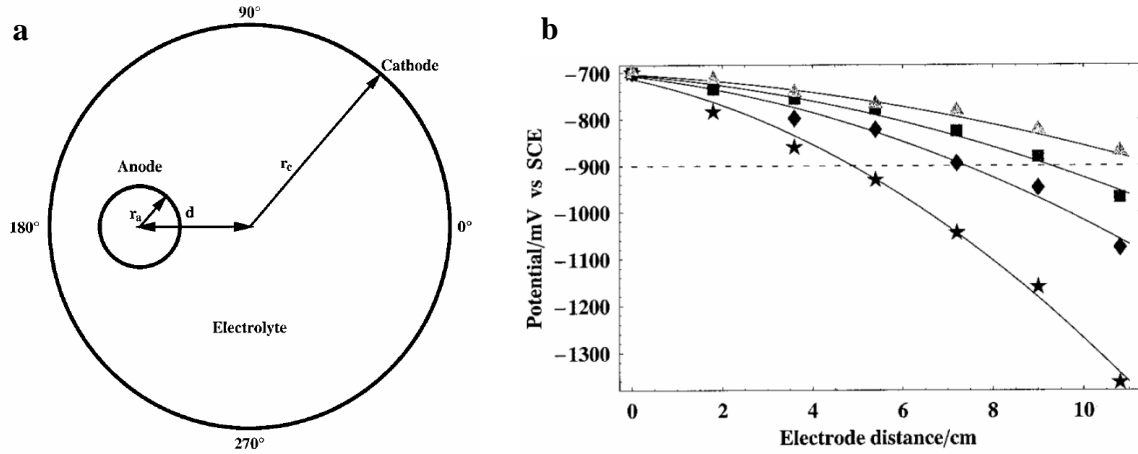


Figure 2-12: (a) Schematic view of a cross-section of the internal CP system investigated in [130], where r_a is the wire anode radius, r_c is the hollow cylinder (cathode) radius, and d is the offset distance from the central axis (b) Steady-state potential measured at 180° in (a) as a function of d in electrolytes of different conductivities (triangle: 1% NaCl, square: 0.6% NaCl, diamond: 0.3% NaCl, and star: 0.15% NaCl)

In soil systems, current distribution in a structure under CP is a function of system geometry, relative magnitudes of O_2 diffusivity and ionic conductivity of the bulk soil, and reaction kinetics at electrode-soil interfaces. However, since soil is porous, tortuous mass-transfer within it obeys multi-phase flow laws which have critical dependence on air-filled void porosity, moisture content, and temperature [131]–[135]. These parameters are interrelated and depend on parameters such as soil structure, for both gas [136] and charge [137] transport.

For evaluation of gas transport within the soil, previous numerical models of CP and corrosion systems often make narrow use of experimental diffusivity measurements like those of [134]. Rather, the rate of transport is determined through use of empirical parameters based on limiting current density such as in [130], [138], [139]. Seldom do models present coupled gas transport (of O_2) and electrolyte potential distribution like in [140], [141], or variable gas diffusivity in bulk porous media like in [142] (yet without CP presence). For evaluation of

electrical current within the soil, the most rigorous technique is to employ Nernst-Planck based on concentrations, diffusivities, and electric mobilities of ionic species within the soil. Difficulties in quantifying such parameters across a wide range of soil types (with different ionic species and concentrations) make it more practical to simplify the method to a governing equation with a single soil conductivity parameter, used by most researchers [125], [129], [130], [138]–[143].

Reaction kinetics at electrode-electrolyte interfaces is a key determiner of final results in any corrosion model. Formerly, problems in obtaining reliable tabulated kinetic parameters have led to a wide range of values being used in studies. Yet, dependable parameter values or models can be obtained from experiments run in conditions simulating a specific system. Such an approach was presented by Riemer and Orazem [138] using polarization curve parameters for reaction kinetics at the corroding buried structure and real coating properties for CP current leakage through disbonded coating sections. The polarization curve used to represent the contributions of the anodic Fe oxidation reaction and the cathodic O₂ reduction and H evolution reactions took the form of {E-2.4}, where i is the net current density, i_{lim,O_2} is the current density for O₂ reduction limited by mass transfer, β is the Tafel slope (specific to each reaction), Φ is the off-potential of the pipe, and E is the effective equilibrium potential specific to each reaction, taking into account the influence of exchange current density.

$$i = 10^{\frac{\Phi - E_{Fe}}{\beta_{Fe}}} - \left(\frac{1}{i_{lim,O_2}} + 10^{\frac{\Phi - E_{O_2}}{\beta_{O_2}}} \right) - 10^{\frac{-(\Phi - E_{H_2})}{\beta_{H_2}}} \quad \{\mathbf{E-2.4}\}$$

Similarly, Muehlenkamp et al. [33] reported using parameter values for their modelled system from measurements presented in [143]. Nonetheless, since almost all examples of this approach involve parameter values being extracted from the experimental results based on the model intended to govern reaction kinetics in the simulation (e.g. Tafel), incongruities between the governing kinetics model and the actual experimental data are inevitable.

2.4.2 Models of the residual strength and integrity of corroded pipelines

The corrosion of load-bearing metals in engineering applications leads to reduction of their structural integrity and eventually complete failure of the overall system. In the pipeline industry, dependable criteria utilized to evaluate the burst pressures and residual strengths of corroded pipeline are very valuable. The most famous of such criteria developed in the past is the ASME B31G code [144], which was later revised for over-conservatism to yield the 0.85*dL* method [145]. The B31G model for predicting the burst pressure (P_b) of a corroded pipeline is evaluated through {E-2.5}, where t is the wall thickness, D is the outer diameter ($D = 2R$, R : outer radius), d is the maximum defect depth, L is the defect length, and σ_y is the material yield stress at an offset strain of 0.5%. Another established code is Det Norske Veritas (DNV), evaluated by {E-2.6}, where γ_m is the partial safety factor for model prediction, σ_{UTS} is the material ultimate tensile strength, γ_d is the partial safety factor for corrosion depth, $(d/t)_{meas}$ is the measured relative corrosion depth, ε_d is the factor defining fractile value for corrosion depth, and $StD \cdot [d/t]$ is the standard deviation of $(d/t)_{meas}$ based on the specification of the inspection tool.

$$P_{b,B31G} = \frac{2t}{D} (1.1S_y) \left[\frac{1 - \left(\frac{2}{3}\right)\left(\frac{d}{t}\right)}{1 - \left(\frac{2}{3}\right)\left(\frac{d}{t}\right)(M_T^{-1})} \right] ; M_T = \sqrt{1 + 0.8 \frac{L^2}{Dt}} \quad \{\mathbf{E-2.5}\}$$

$$P_{b,DNV} = \gamma_m \frac{2t\sigma_{UTS} \left(1 - \gamma_d \left(\frac{d}{t}\right)^*\right)}{(D-t) \left(1 - \frac{\gamma_d \left(\frac{d}{t}\right)^*}{Q}\right)} ;$$

$$Q = \sqrt{1 + 0.31 \left(\frac{L}{\sqrt{Dt}}\right)^2} ; \left(\frac{d}{t}\right)^* = \left(\frac{d}{t}\right)_{meas} + \varepsilon_d StD \left[\frac{d}{t}\right] \quad \{\mathbf{E-2.6}\}$$

In these two codes, only the L and d dimensions are needed to define the corrosion defect. Addressing the simplifications/assumptions of such codes and creating enhanced and more realistic models for corroded pipelines is an active area of research. Netto et al. evaluated the residual strength of pipelines with single longitudinal corrosion defects through small-scale

experiments and finite element simulations [146]. Real defects in the physical pipeline were produced using a spark erosion process, adjustable for different defect sizes. Amongst the geometric parameters, the experimental P_b upon internal pressurization was most affected by the maximum d . P_b values predicted by the computer model were lower than experimental counterparts; thus, they could be used to obtain lower bound estimates of the response of pipes with similar defect sizes and shapes. In numerical investigations, real corrosion defect geometries are hard to replicate, so most models simplify defect geometries to semi-elliptical, semi-spherical, or constant depth contours. Pipeline material models include elasto-plastic, finitely deforming solids with isotropic hardening [146], elastic-plastic simple power hardening [147], and substitutive Bilinear Isotropic Hardening (BISO) material curves [148] adopted from data for grades such as API X60 and API X65 ([149] and [150], respectively). A simulated P_b is the pressure which causes the Von-Mises equivalent stress (σ_{VM}) at the bottom of the defect (i.e. maximum d) to equal the σ_{UTS} of the material.

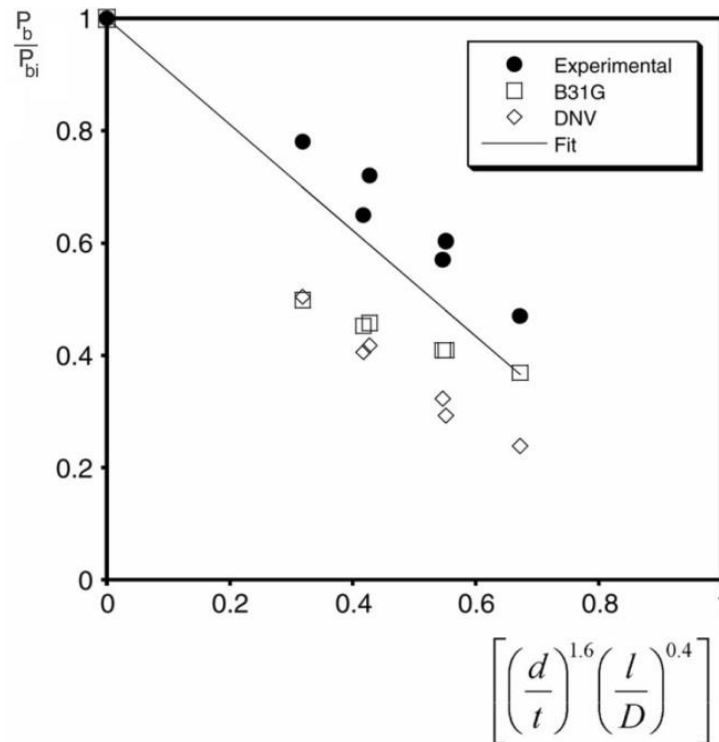


Figure 2-13: Comparisons between experiments, the linear fit (i.e. {E-2.7}), and predictions from DNV and B31G codes [146]

The L dimension of corrosion defects does not influence the P_b values significantly, whereas d does [146], [148]. Circumferential length (or width, c) of the defect has a tangible but minor influence on P_b [146], [151] which increases with the growth of the c/L ratio [148] but is always less of an influence than that of d . Netto et al. used their results to develop a simplified formula, {E-2.7}, to rapidly evaluate structural integrity diminishment due to external corrosion. In this expression, P_{bi} is the burst pressure of an intact pipe. This formula correlates well with their experimental test results, and confirms conservatism of previous B31G and DNV codes (Figure 2-13).

$$\frac{P_b}{P_{bi}} = 1 - 0.9435 \left(\frac{d}{t}\right)^{1.6} \left(\frac{l}{D}\right)^{0.4};$$

$$\frac{c}{D} \geq 0.0785, 0.1 \leq \frac{d}{t} \leq 0.8, \text{ and } \frac{l}{D} \leq 1.5 \quad \{\mathbf{E-2.7}\}$$

Choi et al. presented a three-dimensional (3D) elastic-plastic Finite Element Model (FEM) with a stress-based failure criterion used to simulate pipeline burst tests [151]. σ_{VM} values at the defect are compared to different factored reference strength (S) values (yield strength: S_Y , flow strength: $S_f = 1.1 \cdot S_Y$, and σ_{UTS}). The best correlation with the experimental data is achieved with the σ_{UTS} reference. Regression analysis of the results yield a limit load expression as a function of the non-dimensional parameters \sqrt{Rt} , R/t , and d/t . This produces slightly conservative estimates of excellent overall agreement with experimental results. Recently, Xu and Cheng studied the structural performance of X65, X80, and X100 also using FEM, comparing their results to the established codes B31G, RSTRENG, and DNV [152]. A non-linear elasto-plastic material model was used for all the steel grades. The σ_{VM} -based yield criterion for P_b was less conservative than the codes, for d values up to 40% of the wall thickness t . As d increases, the model results became more conservative. Since pipelines frequently experience external rigid body loads like bending or soil-induced strains, the authors investigated the effect of coupling the presence of a defect with a longitudinal applied pre-strain on the structure. P_b of the corroded

pipe was reduced with applied tensile or compressive pre-strain, though tensile pre-strain was notably more detrimental.

Bedairi et al. recently investigated the hybrid pit-crack defect known to occur during external corrosion of pipelines [53]. The crack initiates from the base of the corroded region (Figure 2-14) simulating the initial stages of SCC, and is termed a Crack-in-Corrosion (CIC) defect. After material characterization determining strength and toughness values (tensile and Charpy V-notch testing, respectively), an elastic-plastic material model is used. For basic corrosion defects, a typical σ_{UTS} -based criterion is used like most other investigations, whereas for crack defects, the criterion was based on energy: if the J-integral value in the vicinity of the crack reaches the critical fracture toughness of the material ($J_{0,2}$), the failure is predicted to occur by fracture. Simulation results were, on average, 17% more conservative than the experimental results obtained by the authors in previous models [153]. This conservatism increased with d , demonstrating the impact of crack profiles and dimensions on P_b . CIC is modeled as a double-profile defect, where both the crack and the corrosion defect are modelled as flat bottom uniform depth profiles (Figure 2-14b) to avoid meshing problems. The authors suggest further studies investigating different pipe geometries, material properties, and crack profiles.

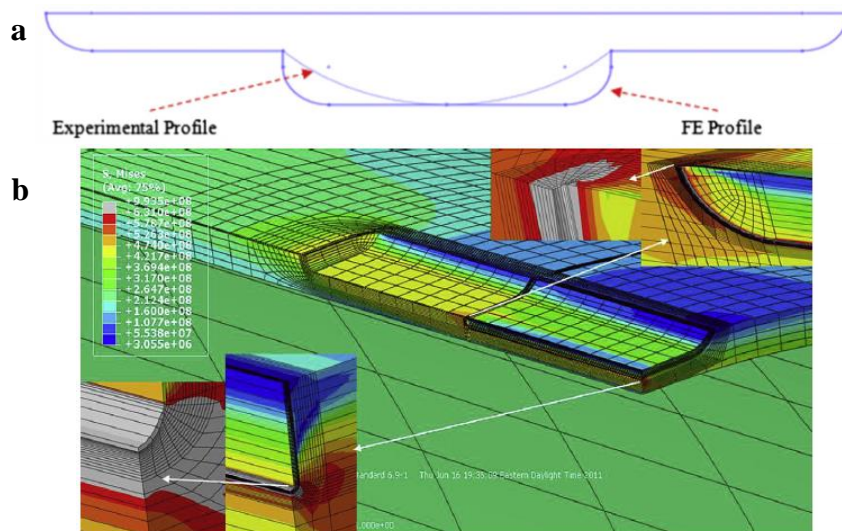


Figure 2-14: (a) Experimental and FEM CIC defect profiles; (b) 3D simulation results for 60% wall thickness CIC defect model, showing spatially-dependent σ_{vM} from a 5.59 MPa internal pressure [53]

3. Objectives

In the multi-faceted review of relevant previous literature presented above, it is apparent that some environmental, material, and surface/interfacial aspects of HSLA steel corrosion in nn-pH soil environments are understudied or completely unexplored. Due to the consequential influence of HSLA steel grade on corrosion and mechanical behaviors, these less studied topics require dedicated investigations on each steel grade. Exploring knowledge gaps therein and contributing to a more complete understanding of corrosion mechanisms in nn-pH soil environments thus has unique novelty when conducted on modern HSLA steels such as API X100. Likewise, developing and improving numerical models of X100 corrosion in nn-pH soil environments based on dedicated laboratory experiments is of particular benefit to the corrosion science and pipeline integrity fields.

The goal of this work is to contribute to a comprehensive understanding and modelling capability of the corrosion of X100 pipeline steel in nn-pH soil environments. Practically, the fulfillment of the key technical objectives outlined in the proceeding section (3.1) contributes towards the improvement of external pipeline corrosion control methods and design guidelines, especially CP standards. The results of this work highlight the specificity of environmental, material, and surface conditions on the external corrosion of buried pipelines. Simple standard testing environments and corrosion control guidelines do not adequately address the full spectrum of integrity-threatening situations present in practice. A better understanding of the fundamental corrosion processes occurring across the full nn-pH range, coupled with enhanced simulation ability of the corrosion processes, can therefore increase the safety and reliability of buried pipeline infrastructure.

3.1 Key technical objectives

- {1} Study the effects of pH-altering electrolyte constituents and properties (HCO_3^- , dissolved CO_2 , and temperature) on X100 corrosion behavior, in concentrations and combinations with resultant nn-pH values in the 5 – 9 range.
- {2} Investigate the impacts of HCO_3^- , Cl^- , SO_4^{2-} , nitrate (NO_3^-), and temperature on anodic/cathodic and passivation processes on X100 in nn-pH HCO_3^- electrolytes, including the semiconductive properties of the passive layer(s).
- {3} Identify the specific role of dissolved O_2 in the formation and evolution of iron-oxides/oxyhydroxides on X100 surfaces in nn-pH aqueous electrolytes, and assess the inhibition effectiveness of an O_2 -scavenger chemical treatment to mitigate corrosion in O_2 -containing nn-pH soil environments.
- {4} Evaluate hydrogen evolution, permeation, and diffusion behaviors for X100 steel in nn-pH HCO_3^- electrolytes, considering the impacts of HCO_3^- and dissolved CO_2 concentration, temperature, and surface condition.
- {5} Develop a numerical model of physiochemical soil/electrolyte phenomena (CP current, O_2 diffusion, and heat transfer) to simulate the corrosion and structural integrity of buried pipelines at coating failure sites.

4. Approach and methodology

In order to achieve the proposed objectives listed in section 3.1, this work includes a comprehensive set of experiments coupled with numerical multiscale models and simulations. The electrochemical tests of corrosion, passivation, and hydrogen-related processes are designed to achieve objectives {1} to {4} separately. Fulfillment of objective {5} is achieved through the incorporation of laboratory results from previous objectives into numerical models developed on a commercial Multiphysics software package, as described in section 4.3 and chapter 9.

Each set of laboratory experiments is performed using a combination of the following electrochemical techniques: OCP, Linear Polarization Resistance (LPR), Potentiodynamic Polarization (PDP), Potentiostatic Polarization (PSP), EIS under OCP or PDP conditions, and Mott-Schottky. Optical Microscopy and Scanning Electron Microscopy (SEM) are used to determine the microstructure of the X100 specimen and the morphologies of corrosion products and passive layers. Evaluations of the chemical composition of the steel or the corrosion products forming under different test conditions is conducted using one or more of the following techniques: Energy-dispersive X-ray Spectroscopy (EDX/EDS), X-ray Diffraction (XRD), X-ray Photoelectron Spectroscopy (XPS), Inductively Coupled Plasma Mass Spectrometry (ICP-MS), and Raman Spectroscopy. Hydrogen permeation and diffusion tests are performed in a hydrogen permeation electrochemical setup [154] (also known as a Devanathan-Stachurski cell [155]).

4.1 Material and specimen preparation

API X100 pipeline steel is the material used throughout this work. All the specimens tested in the laboratory studies of this work are cut from a larger steel section removed from an oil pipeline manufactured by Evraz Inc. The chemical composition of this HSLA steel section is evaluated with ICP-MS, the results of which are listed in Table 4-1 along with the corresponding carbon equivalent (CE), which is calculating using: $CE = \%C + \%Mn/6 + \%Cr/5 + (\%Mo+\%V)/4 + (\%Cu+\%Ni)/15$.

Table 4-1: Chemical composition and carbon equivalent (CE) of API X100 steel used in laboratory tests

Composition [wt%]	C	Mo	Mn	Al	Ni	Cu	Ti	Cr	V	Nb	CE
	0.1	0.19	1.66	0.02	0.13	0.25	0.02	0.016	0.003	0.043	0.45

4.1.1 Microstructural evaluation

Microstructural evaluation of the X100 steel is performed using a Nikon EPIPHOT 300 series Optical Microscope and ImageJ analysis software. Polishing is performed with 6 and 1 μm diamond suspension abrasives, then samples are etched with freshly prepared 2% nital (2 mL nitric acid (HNO_3) and 98 mL ethanol ($\text{C}_2\text{H}_6\text{O}$)) or LePera solution [156] (1:1 ratio of 4 g picric acid ($\text{C}_6\text{H}_3\text{N}_3\text{O}_7$) in 100 ml $\text{C}_2\text{H}_6\text{O}$ and 1 g sodium metabisulfite ($\text{Na}_2\text{S}_2\text{O}_5$) in 100 ml deionized H_2O , mixed immediately beforehand) to reveal ferrite or martensite-retained austenite (M-A) phases, respectively. Samples are etched for ~ 15 s in 2% nital or for ~ 35 s in LePera solution.

The formation of different phases in HSLA steels is reported to be reliant on three main factors: prior austenite grain size before cooling, the cooling rate during processing, and the state of Nb (i.e. in solution or precipitated) [157]. Grain boundaries are preferential sites for new phase nucleation, and since the ferrite nucleating on the austenite grain boundaries grows into grains through a diffusional transformation, cooling rate influences the process. From the micrograph of the X100 steel sample etched in 2% nital (Figure 4-1a), the presence of ferrite structures is evident in different forms as identified by arrows. In general, the majority of ferrite observed in the steel sample is irregular; featureless grains with non-smooth borders or, in many instances, needle-like ferrite formations are seen. Phase quantification of the ferrite was performed based on color contrast with bainitic regions, which also contain M-A, yielding a content around 45%. This result depends on the color intensity and shape criteria employed in the image analysis. Phase quantification was therefore done with a range of realistic intensity and shape criteria, and conducted on micrographs from other regions. The results yielded were generally within an acceptable $\pm 10\%$ range of the value reported here. Indeed, this 45% ferrite content compares favorably with similar HSLA pipeline steels like X80 in the as-received condition [158].

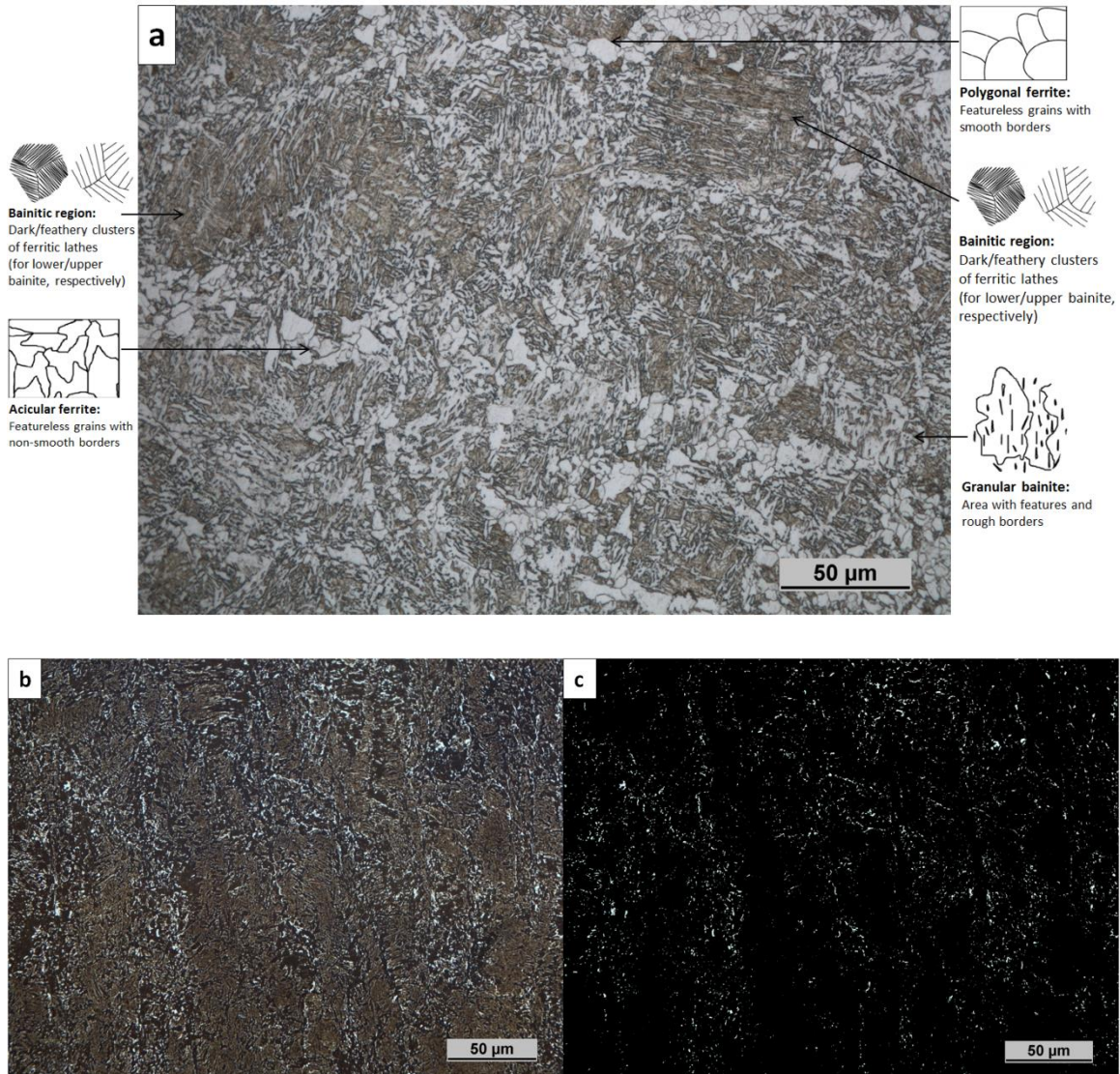


Figure 4-1: Microstructure of API X100 steel sample etched with: (a) 2% nital, with corresponding differentiation of ferrite and bainite phases according to ASTM E562-08; and (b) LePera solution; (c) graphical representation of M-A phase identification using ImageJ analysis software

It is established that prior austenite grain boundaries cannot be observed for ferritic structures, whereas they are noticeable for bainitic structures. Bainitic regions in the steel microstructure are observed in Figure 4-1a, yet it is difficult to identify specific forms of bainite (aside from the granular form) or M-A phases in these regions with a 2% nital etchant. Instead, LePera etchant was used, with which M-A phases appear white, bainite appears black, ferrite appears tan, and grain boundaries are not strongly etched [156]. Figure 4-1b shows the results of

LePera etching and the corresponding Figure 4-1c shows isolation of the martensite phase for fractional content measurement using ImageJ. Based on the analysis of several captured micrographs after LePera etching, the M-A content of the sample is deemed to be within the 4-5% range. The remaining phase (i.e. bainite of all forms) constitutes around 50%. Both increased prior austenite grain size (which decreases the concentration of preferential nucleation sites at grain boundaries) and Nb presence will necessitate a higher driving force for phase transformations to happen, through increasing the transformation temperature. Hence, the increased M-A% of as-received X100 compared to weaker grades such as X80 is closely related to the higher Nb presence (0.043 vs. 0.034 wt. %, respectively [158]).

4.1.2 Preparation of specimens

Laboratory specimens for all electrochemical tests are connected to wires using conductive silver (Ag) paste and then mounted in hard cold-curing epoxy resins. High-temperature epoxy resins are used for any test which involved temperatures $\geq 50^{\circ}\text{C}$. Only a flat surface is exposed to solutions in all tests. ASTM G1-03 standards are followed for chemical cleaning [159]. Before each experiment, specimens are sequentially wet-ground with 320, 600, and 1200 grit silicon carbide (SiC) papers and subsequently degreased ultrasonically in acetone ($\text{C}_3\text{H}_6\text{O}$) for 10 minutes. Then, they are rinsed in deionized H_2O and dried in a stream of cool air.

For H permeation and diffusion tests, the X100 pipeline section is cut from the half-thickness plane to produce thin square sheets, with a side length of 15 mm. Both sides of the thin steel samples used for these experiments are ground with 800 grit SiC paper to obtain a final thickness of 1 mm. One side of the samples is further ground and polished with 1 μm diamond suspension for Palladium (Pd) coating. The choice of this sample thickness ensures a diffusion controlled regime during permeation experiments [160], [161]. This behavior is validated through calculations on preliminary results, but the details are not presented here. After sonication in ethanol for 5 min and then drying in air, the detection side (also referred to as oxidation or exit

side) of each sample is immediately coated with 99.99% Pd using a vapor deposition Edwards Coating System E306A [162]. In this coating system, the solid Pd source cube to be evaporated is placed in a filament crucible through which a large current is passed. The crucible and Pd coating metal are placed at the base of a sealed dome which is kept at a vacuum pressure. On the top end of this dome is the steel sample, with the detection side facing the crucible. As the Pd melts in the crucible then evaporates, a very thin film (i.e on the order of 10^{-9} m) is deposited uniformly on the exposed surface of the steel sample. The coated samples are then carefully removed from the machine, cleaned, and stored appropriately in a desiccator until tested (see section 4.2.3).

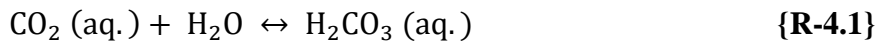
4.2 Test environments and methods

Laboratory tests in this study are conducted in nn-pH HCO_3^- -based solutions between pH 5 – 9, containing different concentrations of Cl^- , SO_4^{2-} , NO_3^- , Na^+ , K^+ , Ca^{2+} , Mg^{2+} , dissolved CO_2 , dissolved O_2 , and temperature. The specifics of each test environment depends on the corrosion and passivation aspects being investigated, and will be described in each corresponding chapter separately. Moreover, test routines are designed with various electrochemical procedures, microscopy methods, and chemical characterization techniques to achieve the key technical objectives outlined in section 3.1. Each particular investigation in this study will utilize a combination of at least three of these various methods, as will be shown in each chapter accordingly. A general overview of the parameters and devices used in the electrochemical, microscopy, and chemical characterization techniques is described in sections 4.2.2 – 4.2.4.

4.2.1 Standard NS4 solution and variants

Generally, a baseline reference solution is used for all the environmental conditions studied here, namely NS4 at 25 °C purged with 5% CO_2 /95% N_2 . NS4 solution has the following ionic composition in M [162]: 5.75×10^{-3} HCO_3^- , 5.75×10^{-3} Na^+ , 4.10×10^{-3} Cl^- , 1.64×10^{-3} K^+ , 1.23×10^{-3} Ca^{2+} , 5.32×10^{-4} SO_4^{2-} , and 5.32×10^{-4} Mg^{2+} . In this standard form, NS4 is one simulation of the nn-pH electrolyte typically found under disbonded pipeline coatings, as

determined through chemical analysis of such electrolytes from real coating disbondments in the field [13]. From this baseline standard reference, more alkaline or more acidic HCO_3^- -based conditions are instigated by changing HCO_3^- content, purging gas, and temperature. Increased CO_2 dissolves in the solution as H_2CO_3 , with a concentration dependent on the partial pressure of CO_2 . This reduces solution pH by shifting the $\text{H}_2\text{CO}_3/\text{HCO}_3^-$ equilibrium of {R-4.2} in the solution. HCO_3^- concentration has a direct influence on this equilibrium – added HCO_3^- increases the pH by pushing {R-4.2} to the left.



The varying of HCO_3^- content, purging gas, and temperature simulates the wide diversity of nn-pH electrolytes and addresses the need to study different environmental parameters within the nn-pH range, arising from the concentration cell effect in the disbondment crevice. Cl^- and SO_4^{2-} additions to solutions are also studied, although they do not change their corresponding solution's pH. All environments throughout this work are created using double-distilled deionized H_2O , analytic grade reagents, and Praxair® 99.99% purity purging gas or gas mixtures.

4.2.2 Electrochemical test methods for corrosion and passivation processes

Electrochemical experiments conducted to investigate corrosion and passivation processes in this study are performed in a glass jacket test cell with a total volume of 0.6 L. Extended immersion experiments are performed either in the same glass jacket test cell or in individual glass containers of a smaller 0.2 ml volume. The temperature of the solution in the glass jacket test cell is regulated by connecting the cell to a circulation water heater equipped with an accurate digital controller. In immersion tests the proper solution temperature is achieved by placing the cells on a digitally controlled hot-plate. In both cases, temperatures are periodically verified using a thermometer inserted in the cells. The cells are sealed from the external atmosphere except for a vent in the gas purger to prevent pressure buildup. Experiments are left

open to air or purged with some form of gas or gas mixture before specimen immersion until test completion.

A conventional three-electrode setup is used for electrochemical measurements. The working electrode in the tests is the studied X100 specimen and the counter electrode or auxiliary electrode is a slender graphite rod or a platinum wire mesh. The reference electrode used is a SCE of $+0.241 V_{SHE}$, isolated in a salt bridge which is electrochemically in contact with the working electrode through a Luggin capillary tube with a low leak-rate Vycor frit. The potentiostats used are either Princeton Applied Research Versastat machines controlled by the accompanying VersaStudio software, or Gamry Reference 600 machines controlled by the accompanying Gamry Electrochemical Suite software package. Figure 4-2 shows a schematic of the experimental setup used to acquire all OCP, LPR, PDP, PSP, EIS under OCP or PDP conditions, and Mott-Schottky results presented throughout this dissertation.

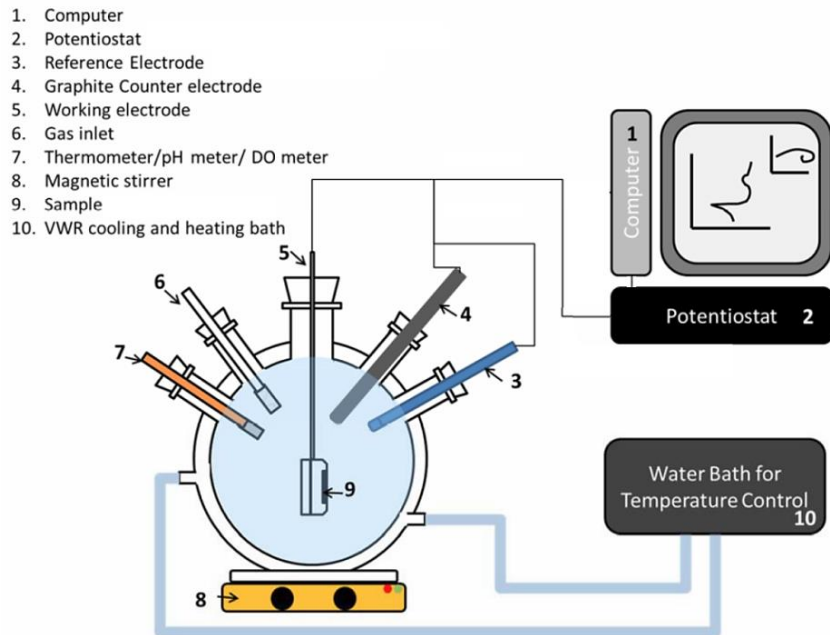


Figure 4-2: Schematic of experimental setup for electrochemical tests of corrosion and passivation [162]

Electrochemical tests are performed after the proper solution temperature is verified ($\pm 1^\circ C$) and the pH of the solution reaches a stable state under the effect of gas purging, if present (maximum change of ± 0.2 pH during 15 minutes). To reach this condition, at least 30 minutes of

pre-immersion gas purging is normally required for all tests. Immediately following specimen immersion, a potentiostatic voltage of $-1.5 V_{SCE}$ is always applied for 1 minute in order to remove any air-oxide film on the steel surface. Each set of tests designed to achieve a specific objective in the overall thesis comprises of at least two electrochemical techniques, for confirmation of measured behaviors. The following is a brief description of the parameters used for each technique:

- **OCP** testing immediately follows immersion and the short cathodic cleaning routine. Specimens are held at OCP until a stable profile is achieved, characterized by fluctuations no greater than ± 0.1 mV/s. This is often achieved within 30 minutes to 1 h of immersion. For extended immersion tests, specimens are held at OCP for 24 h, within which changes in profiles are observed mainly due to corrosion product development on the surface.
- **PDP** testing is carried out following stable early stages of OCP, between cathodic and anodic potentials chosen for the specific processes of interest, described in subsections of each chapter accordingly. Cathodic potentials in the PDP tests are not less than $-2.0 V_{SCE}$, and anodic potentials are not greater than $1.6 V_{SCE}$. PDP sweeps are carried out at a standard scan rate of $1/6$ mV/s [163], 0.5 mV/s, or 1 mV/s deemed suitable for revealing the vital corrosion kinetics features of the system, since previous studies of pipeline steel in HCO_3^- solutions have appropriately used them (1 mV/s upper limit [164]).
- **LPR** tests are performed to extract R_p and corrosion rate information, within ± 10 mV or ± 20 mV of OCP depending on the specific test. These quick sweeps are always conducted at a standard scan rate of $1/6$ mV/s [165] and repeated three times to ensure reproducibility – the corresponding results are averaged and confidence intervals are presented to ensure statistical relevance.
- **EIS** is utilized extensively in this study to evaluate interfacial processes [166] and surface interactions on unpolarized specimen after 1 h immersions and during 24 h extended

immersions, and on polarized specimen in a dynamic EIS routine [167], [168] employed to study anodic and cathodic processes. For EIS tests in this study, the AC disturbance signal is 10 mV, the measurement frequency (ω) range is between 0.01 Hz and 20 kHz (or 0.1 Hz – 10 kHz for some tests), and the sampling rate is 10 points/decade. All EIS results are analyzed and fitted to electrochemical equivalent circuits (EEC) using the ZSimpWin software.

- **PSP** is performed for the tests in section 6.3 to grow passive corrosion product layers for EIS and Mott-Schottky evaluations. Nonetheless, in this PSP or anodizing step conducted at 0.5 V_{SCE} for 1 h, i_{corr} decay behaviors are recorded and used to corroborate the results interpreted from other techniques.
- **Mott-Schottky** tests are performed to study the influence of HCO₃⁻, temperature, and pH on the semiconductive properties of passive corrosion product layers following anodizing. Mott-Schottky tests in this study are scanned between -0.5 V_{SCE} and 1 V_{SCE} at a frequency of 1 kHz and with a step height of 20 mV.

4.2.3 Electrochemical test method for hydrogen permeation and diffusion

Tests of H permeation and diffusion in the thin X100 specimens prepared specifically for this purpose (see section 4.1.2) are performed in a H permeation electrochemical setup [154] (also known as a Devanathan-Stachurski cell [155]). Figure 4-3 shows a general schematic of the setup. In the H permeation and diffusion experiments of this study however, the charging cell (entry compartment) and oxidation cell (exit compartment) are of the same volume, and both reference electrodes are inserted within Luggin capillary tubes with frits close to their corresponding sides of the specimen. The following points, as mentioned in the ASTM G148 standard [154], summarize the hydrogen permeation and diffusion procedure in this apparatus. Further details on the electrochemical apparatus and methods of studying H diffusion, permeation, and solubility in metals can be found in [154], [169].

- The metal membrane (i.e. specimen) of interest is inserted between the hydrogen charging and oxidation cells. The charging cell contains the environment of interest. H atoms are generated on the membrane surface exposed to this environment. In this work, these atoms are the result of corrosion processes on the steel, namely cathodic reduction reactions.
- Some of the H atoms generated on the charging side diffuse through the membrane and are then oxidized on exiting from the other side of the metal in the oxidation cell.
- The conditions (for example, environment and the electrode potential) on the oxidation side of the membrane are controlled so that the metal surface is either passive or immune to corrosion. Additional material (usually Pd), either plated or sputter deposited/coated onto or clamped against the specimen on the oxidation side, may be used to achieve this provided that it is demonstrated that the introduction of this additional interface has no effect on the calculated diffusivity. The background current established under these conditions prior to H transport should be relatively constant and small compared to that of the H atom oxidation current.
- The electrode potential of the specimen in the oxidation cell is controlled at a value sufficiently positive to ensure that the kinetics of oxidation of hydrogen atoms are limited by the flux of hydrogen atoms (i.e. the oxidation current density is diffusion limited).
- The total oxidation current is monitored as a function of time. The total oxidation current comprises the background current and the current resulting from oxidation of hydrogen atoms. The latter is the permeation current.

In the present study, the Pd coated X100 steel sample (as described in section 4.1.2) was mounted between the hydrogen charging and oxidation cells to expose a circular region of approximately 1 cm² area to the solution on each side. The experiment is commenced by filling the Pd coated side (exit or oxidation) compartment with deaerated (100% N₂) 0.01 M NaOH

solution (pH 12), followed by rapidly applying a potential of 140 mV_{SCE} (1.09 V more positive than the H⁺/H₂ reversible potential at pH 12) and recording the background current density (*i_{bg}*). The applied potential on the Pd coated side ensures fast kinetics of the H oxidation reaction and effectively maintain a H atom concentration of near zero at the Pd coated surface. In each test, after the current density on the exit side reaches a stable value of approximately 70 nA/cm², the other compartment (entry or charging) is filled with the deaerated NS4 solution being tested.

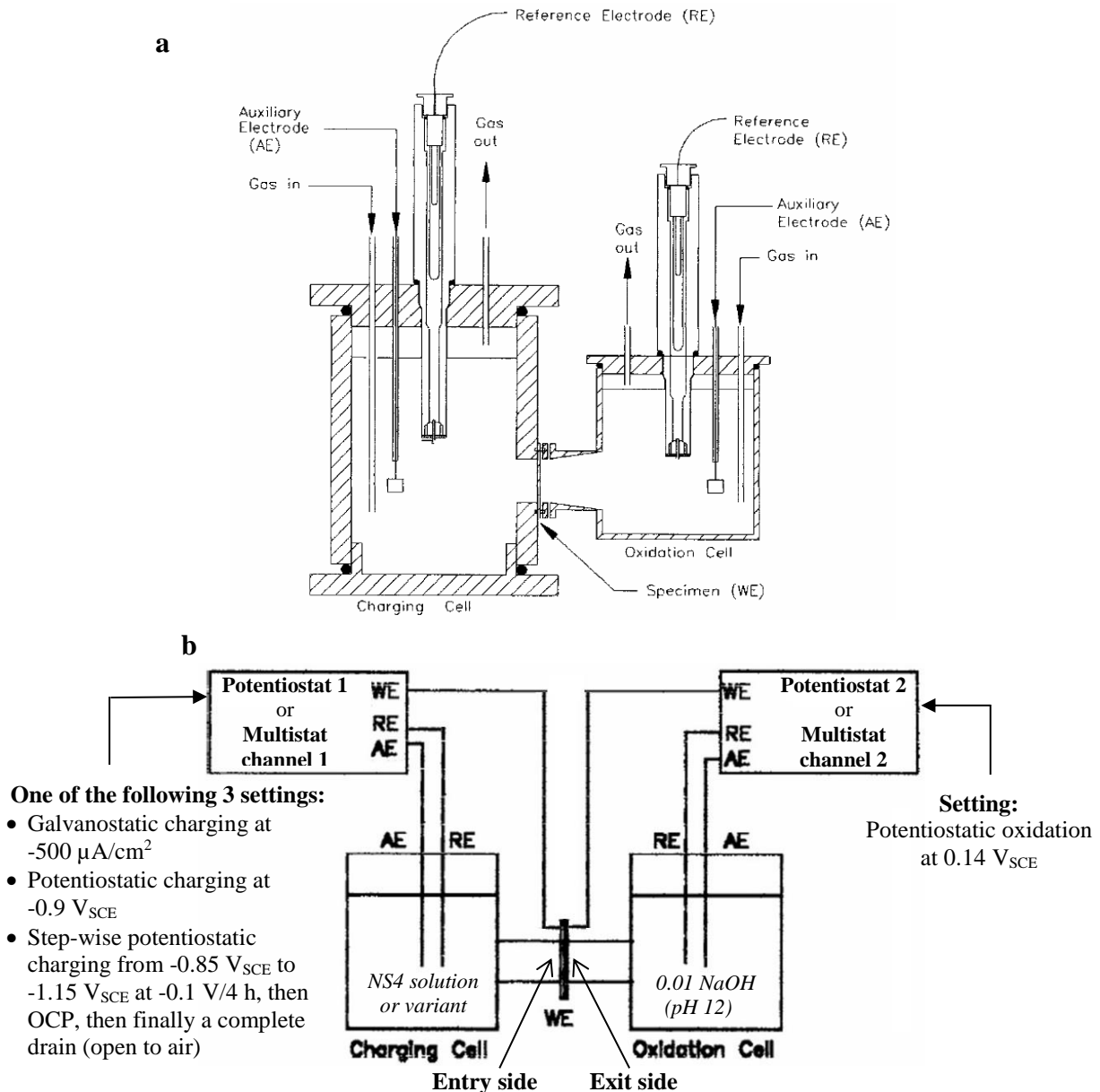


Figure 4-3: Electrochemical H permeation and diffusion cell: (a) components and assembly (b) measuring apparatus and settings (with two potentiostat instruments or two channels of one multistat) [154]

In the entry compartment, H charging is performed under several different conditions. In the first set of experiments, a galvanostatic charging current density of $-500 \mu\text{A}/\text{cm}^2$ is applied to the uncoated face of the sample for up to 10 hours. In the second set of experiments, a constant cathodic potential of $-0.9 V_{\text{SCE}}$ is applied during which the purging gas of the charging solution is switched from 100% N_2 to 5% CO_2 , and then subsequently switched to 100% CO_2 . In the third set of experiments, the surface potential of the steel sample on the entry side is changed by first applying cathodic potentials varying from -0.85 to $-1.15 V_{\text{SCE}}$ with a step size of $-0.1 V$ per step (4 h), then leaving the sample at the OCP, and finally draining the solution in the entry compartment to leave the sample exposed to air.

4.2.4 Microscopy and chemical characterization methods

Morphologies of the corrosion products formed on specimens following laboratory tests are observed using SEM. The SEM images presented in this study are from either a Hitachi S570 model or a Hitachi S3000N Variable Pressure model, both of which use a conventional tungsten hairpin electron gun. All EDX/EDS spectra presented here are obtained using the EDX/EDS capability in the Hitachi 3000N Variable Pressure SEM. XRD characterization results presented throughout this study are obtained using a Rigaku MultiFlex machine with a 2kW x-ray generator, from start angles $\geq 3^\circ$ to a stop angle of 90° . For some XRD routines, corrosion products are scraped off with a clean razor onto a 0-diffraction quartz plate. The x-ray tube $\text{Cu K}\alpha$ settings are 40 kV and 20 mA, and the scan speed is a very slow $0.125^\circ \text{ min}^{-1}$ to minimize noise. XPS characterization is performed on an Omicron & Leybold MAX200 machine with a monochromatic $\text{Al K}\alpha$ X-ray source at 10 kV and 20 mA. For the XPS measurements of this thesis, the system pressure is 2×10^{-7} Pascal (Pa). Raman Spectroscopy is conducted on a Horiba LabRAM HR Raman spectrometer with a 633 nm HeNe laser and a Pelletier-based cooled CCD Si detector. The Raman spectrometer is fitted with an Olympus microscope with a 100x magnification objective lens and has a 1200 line/mm diffraction grating capability.

4.3 Modelling geometries and meshes

This study presents simulation results from two models of the external corrosion of buried pipelines. The first model is at a macroscale, on the order of meters, simulating physicochemical soil phenomena (i.e. heat transfer, CP, and gas diffusion) in soils of various structures and moisture contents, and their effect on corrosion processes at a coating failure site on a buried pipeline. The second model is at a mm-scale in the trapped water region beneath a disbonded external coating of a pipeline. The second model incorporates both a corrosion and a structural stress analysis module – corrosion defect sizes simulated by the former affect the structural integrity of the pipeline, the extent of which is simulated by the latter module.

For the macro m-scale model of pipeline corrosion, and the corrosion module of the mm-scale model beneath a disbonded coating, Comsol Multiphysics® version 4.3a is the modelling software used. The stress analysis module of the second model is developed in ANSYS®. This dissertation will focus more on the first model and the corrosion module of the second model, whereas the development and results from the structural model will only be presented and discussed briefly. In all of the models/modules developed here, the Finite Element Method (FEM) is the numerical technique employed. The presence of spatially varying governing properties in the modelled systems (e.g. diffusivity in soil) is a key reason why FEM is favored over other techniques such as the Finite Difference Method (FDM) or the Boundary Element Method (BEM). FDM has inadequate resolution capabilities & difficulties in handling irregular meshes, moving meshes, and nonlinear effects, while BEM cannot handle the spatially-varying properties of the electrolyte media modelled here.

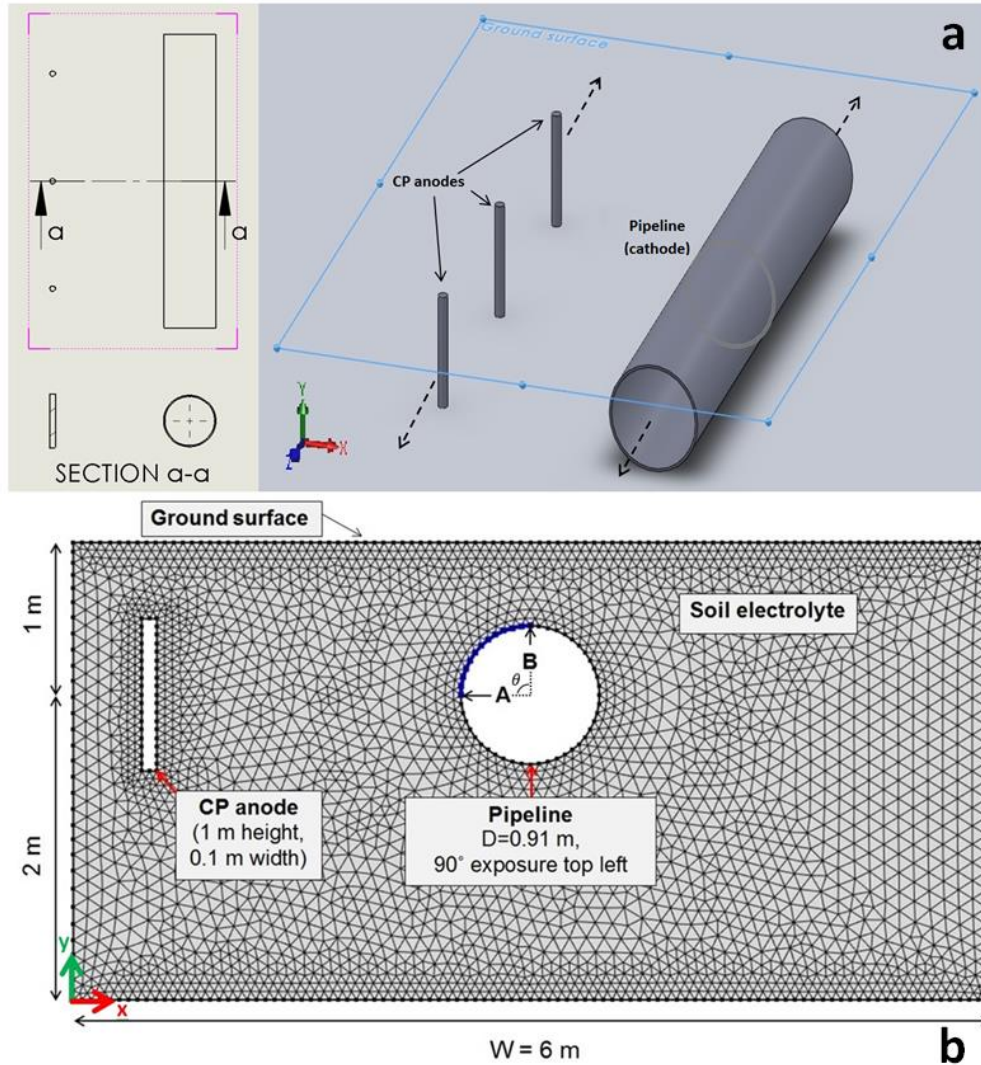


Figure 4-4: (a) 3D representation of buried pipeline with CP anodes (right), and axis of model cross-section (left); (b) 2D representation of model geometry and dimensions

A 3D representation of a sectioned buried CP-pipeline system is shown in Figure 4-4a. A cross-section of this structure is taken at plane a-a resulting in the 2D section shown in Figure 4-4b, which is the basis of the m-scale model in this thesis. The reduction of the 3D geometry to a 2D one permits the use of 2D plane elements and significantly simplifies the model. Consequences of this simplification on simulation results are discussed in chapter 9. Dimensions in the model are the typical values for onshore transmission pipelines [13] in excavated ditches [170]. A 90° arc of the steel is exposed to the corrosive soil environment shown between A and B in Figure 4-4a, representing a site where the protective coating completely

deteriorated. Although the overall size of this defect is larger than would normally be present on a buried pipeline, it is modelled in this way here to identify the varying potential, anodic/cathodic current density, and O_2 concentration distributions at different angles θ . In practice, a single simulation result from the present study can be used to evaluate the disparity between CP and corrosion at $0^\circ \leq \theta \leq 90^\circ$, instead of running separate simulations for each location. Although the influence of localized corrosion is diminished with this approach, the model maintains the ability to investigate localized effects if desired by reducing θ .

A cross-section of the 3D pipeline representation in Figure 4-4a taken on the longitudinal y-z plane results in the 2D section shown in Figure 4-5. The basis of the corrosion module of the mm-scale model is the zoomed portion of this figure, with the assigned dimensions of a suggested coating disbondment in section A-A. CP current availability at the disbondment opening is assumed to be sufficient enough for proper protection (i.e. $-0.85 V_{Cu-CuSO_4}$ or $-0.77 V_{SCE}$ according to the NACE SP0169 standard), while simulating CP shielding and the resulting growth of a corrosion defect at the exposed steel surface. Pipeline wall thickness (t) and coating disbondment width (w) and length (L) dimensions simulated are normal values for standard 36" buried transmission pipelines [35].

Discretization versatility of the FEM is exploited by solving 5 sets of mesh resolutions for the m-scale model, and 3 sets of mesh resolutions for the mm-scale model for all simulated parameters. Field variables within each element are linear throughout this thesis. For the m-scale model, all the meshes are discretized more finely around electrode-soil interfaces and the ground surface boundary for enhanced identification of critical phenomena occurring between the CP anode, the ground surface, and the pipeline's exposed surface. Similarly, all the meshes in the mm-scale model are made finer at the exposed steel surface (electrolyte-electrode interface) for more accurate simulation of the shape and growth of the corrosion defect. Mesh parameter values for the various mesh resolutions are listed in Table 4-2 for the m-scale model of Figure 4-4b. The equivalent mesh details for the mm-scale model can be found in Table E-1 in Appendix E. The

adequacy of the mesh sizes utilized for both models is ensured through suitable convergence in the mesh sensitivity analyses of the results (see section 9.5).

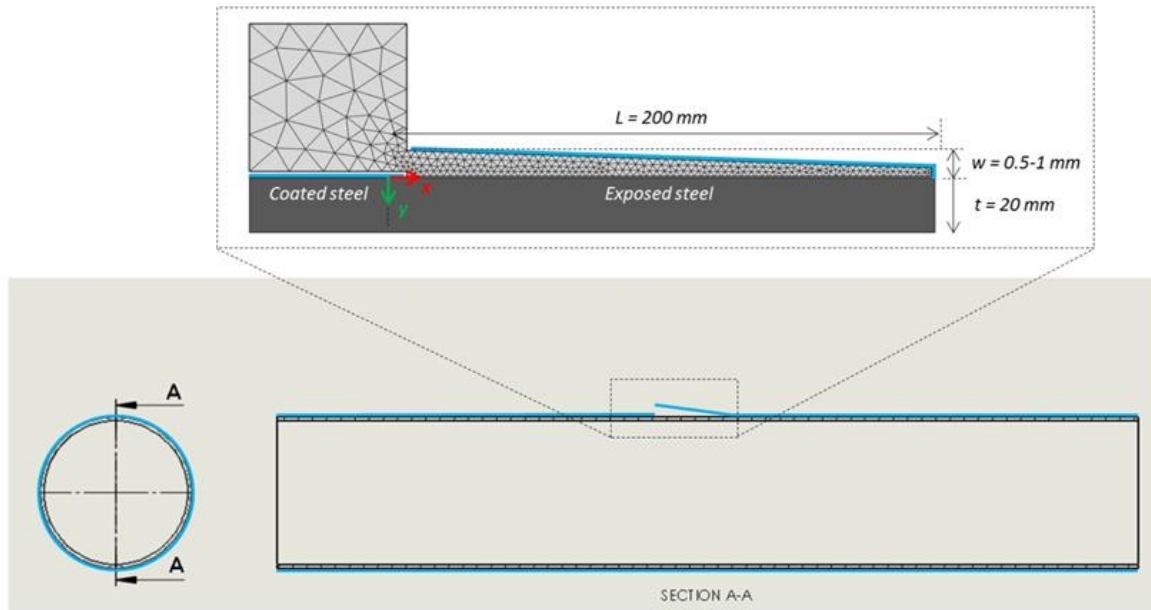


Figure 4-5: 2D cross-section of pipeline in longitudinal plane with coating defect (zoomed section), dimensions, and mesh of trapped water region

Table 4-2: Maximum and minimum element size, maximum element growth rate, and resolution of curvature values for extra coarse to extra fine mesh resolutions, within the soil domain vs. at electrode/ground boundaries in Figure 4-4b

Mesh parameters		Mesh resolution				
		Extra coarse	Coarse	Normal	Fine	Extra fine
In general domain	Maximum/minimum element size	0.402 m/ 1.8×10^{-3} m	0.318 m/ 1.8×10^{-3} m	0.222 m/ 7.5×10^{-4} m	0.120 m / 4.5×10^{-4} m	0.060 m/ 1.2×10^{-4} m
	Maximum element growth rate	1.30 m	1.30 m	1.25 m	1.20 m	1.10 m
	Resolution of curvature	0.30	0.30	0.25	0.25	0.20
At critical boundaries	Maximum element size	0.318 m/ 1.8×10^{-3} m	0.222 m/ 7.5×10^{-4} m	0.120 m / 4.5×10^{-4} m	0.060 m/ 1.2×10^{-4} m	Same as general domain
	Maximum element growth rate	1.30 m	1.25 m	1.20 m	1.10 m	
	Resolution of curvature	0.30	0.25	0.25	0.20	

5. Electrochemical behavior of X100 pipeline steel in deaerated HCO_3^- solutions of near-neutral, mildly acidic, or mildly alkaline pH^{2,3}

External pipeline corrosion and SCC of the nn-pH form occurs in HCO_3^- - CO_3^{2-} trapped water containing small quantities of Cl^- and SO_4^{2-} , with a pH in the range from 5.5 to 8.5 [171]. The role of this local environment on corrosion and the subsequent initiation of cracking in pipeline steels, especially newer HSLA grades, is not completely clear. In specific, an understanding of the effect of changes in pH-altering environmental variables such as H-based electrolyte constituents, % CO_2 in dissolved gases, and temperature on the electrochemical behavior of pipelines steels is lacking. These parameters are coupled in a way that variations in one immediately cause changes in others according to the equilibrium reactions {R-4.1} and {R-4.2} shown in the previous chapter. In addition, the effect of these pH-altering variables on electrochemical behavior appears to be interrelated [64], [65].

The objective of this chapter is to evaluate the influence of combinations of the abovementioned environmental variables on the corrosion behavior of API X100 pipeline steel. The overall pH of the environments tested is kept within or close to the established nn-pH range of 5.5 to 8.5 [13]. A nn-pH solution (NS4 deaerated with a 5% CO_2 /95% N_2 mixture) is used as a reference, and environmental variations are introduced to this condition by changing: ion content (HCO_3^- , Cl^- , and SO_4^{2-}), purging gas (5% CO_2 /95% N_2 , 100% CO_2 , and 100% N_2), and temperature (25, 40, and 55 °C). These three parameters determine the pH of the condition being tested, as shown in Figure 5-1 for a subset of the presented results. An environmental condition matrix stems from different combinations of these variables. Electrochemical kinetics and passivation behavior of the steel are assessed for each condition therein using OCP, LPR, PDP,

² **I. M. Gadala** and A. Alfantazi, *Corrosion Science*, vol. 82, pp. 45–57, May 2014.

³ **I. M. Gadala** and A. Alfantazi, *Metallurgical and Materials Transactions A*, vol. 46, no. 7, pp. 3104–3116, Apr. 2015.

and EIS measurements. This chapter is based on two papers [74], [172] which were published as part of the research work leading towards this PhD thesis.

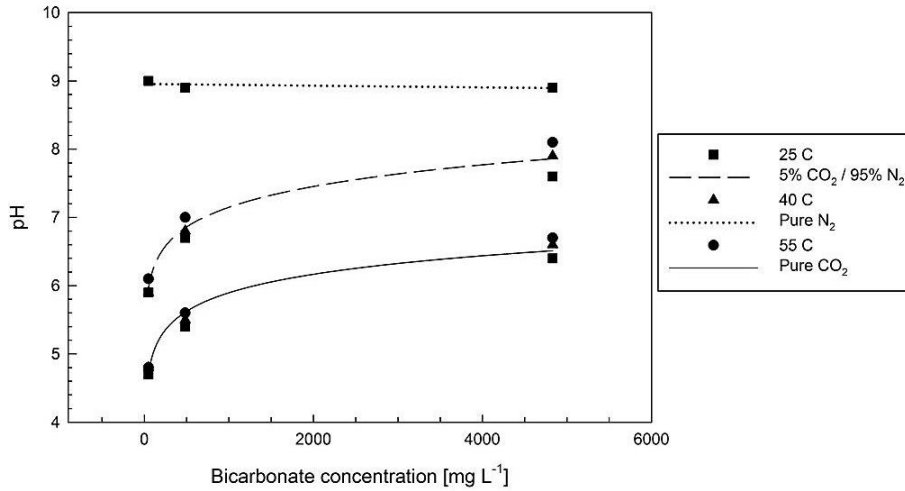


Figure 5-1: Effect of HCO_3^- , purging environment, and temperature on solution pH

5.1 OCP and LPR measurements

The free corrosion potentials (OCP) of the specimens are observed up to about 5000 s to ensure fluctuations are negligible. The OCPs are all below $-710 \text{ mV}_{\text{SCE}}$ and in the anaerobic range [24], consistent with fact that all solutions are deaerated by purging some form of gas or gas mixture. The OCP values for the highest pH solutions are the least noble. As shown in Figure 5-2, OCP values decrease linearly with pH at all temperatures. Each line in this plot represents a single purging environment and temperature. Data points plotted on each line represent the different $[\text{HCO}_3^-]$ investigated (i.e. 48.3, 438, or 4830 mg/L NaHCO_3). Based on the HCO_3^- , dissolved CO_2 , and pH relations discussed in 4.2.1, the trend in Figure 5-2 suggests an increase in the active corrosion of the steel with decreased HCO_3^- content and/or increased CO_2 concentration. A consistent correlation between temperature and OCP is not clear. However, it is observed that in more acidic conditions *within* any single purging environment, higher temperatures increase OCP, and vice versa. This effect is noticed even though the pH of higher temperature solution becomes slightly more alkaline. The trend of decreasing OCP values with pH can be explained by the decrease in cathodic kinetics in {R-5.2} at higher pH.

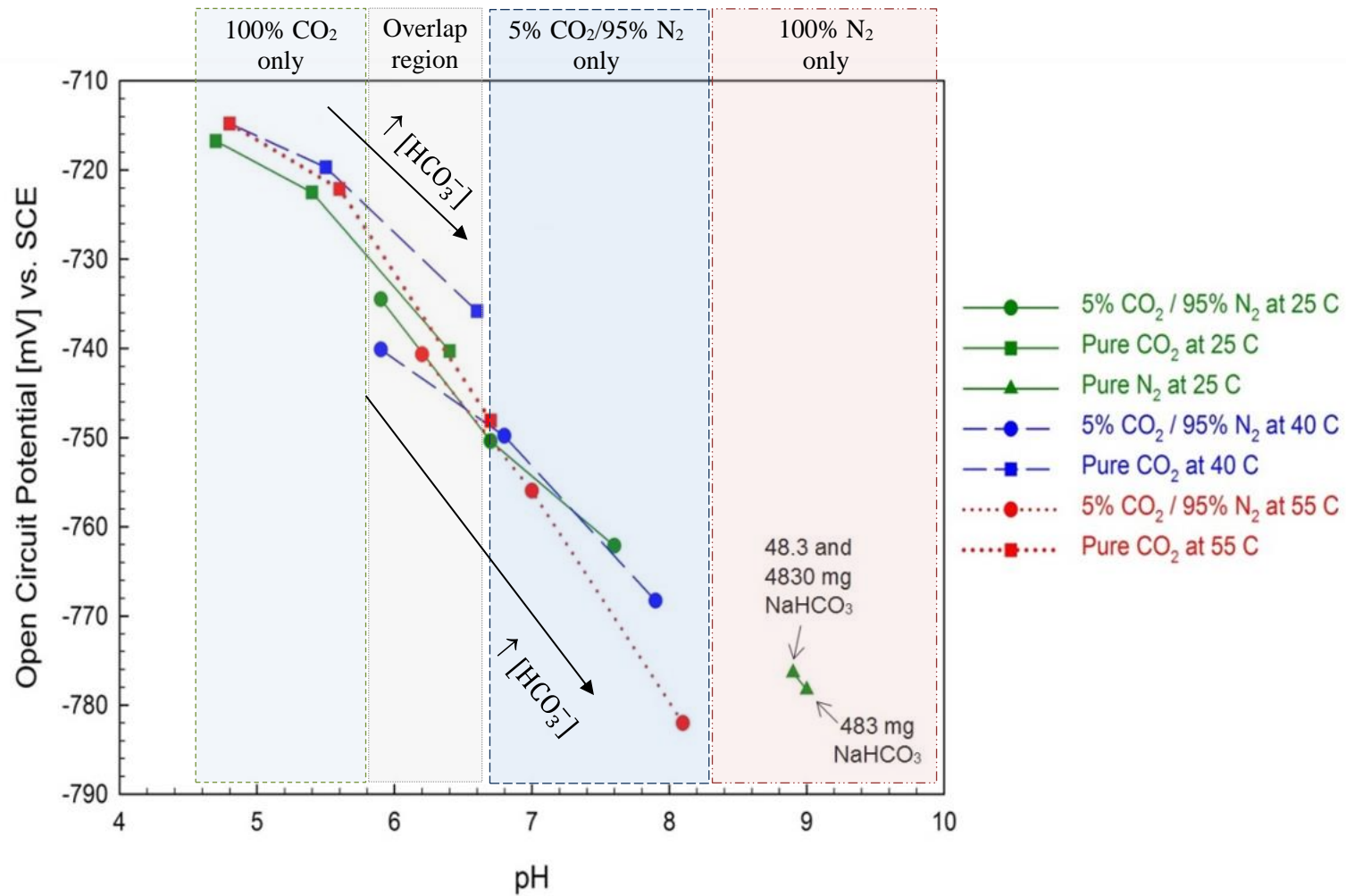


Figure 5-2: Open circuit potentials vs. pH in all solutions free of Cl⁻ and/or SO₄²⁻ additions (varying HCO₃⁻, purging gas, and temperature)



In addition to {R-5.2}, the simultaneous discharge of HCO_3^{-} in {R-5.3} can be present with sufficient HCO_3^{-} content, though it is thermodynamically less favorable than H evolution at lower pH [100]. Larger drops in potential with increased HCO_3^{-} observed in mildly alkaline and nn-pH conditions compared to lower pH conditions is most likely due to {R-5.3} and {R-5.4} becoming more dominant.

Analysis of the “overlap region” between the 100% CO_2 and 5% $\text{CO}_2/95\% \text{N}_2$ purged data in Figure 5-2 advocates that corrosion activity of the steel cannot be determined qualitatively based on the solution pH only. Data points in this region exhibit diverse OCP values although their corresponding solutions possess nearly identical pH. Similarly, a number of points have identical OCPs, such as at the -740 mV or -735 mV mark, although the pH levels of these points vary significantly. The region where this discrepancy occurs in Figure 5-2 is the overlap of data from the HCO_3^{-} -rich solutions purged with 100% CO_2 and the NS4- or below NS4-level HCO_3^{-} solutions purged with 5% $\text{CO}_2/95\% \text{N}_2$. Based on this, it is deduced that quantitative comparisons of corrosion activity in different environments using the pH dependence approach should only be performed in the same purging environment. Other purging environments can be included only if there exists significantly large pH variations (± 1.5 or more) in the solutions.

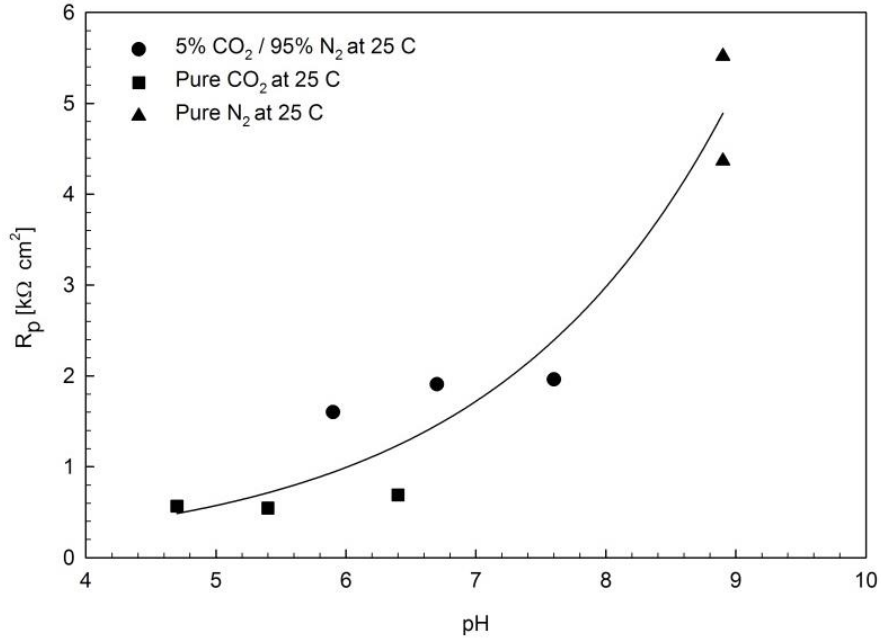


Figure 5-3: Corrosion activity vs. pH based on polarization resistance values of select data

LPR results illustrated in Figure 5-3 are consistent with the OCP findings. The plotted data set in Figure 5-3 was selected from various purging and solution HCO_3^- conditions to observe the overall trend with respect to pH. Between the high pH solutions at 9 (100% N_2 purged NS4 + 10x HCO_3^-) and the low pH solutions at 4.7 (low HCO_3^- content purged with 100% CO_2), an overall decrease in R_p values is observed. Corrosion activity measured through i_{corr} is inversely related to R_p , implicating that corrosion activity increases at lower pH. Yet, for small pH variations, specifically at neutral or nn-pH, such a tendency cannot be precisely discerned. This corroborates the large pH variation requirement (± 1.5 pH or more) mentioned earlier. This central sensitivity to pH variations is extended even further with results presented in [74], which reveal that not only is the pH change itself important, but the cause of the change (e.g. different HCO_3^- content vs. different % CO_2 purging environment) can actually yield opposing influences.

5.2 PDP testing and parameter variations based on E -pH

The PDP profiles for the environments shown in Figure 5-1 manifest different electrochemical behaviors, which are divided here into two groups according to active vs. passive

(and passive-like) responses. Only the latter are shown and discussed in detail in this chapter. Profiles manifesting active responses can be seen in Appendix A.

5.2.1 Passive and passive-like PDP responses

All solutions with HCO_3^- levels 10x the NS4 baseline exhibit passive or passive-like behavior, regardless of the pH (Figure 5-4 to Figure 5-6). The pH of the conditions for the PDP profiles illustrated in Figure 5-4 to Figure 5-6 range from alkaline (8.9) for the 100% N_2 purged NS4 + 10x HCO_3^- , to just below neutral (6.4) for the 100% CO_2 purged NS4 + 10x HCO_3^- , both at 25 °C. This ascertains that passive film formation is possible on HSLA steel in nn-pH conditions, provided that sufficient HCO_3^- is present in the solution. This is contrary to what has been reported previously in [99] and [173] that no stable passive film formation is possible on carbon steel in nn-pH solutions. This is because the conditions investigated in [99] are both low in HCO_3^- (directly added or dissociated from purging gas) and possess a nn-pH. In contrast, here some of the conditions are nn in pH yet contain considerably more amounts of HCO_3^- , both added directly and dissociated from the purging gas. Backed by the findings in [174] and [175], it could be concluded that the increased HCO_3^- content is thus what causes passivation. In [174], addition of HCO_3^- was beneficial to both the formation of a passive film and the inhibition of pitting of X70 micro-alloyed steel. The results of [175] demonstrate that the anodic polarization curves of Fe in 0.01-1.0 mol L⁻¹ HCO_3^- solutions have a typical active-passive-transpassive characteristic, where the form and number of the anodic peaks varies with HCO_3^- concentration. The polarization results of this investigation show that this remains true even for micro-alloyed X100 steel in the presence of small amounts of Cl^- and SO_4^{2-} .

It should be noted that the concentration of HCO_3^- ions originating from the dissociation of dissolved gas in the solution is not trivial. In the work of Xie et al. [176], this concentration was calculated and it affected the H adsorption and ductility of X-65 in stress tests. In this study, calculations of HCO_3^- concentrations from the dissociation of dissolved gas in the solution

(assuming Henry's Law) reveal that purging 5% CO₂/95% N₂ adds 0.0017 mol HCO₃⁻ to the solution. This is the equivalent of 0.1037 g NaHCO₃. Purging 100% CO₂ is equivalent to upwards of 2 g NaHCO₃ added. These HCO₃⁻ ion concentrations have a tangible effect on the polarization results, specifically the formation of passive films and their stability.

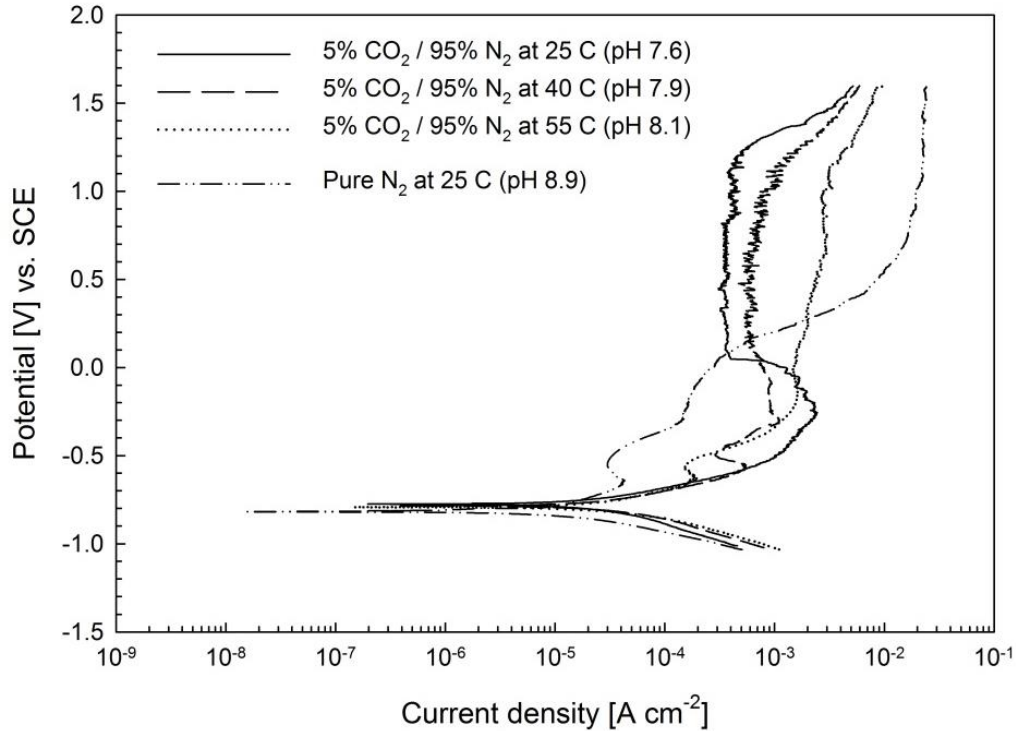
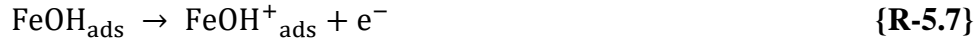
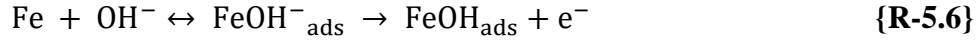
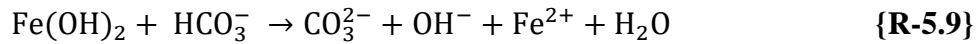


Figure 5-4: PDP in 5% CO₂/95% N₂ purged NS4 + 10x HCO₃⁻ at 25, 40, and 55 °C (pH 7.6, 7.9, and 8.1, respectively)

The PDP profiles for 5% CO₂/95% N₂ purged NS4 + 10x HCO₃⁻ at 25, 40, and 55 °C are shown in Figure 5-4. The anodic branches in Figure 5-4 show clear signs of multi-step dissolution and passive film formation for the higher pH conditions. At potentials between around -500 and -650 mV_{SCE} a decrease in current densities is observed in the 100% N₂ purged condition at 25 °C and the 5% CO₂/95% N₂ purged condition at 40 and 55 °C. The anodic peak potentials at which this deceleration occurs increases with decreased solution pH, indicating the likely involvement of OH⁻. This involvement is in the form of a defective OH⁻-based hydrous film which decelerates the current densities transiently [177]. This film has previously been shown to develop within a narrow potential range [178] and follows the ensuing formation sequence:



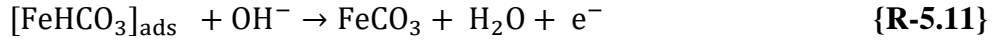
The 25 °C profile exhibits subtle early signs of this iron hydroxide (Fe(OH)₂) film formation at around -500 mV_{SCE}, yet does not fully materialize like the others. It is highly suspected that this is due to insufficient OH⁻ content or solution alkalinity. This suggests that the threshold pH for observable formation of hydrous Fe(OH)₂ in the environments investigated herein is around 7.6. This threshold is dependent on other environmental parameters like temperature and would change for conditions different than the ones explored here. In the profiles which experienced significant Fe(OH)₂ formation, an increase in current density is observed above the -500 and -650 mV_{SCE} potential range where Fe(OH)₂ formed. This is evidence of the Fe(OH)₂ removal process described by {R-5.9} [99]:



The initiation of this removal process is identified by the current density inflection point, which seems to occur fastest in the 5% CO₂/95% N₂ purged condition at 55 °C. This indicates an influence of HCO₃⁻ content, highest in this condition, on the removal process. Nonetheless, for all three cases this inflection point occurs at potentials 150 mV higher than the potential of first current density decrease (Fe(OH)₂ formation). Alternatively, at this potential it has been reported that FeCO₃ may start to form in a double-layered film with Fe(OH)₂ [179]. It is doubted that this occurs in the conditions investigated here, since FeCO₃ possesses better protection properties than Fe(OH)₂ and would thus limit the accelerated current densities observed in this potential range.

Instead, at a potential of approximately -300 mV_{SCE}, independent of purging gas and temperature, the formation of a single-layer FeCO₃ film takes place. This is confirmed by upcoming SEM images and chemical characterization spectra (section 5.2.2). In the profiles which previously experienced the formation of Fe(OH)₂, the FeCO₃ film does not fully form

(100% N₂ purged condition) or is unstable (5% CO₂/95% N₂ purged condition at 40 or 55 °C). In the 100% N₂ purged condition, the FeCO₃ film does not fully form due to the low HCO₃⁻ content from the lack of CO₂ in the purging gas, greatly decelerating the reaction sequence of {R-5.10} and {R-5.11} [180]:



The 5% CO₂/95% N₂ purged conditions at 40 or 55 °C have higher HCO₃⁻ concentrations than the 100% N₂ purged condition, yet these HCO₃⁻ concentrations are suspected to have reduced from the Fe(OH)₂ removal process of {R-5.9} leaving less HCO₃⁻ for the FeCO₃ formation process. As such, these two conditions exhibit passive-like behaviors which do not reach the level of stability or low current density of 5% CO₂/95% N₂ purged condition at 25 °C.

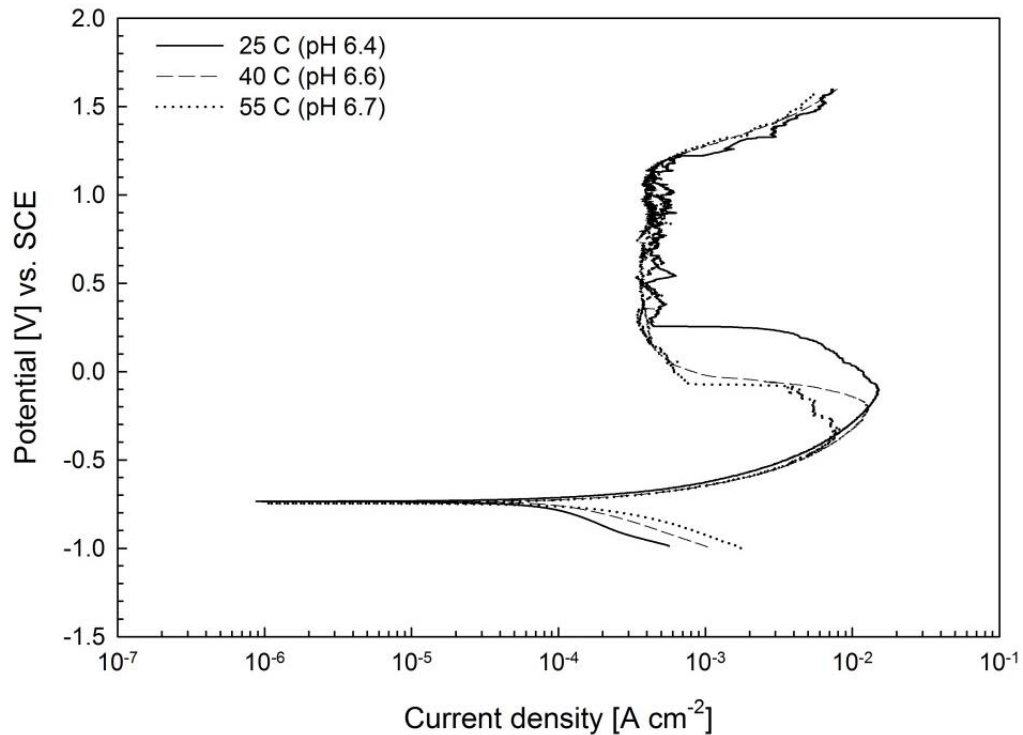


Figure 5-5: PDP profiles in 100% CO₂ purged NS4 + 10x HCO₃⁻ at 25, 40, and 55 °C (pH 6.4, 6.6, and 6.7, respectively)

In the 100% CO₂ purged NS4 + 10x HCO₃⁻ conditions, it is clear that hydrous Fe(OH)₂ does not form due to insufficient alkalinity or OH⁻ involvement in all cases (Figure 5-5). A stable FeCO₃ film is formed at all temperatures, with a passive current density (*i_p*) relatively equal to one another in all cases. The *i_p* in Figure 5-5 is the same as that of the 5% CO₂/95% N₂ purged condition at 25 °C in Figure 5-4. Between the different temperatures in Figure 5-5, evident delay in the onset of passivation is witnessed, signifying a role of temperature (or pH) in the formation of FeCO₃ in nn-pH conditions where Fe(OH)₂ does not form. This finding is corroborated in the results presented in the upcoming chapter 6.6 below

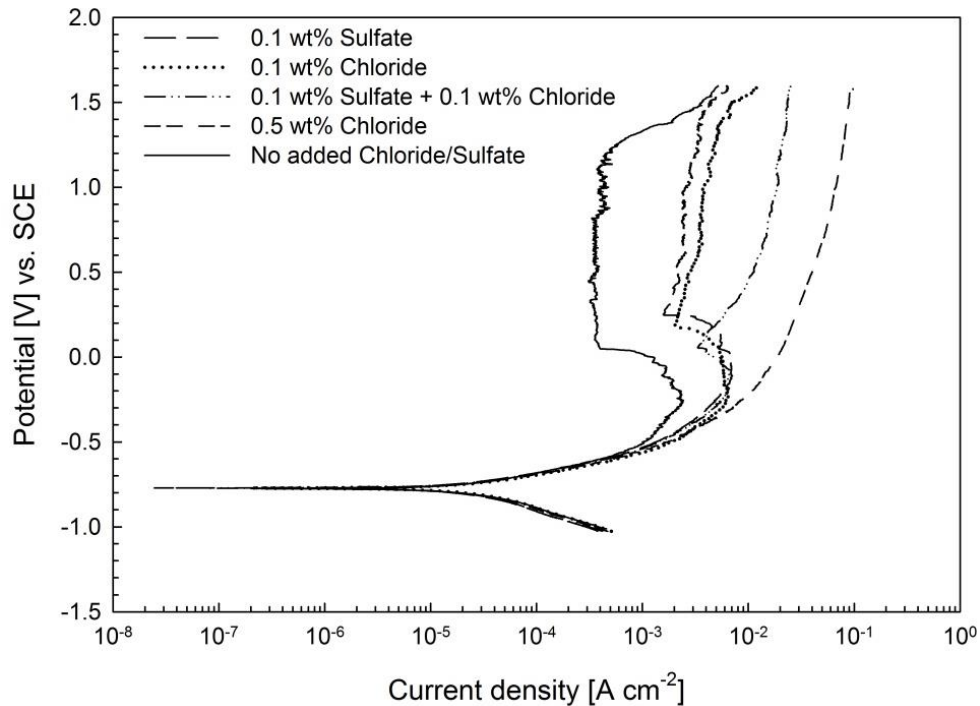


Figure 5-6: PDP in 5% CO₂/95% N₂ purged NS4 + 10x HCO₃⁻ at 25 °C with various chloride and/or sulfate ion content (pH 7.6 for all)

The addition of Cl⁻ and SO₄²⁻ to conditions which are found to cause passivation induced visible kinetic changes. As shown in Figure 5-6, compared to the reference 5% CO₂/95% N₂ purged NS4 + 10x HCO₃⁻ condition at 25 °C, increased current densities are observed especially at higher potentials. The addition of 0.5 wt% Cl⁻ prevents passivation altogether as its anodic profile appears active with no current density decreases. Sufficient Cl⁻ concentration in solutions

is known to prevent passivation [181], [182] and pre-passivation steps on Fe and steels, as recently reported in [183]. Even in concentrations which do not completely prevent passivation, Cl^- has been shown to accelerate anodic reactions on the corroding iron and steel surfaces [184]. This is observed in the 0.1 wt% Cl^- profile when compared to the reference condition of Figure 5-6. The addition of an identical amount of SO_4^{2-} instead has a similar effect, yet the severity is not as high as the Cl^- . On the other hand, when Cl^- and SO_4^{2-} are added together, a compound effect is observed in which the anodic profile of the PDP profile becomes almost completely active and the passivation of the steel surface is practically eliminated.

From Figure 5-6, it can be deduced that the aggressiveness ranking of anion attack on passive layers in nn-pH environments surrounding X100 pipeline steel is $\text{Cl}^- > \text{SO}_4^{2-} > \text{HCO}_3^-$. Also, a compound effect of Cl^- and SO_4^{2-} on passive layer degeneration in nn-pH conditions is established. In the cathodic region though, Cl^- and/or SO_4^{2-} additions garnered no discernible differences, and HCO_3^- retains its dominating influence on the cathodic processes. Similarly, added Cl^- and/or SO_4^{2-} has no practical effect on corrosion rates in the unpassivated states at OCP when extracted from Figure 5-6, although subtle effects on interfacial processes at OCP are detected as reported in the EIS results of section 5.3.

5.2.2 Anodic parameter relationships with E -pH

Based on the consequential impacts of pH and HCO_3^- concentration on corrosion and passivation processes as shown above, it is deemed important to further investigate changes in the onset and the development of passive layer(s) on X100 as a function of pH. Since the electrochemical technique used here is PDP, this also involves electrochemical potential (E). Changes to the pH of the environments in this analysis are instigated through added HCO_3^- ; unlike the approach of the previous section (5.2.1), temperature is maintained at 25 °C and the purging gas is kept consistent as 5% CO_2 /95% N_2 . The baseline NS4 environment of pH 6.7 and 0.00575 M HCO_3^- does not induce any clear passivation in laboratory PDP tests, hence the pH range for

the following analysis is between a mildly alkaline 7.5 and 8.9 instead. The influence of Cl^- and SO_4^{2-} presence, in the concentrations found in the standard NS4 condition, and PDP scan rate are explored.

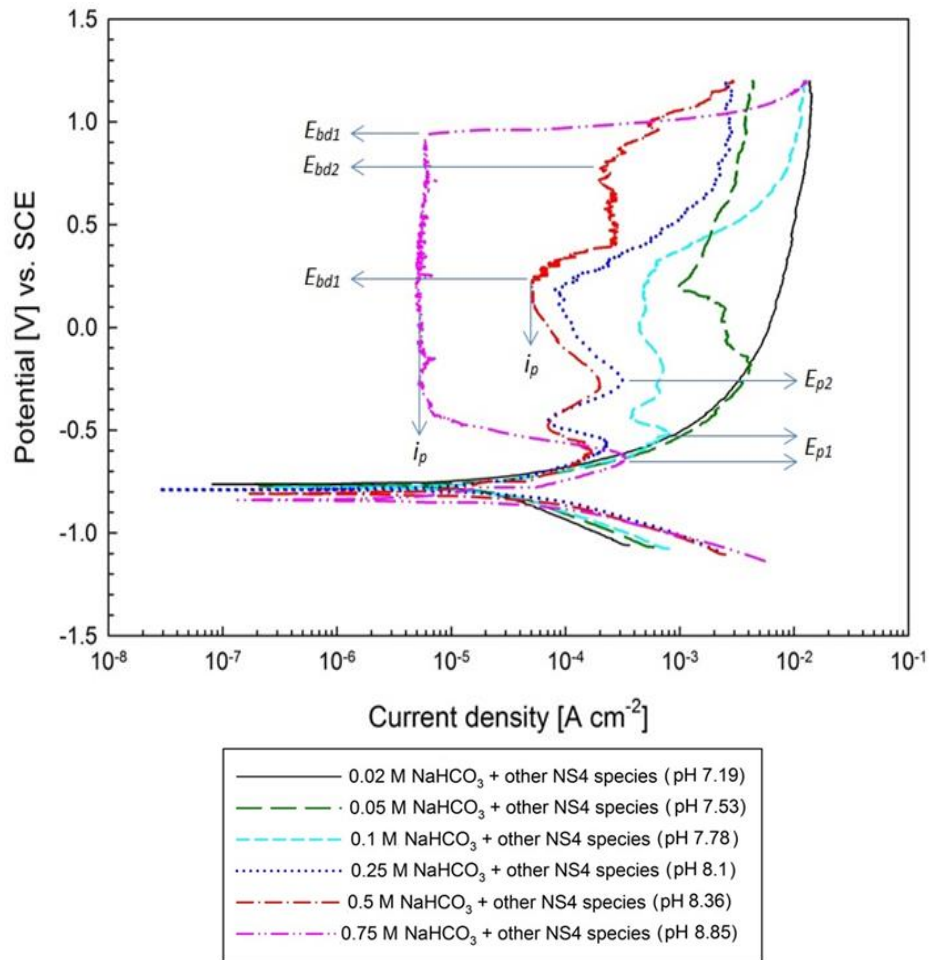


Figure 5-7: 1 mV/s PDP profiles of specimen in NS4 Cl^- and SO_4^{2-} -containing solutions with $7.19 < \text{pH} < 8.85$

In Figure 5-7, E and current density (i) parameters used for analyzing PDP profiles are identified: E_{p1} and E_{p2} are the first and second potentials at which sustained current density decreases occur, respectively; E_{bd1} and E_{bd2} are the first and second potentials at which sustained breakdown or transpassivation occurs, respectively; and i_p is the lowest current density reached in each passive region. As the X100 surface passivates, dissolution is hampered due to the reacting ion barrier covering anodic sites. Even though cathodic reaction rates at higher potentials are

greatly decreased, this should be counteracted by an accelerated dissolution half-cell reaction rate at these more anodic regions. Marked decreases in i_{corr} and corrosion rate values are found in Cl^- - and SO_4^{2-} -free solutions, confirming the accelerated anodic dissolution and Fe^{2+} release of bare steel specimen [57] under the influence of these aggressive anions, not only their attack on passive layers formed. Corrosion rates at the lower and upper bounds of the pH range in this section (at 298 K or 25 °C, 6.7 - 8.9) increase from 0.055 to 0.326 mm per year (mmpy), for solutions with NS4 Cl^- and SO_4^{2-} . This is a significant difference for a relatively small pH change, and only occurs for a short period until dissolution sites are covered by corrosion product(s). Hence, this finding should not be generalized for long term behavior of X100 under these conditions since corrosion product deposition is only possible at higher pH, as discussed below.

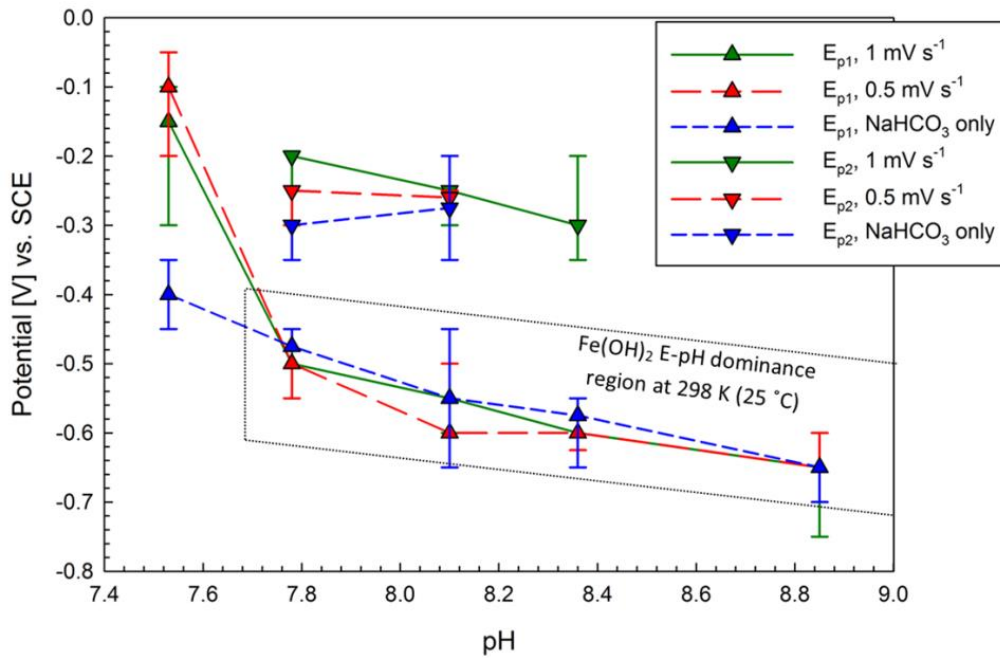


Figure 5-8: Current density peaks E_{p1} and E_{p2} plotted vs. pH for Cl^- - and SO_4^{2-} -containing solutions at 1 mV/s and 0.5 mV/s, and Cl^- - and SO_4^{2-} -free solutions at 1 mV/s

At potentials higher than the active region, passive layer formation is observed in all solutions with $\text{pH} > 7.19$ in Figure 5-7. In the $\text{pH} 7.53$ solution with the presence of Cl^- and SO_4^{2-} , E_{p1} shifts downward by about -0.15 V compared to the $\text{pH} 7.19$ solution. E_{p1} values for all

profiles are plotted in Figure 5-8, with error bars representing the range of values exhibited over the three scans conducted. Error bars extending in one direction only or not appearing at all are for parameter values which were the same for different scans. For the pH 7.53/7.56 solutions, further decrease in E_{p1} occurs when Cl^- and SO_4^{2-} are removed. This is explainable by easier passive layer formation without the attack of these species. Sporadic corrosion product formation in this case is still expected to be FeCO_3 , at an E -pH still below that at which Fe^{3+} becomes viable [185] and well above the metal immunity point [186] (see Fe-H₂O Pourbaix in Figure A-5 in Appendix A). In the presence of Cl^- and SO_4^{2-} , metastable FeCO_3 formation is due to mediocre kinetics of {R-5.10} and {R-5.11} from HCO_3^- , FeHCO_3 , and pH levels which are low. Previous reports attribute broad current density peaks in this potential range to the intersection of the cathodic currents of O_2 reduction with the passive current [187]. Here, this is shown to be unlikely due to its occurrence with nominal O_2 levels.

By increasing HCO_3^- concentration of the solutions further, creating conditions with pH 7.78, 8.1, and 8.36, the FeCO_3 formation potential (2nd peak in these cases, E_{p2}) is driven closer to the immunity-dissolution boundary potential governed by the Fe-H-C-O Pourbaix [186] (see Figure A-6 in Appendix A). Accelerated kinetics of {R-5.10} and {R-5.11}, and thus easier association of FeCO_3 in more alkaline conditions richer in HCO_3^- causes this, provided the thermodynamic viability of Fe dissolution is still valid. E_{p2} values are slightly dependent on scan rate and Cl^- and SO_4^{2-} at both pH 7.78 and 8.1 (Figure 5-8). The slower scan rate facilitates FeCO_3 development at lower potentials due to increased $[\text{Fe}^{2+}]$ in the solution from increased time spent at active potentials. Yet, the absence of Cl^- and SO_4^{2-} appears to be more effective for stable FeCO_3 formation, as E_{p2} of HCO_3^- -only solutions are lower than for 0.5 mV s^{-1} cases (Figure 5-8).

In the mildly alkaline solutions of pH 7.78 - 8.36 in Figure 5-7, the same multi-step dissolution process of Figure 5-4 is observed in the -0.5 to -0.2 V_{SCE} potential range. The

involvement of $\text{Fe}(\text{OH})_2$, interacting with FeCO_3 forming at higher potentials in a multi-layered or intermixed morphology as discussed in section 5.2.1, is again likely here. Theoretically, this $\text{Fe}(\text{OH})_2$ formation cannot occur at a pH less than a mildly alkaline 7.6-8, depending on the presence of other anions in the solution and temperature [185]. The resulting passive layer $\text{Fe}(\text{OH})_2$ vs. FeCO_3 constituent ratio depends on whether HCO_3^- or OH^- dominantly drives the charge-transfer steps on which the growth of the corrosion products depend at higher potentials [187]. This mechanism is independent from O_2 traces in the media as reported by Rangel et al. [188]. Thus, comparability of present results with those of previous tests, some of which containing O_2 [175], [179], [188], is sustained.

The E -pH region of $\text{Fe}(\text{OH})_2$ dominance in the Fe-H-C-O Pourbaix has been superimposed onto Figure 5-8 to demonstrate this interpretation [178]. E_{p1} data points for all pH > 7.5 lie within the $\text{Fe}(\text{OH})_2$ dominance region; yet, not necessarily implying the formation of $\text{Fe}(\text{OH})_2$ in all these cases. At the highest pH of 8.9 it is more likely that FeCO_3 formation takes precedence over $\text{Fe}(\text{OH})_2$ due to the significantly high $[\text{HCO}_3^-]$, making HCO_3^- the main driver of the charge transfer steps ({R-5.10} and {R-5.11}). This is corroborated by the absence of local current minima in this profile. The second stage of the multi-step dissolution indicates $\text{Fe}(\text{OH})_2$ removal under the influence of high $[\text{HCO}_3^-]$ as described by Castro et al. (11) [179], and shown by {R-5.9} in the previous section.

Beyond E_{p2} , the mildly alkaline (pH 7.78 - 8.36) profiles exhibit a region of constant or decreasing current density dependent on $[\text{HCO}_3^-]$, scan rate, and the presence of Cl^- and SO_4^{2-} . Decreasing i_p values in this region with increasing pH indicate the gradually enhancing protectiveness of FeCO_3 at higher anodic potentials [188], [189], plotted vs. pH in Figure 5-9. The potential difference (ΔE) parameter, between the most anodic passive layer development potential (E_{p1} or E_{p2}) and the earliest breakdown potential (E_{bd1}), is plotted vs. pH in Figure 5-10. Fe^{2+} from Fe dissolution is involved in FeCO_3 formation through direct association with CO_3^{2-} or through FeHCO_3 intermediary steps. Direct transformation of $\text{Fe}(\text{OH})_2$ into FeCO_3 through {R-

5.12} is also possible. Although it is difficult to quantitatively specify the ratio of the latter FeCO_3 formation path, it appears that Fe(OH)_2 is always a part of the formation process in the pH 7.78 - 8.36 domain through multi-step passivation-dissolution behavior at these E-pH levels.

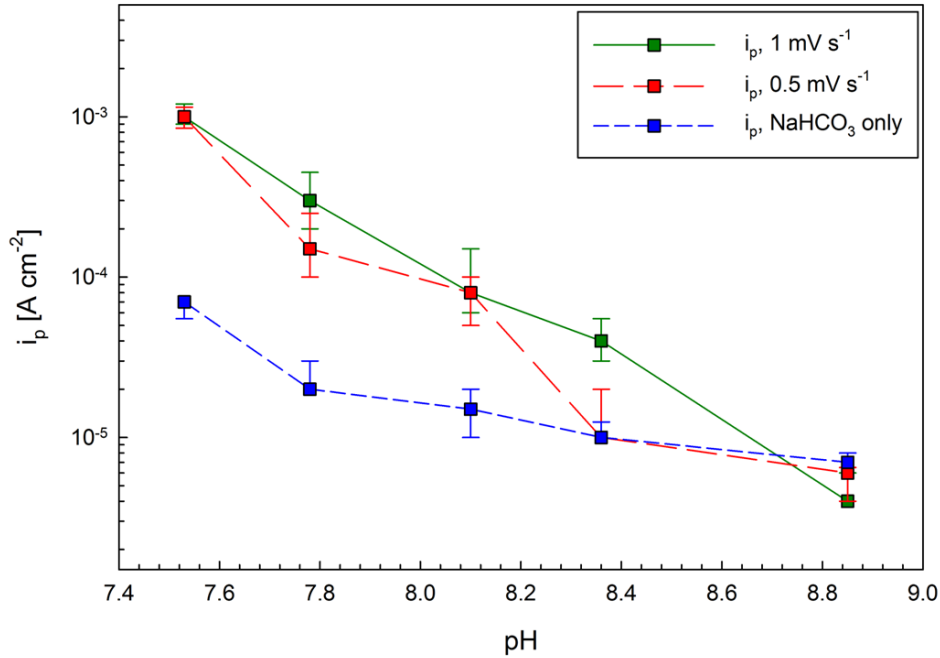
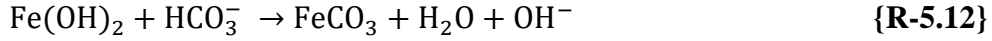


Figure 5-9: Passive current density i_p plotted vs. pH for Cl^- and SO_4^{2-} -containing solutions at 1 mV/s and 0.5 mV/s, and Cl^- and SO_4^{2-} -free solutions at 1 mV/s

The protectiveness of the FeCO_3 layer shows clear dependencies regardless of formation path(s). Prolonging formation times (with slower scan rates) and removing Cl^- and SO_4^{2-} results in lower i_p (Figure 5-9), denoting better protectiveness. Although reducing the scan rate may sometimes have little or no effect on i_p , removing Cl^- and SO_4^{2-} from the solutions always improves protectiveness (except in the pH 8.9 condition, where i_p reaches a minimum). ΔE increases with pH, reduced scan rate, and the absence of Cl^- and SO_4^{2-} , signifying increased protectiveness with those changes. The ΔE trend vs. pH is inversely proportional to i_p , and separations between different conditions are more pronounced. This indicates that although the corrosion rate of the passivated specimen might be the same in NaHCO_3 -only solutions or during

slower scan rates, the passive layer in these conditions will resist dissolution/breakdown more. The ΔE of the NaHCO_3 -only solutions are generally more than 3 times that of the solutions with Cl^- and SO_4^{2-} at the same scan rate, and almost double that of tests conducted at 0.5 mV s^{-1} .

The tests presented in this section are all conducted at $25 \text{ }^\circ\text{C}$, so temperature dependence of FeCO_3 formation cannot be deduced from the results. It has been reported though that siderite's solubility product decreases from 10^{-11} to $10^{-11.5}$ for a 50 degree increase above the temperatures tested here, implying slightly higher siderite precipitation with temperature [190]. However, this effect is offset and likely even overturned by decreased $[\text{HCO}_3^-]$ with lower CO_2 solubility at such higher electrolyte temperatures, due to the stronger influence of $[\text{HCO}_3^-]$ on FeCO_3 formation and robustness presented here and in previous studies.

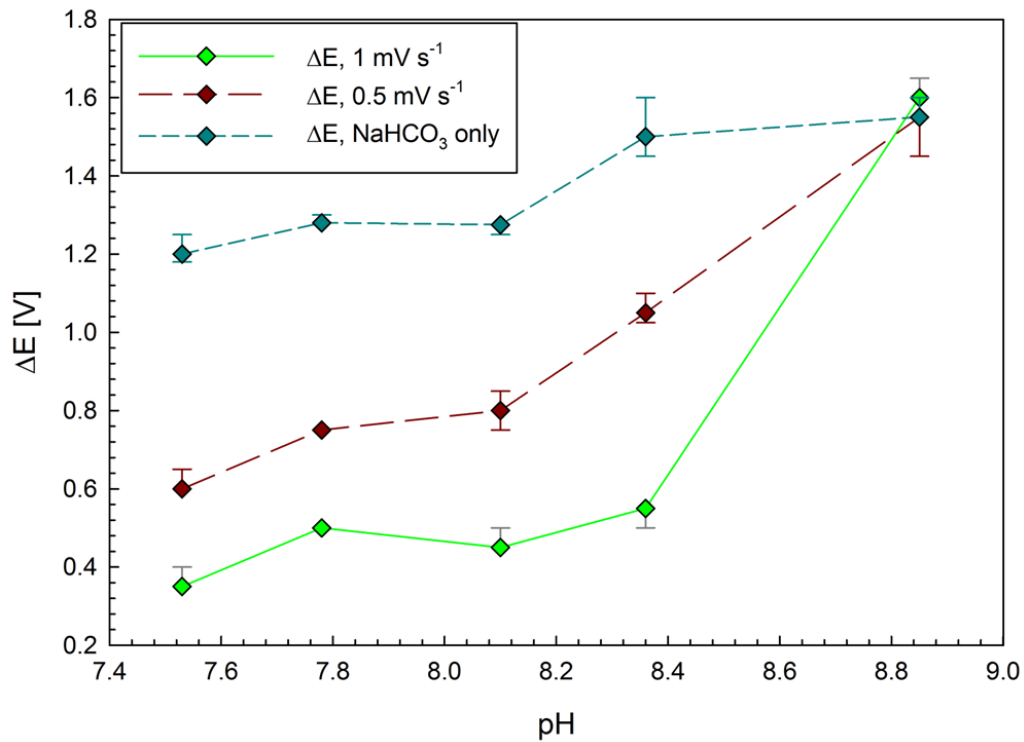


Figure 5-10: Potential difference ΔE plotted vs. pH for Cl^- - and SO_4^{2-} -containing solutions at 1 mV/s and 0.5 mV/s , and Cl^- - and SO_4^{2-} -free solutions at 1 mV/s

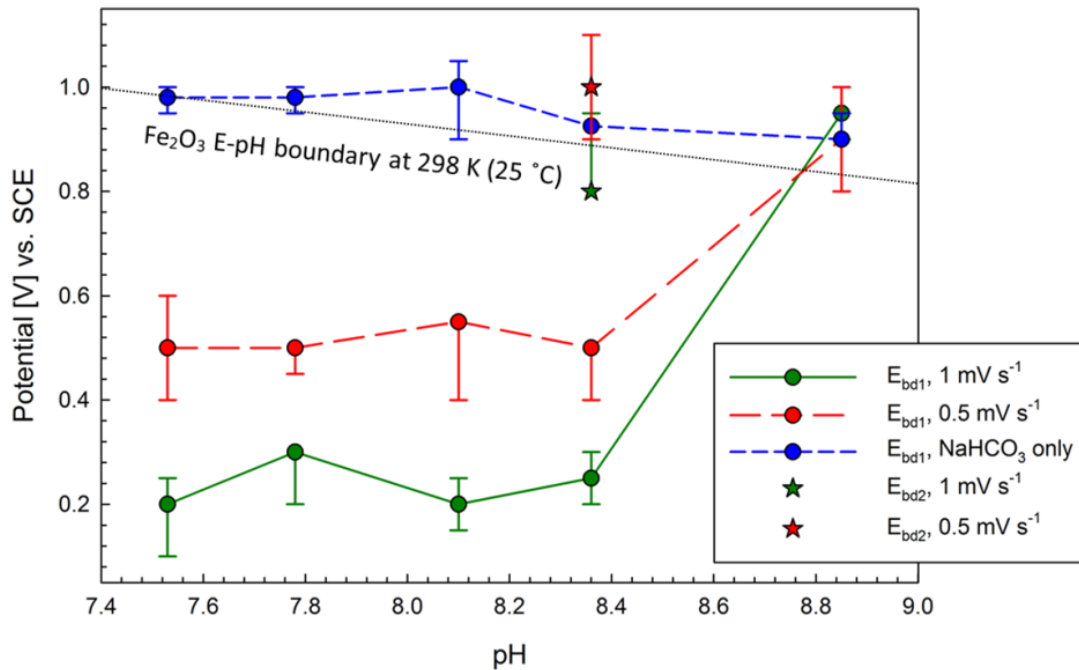
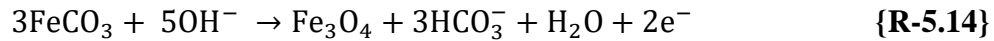
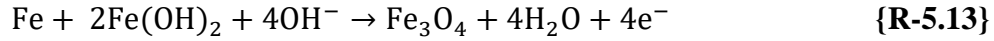


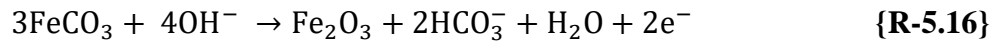
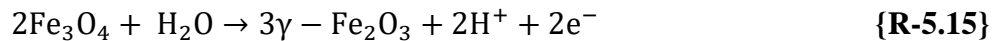
Figure 5-11: Breakdown or transpassivation potentials E_{bd1} and E_{bd2} plotted vs. pH for Cl^- and SO_4^{2-} -containing solutions at 1 mV/s and 0.5 mV/s, and Cl^- and SO_4^{2-} -free solutions at 1 mV/s

A passive-layer breakdown behavior dependent on pH and solution anion content is witnessed at potentials beyond the passive region in Figure 5-7. Here, excluding the lowest and highest pH profiles, an abrupt breakdown commences at around 0.25 V_{SCE} , E_{bd1} and E_{bd2} extracted and plotted vs. pH for all conditions are shown in Figure 5-11. Uniquely, all Cl^- and SO_4^{2-} -containing solutions of $\text{pH} \leq 8.4$ experienced early breakdown at potentials $\leq 0.5 V_{\text{SCE}}$, well below the O_2 evolution potential of around 1 V_{SCE} . E_{bd1} values are relatively independent of pH or $[\text{NaHCO}_3]$ for both the slow and fast scan rates, negating the sole connection of the behavior to weak passive layer formation. Rather, this behavior likely indicates Fe_3O_4 or $\gamma\text{-Fe}_2\text{O}_3$ presence, previously shown to be unaffected by the presence of HCO_3^- or CO_3^{2-} as long as E remains in the passive region, since the oxidation current is practically independent of $[\text{HCO}_3^-]$ or $[\text{CO}_3^{2-}]$ [189]. Corrosion product between E_{bd1} and E_{bd2} loses some but not all of its protective strength, suggesting formation of a more porous or less protective product/pseudomorph is occurring at these particular potentials. Superimposing the upper boundary of the Fe_2O_3 dominance region

from the Fe-H-C-O Pourbaix system [186] to Figure 5-11 further supports the impression that Fe₃O₄ or γ-Fe₂O₃ formation in alkaline media is happening around E_{bd1} . Voltammetric studies of carbon steel in deaerated NaHCO₃ solutions by El-Naggar [191] have shown that former reaction complexes like Fe(OH)₂ can be involved in Fe₃O₄ formation. Likewise, transformation from the more predominant FeCO₃ has been reported by [192]:



These reactions occur in the complete absence of O₂, although its presence can equally enable the pure chemical oxidation of FeCO₃ as shown in [79]. Here, current density accelerations are attributed to both oxidative electron release in {R-5.13}-{R-5.14} and the proven diminished protectiveness of Fe₃O₄ [82]. In contrast to the insulating properties of FeCO₃, Fe₃O₄ is considered to be a good electrical conductor [191]. Intermediary current density levels between E_{bd1} and E_{bd2} indicate retentive protectiveness behavior. Possessing a similar structure to Fe₃O₄ but pronounced enhancement in passivity and diminishment in conductivity, γ-Fe₂O₃ forming from Fe₃O₄ [191] or the original FeCO₃ [175] develops over Fe₃O₄ to create a Fe/FeCO₃/Fe₃O₄/γ-Fe₂O₃/H₂O system as confirmed by XRD results in Figure 5-12b [193]:



SEM imagery in this potential region identifies this proposed FeCO₃ and Fe₃O₄/γ-Fe₂O₃ presence. Ex-situ images taken after the PDP scan on the specimen is stopped prematurely at a final $E < E_{bd2}$. FeCO₃ precipitates of characteristic rhombohedral crystal structure form in a columnar-like fashion [194] with sizes ranging from 10 μm to 30 μm in the top right half of Figure 5-12a. They are covered by distinctive iron-oxide product in the lower left half. The cloud-like oxide morphology is encroaching on the surface of the FeCO₃ formations, almost engulfing individual

crystals at the boundary. The lower magnification image reveals the varying porosity of $\text{Fe}_3\text{O}_4/\gamma\text{-Fe}_2\text{O}_3$ formations.

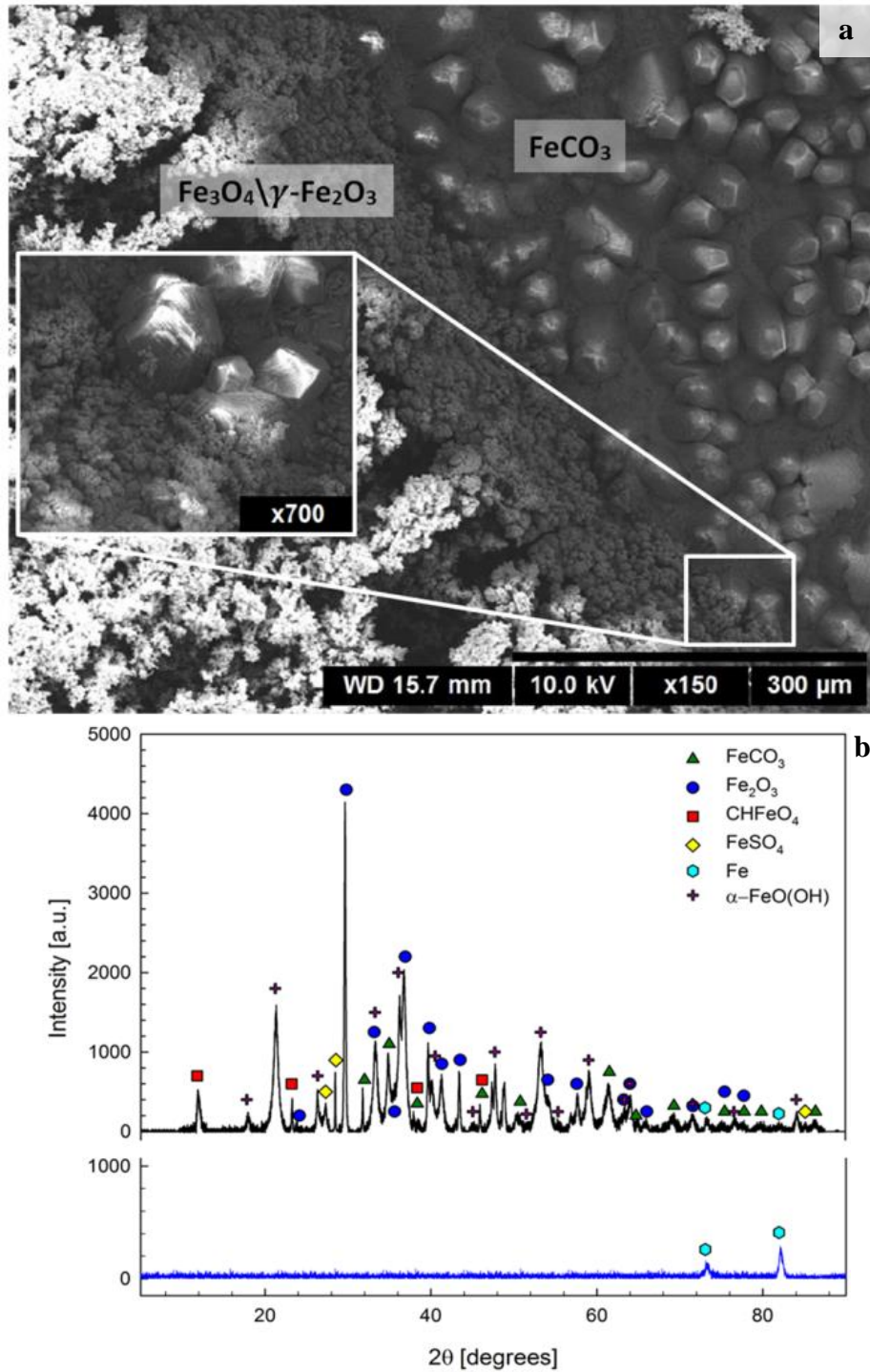


Figure 5-12: (a) SEM image (x150 magnification) of $\text{FeCO}_3\text{-Fe}_3\text{O}_4/\gamma\text{-Fe}_2\text{O}_3$ discrete boundary: (zoom) x700 magnification of Fe_3O_4 growth over FeCO_3 crystals; (b) XRD pattern of a specimen removed from a PDP scan in pH 8.36 solution (top profile), and control sample with no corrosion product (bottom profile)

The exclusivity of this transformation process to environments with Cl^- and SO_4^{2-} is supported by the synergistic effect of both anions, as shown in the previous section [172]. As such, the process is more evident here than in investigations in which similar amounts of only Cl^- was added [195]. Without Cl^- and SO_4^{2-} , breakdown occurs at much higher potentials, generally above the Fe_2O_3 formation region. Similarly, small Cl^- and SO_4^{2-} vs. HCO_3^- ratios in very high $[\text{NaHCO}_3]$ solutions are behind the absence of noticeable $\text{Fe}_3\text{O}_4/\gamma\text{-Fe}_2\text{O}_3$ formations in those conditions, since the FeCO_3 passive layers present are more robust. Combining these findings with results which report the absence of $\text{Fe}_3\text{O}_4/\gamma\text{-Fe}_2\text{O}_3$ in mildly acidic, high temperature 80 °C, CO_2 -saturated conditions representing possible internal conditions of pipelines (Farelas et al. [196]) indicates that higher temperatures make FeCO_3 to Fe_3O_4 transformation kinetics insignificant in the absence of O_2 , and hamper the pure chemical oxidation of FeCO_3 . It is noted that in [196], O_2 levels were < 10 parts per billion (ppb) representing completely anoxic conditions inside a pipeline. External surfaces can certainly anticipate higher O_2 amounts. Also, the flow of corrosive media within a pipeline as simulated in their setup will introduce mass-transfer effects not present in external corrosion of buried pipelines.

5.3 EIS tests at OCP in deaerated nn-pH conditions

EIS tests are performed here to study the influence of pH, within the nn-pH range, on corrosion and auxiliary electrochemical processes on unpolarized X100 specimens. The tests were hence done at OCP following its stabilization to steady levels after 1 h immersion in solution. Changes in pH of the solutions in which EIS was conducted here are instigated in the same way as that illustrated in Figure 5-1, namely through different $[\text{HCO}_3^-]$, purging environment, and temperature combinations. Due to similar responses for the reference NS4 and NS4 – 10x HCO_3^- conditions, plots and results are presented for the first condition only, in addition to NS4 + 10x HCO_3^- environments and solutions with added Cl^- and/or SO_4^{2-} in concentrations greater than the standard NS4 level.

In the standard NS4 solutions, the Nyquist plots of Figure 5-13a readily show the effect of purging gas environment and temperature on the impedance profiles. In the 100% CO₂ gas purging condition, nearly-complete depressed semicircles decrease in size with temperature, and no induction effects are observed at lower frequencies. No positive inflections in the impedance profile are observed at low frequencies of the Nyquist plots either. This characteristic is revealed better by the small phase angle (θ_{EIS}) and nearly constant impedance moduli ($|Z|$) profiles at those frequencies in Figure A-7 and Figure A-8, respectively in Appendix A. This behavior suggests the absence of significant adsorption processes occurring outside the double layer. Combined with the absence of induction or diffusion characteristics to the plots, such a response advocates the triviality of any electrochemical developments occurring outside the double layer in the 100% CO₂ gas purged NS4 solution at all temperatures. Since this reference NS4 [HCO₃⁻] condition does not cause passivation even at potentials more anodic than OCP, the existence of a passive film layer is ruled out for this condition. Thus, a basic single time-constant equivalent circuit comprised of R_{ct} , R_s , and a CPE double layer (Q_{dl}) is used to model the data (Figure 5-13b). The CPE is used instead of ideal capacitor elements to account for frequency dispersion due to distributed time constants and surface heterogeneities. Capacitive idealness of the CPE is governed by the exponent ratio (n) in the CPE impedance (Z_{CPE}) relationship {E-5.1}, first proposed by Brug et al. [197]. The j in {E-5.1} is the imaginary number, $\sqrt{-1}$, and ω is the frequency of the AC input.

$$Z_{CPE} = [Q(j\omega)^n]^{-1} \quad \{\mathbf{E-5.1}\}$$

The results of fits to the EEC correlate well with the experimental data as the χ^2 values of Table 5-1 reveal. R_{ct} decreases with temperature indicating increased corrosion rate of the steel, following well the LPR results presented in section 5.1. This same trend has previously been reported in other investigations for similar CO₃²⁻-HCO₃⁻ conditions [13]. The capacitive

character of the double layer is reflected by the reciprocal relationship between Q_{dl} and R_{ct} . This typical CPE behavior [166] is observed in all the EIS results in this section.

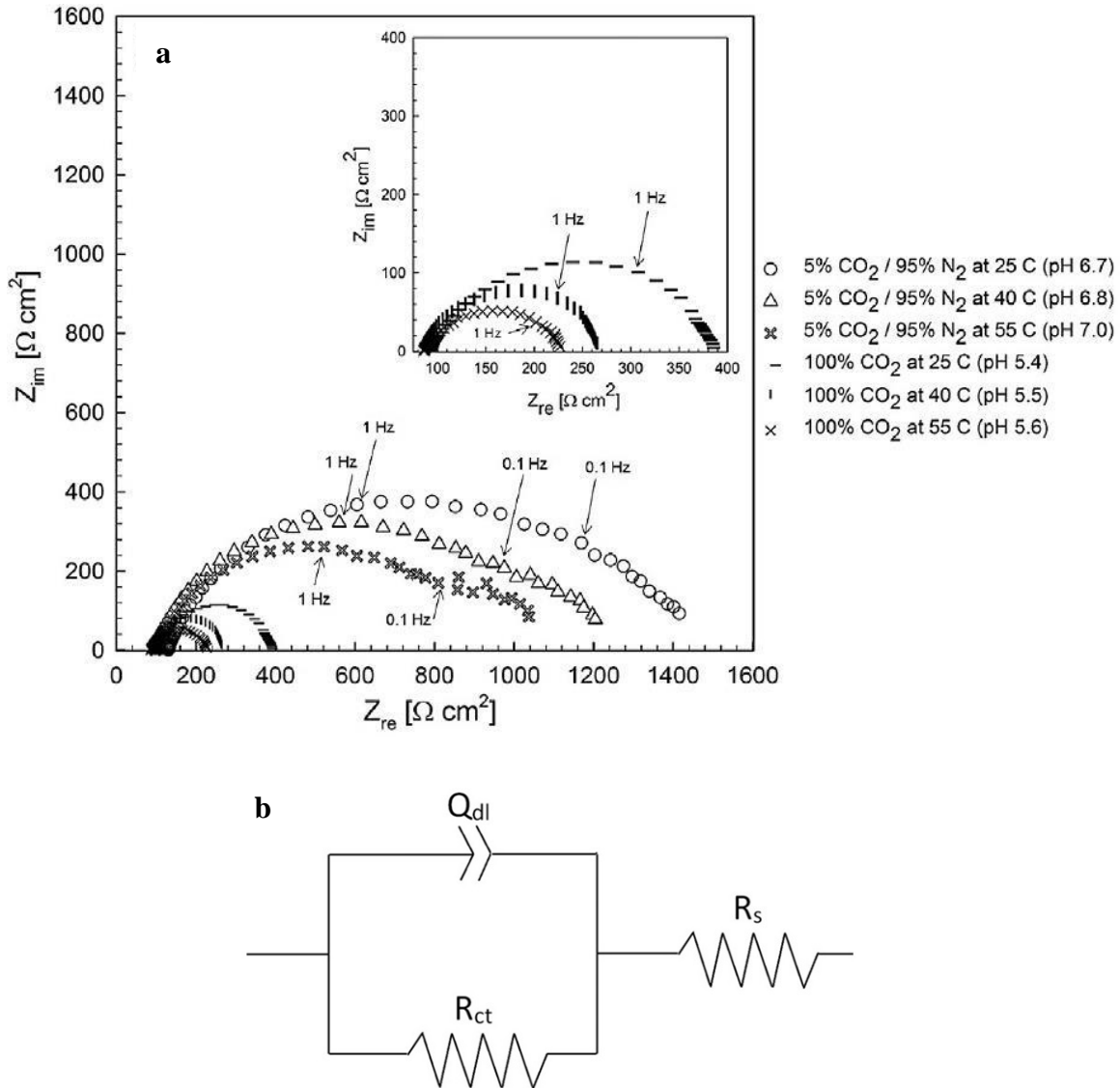


Figure 5-13: EIS for NS4 solution at 25, 40, and 55 °C purged with 5% CO₂/95% N₂ (pH 6.7, 6.8, and 7.0, respectively) or 100% CO₂ (pH 5.4, 5.5, and 5.6, respectively): (a) Nyquist impedance representation, (b) proposed EEC for 100% CO₂ results

Table 5-1: EIS component values for NS4 solution at 25, 40, or 55 °C purged with 5% CO₂/95% N₂, or 100% CO₂

Components	5% CO ₂ / 95% N ₂			100% CO ₂		
	25 °C (pH 6.7)	40 °C (pH 6.8)	55 °C (pH 7.0)	25 °C (pH 5.4)	40 °C (pH 5.5)	55 °C (pH 5.6)
R_s [Ω cm ²]	129.7	98.7	97.0	124.1	87.7	93.2
Q_{dl} [Ω^{-1} s ⁿ]	2.22 x 10 ⁻⁴	2.28 x 10 ⁻⁴	2.92 x 10 ⁻⁴	3.52 x 10 ⁻⁴	4.71 x 10 ⁻⁴	5.45 x 10 ⁻⁴
n_{dl}	0.81	0.82	0.78	0.84	0.80	0.79
R_{ct} [Ω cm ²]	856.3	811.9	761.3	291	188.9	138.3
Q_a [Ω^{-1} s ⁿ]	1.85 x 10 ⁻³	4.74 x 10 ⁻³	1.06 x 10 ⁻²	\	\	\
n_a	0.61	0.65	0.81	\	\	\
R_a [Ω cm ²]	500.8	371.3	287.5	\	\	\
χ^2	1.36 x 10 ⁻⁵	7.36 x 10 ⁻⁵	1.55 x 10 ⁻⁴	6.59 x 10 ⁻⁴	4.54 x 10 ⁻⁴	1.07 x 10 ⁻³

Contrary to the 100% CO₂ case, the 5%CO₂/95%N₂ gas purged NS4 environment exhibits positive inflections in Z and θ_{EIS} at lower ω . Also, θ_{EIS} peaks are higher and more distinct as seen in Figure A-7 (Appendix A). This signifies the importance of processes occurring outside the double layer in this condition and suggests the presence of direct HCO₃⁻ adsorption. This behavior may also be due to relaxation of carbon carrying intermediate species [198]. The contribution of adsorption and/or relaxation of intermediate species external to the double layer is accounted for in the proposed EEC (Figure 5-14) with the addition of a nested parallel circuit to the previous case, comprised of an adsorption resistance R_a and an adsorption CPE Q_a . Other EECs have previously been demonstrated to be accommodating of adsorption processes in CO₃²⁻-HCO₃⁻ solutions [26, 34], yet since those reports involved passive layer formation, those circuits are unsuitable for the specific conditions addressed here.

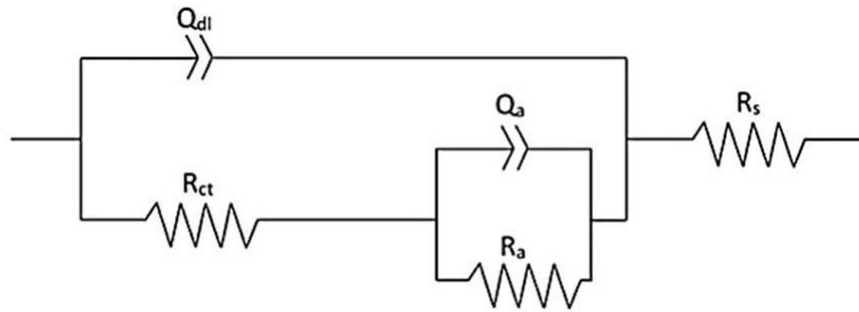


Figure 5-14: Proposed EEC for 5% CO₂/95% N₂ purged NS4 solution at 25, 40, and 55 °C (pH 6.7, 6.8, and 7.0, respectively) and 100% CO₂ purged NS4 + 10x HCO₃⁻ solution (pH 6.4, 6.6, and 6.7, respectively)

The proposed EEC of Figure 5-14 achieves a good fit with the experimental data as shown in Table 5-1, wherein it is seen that resistance to adsorption (i.e. R_a) decreases with increased temperature. This behavior is observable graphically from the difference in impedance magnitude ($|Z|$) at low ω in Figure A-8. This perhaps explains the improved adsorption of hydrous $\text{Fe}(\text{OH})_2$ at higher temperatures (higher pH) witnessed in the polarization results of the previous sections. The R_{ct} values decrease with temperature indicating increased corrosion activity, matching previous polarization results. They are markedly higher than the 100% CO_2 gas purged counterparts, confirming decreased corrosion severity in more alkaline solutions created by removal of dissolved CO_2 .

The Nyquist plots for EIS in NS4 + 10x HCO_3^- solutions at 25, 40, and 50 °C with various purging gases are shown in Figure 5-15a and Figure 5-15b. Bode $|Z|$ and θ_{EIS} plots for EIS in these conditions can be found in Figure A-9 to Figure A-11 in Appendix A. All these plots demonstrate the induced effects of increased solution alkalinity and added $[\text{HCO}_3^-]$. Nyquist plots for the 100% CO_2 case at all temperatures exhibit a similar response to the mildly acidic 5% $\text{CO}_2/95\%$ N_2 purged NS4 condition discussed above. Adsorption effects are evident from the $|Z|$ and θ_{EIS} values at lower ω . Good fit with the experimental data is achieved when modeled with the EEC of Figure 5-14, as seen in Table 5-2. The trend of decreasing R_a with temperature continues to occur, suggesting increased adsorption due to temperature. Judging from the increased Q_a values with temperature, there appears to be a capacitive adsorption region near the specimen surface which behaves similar to the double layer. This adsorption region becomes more dominant at higher temperatures. The decreasing R_a effect with temperature is apparently not due to the associated increase in pH with higher temperatures, since R_a values increase markedly in the more alkaline solutions of 5% $\text{CO}_2/95\%$ N_2 and 100% N_2 conditions in Table 5-2. R_a only decreases with temperature within the 5% $\text{CO}_2/95\%$ N_2 test set, establishing the temperature-only dependence of adsorption even further.

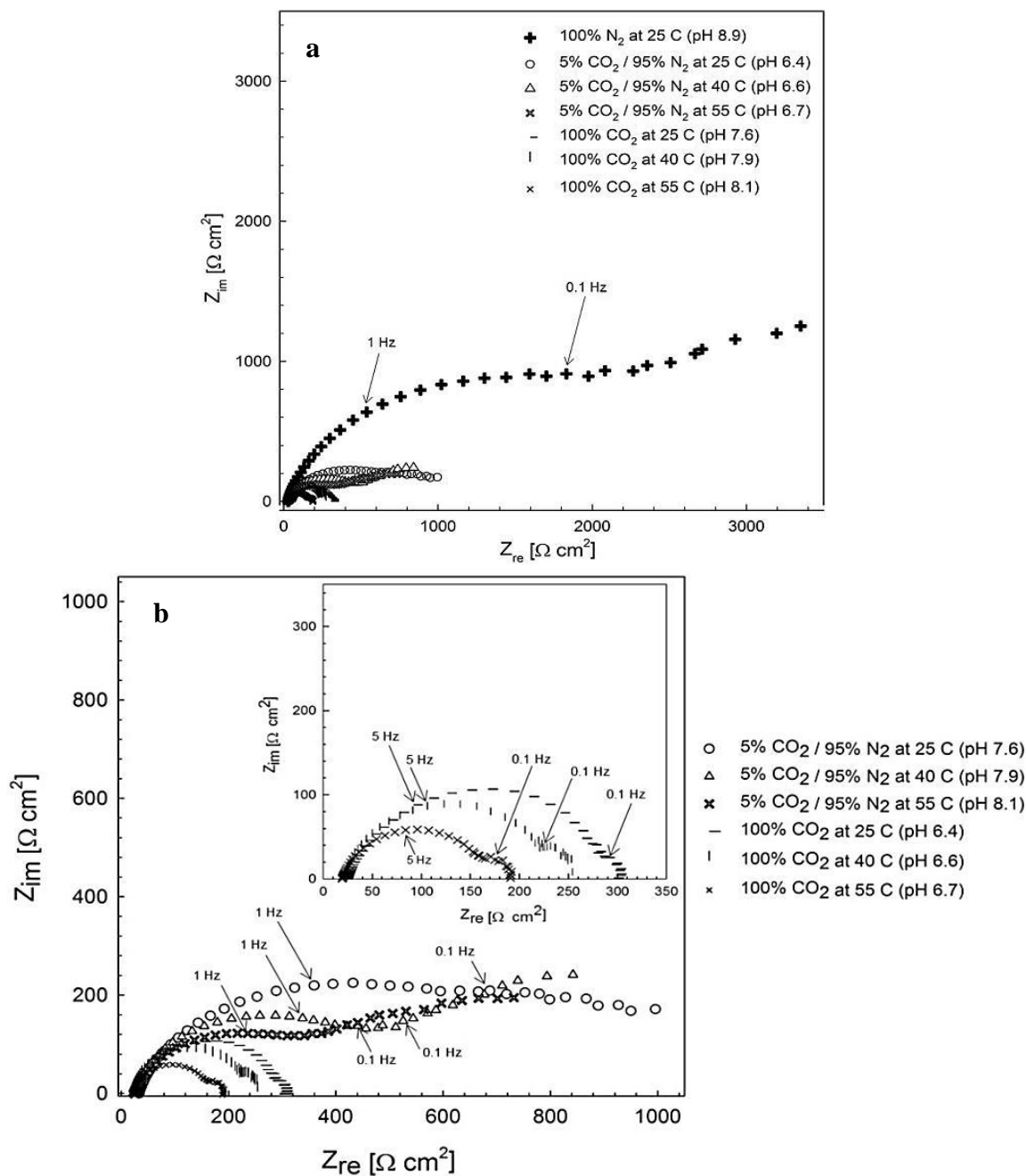
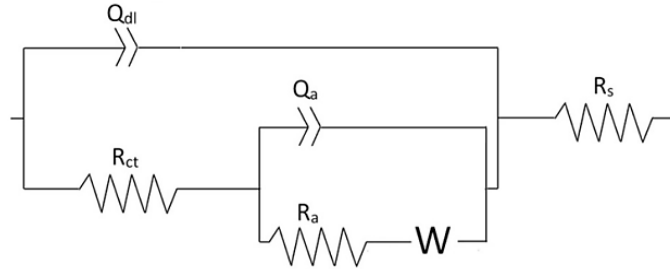


Figure 5-15: NS4 + 10x HCO₃⁻ solution at 25 °C purged with 100% N₂ (pH 8.9), and at 25, 40, and 55 °C purged with 100% CO₂ (pH 6.4, 6.6, and 6.7, respectively), and 5% CO₂/95% N₂ (pH 7.6, 7.9, and 8.1, respectively) (a) Nyquist impedance representation for all cases, (b) enlarged Nyquist impedance representation for 5% CO₂/95% N₂ and 100% CO₂ purged cases

Table 5-2: EIS component values for NS4 + 10x HCO₃⁻ solution

Components	5% CO ₂ /95% N ₂			100% CO ₂			100% N ₂
	25 °C	40 °C	55 °C	25 °C	40 °C	55 °C	25 °C
R_s [Ω cm ²]	33.5	25.5	25.0	32.4	20.9	19.3	29.3
Q_{dl} [Ω^{-1} s ⁿ]	2.33×10^{-4}	5.98×10^{-3}	1.10×10^{-2}	1.32×10^{-4}	3.53×10^{-4}	4.50×10^{-4}	2.75×10^{-4}
n_{dl}	0.83	0.66	0.66	0.96	0.85	0.86	0.85
R_{ct} [Ω cm ²]	534.3	449.6	422.7	300.24	208.2	142.4	930.4
Q_a [Ω^{-1} s ⁿ]	1.64×10^{-4}	2.58×10^{-4}	3.08×10^{-4}	3.43×10^{-2}	0.10	0.44	6.11×10^{-4}
n_a	0.30	0.81	0.81	0.74	1	1	0.87
R_a [Ω cm ²]	527	347.4	291.3	261.6	37.65	24.7	1629
W [Ω^{-1} s ^{0.5}]	\	3.26×10^{-2}	2.43×10^{-2}	\	\	\	2.14×10^{-3}
χ^2	8.69×10^{-5}	7.04×10^{-4}	2.48×10^{-4}	3.92×10^{-4}	5.32×10^{-4}	3.13×10^{-4}	3.55×10^{-4}

In environments with a pH of around 8 or greater, specifically 100% N₂ and higher temperature 5%CO₂/95%N₂ conditions, a significant change in the low ω Nyquist profiles is observed. An incomplete semi-circle at high ω is followed by a nearly linear region at lower ω . The Bode plots for these conditions exhibit a constant θ_{EIS} for almost one decade or more of low ω , from 0.01 to 0.1 Hz or greater (see Appendix A). These $|Z|$ and θ_{EIS} features are characteristic mass transfer controlled behaviors [158], typically modelled with a diffusion element in EECs. This suggests that in these conditions, diffusion of electro-active species to or from the specimen surface occurs, in agreement with findings of Linter and Burstein for similar mildly alkaline solutions [64].

**Figure 5-16:** Proposed EEC for 5% CO₂/95% N₂ purged NS4 + 10x HCO₃⁻ at 25, 40, and 55 °C (pH 7.6, 7.9, and 8.1, respectively), and 100% N₂ purged NS4 + 10x HCO₃⁻ solution at 25 °C (pH 8.9)

An EEC with components to account for parallel diffusion and adsorption control at low ω is proposed in Figure 5-16, where W represents the Warburg diffusion element. The experimental data fits the model well (Table 5-2), and a reciprocal relationship between the

diffusion and adsorption is seen at pH 8.9. Adsorption at this pH is greatly reduced yet not fully eradicated, and diffusion of complex ions at the surface greatly increases, hence contributes much more in controlling the corrosion rate of the specimen. This is witnessed in the 100% N₂ purged column of Table 5-2, through the considerable increase in R_a to 1629 $\Omega \text{ cm}^2$ (indicating decreased adsorption) combined with the significant decrease in W to the order of $10^{-3} \Omega^{-1} \text{ s}^{0.5}$ (indicating increased diffusion). Conversely, in the 5% CO₂/95% N₂ conditions of Table 5-2, parallel adsorption and diffusion processes both slightly increase with temperature between 40 and 55 °C. The relationship between these two processes is thus not only directly pH-dependent, but also temperature-dependent as seen here and potential-dependent as shown further in section 6.2.1 of chapter 6. Here, the solution pH measured for the 25 °C condition with only adsorption effects versus the 40 °C condition with parallel adsorption and diffusion control suggests that the emergence of diffusive effects is pH dependent and occurs at a threshold of around 7.7. In addition, the small pH range between the 25 °C and 40 °C conditions reveals that this adsorption-diffusion transition is abrupt, not gradual.

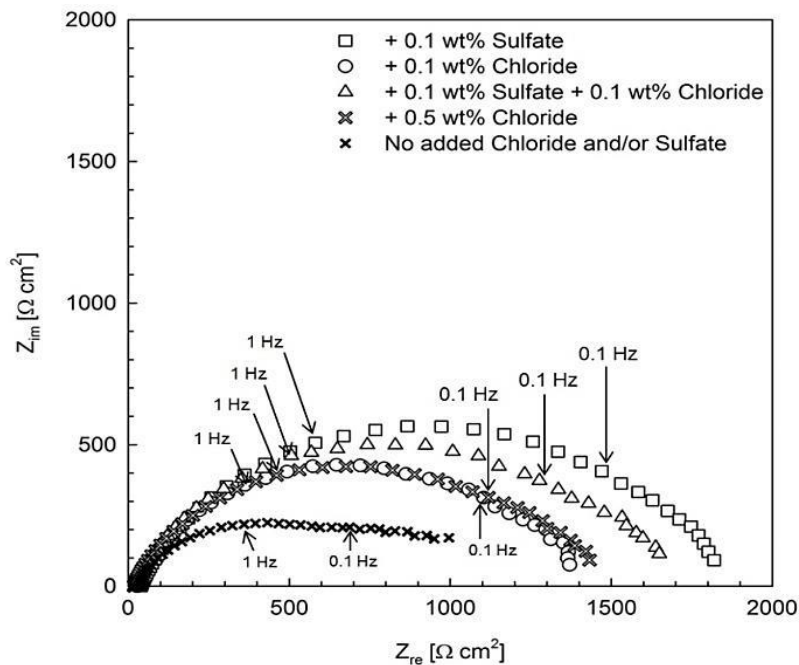


Figure 5-17: Nyquist impedance representation plots for NS4 + 10x HCO₃⁻ solutions with added Cl⁻ and/or SO₄²⁻ at 25 °C, purged with 5% CO₂/95% N₂ (pH 7.6)

Table 5-3: EIS component values for NS4 + 10x HCO₃⁻ solutions with added Cl⁻ and/or SO₄²⁻ at 25 °C, purged with 5% CO₂/95% N₂ (pH 7.6)

Components	5% CO ₂ /95% N ₂ at 25 °C			
	+ 0.1 wt% SO ₄ ²⁻	+ 0.1 wt% Cl ⁻	+ 0.1 wt% SO ₄ ²⁻ + 0.1 wt% Cl ⁻	+ 0.5 wt% Cl ⁻
R_s [Ω cm ²]	36.7	26.2	24.2	18.0
Q_{dl} [Ω^{-1} s ⁿ]	2.52 x 10 ⁻⁴	3.36 x 10 ⁻⁴	2.86 x 10 ⁻⁴	3.11 x 10 ⁻⁴
n_{dl}	0.73	0.77	0.76	0.75
R_{ct} [Ω cm ²]	1722	1344	1617	1392
Q_a [Ω^{-1} s ⁿ]	8.89 x 10 ⁻⁵	1.30 x 10 ⁻⁴	1.91 x 10 ⁻⁴	2.17 x 10 ⁻⁴
n_a	0.86	0.89	0.83	0.81
R_a [Ω cm ²]	619.8	628.9	703.5	683.6
χ^2	5.46 x 10 ⁻⁵	1.56 x 10 ⁻⁴	1.11 x 10 ⁻⁴	7.87 x 10 ⁻⁵

Nyquist impedance plots for NS4 + 10x HCO₃⁻ solution with added Cl⁻ and/or SO₄²⁻ are shown in Figure 5-17. Bode $|Z|$ and θ_{EIS} plots for EIS in these environments can be found in Figure A-12 in Appendix A. These plots show that Cl⁻ and/or SO₄²⁻ additions induce less adsorption than the reference solution free of such additions. The resemblance between features of these plots compared to the other nn-pH solution plots, such as NS4 + 10x HCO₃⁻ solution purged with 100% CO₂, suggests the similarity of electrochemical processes occurring in both. Hence, the adsorption-controlled EEC of Figure 5-14 is used to model the data, resulting in the component values listed in Table 5-3. As seen here, reduction in adsorption propensity occurs, based on the increase in R_a values versus the reference case. An increase in R_{ct} values compared to the reference solution is also observed, indicating a reduction in free corrosion activity due to Cl⁻ and/or SO₄²⁻. However, this behavior is exclusive to OCP conditions, since the results are opposite to those of EIS tests conducted at $E > OCP$ shown in section 6.2.1 of the forthcoming chapter 6. Electrode potential plays an important role in the corrosion severity of Cl⁻ and/or SO₄²⁻, a proposition precluded by the PDP profiles in Figure 5-6. From the Table 5-3 results, no clear trend can be observed in R_{ct} , R_a , or the related Q_a and Q_{dl} values with respect to Cl⁻ and SO₄²⁻ combinations. The effect Cl⁻ and/or SO₄²⁻ additions to HCO₃⁻/CO₃²⁻ solutions have on the corrosion and passivation of X100 steel is hence an area which requires further investigation. Such a study is presented in chapter 6 of this thesis.

5.3.1 Subdivision of electrochemical response based on pH range

Examination of the EIS data presented in the previous section highlights three different regions of electrochemical processes which can occur on X100 steel during free corrosion (i.e. OCP), depending on pH of the environment. It is important to note that the nn-pH range of 5 to 8.5 overlaps each of these three pH regions, signifying the criticality of seemingly minor environmental differences on the progression of corrosion processes. In acidic solutions below a pH of 6, such as NS4 solution at 55 °C purged with 100% CO₂, only a capacitive double layer is present at the steel specimen's surface, with no signs of adsorption or diffusion effects beyond that. In mildly acidic (pH 6.5) and neutral pH solutions such as NS4 solution at 55 °C purged with 5% CO₂/95% N₂, adsorption of electroactive species outside the double-layer becomes evident. Adsorption dominance is decreased with the presence of Cl⁻ and/or SO₄²⁻ ions, even though the presence of these ions does not change the pH of the solution. In alkaline solutions with a pH ≥ 7.7, mass-transfer behavior manifests in the interfacial processes, and mainly the diffusion of complex ions controls the corrosion rate of the steel.

5.4 Summary

In this chapter, X100 pipeline steel specimens are subject to a matrix of environmental conditions characterized by [HCO₃⁻], purging gas, solution temperature, Cl⁻ and/or SO₄²⁻, and resultant solution pH. The reference condition is standard NS4 solution at 25 °C, deaerated with 5% CO₂/95% N₂. OCP values decrease linearly with pH at all temperatures due to accelerated cathodic reactions at lower pH. When pH increase is created by decreasing %CO₂ in the purging gas, the overall trend of the results implies increased corrosion at lower pH, as confirmed by LPR data. An opposing trend of increased corrosion rate with alkalinity manifests at pH > 7.6 in situations where only [HCO₃⁻] is used to adjust pH, indicating not only the importance of the pH change but also the cause of the change. It is stressed that the corrosive aggressiveness of an environment cannot be determined qualitatively based on the solution pH only, for ΔpH < 1.5.

Passive or passive-like behavior is exhibited only in solutions with above-reference $[\text{HCO}_3^-]$, except for 0% CO_2 situations where a defective hydrous $\text{Fe}(\text{OH})_2$ film forms due to the involvement of OH^- . In solutions of $\text{pH} \geq 7.53$, the passive layers formed also include Fe^{2+} with CO_3^{2-} at medium range potentials as found through XRD characterization. At $\text{pH} \geq 7.78$ this is followed by $\text{Fe}_3\text{O}_4/\gamma\text{-Fe}_2\text{O}_3$ formation at higher potentials under the influence of Cl^- and SO_4^{2-} . Passive layer protectiveness is enhanced at slower scan rates due to the greater time given for corrosion product formation and the increased availability of key ionic species (i.e. Fe^{2+}) from increased time spent at active dissolution. Yet, passive layer protectiveness is more sensitive to Cl^- and SO_4^{2-} presence than scan rate. At solution pH levels > 8.5 (thus not within the nn-pH range), it seems $\text{HCO}_3^-/\text{CO}_3^{2-}$ drives FeCO_3 passive layer reaction steps in a manner which takes precedence over $\text{Fe}(\text{OH})_2$ involvement, through direct association with Fe^{2+} or through FeHCO_3 pre-passivation steps. Passive layer breakdown is highly dependent on the presence of Cl^- and SO_4^{2-} , and $\text{Fe}_3\text{O}_4/\gamma\text{-Fe}_2\text{O}_3$ formation over FeCO_3 at high anodic potentials for specific conditions is observed under SEM. A synergistic effect for chloride and sulfate is established, even in tests conducted at OCP.

EIS results reveal three varying surface interactions occurring on the steel based on the environmental conditions. Acidic solutions with a pH below 6 induce impedance responses representing the absence of any adsorptive and/or diffusive effects outside the capacitive double-layer. Solutions of nn-pH introduce a capacitive adsorption region at the steel surface whose dominance increases with solution temperature and decreases with Cl^- and/or SO_4^{2-} additions. Further increase in pH into the alkaline region brings about mass-transfer controlled behavior which, in parallel with adsorption effects, controls the corrosion rate of the steel. Cl^- and/or SO_4^{2-} additions of any amount completely eliminate this diffusion behavior on unpolarized specimen and are found to impede charge transfer at OCP or during free corrosion.

6. Quantitative studies of the properties & growth of corrosion products on X100 steel in mildly alkaline deaerated HCO_3^- solutions using EIS and Mott-Schottky⁴

A main corrosion product causing passivation of steel in HCO_3^- -rich, deaerated, and mildly alkaline environments is FeCO_3 as identified in Figure 5-12 of the previous chapter. A formation threshold pH for FeCO_3 on X100 exists at around 7.6 in solutions with 10x the reference NS4 $[\text{HCO}_3^-]$ (section 5.2.1). The dependence of FeCO_3 formation on pH and $[\text{HCO}_3^-]$ is clear according to {R-2.2} and the previously presented results. Aggressive anions like Cl^- and SO_4^{2-} also play an important role in passive layer development and performance. In $\text{HCO}_3^-/\text{CO}_3^{2-}$ electrolytes, Cl^- positively shifts transpassivation potentials with CO_3^{2-} at different temperatures [200], or eliminates the onset of passivation as shown by Alves et al. [192]. At anodic sites, Cl^- accelerates anodic dissolution and Fe^{2+} release from Fe specimens, as discussed by Lorenz and Heusler in [57] and supported experimentally by Zhang et al. [58]. A synergistic effect of Cl^- and SO_4^{2-} on corrosion acceleration and the elimination of passivation on X100 has been shown earlier in chapter 5. However, quantitative studies of the synergistic influence of Cl^- and SO_4^{2-} on interfacial processes involved in HSLA steel corrosion/passivation in HCO_3^- environments are still needed. This can contribute to forming a mechanistic understanding of more advanced degradation processes in related environments like nn-pH SCC, which until now lacks such an understanding [201].

The nature of corrosion products and the corresponding necessary reaction steps of steel passivation in HCO_3^- solutions are potential dependent. Fundamental cyclic voltammetry studies by El-Naggar [191], [202] on carbon steel in deaerated NaHCO_3 solutions have revealed the

⁴ I. M. Gadala and A. Alfantazi, *Applied Surface Science*, vol. 357, Part A, pp. 356–368, Dec. 2015.

involvement of OH^- , CO_3^{2-} , and O^{2-} complexing reactions with Fe^{2+} at low, medium, and high anodic potentials, respectively. Using EIS to study these potential dependent steps is beneficial. Yet, static EIS at OCP or any higher potential to which a bare sample is immediately polarized overlooks the effect of previous processes and surface states, leading to electrochemical responses which may misrepresent the actual chronological progression of corrosion and passivation. In contrast, EIS under PDP conditions can be used to determine changes in passive layers caused by variations in electrode potential. Linear or step-wise potential change of EIS conditions can capture and quantify the time and/or surface dependence of sequential electrochemical processes such as intermediate diffusion or pitting [167]. A theoretical formulation proving the suitability of this method in studying time-dependent events is outlined by Darowicki in [168].

Since the electronic properties of a passive layer play an essential role in corrosion processes of the underlying steel substrate [203], their analysis for passive layers formed in aqueous media with different environmental parameters such as $[\text{HCO}_3^-]$, temperature, and pH is valuable. It is acknowledged that the electrochemical and protective behavior of a passive layer is related to its electronic properties [204]. Mott-Schottky is commonly used to study the electronic properties of passive films by measuring electrode capacitance (C) as a function of potential [205], [206]. In this chapter, Mott-Schottky tests are performed on anodized specimens in nine different mildly alkaline HCO_3^- environments.

The main objective of this chapter is to further examine and quantify the interfacial and surface processes preceding, during, and following stable passivation in a HCO_3^- -based mildly alkaline solution (pH 7.8) using a dynamic step-wise anodizing-EIS routine. Passive layer protectiveness parameters are quantified for the effect of $\text{Cl}^-/\text{SO}_4^{2-}$. Furthermore, temperature dependent trends are identified using current density decay analysis of PSP tests, and Mott-Schottky is used to evaluate the semiconductive behavior of FeCO_3 layers at normal to high

temperatures (25 – 75 °C). This chapter is based on a paper [75] which was published as part of the research work leading towards this PhD thesis.

6.1 Details of dynamic EIS, PSP, and Mott-Schottky test methods

After reaching a stable OCP, either a step-wise anodizing-EIS routine or an extended anodizing, EIS, and Mott-Schottky routine is implemented in the tests here. The step-wise anodizing-EIS routine, performed in 0.1 M $[\text{HCO}_3^-]$ solution with/without NS4-level $\text{Cl}^-/\text{SO}_4^{2-}$ additions, is a six-stage process where the steel is sequentially anodized at a specific potential for 1200 s and during EIS. The anodizing period following each change ensures sufficient stability for the EIS at each stage. For such non-stationary potential conditions, either multi-sine wave [207] or single sine wave AC inputs could be used. In this study we opt for a single sine wave input (ω range: 10,000 - 0.1 Hz; AC disturbance signal: 10 mV; and sampling frequency: 10 points/decade) to allow comparability with the proposed EECs and results of other studies, the majority of which also use single sine wave input.

Table 6-1: Anodizing potentials (E_{an}) in each potential range for step-wise anodizing-EIS routine

		Potential (E) range in Figure 6-1				
		Active (early/late)	Transition	Passive formation	Passive	Transpassive /Breakdown
Anodizing potential (E_{an}) [V _{SCE}]	<i>Solution with NS4 $\text{Cl}^-/\text{SO}_4^{2-}$</i>	-0.65/-0.5	-0.475	-0.1	0.175	0.65
	<i>Solution without NS4 $\text{Cl}^-/\text{SO}_4^{2-}$</i>	-0.65/-0.5	-0.4	-0.25	0.5	1.1

A comparative plot of the PDP profiles for 0.1 M $[\text{HCO}_3^-]$ solution (pH 7.8) with/without NS4-level $\text{Cl}^-/\text{SO}_4^{2-}$ additions is shown in Figure 6-1, displaying key multi-step dissolution, passive layer formation, and early passive layer breakdown or transformation features. This environment is selected for the step-wise anodizing-EIS tests due to its multifaceted response to accelerated corrosion/passivation through PDP, which gives opportunities for a more complete understanding of the chronological electrochemical step processes. The potential ranges of the main electrochemical processes of interest, for both the 0.5 mV s^{-1} and HCO_3^- -only cases are

labelled in Figure 6-1 for their importance in the step-wise anodizing-EIS routine. The specific anodizing potentials (E_{an}) at which the PSP and each subsequent EIS are performed within each range are listed in Table 6-1. In general, E_{an} are chosen to be in the middle of each E range to minimize any inaccuracies in determining the range boundaries and to isolate the specific processes occurring in each range for spectroscopic analysis.

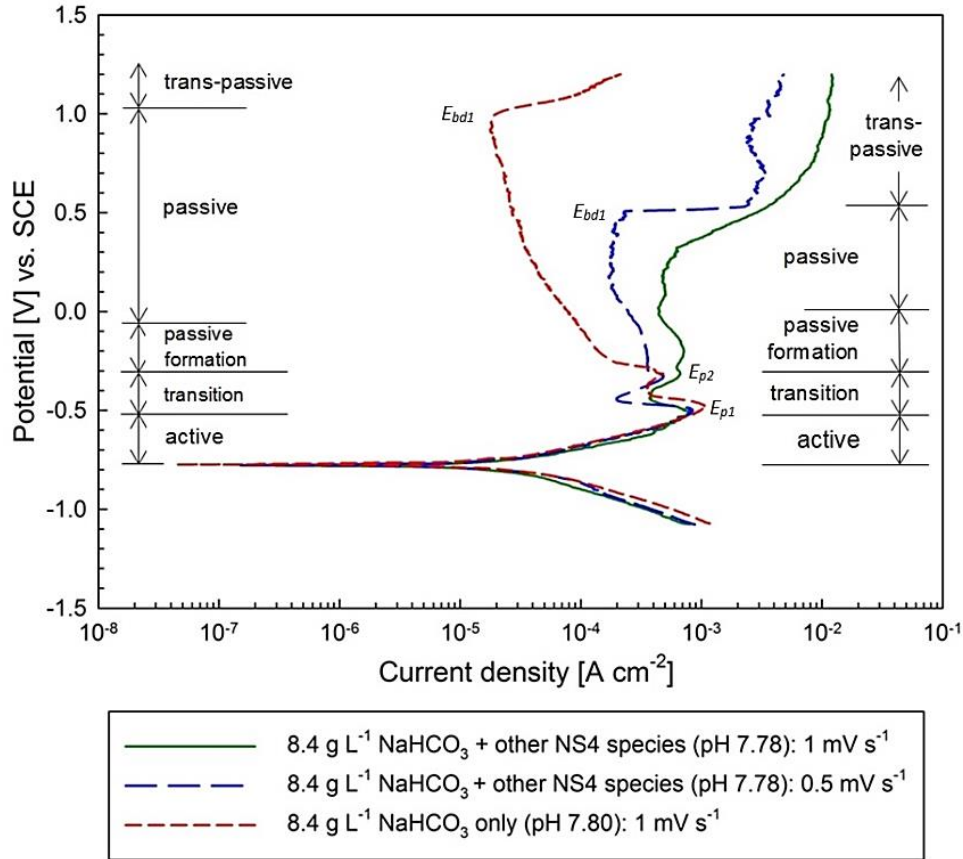


Figure 6-1: Comparative PDP plot for 0.1 M [HCO₃⁻] solution with and without NS4 Cl⁻/SO₄²⁻ scanned at 0.5 mV/s or 1 mV/s, labelled for potential regions of step-wise anodizing-EIS routine

The second independent test routine consists of a PSP or anodizing session at 0.5 V_{SCE} for 1 h, followed by EIS and Mott-Schottky. The effects of higher alkalinity (pH 7.8 - 9.3) and temperature (25 - 75 °C) on the electronic and protective properties of the anodized passive layers are evaluated. Passive layer attack by Cl⁻/SO₄²⁻ is eliminated in order to properly study the protective and electronic properties of well-formed FeCO₃ under these environmental influences. Mott-Schottky tests are scanned between -0.5 V_{SCE} and 1 V_{SCE} at a frequency of 1 kHz and with a

step height of 20 mV. Figure 6-2 is a schematic of the two test routines of this study, and Figure B-1 in Appendix B illustrates the $[\text{HCO}_3^-]$, temperature, and pH relationships of the solutions tested.

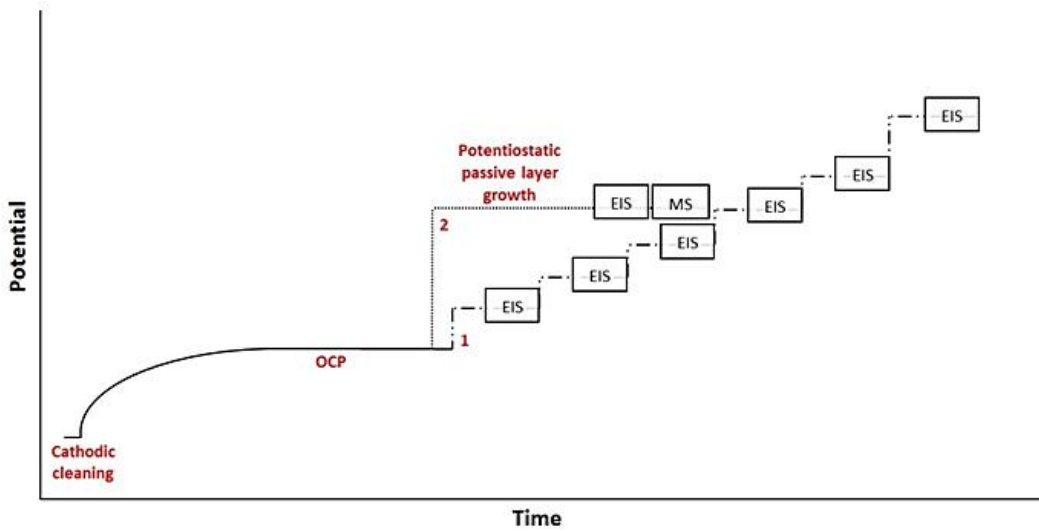


Figure 6-2: Schematic of the two independent electrochemical test routines conducted in this chapter

6.2 Dynamic step-wise anodizing EIS test

The following discussion of EIS results under PDP conditions follows the same order of the potential regions examined in each PDP scan of Figure 6-1 (i.e. from the active potential region to the transpassive/breakdown region, scanned in the anodic direction).

6.2.1 Active corrosion at $E < E_{pl}$

In the active potential region from OCP to just above $-0.5 V_{SCE}$, nearly complete depressed semicircles were exhibited in the Nyquist profiles (Figure 6-3) of solutions with and without $\text{Cl}^-/\text{SO}_4^{2-}$. The existence of ancillary electrochemical processes is observable at lower ω . In the $-0.65 V_{SCE}$ profiles of Figure 6-3, slight positive inflections in the Nyquist profile at 1 Hz are the result minor impedance increases from a ω -dependent surface process on the otherwise bare steel. At this early active potential, well before the significant i_{corr} decreases above E_{pl} , adsorption of pre-passive ferrous bicarbonates ($[\text{FeHCO}_3^-]_{ads}$ and $[\text{FeHCO}_3]_{ads}$, [180]) occurs prior to formation of FeCO_3 . In addition, the adsorption of FeOH_{ads} is a necessary prerequisite to

the development of $\text{Fe}(\text{OH})_2$ as shown in [178]. These pre-passivation steps are involved with anodic dissolution of the substrate at anodic sites which cover the majority of the surface at this stage.

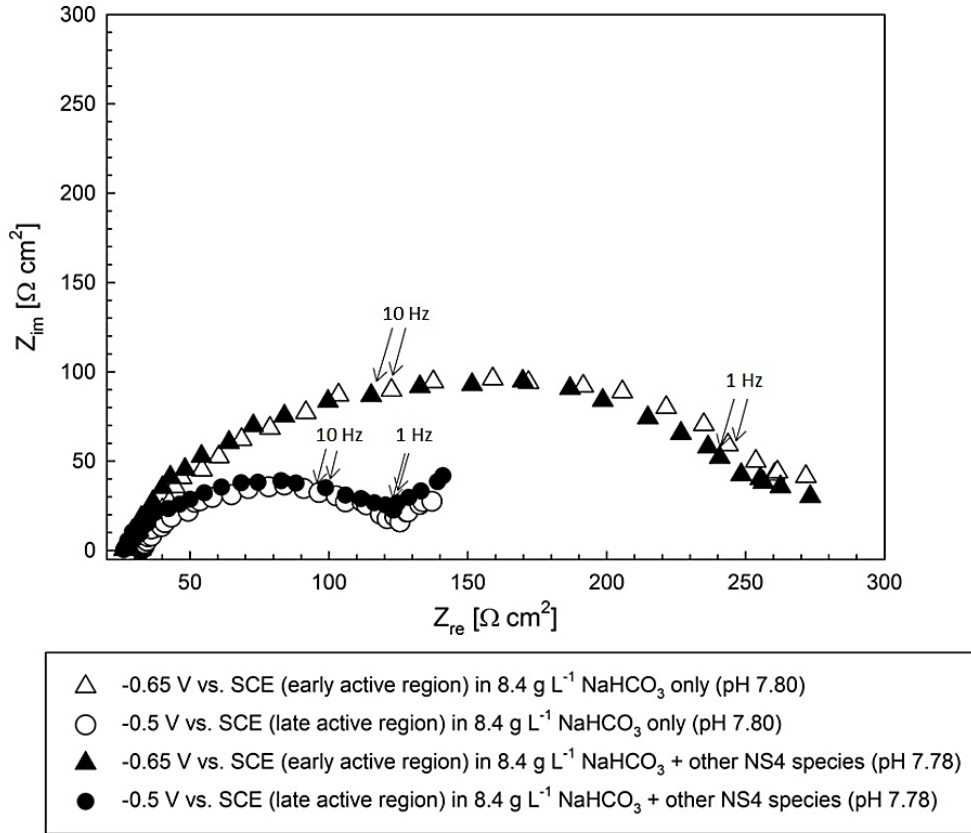


Figure 6-3: Nyquist impedance representation in active corrosion region ($\text{OCP} < E \leq E_{pi}$)

This parallel dissolution-adsorption process is adsorption-controlled and ω -dependent based on its influence beyond 1 Hz only. Modelling this process using an EEC with a capacitive-resistive element pair in a parallel orientation [208] can accommodate the less restricted movement of current through capacitive branches at higher ω , as the resistive branches are shorted. In situations with more compliant adsorption processes, the applicability of a nested parallel adsorption layer within the double layer of the proposed EEC has been shown before [208]. The configuration is $\{R(C(R(C(R))))\}$ as illustrated earlier in Figure 5-14 on page 77. This proposed EEC orientation is used to model the present adsorption-controlled process, achieving a better fit than the $\{R(CR)(CR)\}$ configuration in which the adsorption elements are outside of the

double layer. EEC elements are the same as with the previous usage of this model, where CPE double-layer and adsorption elements are again governed by {E-5.1} on page 75

Good correlation between the $-0.65 V_{SCE}$ experimental data and $\{R(C(R(C(R))))\}$ is achieved, as seen from χ^2 values on the order of 1.0×10^{-4} and a maximum error in fit of 2.25% (Table 6-2). The Westing-Mertens method described in {E-6.1} is used to convert CPE amplitudes Q_{dl} and Q_a to corresponding equivalent capacitances C_{dl} and C_a , where ω_θ is the inflection ω at which the absolute value of θ_{EIS} reaches a maximum [209]. This method is appropriate for multiple time constant nested RC circuits, and $n > 0.8$ for all instances in Table 6-2 meets CPE usage recommendations.

Table 6-2: EIS component values for 0.1 M $[HCO_3^-]$ solution with and without Cl^-/SO_4^{2-} at $E_{an} = -0.65 V_{SCE}$ (early active E region)

Components	Solution with Cl^-/SO_4^{2-} at $-0.65 V_{SCE}$	Solution without Cl^-/SO_4^{2-} at $-0.65 V_{SCE}$
R_s [$\Omega \text{ cm}^2$]	24.1	19.6
Q_{dl} [$\Omega^{-1} \text{ s}^n$]	2.03×10^{-4}	2.38×10^{-4}
n_{dl}	0.87	0.84
C_{dl} [$F \text{ cm}^2$]	1.32×10^{-4}	1.41×10^{-4}
R_{ct} [$\Omega \text{ cm}^2$]	158	181
Q_a [$\Omega^{-1} \text{ s}^n$]	4.01×10^{-3}	3.76×10^{-2}
n_a	0.82	0.87
C_a [$F \text{ cm}^2$]	2.24×10^{-3}	2.45×10^{-2}
R_a [$\Omega \text{ cm}^2$]	34.9	75.6
χ^2	5.5×10^{-4}	4.05×10^{-4}
% error in fit	< 2.25	< 1.93

$$C_i = \frac{Q_i \cdot (\omega_{\theta,i})^{n_i-1}}{\sin(\frac{\pi n_i}{2})} \quad \{\mathbf{E-6.1}\}$$

In Table 6-2, R_{ct} values increase in the absence of Cl^-/SO_4^{2-} , and it appears that Cl^-/SO_4^{2-} also promote adsorption on the exposed steel surface, judging from decreased R_a values in their presence. These effects are opposite to those induced by Cl^-/SO_4^{2-} additions at OCP seen in the previous chapter. The anodic polarization of the specimen proliferates anodic site coverage more so than when left at OCP, which attracts dissolved anions and is likely what increases Fe^{2+} release and anion adsorption. It is proposed that due to the adsorbed anions hampering the

establishment of a complete first $[\text{FeHCO}_3]_{ads}$ layer on the steel adsorbent, the attractive strength between the steel and the $\text{Cl}^-/\text{SO}_4^{2-}$ adsorbates remain high. Once a first $[\text{FeHCO}_3]_{ads}$ layer is formed, further adsorption to this layer is greatly impeded as established by numerous adsorption models, such as Hill-Langmuir in {E-6.2} [210]. In this specific model, θ_{ads} is the fractional coverage of the surface, C_{ads} is the concentration of the adsorbed electroactive species/compound, and α_{ads} is a constant. Impedance to further adsorption, represented by R_a in the present EIS results, is higher for surfaces with more filled particle sites.

$$\theta_{ads} = \frac{\alpha_{ads} \cdot C_{ads}}{1 + \alpha_{ads} \cdot C_{ads}} \quad \{\mathbf{E-6.2}\}$$

At $E_{an} = -0.5 \text{ V}_{\text{SCE}}$, the Nyquist plots in Figure 6-3 reveal more noticeable supplemental electrochemical processes at low $\omega < 1 \text{ Hz}$, suggesting change in governing mechanism(s) [211]. The positive linearity of the Nyquist plots at $\omega < 1 \text{ Hz}$ suggests a contribution of diffusion in the electrochemical process occurring. Mass-transfer controlled behavior, characterized especially by the linear slope segments in the Nyquist plots, give evidence for the necessary diffusion of electro-active species towards the specimen surface in support of the pre-passivation step reactions ensuing at this potential. In the mildly alkaline media here, these species are suggested to be HCO_3^- and OH^- [212] diffusing due to a concentration gradient arising from depletion caused by earlier adsorption reactions. Due to continued association of the electrochemical process with R_{ct} and Q_{dl} , this diffusion is best accommodated in the proposed EEC by the W diffusion element. This element induces a ω -dependent impedance (Z_W) which decreases at higher ω values as described by {E-6.3}, where W_A is the Warburg constant:

$$Z_W = \frac{W_A}{\sqrt{\omega}} + \frac{W_A}{j\sqrt{\omega}} \quad \{\mathbf{E-6.3}\}$$

The configuration with the diffusive element within the adsorption subset of the electrochemical circuit, namely {R(Q(R(Q(RW))))} as previously shown in Figure 5-16, achieves better fit than when the diffusive element is placed in series with R_s . Overall, very good

compatibility with the experimental results is attained, with the maximum error in fit not surpassing 2% as seen in Table 6-3.

Table 6-3: EIS component values for 0.1 M $[\text{HCO}_3^-]$ solution with and without $\text{Cl}^-/\text{SO}_4^{2-}$ at $-0.5 \text{ V}_{\text{SCE}}$ (late active potential region), and 0.1 M $[\text{HCO}_3^-]$ solution without $\text{Cl}^-/\text{SO}_4^{2-}$ at $-0.4 \text{ V}_{\text{SCE}}$ (transition potential region)

Components	Solution with NS4 $\text{Cl}^-/\text{SO}_4^{2-}$ at $-0.5 \text{ V}_{\text{SCE}}$	Solution without NS4 $\text{Cl}^-/\text{SO}_4^{2-}$ at $-0.5 \text{ V}_{\text{SCE}}$	Solution without NS4 $\text{Cl}^-/\text{SO}_4^{2-}$ at $-0.4 \text{ V}_{\text{SCE}}$
R_s [$\Omega \text{ cm}^2$]	20	24	24
Q_{dl} [$\Omega^{-1} \text{ s}^n$]	5.28×10^{-4}	3.56×10^{-4}	3.43×10^{-4}
n_{dl}	0.79	0.81	0.85
C_{dl} [F cm^{-2}]	2.70×10^{-4}	1.93×10^{-4}	2.40×10^{-4}
R_{ct} [$\Omega \text{ cm}^2$]	38.1	55.3	339
Q_a [$\Omega^{-1} \text{ s}^n$]	2.87×10^{-2}	2.72×10^{-2}	5.11×10^{-3}
n_a	0.80	0.84	0.96
C_a [F cm^{-2}]	1.51×10^{-2}	1.61×10^{-4}	4.62×10^{-3}
R_a [$\Omega \text{ cm}^2$]	91.7	115	84.9
W [$\Omega^{-1} \text{ s}^{0.5}$]	4.42×10^{-2}	3.28×10^{-2}	2.53×10^{-2}
χ^2	2.21×10^{-4}	2.72×10^{-4}	2.16×10^{-4}
% error in fit	< 1.52	< 1.63	< 1.51

The applicability of the Figure 5-16 configuration for nested parallel circuits with two time constants has previously been shown by Chen and Jepson in [213], albeit for a situation where the second time constant paired with the double layer is from a passive film (R_f and Q_f). Practically though, for the processes occurring in the present conditions adsorption and diffusion effects exist together due to the direct physical reliance of the former on the species transported by the latter. Thus, the proposed model configuration of Figure 5-16 is more representative of the suggested physical process. As such, increased diffusion W in Table 6-3 upholds well the accompanying increased adsorption (decreased R_a) at more anodic potentials. It is noted that increased diffusion is indicated by higher corresponding Z_W and that the W results in Table 6-3 are for ω -dependent units containing Ω^{-1} . Compared to results for EIS at OCP in section 5.3, it is clear here that anodic polarization enhances the movement and adsorption of dissolved anions to an active corroding steel surface. Compared to the $-0.65 \text{ V}_{\text{SCE}}$ results, decreased R_{ct} values are anticipated in the $-0.5 \text{ V}_{\text{SCE}}$ case due to higher dissolution with increased anodic polarization in

the active region. In both the $-0.65 \text{ V}_{\text{SCE}}$ and $-0.5 \text{ V}_{\text{SCE}}$ cases C_{dl} exhibits an inverse trend with R_{ct} reflecting the capacitive character of the double layer [57].

6.2.2 Corrosion and passive-like behavior in the $E_{p1} < E < E_{p2}$ transition

In the active-passive transition potential region above $-0.5 \text{ V}_{\text{SCE}}$, the E at which the i minima occurs in Figure 6-1 most likely represents the change from $\text{Fe}(\text{OH})_2$ formation to its dissolution in HCO_3^- media [189]. The short E range where i decrease and subsequent acceleration occurs with the development and dissolution of this product substantiates the likelihood of it being $\text{Fe}(\text{OH})_2$. $\text{Fe}(\text{OH})_2$ development follows the reaction steps {R-5.6} – {R-5.8} shown before in section 5.2.1 [178], and its adherence to the surface in the final step {R-5.8} results in the intermittent current density decrease observed between E_{p1} and E_{p2} in Figure 6-1. The mechanism has been reported to be independent of O_2 traces in the media [188]; hence, its occurrence in the deaerated solutions of the present investigation is not anomalous.

Since the E range of the $\text{Fe}(\text{OH})_2$ formation and dissolution region is very small, it is difficult to target the specific regions of decreasing or increasing i with a PSP. As such, polarization performed in this region might drive either $\text{Fe}(\text{OH})_2$ formation or dissolution, a result which can only be determined by observing i behavior during polarization or EIS analysis after it. From the Nyquist plot of 0.1 M HCO_3^- in the absence of $\text{Cl}^-/\text{SO}_4^{2-}$ polarized at $-0.4 \text{ V}_{\text{SCE}}$ (Figure 6-4a), it is more likely that the process being driven at this E is the formation of $\text{Fe}(\text{OH})_2$ below the current minima in Figure 6-1. The extended low ω portion of the Nyquist plot suggests that dissolution is not the only electrochemical process occurring. Rather, the diffusion of OH^- and the adsorptive effect of FeOH_{ads} are still present. Continued $\text{Fe}(\text{OH})_2$ formation triggers OH^- diffusion to counteract OH^- depletion in early and late steps of the process (i.e. {R-5.6} and {R-5.8}, respectively). Adsorption, specifically of FeOH , is also inherently involved therein. Subsequent adherence of the final $\text{Fe}(\text{OH})_2$ product to the surface, as illustrated schematically in Figure 6-4b, leads to the observable increase of Z_{im} and Z_{re} values of the $-0.4 \text{ V}_{\text{SCE}}$ case in

Figure 6-4a compared to the $-0.5 V_{SCE}$ case of Figure 6-3. The increased Z at the interface in the presence of this $Fe(OH)_2$ product has the capability of causing noticeable declines in current density as reported in [177], a finding corroborated by the i minima between E_{p1} and E_{p2} exhibited in the PDP curves of Figure 6-1.

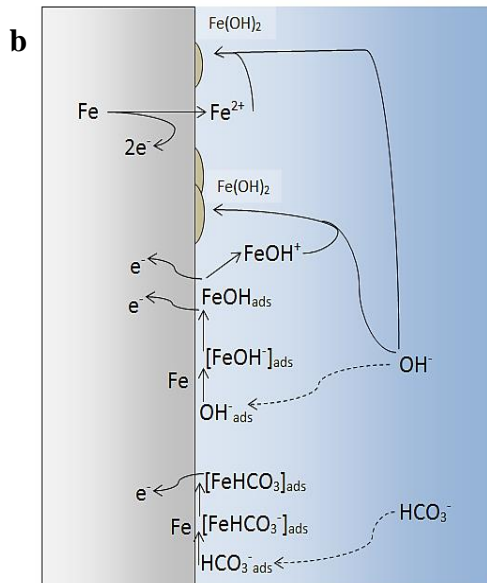
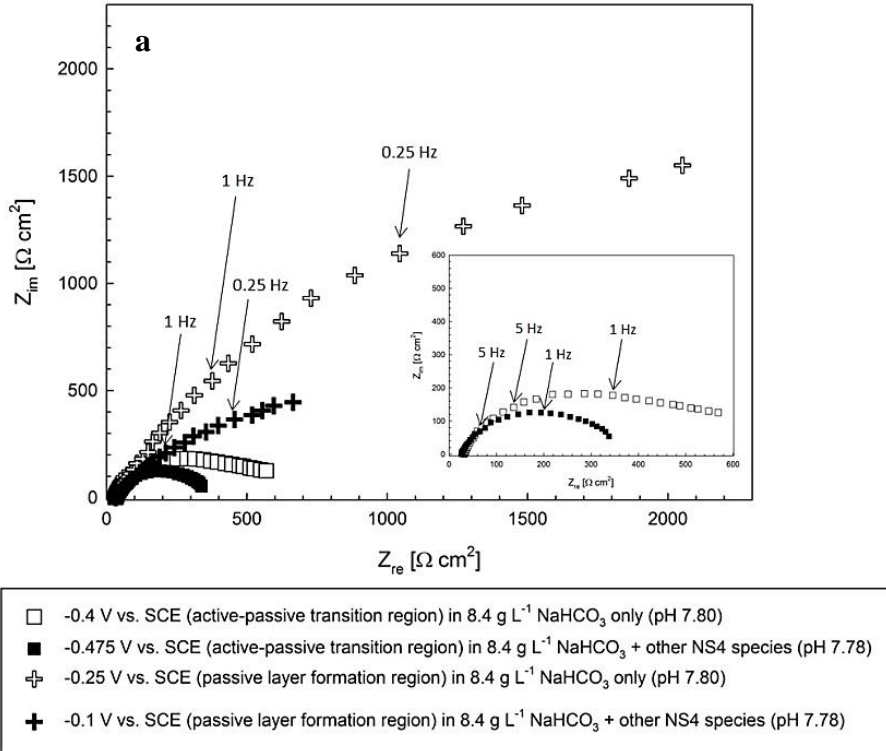


Figure 6-4: (a) Nyquist impedance representation in transition and passive layer formation region ($E_{p1} < E \leq 0 V_{SCE}$); (b) Proposed physical occurrences for EIS at $-0.4 V_{SCE}$ in solution without NS4 Cl^- / SO_4^{2-}

Although $\text{Fe}(\text{OH})_2$ formation does partially cover the specimen surface, causing the increase in the impedance modulus of the $-0.4 \text{ V}_{\text{SCE}}$ case, the continued applicability of the $\{\text{R}(\text{Q}(\text{R}(\text{Q}(\text{RW}))))\}$ EEC configuration in modelling this stage is suggested. The Nyquist plot indicates the sustained involvement of adsorption-diffusion processes which precede and upkeep the $\text{Fe}(\text{OH})_2$ formation reactions (Figure 6-4b), requiring the inclusion of R_a , Q_a , and W elements. The validity of including a third time constant with a parallel R_f and Q_f configuration is considered to be poor. This is because the $\text{Fe}(\text{OH})_2$ is defective and does not completely passivate the surface [177], causing only transitory impediment of the dissolution process. In fact, even in situations where stable passive layers develop, Eliyan et al. [214] reported limited applicability of EECs with three time constant such as $\{\text{R}(\text{QR})(\text{QR})(\text{QR})\}$ and $\{\text{R}(\text{QR})(\text{QR})(\text{Q}(\text{RW}))\}$ for situations with possible adsorption and/or insertion processes. Modelling the $-0.4 \text{ V}_{\text{SCE}}$ case with the parallel diffusion-adsorption circuit illustrated of Figure 5-16 achieves a very good fit as seen by χ^2 and % error values in Table 6-3. The fitting results show sustained anion diffusion, mainly OH^- based on the previous discussion, and increased adsorption compared to $E_{an} = -0.5 \text{ V}_{\text{SCE}}$ in the late active E region. The increased adsorption represented by the decreased R_a values is attributed to the depletion of adsorbed OH^- species and complexes (OH^-_{ads} , $[\text{FeOH}]_{\text{ads}}$, and FeOH_{ads}) due to the development of $\text{Fe}(\text{OH})_2$. The FeOH_{ads} oxidation product FeOH^+ is a reactant in the $\text{Fe}(\text{OH})_2$ deposition mechanism, as shown schematically in Figure 6-4b. The depletion of adsorbed species/complexes decreases θ_{ads} in {E-6.2}, or likewise in other models, thus causing more adsorption and supporting diffusion to sustain original concentrations.

Contrary to the $-0.4 \text{ V}_{\text{SCE}}$ case, the complex plot for specimen polarized at $-0.475 \text{ V}_{\text{SCE}}$ in Figure 6-4a lack any evident auxiliary effects at low ω . Even though the polarizing E is less anodic compared to $-0.4 \text{ V}_{\text{SCE}}$, it appears that the dissolution of exposed areas of the steel substrate is the controlling electrochemical process at this stage in these conditions. The strong influence of even small amounts of $\text{Cl}^-/\text{SO}_4^{2-}$ is apparent here. These anions inhibit stable

adsorption of OH^- species and OH^- complexes, in addition to hampering the adherence of subsequently-formed products like $\text{Fe}(\text{OH})_2$. At this potential, any $\text{Fe}(\text{OH})_2$ deposit can also suffer from pure chemical breakdown into Fe^{2+} , OH^- , and CO_3^{2-} ions, under the influence of HCO_3^- as seen in {R-5.9} [178], [215]. Combined with the accelerated Fe^{2+} release Cl^- inflicts on the exposed steel [57], the chemical breakdown in {R-5.9} causes clear electrochemical dissolution-control at this E in the active-passive transition region. This process is electrochemically modelled by a single time-constant Randles EEC [216], namely{R(QR)}, resembling the active dissolution of stages at -0.65 and -0.5 V_{SCE} except without adsorptive or diffusive effects. A CPE element is still used for the double layer, but the Brug method of {E-6.4} [197] is used instead of Westing-Mertens to convert its result to C_{dl} . The Brug method applies only to the single time constant Randles circuit and depends on resistances R_{ct} and R_s , not ω :

$$C_i = \left[Q_i \left(\frac{1}{R_s} + \frac{1}{R_{ct}} \right)^{n_i} \right]^{1/n_i} \quad \{\mathbf{E-6.4}\}$$

Table 6-4: EIS component values for 0.1 M $[\text{HCO}_3^-]$ solution with $\text{Cl}^-/\text{SO}_4^{2-}$ at -0.475 V_{SCE} (transition potential region)

Components	Solution with $\text{Cl}^-/\text{SO}_4^{2-}$ at -0.475 V_{SCE}
R_s [$\Omega \text{ cm}^2$]	19
Q_{dl} [$\Omega^{-1} \text{ s}^n$]	9.10×10^{-4}
n_{dl}	0.82
C_{dl} [F cm^{-2}]	3.68×10^{-4}
R_{ct} [$\Omega \text{ cm}^2$]	253
χ^2	6.04×10^{-4}
% error in fit	< 2.38

It is important to note that the proposed Randles circuit only models the active dissolution of the exposed sites of the steel substrate, not the $\text{Fe}(\text{OH})_2$ removal. The use of additional elements to represent any $\text{Fe}(\text{OH})_2$ presence on the surface is neglected for the same reasons outlined earlier in this section. R_{ct} values can sufficiently gauge the impedance effect caused by the presence of any $\text{Fe}(\text{OH})_2$ deposits on the specimen. Indeed, the R_{ct} value in

Table 6-4 agrees well with the PDP of Figure 6-1: the i of the solution containing $\text{Cl}^-/\text{SO}_4^{2-}$ in the active-passive transition E region is more than the $\text{Cl}^-/\text{SO}_4^{2-}$ -free solution in the same E region (Table 6-3), yet less than the same solution at a lower $E = -0.65 \text{ V}_{\text{SCE}}$ (Table 6-2).

6.2.3 Corrosion and passivation processes at $E > E_{p2}$

With further increase of anodizing E into the passive-layer formation and passive regions above E_{p2} , passive layers develop stably as manifested by markedly higher impedance values in Figure 6-4a and Figure 6-5a (cross and star data points). Bode $|Z|$ profiles for the star data points can be found in Figure B-2 in Appendix B. HCO_3^- in the electrolyte previously driving the complexing of pre- FeCO_3 formation compounds at lower E [189] also contributes to the formation of FeCO_3 at $E > E_{p2}$ as shown in the bottom half of Figure 6-5b. The degeneration of $\text{Fe}(\text{OH})_2$ deposits leads to increased FeCO_3 either through direct transformation (shown in [217]) or through the increase of $[\text{CO}_3^{2-}]$ in the solution, which can later associate with Fe^{2+} from the substrate dissolution. Thus, the growth of the FeCO_3 layer depends on HCO_3^- driving the charge-transfer steps, and forms over $\text{Fe}(\text{OH})_2$ in a multi-layer as illustrated in the top half of Figure 6-5b.

The noticeable increase in impedance in the Nyquist plots in this E region is expected from increased R_{ct} and the introduction of a robust barrier between the steel and the environment. This is modeled in the corresponding EEC with a second time-constant as proposed in [59] for steels in concentrated HCO_3^- solutions, with the configuration $\{\text{R}(\text{QR})(\text{QR})\}$ in Figure 6-6a. R_f and Q_f in this EEC are the passive film resistance and passive constant phase elements, respectively. This EEC is used to model Z spectra from both the passive-layer formation and passive regions below E_{bd1} in the PDP plots, as only the growth of the FeCO_3 layer and its level of protectiveness changes between these regions. The circuit achieves a good agreement with the experimental data (Table 6-5). R_f values are E -dependent and superior in the absence of $\text{Cl}^-/\text{SO}_4^{2-}$, indicating increased protectiveness. R_{ct} values achieve agreeable compatibility with R_f

values due to decreased dissolution with greater FeCO_3 growth, either at higher E or in $\text{Cl}^-/\text{SO}_4^{2-}$ -free solutions. CPEs of both the double layer and the passive layer exhibit typical reciprocity with their corresponding resistances, again reflecting their capacitive character.

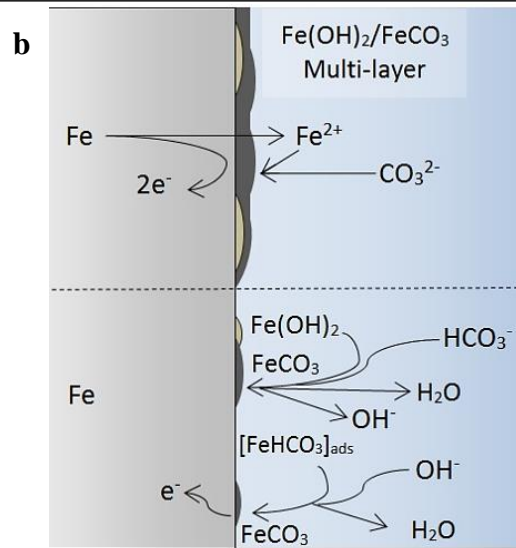
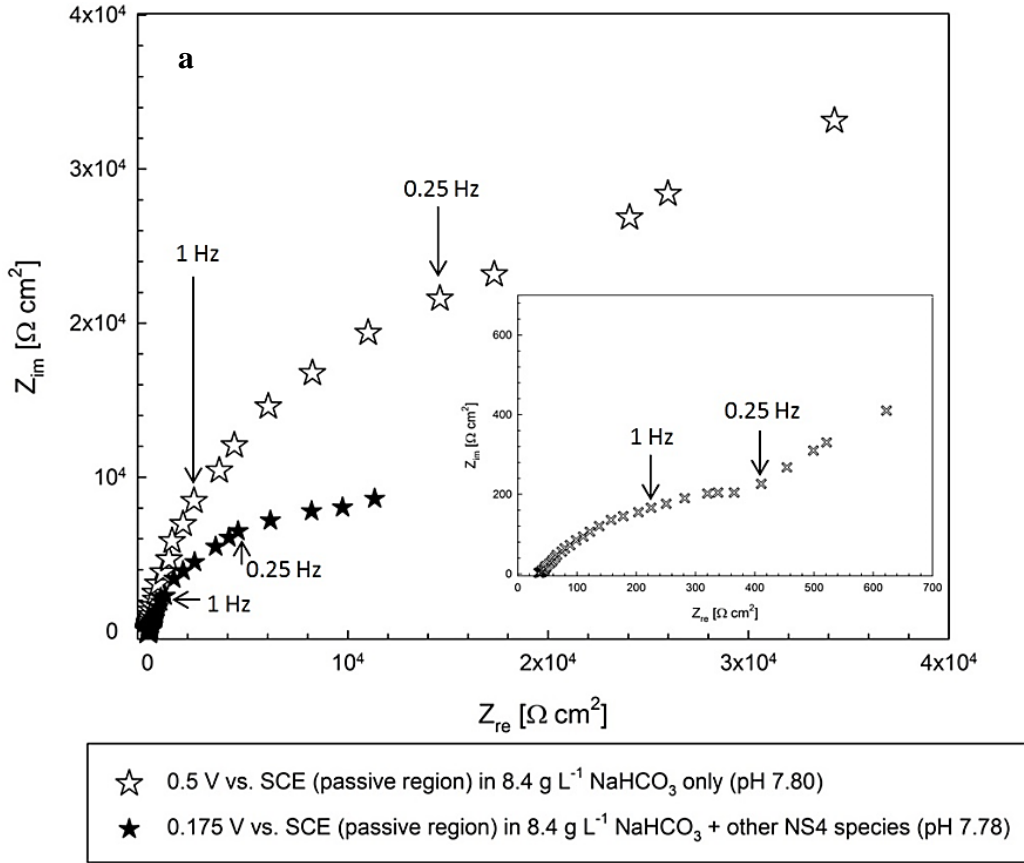


Figure 6-5: (a) Nyquist impedance representation in passive and transpassive region ($E > 0 \text{ V}_{\text{SCE}}$); (b) Proposed corresponding physical occurrences for EIS at $-0.25 \text{ V}_{\text{SCE}}$, $-0.1 \text{ V}_{\text{SCE}}$, $0.5 \text{ V}_{\text{SCE}}$ and $0.175 \text{ V}_{\text{SCE}}$

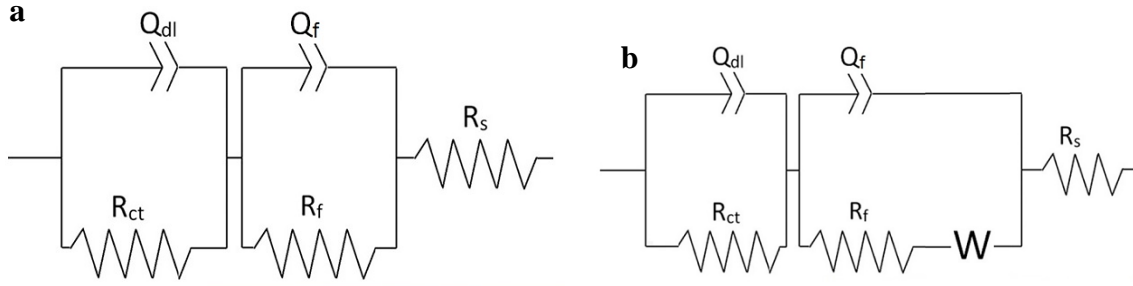


Figure 6-6: (a) Proposed EEC and corresponding physical occurrences for EIS at $-0.25 V_{SCE}$, $-0.1 V_{SCE}$, $0.5 V_{SCE}$ and $0.175 V_{SCE}$; (b) Proposed EEC for EIS at $1.1 V_{SCE}$ in solution without Cl^-/SO_4^{2-}

Table 6-5: EIS component values for 0.1 M $[HCO_3^-]$ solution with Cl^-/SO_4^{2-} at $-0.1 V_{SCE}$ (passive formation potential region) and $0.175 V_{SCE}$ (passive potential region), and without Cl^-/SO_4^{2-} at $-0.25 V_{SCE}$ (passive formation potential region) and $0.5 V_{SCE}$ (passive potential region)

Components	Solution with NS4 Cl^-/SO_4^{2-} at $-0.1 V_{SCE}$	Solution without NS4 Cl^-/SO_4^{2-} at $-0.25 V_{SCE}$	Solution with NS4 Cl^-/SO_4^{2-} at $0.175 V_{SCE}$	Solution without NS4 Cl^-/SO_4^{2-} at $0.5 V_{SCE}$
R_s [Ωcm^2]	32	29	32	34
Q_{dl} [$\Omega^{-1} s^n$]	9.14×10^{-3}	7.40×10^{-3}	7.54×10^{-3}	3.35×10^{-5}
n_{dl}	0.84	0.81	0.94	0.99
C_{dl} [$F cm^2$]	7.85×10^{-3}	6.22×10^{-3}	6.97×10^{-3}	3.29×10^{-5}
R_{ct} [Ωcm^2]	1.00×10^3	1.40×10^3	4.42×10^3	8.82×10^3
Q_f [$\Omega^{-1} s^n$]	9.97×10^{-4}	6.54×10^{-5}	5.24×10^{-5}	2.09×10^{-5}
n_f	0.84	0.84	0.83	0.90
C_f [$F cm^2$]	8.56×10^{-4}	5.62×10^{-5}	4.29×10^{-5}	1.76×10^{-5}
R_f [Ωcm^2]	1.54×10^3	3.71×10^3	1.07×10^3	2.26×10^3
χ^2	7.78×10^{-4}	1.87×10^{-4}	1.38×10^{-4}	5.66×10^{-4}
% error in fit	< 2.76	< 1.44	< 1.33	< 2.29

At transpassive potentials above E_{bdl} , passive layer breakdown occurs as revealed by the sharp drop in $|Z|$ values in Figure B-2 compared to spectra at passive potentials. The Nyquist profile of the $0.65 V_{SCE}$ case was omitted from Figure B-2 due to its incoherence. The breakdown mechanism in Figure B-2 is dependent on Cl^-/SO_4^{2-} , manifested by the unstable fluctuation of the $0.65 V_{SCE}$ case with Cl^-/SO_4^{2-} therein, compared to the orderly profiles of the higher applied $E = 1.1 V_{SCE}$ case without NS4 Cl^-/SO_4^{2-} in Figure 6-5a and Figure B-2. Here, Cl^-/SO_4^{2-} ions attack pre-existing deposits, increasing the density of anodic sites on the specimen exposed to electrolyte. Subsequently, $Fe_3O_4/\gamma-Fe_2O_3$ formation is likely occurring at this high anodic potential, resulting in a less protective more porous passive layer structure. Modeling the $Fe_3O_4/\gamma-$

Fe₂O₃ covered surface above E_{bd1} involves an added time-constant to quantify pore impedance, but reliable fitting results were unachievable here. Separate EIS investigations dedicated to oxide and oxyhydroxides of Fe on X100 are presented in the next chapter (see section 7.4.2).

Table 6-6: EIS component values for 0.1 M [HCO₃⁻] solution without Cl⁻/SO₄²⁻ at 1.1 V_{SCE} (transpassivation potential region)

Components	Solution without Cl ⁻ /SO ₄ ²⁻ at 1.1 V _{SCE}
R_s [Ω cm ²]	30
Q_{dl} [Ω^{-1} s ⁿ]	2.22×10^{-3}
n_{dl}	0.82
C_{dl} [F cm ⁻²]	1.88×10^{-3}
R_{ct} [Ω cm ²]	1.28×10^3
Q_f [Ω^{-1} s ⁿ]	3.80×10^{-4}
n_f	0.88
C_f [F cm ⁻²]	3.37×10^{-4}
R_f [Ω cm ²]	1.90×10^3
W [Ω^{-1} s ^{0.5}]	2.58×10^{-2}
χ^2	1.09×10^{-4}
% error in fit	< 1.27

The EIS response for the transpassive region in the solution free of Cl⁻/SO₄²⁻ (1.1 V_{SCE}) is stable, and diffusive effects appear once again after withdrawing during passive formation and passive regions. The lower $|Z|$ values accompanying this suggests greater mobility of electroactive species driving the passive layer breakdown steps through increased transfer channels in the passive films. This resembles the interfacial process occurring on steel with weak passive layers created in more dilute HCO₃⁻ solutions in [218]. The increased transfer channels within the passive film require the diffusion element to be within the film section of the EEC, in a configuration similar to the Figure 5-14 model used for parallel diffusion-adsorption controlled processes at lower E . In principle, diffusion is also present within the electric double layer, including both the Gouy-Chapman layer below 200 Å and the thicker Nernst diffusion boundary. However, in the present proposed model any mass-transfer within the double-layer is neglected for simplicity. The parallel kinetics-diffusion controlled process observed here has been shown to be modeled well with the {R(QR)(Q(RW))} configuration of Figure 6-6b [219]. This circuit

achieves a good fit with the present experimental data at the transpassivation E in $\text{Cl}^-/\text{SO}_4^{2-}$ -free media (Table 6-6). R_f and R_{ct} values drop significantly compared to passive E of Table 6-5, and it appears that species mobility is quite high, at a level almost comparable to pre-passivation active stages in Table 6-3.

6.3 Protective and semiconductive properties of anodized FeCO_3

6.3.1 Current density decay and qualitative analysis of Bode $|Z|$ results

The transient i decay profiles under a PSP voltage of $0.5 \text{ V}_{\text{SCE}}$ are illustrated in Figure 6-7. The steepest decline is observed in the pH 8.5, $25 \text{ }^\circ\text{C}$ environment, reaching a stable i on the order of $1 \text{ } \mu\text{A cm}^{-2}$ in less than 200 s of polarization. All profiles at $25 \text{ }^\circ\text{C}$ demonstrate rapid decay and stable steady-state i approaching 1 h PSP. Conversely, with increasing solution temperature, i reaches $5 \text{ } \mu\text{A cm}^{-2}$ in approximately 800 s. Values of i shift higher with temperature and decreased pH due to less added $[\text{HCO}_3^-]$, and changes due to $[\text{HCO}_3^-]$ are more pronounced at higher temperatures. Transient profiles of tests conducted at $75 \text{ }^\circ\text{C}$ have stability times greater than the time domain of the figure (i.e. $> 1500 \text{ s}$) and still exhibit observable decrease after 1 h. Volatility in the decaying portion of the profiles alludes to unstable passivation development due to the thinner and less robust passive layer formed from sluggish film growth.

The trend of Figure 6-7 confirms the development of a more robust and protective passive layer in colder, more alkaline, HCO_3^- -rich conditions. FeCO_3 formation is generally accelerated with both increased alkalinity and $[\text{HCO}_3^-]$ as described in [180]. Large $\text{Fe}(\text{OH})_2$ involvement in the formed passive layer is unlikely here due to thermodynamic unviability at a direct PSP E of $0.5 \text{ V}_{\text{SCE}}$, based on E -pH diagrams of the $\text{Fe-HCO}_3^- \text{-CO}_3^{2-} \text{-H}_2\text{O}$ system. At any single $[\text{HCO}_3^-]$, increasing solution temperature increases alkalinity due to decreased CO_2 solubility and the resulting H_2CO_3 dissociation at higher temperatures. Yet, it is observed that this decreases passive layer protectiveness at any single $[\text{HCO}_3^-]$. This is due to decreased kinetics of pre- FeCO_3 HCO_3^- complexation steps in {R-5.10} and {R-5.11} due to lower dissociated $[\text{HCO}_3^-]$

from the lower $[H_2CO_3]$ at higher temperatures, hampering $FeCO_3$ growth. Interestingly, this behavior offsets reduced $FeCO_3$ solubility at higher temperatures, which would lead to increased precipitation. Previously, Benezeth et al. experimentally found that the solubility product (K_{sp}) of $FeCO_3$ decreases from 10^{-11} to $10^{-11.5}$ for a temperature change from 25 to 75 °C [220]. This influence is not enough to overcome sluggish $FeCO_3$ growth at higher temperatures, leading to the observed reduced protectiveness at 50 and 75 °C.

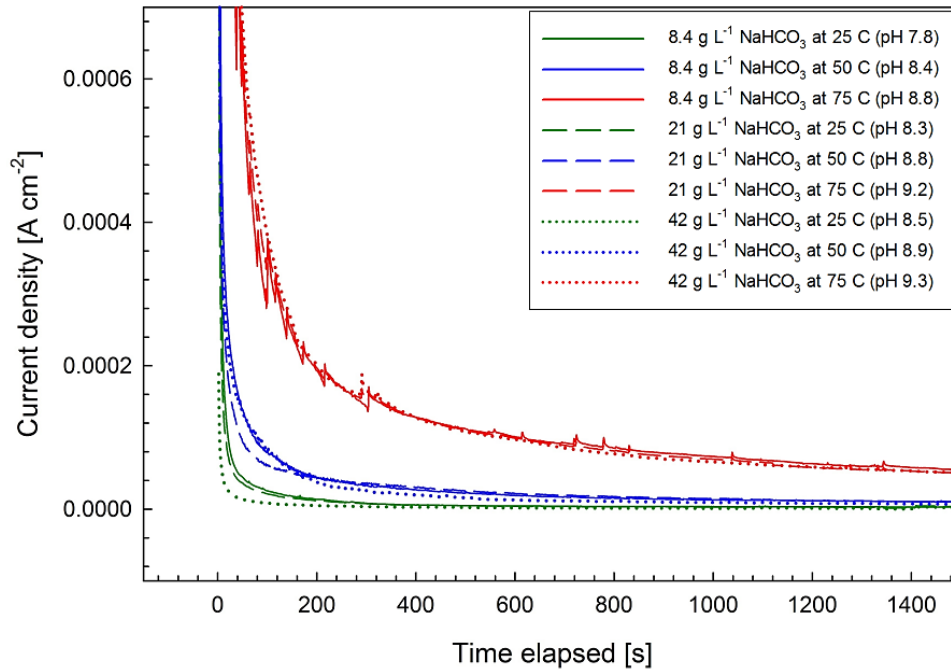


Figure 6-7: Current density decay profiles of specimen anodized at $0.5 V_{SCE}$ in 0.1, 0.25, or 0.5 M $NaHCO_3$ at 25, 50, or 75 °C (pH 7.8 – 9.3)

Identifying a passive layer protectiveness ranking based on temperature or $[HCO_3^-]$ requires isolation of either variable to determine the individual effect of each. EIS is conducted on passivated specimen immediately following PSP to corroborate former interpretations. Only $|Z|$ results are presented here for qualitative comparisons (Figure 6-8), and the EEC referred to herein is that which we used previously to model a well-developed passive layer which is not breaking down (Figure 6-6a). At $\omega < 100$ Hz, $|Z|$ are less influenced by the ω -dependent capacitive effects of Q_f and Q_{ct} and hence the EIS spectra on the left half of Figure 6-8 follow the protectiveness trend of i decay results identically. In this ω range the resistances R_f and R_{ct} , which are of physical

importance in identifying passive layer strength, are less skewed by the parallel CPE branches in the EEC. In contrast, at $\omega > 100$ Hz, the capacitive branches experience reduced individual Z , decreasing the total $|Z|$ and drawing current (I) from the resistive branches. Thus, $|Z|$ at these ω represent less the combined resistivity of the passive and double layers, explaining the diminished separation of the data and the loss of the observed protectiveness trend. The reduced-slope region at $0.1 < \omega < 100$ Hz can be attributed to remnants of sustained mass-transfer, especially at high temperatures where full steady-state behavior is not achieved after 1 h of PSP. Comparing the $|Z|$ spectra of Figure 6-8 to those of passivated surfaces in the step-wise anodizing-EIS tests (Figure B-2 in Appendix B) demonstrates that increasing temperature to 75 °C has a detrimental effect on passive layer strength almost equivalent to the presence of aggressive $\text{Cl}^-/\text{SO}_4^{2-}$. In fact, the effect of higher temperature can be comparable to partial breakdown of the passive layer above E_{p1} , as $|Z|$ approaches $10^3 \Omega \text{ cm}^2$ in both situations alike.

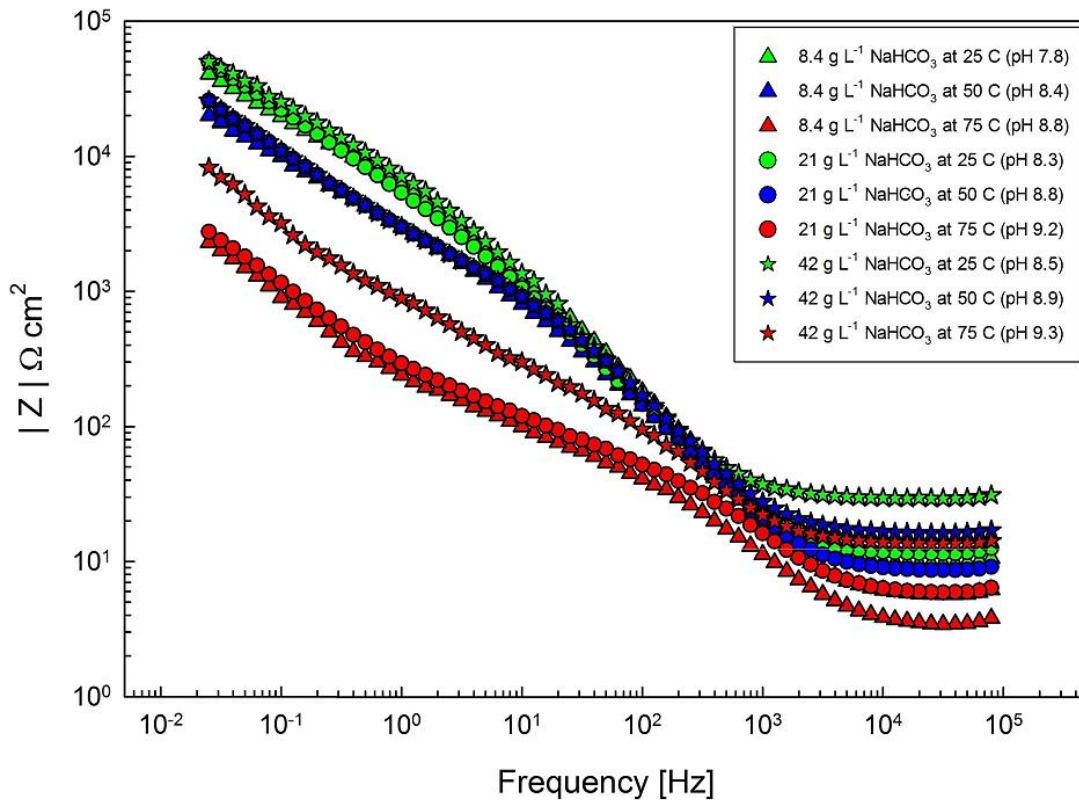


Figure 6-8: Bode $|Z|$ profiles of specimen after 1 h PSP in at 0.5 V_{SCE} in 0.1, 0.25, or 0.5 M NaHCO_3 at 25, 50, or 75 °C (pH 7.8 – 9.3)

6.3.2 Semiconductive properties analysis using Mott-Schottky

Mott-Schottky analysis relies on the assumption that the capacitance of the space charge layer (C_{sc}) is much less than that of the Helmholtz layer. At high applied ω , such as 1 kHz used in the present investigation, the capacitance at the passive layer's interface with the electrolyte mainly expresses C_{sc} , since the contribution of Helmholtz capacitance to measured electrode capacitance is negligible [221]. As such, the C_{sc}^{-2} versus E plots describe the semiconductive behavior of the depletion region. Quantitatively, the charge distribution as a function of E can be determined using {E-6.5} for n -type semiconductors [221], where N_d , E_{fb} , k , T , ε , ε_0 , and e parameters hold the same definitions as those given earlier in section 2.1.

$$\frac{1}{C_{sc}^2} = \frac{2}{\varepsilon\varepsilon_0eN_d} \left(E - E_{fb} - \frac{kT}{e} \right) \quad \{\mathbf{E-6.5}\}$$

N_d is determined from the slope of the experimental C_{sc}^{-2} vs. E plots (i.e. the $\frac{2}{\varepsilon\varepsilon_0eN_d}$ term), whereas E_{fb} is the potential intercept for $C_{sc}^{-2} = 0$. The thickness of the space-charge layer (δ_{sc}) for n -type semiconductors is evaluated using {E-2.1} in section 2.1.

After passive layer formation through PSP at 0.5 V_{SCE} for 1 h, all the Mott-Schottky tests are scanned from $E < E_p$ to $E > E_{bd}$. The C_{sc}^{-2} vs. E plots exhibit positive slopes in the passive region of interest as shown in Figure B-3 and Figure B-4 in Appendix B, indicating n -type semiconductive behavior. These two figures illustrate examples of the temperature and $[\text{HCO}_3^-]$ dependencies, respectively. The influence from $[\text{HCO}_3^-]$ and temperature results in decreased N_d with increased $[\text{HCO}_3^-]$ at any fixed temperature, or increased N_d with temperature at any fixed $[\text{HCO}_3^-]$ (Figure 6-9), corresponding to the findings of [173]. Consistencies are found with respect to slope nonlinearity also, specifically at the critical potential (E_c) of approximately 0.3 V_{SCE} in the 75 °C data of Figure B-4, where a noticeable slope increase (resulting in a drop in N_d) is observed. Slope nonlinearity in Mott-Schottky plots has previously been attributed to the distribution of donor states over a broad range of energies, the presence of surface states altering

the ΔE across the Helmholtz layer, or surface roughness and nonlinear donor distribution [222], [223]. Since the system of the present study involves oxidized states of Fe, slope nonlinearity is attributed to the influence of iron (III) ions (Fe^{3+}) on the electronic structure of passive layers developing at potentials beyond E_c [224]. This interpretation is thermodynamically supported by E_c , representing the E for the ionization of the deep level in the space charge layer, coinciding with the Pourbaix boundary between Fe^{2+} and Fe^{3+} valence states found in [225]. As such, a separate N_d value is required for $E > E_c$ in the 75 °C data, represented by N_{d2} and evaluated using the slope relationship in {E-6.6b}:

$$S_1 = \frac{2}{\varepsilon\varepsilon_0 e N_{d1}} \quad \text{for } E < E_c \quad \text{\{E-6.6a\}}$$

$$S_2 = \frac{2}{\varepsilon\varepsilon_0 e (N_{d1} + N_{d2})} \quad \text{for } E > E_c \quad \text{\{E-6.6b\}}$$

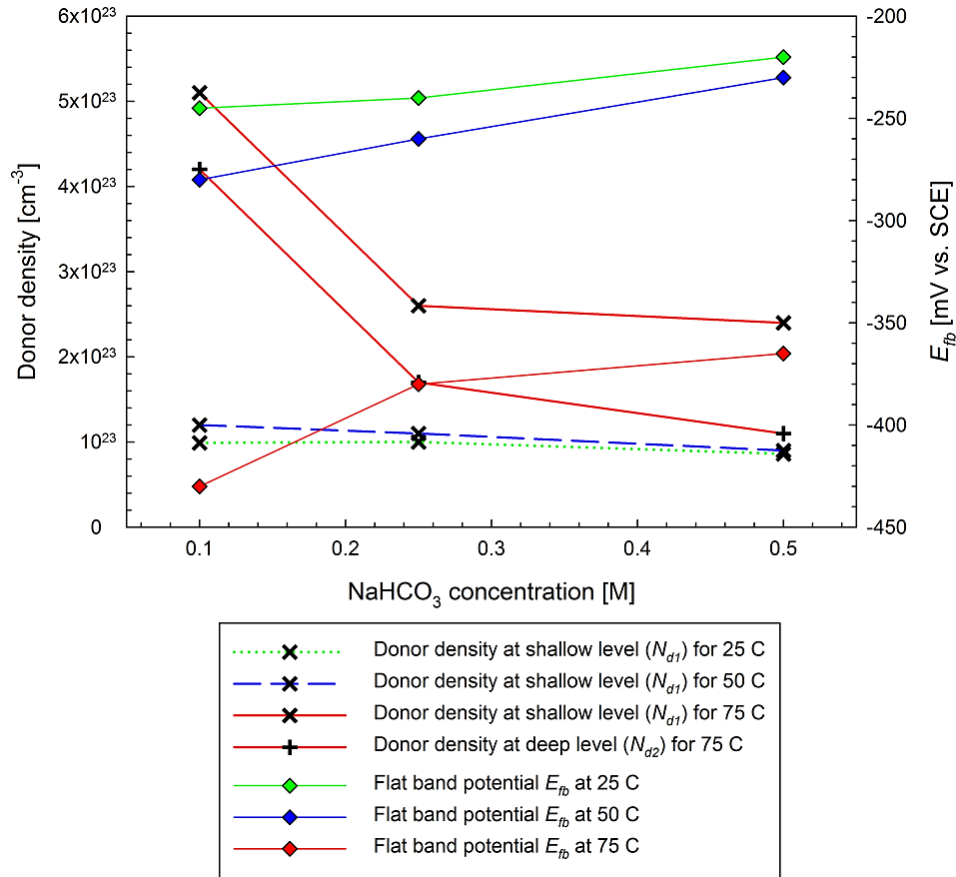
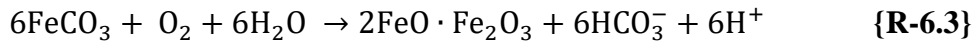
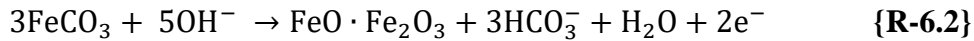


Figure 6-9: Dependence of N_{d1} , N_{d2} , and E_{fb} of passive layer on $[\text{NaHCO}_3]$ (0.1, 0.25, or 0.5 M) and temperature (25, 50, or 75 °C)

Passive layer charge neutrality and the higher tendency for Fe²⁺ to Fe³⁺ oxidation with temperature make slope nonlinearity in the Mott-Schottky plots highly temperature-dependent. However, as opposed to being almost equally influenced over a large range of temperatures as reported in [224], it appears from Figure B-3 that this dependence may be controlled by a minimum temperature threshold, since the change is almost non-existent at temperatures ≤ 50 °C. It is likely that the higher temperature which impedes robust FeCO₃ coverage of the steel as shown by *i* decay results leaves anodic sites where oxidation to Fe₃O₄/γ-Fe₂O₃ occurs. This results in decreased passive layer protectiveness. FeCO₃ can also transform directly to Fe²⁺-Fe³⁺-oxide (FeO·Fe₂O₃ or Fe₃O₄) at higher anodic *E* in anoxic conditions or with the influence of O₂ in the solutions as shown in {R-6.2} and {R-6.3}, respectively [226]. It appears that the higher temperatures accelerate the kinetics of these transformations through higher alkalinity, supported by inflections becoming more pronounced in higher [HCO₃⁻] solutions of pH 9.3 and 9.2 (Figure B-4).



The larger reductions in N_{d2} with [HCO₃⁻] or pH witnessed in the 75 °C plots in Figure 6-9 supports the suggested Fe₃O₄ involvement, since increased alkalinity reduces Fe²⁺ presence thereby resulting in a bigger influence of Fe³⁺ on the electronic behavior of the overall layer. Even though both Fe₃O₄ and Fe₂O₃ have similar crystallographic structures possessing an O²⁻ sub-lattice which is cubic close-packed (ccp) [58], conversions therein have previously been shown to yield structural change and enhance transport pathways through passive layers [227].

The N_d values of Figure 6-9 are comparable to those for passive layers on other alloy steels or Fe [228], signifying a highly disordered nature for the passive layer. Generally, the breakdown/pitting susceptibility of a passive layer increases with N_d , a correlation which is not violated in the present results; previous *i* and EIS results reveal that the weaker passive layers

formed in dilute solutions or higher temperatures experiences easier breakdown than those in colder conditions with greater $[\text{HCO}_3^-]$. E_{fb} values, critical in determining the positions of semiconductor energy bands as a function of the redox potentials of electroactive ions in the electrolyte, are extracted from the Mott-Schottky plots and reveal an inverse relationship with N_d . Since these positions are governed by the thermodynamic stability of the passive layer and the charge transfer across its interface with the electrolyte, E_{fb} is expected to increase for more stable, protective layers. This entails an increase at lower temperatures and higher $[\text{HCO}_3^-]$. It is noted that E_{fb} data for the 75 °C case is calculated using the average of N_{d1} and N_{d2} . The E_{fb} data in Figure 6-9, along with the corresponding increase of δ_{sc} with $[\text{HCO}_3^-]$, E , and reduced temperatures as shown in Figure 6-10, correspond well with these expectations. They are also in agreement with the steady-state i decay and EIS results presented earlier in section 6.3.1 above.

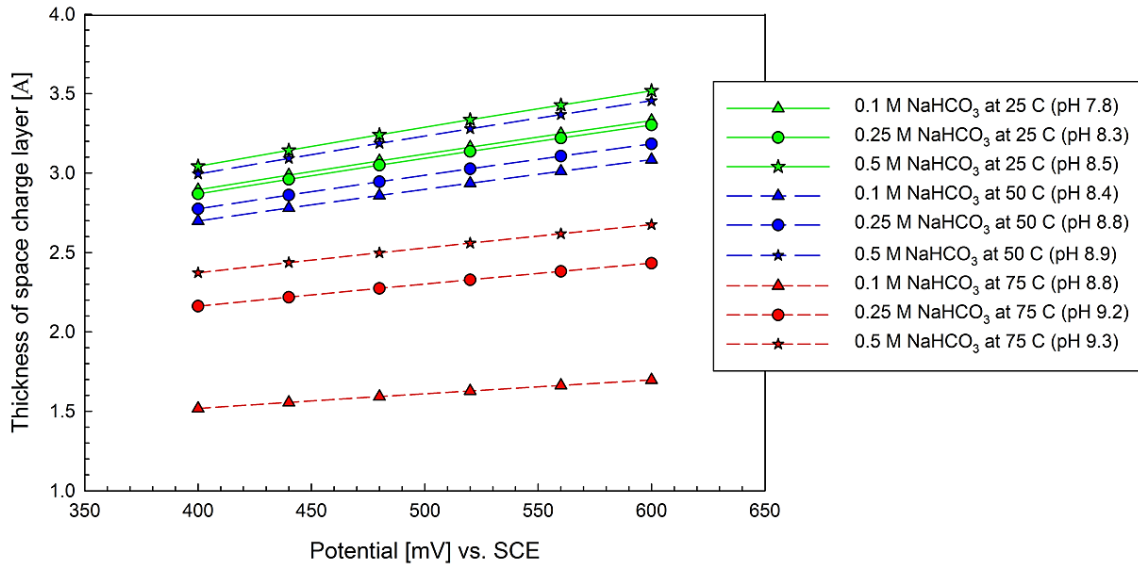


Figure 6-10: Dependence of (δ_{sc}) with respect to E , $[\text{NaHCO}_3]$ (0.1, 0.25, or 0.5 M), pH, and temperature (25, 50, or 75 °C)

6.4 Summary

In this chapter, the properties and growth of corrosion product on an API X-100 pipeline steel sample in mildly alkaline HCO_3^- solutions are studied using EIS (under both PDP and PSP conditions), i decay analysis, and Mott-Schottky. Auxiliary electrochemical processes are

observed and quantified at lower applied ω in pre-passive, active-passive transition, and transpassive E regions. EECs with nested parallel subsets are used to numerically model the responses during dissolution-adsorption, adsorption-diffusion, and diffusion controlled processes. Adsorption of pre-passive complexes of Fe^{2+} with HCO_3^- and OH^- is necessary prior to the formation of FeCO_3 or $\text{Fe}(\text{OH})_2$, respectively. Steel dissolution at active sites is accelerated by $\text{Cl}^-/\text{SO}_4^{2-}$ at applied $E > \text{OCP}$, contrary to the inhibitive effect these anions are seen to have in chapter 5. This is suggested to be because here, anodic polarization of the specimen proliferates anodic site coverage more so than during free corrosion or OCP, attracting these $\text{Cl}^-/\text{SO}_4^{2-}$ and other anions more readily. This is also suggested to be what causes increased adsorption and Fe^{2+} release (charge transfer and hence, corrosion). Conversely, diffusion during pre-passive steps is inhibited by $\text{Cl}^-/\text{SO}_4^{2-}$.

The applicability of film resistance and capacitance elements to model defective $\text{Fe}(\text{OH})_2$ presence on the steel surface is negated, and R_{ct} is used instead to gauge the Z effects of such deposits. Stable passive layer formation and protectiveness is evaluated with a second time constant, revealing improved performance at higher potentials and in $\text{Cl}^-/\text{SO}_4^{2-}$ -free solutions. Transpassive EIS response is modelled when stable, where diffusive effects reappear as increased transfer channels form within the passive films. Decay of i during PSP, in addition to EIS and Mott-Schottky tests after PSP, all indicate improved passive layer robustness in colder, more alkaline, and HCO_3^- -rich environments. Passive layer dependencies on $[\text{HCO}_3^-]$ and temperature are supported by the changes observed in semiconductive behavior under the influence of these parameters: N_d values decrease, E_{fb} values increase, and the δ_{sc} decreases.

7. Extended immersion studies of the formation of oxide/oxyhydroxide corrosion products on X100 steel⁵ during exposure to nn-pH HCO₃⁻ solutions with O₂, N₂H₄, and/or NO₃⁻

Corrosion evaluations of HSLA steels in actual and simulated environments identify multi-component corrosion products forming, including complexes of Fe²⁺ and/or Fe³⁺ with OH⁻ (Fe(OH)₂), CO₃²⁻ (FeCO₃), oxide (Fe₃O₄ and Fe₂O₃), and oxyhydroxide (γ/α -FeOOH) as shown in [30], [42], [72]–[78] and the previous chapters above. This formation is repeatedly seen to depend on aspects such as solution constituents, dissolved CO₂ or O₂ concentrations, and polarization potentials. Oxidation reactions of compounds found in these multi-layer corrosion products are viable at different O₂ concentrations ([O₂]), such as the oxidation of FeCO₃ in nominal O₂ conditions [79] versus that of Fe(OH)₂ in the complete absence of O₂ [32], [80]. This O₂ dependency raises concerns regarding the precise influence of [O₂] in overall multi-layer corrosion product development. This is important since O₂ presence in environments is variable in practical situations such as marine and soil conditions. Corrosion severity is affected by physicochemical properties, depths, temperatures, reduction/depletion rates, and natural cycles (e.g. drying-wetting) [39], [40], [80], [229]. The formation and evolution of corrosion products on HSLA steels upon exposure to O₂-containing electrolytes is therefore still of particular interest.

The recognized detrimental influence which O₂ has on external pipeline corrosion, combined with its foreseen presence in small quantities at exposed surfaces, is the motivation behind studying the inhibitive behavior of an O₂ scavenger in this chapter. Mechanical steps for the removal of trace O₂ amounts from critical industrial equipment (e.g. N₂ purging or “scrubbing”, vacuum degasification, and heating [230]) are impractical in buried pipeline

⁵ **I. M. Gadala**, H. M. Ha, P. Rostron, and A. Alfantazi, *Corrosion*, vol. 73, no. 3, pp. 221-237, March 2017.

systems. However, chemical scavenging can be feasibly incorporated in such systems at predetermined critical locations. Hydrazine (N_2H_4) is a known effective O_2 scavenger and reducing agent in the chemical, petroleum, and energy generation industries [231]–[233]. The kinetics of its reaction with O_2 has formerly been proven in alkaline CO_3^{2-} - HCO_3^- systems, exhibiting accelerated depletion at high temperatures ($\sim 80\text{ }^\circ\text{C}$) [232]. At $40\text{ }^\circ\text{C}$ and within a 160 min time frame, its depletion behavior is nearly linear with respect to time. Although being an environmentally unfriendly substance, N_2H_4 deployment in minute ppm amounts at these temperatures will ensure its complete reaction with O_2 through a process which yields simply H_2O and gaseous N_2 . Additionally, N_2H_4 treatments can serve to remove nitrate (NO_3^-) from corrosive trapped water [233], a further beneficial outcome considering nitrate's reported acceleration of carbon steel's anodic dissolution in HCO_3^- solutions [183]. For these reasons, N_2H_4 treatments in concentrations ≤ 1 ppm are chosen for the investigative tests in this chapter.

Previous chapters in this thesis have discussed in detail the strong pH influence on corrosion and passivation processes [74], [75], [172], [234]. Many of the nn-pH environments studied are low in electrical conductivity (on the order of $1 - 10\text{ mS/cm}$) whilst containing the HCO_3^- , Cl^- , and/or SO_4^{2-} anions commonly found in natural environments. This combination of low electrolyte conductivity and nn-pH is prevalent in many corrosion situations, such as in potable or tap waters, freshwaters, closed-loop piping circuits, crevices, and infrastructure reinforcement of both buried and concrete-embedded types [29]–[33], [141]. The breadth of these applications has not been met with an understanding of a broad range of species which could be present therein. For example, NO_3^- facilitates carbon steel passivation in concentrated HCO_3^- solutions [202], yet its influence on HSLA steel corrosion in more dilute lower conductivity solutions has not been widely reported. NO_3^- could appear in natural environments from a variety of bacterial, industrial/agricultural (e.g. fertilizers), and mineralogical (e.g. naturally occurring Nitratine or NaNO_3) sources [235], [236]. An objective of the present chapter is to study the

influence of NO_3^- on the evolution of corrosion rates and products on HSLA steel in nn-pH solutions with conductivities on the order of 1 – 10 mS/cm.

In addition to environmental influences, structural factors of corrosion products (e.g. compactness and porosity) forming on HSLA steel during corrosion are critical as reviewed in section 2.2 of chapter 2 [75], [77], [78], [237]. Films of uniform corrosion products containing few cracks tend to form on homogenous microstructures such as ferrite and bainite [237]. Microstructural effects arising from welding processes greatly differentiate corrosion product growth behaviors. Dense and fine corrosion product layers seen forming on base metals and weld metals with SEM yield the highest corrosion resistance, whereas coarse and porous layers on the heat-affected zones yield the lowest [158], [238]. This is supported by findings from microscopic studies using SVET and localized EIS [79], [239]. This chapter investigates the impact of structural factors of corrosion products on the corrosion behavior of HSLA steel in low conductivity nn-pH environments containing O_2 and NO_3^- .

In this work, combinations of O_2 , N_2H_4 , and/or NO_3^- concentrations constitute array environments in which samples are tested for various times and using various procedures (see below). Electrochemical techniques are periodically conducted to determine the evolution of corrosion processes during immersions. Mechanisms for the formation and evolution of corrosion products are proposed. The findings are corroborated by surface morphologies observed on specimens and by chemical compounds identified in the corrosion products.

7.1 Test environments and experimental procedures

Similar to the tests in chapter 5, low conductivity test solutions in the present chapter are based on the standard NS4 solution which is deaerated with 5% CO_2 /95% N_2 and has a nn-pH of 6.6 or 6.7. O_2 in this reference condition is varied between around 0 ppm (anoxic), 6 ppm, and 20 ppm. The 6 ppm condition represents natural aeration around atmospheric air pressures, whereas the 20 ppm condition represents O_2 levels which are significantly higher than expected in natural

environments. The latter is simulated here for mechanistic insight. The influence of NO_3^- is investigated at 0.005 and 0.015 M. In studies of corrosion inhibition through O_2 scavenging, environments are treated with 0.5 ppm or 1 ppm N_2H_4 using a graduated syringe. Only environments with a 6 ppm initial O_2 concentration ($C_{\text{O}_2,i}$) are treated. All O_2 scavenging tests are conducted at both 25 and 50 °C to evaluate the influence of temperature.

Table 7-1 summarizes the combinations of $[\text{O}_2]$ and $[\text{NO}_3^-]$ studied in this chapter with corresponding measured pH and conductivities. Likewise, the temperature and $[\text{N}_2\text{H}_4]$ combinations studied in corrosion inhibition are listed in Table 7-2 and Table 7-3 for short-term electrochemical studies (1 h OCP and PDP thereafter) and 168 h immersion tests, respectively. In all tests, the stable pH, $C_{\text{O}_2,i}$, and solution conductivities are measured beforehand using a bench top pH meter ($\pm 1\%$ rated measurement precision), a new calibrated O_2 probe cell, or a calibrated conductivity/TDS meter, respectively.

Table 7-1: List of $[\text{O}_2]$ and $[\text{NO}_3^-]$ combinations studied in this chapter, based on the reference NS4 electrolyte of A, with corresponding measured $C_{\text{O}_2,i}$, pH, and conductivities of solutions

Environment	NO_3^- [M]	$C_{\text{O}_2,i}$ [ppm]	pH ^a	Conductivity[mS/cm]
A	0	0.2	6.6	1.11
B	0	5.7	7.5	
C	0	21.6	8.3	
D	0.005	0.2	6.7	1.62
E	0.005	5.8	7.7	
F	0.005	20.4	8.6	
G	0.015	0.1	6.7	2.61
H	0.015	6.0	7.8	
I	0.015	21.2	8.9	

^a: stable value measured at 25 °C over at least 30 minutes

Mainly low polarization electrochemical techniques are used in the tests of this chapter, since many relevant low conductivity nn-pH environments suffer from restriction of CP due to aspects like the high R_s (e.g. tap waters), the shielding of CP current (e.g. under coating disbondments and crevices), or the lack of CP altogether (e.g. internal pipe surfaces). Two test routines are conducted for each test environment in Table 7-1. The first involved a short OCP period < 1 h followed by a PDP scan between -1.25 to 1.25 V_{SCE} at a standard scan rate of 1/6 mV/s. This test routine is also conducted on each environment in Table 7-2. Scans are repeated at

least twice to ensure reproducibility. The second routine consists of 24 h immersion with continuous OCP monitoring, where LPR (± 10 mV of OCP at $1/6$ mV s⁻¹) and static EIS (10,000 - 0.01 Hz, AC amplitude = 10 mV, and 10 points/decade sampling frequency) is conducted at prescribed 1 h intervals. All LPR and EIS measurements are conducted three times to ensure reproducibility of the results at each interval and for each environment.

For the N₂H₄ treatment tests of Table 7-3, specimens are fully immersed in their corresponding environment for 168 hours. Only environments with a non-zero C_{O₂i} are tested here, as shown in Table 7-3. Treatments of 1 ppm N₂H₄ are periodically added to the environment every 24 h. After completion of either the first or second test routines, specimens are carefully removed from environments and dried in an inert gas stream of N₂ or Argon (Ar) to avoid air oxidation, placed in previously deaerated sealed containers, and stored in a glass desiccator until ex-situ SEM, XPS, Raman Spectroscopy, and/or XRD examinations are conducted, where applicable. Details on the microscopy and chemical characterization equipment used in this chapter have previously been specified in section 4.2.4 on page 49.

Table 7-2: List of temperature and [N₂H₄] combinations studied in short term corrosion inhibition tests of this chapter based on reference NS4 electrolyte of environment AA*, with corresponding measured C_{O₂i}

Environment	Temperature [°C]	Aeration condition	[N ₂ H ₄] in ppm	C _{O₂i} [ppm]
AA*	25	Deaerated	0	0.2
CC		Naturally	0	5.8
EE		Aerated	0.5	5.6
GG			1	5.8
BB	50	Deaerated	0	0.1
DD		Naturally	0	4.9
FF		Aerated	0.5	4.7
HH			1	4.9

Table 7-3: List of temperature and [N₂H₄] combinations studied in extended 168 h immersion corrosion inhibition tests of this chapter based on environment AA* in Table 7-2, with corresponding measured C_{O₂i}

Environment	Temperature [°C]	[N ₂ H ₄] in ppm, added every 24 hours	C _{O₂i} [ppm]
CC	25	/	5.8
GG		1	5.7
DD	50	/	4.9
FF		1	4.8

7.2 Short-term electrochemical tests at immersion times ≤ 1 h

7.2.1 OCP < 1 h

The OCP transients stabilize within 5 minutes of immersion, extending until the PDP scans are conducted in the first test routine (at 1 h). Figure C-1 in Appendix C illustrates these stable OCP profiles approaching the 1 h mark, and Figure 7-1 shows the final values at 1 h in terms of $[O_2]$. Different redox conditions at the steel surface depending on $[O_2]$, specifically the reduction of O_2 in {R-7.1} versus that of H_2O previously shown in {R-5.4}, cause clear separation in the profiles.

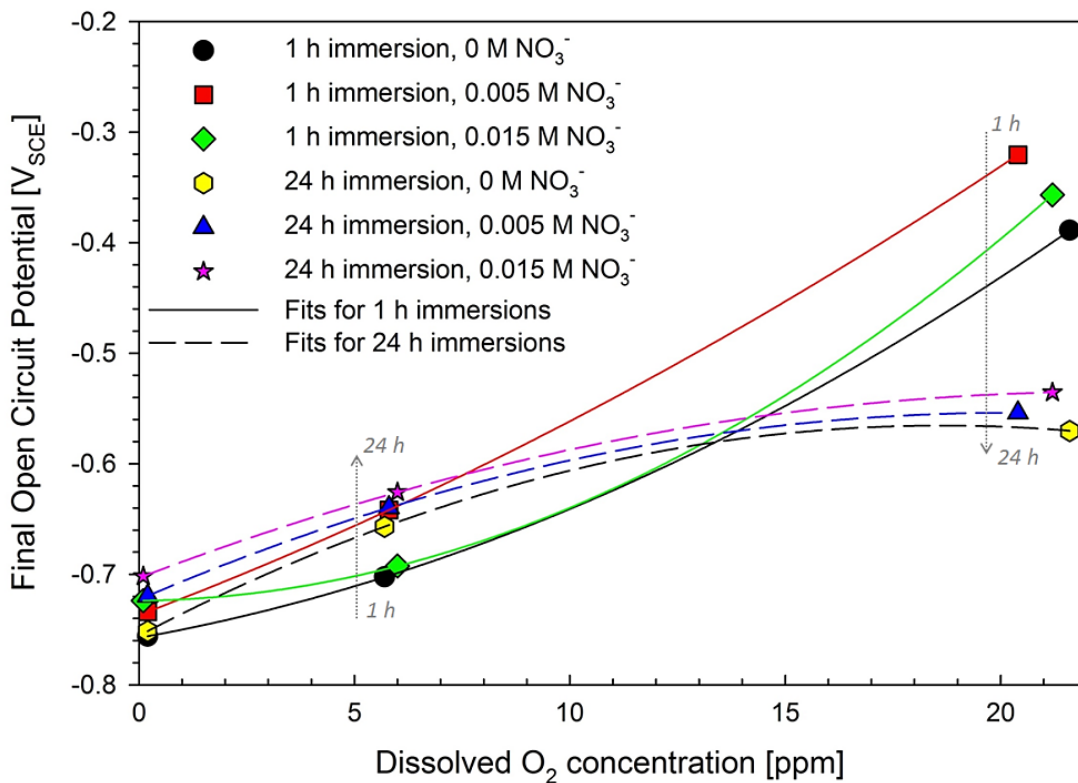


Figure 7-1: Final OCPs reached after 1 h and 24 h immersion (separate tests) as a function of $[O_2]$, with nonlinear fit profiles overlaid

OCP becomes more anodic with increased $[O_2]$ in the solution at any single $[NO_3^-]$. Values are close to those reported for carbon steel in similar pH and HCO_3^- environments

although the alloy and electrolyte compositions are different [40], [240]. In high [O₂] conditions it is clear that O₂ has the most consequential influence on OCP. In deaerated and 6 ppm O₂ conditions though, the influence of HCO₃⁻, other anions, and %CO₂ in the purging gas become the controlling factors. In deaerated solutions specifically, alloy and electrolyte composition differences compared to previous reports reveal discrepancies in results. The deaerated OCP values between -0.71 and -0.75 V_{SCE} here are 100 mV more anodic than those reported by Lee et al. [215] and Sherar et al. [68] in similar mixed anion solutions. Anion concentration and alloy composition differences (carbon steel vs. HSLA steel) between previous reports and the present work are influential but likely not greatly so. Instead, the most substantial influence is suggested to be a synergy of electrolyte pH and the surface condition of the specimen. Supporting this is the fact that OCP is less anodic when specimens have a pre-grown CO₃²⁻ and O²⁻ compound layer from a pre-treatment stage [68], which unmistakably protects the steel surface compared to the bare surface state here. Furthermore, the slightly more acidic pH of solutions here owing to the 5% CO₂ content in the purging gas for the deaerated condition, causes increased OCP values compared to 0% CO₂ conditions, a finding which has been established by results presented in previous chapters [172].

Using these results, it is beneficial to identify a quick method of determining the change in OCP from a benchmark condition based on the change in [O₂] (ΔO_2). In the present conditions, a nearly linear response to ΔO_2 is seen (Figure 7-1) based on the measured OCP in 6 ppm conditions compared to 0 ppm conditions. This is in agreement with OCP transients measured for other structural materials in soil environments [241] although different ion concentrations and temperatures alter [O₂] in electrolytes (shown before for NaCl solutions [242]). Here, it can be said that preliminary predictions of X100 OCP upon exposure to nn-pH NS4 can be calculated using an approximate 3 mV anodic shift per unit ppm change in [O₂] from the base-line deaerated condition. It should be noted that this 3 mV anodic shift value is only valid for the 0 – 6 ppm [O₂]

range for times < 24 h. With higher [O₂] and exposure times this number is expected to change, in addition to the linearity of the dependency.

The effect of increased [NO₃⁻] is generally similar to the influence of higher [O₂], causing potential shifting in the anodic direction. It is suggested that the impact of NO₃⁻ reduction of {R-7.2} involving H⁺ in the media, as alluded to by El-Naggar [202], is causing this. However, a consistent trend is not observed here. In both 6 ppm and 20 ppm O₂ solutions the 0.005 M profiles are more anodic than 0.015 M profiles upon reaching the 1 h mark, whereas in the deaerated case the 0.015 M profile is more anodic.



The tendency for the reduction of NO₃⁻ is very low due to its more stable electronic structure. Thus, it is the single step reduction of NO₃⁻ which plays a role in intensifying corrosion in NO₃⁻-containing environments (seen in 24 h OCP transients also). As NO₃⁻ reduction competes with O₂ reduction here, the reaction of NO₃⁻ in lower [O₂] environments is aided by its better kinetic feasibility versus that of O₂ [202]. In the higher [O₂] environments of B, C, E, F, H, and I in Figure C-1, this greater kinetic feasibility is less noticed, likely due to: (a) weakened NO₃⁻ reduction kinetics (based on {R-7.2}) in the more alkaline conditions of 6 ppm (pH ≈ 7.5) and 20 ppm O₂ (pH ≈ 8.5) compared to the deaerated condition of pH 6.7, and (b) increased O₂ reduction kinetics with more O₂ availability. Also noted is that NO₃⁻ diminished in the {R-7.2} reaction is not resupplied with added NaNO₃ during the immersion. In contrast, [O₂] remains constant throughout the test due to continuous gas supply. This artifact of the experimental procedure can also contribute to the weakened influence of NO₃⁻ in 6 ppm and 20 ppm O₂ conditions, since a lower NO₃⁻ is advantageous to O₂ in the competitive reduction. Nonetheless, this latter factor is less important than pH or [O₂], as NO₃⁻ will not deplete considerably during 1 h immersions. It becomes a more contributing influence during much longer exposures.

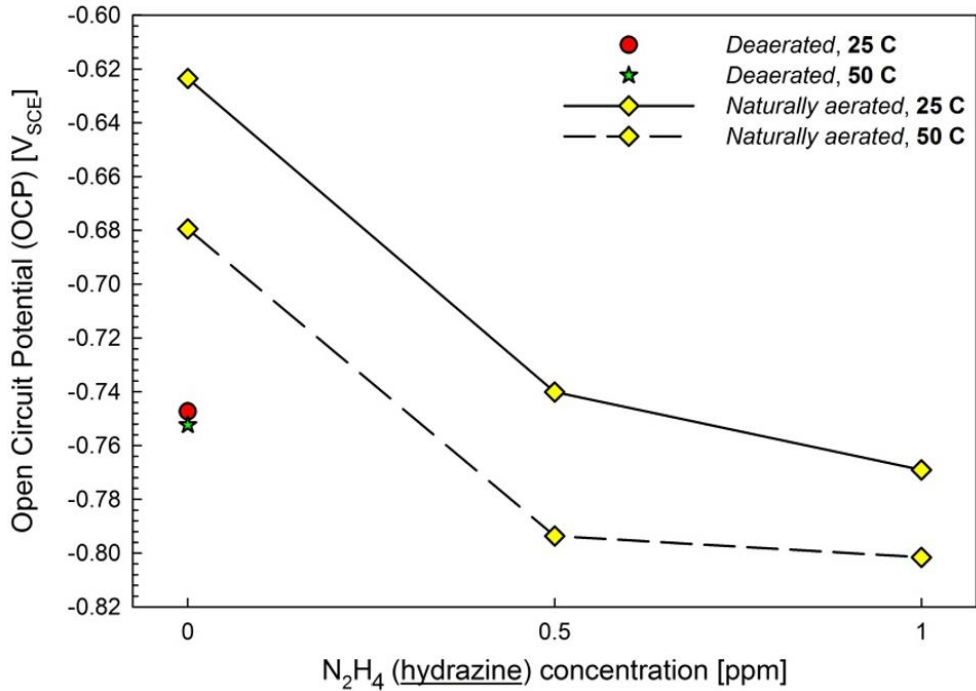


Figure 7-2: Influence of N₂H₄ treatment concentration on 1 h OCP values at 25 and 50 °C

Figure 7-2 shows the influence of [N₂H₄] on the OCP values reached after 1 h of immersion in 6 ppm [O₂] conditions at 25 and 50 °C. Figure C-2 in Appendix C shows the OCP transients approaching 1 h immersion in these same Table 7-2 environments investigating N₂H₄ treatment. It is clear here that the 50 °C case with a 1 ppm treatment of N₂H₄ results in the most cathodic OCP, partly attributed to this condition having the lowest [O₂] of all the conditions tested. Figure 7-2 also shows that the drop in OCP is larger with a 0.5 ppm N₂H₄ treatment compared to a rise in temperature from 25 to 50 °C. Yet, the most important revelation from Figure 7-2 is that the OCP of conditions with 1 ppm N₂H₄ treatment (at either 25 to 50 °C) and that of the 50 °C condition with 0.5 ppm N₂H₄ addition stabilize at a value more cathodic than the deaerated case. This alludes to possible further protection of the steel surface with N₂H₄ treatment in a mechanism additional to the lessening of O₂ levels in solution. This revelation is corroborated by findings in subsequent sections using other electrochemical and characterization techniques.



The anodic shift between 6 and 0 ppm O₂ concentration OCP values is much larger than that between the former and the N₂H₄ treated conditions of any concentration. This shows that although even a minute 0.5 ppm addition of N₂H₄ will react with the equivalent molar concentration of O₂ present in the electrolyte, doubling this N₂H₄ amount to 1 ppm will not necessarily double the resulting effect on the redox conditions on the steel. The mechanism by which N₂H₄ additions lessen O₂ presence in the solution is shown in {R-7.3}. Hydrazine is known to be a volatile compound, and its reaction with dissolved O₂ is considered to occur quickly. However, based on results observed throughout this chapter, this reaction seems to not occur alone, rather in conjunction with other processes involving N₂H₄. The reasons for this postulation are alluded to in the following discussion.

A ratio of 1 ppm N₂H₄ to 1 ppm O₂ corresponds to a 0.9375:1 molar concentration ratio. Hence, it is expected that even with a 1 ppm N₂H₄ addition to 6 ppm O₂ conditions, a considerable amount of O₂ will remain unreacted. This small change in [O₂] may be the reason behind the small change in 1 h OCP behavior when [N₂H₄] is doubled (Figure 7-2). However, the exact reason why the N₂H₄ treated conditions with non-zero O₂ concentrations exhibit improved corrosion performance over their completely deaerated counterparts is unknown. One possible explanation is that N₂H₄ additions ≤ 1 ppm do not react completely with the O₂ in the solution; being a strong oxidizer, the remaining N₂H₄ might act as an anodic inhibitor by accelerating the formation of a protective corrosion (oxidation) product on the steel surface. This explanation is plausible based on the appearance of weak passivation characteristics in the PDP profiles of N₂H₄ treated tests after 1 h (see Figure 7-5). Also, film formations are observed on the sample surfaces during extended 168 h immersions with periodic N₂H₄ treatments (see section 7.3).

7.2.2 PDP at 1 h

Figure 7-3 illustrates PDP profiles in nn-pH solutions of varying [O₂] with 0.015 M NO₃⁻. PDP profiles for 0 M and 0.005M NO₃⁻ solutions are shown in Figure C-3 and Figure C-4,

respectively in Appendix C. Also, Figure 7-4a and Figure 7-4b reveals the effect of changing $[\text{NO}_3^-]$ in 6 ppm and 20 ppm O_2 solutions, respectively. All PDP results are in good agreement with OCP profiles and support the greater influence of $[\text{O}_2]$ versus $[\text{NO}_3^-]$. In 6 ppm and 20 ppm O_2 conditions, corrosion rate is not calculated from PDP results due to the absence of prerequisites for Tafel extrapolation such as the existence of well-defined Tafel regions [243]. Conversely, for deaerated environments Tafel extrapolation is appropriate and is conducted using the Tafel Curve Fitting Method [244]. The results are shown in Table C-1, where the trend of increased i_{corr} with $[\text{NO}_3^-]$ supports the OCP findings. However, the quantitative results of the extrapolation are not intended for stand-alone use, even though anodic and cathodic Tafel constants (β_a and β_c , respectively) correlate well with previous reports on anaerobic corrosion of steel in similar nn-pH environments (e.g. $\beta_a = 86$ mV and $\beta_c = 200$ mV) [68]. These extrapolation results serve as a qualitative corroboration of the 24 h EIS and LPR tests on unpolarized samples in this chapter.

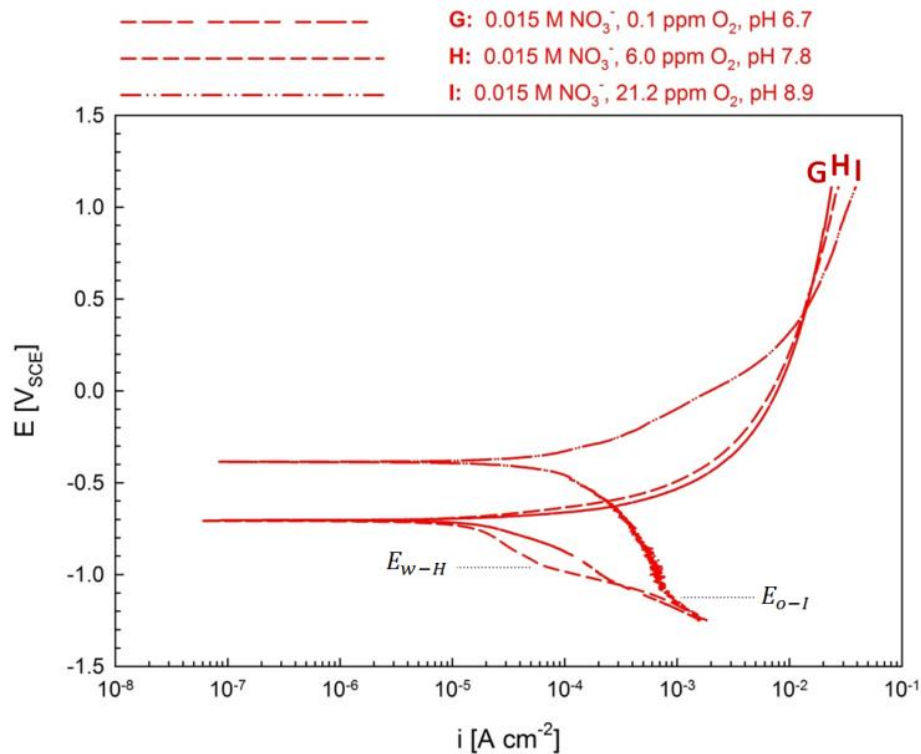


Figure 7-3: PDP in 0 ppm, 6 ppm, and 20 ppm O_2 solutions with 0.015 M added NO_3^-

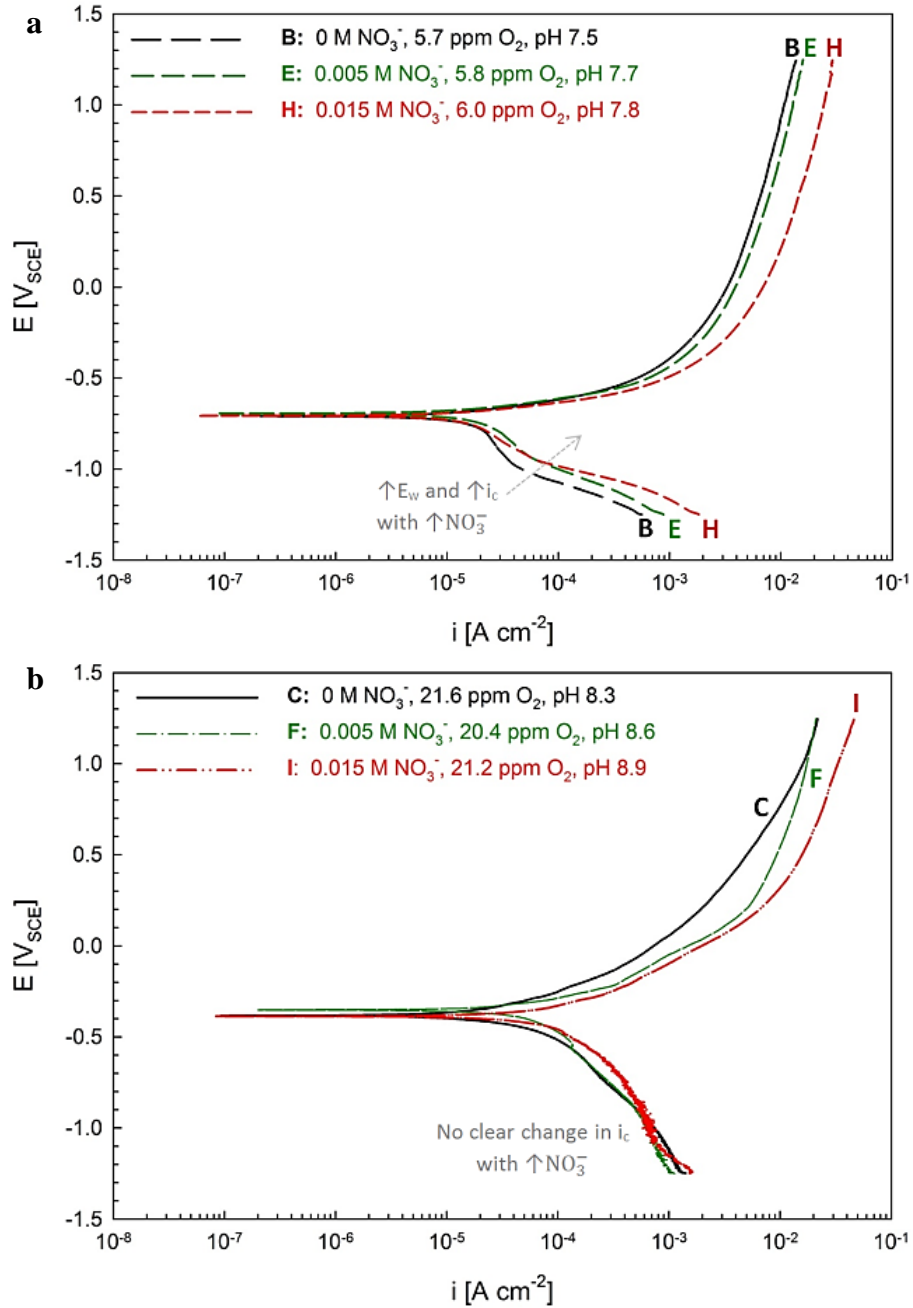


Figure 7-4: PDP in (a) 6 ppm O_2 solutions with 0, 0.005, and 0.015 M added NO_3^- , and (b) 20 ppm O_2 solutions with 0, 0.005, and 0.015 M added NO_3^-

Figure 7-4a indicates that even dilute $[\text{NO}_3^-]$ will contribute to net anodic dissolution, much like Cl^- causing the accelerated Fe^{2+} release from iron specimen at anodic sites [57]. Cathodic polarization branches below OCP for all non-zero $[\text{O}_2]$ tests show O_2 diffusion behavior. At around $-1 \text{ V}_{\text{SCE}}$ for 6 ppm O_2 environments (i.e. B, E, and H) this behavior

subsequently withdraws completely (withdrawal E : E_w), as shown with the symbols E_{w-B} , E_{w-E} , and E_{w-H} in Figure 7-3, Figure C-3, and Figure C-4, respectively. Below E_w the 6 ppm O_2 profiles inflect to first follow the deaerated case with matching $[NO_3^-]$, and then eventually the 20 ppm O_2 profile with matching $[NO_3^-]$. The latter occurs at a potential where all three $[O_2]$ environments overlap (denoted E_o). Increased $[NO_3^-]$ upwardly shifts this E_o point, as seen by comparing E_{o-F} in Figure 7-3 with E_{o-I} in Figure C-4. Since increased $[NO_3^-]$ accelerates {R-7.3} resulting in higher cathodic reaction rates, the associated i reach that of the shared E_o faster. The cathodic region in Figure 7-4a supports this, because for equal 6 ppm O_2 at different $[NO_3^-]$, E_w and cathodic current densities (i_c) below E_w both increase, as shown by the arrow in the figure. The strongest i inflection beyond this is manifested in the 0.015 M NO_3^- profile.

It is noted that in the NO_3^- -free conditions in Figure C-3, E_o occurs beyond the measured cathodic potential range and thus was not captured. Its occurrence at a $E_o < -1.25$ V_{SCE} is consistent with the downwardly shift decreased $[NO_3^-]$ has on E_o values. This supports the attribution of changing E_o values on the rate of {R-7.3}, since in NO_3^- -free environments there is no added i from NO_3^- and hence the profiles reach the shared E_o the slowest (i.e. at the lowest potential). This interpretation relies on the fact that changing $[NO_3^-]$ between 0 – 0.015 M in 20 ppm O_2 environments does not influence i_c values observably; this is shown in Figure 7-4b, where the cathodic profiles C, F, and I have no consistent difference. The dissimilar cathodic behaviors of Figure 7-4a and Figure 7-4b thus follow the results in the previous section and corroborate the suggested two main factors for decreased NO_3^- influence at higher $[O_2]$ (i.e. weakened NO_3^- reduction kinetics with alkalinity, and increased O_2 reduction kinetics with $[O_2]$).

Overall, the observable two-region cathodic profile in the 6 ppm O_2 and 20 ppm O_2 conditions is attributed to the domination of other cathodic reactions independent of $[O_2]$ below E_w . It is established that O_2 -free HCO_3^- -based solutions such as the baseline deaerated NS4 environment of Figure C-3 induce the discharge of HCO_3^- , {R-5.3}, along with H evolution in

acidic environments, {R-5.2}, or {R-5.4} in alkaline environments [64], [65], [74], [100]. The corresponding equilibrium E (E_{eq}) of {R-5.3}, denoted $E_{eq_{5.3}}$, is a function of pH. It is calculated by combining the expressions for the hydration constant of CO_2 with the ionization constants and reversible E of H_2CO_3 and HCO_3^- discharge reactions (at 20 °C) [245]. At pH 10.3, $E_{eq_{5.3}} = -0.85 V_{SCE}$, equaling the standard E_{eq} , hence validating its correctness since $[\text{HCO}_3^-] = [\text{CO}_3^{2-}]$ at this pH in $\text{H}_2\text{CO}_3\text{-HCO}_3^-\text{-CO}_3^{2-}$ speciation. The pH range of the present environments of Table 7-1 is between 6.6 and 8.9, thus the corresponding $E_{eq_{5.3}}$ of -0.75 to -0.81 V_{SCE} proves the viability of {E-7.1} involvement at the cathodic E of $E_w \sim -1 V_{SCE}$. In NO_3^- -containing conditions, the reduction reaction described by {R-7.3} ensues for $E < E_w$ at rates dependent on $[\text{NO}_3^-]$ and pH. Cathodic reactions not concerning O_2 , namely those involving HCO_3^- , H^+ , H_2O , and/or NO_3^- , do not significantly affect i at $E > E_w$ or $E < \text{OCP}$ since O_2 reduction is the dominant process in this range. Below E_w the tendency for 6 ppm O_2 and deaerated profiles to overlap in all presented figures, and then eventually include 20 ppm O_2 at potentials below E_o , strongly verifies the absence of significant O_2 -dependent cathodic processes at $E < E_w$.

$$E_{eq_{5.3}} = -5.55 \cdot 10^{-1} - (2.9 \cdot 10^{-2}) \cdot pH \text{ [V}_{SCE}] \quad \{\mathbf{E-7.1}\}$$

In the N_2H_4 treated environments of Table 7-2, it is clear from Figure 7-5 that within the 500 mV region above OCP where anodic processes would be important, N_2H_4 treatments result in lower i compared to untreated conditions. In fact, the results reveal a short-lived passive region in which i are around 2 orders of magnitude lower than what they would be if there were no N_2H_4 added. This passive region has boundaries specific to each $[\text{N}_2\text{H}_4]$ and temperature, which are easily identified due to the sharp decrease in i to near zero levels. These are termed E_{co1} and E_{co2} based on their attribution to new couples in the anodic and cathodic reactions. These newly introduced couples are not related to $[\text{O}_2]$ due to their complete absence in aerated but untreated environments of Figure 7-3 and Figure 7-4. Furthermore, the introduction of a new anodic reaction not involving N_2H_4 or one of its products is highly unlikely, since such a reaction would

be Fe-based and Fe is not known to be in a reaction other than Fe/Fe²⁺ oxidation at these E -pH levels. These newly introduced couples are hence attributed to N₂H₄ in some way, where the anodic and cathodic current under the influence of N₂H₄ results in a net i of nearly zero at E_{co1} and E_{co2} .

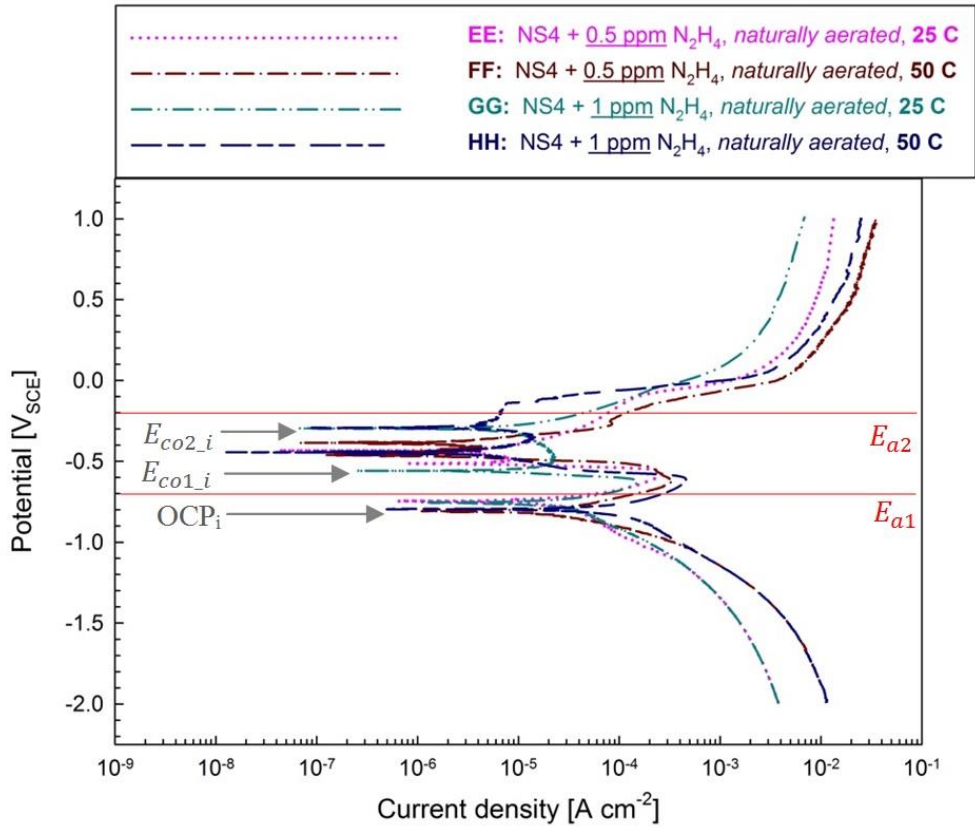


Figure 7-5: PDP profiles of aerated environments at 25 and 50 °C, treated with N₂H₄

Table 7-4: Values of E_{co1} and E_{co2} extracted from PDP plots of N₂H₄ treated environments, with corresponding ranges of the low-current region

Environment	Temperature [°C]	E_{co1} [mV _{SCE}]	E_{co2} [mV _{SCE}]	$\Delta E_{co} = E_{co2} - E_{co1}$ [mV]
EE: NS4 + 0.5 ppm N ₂ H ₄	25	-513	-434	79
GG: NS4 + 1 ppm N ₂ H ₄		-558	-296	262
FF: NS4 + 0.5 ppm N ₂ H ₄	50	-495	-385	110
HH: NS4 + 1 ppm N ₂ H ₄		-443	-292	151

The magnitude of the potential range of the low i region between E_{co1} and E_{co2} is important, since it is a parameter which can describe the efficiency of the inhibition of corrosion

with N₂H₄ treatments. The values of this potential range, termed ΔE_{co} , for all the relevant Table 7-2 environments are extracted from the PDP plots and are listed in Table 7-4. The results in this table indicate that the most persistent passive region of the conditions tested forms with 1 ppm N₂H₄ treatment at 25 °C. Likewise at 50 °C ΔE_{co} of the low i region is higher with 1 ppm N₂H₄ treatment than with the 0.5 ppm. This is expected, since the introduction of the low i region bounded by the E_{co1} and E_{co2} is itself due to N₂H₄ addition. However, it appears that increased temperature has a mixed effect on the persistence of this low i region depending on the [O₂] in the environment. In lower [O₂] due to 1 ppm treatment, higher temperature reduces ΔE_{co} , whereas with 0.5 ppm treatment the range is increased in size. Upcoming EIS results do not offer a clarification to these mixed trends, which also appear in the Table 7-5 results of i below.

Table 7-5: Values of i_{a1} and i_{a2} extracted from PDP plots of N₂H₄ treated environments, with corresponding i_{max} values in low i region and minimum percent decrease in i

Environment	Temperature [°C]	i_{a1} at -0.2 V _{SCE} [A cm ⁻²]	i_{a2} at 0 V _{SCE} [A cm ⁻²]	i_{max} in ΔE_{co} range [A cm ⁻²]	Minimum decrease in i [%]
EE: NS4 + 0.5 ppm N ₂ H ₄	25	5.85 x 10 ⁻⁵	1.25 x 10 ⁻³	1.02 x 10 ⁻³	18
GG: NS4 + 1 ppm N ₂ H ₄		7.25 x 10 ⁻⁵	4.50 x 10 ⁻⁴	2.31 x 10 ⁻⁵	68
FF: NS4 + 0.5 ppm N ₂ H ₄	50	1.50 x 10 ⁻⁴	3.66 x 10 ⁻³	9.45 x 10 ⁻⁵	37
HH: NS4 + 1 ppm N ₂ H ₄		2.70 x 10 ⁻⁵	1.00 x 10 ⁻³	1.46 x 10 ⁻⁵	46

To further identify the performance of the two levels of N₂H₄ treatment in different temperatures, the i reached at E within the two active regions before and after the short-lived low i region are extracted from the profiles of Figure 7-5. The E within the active regions are denoted as E_{a1} and E_{a2} for the region before E_{co1} and the region after E_{co2} (and clear i acceleration) in the profiles, respectively. Their corresponding values are -0.7 V_{SCE} and 0 V_{SCE}, respectively. Coincidentally, the -0.7 V_{SCE} case is a useful E to study since it coincides with the free corrosion potential or OCP of the typical deaerated nn-pH NS4 environment. The values of the i at these E for all the environments tested are extracted from the PDP plots and are listed in Table 7-5. In addition, the i in the low i region between E_{co1} and E_{co2} are studied to identify the maximum i in

the region, denoted i_{max} . The values of this parameter are used to evaluate the minimum decrease in i between the active region and the passive-like region of each profile, using {E-7.2}.

$$\%i_{decrease} = \min \left\{ \left(1 - \frac{i_{max, \Delta E_{CO}, i}}{i_{a1, i}} \right), \left(1 - \frac{i_{max, \Delta E_{CO}, i}}{i_{a2, i}} \right) \right\} \cdot 100 \quad \{\mathbf{E-7.2}\}$$

Since the i of the active regions of all profiles are relatively similar to the untreated case, and it is the corresponding i from these regions which are used in the $\%i_{decrease}$ calculation, the results of this procedure are a preliminary measure of the inhibition efficiency of N_2H_4 treatments. The results of this evaluation are in good correspondence with the trends revealed in the Table 7-4 interpretation, where the best performing situation from a corrosion control standpoint is the 1 ppm N_2H_4 treated environment at 25 °C. This $[N_2H_4]$ is significantly better than the 0.5 ppm counterpart at the same temperature. Similarly, at 50 °C the higher $[N_2H_4]$ offers more reduction in i . As mentioned earlier, for each $[N_2H_4]$ pair, the influence of temperature is mixed between favorable and unfavorable to corrosion control, hence leaving the influence of temperature on the efficiency of N_2H_4 treatment unknown without further more dedicated studies on this subject.

7.3 Surface analysis following 24 h or 168 h immersions

Specimens immersed in each environment of Table 7-2 are analyzed with SEM after 24 hours. Ex-situ characterization with XPS, Raman Spectroscopy, and XRD are only conducted on samples with visible corrosion products. NO_3^- did not affect characterization results greatly, so only NO_3^- -free spectra are shown. A reddish-orange corrosion “tubercle” forms on the specimen surface in 6 ppm and 20 ppm O_2 environments, for every $[NO_3^-]$ tested. In contrast, no significant corrosion product is observed on the specimens immersed in deaerated environments of any $[NO_3^-]$. The tubercles appearing in O_2 -containing environments cover approximately 50% of the specimen surface for 20 ppm O_2 conditions. Coverage decreases in 6 ppm O_2 conditions, yet does not change noticeably with $[NO_3^-]$ for any $[O_2]$. Surfaces of the specimen are imaged at the

microscopic scale using SEM, to identify differences in morphologies. The absence of observable corrosion product formations following immersion in deaerated conditions of any $[\text{NO}_3^-]$ is confirmed, as seen in Figure C-5 in Appendix C for the 0.015 M NO_3^- (0.1 ppm O_2 , pH 6.7) case.

In the 6.0 ppm O_2 environment of pH 7.8 and with 0.015 M NO_3^- , the tubercle formed (Figure 7-6) contains a mix of equally distributed large and small pores ranging in size from around 0.1 mm (largest pore size under 45x magnification) to $< 10 \mu\text{m}$ (smallest pore sizes under higher magnification). Using image analysis software the pixels in the higher magnification image at and below a fixed brightness level are colored red, as shown in the bottom-right image in Figure 7-6. These red sections cover 30.4% of the total area, and the average size of the largest dimension of the coalesced pore openings they create is $9.0 \mu\text{m}$ (standard deviation: $2.6 \mu\text{m}$).

In the 20 ppm O_2 environment of pH 8.9 and with 0.015 M NO_3^- , the tubercle formed is uniform as shown in Figure 7-7, but observably more compact than the 6 ppm O_2 case of Figure 7-6. Higher magnification shows that the smallest pore size in the tubercle formed in 20 ppm O_2 environments is $< 5 \mu\text{m}$ (top-right corner). Using the same brightness level for image analysis as that employed in Figure 7-6, the red pores of Figure 7-7 cover only 11.7% of the total area, with an average coalesced pore size of $4.7 \mu\text{m}$ (standard deviation: $0.6 \mu\text{m}$) in the largest dimension orientation. At the edges of the tubercles formed in both 6 ppm and 20 ppm O_2 environments, the growth of corrosion product directly over the steel surface is seen in Figure C-6 of Appendix C, in a similar manner to that shown in Figure 5-12 of section 5.2.2 above. Here, two different corrosion product structures are identified, one of spherical or cylindrical large crystal structures, and the other of cloud-like formations of small globules. It is the latter structure which grows to form the tubercles observed on the surface in the images of Figure 7-6 and Figure 7-7.

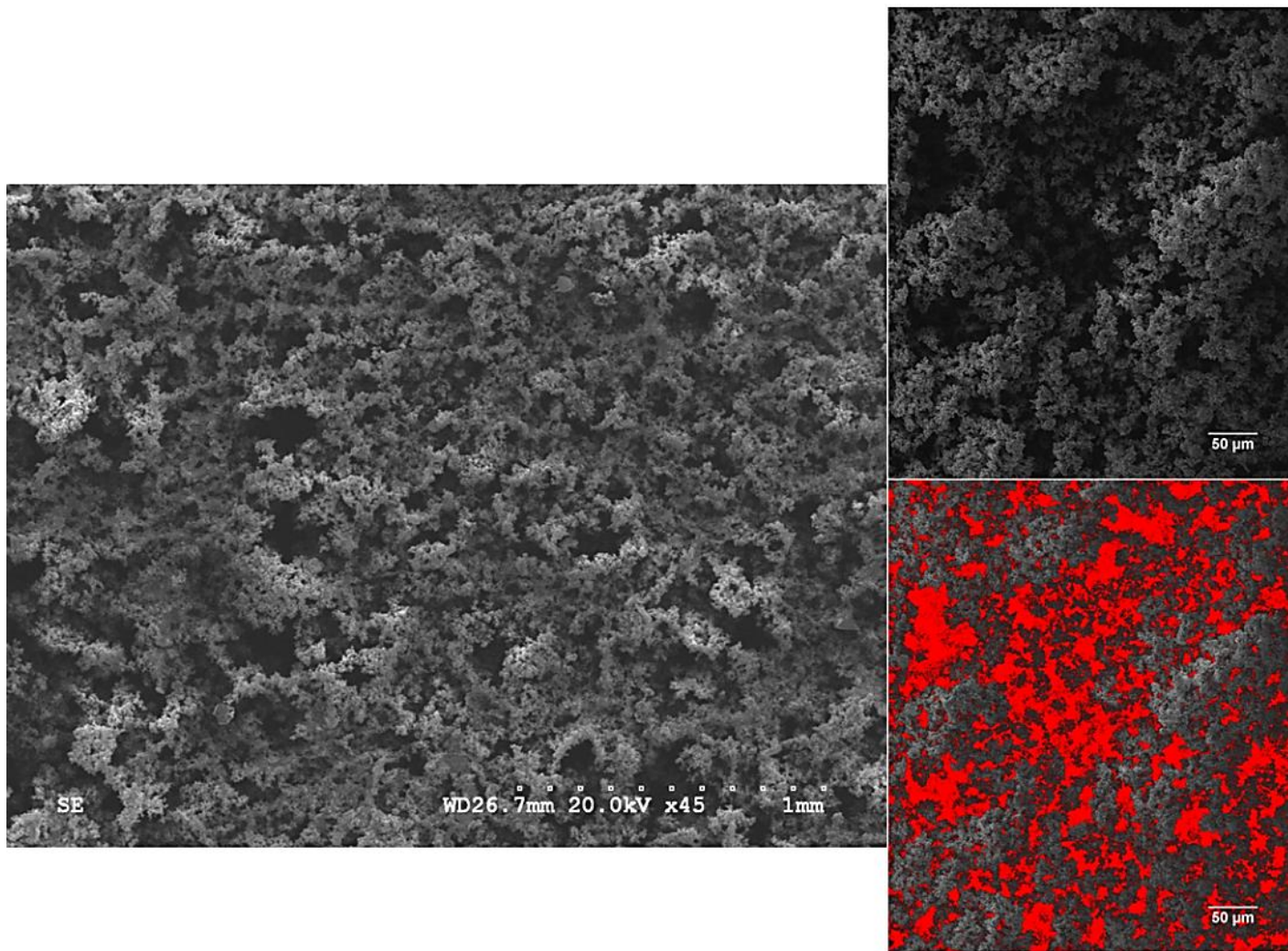


Figure 7-6: SEM images of steel specimen surface following immersion in solution containing 6.0 ppm O₂ (pH 7.8) and 0.015 M NO₃⁻: (left) low magnification; (top-right) as imaged high magnification with 50 μm scale bar; and (bottom-right) high magnification with 50 μm scale bar analyzed by color threshold

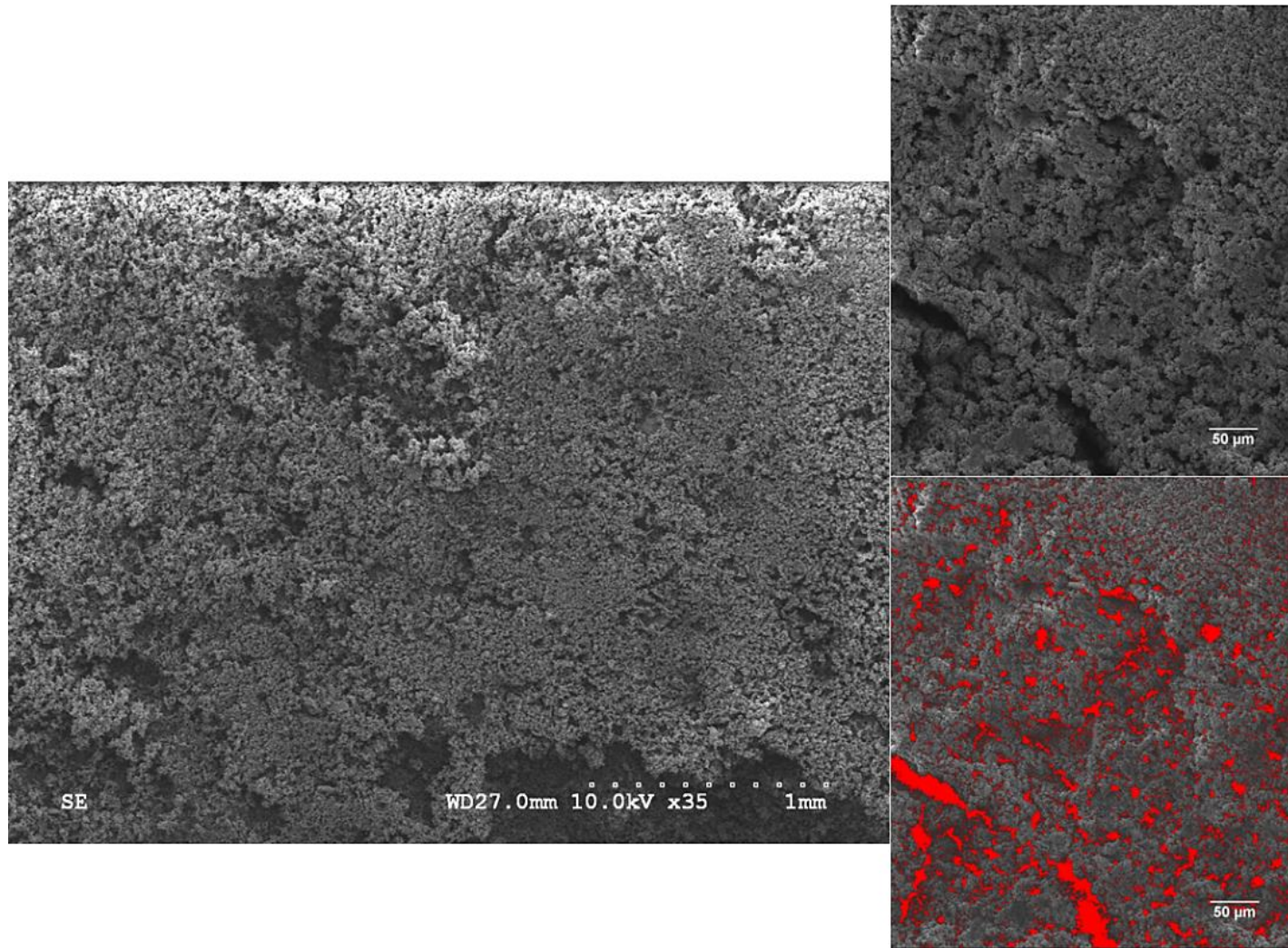


Figure 7-7: SEM images of steel specimen surface following immersion in 21.2 ppm O₂ (pH 8.9) and 0.015 M NO₃⁻: (left) low magnification; (top-right) as imaged high magnification with 50 µm scale bar; and (bottom-right) high magnification with 50 µm scale bar analyzed by color threshold

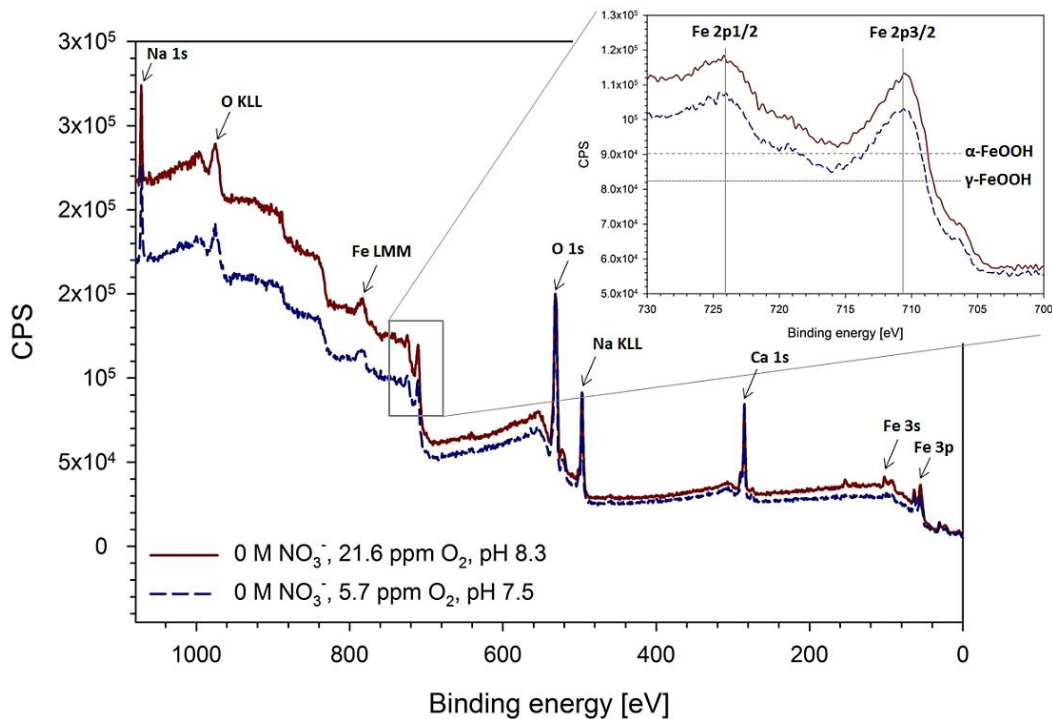


Figure 7-8: Ex-situ XPS spectra of specimen immersed in 6 ppm and 20 ppm O₂ solutions free of NO₃⁻

From the peaks identified in Figure 7-8, ex-situ XPS reveals the involvement of Fe²⁺ and Fe³⁺ complexes with oxides and/or oxyhydroxides. Other peaks are artifacts of contamination during drying of the NaHCO₃ electrolyte and the influence of the steel alloy substrate (Na 1s, Na KLL, and Fe LMM). The 2p_{3/2} peak shape strongly indicates the presence of high-spin Fe²⁺ and Fe³⁺ compounds due to its broadened appearance compared to Fe⁽⁰⁾ or low-spin Fe²⁺ [246]. Electrostatic interactions, spin-orbit coupling between the 2p core hole and unpaired 3d electrons of the photoionized Fe cation, and crystal field interactions have been shown to cause this peak shape [247]. The 2p_{3/2} peak spectra for both [O₂] cases shown resemble those attributed to Fe₂O₃ (of α and γ phases alike) and α -FeOOH in separate accounts [246],[248]. Based on the findings of Grovesnor et al. [246], the Fe 2p_{1/2} and Fe 2p_{3/2} peaks can identify specific compounds depending on the extrinsic loss as well as the intrinsic structures, both of which are distinct to γ/α -FeOOH, γ/α -Fe₂O₃, and Fe₃O₄ products. The intensities of α -FeOOH and γ -FeOOH reported in the high resolution photoelectron spectra are plotted over the zoomed portion of Figure 7-8 [246]. The

close match between the added lines and spectra of the products formed in the environments tested here strongly indicates the formation of both FeOOH phases on the steel surface.

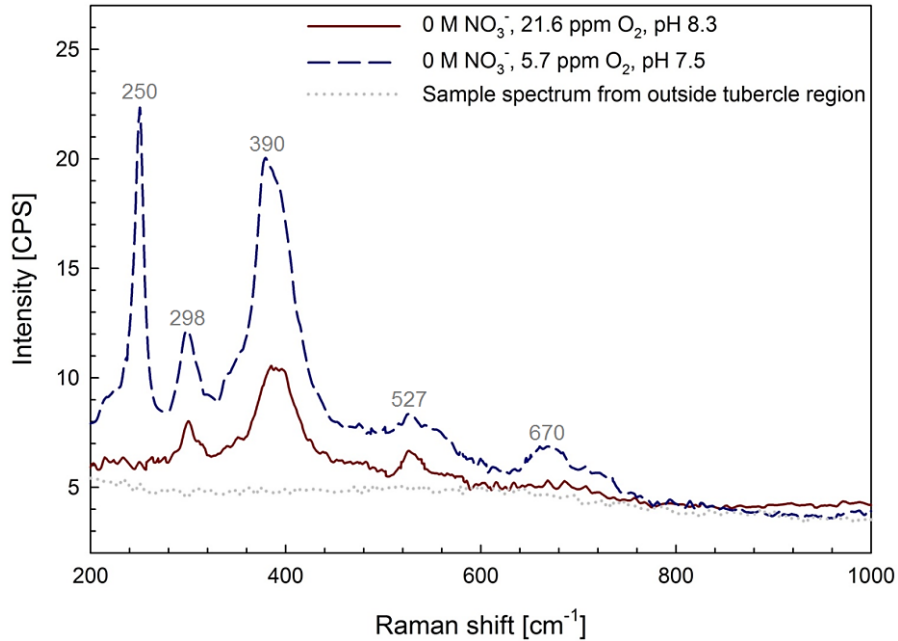


Figure 7-9: Ex-situ Raman spectra of specimen immersed in 6 ppm and 20 ppm O₂ solutions free of NO₃⁻

Surface analysis through Raman Spectroscopy further indicates the primarily Fe-oxide/oxyhydroxide constituents of the multi-layer corrosion product, as seen in Figure 7-9. By reference to standard spectra, the peaks at 390 cm⁻¹ can be attributed to α -FeOOH (reference: 392 cm⁻¹), whereas those at 298 and 527 cm⁻¹ indicate Fe₃O₄ presence (reference: 297 and 523 cm⁻¹, respectively) [249]. These two compounds are detected in the corrosion product of both 6 ppm and 20 ppm O₂ conditions. Conversely, the peaks at 250 cm⁻¹ and 670 cm⁻¹ appear only in the 6 ppm O₂ environment. Based on reference standard spectra, the 670 cm⁻¹ peak can be attributed to either α -FeOOH again (reference: 674 cm⁻¹), or could indicate the presence of γ -Fe₂O₃ (reference: 665 cm⁻¹) [249]. Since the peak at 250 cm⁻¹ is most corresponding to α -Fe₂O₃ (reference: 247 cm⁻¹), it is evident that Fe₂O₃ forms in at least the α phase in 6 ppm O₂ environments. The clear presence of γ/α -FeOOH in the corrosion product seen in the Raman spectra is further confirmed through distinct XRD peaks of Figure C-7 in Appendix C, appearing mainly around 20°, 30°, 35°, and 47.5°, and 52.5°. The existence of both phases is partially attributed to γ -FeOOH isomerizing

to α -FeOOH of a rhombic structure, a process which is dependent on water activity [80], [250]. Distinctly noticeable in the spectra of Figure 7-9 are the higher intensities of peaks associated with Fe₂O₃ in the 6 ppm O₂ vs. the 20 ppm O₂ environment, supporting the Raman findings. Peaks in the latter are much lower at ~40° or completely absent at ~33°.

In contrast to Figure 7-6 and Figure 7-7, the surfaces of the specimens immersed in N₂H₄ treated environments manifest much less corrosion product in total, if observed at the same magnification (Figure 7-10a and Figure 7-10c). At higher magnifications some minor crystal structures (likely FeCO₃ based on rhombohedral crystal structure forming in columnar-like fashion [251]) and a uniform base product film appear on the surface, the latter being cracked, holed, or flaked all across the surface. Based on the present system, the four peaks seen in both XRD spectra are attributed to γ -FeOOH at around 29°, FeCO₃ at around 44° and 65°, and substrate Fe at around 82°. The base product film seen with SEM is suggested to be causing the weak passivation effect observed in the PDP results of Figure 7-5, which improves the corrosion performance of specimen in N₂H₄ treated environments to a level beyond that seen even in completely deaerated conditions. It is noted however that the surfaces illustrated in Figure 7-10a and Figure 7-10c are for the 168 h immersion tests which were treated with 7 ppm of N₂H₄ in total (i.e. 1 ppm every 24 h). Thus, in these conditions, even if all the stoichiometric [N₂H₄] needed to deplete the 6 ppm O₂ is used, some N₂H₄ will remain. Then, with the O₂ fully depleted and the test containers sealed from further O₂ ingress, the remaining N₂H₄ will likely interact with the substrate in a manner similar to an anodic inhibitor, as previously proposed. Nonetheless, based on the 1 h N₂H₄ treatment results presented earlier in this chapter, it seems that even without a larger stoichiometric concentration ratio of N₂H₄:O₂, some N₂H₄ will not participate in {R-7.3}, and will instead interact with or oxidize the Fe substrate. Though not a specific objective of this work, further analysis by future studies to discern the chemical characteristics of surface layers forming with N₂H₄ treatments would be particularly beneficial to support this hypothesis.

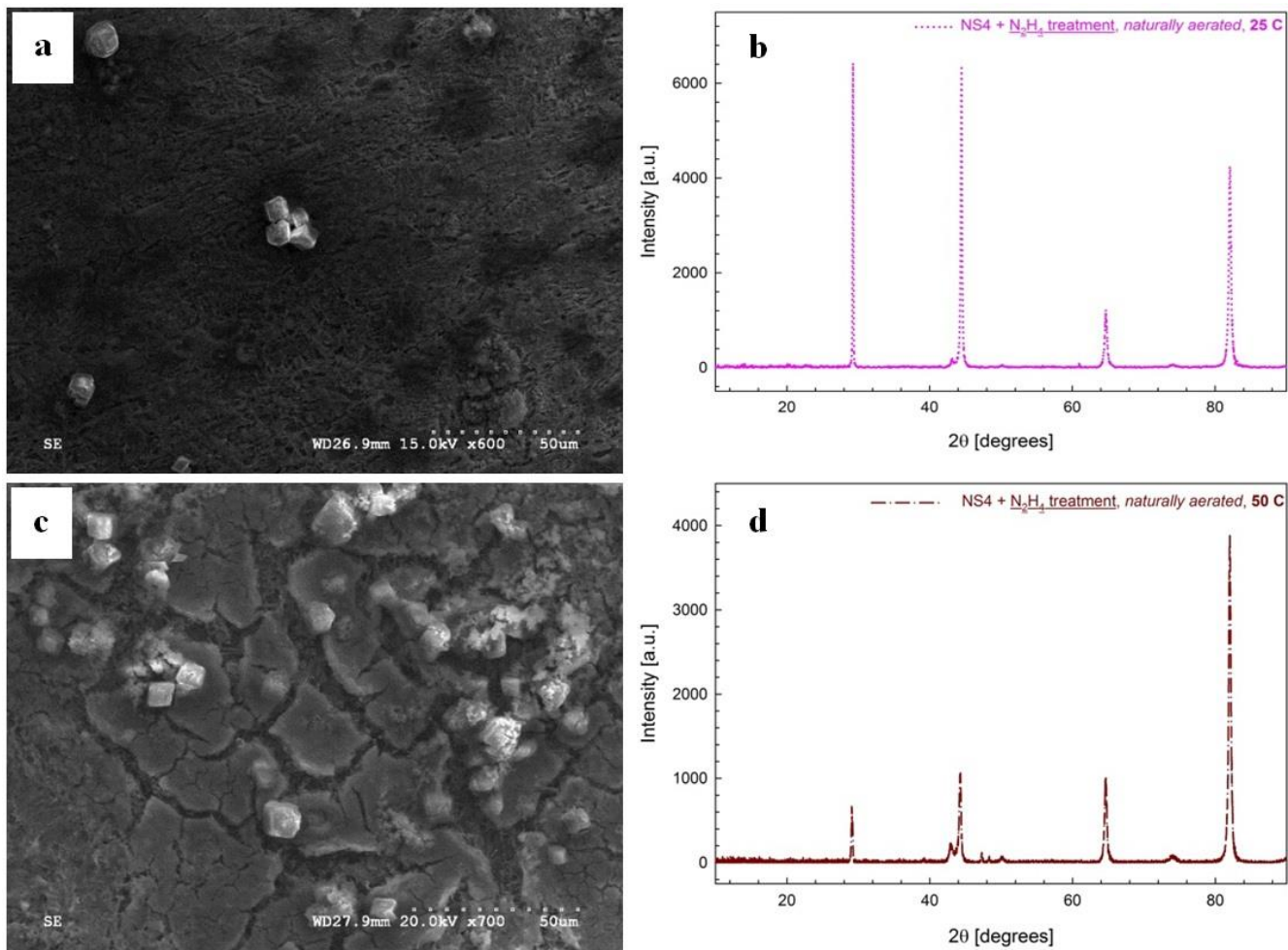


Figure 7-10: SEM images and corresponding ex-situ XRD spectra of X100 specimen surface following 168 h immersion in environments periodically treated with N₂H₄ as described in Table 7-3: (a), (b) 25 °C; (c), (d) 50 °C

7.4 Periodic electrochemical tests during 24 h immersions in 0 – 20 ppm [O₂] and 0 – 0.015 M [NO₃⁻] conditions

7.4.1 OCP

OCP transients during extended immersion until 24 h in the environments of Table 7-1 are shown in Figure 7-11 (same legend as Figure C-1). In deaerated conditions, a slight increase in OCP occurs over the 24 h period due to HCO₃⁻ presence accelerating active dissolution of the substrate as reported before [73]. Normally, in the absence of O₂, ensuing cathodic reduction can only be of either H⁺ or of reducible corrosion products on the surface. The absence of corrosion product following immersion in deaerated conditions of any [NO₃⁻] (Figure C-5) rules out the latter case, as well as the near impossibility of such reduction occurring in the present conditions, unaided by cathodic polarization or high temperatures [252]. Conversely, acceleration of corrosion in the presence of HCO₃⁻ stems from its role as an alternative H⁺ donor to pure H₂O reduction in anaerobic nn-pH; the sluggish nature of the latter is considered to be rate-limiting [253]. H evolution as the cathodic half-cell in deaerated conditions is supported by OCP being noticeably lower than O₂-containing conditions, dismissing O₂ as the predominant depolarizer. OCPs are also below the (E_{eq}) for H evolution assuming a H₂ partial pressure of 1 atm (-0.736 V_{SCE} for pH 8.33) [73].

Corrosion product growth on the steel samples immersed in 20 ppm O₂ conditions decreases OCP transients as shown in Figure 7-11. The final OCP values reached in both 1 h and 24 h immersion tests were shown previously in Figure 7-1 above, as a function of [O₂]. Results of regression fits on this data are shown in Table C-2 of Appendix C. In a recent study, Lu et al. have also shown that OCP drops occur with greater coverage of α -FeOOH following initial formation stages [73]. The 6 and 20 ppm O₂ profiles in Figure 7-11 appear to be converging to the -0.5 to -0.6 V_{SCE} plateau reached after month long immersions in solution of similar constituents [68]. During aerobic stages of cyclic aeration-deaeration junctures, OCPs settle

habitually to between -0.5 to -0.6 V_{SCE} shown in the figure with a shaded band [39], [40]. In such studies, the variable causing the OCP change at the boundaries of the cyclic aeration-deaeration intervals is $[O_2]$, directly altered with different purging gases. The growth of corrosion product also influences $[O_2]$ levels at preferential reduction sites and the kinetics of this reduction compared to that on a bare surface. In the present study, $[O_2]$ in the bulk solution is constant throughout the immersion, yet the movement of OCP transients still coincides with corrosion product growth. These results suggest that the presence of these oxide- and oxyhydroxide-based corrosion products on the surface, as shown with surface analyses, influences the $[O_2]$ at the steel-environment interface (below the tubercle), hence affecting redox conditions and OCPs. Both γ -FeOOH and α -FeOOH are the main tubercle products formed here in the presence of O_2 . The tubercle growth is driven by Fe^{2+} reacting with O_2 not reduced to OH^- (e.g. {R-7.4}) [80]. Similar tubercle formations containing γ/α -FeOOH have been observed following anaerobic-aerobic cycling of steel in solutions with Cl^- [254].

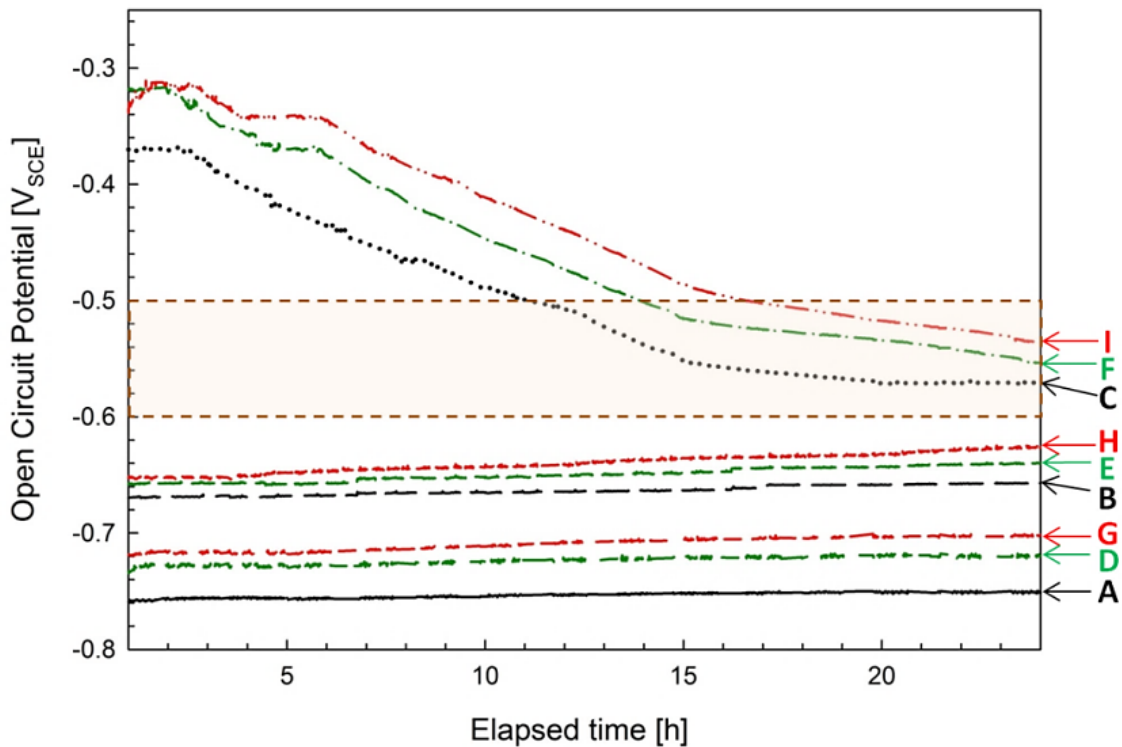


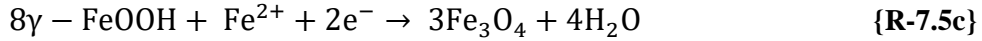
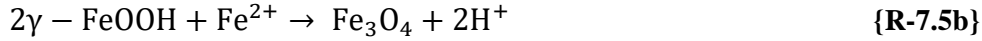
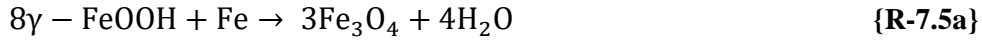
Figure 7-11: Full spectrum OCP transients Table 7-1 conditions during 24 h (same legend as Figure C-1)



The growth of this oxyhydroxide corrosion product on the surface gradually decreases the surface area of the exposed steel at which O₂ reduction formerly occurred during OCP < 1 h. Preferential O₂ reduction occurs on covered areas, not at the interface of the exposed steel with the electrolyte [255], resulting in the intensification of corrosion through separation of anode and cathode sites. Based on mixed potential theory, when the rate of the anodic half-cell reaction branch increases its intersection with the cathodic branch sum occurs at a lower corrosion potential (lower OCP) and a higher i_{corr} . OCP can also go lower from a decrease in the total rate of the cathodic half-cell reactions, yet at a lower i_{corr} . The unmistakable drop in R_p (indicating increasing i_{corr}) during the 24 h test in 20 ppm O₂ conditions (see LPR and EIS results below) is evidence that i_{corr} increases during this period, hence the associated OCP decrease in Figure 7-11 can be attributed to increased steel oxidation.

Amongst typical oxide/oxyhydroxide products known to form in O₂-containing conditions, such as γ -FeOOH, Fe₃O₄, and γ/α -Fe₂O₃, O₂ reduction occurs preferentially on Fe₃O₄, not γ -FeOOH or insulating Fe₂O₃ [202]. The clear detection of Fe₃O₄ in the corrosion products forming in 20 ppm O₂ conditions could therefore partially explain the increased redox reactions occurring at OCP, simultaneously increasing i_{corr} and moving the OCP in the cathodic direction. The preferential O₂ reduction on Fe₃O₄ (cathodic sites) accelerating oxidation of the steel substrate at separate anodic sites has previously been shown to occur in similar conditions by Sherar et al. [68], supporting the present interpretations. Fe₃O₄ develops from γ -FeOOH through various system-dependent reactions [80], [256]–[259], accelerated by Fe²⁺ presence. Specifically, the reduction of γ -FeOOH to Fe₃O₄ occurs through one of a set of virtually identical reactions either involving Fe directly {R-7.5a} [256], [257], Fe²⁺ chemically {R-7.5b} [258], or Fe²⁺ electrochemically {R-7.5c} [80] in low or zero [O₂] environments. It is noted that although being

influenced by temperature, all these reactions are reported to be viable at an ambient temperature of 25 °C.



The strong pH and Fe^{2+} dependence of the {R-7.5b} reaction corroborates the likelihood it being the reaction which occurs in the present conditions. In experiments conducted by Tamaura et al. [258], it was found that the transformation only occurs at a pH above 7.3, triggered by the adsorption of Fe^{2+} on the γ -FeOOH. The environments in which Fe_3O_4 forms here are all above this threshold pH. Furthermore, Fe^{2+} plays a critical role in lowering the electron transfer barrier of the corrosion product layer [256], or likewise the facilitation of γ -FeOOH “autoreduction” to Fe_3O_4 from Fe [257]. Either of these effects explains the trend of increasing corrosion rate with immersion observed for the full length of the tests in 20 ppm O_2 conditions and until 7 h in 6 ppm O_2 conditions (see LPR and EIS sections). γ -FeOOH has a band gap of 2.06 eV between conduction and valence whereas Fe_3O_4 has a band gap on the order of 0.1 eV [259], representing a stark reduction in electron transfer barrier strength, hence the augment of corrosion rate found here.

Even with the definite O_2 presence in 6 ppm O_2 conditions, OCP slowly moves in the anodic direction in contradiction with behavior in 20 ppm O_2 conditions (shown in Figure 7-1 also). Three main differences are present between the two environments and the resultant corrosion product formations: (1) the $[\text{O}_2]$ and pH of the bulk solution, (2) the morphology of the γ/α -FeOOH tubercle forming during the immersion as seen in section 7.3, and (3) the presence of Fe_2O_3 exclusively in 6 ppm O_2 conditions as revealed by both Raman Spectroscopy and XRD. It is therefore reasonable to attribute the different OCP transient behavior in 6 ppm O_2 versus 20 ppm O_2 conditions to one or more of these factors. Through the reciprocal of the methodology

used to explain the opposite OCP movement in 20 ppm O₂ environments, when the rate of the anodic branch sum decreases its intersection with the cathodic branch sum occurs at a higher corrosion potential (higher OCP) and a lower i_{corr} . This justification is consistent with the increased R_p values measured in LPR and EIS tests during the same 7 – 24 h period (as shown below), and is the basis for the proposed corrosion evolution mechanism in 6 ppm O₂ environments.

7.4.2 EIS

Results from the periodic EIS scans during immersion reveal clear [O₂] and time dependencies. Responses for different [NO₃⁻] at any single [O₂] are similar, so only 0.005 M NO₃⁻ results are presented.

The Nyquist plots of Figure 7-12a and Figure 7-12b readily show the stability of Z during 24 h of immersion in deaerated conditions. Nearly complete semicircles which do not change in size significantly with time reveal steady corrosion with no notable diffusion or induction effects at lower ω . For the same reasons outlined in the previous EIS analyses of sections 5.3 and 6.2 (i.e. slight positive inflections in Z and θ_{EIS} (not shown) at lower ω indicating adsorption of electroactive species or the relaxation of carbon carrying intermediate species [198]), the same EEC of Figure 5-14 with a nested parallel adsorption section shown in the corner of Figure 7-12a is used to model the results, where component symbols are the same as in earlier uses. This EEC once again achieves very good correlation with measured spectra as seen in the select fits (2 and 8 h) superimposed on the figures, and by χ^2 values on the order of 10^{-4} in Table C-3 of Appendix C. The inflections in Z_{re} caused by adsorption effects are readily observed by comparing the fit curves from the proposed EEC with those from a basic Randles circuit (no nested parallel adsorption circuit) at 10 and 20 h immersions in Figure 7-12a and Figure 7-12b, respectively. The Westing-Mertens method of conversion from Q to C compatible with the two time constant of the EEC is used, the results of which are shown in Table C-3 [209].

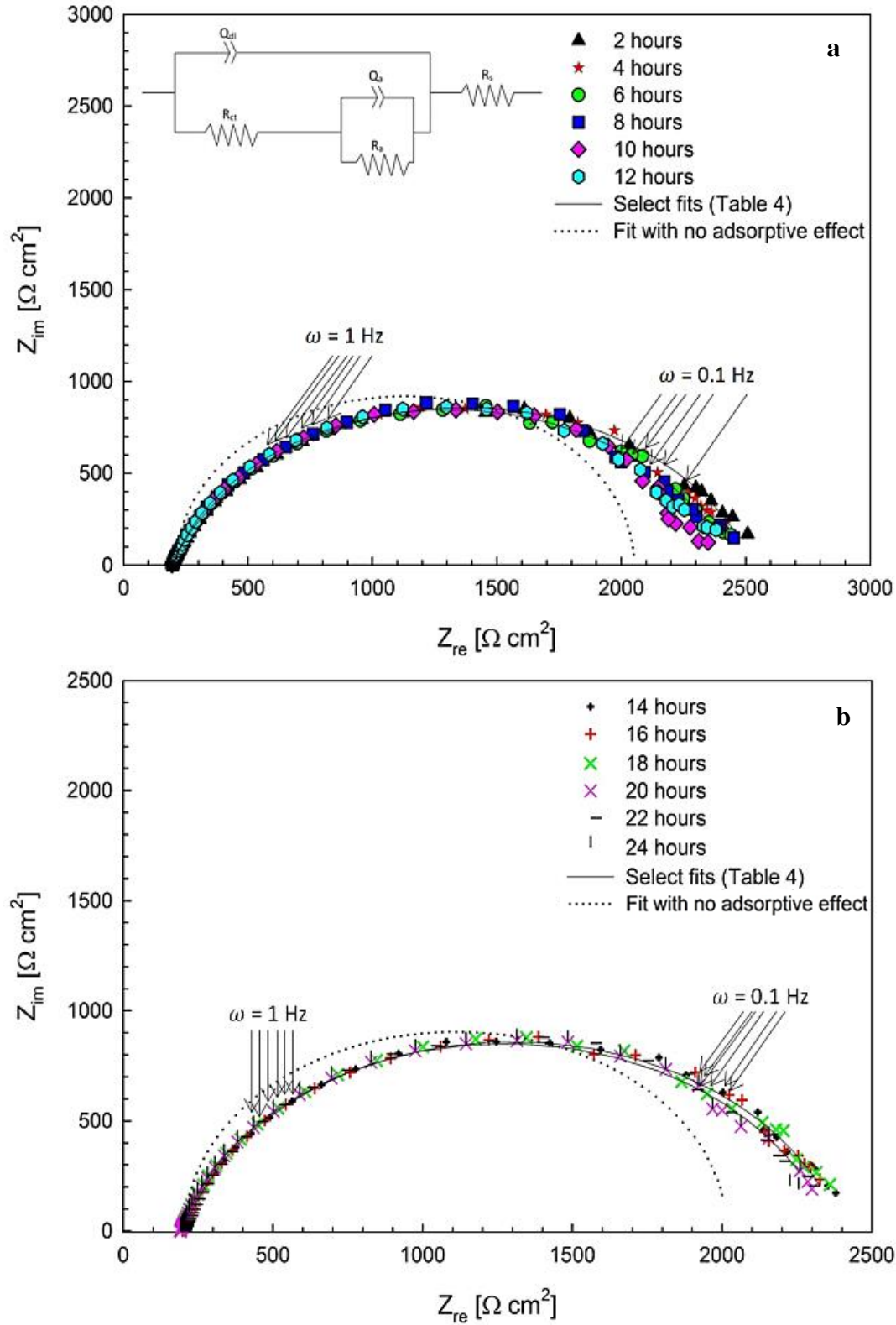


Figure 7-12: Nyquist impedance representation and fit profiles for deaerated solution containing 0.005 M NO_3^- (0.2 ppm O_2 , pH 6.6): (a) at 2, 4, 6, 8, 10, and 12 h immersion times, with proposed EEC; (b) at 14, 16, 18, 20, 22, and 24 h immersion times

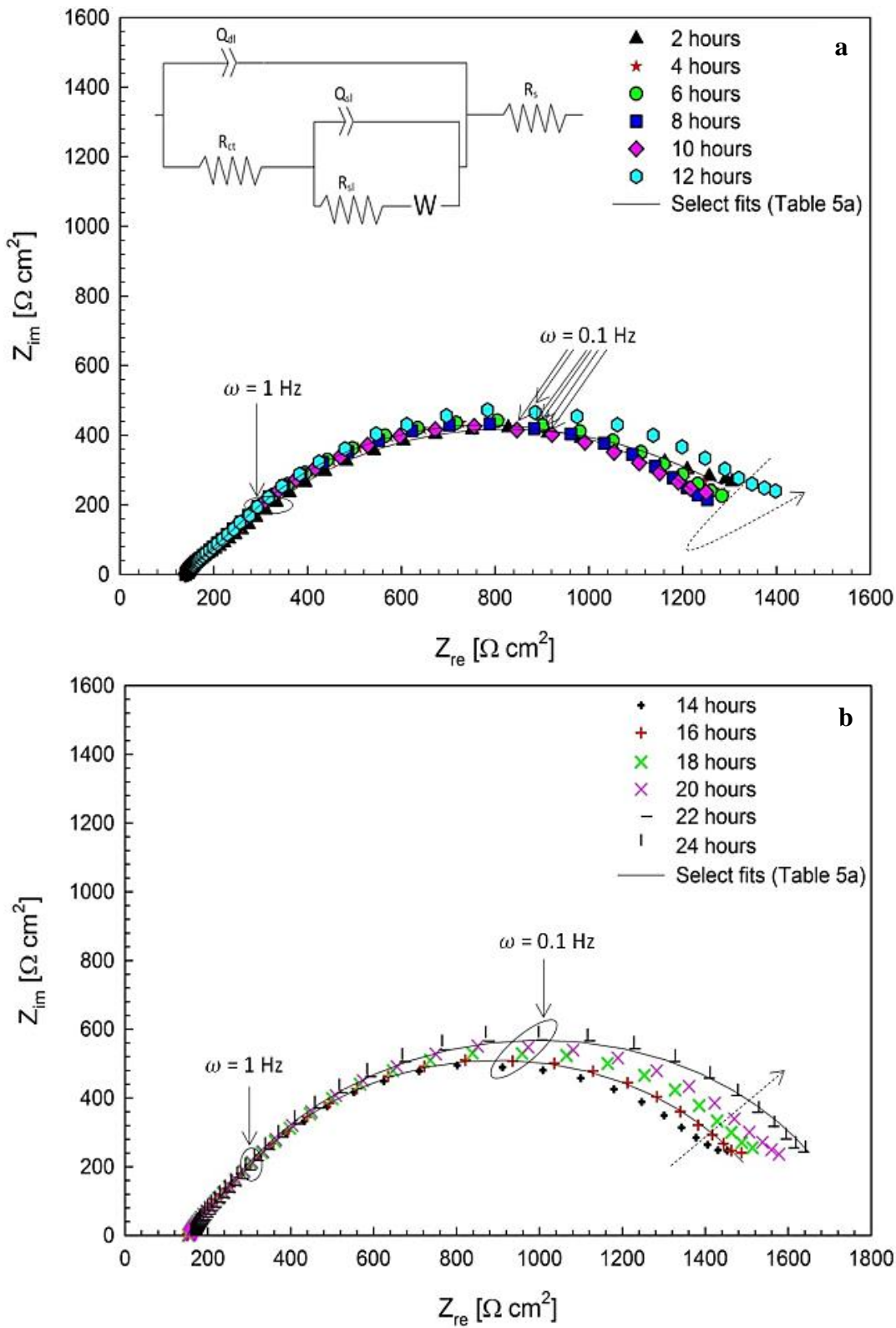


Figure 7-13: Nyquist impedance representation and fit profiles for 5.8 ppm O_2 solution (pH 7.7) containing 0.005 M NO_3^- : (a) at 2, 4, 6, 8, 10, and 12 h immersion times, with proposed EEC; (b) at 14, 16, 18, 20, 22, and 24 h immersion times

The steady R_{ct} values for the deaerated condition are higher than their 6 ppm and 20 ppm O_2 counterparts (Table C-4 and Table C-5, respectively) throughout the 24 h immersion, indicating lower corrosion. Increased R_a with time demonstrates the decreasing attractive strength between the steel and the adsorbate(s), a finding which is once more explainable through basic dilute solute adsorption theory valid here, in which increasing θ_{ads} of the surface with the growth of an adsorbate layer decreases the number of sites capable of binding the adsorbate. In section 6.2.1 the Hill-Langmuir model for adsorption was shown as an example; nonetheless, competing adsorption of dissolved electroactive species can also be represented by the classic Everett isotherm {E-7.3}, where θ_i^s is the fractional coverage of adsorbate i on the solid (single component steel surface), x_i^l is the molar fraction of adsorbate i ($\sum_{i=1}^k x_i^l = 1$), and K_{eq}^i is the adsorbate equilibrium constant [210], [260]. Monolayer capacity a_m is assumed to be the same as surface phase capacity n_m (i.e. monolayer adsorption analogous to Langmuir isotherm for gas adsorption), thus more filled binding sites on the adsorbent hinders further binding (increases R_a).

$$\theta_i^s = \frac{K_{eq}^i [x_i^l / (1 - x_i^l)]}{1 + K_{eq}^i [x_i^l / (1 - x_i^l)]} \quad \text{assuming } n_i / n_m \approx a_i / a_m = \theta_i^s \quad \{\mathbf{E-7.3}\}$$

Nyquist plots for 6 ppm and 20 ppm O_2 nn-pH solutions containing 0.005 M NO_3^- are shown in Figure 7-13a-b and Figure 7-14a-b, respectively. The plots demonstrate the effects induced by above-nominal $[O_2]$ and mildly alkaline pH values. The 6 ppm O_2 results during the first half of the immersion (Figure 7-13a) immediately reveal higher corrosion activity compared to the deaerated case, judging from the drop in maximum Z_{re} and Z_{im} values, respectively, at the same ω identified. Simultaneous to this reduced Z is a noticeable change in the shape of the Nyquist profile compared to Figure 7-12a and Figure 7-12b, characterized by: a smaller rise (lower slope) in the high ω region above 1 Hz, an extension in the Z_{re} direction at low $\omega < 0.1$ Hz, and an elevated Z_{im} at the lowest applied ω of 0.01 Hz. The two latter characteristics are relative to overall Z , so even though quantitatively the values are similar to the deaerated case, since overall Z values are less their effect is magnified. These Z features signify mass transfer

behaviors, which manifest in increased Z_{re} and Z_{im} at lower ω and could be accommodated by the EEC shown in Figure 7-13a. The W diffusion element has previously been described in {E-6.3} of section 6.2.1. The new R_{sl} and Q_{sl} elements in the EEC of Figure 7-13a represent total surface layer R and C , respectively. These elements are included to gauge the protectiveness of the multi-layer developed, especially at immersion times ≥ 8 h as revealed by OCP behaviors in Figure 7-1 and Figure 7-11. R_{sl} and Q_{sl} are like the adsorption subset in Figure 7-12a, but with the influence of corrosion product presence added to adsorption effects. The W in this nested circuit represents the proposed parallel diffusion-adsorption mechanism, and the ensuing corrosion is modelled by the R_{ct} - Q_{dl} parallel. A better fit is achieved with this configuration than when W is placed in series with R_s .

Goodness of fits for 6 ppm O_2 condition spectra are highly favorable, with χ^2 values on the order of 10^{-5} and errors in fit below 1% in general. R_{sl} of Table C-4 and Table C-5 is considerably higher in magnitude than R_a of Table C-3, indicating the protectiveness of the corrosion product layers. The value of this element increases with immersion time, an expected result of tubercle and sub-tubercle growth. This is naturally accompanied by decreasing W (lower diffusion in the product) as revealed by the results. Q_{sl} (or C_{sl}) and corresponding high n values demonstrate what appears to be a capacitive region near the specimen surface stemming from the surface layer and adsorptive effects, which behaves similar to the double layer. This region becomes less dominant with immersion time akin to the overall trend in Q_{dl} or C_{dl} . The opposite trend is exhibited by R_{ct} which yields values lowest at 8 h and noticeably higher thereafter (shown graphically with arrows in Figure 7-13a and Figure 7-13b), a behavior which aligns with the OCP results in section 7.4.1 and the LPR results below. It is suggested that Fe_2O_3 , found in the corrosion product of 6 ppm O_2 conditions as shown by XRD and Raman Spectroscopy, is a main cause of this behavior. The insulating nature of γ - Fe_2O_3 in comparison with Fe_3O_4 (the latter has a very low energy band gap on the order of 0.1 eV) impedes charge transfer resulting in a

decreasing corrosion rate coinciding with its development [259]. Furthermore, the pseudo-morphing of γ -FeOOH to γ -Fe₂O₃, as seen in {R-7.6}, has previously been shown to be supported by [O₂], and occurs in relatively low corrosion rates, two features which do not contradict with the present findings: (1) diffusion processes are occurring in the FeOOH tubercle as identified by W in Table C-4, and (2) R_{ct} values are near those in deaerated conditions [80], [250].



In contrast, the evolution of 20 ppm O₂ spectra in Figure 7-14a-b is void of a Z inversion, manifesting profiles continually decreasing in size. The same characteristics of mass-transfer influence found in 6 ppm O₂ conditions are seen here, where the low ωZ_{re} extension is unmistakable in the context of the much smaller profile sizes. This region traverses nearly horizontally in many cases, especially at longer immersion times. Despite the difference in $|Z|$ evolution with time between 20 ppm and 6 ppm O₂ EIS results, the same proposed EEC is suitable; the processes leading up to and causing multi-layer corrosion product growth are the same although magnitudes of these processes and the characteristics of resulting developments are different.

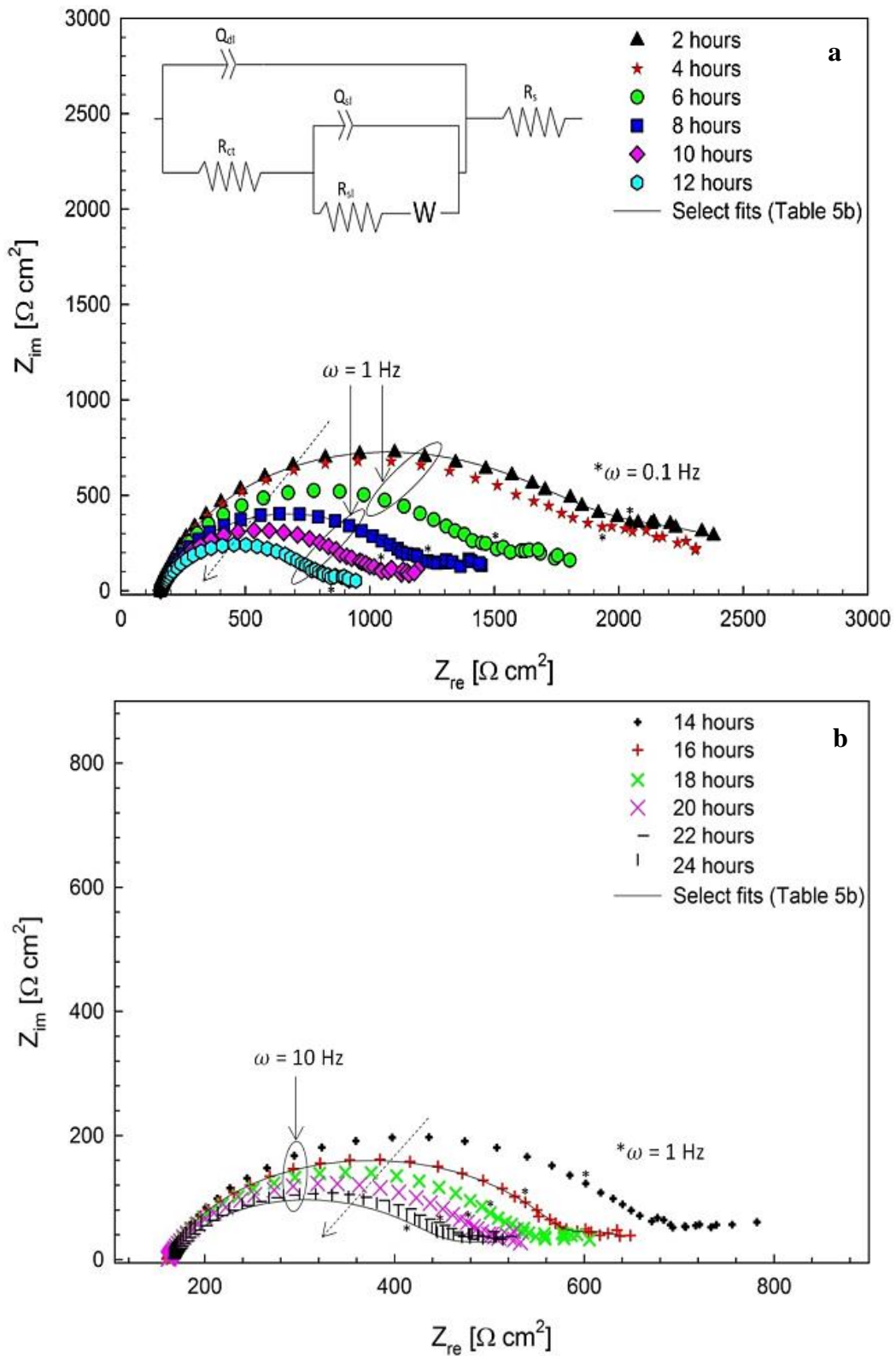


Figure 7-14: Nyquist impedance representation and fit profiles for 5.8 ppm O_2 solution (pH 7.7) containing 0.005 M NO_3^- : (a) at 2, 4, 6, 8, 10, and 12 h immersion times, with proposed EEC; (b) at 14, 16, 18, 20, 22, and 24 h immersion times

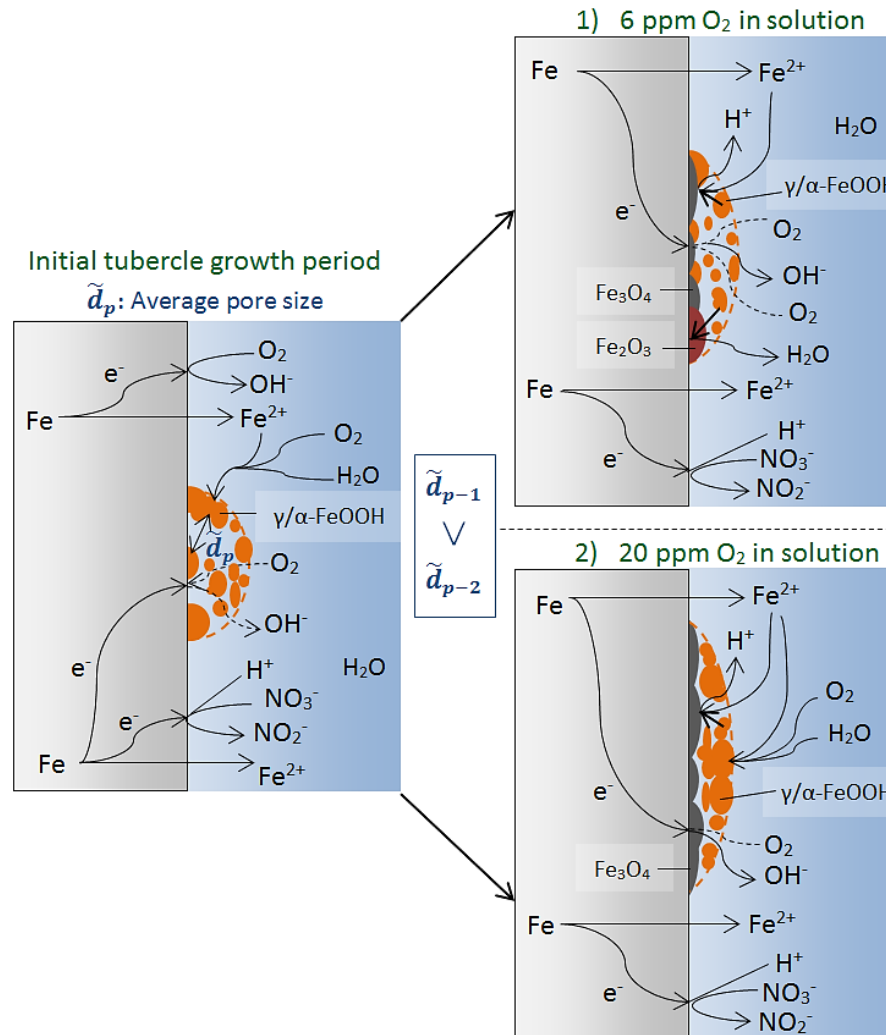


Figure 7-15: Diagram illustrating the influence of $\Delta[\text{O}_2]$ between: (1) 6 ppm O_2 and (2) 20 ppm O_2 conditions on the evolution mechanism of the Fe-oxyhydroxide tubercle and sub-tubercle Fe-oxide layer(s), where \tilde{d}_p represents the average pore size in the tubercle

Quantitatively, this difference is identified through the results of the three key parameters: R_{ct} , R_{sl} , and W in Table C-5. R_{ct} is initially large and then decreases substantially to end at a level an order of magnitude less than 6 ppm O₂ and deaerated condition counterparts. Conversely, R_{sl} of the 20 ppm O₂ conditions is generally higher than that of 6 ppm O₂ conditions, considered to be the influence of the less porous tubercle layer of the former. The development and growth of the γ/α -FeOOH tubercle with this morphology limits diffusion, as verified by the lower W values relative to 6 ppm O₂ results (except at 2 h). Hence, the values and evolution of the electrochemical parameters are corroborative of the OCP transients and surface analyses discussed above. The absence of the Z inversion in the 20 ppm O₂ conditions further supports the critical role of charge-transfer behavior of the intermediary corrosion products developing in different environments. Only Fe₃O₄ is detected in 20 ppm O₂ conditions, on which preferential charge-transfer continually increases corrosion as opposed to insulating Fe₂O₃ in 6 ppm O₂ conditions [202]. Figure 7-15 is a cumulative schematic summarizing the main differences identified and proposed in this chapter between 6 ppm O₂ and 20 ppm O₂ conditions, as supported by morphological, product characterization, and electrochemical evidences from experiments.

7.4.3 LPR

The R_p results of the specimen immersed in deaerated and 6 ppm O₂ conditions are shown in Figure 7-16a, whereas Figure 7-16b shows the results for immersions in 20 ppm O₂ conditions. Error bars show the range of values obtained for the three repetitions conducted for each test. The results agree well with the higher R_{ct} (lower corrosion rate) values of deaerated and 6 ppm O₂ versus 20 ppm O₂ conditions from EIS. Quantitatively, the sums of EIS resistance values in the deaerated environments ($R_p^* = R_s + R_{ct} + R_a$) compare very well with measured R_p values in the LPR tests, shown correspondingly in Table 7-6. This is also true for the non-zero [O₂] tests in the same table, where R_p^{**} (sum of ω -independent resistances plus W , or $R_p^* + W$) is

similar to R_p for each corresponding time and environment. LPR results also indicate increased anodic dissolution with $[\text{NO}_3^-]$, a finding discussed earlier.

In all 6 ppm O_2 conditions R_p reaches a minimum at around 7 h followed by increasing corrosion protectiveness of the product layers until 24 h. At times < 7 h the formation of mainly $\gamma/\alpha\text{-FeOOH}$ and Fe_3O_4 underneath is conducive to corrosion, and diffusivity of species occurs through the porous tubercle as suggested by surface analysis and EIS findings. Yet, at times > 7 h the proposed localized influence of $\gamma\text{-Fe}_2\text{O}_3$ forming from $\gamma\text{-FeOOH}$ diminishes the overall reduction rate of O_2 due to its insulating nature, thereby reducing the corrosion of coupled anodic sites on the unpolarized steel specimen. If formed over Fe_3O_4 , $\gamma\text{-Fe}_2\text{O}_3$ can also steadily lessen the significance of O_2 reduction on the dual-layer with time [39]. The time at which R_p upsurges in Figure 7-16a coincides with the Z inversion in the EIS results. In contrast, deaerated conditions exhibit nearly flat R_p evolution with time and 20 ppm O_2 conditions show continually decreasing profiles, both trends matching their corresponding $[\text{O}_2]$ case behavior in the OCP transients and EIS spectra fits.

Table 7-6: Comparison of R_p values from LPR with R_p^* or R_p^{**} from EIS component sums, in solutions with 0, 6, and 20 ppm O_2 at 2, 8, 16, and 24 h immersion

Condition	Resistance parameter	2 h	8 h	16 h	24 h
0.2 ppm O_2 pH 6.7 0.005 M NO_3^-	R_p^* [$\text{k}\Omega \text{ cm}^2$]	2.22	2.32	2.20	2.37
	R_p (LPR) [$\text{k}\Omega \text{ cm}^2$]	2.20 ± 0.05	2.15 ± 0.01	2.14 ± 0.04	2.23 ± 0.03
5.8 ppm O_2 pH 7.7 0.005 M NO_3^-	R_p^{**} [$\text{k}\Omega \text{ cm}^2$]	1.8	1.6	1.8	2.0
	R_p (LPR) [$\text{k}\Omega \text{ cm}^2$]	1.54 ± 0.02	1.45 ± 0.03	1.72 ± 0.01	1.88 ± 0.04
20.4 ppm O_2 pH 8.6 0.005 M NO_3^-	R_p^{**} [$\text{k}\Omega \text{ cm}^2$]	1.9	1.1	0.9	0.6
	R_p (LPR) [$\text{k}\Omega \text{ cm}^2$]	1.80 ± 0.05	0.98 ± 0.03	0.59 ± 0.13	0.46 ± 0.05

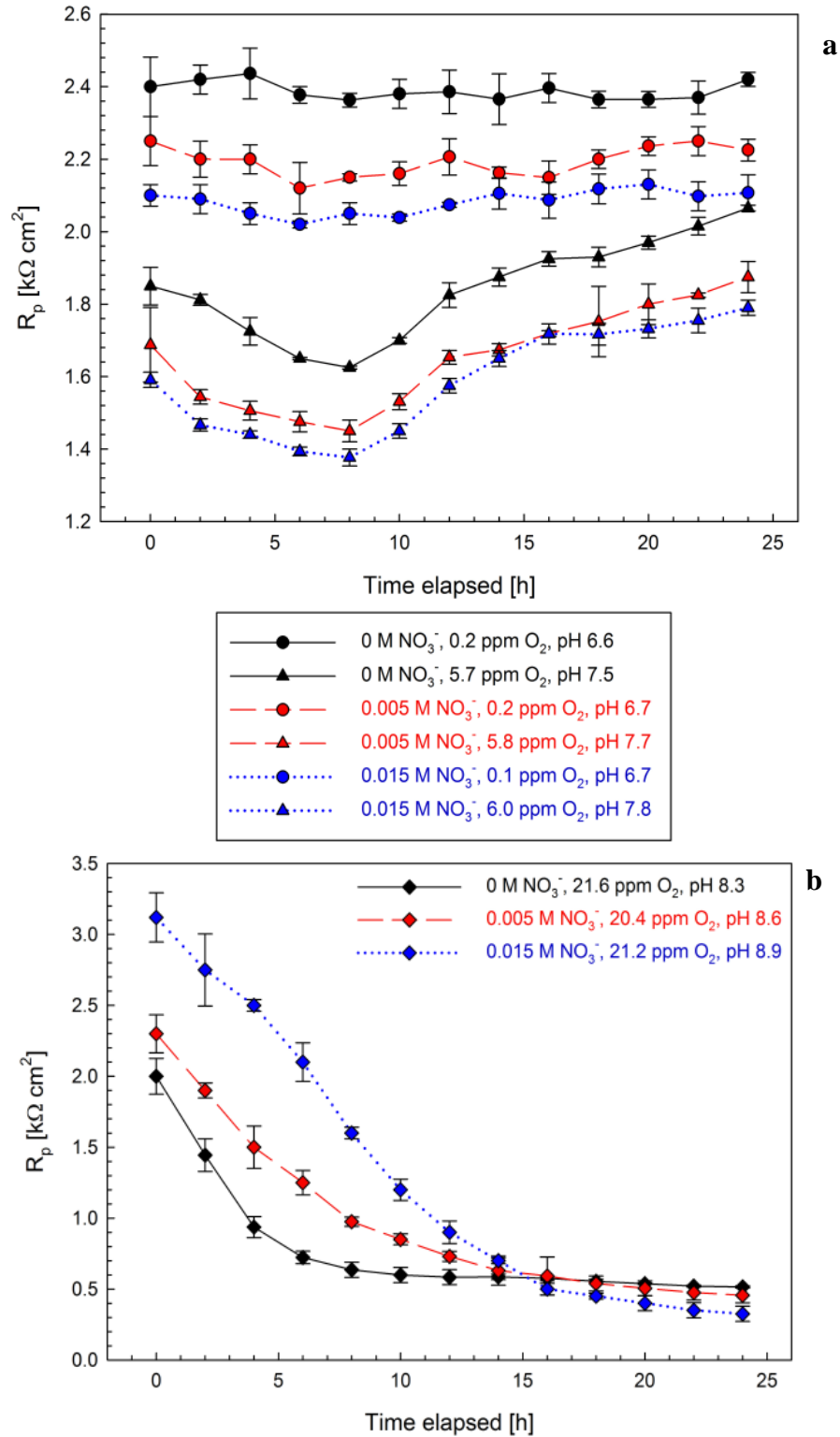


Figure 7-16: Polarization resistance (R_p) vs. immersion time, calculated from periodic LPR scans conducted in: (a) deaerated and 6 ppm O $_2$ solutions containing 0, 0.005, or 0.015 M NO $_3^-$; (b) 20 ppm O $_2$ solutions containing 0, 0.005, or 0.015 M NO $_3^-$

7.5 Summary

In this chapter, the electrochemical corrosion behavior of X100 steel specimens is tested in nn-pH NS4 solutions of $0.1 \text{ ppm} \leq [\text{O}_2] \leq 21.6 \text{ ppm}$, $0 \text{ M} \leq [\text{NO}_3^-] \leq 0.015 \text{ M}$, $0 \text{ ppm} \leq [\text{N}_2\text{H}_4] \leq 1$, and temperatures of 25 °C and 50 °C. $[\text{O}_2]$ and $[\text{NO}_3^-]$ are studied at $1 \text{ h} \leq$ immersion times $\leq 24 \text{ h}$, whereas temperature and N_2H_2 treatment combinations are studied during immersion times $\leq 1 \text{ h}$ and following a 168 h extended immersion session. During the first hour of immersions, stable OCP profiles are more anodic with increased O_2 and increased $[\text{NO}_3^-]$ owing to the latter's single stage reduction leading to intensified corrosion. The influences of higher $[\text{O}_2]$ and $[\text{NO}_3^-]$ are clear in the cathodic region of PDP profiles, driving both diffusion-controlled i and overall cathodic i higher. NO_3^- imposes an upward shift on the E where H evolution dominates over O_2 reduction. Where Tafel extrapolation is appropriate, NO_3^- is also found to increase i_{corr} as corroborated by all electrochemical tests. N_2H_4 treatments in ppm concentrations impacts X100 corrosion by shifting the OCP and i of the steel to values less than those exhibited in the 5% CO_2 deaerated environment. Increasing the concentration of N_2H_4 treatment always improves the creation of a weak passivation effect appearing at low anodic polarizations, enhancing corrosion control of the steel through partial covering of the surface (seen in SEM).

Upon extended immersion, X100 in deaerated conditions exhibits the least noble OCPs governed cathodically by H evolution, and no corrosion products form. Both 6 ppm and 20 ppm O_2 conditions appear to converge to an OCP between -0.5 to -0.6 V_{SCE} through movement in either anodic or cathodic directions, respectively. Tubercles form in all above-nominal $[\text{O}_2]$ conditions and are characterized as FeOOH of both γ and α phases, with markedly higher porosities in conditions with lower $[\text{O}_2]$ in solution. Fe_3O_4 , FeCO_3 , and Fe_2O_3 are also identified in the corrosion product, the latter being noticeably more extensive with higher porosity tubercles of the 6 ppm O_2 conditions. N_2H_4 treatments in 0.5 ppm – 1 ppm concentrations virtually eliminate the formation of Fe-oxides and Fe-oxyhydroxides during immersion in O_2 -containing

nn-pH NS4 conditions. In cases where it forms, the insulating properties of Fe_2O_3 causes an upsurge in R_p and R_{ct} values at around 7 h immersion, which otherwise continually decreases due to more enhanced cathodic kinetics (of O_2 reduction) occurring preferentially on Fe_3O_4 beneath the γ/α -FeOOH tubercle. The growth of the multi-layered corrosion product formations including the porous tubercle is modelled with surface layer EEC elements, which also gauge adsorption effects. Lower diffusivity of O_2 in the more compact tubercles formed in 20 ppm O_2 conditions is revealed by EIS modelling results.

8. Evaluation of hydrogen evolution, absorption, and diffusion in X100 steel exposed to nn-pH HCO_3^- solutions of various ion constituents and temperatures⁶

Transgranular SCC of underground pipelines occurs in nn-pH environments and is distinct from the classic intergranular (IG) SCC often found in high pH environments [28], [87], [261]–[263]. Experiments in dilute aqueous solutions concluded that transgranular SCC occurs with or without the presence of O_2 , HCO_3^- - CO_3^{2-} , or dissolved CO_2 [264]. Nevertheless, it is widely established that transgranular SCC in nn-pH simulated soil environments is greatly enhanced by the presence of dissolved CO_2 [21], [50], [265]. Transgranular SCC in underground pipelines is characterized by wide cracks with quasi-cleavage morphology and little branching [28], [87], [88]. The crack sides often suffer significant lateral corrosion resulting in the destruction of the original crack faces. The mechanism of transgranular SCC in underground pipelines is not yet fully understood, albeit a combination of anodic dissolution and HE is proposed to be responsible for the cracking [21], [91], [92], [266]. Evidences supporting the contribution of H to the crack growth are reported in literature [51], [93], [94]; the morphology of the fracture surface resembles those observed in HIC [21], [97], and secondary cracks manifest in isolation of the surface of the specimen, whilst nucleating on bands of pearlitic material [21], [28]. In addition, the increase in the susceptibility of steels to transgranular SCC at more cathodic E also supports the proposed HE mechanism [92], [95], [96].

Electrochemical and corrosion studies of steels in nn-pH environments mainly focus on the anodic process [97], [172], [217], [267]. The cathodic processes on steels, particularly the hydrogen evolution reactions (HER) which might play an important role in controlling transgranular SCC mechanisms in the nn-pH environment, are not thoroughly understood. Knowledge regarding the HER in HCO_3^- - CO_3^{2-} solution is mainly obtained from studies of

⁶ H. M. Ha, I. M. Gadala, and A. Alfantazi, *Electrochimica Acta*, vol. 204, pp. 18–30, June 2016.

internal corrosion of pipelines exposed to CO₂ solutions [36], [64], [100], [101], [268], [269]. Such electrolytes are far more concentrated and more acidic than any corrosive electrolyte surrounding pipelines at locations where transgranular SCC is found [21], [24], [265]. In these internal pipeline corrosion studies though, the presence of CO₂ increases the corrosion rate of Fe by increasing the rate of the HER [36], [64], [100], [268]. It is widely suggested that the i_c is the sum of the i for H⁺ reduction and H₂CO₃ discharge, at least in nn-pH and alkaline environments. However, at higher pH the direct discharge of HCO₃⁻ becomes important near the corresponding OCP of steels [65]. Understanding the effects of parameters such as solution chemistry, aeration condition, CO₂, pH, and temperature on the kinetics of the cathodic reactions, particularly HER on steels, is important in studies of the nn-pH environments and transgranular SCC.

The kinetics of H generation on the steel surface will affect the amount of H ingress into the material and subsequently assist SCC crack growth. Recent studies on H damage manifestations in X100 steels, including HIC under severe cathodic charging in both acidic and alkaline environments [104], [108], [109] and HE under different E ranges in HCO₃⁻ solutions [90], emphasize the need to understand the H generation/evolution, absorption, and diffusion kinetics in this modern HSLA material in specific. This chapter addresses the shortage of studies investigating cathodic reaction kinetics particularly on X100 steels in nn-pH electrolytes relevant to underground pipeline corrosion. The effects of environmental parameters, specifically ion constituents, %CO₂, temperature, and pH, in addition to surface states of the steel (i.e. bare versus covered with corrosion product) are examined. The significance of H uptake and H diffusion kinetics in X100 exposed to these environments is also studied. This chapter is based on a paper [245] which was published as part of the research work leading towards this PhD thesis.

8.1 Environments and hydrogen permeation conditions

HSLA X100 steel samples are used for all the corrosion, permeation, and diffusion tests conducted in this chapter. The microstructural features of this steel have been discussed earlier in

this thesis (see section 4.1.1). The standard NS4 solution used in all previous chapters is the baseline test electrolyte for the tests conducted here. Reagent-grade chemicals and ultra-pure deionized water are used to synthesize this reference condition and all other modifications of it. Modified NS4 solutions with varying anion and cation contents are prepared to investigate the effect of these ion species on the corrosion and corresponding H-related phenomena. This is done by increasing the amount of KCl, NaHCO₃, CaCl₂·2H₂O, or MgSO₄·7H₂O in the test environments by 10 times. Similarly, in pursuing a better understanding of CO₂ and O₂ influences on the overall degradation mechanism, solutions are either left open to air (natural aeration) or purged with pure N₂, pure CO₂, or the mixture of 5% CO₂/95% N₂ of the reference NS4 condition. Although not practically expected in service, 100% CO₂ purging environments were tested here for mechanistic insight. All purging gases are of a purity $\geq 99.99\%$ (Praxair® Inc.). Generally, purging is conducted for at least 30 minutes in order for environments to achieve their natural pH; yet, in some experiments the pH of the solution is adjusted by adding 1 M NaOH or 1 M HCl.

The influence of temperature is included in selected environments, simulating levels normally encountered in industrial applications in practice, specifically those of buried pipelines. The conductivity of the base-line NS4 solution is 1.11 mS/cm and varied in the range of 1.11 to 7.74 mS/cm in the modified NS4 solutions of this chapter. Table D-1 in Appendix D lists details of the test conditions studied here. Although some of the environments therein do not represent typical field conditions (specifically the pure CO₂ purging situations), their inclusion is important to support a thorough understanding of H-related corrosion and transport phenomena on X100 steel sought here. Moreover, actual environments are irregular in nature as shown in section 2.1, depending on a wide variety of physicochemical soil variables; hence, simulations thereof should evaluate individual parameter changes built on an established base-line situation as presented in this study. Modifications from this central situation are amplified to properly magnify and identify the effects caused by the changes involved.

In this chapter, PDP experiments are commenced by leaving the specimens to freely corrode at OCP for 1 h. Then, E is swept from 50 mV > OCP to more negative E (cathodic polarization) at a 2 mV/s scan rate. As in all the test polarization tests of this thesis, iR-drop in low conductivity test solutions is compensated by the current interruption technique within the potentiostats used (Gamry Reference 600 is used in the experiments of this chapter). Anodic behavior of X100 in the environments of Table D-1 has been discussed in detail in previous chapters, hence will not be presented here.

8.1.1 Hydrogen permeation conditions

Under the diffusion controlled regime, the permeation flux will follow Fickian behavior. The solution for the permeation transient is solved assuming no mobile H exists inside the sample at the beginning of the permeation experiment and the concentrations of H at the entry side and the exit side during the permeation experiment are fixed at a constant value of C_o and zero, respectively [160], [270]. The analytical solution gives the relationship between the permeation current density and the effective hydrogen diffusivity as follows [160], [271]:

$$\log[(i_{perm} - i_{bg})t^{0.5}] = C - \frac{L^2 \log e}{4D_{eff}} \cdot \frac{1}{t} \quad \{\mathbf{E-8.1}\}$$

where i_{perm} is the permeation current density (A/cm²) at time t (s), i_{bg} the background permeation current densities prior to charging (A/cm²), C is a constant, D_{eff} is the effective hydrogen diffusivity (cm²/s), and L is the specimen thickness (cm). At steady state, the permeation current density is expressed by [155], [272]:

$$i_{ss} = \frac{nFD_{eff}C_s}{L} \quad \{\mathbf{E-8.2}\}$$

where i_{ss} is the H permeation current density at steady state (A/cm²), n is the charge of proton ($n = 1$ equivalent), F is the Faraday constant, and C_s is the subsurface H concentration at the entry side (mol/cm³).

The effective hydrogen diffusivity, D_{eff} , could be determined from the plot of $\log[(i_{bg})t^{0.5}]$ vs. $1/t$ according to {E-8.1}. The D_{eff} could also be determined from the breakthrough time t_b , which is the time when the permeation transient starts to rise, or from the lagging time t_{lag} , which is the time when the permeation current achieves 63% of the steady state current [155]:

$$D_{eff} = \frac{L^2}{15.3t_b} \quad \text{\{E-8.3\}}$$

$$D_{eff} = \frac{L^2}{6t_{lag}} \quad \text{\{E-8.4\}}$$

8.2 Results of OCP and cathodic polarization ($E < -1.2 V_{SCE}$)

The OCP of API X100 steel in different solutions at 20 °C is shown in Figure 8-1. The figure shows the average values of OCPs and the standard deviation determined from 3 measurements. Samples in solutions left open to air exhibited the highest OCP while those in solutions purged with 100% N₂ gas exhibited the lowest OCP. Higher concentrations of CO₂ in the mixed gas resulted in increased OCP values for the steel. Adding NaHCO₃ to NS4 solution reduced the OCP of the steel in all gas atmospheres, whereas adding KCl, MgSO₄, and CaCl₂ did not significantly alter the steel's OCP.

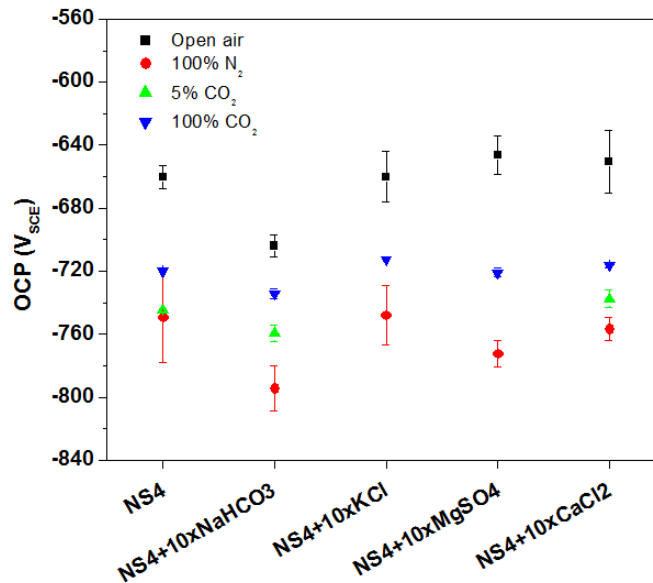


Figure 8-1: Open circuit potential of X100 steel in different test solutions of Table D-1 at 20 °C

8.2.1 Environmental effects on cathodic polarization results

Cathodic polarization curves of the X100 steel sample in test solutions at 20 °C and deaerated with 100% N₂ are shown in Figure 8-2a. In these solutions, the cathodic reactions on the steel start at approximately -760 mV_{SCE} and exhibit a Tafel slope of approximately 120 mV/decade in the whole range of E down to -1.2 V_{SCE}. However, the cathodic behavior of the steel in NS4 + 10x NaHCO₃ is an exception in that its cathodic polarization curve exhibits higher i_c compared to those in other 100% N₂ purged solutions, suggesting additional cathodic reactions. The behavior exhibited by the X100 steel sample is similar for all open air solutions (Figure 8-2b), showing a diffusion controlled regime at OCP > E > -1.1 V_{SCE} and approaching a linear behavior at E < -1.1 V_{SCE}. The limiting current density (i_{lim}) in the diffusion controlled regime is approximately 10⁻⁴ A/cm². The Tafel slope of the linear segment at E < -1.1 V_{SCE} is approximately 120 mV/decade. Compared to the i_c in 100% N₂ NS4 solution, the i_c in open air solutions is significantly higher in the E range near OCP but gradually approaches the 100% N₂ curve at more negative E .

Similarities are also observed in the cathodic polarization behavior of the X100 steel sample in all 100% CO₂ solutions (Figure D-1 in Appendix D). The i_c of the steel in this condition is 2 to 10 times higher than that in 100% N₂ solutions. Figure 8-3a shows the cathodic polarization curves in NS4 solution with different purging gas, plotted in the same graph. An increase in i_c is observed at all cathodic E when the 5% CO₂ gas mixture is used (vs. 100% N₂), and i_c values further increase as the concentration of CO₂ in the purging gas becomes 100%. The effect of CO₂ on the cathodic reaction kinetics is clearly seen one more time in Figure 8-3b when the gas atmosphere is switched during PSP experiments at -0.8, -0.9 and -1.0 V_{SCE}. In 100% N₂ NS4 solution, i_c at -0.8, -0.9 and -1.0 V_{SCE} reaches stable values of approximately 1, 20 and 60 μA/cm², respectively. The stable i_c increases and establishes new, higher stable values as the gas atmosphere is changed from 100% N₂ to 5% CO₂ to 100% CO₂.

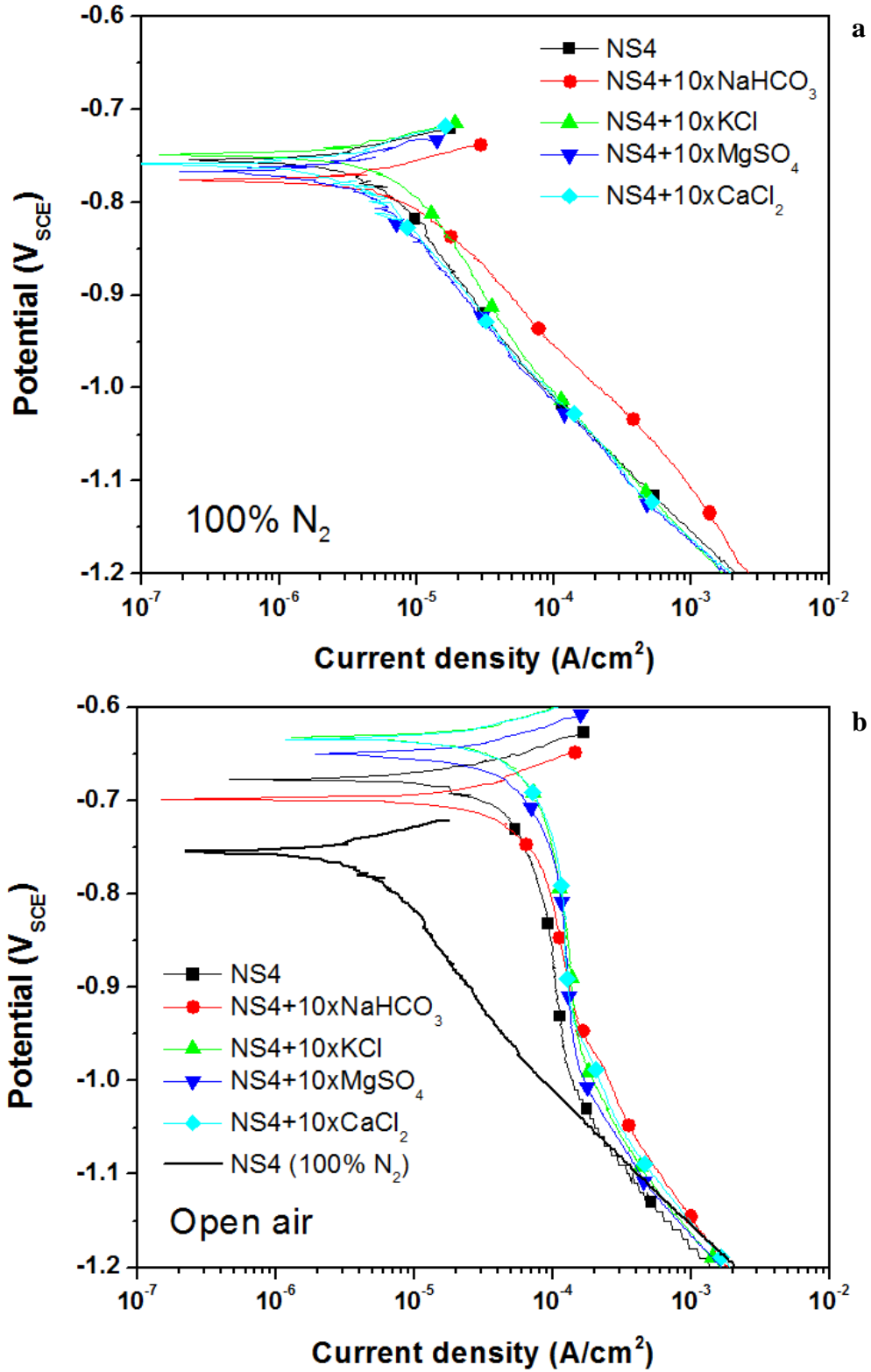


Figure 8-2: Cathodic behavior of X100 steel in: (a) deaerated (100% N₂) NS4 and modified NS4 solutions at 20 °C; (b) open air NS4 and modified NS4 solutions at 20 °C

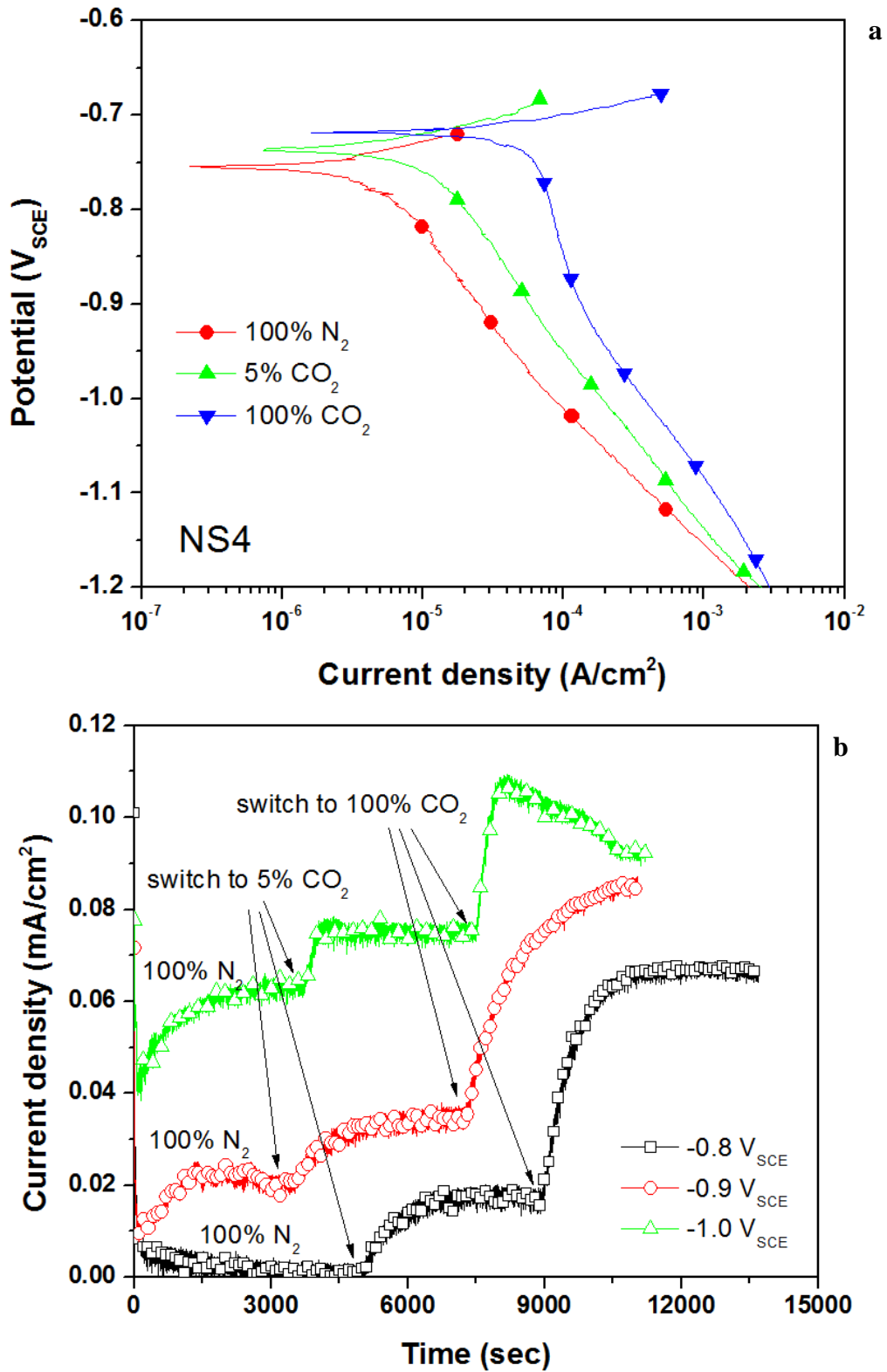


Figure 8-3: Cathodic behavior of X100 steel in: (a) NS4 solution under different gas atmospheres; (b) NS4 solution under different gas atmospheres during constant potential holds at -0.8, -0.9 and -1.0 V_{SCE}

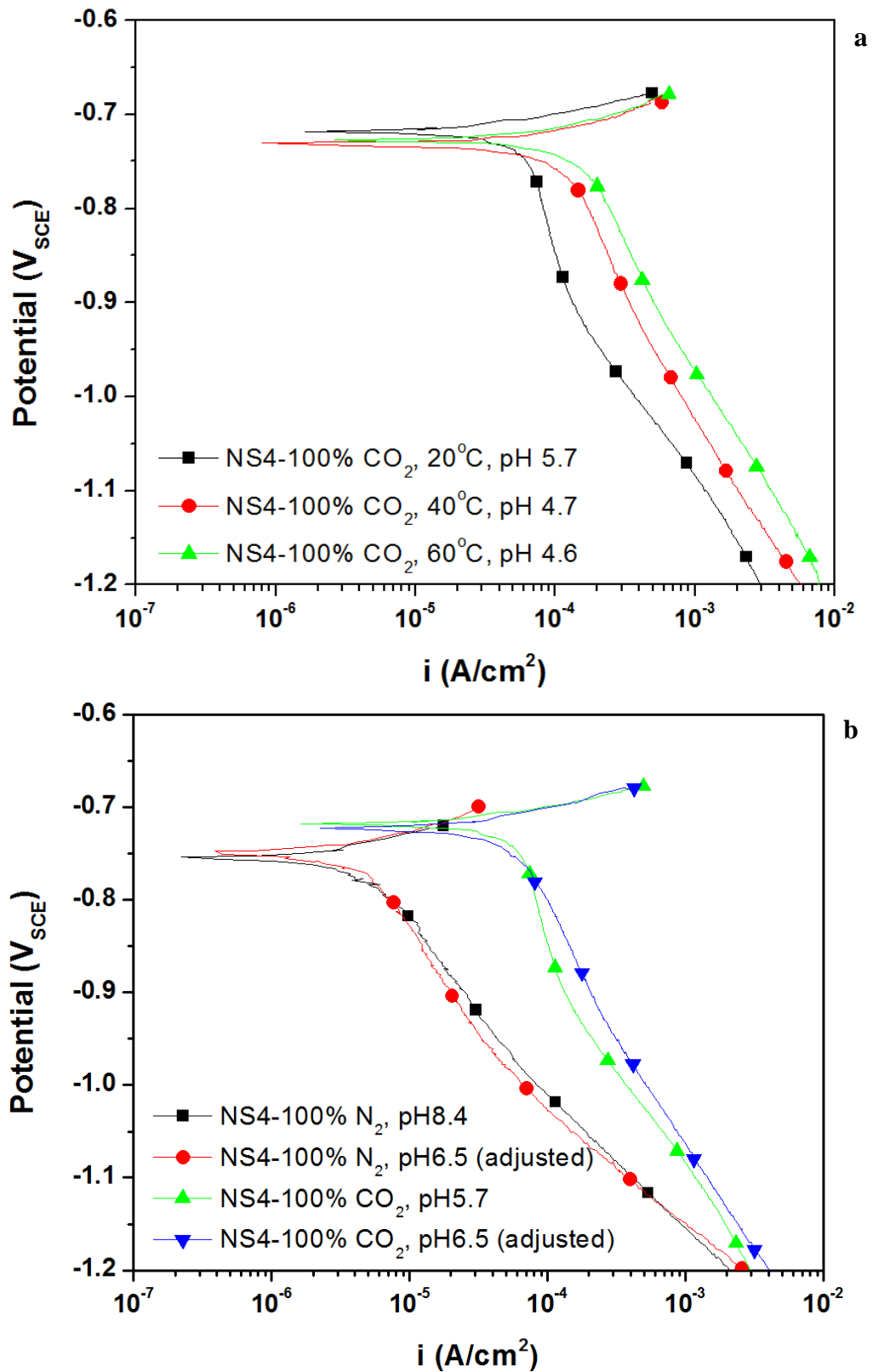


Figure 8-4: Cathodic polarization curves of X100 steel in: (a) 100% CO_2 NS4 solution at 20, 40, and 60 °C, natural pHs; (b) NS4 solution with adjusted pH at 20 °C

The cathodic behavior of the steel in 100% CO₂ NS4 and NaHCO₃-added NS4 solutions at 20, 40 and 60 °C are presented in Figure 8-4a and Figure D-2a in Appendix D, respectively. In general, cathodic kinetics increase with temperature, indicated by a shift in the polarization curves to higher i_c levels. The polarization curves of X100 steel in NS4 solution at different pH levels is shown in Figure 8-4b. In 100% N₂ solution, the curves are slightly shifted in the direction of higher i_c as the pH is increased from 6.5 to 8.4. A similar behavior occurs in 100% CO₂ solution as the pH is increased from 5.7 to 6.5. This behavior is reproducible in replicated experiments. In 100% N₂ NaHCO₃-added NS4 solution (Figure D-2b in Appendix D), the cathodic polarization curve in the natural pH 8.4 solution shows significantly higher i_c compared to the curve in NS4 pH 8.4 solution. However, this increased i_c behavior disappears when the pH of the NaHCO₃-added NS4 is adjusted to 5.7.

8.2.2 Surface deposit effects on cathodic polarization results

The nature of the deposit on samples after a 1 h PSP at -1.2 V_{SCE} in 100% CO₂ NS4 solutions is examined by SEM and EDX/EDS. Small spherical particles approximately 5 μm in diameter are observed on the sample surface as shown in Figure 8-5a. After 10 h, the sample surface is completely covered by a continuous layer. EDX/EDS analysis indicates the existence of C, O, Mg, and Ca in the composition of the deposit, which is in agreement with the chemical nature of the commonly found Ca_xMg_{1-x}CO₃ scale on steels in this environment [273]–[275]. The cathodic behavior of the scale-covered X100 steel in NS4 solution is shown in Figure 8-5b. The cathodic polarization curve of the sample after a 1 h PSP session at -1.2 V_{SCE} is shifted to i_c lower than those of the freshly polished sample. In addition, the extent of the shift in the cathodic polarization curve increases as the duration of the PSP at -1.2 V_{SCE} increases from 1 to 10 h.

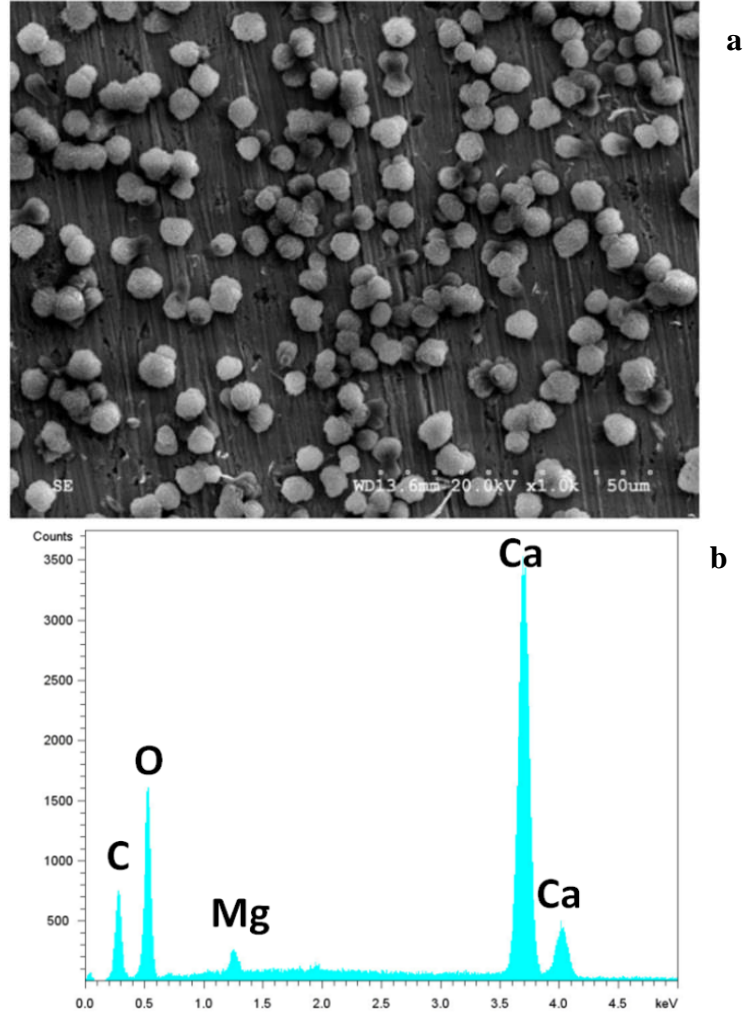


Figure 8-5: Characterization of the deposit on X100 steel held at $-1.2 \text{ V}_{\text{SCE}}$ in 100% CO_2 NS4 solution: (a) SEM photo after 1 h; (b) EDX/EDS spectrum of a particle formed

8.3 Results of hydrogen permeation experiments

The H flux transient in the X100 thin sheet sample when a charging current density (i_{charge}) of $-500 \mu\text{A}/\text{cm}^2$ is applied on the entry side is shown in Figure 8-6a. After a breakthrough time, the i_{perm} increases to a steady state value of $i_{\text{ss}} = 0.4 \mu\text{A}/\text{cm}^2$ in approximately 9000 s. The t_b and the t_{lag} of the permeation transient are 1594 s and 3398 s, respectively. Hence, D_{eff} in X100 steel is determined to be 4.1×10^{-7} and $4.9 \times 10^{-7} \text{ cm}^2/\text{s}$ using {E-8.3} and {E-8.4}, respectively. Hydrogen diffusivity could also be determined from the slope of $\log[(i_{\text{perm}} - i_{\text{bg}})t^{0.5}]$ vs. $1/t$ which returns a value of $4.3 \times 10^{-7} \text{ cm}^2/\text{s}$ for D_{eff} (Figure 8-6b). The average D_{eff} calculated by these three different methods yields a value of $4.4 \times 10^{-7} \pm 4 \times 10^{-8} \text{ cm}^2/\text{s}$.

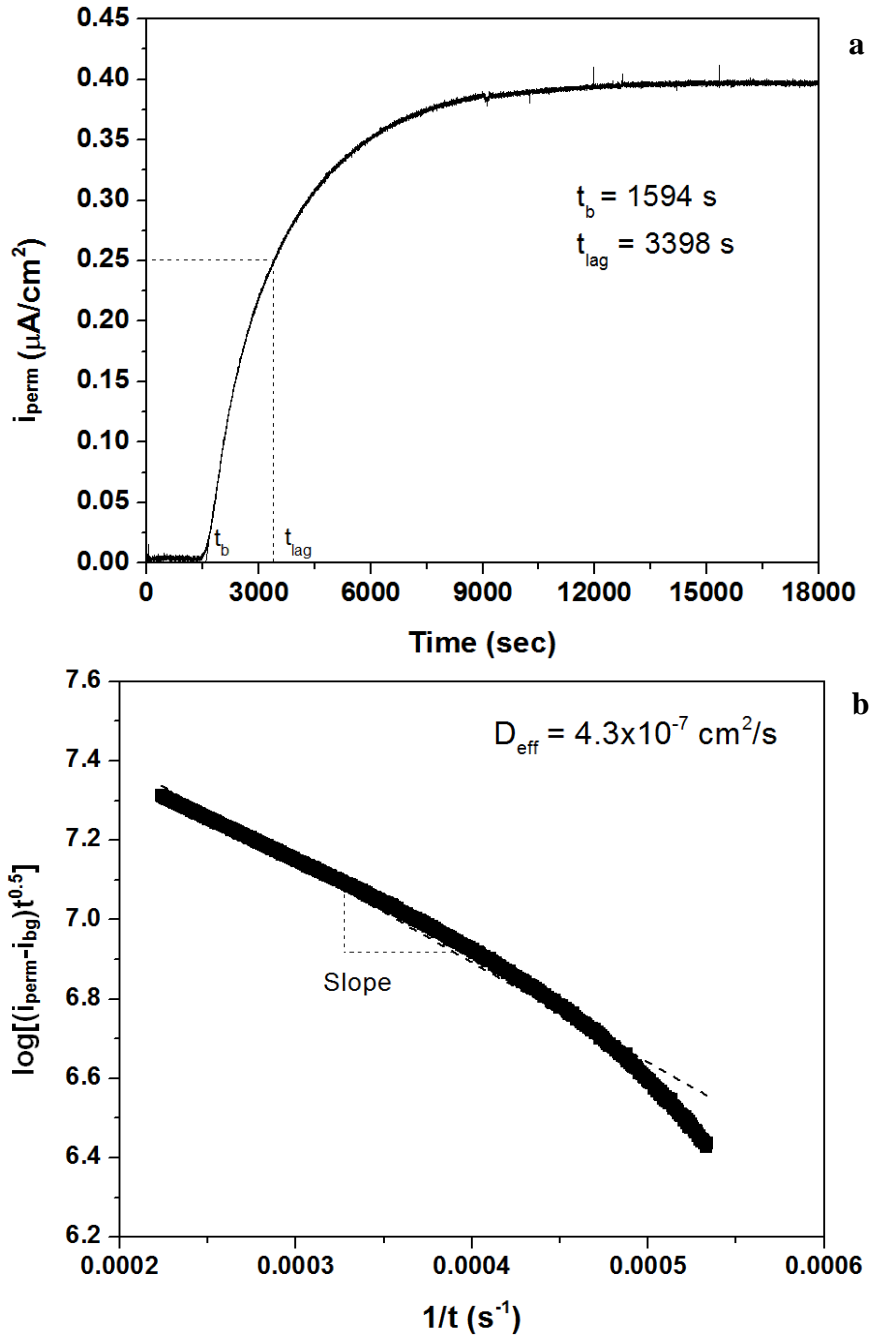


Figure 8-6: (a) Permeation current transient of X100 steel exposed to 100% CO₂ NS4 solution (20 °C) at a hydrogen charging current density of -500 μA/cm²; (b) determination of D_{eff} of the X100 steel from permeation current transient using {E-8.1}, where the slope of the $\log((i_{perm}-i_{bg}) \times t^{0.5})$ vs. $1/t$ plot is obtained by linear fitting

The response of i_{charge} and i_{perm} when the purging gas in the entry compartment is switched from 100% N₂ to 5% CO₂ to 100% CO₂ is plotted in Figure 8-7. Here, i_{charge} values are kept negative to show that they are a measure of cathodic/reduction reaction rates versus that of

the anodic/oxidation reaction rates measured on the exit side (i.e. i_{perm}). The magnitude or absolute value of i_{charge} on the entry side (i.e. $|i_{charge}|$) increases from approximately 10 to 20 to 95 $\mu\text{A}/\text{cm}^2$ as the entry compartment is purged with 100% N_2 , 5% CO_2 , and 100% CO_2 , respectively. These values are within around 10 $\mu\text{A}/\text{cm}^2$ of the corresponding cathodic current densities of separate tests in the same conditions (i.e. NS4 solution and -0.9 V_{SCE} charging potential, shown in Figure 8-3b). These are overlaid on Figure 8-7 with dashed lines. Similarly, i_{perm} on the exit side increases from approximately 0.03 to 0.05 to 0.1 $\mu\text{A}/\text{cm}^2$ corresponding to the switching of the purging gas in the entry compartment from 100% N_2 to 5% CO_2 to 100% CO_2 , respectively.

Several remarks could be made about this data. Regarding the increased amount of H generated on the steel sample (i_c at the entry side) at higher % CO_2 , this is primarily due to the increased acidity of the solution (i.e. increased $[\text{H}^+]$). At decreased pH levels the kinetics of H evolution through H^+ reduction increases, partly due to the increased $[\text{H}^+]$ in the solution. Perhaps more important than the increased $[\text{H}^+]$ though is the increase in E_{eq} of the HERs with acidity. It is shown in {E-8.8}, {E-8.9}, {E-8.12}, and {E-8.13} of section 8.4.2 below that in more acidic solutions, the E_{eq} of H evolution increases for all the available cathodic reaction paths. Thus, even at a constant charging potential of -0.9 V_{SCE} , the overpotential driving the cathodic reactions will be larger at lower pH due to the corresponding increases in E_{eq} of the HERs involved. Inherently, due to additional HERs involving H_2CO_3 or HCO_3^- becoming viable through increased E_{eq} at lower pH, and since the charging potential remains constant at a level more negative than these reversible potentials, the i_c values measured at the entry side is augmented by the additional involvement of these reactions. The influence of CO_2 on the kinetics of HERs will be elaborated further in subsequent sections below. The results in Figure 8-7 also reveal that the amount of H absorbed and transported through the steel sample in NS4 solutions is only 0.1 to 0.3% of the H generated at the charging side. Hence, most of H is harmless to the steel and bubbles out. Finally, it takes some time for i_{perm} on the exit side to respond to the change in i_{charge} on the entry side as the result of the delay associated with the diffusion of H through the sample.

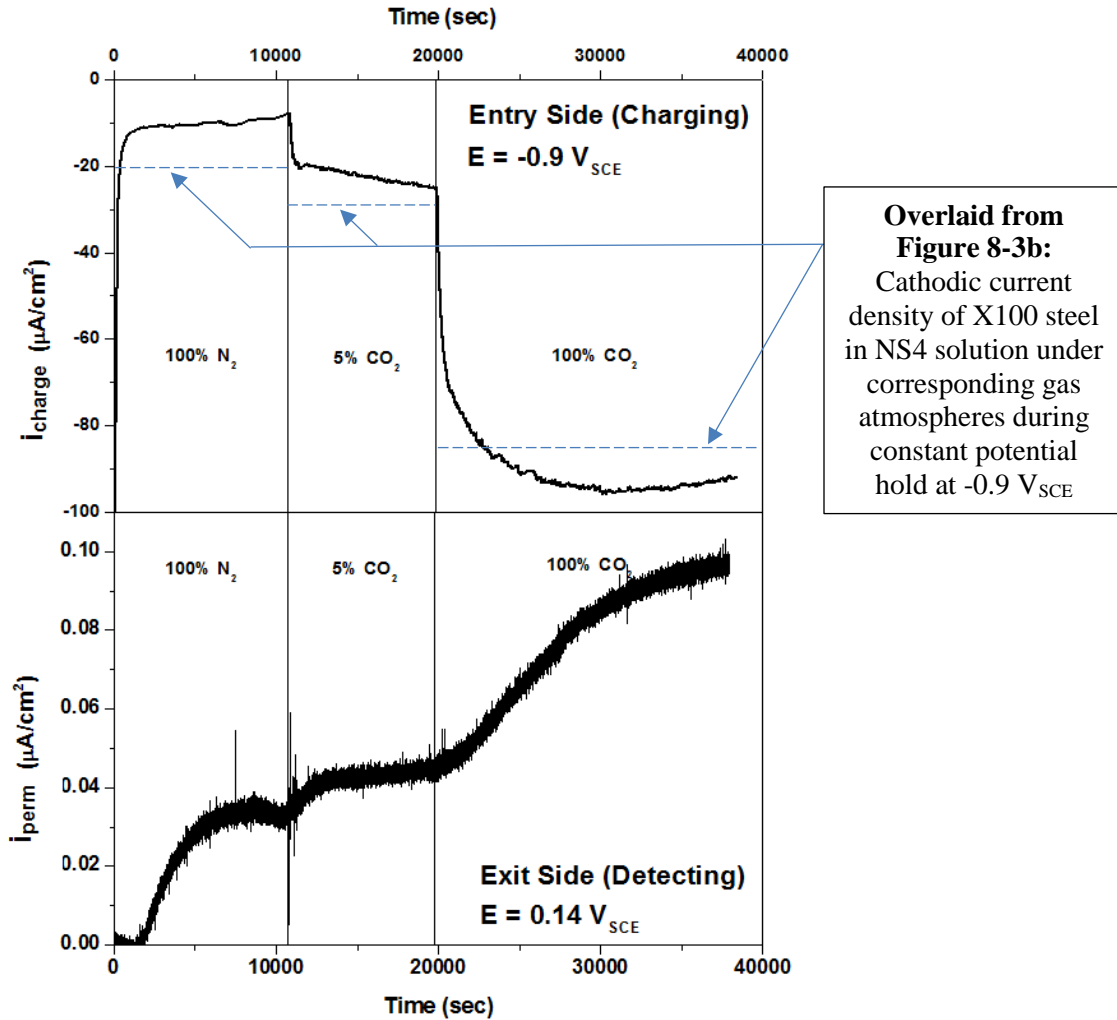


Figure 8-7: The current response in the H entry and exit sides (cathodic i_{charge} and anodic i_{perm} , respectively) during the permeation experiment in NS4 solution. The purging gas in the charging compartment is switched from 100% N_2 to 5% CO_2 to 100% CO_2

Figure 8-8 shows the transients of both i_{charge} and i_{perm} as the applied cathodic E on the entry side is changed from -0.85 to -0.95 , -1.05 , and finally $-1.15 V_{SCE}$. The magnitude of the H i_{charge} density increases from approximately 70 to $200 \mu A/cm^2$ for the full spectrum of the applied E change (i.e. from -0.85 to $-1.15 V_{SCE}$). This indicates an increase in H generation kinetics on the entry side of the steel sample at more negative cathodic E . On the exit side, i_{perm} also increases from 110 to $310 nA/cm^2$ correspondingly. However, after H charging on the entry side is halted (i.e. left unpolarized), i_{perm} does not decay to zero but only decreases to approximately $60 nA/cm^2$. Only when all the solution in the entry compartment is drained out and the sample is left exposed

to air does i_{perm} decay to zero. This indicates H entry in the sample continues to occur even at OCP.

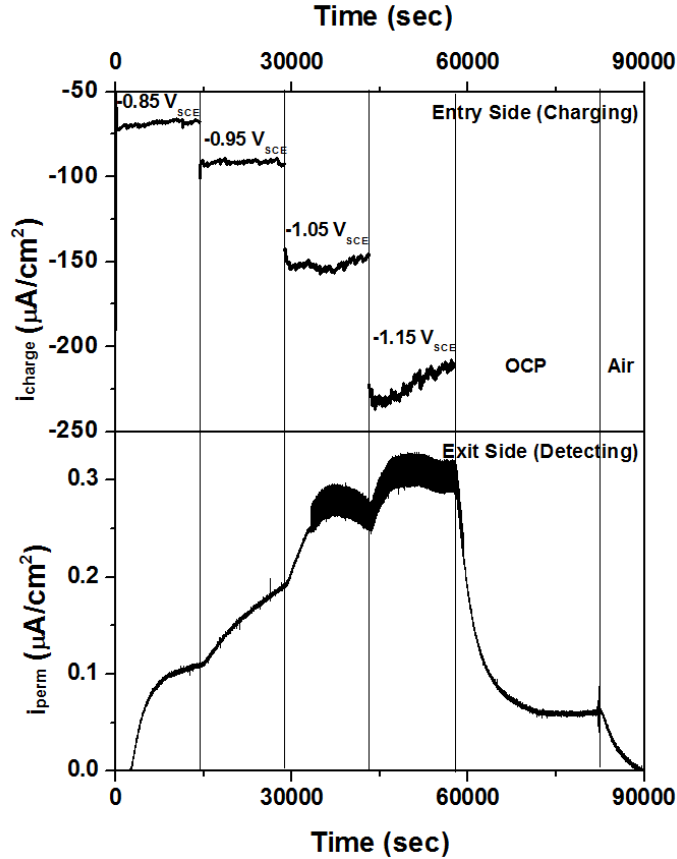


Figure 8-8: The current response at the H entry and exit sides during the permeation experiment in 100% CO₂ NS4 solution at 20 °C. The surface potential of the steel sample at the entry side is first switched from -0.85 to -1.15 V_{SCE} with 100 mV/step/4 h then is left at unpolarized (i.e. OCP) before the solution in the entry compartment is drained out to leave the sample open to air

8.4 Discussion of OCP, cathodic PDP, and permeation results

8.4.1 Hydration of CO₂ and [HCO₃⁻-CO₃²⁻] in CO₂-H₂O system

Gaseous CO₂ dissolves in water to form CO_{2(aq)} of {R-4.1} at a mole fraction solubility of $x_{CO_2(aq)} = 6.15 \times 10^{-4}$ at 25 °C [276], based on a Henry's constant for the $pCO_2/x_{CO_2(aq)}$ ratio of $1.63 \times 10^3 \frac{\text{atm} \cdot \text{mol}_{H_2O}}{\text{mol}_{CO_2(g)}}$ (see Table D-2 in Appendix D) [277], [278]. The dissolved CO₂ reacts with

water to form H_2CO_3 , which dissociates to form HCO_3^- as shown previously in {R-4.1} and {R-4.2}, respectively. HCO_3^- dissociates to form CO_3^{2-} according to {R-8.1} below:



The temperature dependence of the hydration constant of CO_2 forming H_2CO_3 in reaction {R-4.1}, K_0 , the ionization constant of H_2CO_3 forming HCO_3^- in {R-4.2}, K_1 , and the equilibrium constant of HCO_3^- forming CO_3^{2-} in {R-8.1}, K_2 , are expressed by [279]:

$$pK_0 = -\log K_0 = \frac{-2385.73}{T} - 0.0152642 \cdot T + 14.0184 \quad \{\mathbf{E-8.5}\}$$

$$pK_1 = -\log K_1 = \frac{3404.71}{T} + 0.032786 \cdot T - 14.8435 \quad \{\mathbf{E-8.6}\}$$

$$pK_2 = -\log K_2 = \frac{2902.39}{T} + 0.02379 \cdot T + 6.4980 \quad \{\mathbf{E-8.7}\}$$

The above equations are practically equivalent to the equations reported by other researchers [280], [281]. The equilibrium concentrations of CO_2 , H_2CO_3 , HCO_3^- , and CO_3^{2-} in the CO_2 - H_2O system could thus be fully determined from the pressure of CO_2 gas and the system temperature, with the latter defining the values of the necessary equilibrium constants listed above. As an example, the speciation diagram of the CO_2 - H_2O system at 25 °C calculated based on thermodynamics using Medusa[®] software is plotted in Figure 8-9. The diagram shows that $\text{pH} < 4$, H_2CO_3 is the dominant species. As the solution pH increases from 4 to 8, the fraction of H_2CO_3 to the combined concentrations of H_2CO_3 , HCO_3^- , and CO_3^{2-} decreases to approximately zero while the corresponding fraction of HCO_3^- increases and approaches a maximum at pH 8.35. At $\text{pH} < 8$ the concentration of CO_3^{2-} is several orders of magnitude less than either H_2CO_3 or HCO_3^- , hence its fraction to the overall sum of concentrations is practically zero. In more alkaline solutions, the fraction of HCO_3^- decreases and CO_3^{2-} gradually becomes dominant, with the concentration of both species equaling one another at around pH 10. It should be noted that although the concentration of HCO_3^- increases at pH levels more alkaline than 8.35, the fraction of HCO_3^- to the overall sum of concentrations decreases with further alkalinity since the

concentration of CO_3^{2-} increases at a faster rate, and the concentration of H_2CO_3 remains constant. This behavior is apparent in the concentration plots of Figure 8-10a to Figure 8-10c.

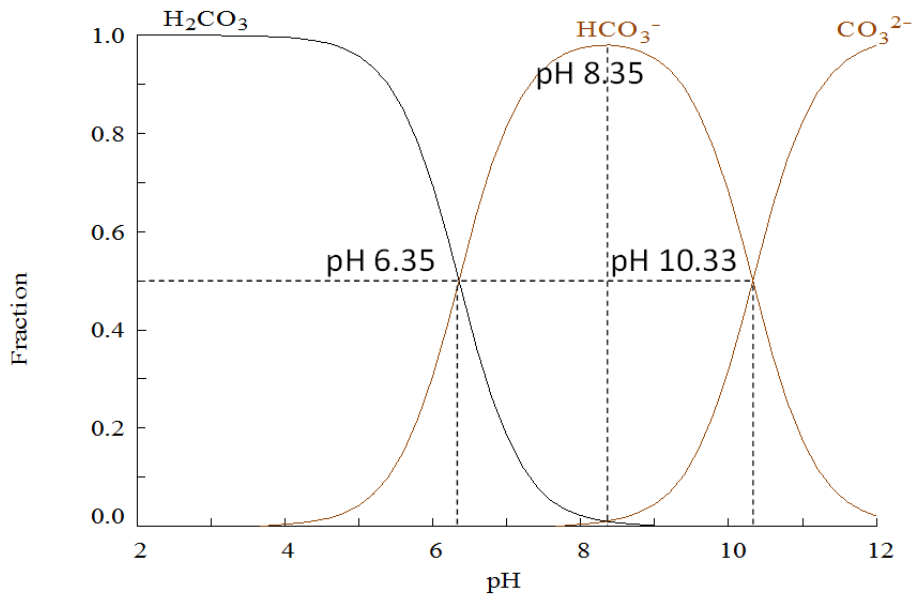


Figure 8-9: Speciation diagram of the CO_2 - H_2O system calculated at 25 °C using Medusa software

The concentration of each carbonate species in the solution at 20, 40, and 60 °C in a 1 atm (~100 kPa) CO_2 atmosphere determined from the aforementioned equilibria is shown in Figure 8-10. The concentration of H_2CO_3 and dissolved CO_2 are independent of pH, as expected due to the absence of H^+ in the dissolving of $\text{CO}_{2(\text{g})}$ and its hydration forming H_2CO_3 , {R-4.1}. Conversely, the concentrations of HCO_3^- and CO_3^{2-} increase as pH increases. It is important to note that this increase is in fact exponential, not linear, due to the log scale of the y-axis. In acidic and nn-pH conditions, dissolved CO_2 accounts for most of the total concentration of carbonate species whereas in alkaline solutions HCO_3^- and CO_3^{2-} are dominant. The concentration of H^+ is also plotted in the same graph for comparison. At low pH, $[\text{H}^+]$ is much higher than $[\text{HCO}_3^-]$ and $[\text{CO}_3^{2-}]$ but at nn-pH and higher, the later species are more abundant in the solution. Using these concentration plots, specifically Figure 8-10a at 20 °C, it becomes apparent for Figure 8-9 how the fractions of H_2CO_3 and HCO_3^- concentrations are equal at around pH 6. Likewise, it can be seen how the fractions of H_2CO_3 and CO_3^{2-} are equal at around pH 8, corresponding to the HCO_3^-

fraction being almost 1 due to $[\text{HCO}_3^-] \gg [\text{CO}_3^{2-}]$ and $[\text{HCO}_3^-] \gg [\text{H}_2\text{CO}_3]$. Finally, the fractions of HCO_3^- and CO_3^{2-} are equal at around pH 10, and since the concentration of either specie is much larger than $[\text{H}_2\text{CO}_3]$ at that pH, the fraction of H_2CO_3 is negligible there. To illustrate these relationships numerically, the concentrations of H_2CO_3 , HCO_3^- , and CO_3^{2-} are extracted from Figure 8-10a at four pH values: 4, 6.3, 8.3, and 10.3. Then, the fraction of each specie at each pH is calculated through the division of the concentration of that respective specie by the total sum of $[\text{H}_2\text{CO}_3]$, $[\text{HCO}_3^-]$, and $[\text{CO}_3^{2-}]$. The results are shown in Table 8-1 below, with the fractions matrix being numerically consistent with the graphical speciation in Figure 8-9.

Table 8-1: Approximate concentrations and % fractions of H_2CO_3 , HCO_3^- , and CO_3^{2-} in the CO_2 - H_2O system for a temperature of 20 °C and 1 atm CO_2

pH	Concentration [M]				Fraction			
	H_2CO_3	HCO_3^-	CO_3^{2-}	Total	H_2CO_3	HCO_3^-	CO_3^{2-}	Total
4	1×10^{-6}	5×10^{-9}	2×10^{-15}	1×10^{-6}	99.5%	0.5%	0.0%	100.0%
6.3	1×10^{-6}	1×10^{-6}	5×10^{-11}	2×10^{-6}	50.0%	50.0%	0.0%	
8.3	1×10^{-6}	1×10^{-4}	1×10^{-6}	1×10^{-4}	1.0%	98.0%	1.0%	
10.3	1×10^{-6}	4×10^{-3}	4×10^{-3}	8×10^{-3}	0.0%	50.0%	50.0%	

In addition to the pressure of CO_2 , the temperature of the CO_2 - H_2O system determines the equilibrium concentrations of the carbonate species. This mainly is due to the temperature dependent solubility of CO_2 ; when temperature increases, the solubility of CO_2 in aqueous solutions decreases significantly. For instance the mole fractions of CO_2 in the solution at 20, 40, and 60 °C in a 100 kPa CO_2 atmosphere are 0.70, 0.43, and 0.30, respectively [276]. Meanwhile pK_1 and pK_2 only slightly decrease and pK_0 slightly increases as the temperature increases. Overall, these changes result in a shift of all concentration distributions vs. pH to lower concentration as temperature increases (Figure 8-10). This means that the concentrations of H_2CO_3 and carbonate species in higher temperature solutions are lower than those in lower temperature solutions at the same pH. As seen in the next sections, the concentrations of H_2CO_3 and carbonate species in solution play a crucial role in the kinetics of HER.

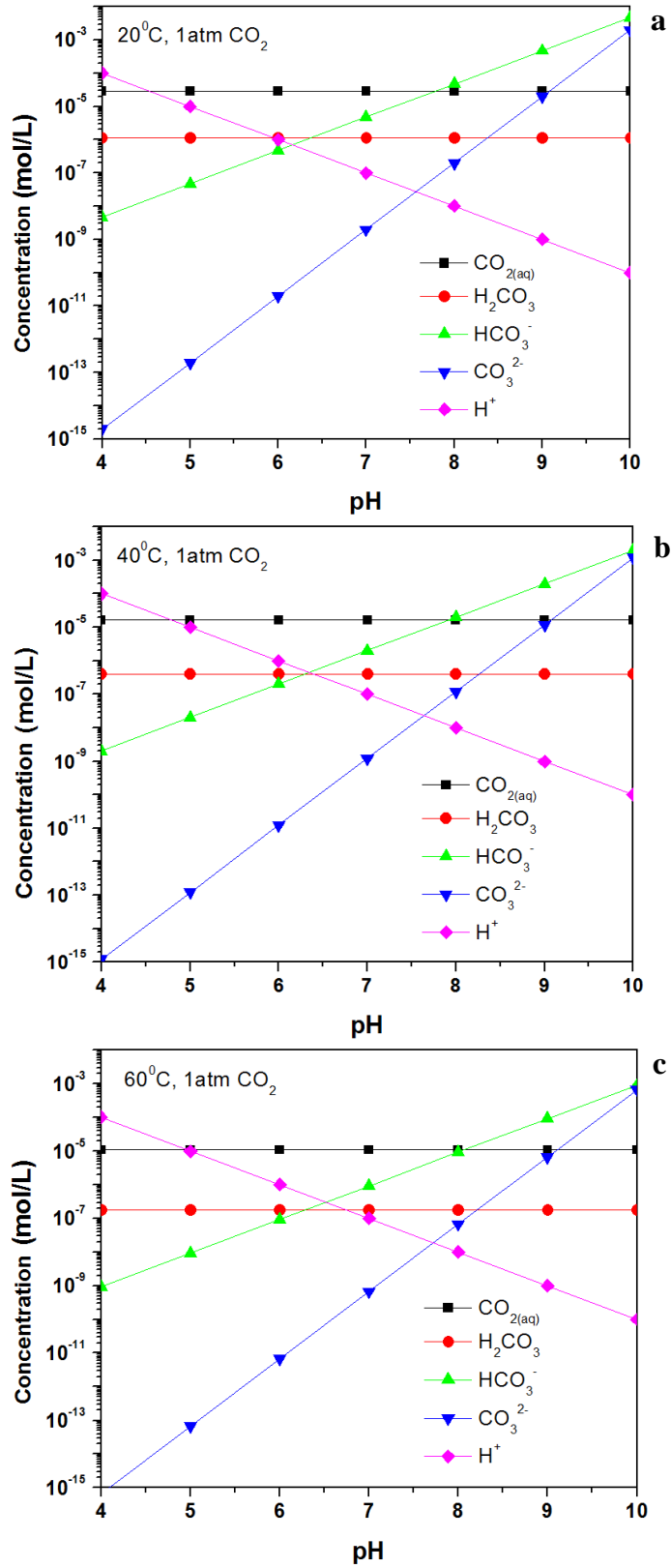


Figure 8-10: Concentration of dissolved CO₂ and carbonate species in solution with respect to pH, with pCO₂ = 1 atm at: (a) 20 °C; (b) 40 °C; and (c) 60 °C

8.4.2 HER on X100 at OCP and cathodic potentials

In acidic CO_3^{2-} -free and O_2 -free solutions, H^+ reduction shown earlier in {R-5.2} is the dominant cathodic reaction, with an E_{eq} at 20 °C expressed by [124]:

$$E_1 = -241 - 58pH \text{ (mV}_{SCE}) \quad \{\mathbf{E-8.8}\}$$

At higher pHs, H evolution by direct reduction of water, as shown previously in {R-5.4}, becomes more important as the concentration of H^+ is negligible compared to the concentration of OH^- [124], [268]. The E_{eq} of this reaction at 20 °C is expressed by [124], [268]:

$$E_2 = -58pH \text{ (mV}_{SCE}) \quad \{\mathbf{E-8.9}\}$$

In solutions containing dissolved CO_2 and HCO_3^- , additional cathodic reactions might occur by the direct discharge of these species according to {R-8.2} below and {R-5.3} from chapter 5 (reproduced here as {R-8.3}) [36], [64], [100], [268], [282]:



The E_{eq} corresponding respectively to {R-8.2} and {R-8.3}:

$$E_3 = -622 - 58 \log \frac{[\text{HCO}_3^-]}{[\text{H}_2\text{CO}_3]} \text{ (mV}_{SCE}) \quad \{\mathbf{E-8.10}\}$$

$$E_4 = -856 - 29 \log \frac{[\text{CO}_3^{2-}]}{[\text{HCO}_3^-]} \text{ (mV}_{SCE}) \quad \{\mathbf{E-8.11}\}$$

Combining {E-8.5}, {E-8.6}, {E-8.10}, and {E-8.11} gives the E_{eq} at 20 °C:

$$E_3 = -251 - 58pH \text{ (mV}_{SCE}) \quad \{\mathbf{E-8.12}\}$$

$$E_4 = -555 - 29pH \text{ (mV}_{SCE}) \quad \{\mathbf{E-8.13}\}$$

Figure 8-11 illustrates the OCP values of API X100 steel in NS4 and modified NS4 solutions with respect to pH, under different purging gas atmospheres at 20 °C. The E_{eq} for HER are superimposed onto the plot. Figure 8-11 indicates that H evolution is feasible even in aerated solutions at the OCP or free corrosion condition because the E_{eq} of direct water reduction, {R-

5.4}, is more positive than the OCPs of the steel. It is consistent with the result of the H permeation experiment which shows a H flux at OCP (Figure 8-8). In O₂-free (100% N₂) solutions, in addition to the direct water reduction, H⁺ reduction through {R-5.2} may also occur at the freely corroding surface. However, because the pH of the O₂-free (100% N₂) solution is 8.8, the [H⁺] is low and so is the kinetics of H⁺ reduction. Therefore, the direct water reduction reaction is the dominant cathodic reaction in this condition. In O₂-free (5% and 100% CO₂) solutions, H₂CO₃ discharge through {R-8.2} is possible over the whole pH range while the discharge of HCO₃⁻ is only possible in solutions with pH below 5.4. However at this low pH, the concentration of HCO₃⁻ is negligible as indicated in the speciation diagram and the carbonate species concentration plot (Figure 8-9 and Figure 8-10, respectively). Therefore H evolution due to HCO₃⁻ discharge in NS4 solution at OCP is unlikely.

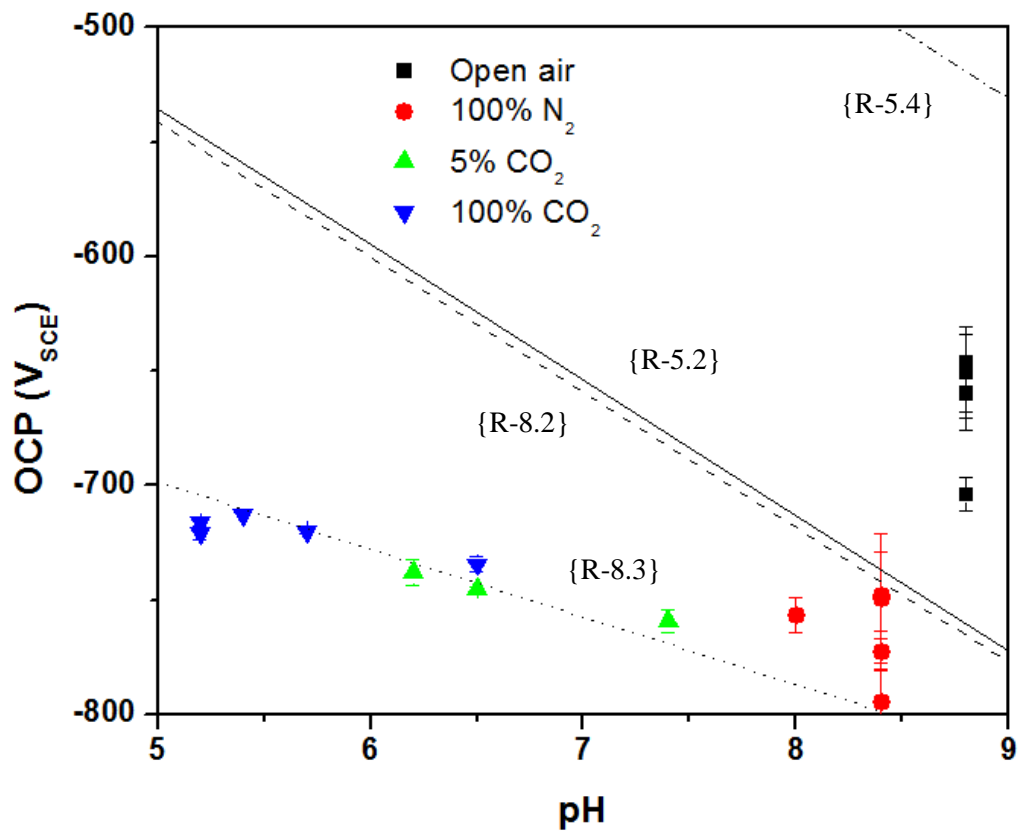


Figure 8-11: OCP of X100 steel in NS4 and modified NS4 solutions under different purging gas atmospheres at 20 °C

It is noticed that adding HCO_3^- to the solution significantly reduces the OCP of the steel, particularly in open air and deaerated (100% N_2) NS4 solutions (Figure 8-1). This is mainly due to the increase in the anodic dissolution kinetics in more concentrated HCO_3^- environments as can be seen from the shift of the anodic polarization curves towards higher i in the figures of previous chapters. Another reason for the OCP decrease in HCO_3^- -added solutions is the lower $[\text{H}^+]$ in these solutions as a result of the buffering effect of HCO_3^- . Solution pH increases by almost a full unit when NaHCO_3 is added to the NS4 solution, as shown in Table D-1. In practice, for a buried pipeline application the E of the pipe surface is affected by CP and might be polarized to much more negative values. In this case, all four HERs will be possible, but each of them will have a different contribution to the overall kinetics of the cathodic process.

During cathodic polarization in the results shown above, E is swept from OCP to $-1.2 V_{\text{SCE}}$, which makes all four cathodic reactions in {R-5.2}, {R-5.4}, {R-8.2}, and {R-8.3} possible. In O_2 -free (100% N_2) NS4 solution (Figure 8-2a), the cathodic polarization curve exhibits a Tafel slope of 120 mV/decade. As discussed earlier, H^+ discharge is not significant in this solution due to its alkalinity (pH 8.8). Therefore, this Tafel behavior is attributed mainly to the HER of direct water reduction, {R-5.4}. Similar Tafel slopes for the cathodic polarization curve of steel in HCO_3^- - CO_3^{2-} solutions have been observed by other researchers [268]. In open air solutions (Figure 8-2b), the acceleration of cathodic kinetics near the OCP is attributed to the reduction reactions of dissolved O_2 in the open air solutions. Here, the Tafel behavior at the more negative potential range, which overlaps with the polarization curve in deaerated (100% N_2) conditions, is again attributed to the HER of direct water reduction. In O_2 -free, 100% CO_2 solution (Figure D-1 in Appendix D), the increase in the cathodic process observed could be attributed to the HER of H_2CO_3 and HCO_3^- discharge ({R-8.2} and {R-8.3}, respectively).

The effect of pH on the cathodic polarization provides some interesting insight into the nature of the cathodic reactions in the potential range from OCP to $-1.2 V_{\text{SCE}}$. Cathodic kinetics in

all solutions is suppressed when the pH of the solution decreases from 8.4 to 5.7 given the same purging gas is used (Figure 8-4b). The effect is particularly pronounced when the pH of NaHCO₃-added solution is adjusted from 8.4 to 5.7 (Figure D-2b). The cathodic polarization curve in the NaHCO₃-added solution after the pH is adjusted is similar to the polarization curve in HCO₃⁻-free solution. This indicates that the additional HER reactions in CO₃²⁻-containing solutions are suppressed by decreasing the pH. Because the [H₂CO₃] is independent of pH (Figure 8-10), the suppression of the HER reaction when pH decreases from 8.4 to 5.7 is attributed to the decrease in the [HCO₃⁻] in the solution. This suggests the HER due to HCO₃⁻ discharge, {R-8.3}, is probably the dominant cathodic reaction over the discharge of H₂CO₃, {R-8.2}, in the OCP > E > -1.2 V_{SCE} range, so a change in the [HCO₃⁻] due to pH directly affects the cathodic kinetics.

The shift of the cathodic polarization curve to higher i_c when the temperature increases from 20 to 60 °C (Figure 8-4a) indicates a strong temperature dependence of the HER kinetics on X100 steel. It is shown in Figure 8-10 that the solubility of CO₂ in aqueous solution decreases when the temperature increases. As a result, the concentration of H₂CO₃ and carbonate species also decreases when the temperature increases. Therefore, the temperature dependence of the HER kinetics cannot be explained based on the reduction/discharge reactions of carbonate species. This points to the role of the H⁺ reduction reaction which is facilitated by lower pH as the result of increased temperature. It is noted that the pH of the solution decreases from 6.5 to 5.1 in 100% CO₂ NaHCO₃-added NS4 solution and from 5.7 to 4.7 in 100% CO₂ NS4 solution when temperature increases from 20 to 60 °C. It is the increase in the [H⁺] that causes the increase in the HER kinetics observed in Figure 8-4a. In addition, Figure 8-10 also shows that in the pH range between 5.7 and 4.7, H⁺ is dominant over HCO₃⁻.

The role of CO₂ in the cathodic process is demonstrated in the gas switching experiments as well as in the PDP experiments. It is clearly shown that i_c significantly increases as the purging gas atmosphere is switched from 100% N₂ to 5% CO₂ to 100% CO₂ (Figure 8-3b and Figure 8-7).

This is in agreement with studies of CO₂ corrosion of pipeline steels which conclude that corrosion of steels is accelerated in the presence of CO₂ [64], [100], [268]. Also, the role of calcareous deposits on the H evolution kinetics on steels can be seen when comparing the cathodic polarization of a freshly-polished sample and samples after cathodic holding at -1.2 V_{SCE} (Figure 8-12). The cause of the shift to lower i_c in the cathodic polarization curve of samples after cathodic PSP appears to be due to the deposition of a CO₃²⁻ scale on the sample surface, which results in the inhibition of the cathodic reactions. Such scale is confirmed to be present in SEM images shown in Figure 8-5. The deposition of a CaCO₃ layer might block the cathodic reaction sites and therefore reduce the HER kinetics.

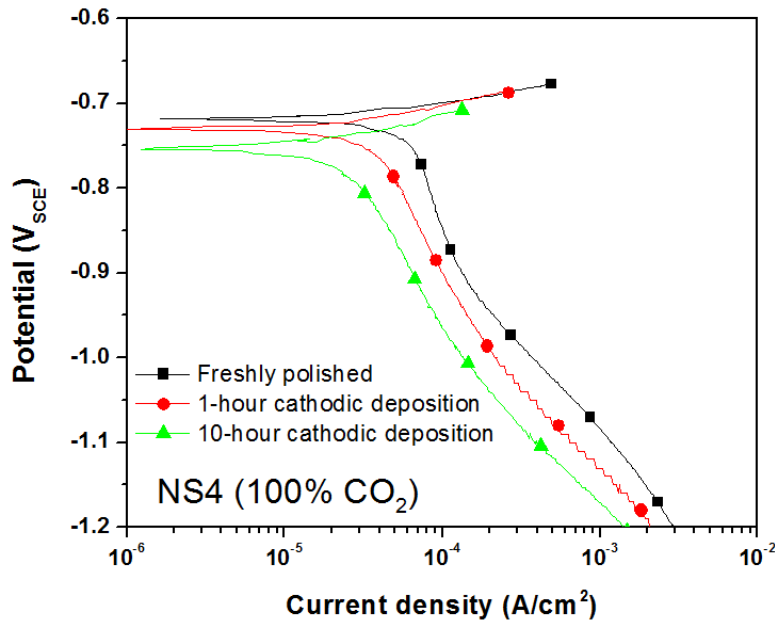


Figure 8-12: Cathodic polarization curves of scale-covered X100 steel in NS4 solution at 20 °C

8.4.3 Hydrogen permeation in X100 exposed to nn-pH HCO₃⁻ solutions

From the permeation experiments, D_{eff} in the X100 steel is determined to be $4.4 \times 10^{-7} \pm 4 \times 10^{-8}$ cm²/s (Figure 8-6a and Figure 8-6b). This value is comparable to the H diffusivity normally measured in pipeline steels of difference grades [104], [161], [261], [262], [283], [284]. The amount of H absorbed in X100 steel at OCP in 100% CO₂ NS4 solution can be quantified from i_{ss} using {E-8.14} which is derived from {E-8.2}:

$$C_s = \frac{i_{ss}L}{nFD_{eff}} \quad \{\mathbf{E-8.14}\}$$

Using the average value of D_{eff} calculated from the range mentioned above, the sample thickness of 1 mm, and $i_{ss} = 60 \text{ nA/cm}^2$ determined from Figure 8-8, the diffusible hydrogen concentration in X100 steel exposed to 100% CO_2 NS4 solution in the freely corroding condition is $1.4 \times 10^{-7} \text{ mol/cm}^3$ or 1 atomic ppm (appm).

Table 8-2: Summary of steady state permeation current densities and diffusible hydrogen concentrations in the X100 steel exposed to the NS4 solution under different charging conditions

Charging condition	i_{ss} ($\mu\text{A/cm}^2$)	C_s (mol/cm^3)	C_s (appm)
-0.9V _{SCE} , 100% N ₂	0.03	7.0×10^{-8}	0.5
-0.9 V _{SCE} , 95% N ₂	0.05	1.17×10^{-7}	1.3
-0.9 V _{SCE} , 100% CO ₂	0.1	2.33×10^{-7}	1.7
OCP, 100% CO ₂	0.06	1.4×10^{-7}	1
-0.85 V _{SCE} , 100% CO ₂	0.11	2.57×10^{-7}	1.8
-0.95 V _{SCE} , 100% CO ₂	0.19	4.43×10^{-7}	3.2
-1.05 V _{SCE} , 100% CO ₂	0.25	5.83×10^{-7}	4.2
-1.15 V _{SCE} , 100% CO ₂	0.29	6.44×10^{-7}	4.8

The values for diffusible hydrogen concentration in X100 steel exposed to NS4 solution at different applied cathodic E and under different purging gas atmospheres are calculated in the same way. A summary of the resulting diffusible hydrogen concentrations is presented in Table 8-2. As the purging gas is switched from 100% N₂ to 5% CO₂ to 100% CO₂, the diffusible H concentrations change from 7×10^{-8} to 1.2×10^{-7} to $2.3 \times 10^{-7} \text{ mol/cm}^3$ (or 0.5, 0.8, and 1.7 appm), respectively. Certainly the increase in the diffusible H concentration in the steel is associated with an increase in the kinetics of the HER at the charging side of the sample when the purging is switched from N₂ to CO₂. This again confirms the role of dissolved CO₂ in facilitating the ingress of H in steels exposed to the nn-pH HCO₃⁻ environments. The concentration of diffusible H also increases from 2.6×10^{-7} to $6.8 \times 10^{-7} \text{ mol/cm}^3$ (1.8 to 4.8 appm) as the applied cathodic E is augmented from -0.85 to -1.15 V_{SCE}.

Hydrogen in steel could reduce the threshold stress intensity and therefore cause cracking in materials. The dependence of the threshold stress intensity (K_{th}) on H concentration is described by {E-2.2} (reproduced as {E-8.15} below), with the parameters given earlier in section 2.3 [70]:

$$K_{th} = \frac{1}{\beta'} \exp \left[\frac{(k_{IG} - \alpha C_{H\sigma,T})}{\alpha^n \sigma_{YS}} \right] \quad \{\mathbf{E-8.15}\}$$

$$C_{H\sigma,T} = C_s \exp \left[\frac{\sigma_{HVH}}{RT} \right] \quad \{\mathbf{E-8.16}\}$$

The H concentration at the crack tip ($C_{H\sigma,T}$) is proportional to the diffusible hydrogen concentration (C_s) in the material through {E-8.16} (see section 2.3 again for parameter descriptions). Based on this relationship, an increase in the diffusible H concentration in the steel reduces K_{th} and hence the toughness of the material (i.e. resistance to fracture). The H concentrations in X100 steel exposed to nn-pH HCO_3^- environments here are relatively low compared to the diffusible H concentration in pipeline steels exposed to environments containing sulfide (S^{2-}) [161], [285]–[287]. This is because S^{2-} -containing environments are known to promote H ingress into steels due to the poisoning effect of S^{2-} on the H combination reaction. However, such low diffusible H concentrations in the nn-pH HCO_3^- environments shown here can still affect material toughness and cause HE and HIC issues in pipeline steels [19], [93]–[96], [264], [288].

8.5 Summary

In this chapter, the H generation kinetics on HSLA X100 steel in nn-pH HCO_3^- solutions simulating external pipeline corrosion environments are studied. Dissolved CO_2 in the solution accelerates H evolution kinetics through the H_2CO_3 discharge and HCO_3^- discharge reactions. At OCP, H evolution due to direct water reduction is the dominant reaction in O_2 -free and CO_3^{2-} -free solutions; however, the H_2CO_3 discharge becomes the dominant reaction in solutions with

dissolved CO_2 . At $E < \text{OCP}$, H evolution due to HCO_3^- discharge is proven to be thermodynamically inevitable and gradually dominates the other reactions occurring at the OCP.

Through permeation tests in a H permeation setup and subsequent analysis of permeation currents, the H diffusivity in X100 steel is found to be approximately $4.4 \times 10^{-7} \text{ cm}^2/\text{s}$. The concentration of diffusible H in X100 exposed to external nn-pH HCO_3^- environments is hence relatively low compared to that in S^{2-} -containing environments. However, a measurable amount of diffusible hydrogen of approximately 1 appm is detected in the steel at the freely corroding condition. This H concentration in the steel increases at more negative applied E which could arise from CP of buried pipeline infrastructure. The H concentration also increases with higher CO_2 partial pressure in the local electrolyte environment. The evidence shown in this chapter therefore supports the proposed role of H (through H embrittlement) in the transgranular SCC mechanism of pipeline steels exposed to dilute HCO_3^- environments of nn-pH.

9. FEM of the external corrosion and structural integrity of buried pipelines under the influences of CP, gas diffusion, and environment physicochemistry⁷

Strategies which mitigate the external corrosion of underground pipelines revolve around two methods: CP and protective coatings [35], [122]. Chemical degradation of pipeline steels at coating failure sites is lessened by CP systems, in which performance is heavily affected by physicochemical soil properties. As summarized in various sections of the literature review presented earlier, spatial- and time-dependent soil corrosivity is related to numerous physicochemical properties including: position of water table, soil moisture content, soil type, soil resistivity, soil pH, soluble salt content, structure-to-soil potential, redox potential, microbes in the soil, and stray currents [123]. Complexities arise from the interdependence of electrical resistivity, O₂ diffusivity, or heat transfer on one or more soil properties such as particle distribution, porosity, moisture, and temperature [289].

Simplification of complex soil parameter interdependencies is often done when developing empirical correlations of soil corrosivity. Merely soil's electrical resistivity is considered by some to be a sufficient predictor of corrosivity [126], whilst others consider soil type and structure as the determining factors regardless of position with respect to the water table [127]. Simply the wt% moisture content of the soil is also deemed sufficient in determining the aggressiveness category of soils [126]. Such empirical guidelines unduly simplify gas transport, heat transfer, and reaction kinetics phenomena (and complex interdependencies therein), making them generally inadequate for detailed evaluations. Instead, numerical simulations can capture a larger spectrum of the fundamental processes occurring on corroding pipelines and better predict perilous operating parameters and critical corrosion locations on exposed surfaces.

⁷ **I. M. Gadala**, M. Abdel Wahab, and A. Alfantazi, *Materials and Design*, vol. 97, pp. 287–299, May 2016.

Finite element modelling has been used to compare the relative influence of coating quality, soil electrical conductivity, and CP anode size, position, and type on the corrosion of buried steel tanks [125]. By incorporating the influence of diffusion-controlled O₂ reduction with electrolyte conductivity, the distribution of electrical potential within the electrolyte can be computed [129]. Yet, spatial- and time-dependent differences in electrolyte properties are normally not accounted for in previous reports. Similarly, available numerical models of CP and corrosion systems often make narrow use of experimental diffusivity measurements. Rather, the rate of transport is determined with empirical parameters [130], [138]. Seldom do models present coupled gas transport and electrolyte potential distribution like in [140] or variable gas diffusivity in bulk porous media like in [141]. In porous soil, tortuous mass-transfer obeys multi-phase flow laws which depend on air-filled void porosity, moisture content, and temperature. These parameters are interrelated and depend on other conditions such as soil type and structure, for both O₂ and CP.

The macro meter-scaled model (m-model) presented in this chapter uniquely simulates the variable diffusivity of O₂ within soil based on established soil science models. For CP, the Nernst-Planck formulation relies on concentrations, diffusivities, and electric mobilities of ionic species within the soil. This method is simplified to a governing equation with a single soil conductivity parameter (spatially variable, based on experimental measurements) due to difficulties in quantifying Nernst-Planck variables for irregular soils [125], [129], [130], [138], [140], [141]. The conductivity is adjusted for the temperature and moisture content of the soil in each simulation of the m-model, or simply the temperature of the trapped water in the millimeter-scaled model (mm-model) presented in the second part of this chapter.

Reaction kinetics at electrode-electrolyte interfaces are vital in any corrosion model. Formerly, problems in obtaining reliable kinetic parameters have led to a wide range of values being used. Difficulties in obtaining accurate tabulated kinetic parameters to simulate corrosion rates at electrode-electrolyte interfaces are often overcome by instead extracting them from

dedicated laboratory experiments simulating the system [138][33]. Muehlenkamp et al. [33] reported using parameter values for their modelled system from measurements. In almost all such previous works though, a prescribed number of parameter values are extracted from the experimental results based on the type of formulation intended to govern reaction kinetics. Incongruities between the kinetics model and the actual experimental data are inevitable. In the models presented in this chapter, such discrepancies are eliminated by integrating the full spectrum temperature-controlled polarization results into the governing equations. Critical temperature influences on corrosion behavior, shown in earlier chapters of this thesis, are carried through from the first step heat transfer simulations in the present chapter. This feature of the models presented here enables more accurate predictions of CP effectiveness and material corrosion in practical operating temperature ranges.

The objective of the m-scale model developed in the first part of this chapter is to allow for the study of synergistic interactions between heat transfer, CP, O₂ diffusion, and corrosion of buried pipelines. This helps elucidate the strong implications of physiochemical soil parameters on CP, corrosion, and pipeline system design. The objective of the mm-scale model in the second part of this chapter is to simulate transient corrosion defect growth in X100 pipeline steel exposed to nn-pH trapped water under disbonded external coatings, and the resulting diminishment of the pipeline's structural integrity. To date, this latter time-dependent corrosion model is the first to specifically simulate defect growth in trapped water relevant to the nn-pH SCC phenomena of buried pipeline applications. Both models are intended for simulations of buried high-pressure gas transmission pipelines, and present opportunities for rapid scalability to different system dimensions or adjustment for different pipeline applications. Furthermore, they can be integrated into a single multi-scale model with additional work. This chapter is based on a paper [290] which was published as part of the research work leading towards this PhD thesis.

9.1 Modelling details: governing phenomena and equations

Comsol Multiphysics® version 4.3a, in which the established FEM is the numerical technique employed, is the modelling software used in all the simulations of this chapter. The visual representations of both models and the associated geometries have been detailed earlier in section 4.3. The mesh parameters of the m-model were given in Table 4-2 on page 53, whereas the mesh parameters of the mm-model can be found in Table E-1 of Appendix E.

9.1.1 Heat transfer, CP, and O₂ diffusion phenomena

The m-scale model of this chapter includes heat transfer, CP, and O₂ diffusion modules. Conversely, the mm-scale model does not simulate heat transfer since the small disbondment region is considered to be uniform at the temperature of the pipeline. Significant O₂ diffusion within the disbondment is disregarded and only deaerated (standard 5% CO₂ and nonstandard 0% CO₂) environments are simulated. Sand, clay, and peat soil structures are simulated in the m-scale model of this chapter, at moisture contents (herein termed volumetric wetness, ψ) ranging from 0.1 to 0.6 depending on air porosity ratios (ϕ). The ψ of a soil is 0 if it contains absolutely no water (i.e. completely dry) and cannot be 1 unless the media is completely liquid phase. The latter case would constitute a different modelling situation, simulating phenomena related to submerged or underwater structures (not addressed here). Likewise, the ϕ of the soil is 1 if it contains absolutely no air pockets/pores and cannot be 0 unless the media is completely gas phase. These boundary values for both ψ and ϕ are not addressed in this work.

Table 9-1a: Governing transport equations in each module of the m-model [290]

Module	Number	Equation	Condition
Heat transfer	{E-9.1}	$C_v \partial T / \partial t = \nabla(\lambda \nabla T) + Q$	\
CP	{E-9.2}	$i_l = -\sigma_i \nabla \phi_i$	$\nabla \cdot i_l = Q_l = 0$
O ₂ diffusion	{E-9.4}	$\nabla \cdot (-D_{O_2} \nabla c_{O_2}) = R_{O_2}$	\

1a. Heat transfer: The thermal parameters studied in the m-model are listed in Table E-2 in Appendix E [291] and have been experimentally validated in the work of Abu-Hamdeh and Reeder [131]. The governing equation for heat flow in the soil ({E-9.1}, Table 9-1a) is a function

of thermal conductivity (λ) and the volumetric heat capacity (C_v), where T is temperature in °C, t is time in s, ∇ is the gradient in the 2D spatial domain (i.e. $\frac{\partial}{\partial x}$ and $\frac{\partial}{\partial y}$), and Q is a constant heat flux density in W/m² (for the 2D case) in the presence of heat sources or sinks. Air's contribution to C_v can generally be neglected since $C_{air} = 0.0012 \ll C_{water} = 4.18 \text{ MJ/m}^3\text{K}$ [292].

Table 9-2b: Values or expressions for the thermal, electrical, and diffusion properties of the soil media in the m-model [290]

Module	Number	Material property values/equations
Heat transfer	/	See Table E-2 in Appendix E for λ and C_v values
CP	{E-9.3}	$\sigma_i = \sigma_{298K}(1 + 0.02(T_i - 298)) \cdot \psi$
O ₂ diffusion	{E-9.5a}	$D_{O2_sand} = D_{O2_T} \cdot (\phi - \psi)^{5/3}$
	{E-9.5b}	$D_{O2_clay} = D_{O2_T} \cdot (\phi - \psi)^{2.51} \cdot \phi^{-2}$
	{E-9.5c}	$D_{O2_peat} = 0.66 D_{O2_T} \cdot (\phi - \psi) \cdot [(\phi - \psi) / \phi]^2$

1b. CP: In both the m-model and the mm-model, a single electrical conductivity (σ) parameter simulates the complex process of ionic transport within the electrolyte. In the m-model, the electric field between the CP anode and the exposed pipeline surface drives the transport of dissolved ions in the soil moisture (liquid phase). The gradient of the potential (ϕ) multiplied by σ at a point in the soil domain yields the current density vector \mathbf{i}_l at that point ({E-9.2} in Table 9-1a and identical {E-E.2} in Table E-3 in Appendix E). Upon reaching the steady state of the simulations in the m-model, the charge flux (Q_l) in the soil should equal zero. On the other hand, the mm-model simulations and analyses are transient, hence the Q_l in the trapped water electrolyte therein is consistently non-zero. In both models the influence of temperature on σ [137] is simulated with an experimentally validated 2% per degree Kelvin linear compensation ({E-9.3} in Table 9-1b). A nominal σ value at 298 K (25 °C) has been experimentally measured for the representative NS4 simulated soil solution ($\sigma_{298K} = 0.11 \text{ S m}^{-1}$) using a calibrated Jenway® 4510 benchtop conductivity meter, as mentioned earlier in this thesis.

1c. O₂ diffusion: In the m-model, O₂ diffusion occurs due to the gradient in the soil O₂ concentration (C_{O2}), denoted ∇C_{O2} , between the ground-atmosphere interface and deeper soil coordinates. Depletion mainly occurs due to O₂ reduction at the exposed pipeline surface. Charge

neutrality of the molecular O₂ nullifies migration effects due to $\nabla\phi$. In {E-9.4} shown in Table 9-1a, D_{O_2} is the effective O₂ diffusivity and R_{O_2} is a flux term accounting for systematic O₂ depletion from reduction at the exposed pipeline surface, the kinetics of which is defined in section 9.1.3 below. D_{O_2} is dependent on temperature, ϕ , ψ , tortuosity, capillary effects, and other factors within the soil. A nominal O₂ diffusivity parameter at a reference temperature of 298 K ($D_{O_2,0} = 1 \times 10^{-6} \text{ m}^2/\text{s}$ [293]) is adjusted for the actual soil temperature based on the heat transfer module solution through $D_{O_2,T} = D_{O_2,0} \cdot (T/T_{ref})^{1.5}$, then is used to evaluate the actual effective diffusivity through empirical correlations derived by soil researchers: Lai et al. for sand in {E-9.5a} of Table 9-1b, Xu et al. for clay in {E-9.5b}, and Moldrup et al. for peat in {E-9.5c}. These correlations capture complex ϕ , ψ , tortuosity, and capillary effects on the diffusion, and have been experimentally validated in dedicated works such as [134].

9.1.2 Initial conditions and boundary conditions for governing phenomena

2a. Heat transfer: In the m-scale model of this chapter, λ and C_v of the soil are considered to be homogenous and depth-independent. Natural annual periodicity in atmospheric conditions changes the soil's thermal regime. Ground surface temperatures of 303 K (30 °C, maximum) in the summer and 263 K (-10 °C, minimum) in the winter are imposed, while the pipeline wall temperature (T_{wall}) fluctuates between 323 K (50 °C) and 303 K (30 °C) inclusive during both those seasons, respectively. Initial soil temperature profiles of the complete 2D model section (Figure 9-1) are evaluated using {E-9.6} below [292], where z is depth below surface in m, t is ratio of annual cycle ($0 \leq t \leq 1$), \bar{T} is average annual temperature in K, A_0 is amplitude of the annual temperature cycle in K, d is the characteristic annual damping depth in m ($d = \sqrt{365\lambda/\pi C_v}$), and ω is angular frequency in 1/s. To solve for induced temperature profiles, side boundaries are set to the boundary condition described by {E-9.7a}.

$$T(z, t) = \bar{T} + A_0 e^{-\frac{z}{d}} \sin \left[\omega(t - 8) - \frac{z}{d} \right] \quad 0 \leq z \leq d \quad \{\mathbf{E-9.6}\}$$

$$-\nabla T \cdot \vec{n} = 0 \quad \text{where } \vec{n} \text{ is a unit vector normal to the surface} \quad \{\mathbf{E-9.7a}\}$$

$$-\sigma_i \nabla \phi_i \cdot \vec{n} = 0 \quad \{\mathbf{E-9.7b}\}$$

$$-D_{O_2} \nabla c_{O_2} \cdot \vec{n} = 0 \quad \{\mathbf{E-9.7c}\}$$

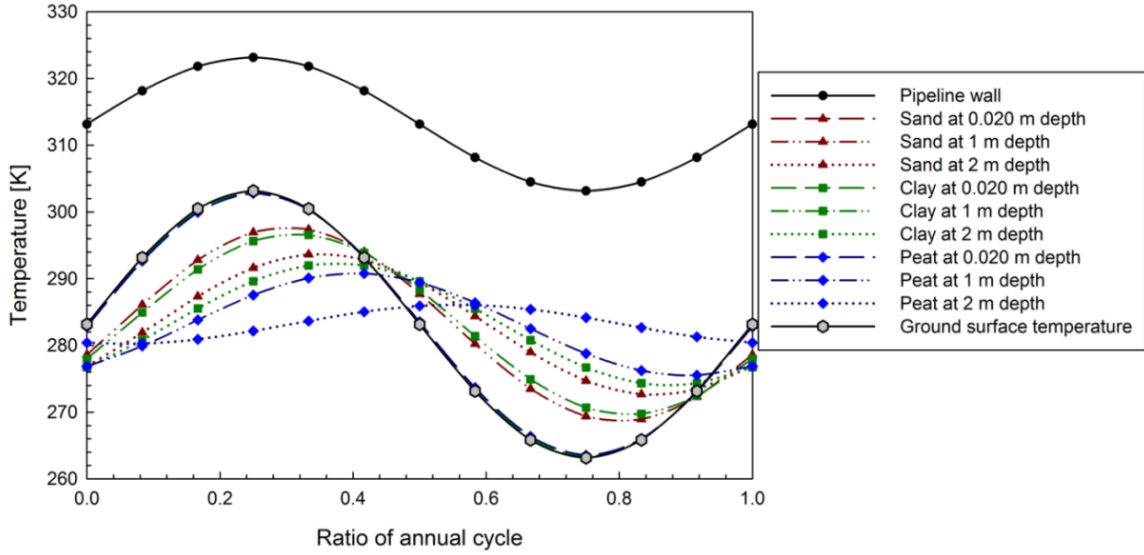


Figure 9-1: Pipeline wall and initial (ambient) soil temperature fluctuations with respect to soil structure, depth, and time in m-model

2b. CP: In the CP module of the m-model, initial potentials are imposed onto the boundary of the CP anode (represented as E_{anode}) and the pipeline electrode (represented as E_{app}) in Figure 4-4b presented in section 4.3 above. It is assumed that: (1) the CP anode has negligible resistivity; (2) the anode-soil interface has a constant interfacial $\Delta\phi$ due to very fast kinetics; and (3) aging effects such as deposition of corrosion products on the anode are insignificant. E_{app} is the potential applied between the pipeline and the CP anode, with the anode treated as ground. This is set to -1 V for the majority of simulations, yet -0.75 V and -1.25 V are also simulated. E_{anode} for all simulations is set to -2.37 V_{SCE} [124], a parameter which could be easily modified to evaluate the performance of specific anode materials such as ferrosilicon. Boundaries which are neither the CP anode nor the exposed surface are set to the electrically insulated boundary condition of {E-9.7b}, with complete insulation assumed.

Initial conditions in the mm-model of the disbondment region are imposed to simulate the three CP region situation shown to exist under coating disbondments [26], [27], [294]: (1) CP

potential sufficient region at the opening, (2) CP potential insufficient region in the middle, and (3) CP potential absent region at the leading edge. The potential applied to the pipeline is again denoted as E_{app} , considered constant based on an uninterrupted CP power supply, and set to either -1 V or -0.75 V to investigate the impact of applied CP voltages. The coated and detached coating boundaries of Figure 4-5 are set to the electrically insulated boundary condition of {E-9.7b}, also assuming perfect insulation from charge/ion transport. Conversely, the exposed steel surface is modelled as a moving boundary at which the mesh is periodically regenerated. The boundary's movement is correlated to the anodic corrosion rate, governed by the spatially-dependent reaction kinetics on the exposed surface as shown in section 9.1.3 below.

2c. O₂ diffusion: In the O₂ diffusion module of the m-model, C_{O_2} is constantly equal to a reference atmospheric $C_{O_2,ref}$ of 9 mol/m³ at the ground-atmosphere interface. All boundaries and surfaces excluding the ground-atmosphere interface and the exposed pipeline steel section (at which O₂ reduction occurs) have the no-flux diffusion boundary condition of {E-9.7c} imposed.

9.1.3 Reaction kinetics at exposed steel surface

The three electrochemical reactions considered at the exposed pipeline surface interface with the soil in the m-model are Fe oxidation ($Fe \rightarrow Fe^{2+} + 2e^-$, {R-5.1}), O₂ reduction ($O_2 + 2H_2O + 4e^- \rightarrow 4OH^-$, {R-7.1}), and water reduction/H evolution ($2H_2O + 2e^- \rightarrow H_2 + 2OH^-$, {R-5.4}) for nn-pH conditions. In the mm-scale model, since no O₂ presence is simulated in the disbondment region, water reduction through {R-5.4} is the only cathodic reaction considered. In both models, the effect of corrosion product buildup on the steel surface is not simulated. The following two subsections describe the reaction kinetics equations for the two models developed.

3a. m-model: In this model the total current density (i_{total}) at any T_{wall} and any point along the exposed arc angle θ (see Figure 4-4b) must equal the total i passing from the bulk soil evaluated at that same θ , normal to the surface ({E-9.8}, Table 9-3). No voltage accumulation can

occur in the complete electrical circuit of the CP system. As shown in {E-9.9a}, this includes E_{anode} (equilibrium potential of the anode-soil half-cell), $\Delta\phi$ (ohmic potential drop in soil between anode and cathode), E_{Fe} (potential difference at pipeline-soil interface), and E_{app} (applied voltage between pipeline and anode). The relationships can be simplified and rearranged to {E-9.9b} yielding E_{Fe} , since the anode-soil interface potential ($\phi|_{anode}$) is equal to E_{anode} and since E_{app} takes E_{anode} as ground.

As shown in {E-9.10}, the flux associated with the depletion of O_2 (R_{O_2}) is evaluated in the same way as i_{total} . As exhibited in this balance, R_{O_2} is undoubtedly a function of the stoichiometric coefficient of O_2 reduction in {R-5.4} (ν_{O_2} , negative for depletion), the number of electrons exchanged (n_{O_2} : $4e^-$ /equivalent), the Faraday constant (F: 96,500 C/mol per equivalent), and the O_2 reduction current density (i_{O_2} in A/m²) as a function of θ and T_{wall} . Table 9-3 also shows i parameters evaluated using Tafel kinetics for the “uncoupled” simulations. Parameter values used here are within ranges obtained from previous modelling studies relevant to this system [33], [123], [138], [141], [142], and are averaged where applicable. The Fe oxidation i , i_{Fe} , is spatially-dependent (function of θ) and temperature-dependent (function of T_{wall}), where $i_{Fe}^{o.ref}$ is the exchange Fe oxidation i ($= 7 \times 10^{-5}$ A/m²), η_{Fe} is the overpotential for Fe oxidation in V, and β_{Fe} is the Tafel slope for Fe oxidation ($= 0.3$ V/decade). The overpotential η_{Fe} is that which is between $E_{Fe}(\theta)$ and the temperature-dependent equilibrium potential (E_{Fe}^{eq}) for Fe corrosion. Hence, the only outstanding relationship to evaluate i_{Fe} is that of the temperature dependence of E_{Fe}^{eq} using the Nernst equation in {E-9.11c}. Values of -0.833 V_{SCE} and 2 are used for the standard E_{eq} for Fe corrosion (E_{Fe}^{eq-std}) and n_{Fe} , respectively. The dissolved $[Fe^{2+}]$ in the aqueous layer is assumed as a constant at 10^{-6} M [124].

Uncoupled O_2 reduction and H evolution kinetics governed by Tafel ({E-9.12} and {E-9.13}, respectively) are the equivalents of {E-9.11} for Fe corrosion. O_2 reduction at any θ is considered proportional to the steady-state C_{O_2} at that location through the $C_{O_2}(\theta)/C_{O_2.ref}$ ratio.

Values of -0.2 V/decade, 0.166 V_{SCE}, 4e⁻/equivalent, and 7.7 x 10⁻⁷ A/m² are used for β_{O₂}, E_{O₂}^{eq,std}, n_{O₂}, and i_{O₂}^{°ref}, respectively. Considering that the measured pH of aerated NS4 simulated soil solution is 7.5 at 303 K (30 °C) and 8.1 at 323 K (50 °C), the pOH used to find [OH⁻] in {E-9.12c} is 6.5 and 5.2, respectively (water self-ionization constant of 14 and 13.3, respectively). For H evolution kinetics, values of -0.15 V/decade, -0.241 V_{SCE}, 2e⁻/equivalent, and 7 x 10⁻⁷ A/m² are used for β_{H₂}, E_{H₂}^{eq,std}, n_{H₂}, and i_{H₂}^{°ref}, respectively. The same pOH methodology for calculating [OH⁻] in {E-9.12c} is extended to {E-9.13c}. Equations {E-9.11} to {E-9.13} fully define the Tafel-based reaction kinetics of the m-model developed in this chapter, for uncoupled simulations.

Table 9-3: Overall formulations and reaction-specific equations governing reaction kinetics in the uncoupled m-model

Reaction type	Number	Equation						
Overall formulations	{E-9.8}†	$i_{total}(\theta, T_{wall}) = i_{Fe}(\theta, T_{wall}) - i_{O_2}(\theta, T_{wall}) - i_{H_2}(\theta, T_{wall})$ $= (-\sigma \nabla \varphi \cdot \vec{n}) _{\theta, T_{wall}}$						
	{E-9.9a}	$E_{anode} - \Delta\varphi - E_{Fe}(\theta) + E_{app} = 0 \quad \text{where } \Delta\varphi = \varphi(\theta) - \varphi _{anode}$						
	{E-9.9b}	$E_{Fe}(\theta) = E_{app} - \varphi(\theta) + E_{anode}$						
O ₂ depletion	{E-9.10}	$R_{O_2}(\theta, T_{wall}) = \frac{\nu_{O_2} \cdot i_{O_2}(\theta, T_{wall})}{n_{O_2}F} = (-D_{O_2} \nabla c_{O_2} \cdot \vec{n}) _{\theta, T_{wall}}$						
Fe corrosion*	{E-9.11}†	<table border="0" style="width:100%; border-collapse: collapse;"> <thead> <tr> <th style="text-align: center;">{A} <i>i</i></th> <th style="text-align: center;">{B} <i>η</i></th> <th style="text-align: center;">{C} <i>E^{eq}</i></th> </tr> </thead> <tbody> <tr> <td style="vertical-align: top;">$i_{Fe}(\theta, T_{wall}) =$ $i_{Fe}^{\circ ref} e^{\left\{\frac{2.3\eta_{Fe}(\theta)}{\beta_{Fe}}\right\}}$</td> <td style="vertical-align: top;">$\eta_{Fe}(\theta, T_{wall})$ $= E_{Fe}(\theta)$ $- E_{Fe}^{eq}(T_{wall})$</td> <td style="vertical-align: top;">$E_{Fe}^{eq}(T_{wall}) = E_{Fe}^{eq,std}$ $+ \frac{RT_{wall}}{n_{Fe}F} \ln([Fe^{2+}])$</td> </tr> </tbody> </table>	{A} <i>i</i>	{B} <i>η</i>	{C} <i>E^{eq}</i>	$i_{Fe}(\theta, T_{wall}) =$ $i_{Fe}^{\circ ref} e^{\left\{\frac{2.3\eta_{Fe}(\theta)}{\beta_{Fe}}\right\}}$	$\eta_{Fe}(\theta, T_{wall})$ $= E_{Fe}(\theta)$ $- E_{Fe}^{eq}(T_{wall})$	$E_{Fe}^{eq}(T_{wall}) = E_{Fe}^{eq,std}$ $+ \frac{RT_{wall}}{n_{Fe}F} \ln([Fe^{2+}])$
		{A} <i>i</i>	{B} <i>η</i>	{C} <i>E^{eq}</i>				
$i_{Fe}(\theta, T_{wall}) =$ $i_{Fe}^{\circ ref} e^{\left\{\frac{2.3\eta_{Fe}(\theta)}{\beta_{Fe}}\right\}}$	$\eta_{Fe}(\theta, T_{wall})$ $= E_{Fe}(\theta)$ $- E_{Fe}^{eq}(T_{wall})$	$E_{Fe}^{eq}(T_{wall}) = E_{Fe}^{eq,std}$ $+ \frac{RT_{wall}}{n_{Fe}F} \ln([Fe^{2+}])$						
O ₂ reduction*	{E-9.12}†	<table border="0" style="width:100%; border-collapse: collapse;"> <tbody> <tr> <td style="vertical-align: top;">$i_{O_2}(\theta, T_{wall}) =$ $\frac{C_{O_2}(\theta)}{C_{O_2,ref}} i_{O_2}^{\circ ref} e^{-\left\{\frac{2.3\eta_{O_2}(\theta, T_{wall})}{\beta_{O_2}}\right\}}$</td> <td style="vertical-align: top;">$\eta_{O_2}(\theta, T_{wall})$ $= E_{Fe}(\theta)$ $- E_{O_2}^{eq}(T_{wall})$</td> <td style="vertical-align: top;">$E_{O_2}^{eq}(T_{wall}) = E_{O_2}^{eq,std}$ $- \frac{RT_{wall}}{n_{O_2}F} \ln([OH^-]^4)$</td> </tr> </tbody> </table>	$i_{O_2}(\theta, T_{wall}) =$ $\frac{C_{O_2}(\theta)}{C_{O_2,ref}} i_{O_2}^{\circ ref} e^{-\left\{\frac{2.3\eta_{O_2}(\theta, T_{wall})}{\beta_{O_2}}\right\}}$	$\eta_{O_2}(\theta, T_{wall})$ $= E_{Fe}(\theta)$ $- E_{O_2}^{eq}(T_{wall})$	$E_{O_2}^{eq}(T_{wall}) = E_{O_2}^{eq,std}$ $- \frac{RT_{wall}}{n_{O_2}F} \ln([OH^-]^4)$			
$i_{O_2}(\theta, T_{wall}) =$ $\frac{C_{O_2}(\theta)}{C_{O_2,ref}} i_{O_2}^{\circ ref} e^{-\left\{\frac{2.3\eta_{O_2}(\theta, T_{wall})}{\beta_{O_2}}\right\}}$	$\eta_{O_2}(\theta, T_{wall})$ $= E_{Fe}(\theta)$ $- E_{O_2}^{eq}(T_{wall})$	$E_{O_2}^{eq}(T_{wall}) = E_{O_2}^{eq,std}$ $- \frac{RT_{wall}}{n_{O_2}F} \ln([OH^-]^4)$						
H ₂ O reduction/H evolution*	{E-9.13}†	<table border="0" style="width:100%; border-collapse: collapse;"> <tbody> <tr> <td style="vertical-align: top;">$i_{H_2}(\theta, T_{wall}) =$ $i_{H_2}^{\circ ref} e^{-\left\{\frac{2.3\eta_{H_2}(\theta, T_{wall})}{\beta_{H_2}}\right\}}$</td> <td style="vertical-align: top;">$\eta_{H_2}(\theta, T_{wall})$ $= E_{Fe}(\theta)$ $- E_{H_2}^{eq}(T_{wall})$</td> <td style="vertical-align: top;">$E_{H_2}^{eq}(T_{wall}) = E_{H_2}^{eq,std}$ $- \frac{RT_{wall}}{n_{H_2}F} \ln([OH^-]^2)$</td> </tr> </tbody> </table>	$i_{H_2}(\theta, T_{wall}) =$ $i_{H_2}^{\circ ref} e^{-\left\{\frac{2.3\eta_{H_2}(\theta, T_{wall})}{\beta_{H_2}}\right\}}$	$\eta_{H_2}(\theta, T_{wall})$ $= E_{Fe}(\theta)$ $- E_{H_2}^{eq}(T_{wall})$	$E_{H_2}^{eq}(T_{wall}) = E_{H_2}^{eq,std}$ $- \frac{RT_{wall}}{n_{H_2}F} \ln([OH^-]^2)$			
$i_{H_2}(\theta, T_{wall}) =$ $i_{H_2}^{\circ ref} e^{-\left\{\frac{2.3\eta_{H_2}(\theta, T_{wall})}{\beta_{H_2}}\right\}}$	$\eta_{H_2}(\theta, T_{wall})$ $= E_{Fe}(\theta)$ $- E_{H_2}^{eq}(T_{wall})$	$E_{H_2}^{eq}(T_{wall}) = E_{H_2}^{eq,std}$ $- \frac{RT_{wall}}{n_{H_2}F} \ln([OH^-]^2)$						

*: represents uncoupled case based on theoretical parameters provided in sub-section 3a above

†: the convention for current density ensures that cathodic current density always has an opposite sign to that of anodic current density

3b. mm-model: The reaction kinetics formulations in the mm-model are similar to the m-model presented above. Here, the two main electrochemical reactions considered to occur at the trapped water-electrode interface in Figure 4-5b are the anodic oxidation reaction of Fe and the

cathodic H evolution reduction reaction for nn-pH conditions. It is assumed the availability of water does not limit the reduction reaction. Again, no voltage accumulation occurs, thus the sum of E_{bulk} (electrolyte potential in bulk solution outside the disbondment, top left corner in Figure 4-5b), $\Delta\phi$ (ohmic potential drop, within the disbondment in the mm-model), $E_s(x)$ (potential difference at interface of exposed steel electrode with trapped water), and E_{app} all equals zero (mathematically shown as {E-E.3} in Table E-3 in Appendix E). With $\phi|_{bulk}$ being equivalent to E_{bulk} , and E_{bulk} being the reference for E_{app} , the voltage sum of {E-E.3} can be rearranged and reduced to {E-E.4}. The total i ($i_{total}(x, T_{wall})$) from the anodic and cathodic reactions at any T_{wall} , summed at any point x along the exposed surface, must equal the total current density passing from the electrolyte evaluated at that same x , normal to the surface ($(-\sigma\nabla\phi \cdot \vec{n})|_{x, T_{wall}}$). The convention in {E-E.5} is negative for cathodic i ($i_c(x, T_{wall})$) and positive for anodic i ($i_a(x, T_{wall})$).

The kinetics of i_a and i_c at the exposed steel surface depend on $E_s(x)$, T_{wall} , and pH (through %CO₂) based on experimental results. For the full spectrum of $E_s(x)$ potentials, i_c is evaluated with an exponential function following the format of {E-E.6}, where C_1 and C_2 are T_{wall} - and %CO₂-dependent fitting parameters. Since %CO₂ diminishes at locations deeper within the disbondment, the expression is designed to equal $i_c(T_{wall}, 5\% \text{ CO}_2)$ at $x = 0$ cm and $i_c(0\% \text{ CO}_2)$ at $x = L$, based on a linear (x/L) ratio. {E-E.6} evaluates i_c for $E_s(x)$ values above and below OCP, since experimental profiles follow Tafel behavior as shown in section 9.2.2.

On the other hand, i_a evaluation methodology is divided into two forms separating the $E_s(x)$ values above OCP from those below OCP. Since anodic branches (i.e. $E_s(x) > \text{OCP}$) of PDP plots represent the total anodic current density, $i_a(E_s(x) > \text{OCP})$ is directly evaluated from experimental results, again with linear x/L proportionality for CO₂. Below OCP, total i_c controls the polarization plots, so the i_a must be determined differently; LPR test results here determine the critical parameters for $i_a(E_s(x) < \text{OCP})$ in {E-E.7}, where i_a° is the exchange Fe oxidation i

(calculated from a reference value of $i_a^{\circ-ref} = 7 \times 10^{-5} \text{ A/m}^2$ using {E-E.11}), η_s is the overpotential for Fe oxidation (evaluated through {E-E.8}), and β_a is the Tafel slope for Fe oxidation (calculated from a standard value of $\beta_a = 0.4 \text{ V}$ per decade using {E-E.12}). The formulation of {E-E.7} is adjusted for CO_2 depletion in the same way as {E-E.6}, using an x/L ratio. The temperature dependence of E_s^{eq} is expressed using the form of the Nernst equation in {E-E.9}, where a value of $-0.83 \text{ V}_{\text{SCE}}$ is used for the standard E_{eq} for Fe oxidation in the steel (E_s^{eq-std}), and 2 for n_a based on the $2e^-$ in {R-5.1}. Again, it is assumed the concentration of dissolved ferrous in the aqueous electrolyte is constant (standard $[\text{Fe}^{2+}] = 10^{-6} \text{ M}$) [124].

The i_a evaluated from either method is used to determine the penetration rate in the exposed steel (R_{steel}), which is location, temperature, and pH dependent as seen in {E-E.10}. It is proportional to atomic weight (A_W), charge on ion of each corresponding element in material (n_i), and the density of Fe in X100 (ρ_{Fe} , Fe > 97.5% of X100 steel) [295]. Remaining discussion of these reaction kinetics formulations requires experimental data and thus will be presented in the sections below.

9.2 Polarization experiments and equations for coupled simulations

Simulations in the m-model which use the equations presented in this section are termed “coupled” due to their reliance on (i.e. coupling with) actual experimental results. Alternatively, simulations which use the unmodified Tafel formulations of {E-9.11} to {E-9.13} in Table 9-3 are termed “uncoupled” in forthcoming discussions. It is important to note that all the mm-model simulations rely on experimental results, thus have no “uncoupled” counterparts.

9.2.1 Temperature- and O_2 -dependent fittings for m-model

Figure 9-2a illustrates the PDP profiles for X100 steel in the conditions relevant for the m-model. At $E < \text{OCP}$, increased C_{O_2} results in diffusion-controlled behavior causing i_{lim} in the cathodic polarization branches for the two aerated tests, which withdraws at around $-1 \text{ V}_{\text{SCE}}$. Profiles below that follow corresponding deaerated cases identically until $-1.25 \text{ V}_{\text{SCE}}$. The two

aerated cathodic profiles are shown closer in Figure 9-2b. Limiting of i_c in the O₂ reduction dominated section is more pronounced in the lower temperature (30 °C) case. This is attributed to the higher dissolvability of O₂ in lower temperature solutions. A higher C_{O_2} of 7.3 mol/m³ measured in 30 °C drives O₂ reduction to $i_c = 10^{-4}$ A/cm², even at cathodic E less than the 50 °C profile (i.e. -0.6 vs. -0.7 V_{SCE}, respectively). Even with the increased cathodic E in the 50 °C situation, the lower C_{O_2} of 6 mol/m³ does not sustain the same O₂ reduction kinetics as the 30 °C case, until the two profiles intersect at a transition potential (E_{trans}) \approx -0.9 V_{SCE}. The 20 degree temperature difference between the two profiles hence reveals the lessened influence of diffusion-control at higher temperatures. Here, although there exists a clear inflection in current density at E_{trans} , the O₂ reduction dominated region in the 50 °C case still exhibits characteristics of activation-control. As such, the O₂ reduction rate (i.e. i_{O_2}) will depend on the E_{Fe} induced by the CP more in hotter soils, for the potential within the $OCP > E > E_{trans}$ range.

Below E_{trans} , other cathodic reaction(s) not directly dependent on C_{O_2} dominate. HCO₃⁻-containing solutions induce the cathodic reduction of H₂CO₃ near OCP over the whole nn-pH range, where HCO₃⁻ discharge becomes more dominant at lower E as shown in chapter 8 above [64]. However, lower quantities of CO₂ dissolve in solution at higher temperatures, leading to decreased [HCO₃⁻] based on the CO₂-H₂O system equilibria of {R-4.1} and {R-4.2}. Hence, a lower rate of HCO₃⁻ discharge (i.e. {R-8.2}) manifests for the 50 °C (pH 8.1) condition compared to the 30 °C (pH 7.5) condition. In Figure 9-2a the 50 °C deaerated cathodic profile instead shifts to higher i_c , signifying enhanced reaction kinetics. This is the result of a higher reaction rate in {R-8.2} produced by the higher temperature offsetting the sluggishness caused by lower [HCO₃⁻]; temperature clearly influences the net result more. Thus, the merger point between the aerated and deaerated regions (i.e. E_{trans}) occurs at a more noble E in 50 °C when the deaerated cathodic kinetics are accelerated. The E_{eq} for HCO₃⁻ discharge, shown previously in {E-7.1}, is near E_{trans} and confirms the viability of {R-8.2} in the cathodic E region illustrated in Figure 9-2a-b.

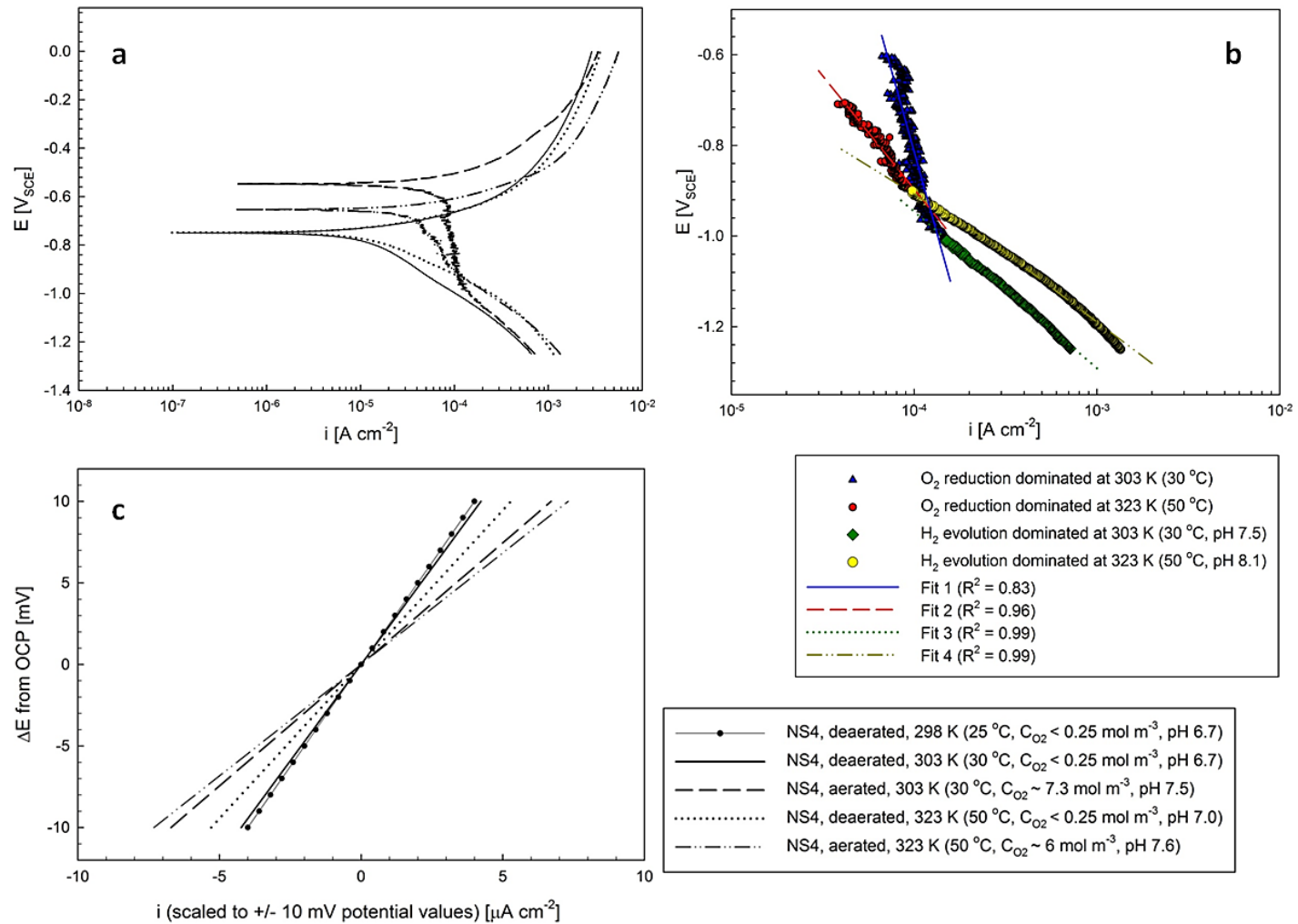


Figure 9-2: (a) PDP profiles of X100 steel sample in deaerated and aerated NS4 solutions at 30 and 50 °C; (b) cathodic regime of PDP profiles (with regression fits) showing E - and temperature-dependent O₂ reduction and H evolution kinetics; and (c) LPR fitting results for X100 specimen immersed in NS4 with combinations of deaeration, aeration, and temperature

Table 9-4: Regression fit equations and corrosion parameters governing reaction kinetics[†] in the coupled simulations of the m-model, extracted from polarization plots

Reaction type	Number	Equation		
		a) <i>i</i>		b) β
		303 K (30 °C)	323 K (50 °C)	
<i>O₂ reduction</i>	{E-9.14}	$i_{O_2}(\theta, 303 K) = \{C_{O_2}(\theta)/C_{O_2,ref}\} \cdot e^{\left\{\frac{E_{Fe}(\theta)+6.6}{-0.6}\right\}} \cdot 10^4$	$i_{O_2}(\theta, 323 K) = \{C_{O_2}(\theta)/C_{O_2,ref}\} \cdot e^{\left\{\frac{E_{Fe}(\theta)+2.9}{-0.2}\right\}} \cdot 10^4$	\
<i>H evolution</i>	{E-9.15}	$i_{H_2}(\theta, 303 K) = e^{\left\{\frac{E_{Fe}(\theta)+2.3}{-0.15}\right\}} \cdot 10^4$	$i_{H_2}(\theta, 323 K) = e^{\left\{\frac{E_{Fe}(\theta)+2.1}{-0.13}\right\}} \cdot 10^4$	\
<i>Fe corrosion</i>	{E-9.16}	$i_{Fe}^\circ(T_{wall}) = i_{Fe}^{\circ,ref} \cdot \left\{ \left(\frac{\partial E_{LPR,298K}}{\partial i_{LPR,298K}} \right) / \left(\frac{\partial E_{LPR,T_{wall}}}{\partial i_{LPR,T_{wall}}} \right) \right\}$		$\beta_{Fe}(T_{wall}) = \beta_{Fe}^{std} \cdot \left\{ \left(\frac{\partial E_{LPR,T_{wall}}}{\partial i_{LPR,T_{wall}}} \right) / \left(\frac{\partial E_{LPR,298K}}{\partial i_{LPR,298K}} \right) \right\}$

[†]: final unit of *i* from any reaction is that which corresponds to Fig. 9-2a-b, namely A/cm²

These intricate temperature- and E -dependent behaviors are not captured by the reaction kinetics equations presented in Table 9-3 (section 9.1.3 above) or similar ones used in the literature. Thus, experimentally-derived formulations are used to provide the basis for the more accurate coupled simulations. Each combination of T_{wall} (30 and 50 °C) and reduction regime (O₂ reduction and H evolution) in Figure 9-2b is fitted to the nonlinear regression model in {E-9.17} using a data analysis software (SigmaPlot® version 11.0). Here, at each data point j : $\overline{E_{Fe-j}}$ is the θ -dependent soil-structure E difference, i_j is the cathodic current density, and E_j and A_j are constants. The best fit for each combination is ensured by minimizing the χ^2 sum for all j , where $E_{Fe-j}(\theta)$ is the result from the fit equation, $\overline{E_{Fe-j}}(\theta)$ is the experimental (actual) value, w_j is a weighting factor, and n is the number of data points in the fit. The maximum averaged error did not surpass 1.35% for any final fit equation. As shown in Figure 9-2b, R^2 averages more than 0.94 for all cases. Table 9-4 shows the resulting fit equations ({E-9.14} and {E-9.15} for each T_{wall}), rearranged to solve for i_j . A ratio coefficient is added to the i_{O_2} expressions to retain their proportionality with $C_{O_2}(\theta)$, where if $C_{O_2}(\theta) = 0$ the i_c will simply be equal to i_{H_2} at the corresponding E_{Fe} . No temperature proportionality is necessary for reaction kinetics equations since reactions happen at the pipeline wall which always remains at T_{wall} .

$$\overline{E_{Fe-j}}(\theta) = E_j + A_j \cdot \ln(i_j)$$

$$\text{where } \chi^2 = \sum_{j=1}^n \left\{ w_j E_{Fe-j}(\theta) - \overline{E_{Fe-j}}(\theta) \right\} \text{ is minimized} \quad \{\mathbf{E-9.17}\}$$

The E - i LPR responses are fit to linear polynomials (Figure 9-2c, with $R^2 \geq 0.99$). The slopes, which are directly proportional to R_p and hence inversely proportional to corrosion rate, decrease with temperature and C_{O_2} . LPR is used instead of PDP in determining Fe corrosion behavior due to the limited validity of the latter in diffusion-controlled systems [243]. For coupled simulations in both the m-model and mm-model of this chapter we supplement the Fe corrosion reaction formulations of {E-9.11a} to {E-9.13a} in Table 9-3 with the temperature

influence revealed by LPR results. Only temperature dependence is added to these formulations to yield {E-9.16} in Table 9-4, whereas C_{O_2} -dependence is dealt with by {E-9.14}. The two corrosion parameters which capture this change are the exchange i (i_{Fe}°) and the Tafel slope (β_{Fe}). At higher temperatures, i_{Fe}° increases from the reference $i_{Fe}^{\circ-ref}$ value of 7×10^{-5} A/m² and β_{Fe} decreases from the standard β_{Fe}^{std} of 0.3 V/decade, according to $\partial E_{LPR}/\partial i_{LPR}$ ratios representing the slopes in Figure 9-2c evaluated at any T_{wall} .

9.2.2 Temperature- and %CO₂-dependent fittings for mm-model

Figure E-1a in Appendix E shows the LPR results below OCP necessary for evaluating $i_a(E_s(x) < OCP)$. The results are scaled to superimpose the different OCPs for each environment j (OCP_{*j*}) onto the same $0 \Delta E_j$ line. A near perfect fit ($R^2 \geq 0.99$) of the E - i response is thus achievable with linear polynomials. The slopes in Figure E-1a, again directly proportional to R_p and inversely proportional to oxidation rate [296], show that i_a increases with temperature and generally decreases with pH, behaviors once more captured through factoring of the exchange i , i_a° , and the Tafel slope, β_a , in {E-E.7} using the ratios shown in {E-E.11} and {E-E.12} (Table E-3 in Appendix E). The ratio orientations ensure that i_a° increases and β_a decreases to yield an increased i_a in corresponding environments, and vice-versa. The $\frac{\partial E_{LPR}}{\partial i_{LPR}}$ terms represent the slopes in Figure E-1a evaluated at any given T_{wall} and %CO₂ combination.

Table 9-5: List of OCP values for environments studied for mm-model, characterized by temperature, %CO₂ concentration in deaerating purging gas, and pH

Environment	Temperature [°C]	[%CO ₂]	pH ^a	OCP [mV _{SCE}]
1	25	5	6.7	-748
2	50	5	7.0	-750
3	25	0	8.5	-793

^a: stable value measured over at least 30 minutes of purging

Table 9-6: C_1 and C_2 parameter results of regression fits for i_c evaluation (i_c as a function of $E_s(x)$, C_1 , and C_2)

Environment	Temperature [°C]	pH	C_1	C_2
1	25	6.7 (5% CO ₂)	2.07	-11.6 x 10 ⁻²
2	50	7.0 (5% CO ₂)	1.92	-10.8 x 10 ⁻²
3	25	8.5 (0% CO ₂)	1.55	-6.1 x 10 ⁻²

Figure E-1b and Figure E-1c illustrate the cathodic and anodic branches of the PDP profiles in the environments tested, respectively. Both sets of profiles asymptote at the OCP_j values used to determine the dashed line boundary in Figure E-1a. Table 9-5 lists the specific OCP value from each tested condition, where it is seen to become less noble with increased alkalinity. In Figure E-1b, it is clear that i_c at 25 °C is augmented with less alkalinity above $-1 V_{SCE}$. Decreased alkalinity drives water reduction forward, resulting in higher i_c for the pH 6.7 profile over the pH 8.5 profile. Similar to Figure E-1a, the higher temperature of the pH 7.0 profile in Figure E-1b manifests the highest i even though it is more alkaline than the pH 6.7 profile; this is attributed to the direct effect of temperature on increasing the reaction rates. The increased i_c of PDP profiles in less alkaline environments agrees with the general trend of the OCP values in Table 9-5. Also, the activation-controlled characteristics of the profiles in Figure E-1b ensure the validity of extending their line fits into the $E_s(x) > OCP_j$ range [243].

Each cathodic profile in Figure E-1b is fitted to an exponential $i_c = e^{((E_s(x)+C1)/C2)}$ model using SigmaPlot. Again, the best fit for each combination is ensured by minimizing the χ^2 sum for all data points j , through {E-E.13} in Table E-3 where: i_{c-j} is the result from the fit equation, $\overline{i_{c-j}}(x)$ is the experimental (actual) value (i_{c_exp} in Figure E-1b), w_j is a weighting factor, and n is the number of data points in the fit. Table 9-6 shows the resulting values for C_1 and C_2 in each condition. The R^2 values for the fits are all ≥ 0.96 .

The observed influence of alkalinity on reaction kinetics also appears in the anodic regime profiles of Figure E-1c. At pH 8.5 a short-lived i reduction appears until around $-0.3 V_{SCE}$. Although not considered to be completely passive (due to the weak and hydrous nature of the $Fe(OH)_2$ product shown to cause it in earlier chapters of this thesis), surface corrosion in this E range is an order of magnitude below the less alkaline counterparts. The formation of $Fe(OH)_2$ exclusively in the pH environment above 7.0 in Figure E-1c agrees well with the $Fe(OH)_2$ formation threshold of pH 7.6 previously found in chapter 5 [172]. These details could not have

been captured by extending the LPR profiles above OCP, which is a further reason why $i_a((E_s(x) > \text{OCP}_j))$ in the mm-model is a point-to-point reproduction of the profiles in Figure E-1c.

9.3 E_{Fe} , C_{O_2} , and i simulation results from m-model

9.3.1 Temperature, ϕ , and C_{O_2} contours

In the m-model, solutions of the heat-transfer module yield induced temperature contours based on T_{wall} , $T(z, t)$, and the governing thermal parameters. A typical isothermal contour result is shown in Figure 9-3a for peat soil structure with $\psi = 0.6$ at the maximum initial temperature conditions in Figure 9-1. Temperature gradients below the pipeline in Figure 9-3a are greater than above the pipeline, leading to more heat flux (arrows) downwards than towards the ground surface. In colder conditions heat flux moves more upwards (not shown) since 0.02 m depth temperatures are damped and lag the 2 m depth temperatures. Analysis of all thermal contours concludes that ψ has little to no influence on induced soil temperatures within any specific soil structure. Induced soil temperature profiles will influence σ and D_{O_2} and hence, the coupled ϕ and C_{O_2} results. The equipotential contours in Figure 9-3b show an example of the ϕ drop between the CP anode and the pipeline, for sand structure with $\psi = 0.2$ at the maximum *induced* soil temperature profile. The σ averages approximately 4.8×10^{-2} S/m in this figure, and ϕ drops from above 2 V_{SCE} at the CP anode to below 0 V_{SCE} at the pipeline surface. At lower ψ values the level of ϕ and corresponding i_l arrow uniformity near the anode decreases, owing to lower σ causing greater $\Delta\phi$. At the exposed pipeline surface clear spatial dependence of ϕ is observed, translating to less corrosion protection of the exposed sites at the top of the pipeline.

The O₂ diffusion and depletion behavior within the soil depends on the temperature and i_l profile of each simulation. Parameters taken from Figure 9-3a and Figure 9-3b are used in the diffusion calculations, culminating in C_{O_2} contours within the soil shown in Figure 9-3c example, where the temperature- and soil structure/ ψ -dependent D_{O_2} averages around 1×10^{-7} m²/s. The lowest C_{O_2} values appear at around $\theta = 0^\circ$, registering diffusion flux (arrows) mainly in the

second quadrant of the soil section. The C_{O_2} contour line buildup to the top of the pipeline (due to smaller diffusion distances between the source and depletion sites) suggests O_2 reduction rate-limiting behavior, creating a gradient along the exposed surface. Corrosion macro-cells from differential aeration in porous media have been identified on structural metals before and are known to accelerate degradation [241]. Diffusion-control occurs in the present investigation although $\psi = 0.2$ conditions allow freer gas transport than $\psi = 0.3$ conditions would. Lower ψ values for any soil structure will yield a smaller C_{O_2} spectrum on the scale of the exposed pipeline section between $C_{O_2}(0^\circ)$ vs. $C_{O_2}(90^\circ)$. The magnitude of η_{O_2} controls the steady-state C_{O_2} profile more than the geometrical distance for the diffusion gradient, supported by soil moisture facilitating low E_{Fe} and thus increased reduction kinetics. This effect is pronounced for higher T_{wall} situations in which i_{O_2} is more sensitive to overpotential, as shown in the O_2 reduction regime in Figure 9-2b and previously discussed in section 9.2.1 above.

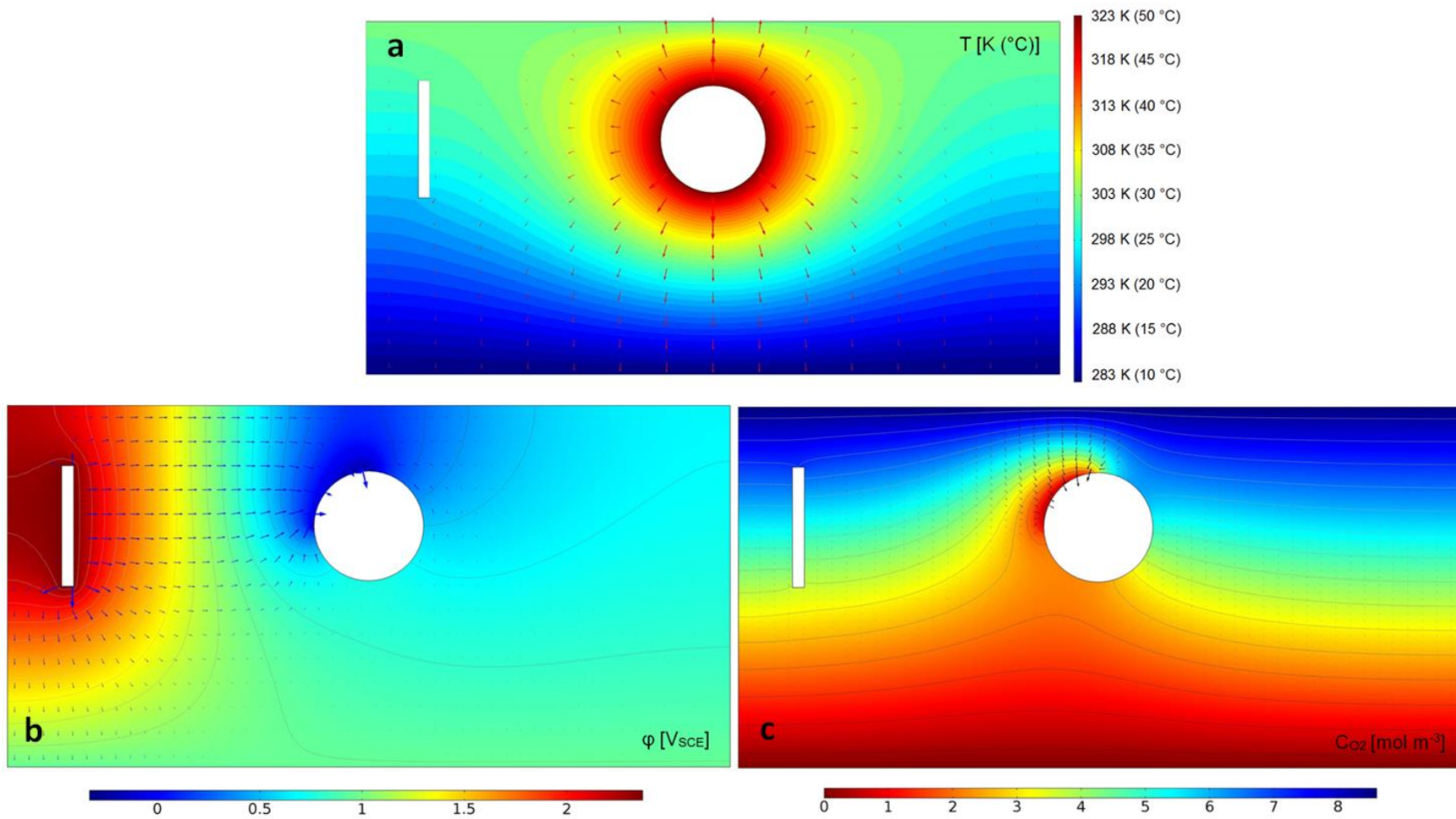


Figure 9-3: Contours of: (a) induced soil temperature [K (°C)] for peat with $\psi = 0.60$ at hottest conditions; (b) ϕ [V_{SCE}] for sand with $\psi = 0.60$ at hottest induced temperatures; and (c) C_{O_2} [mol/m³] for clay with $\psi = 0.20$ at hottest induced temperatures

9.3.2 E_{Fe}

E_{Fe} values in Figure 9-4 are significantly more anodic in drier soils, and sensitivity to ψ is temperature- and soil-dependent. Changes in ψ do not have a significant effect on induced temperatures, so ψ influence on E_{Fe} is primarily due to the availability of conductive media and not the 2% linear temperature compensation. However, increases in temperature from the annual seasonal cycle cause slight cathodic shift (50-100 mV) in E_{Fe} values, mainly due to increased σ of the available liquid phase. Spatial effects are even more consequential, shifting potentials by almost 150-250 mV between the least and most severe cases, respectively. Spatial sensitivity of E_{Fe} decreases in moister soils, implying the easier protection of sites near the CP anode in high ψ soils. This coincides with fundamentals of CP design [297] and the results of CP simulations in other porous media such as [33]. While these studies typically rely on a single physicochemical parameter, here three different soil structures are simulated. The importance of other media properties such as ϕ and temperature is thus revealed; for example, at $\psi = 0.3$, E_{Fe} can be as high as -0.2 V_{SCE} or as low as -0.8 V_{SCE} depending on all soil properties involved (Figure 9-4b).

These interdependencies are more apparent in the coupled simulations, the results of which exhibit clear differences to their uncoupled counterparts. The most obvious of these differences is $|E_{Fe}|$, which gets shifted by around 0.3 V in the cathodic direction in the coupled Figure 9-4b results. The extent of the E_{Fe} drop with respect to ψ is excessive in Figure 9-4a, whereas the more uniform slopes of Figure 9-4b represent actual behavior more accurately. In Figure 9-4b, $E_{Fe}(0^\circ)$ is clearly less affected than $E_{Fe}(90^\circ)$ by ψ at either T_{wall} , which is a logical result judging from the shorter current path in the former case. The results for colder T_{wall} have more sensitivity to lower ψ , attributed to the combined effect of lower liquid phase availability for CP currents and the significantly lower σ of what is still available compared to hotter conditions. This is perhaps the most revealing testament of inaccuracies of the uncoupled results, in which coordinates and temperature seem to have equal effects at different ψ .

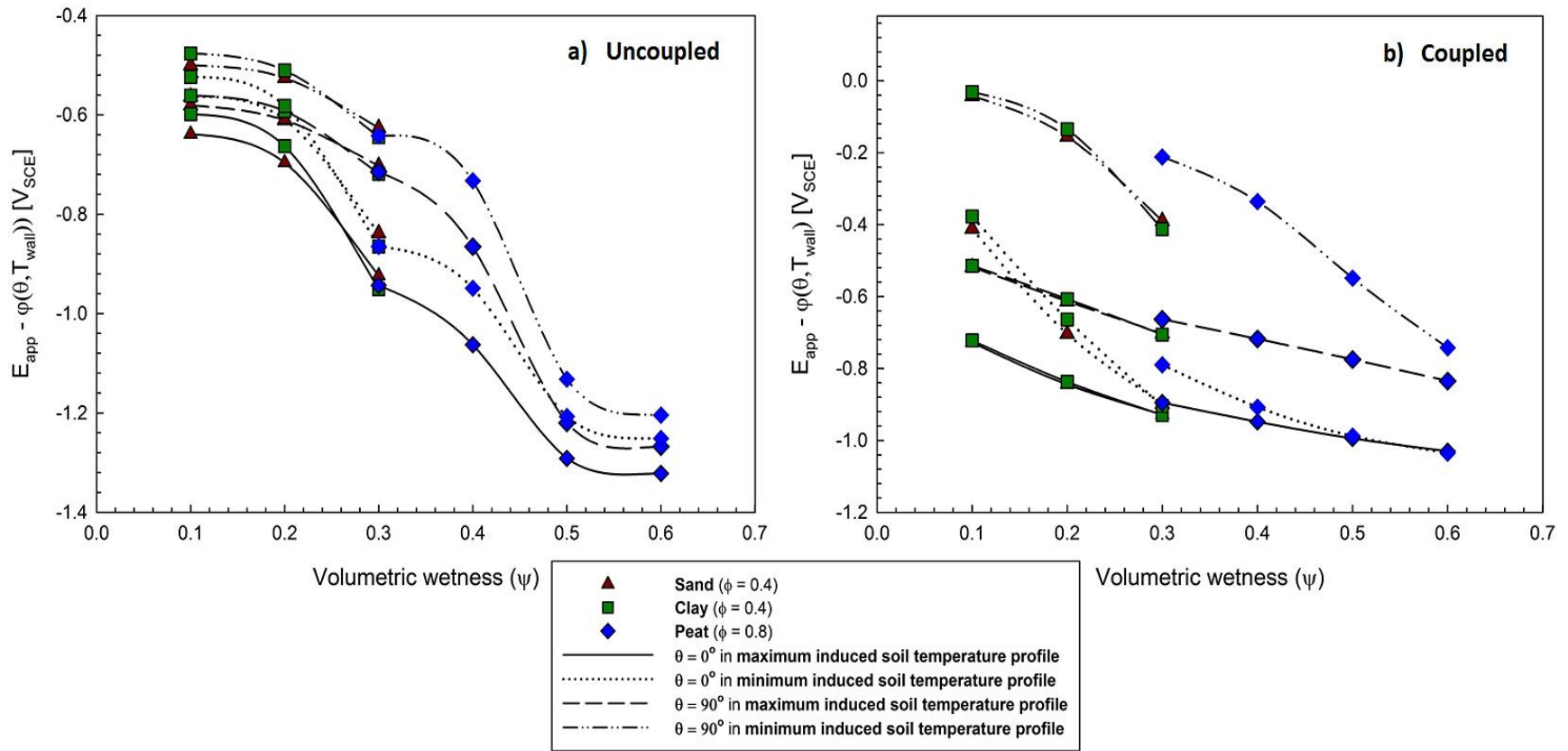


Figure 9-4: E_{Fe} evaluated at $\theta = 0^\circ$ and $\theta = 90^\circ$ in minimum and maximum induced temperature profiles, different soil structures, and ψ using: (a) uncoupled governing equations; and (b) coupled governing equations

9.3.3 i_{Fe}

Results from evaluating i_{Fe} in different soil structures, temperatures, θ , and ψ are shown in Figure 9-5. The most corrosion happens in drier soils of colder temperatures, at exposed sites farther away from the CP anode. The interplaying physicochemical parameters affecting corrosion of the exposed pipeline steel section appear highly consequential, causing a change of around 1 order of magnitude between the lowest and highest i_{Fe} . In the driest, coldest conditions at $\theta = 90^\circ$, i_{Fe} for sand and clay structures is around 3×10^{-5} A/cm² (equivalent to a penetration rate of 13.8 milli-inches per year (mpy) using a density for Fe of 7.81 g/cm³). This value does not meet the acceptable 1 mpy standard for the corrosion of mild steel in industrial applications [298]. Yet, in light of the aforementioned inaccuracies of the uncoupled model, and since most i_{Fe} values in Figure 9-5b translate to a corrosion rate < 1 mpy, the CP system setup modelled here is considered to be a suitable protector of the pipeline at the Figure 4-4b coating failure location.

In conditions colder and/or drier than those simulated here, with exposed sections of the pipeline not facing the CP anode, a CP setup like the one simulated will not provide sufficient protection. Design modification options should therefore be considered in such situations, like positioning the CP anode closer to the pipeline. Inversely, in conditions where it is shown that the CP system overprotects the structure causing unnecessary energy consumption and the acceleration of H evolution, opposite design modification measures should be taken. Efficient energy use and the avoidance of derivative H-related problems is especially important considering the fact that even the coupled simulation results here are assumed to be independent of surface condition effects, mainly corrosion product deposition. The $\text{Ca}_x\text{Mg}_{1-x}\text{CO}_3$ scale commonly found on steels in environments similar to NS4 has previously been shown in chapter 8 above to greatly accelerate H generation on X100 [245]. Similarly, multi-layer Fe-oxide (e.g. Fe_3O_4) and Fe-oxyhydroxide (e.g. $\alpha\text{-FeOOH}$) formations in O_2 -containing environments can accelerate cathodic reactions through separation of anodic and cathodic sites as shown in chapter 7 [290]. Hence, the risk associated with CP overprotection in these cases is heightened.

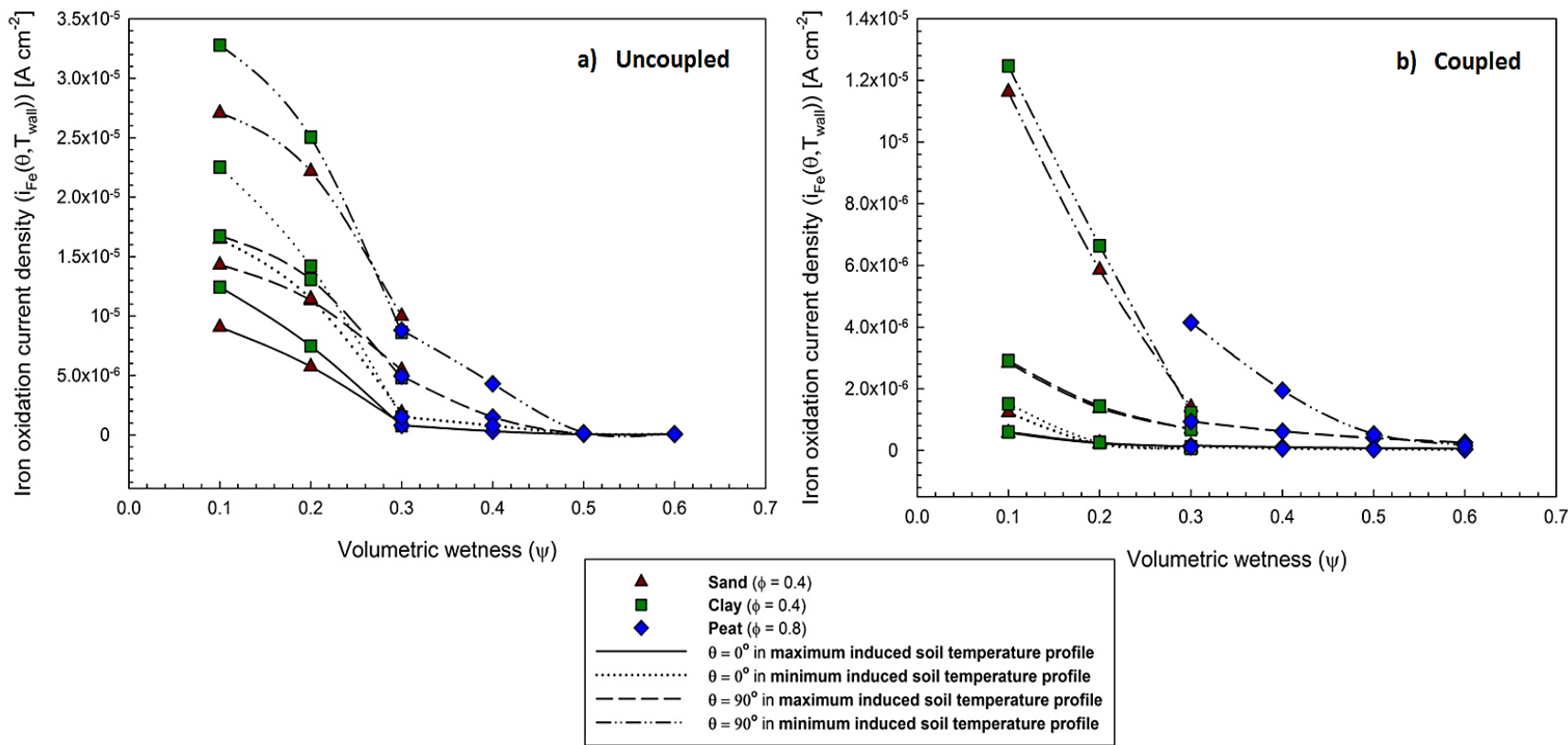


Figure 9-5: i_{Fe} evaluated at $\theta = 0^\circ$ and $\theta = 90^\circ$ in minimum and maximum induced temperature profiles, different soil structures, and ψ using: (a) uncoupled governing equations; and (b) coupled governing equations

9.3.4 C_{O_2} , i_{O_2} , and i_{H_2}

Figure E-2 in Appendix E shows the results for C_{O_2} at the exposed pipeline surface for different soil structures, induced temperatures, θ , and ψ . Generally, C_{O_2} levels decrease in colder temperatures, wetter moistures, and at locations of lower θ . These steady-state values are where the O_2 diffusion flux reaching the surface ($(-D_{O_2}\nabla C_{O_2} \cdot \vec{n})|_{\theta, T_{wall}}$) is balanced by the reduction rate (R_{O_2}) in {E-9.10}. Two unique phenomena are revealed by the C_{O_2} results in Figure E-2 and the related i_{O_2} results in Figure 9-6. The first is the inverse effect of ψ on D_{O_2} and σ . For example, lower ψ increases D_{O_2} in the bulk electrolyte leading to more diffusion, but decreases σ and hence O_2 reduction rate (through more noble E_{Fe} potentials). Both these effects combined cause higher C_{O_2} at the surface. With basic Tafel kinetics of the uncoupled simulations, this joint influence leads to the high sensitivity of C_{O_2} to $\Delta\psi$ as witnessed in Figure E-2a. Here, any profile with $\psi \geq 0.3$ has virtually zero C_{O_2} at the surface, since any O_2 which can diffuse in these low D_{O_2} situations is quickly reduced by the markedly cathodic E_{Fe} . In the more representative coupled C_{O_2} results though, extreme sensitivity to $\psi \geq 0.3$ is eradicated due to the much lower dependence of experimental i_{O_2} values on E_{Fe} (Figure 9-2b), especially at $T_{wall} = 303$ K (30 °C). Here, R_{O_2} at a very cathodic E_{Fe} potential from a high ψ is comparable to that at an E_{Fe} potential near OCP. Hence, the low O_2 levels diffusing in low D_{O_2} situations do not get immediately reduced, and C_{O_2} values are non-zero and correlate to ψ .

The i_l behavior governing the coupled C_{O_2} results yields the i_{O_2} profiles shown in Figure 9-6a. These profiles corroborate the inverse D_{O_2} and σ dependence on ψ . Since i_{O_2} is evaluated as a function of both C_{O_2} and E_{Fe} (see {E-9.14}), values remain relatively the same at low ψ (low cathodic overpotential but high C_{O_2}) vs. high ψ (high cathodic overpotential but low C_{O_2}). In contrast, average ψ values do not have low cathodic overpotential nor C_{O_2} , thus inducing relatively higher i_{O_2} magnitudes creating a bell-shaped profile. This is less observable in the two $\theta = 0^\circ$ peat profiles since at $\psi = 0.3$ there is still sufficient air porosity to sustain enough D_{O_2} , but

if simulations were extended to $\psi = 0.1$ in peat the bell-shape would emerge. As expected, $\theta = 0^\circ$ profiles manifest this peak behavior the most due to the closer distance to the CP anode (more E_{Fe} variations) and the farther distance from the ground surface (more C_{O_2} variations).

The second unique phenomenon revealed by Figure E-2 and Figure 9-6 relates to the geometry of the modelled system. This geometry enhances aeration in the soil surrounding $\theta = 90^\circ$ sites, since these sites are both closer to ground (higher C_{O_2}) and farther away from the CP anode (causing more anodic E_{Fe} potentials and thus less O_2 depletion). An understanding of these C_{O_2} variations along the material surface helps the designer in identifying sites where corrosion acceleration is expected due to corrosion macrocells. This degradation is likely exacerbated if such sites are also sustaining high mechanical tension from pipeline hoop stress, as described in section 8.4.3. Combined with the generation of H from cathodic processes, embrittlement of the remaining material at corroded sites further threatens the integrity of the overall structure.

The i_{H_2} results for all the conditions simulated are shown in Figure 9-6b, demonstrating a steady increase in H generation with ψ for all combinations of ϕ and θ . Unlike i_{O_2} , this cathodic process is uncomplicated by diffusion and i_l issues since the relevant species (mainly HCO_3^-) are considered uniform in concentration on the exposed surface. The magnitude of i_{H_2} increases in moister, hotter conditions around $\theta = 0^\circ$ sites, essentially due to more cathodic E (from increased σ) and increased reduction kinetics at sites facing the CP anode. The effective H diffusivity in the X100 pipeline steel simulated in the model of this chapter was previously shown in chapter 8 to be approximately $4 \times 10^{-7} \text{ cm}^2/\text{s}$, a value similar to other pipeline steel grades [299]. Even though the H concentration in X100 in nn-pH NS4 conditions is relatively low (on the order of 1 ppm) compared to other environments [285], it could still cause embrittlement and affect crack growth dynamics [94]. Accurately simulating i_{H_2} is therefore an important functionality of the present model, and is a key prerequisite for predicting the risk of H-related pipeline damage.

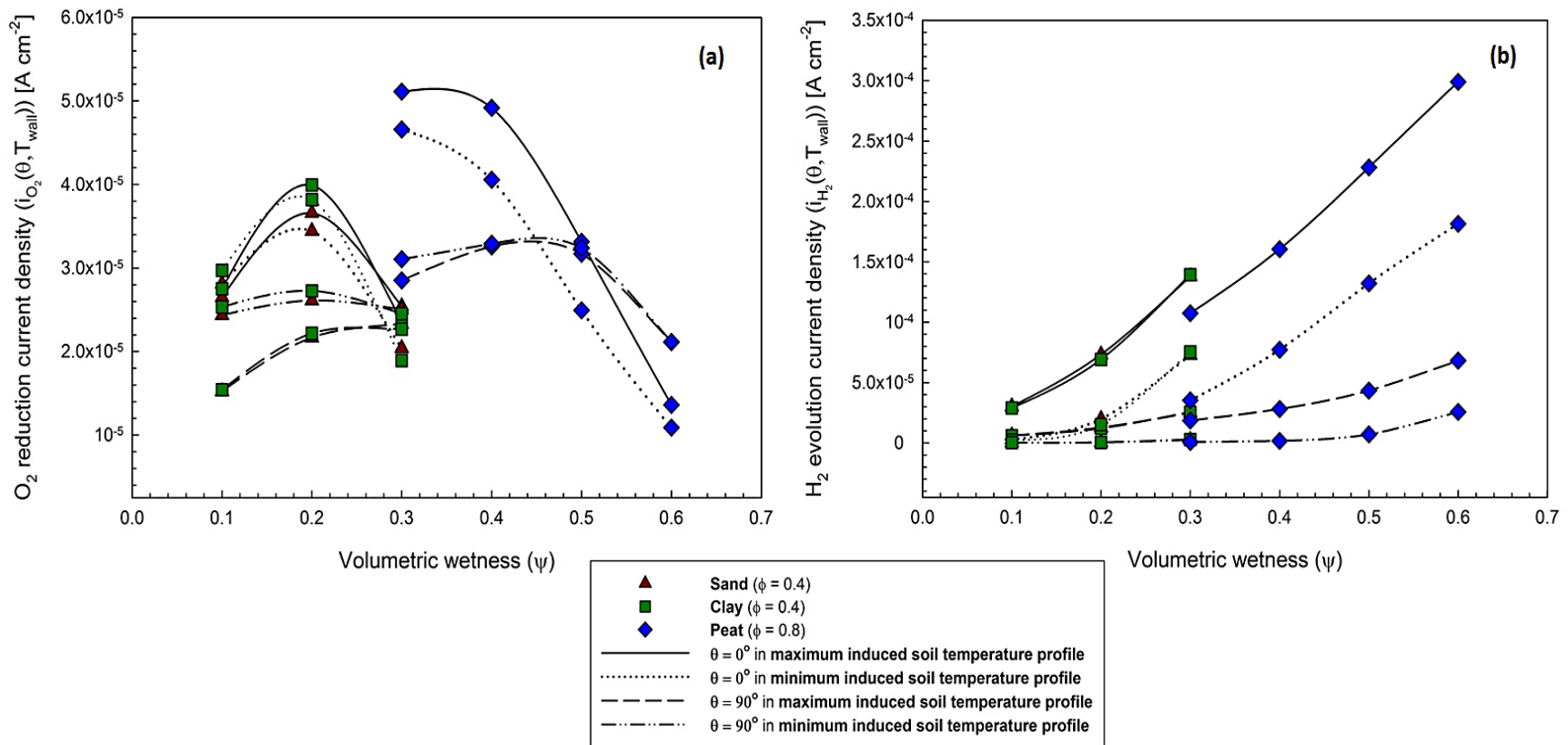


Figure 9-6: (a) i_{O_2} and (b) i_{H_2} , evaluated at $\theta = 0^\circ$ and $\theta = 90^\circ$ in minimum and maximum induced temperature profiles, different soil structures, and ψ using coupled governing equations

9.3.5 Practical CP design applications

The m-model developed here also demonstrates applicability in providing insight on consequences of changes to CP system design, tailored to simulate different soils, initial conditions, geometries, and coating failure locations. A wide range of possibilities are available in this realm, from which the influence of CP anode distance and E_{app} are briefly demonstrated in the following paragraphs.

In Figure 9-7a, E_{Fe} and i_{Fe} at the exposed pipeline surface are simulated for various CP anode distances away from the pipeline. For a prospective coating breakdown location, such a study elucidates whether enough protection is provided at any point on the exposed surface with respect to CP anode placement, and furthermore predicts the rate of cathodic reactions ensuing in these environments (i_{O_2} and i_{H_2} yielded but not shown). Experimental findings are superimposed, revealing that the CP anode need not be placed closer than 1.5 m away from the pipeline for any of the environments simulated. In such simulations, governing simplifications and assumptions in the model influence the exactness of results. For example, the use of a 2D cross-section representation for the overall geometry simplifies the model, but neglects electrical current and O_2 diffusion in the out-of-plane direction (z-axis). This simplification yields less conservative results, as extra current from other anodes or other faces of the sectioned anode itself would most definitely add to the protection of the exposed steel. Similarly, additional O_2 diffusion in the z-axis will likely increase C_{O_2} at coating failure site, albeit followed by its accelerated depletion due to more cathodic E_{Fe} from increased CP currents. Evaluation of the difference between the 2D and 3D representations would require a dedicated study; however, for the 2D results presented here, and based preliminarily on the aforementioned reasoning, a cathodic shift in E_{Fe} of approximately 100 mV (obtained from Figure 9-4b) coupled with a slight increase in C_{O_2} across all ψ (in Figure 9-6) is expected. In the more consequential E_{Fe} result, this represents a difference of 10-15% for the majority of simulated cases, where the 3D results are more conservative.

Conversely, the assumption of perfect coating protectiveness yields simulation values below design requirements. In practice, even the best quality application will produce a coating initially at least 1% less protective than in theory [300]. With time associated breakdown, this number grows to 10% or more, thereby requiring more CP resources to account for the leakage. A design factor of 1.15 or more can accommodate the increased CP needed due to this deterioration, but may lead to overprotection early during the pipeline's service. Instead, the physicochemical properties of coatings should be adopted from material data sheets to develop transient models. Baeckmann et al. have identified the permeation coefficients of H₂O, CO₂, and O₂ in tar, polyethylene, and epoxy coatings (ranging from 0.5 x 10⁻⁹ to 2 x 10⁻⁶ cm² s⁻¹ bar⁻¹), which can be used in governing breakdown equations at coated sites of the pipeline [301]. For advanced design scenarios, the designer may choose to employ further correlations for specific phenomena; nonetheless, a trade-off between model complexity and accuracy must always be made.

Ideally, E_{Fe} should be in the O₂ reduction dominated region of Figure 9-6b, but should provide at least a -100 mV shift from OCP according to industry standards [302]. A -300 mV shift criterion has been criticized in reviews of CP standards as overprotective and inducing of unwanted H evolution [303], a finding corroborated for the environments simulated in this work. The exact level of i_{H_2} vs. i_{O_2} can be obtained for a variety of system design parameters, shown with respect to E_{app} in Figure 9-7b as an example. The arrows indicate the E_{app} at which H evolution rates will exceed O₂ reduction, a convenient margin for determining overprotection. As such, according to recommended NACE criteria for CP design (SP0169 standard [297]), ensuring polarization to a level where Tafel behavior is observed is unnecessary, whereas guaranteeing an E_{Fe} of at least -0.85 V_{Cu-CuSO₄} (-0.77 V_{SCE}) appears to be essential with this analysis. Coupled with field measurements of soils surrounding a buried pipeline, these types of analyses can help determine the correct operating parameters for a CP system to maximize efficiency and safety. The m-model developed herein provides a versatile tool to perform such analyses proficiently.

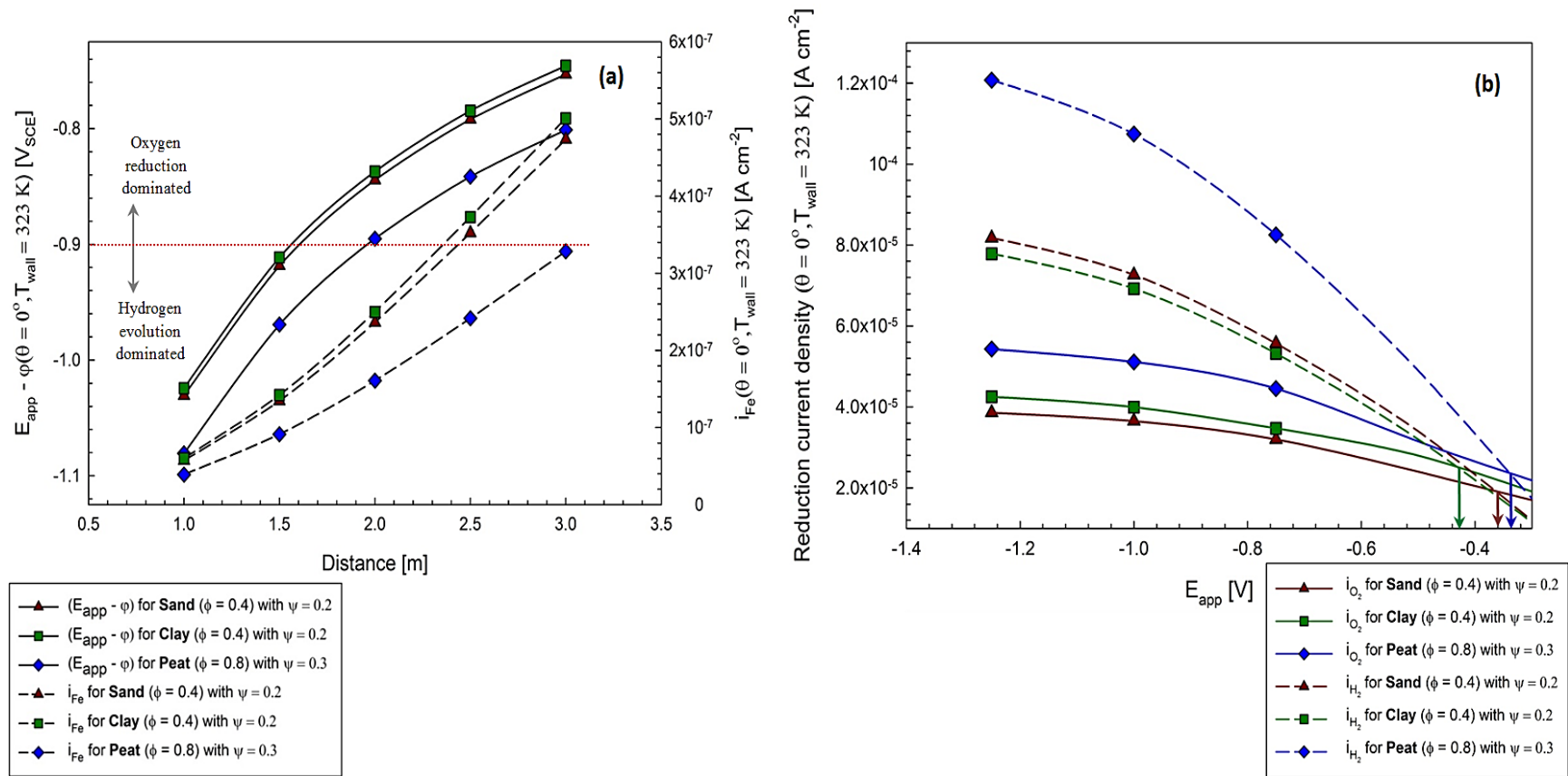


Figure 9-7: Influence of CP design parameters on the model results for simulations at $T_{wall} = 323$ K, $\theta = 0^\circ$, and $\psi = 0.2$ or 0.3 : (a) E_{Fe} and i_{Fe} as a function of CP anode distance from exposed pipeline surface; and (b) i_{O_2} and i_{H_2} as a function of E_{app}

9.4 ϕ evolution, defect growth, and stress analysis in mm-model

9.4.1 ϕ evolution within the disbondment

Corrosion simulations in the mm-model begin with the initial conditions and dimensions outlined in earlier sections, then the applicable governing equations {E-E.1}, {E-E.2}, and {E-12.3} to {E-E.12} are solved within the boundary conditions set for the system. Figure 9-8 illustrates an example result of corrosion defect growth during 150 weeks (~ 3 years), and the evolution of ϕ distribution (for $E_{app} = -1 V_{SCE}$, $T_{wall} = 25^\circ C$, and $w = 1$ mm). The ϕ outside the disbondment in Figure 9-8 remains nearly constant within the 3 year simulation, whereas it is seen that the ϕ drop within the 20 cm long coating disbondment is approximately 600 mV. Based on the E_{app} for this condition, the corresponding range of effective CP for $0 \text{ cm} \leq x \leq 20 \text{ cm}$ is $-1.2 V_{SCE} \leq E_s(x) \leq -0.60 V_{SCE}$, matching well with the potential distributions reported on page 2321 in [26] using measurements on a CP-shielded electrode.

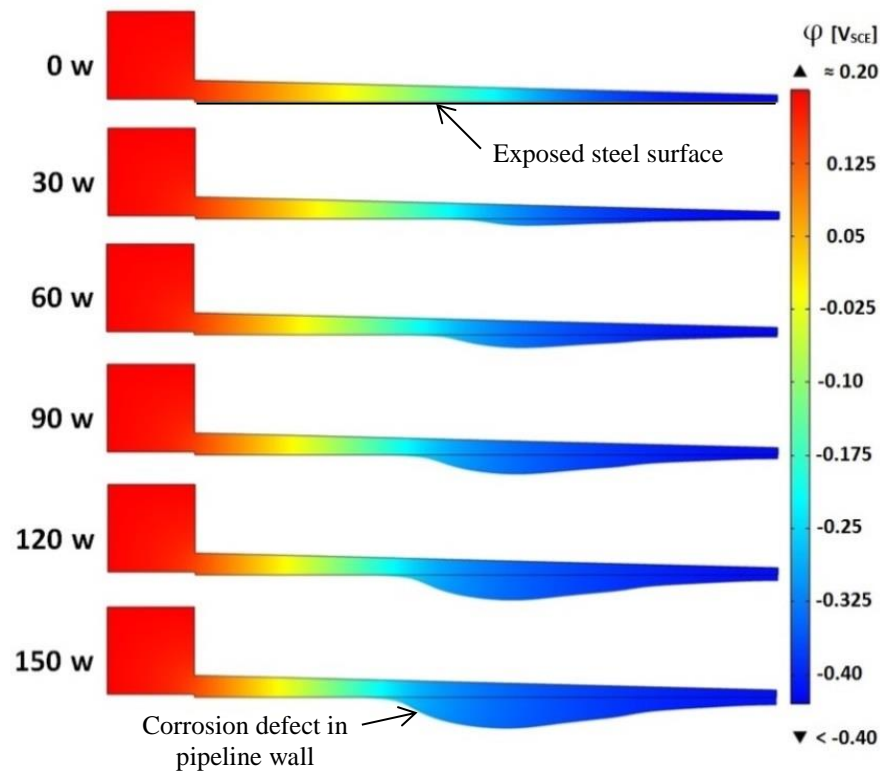


Figure 9-8: Timeline of corrosion defect growth into the exposed steel surface and ϕ evolution throughout the 150 week exposure, for $E_{app} = -1 V_{SCE}$, 1 mm coating disbondment opening, and $T_{wall} = 25^\circ C$

On page 3752 in [294], using an experimental CP setup to mimic a disbondment, it was found that after 90 days of exposure the potential of the steel-electrolyte interface barely registers a 15 mV drop at the deepest point in a 15 cm long disbondment. In comparison, in Figure 9-8 above the loss of CP reach amounts to almost 100 mV over the 3 year period based on the leftward shift of ϕ within the disbondment by nearly $L/5$. This potential drop translates to a rate of approximately 10 mV per 90 days, assuming the rate is linear throughout the 3 years simulated. Thus, the simulated potential drop results generally equal experimental counterparts, and minor discrepancies are likely the result of differences in system conditions such as disbondment length (15 cm vs. 20 cm) and electrolyte composition (C2 vs. NS4 solution).

9.4.2 Growth of corrosion defect and implications on structural integrity

It is clearly seen from the defect shape that the most corrosion (maximum defect depth, d_{defect_max}) occurs in the middle section of the exposed surface, followed by the furthest section in the disbondment. At $0 \text{ cm} \leq x \leq 5 \text{ cm}$, CP can be considered as completely unshielded judging from $\phi \approx 0 \text{ V}_{SCE}$ ($E_s(x) \approx -1 \text{ V}_{SCE}$). This causes suppression of i_a to 10^{-6} and even 10^{-7} A/cm^2 levels, resulting in metal loss not occurring before $x = \sim 5 \text{ cm}$ for any E_{app} and geometry combination (Figure 9-9). The coupled high i_c levels therein produce a more alkaline local environment due to the ensuing water reduction reaction. This has a compound effect on the penetration rates in this region, further decreasing i_a based on the pH proportionality of {E-E.6}. It is particularly notable where the first metal removal from the wall is observed for the conditions simulated in Figure 9-8 at 30 weeks exposure (shown in Figure 9-9a also) – it starts to appear at 8 cm and a corresponding $\phi \approx -0.2 \text{ V}_{SCE}$ ($E_s(x) \approx -0.8 \text{ V}_{SCE}$). This $E_s(x)$ coincides directly with the OCP results, at which i_a first surpasses i_c . Above this, in both 25 and 50 °C conditions, the rate of i_a increase is substantial (Figure E-1c), explaining why the d_{defect_max} is reached only a short distance further into the disbondment ($x = 10 \text{ cm}$ at 30 week triangle data point in Figure 9-9a).

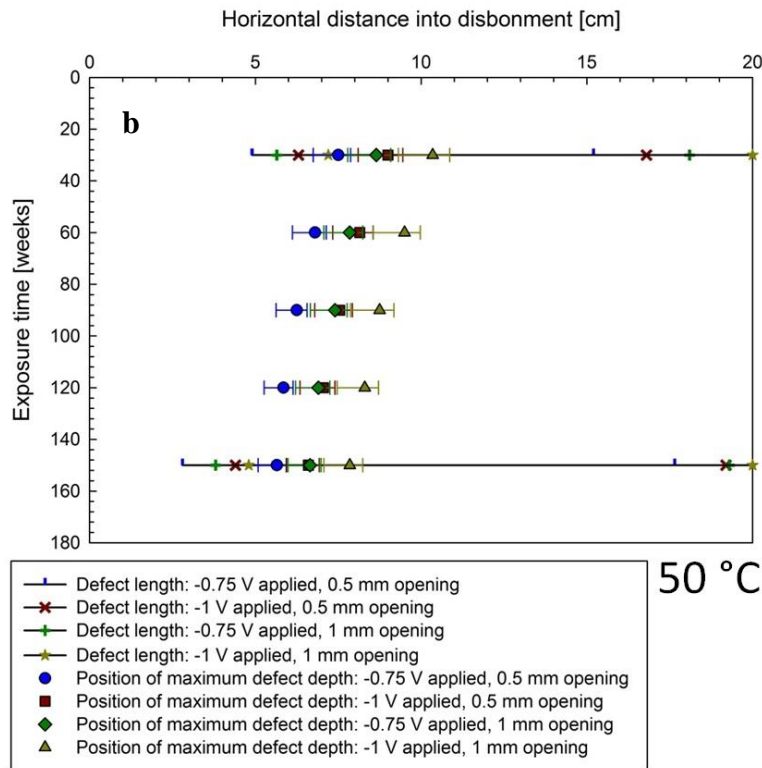
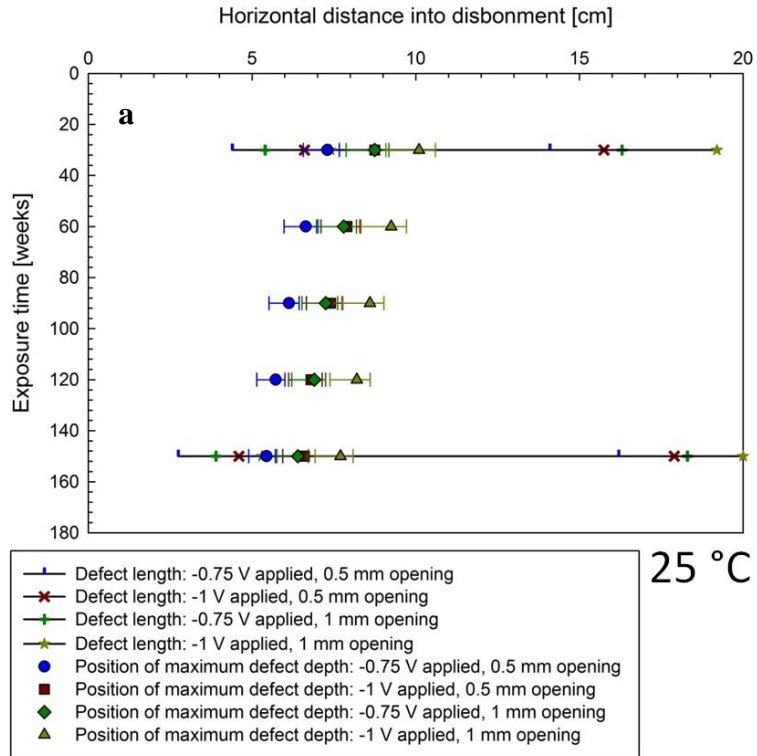


Figure 9-9: Length of corrosion defect (l_{defect}) [mm] along exposed steel surface and x -position of d_{defect_max} (maximum defect depth) [mm] reached during 0 – 150 weeks of exposure, for all E_{app} , coating disbondment opening, and T_{wall} values simulated: (a) $T_{wall} = 25\text{ °C}$, (b) $T_{wall} = 50\text{ °C}$

Beyond the x location of d_{defect_max} in Figure 9-8, d_{defect} becomes shallow again as it approaches L . This behavior contradicts the expectation that the highest corrosion rate, causing the most metal loss, would simply occur at the location with the least CP level (i.e. $x = 20$ cm). Yet, the defect shapes simulated here agree with experiments which measure corrosion rates of pipeline steel in CP shielded situations [27], [177]; such studies report the existence of a critical region between $x = 0$ and $x = L$ where conditions for formation of large corrosion pits and surface microcrack are favorable. In Figure 9-8, the ϕ distributions reveal that the drop in potential beyond the first metal loss point in the disbondment (~ 150 mV) is dwarfed by that before it (~ 450 mV). The drop beyond d_{defect_max} becomes even less, agreeing with the experimental measurements of [294, p. 3752] where the potential was virtually unchanged beyond 9 cm in a 15 cm disbondment. As such, CP levels at $x = 20$ cm are not significantly less than those around $x = 11$ cm. Hence, if i_a values were solely dependent on $E_s(x)$ the penetration depth would be almost equal beyond $x = 11$ cm.

The reason why $d_{defect_max} > d_{defect}(x = 20\text{cm})$ in Figure 9-8 is therefore left to be because of variations in local pH causing $i_a(x = 20\text{cm}) < i_a(d_{defect_max})$, pH differences which are due to the unequal %CO₂ levels within the disbondment. Through experiments, corrosion rates under disbonded coating have previously been shown to be affected by CO₂ through the rate of CO₂ generation and production in the disbondment, and preferential gas-phase transport of CO₂ [18]. As CO₂ concentration decreases with larger x , corrosion rate under the aqueous boundary layer also decreases as shown by numerous previous works [36], [140], [304]. The decreasing corrosion rate distribution due to CO₂ concentration, overlapped with the increasing corrosion rate distribution due to CP reach, results in the x location of d_{defect_max} being near the middle of the disbondment where the net corrosion rate is the highest (referred to as “sweet spot” [27]). It is also likely that the acidification of the electrolyte (a well-established and proven phenomena in pits and crevices [55]) in the d_{defect_max} region further accelerates its growth.

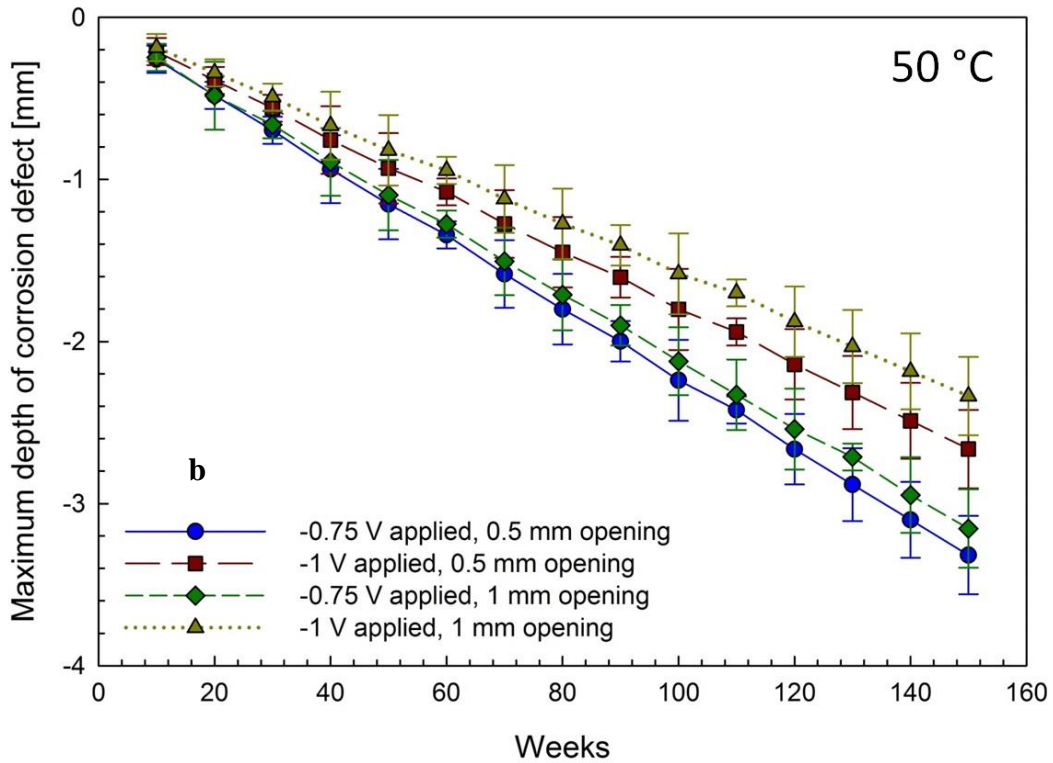
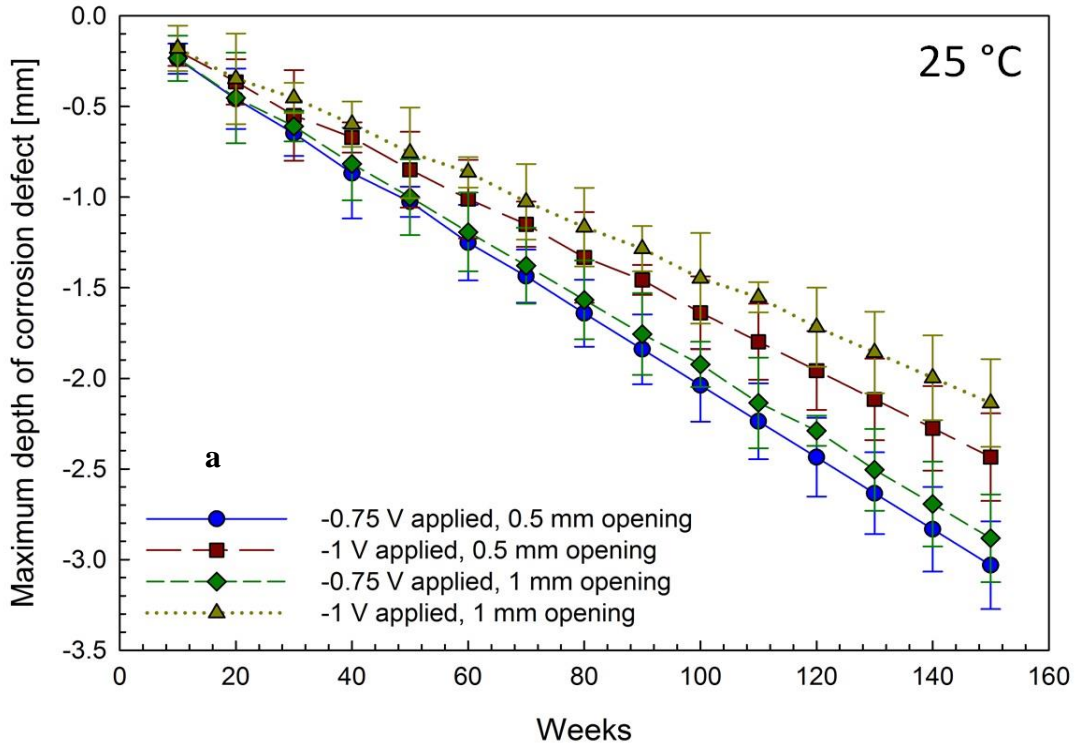


Figure 9-10: Maximum depth [mm] of corrosion defect (d_{defect_max}) below original steel surface from 0 – 150 weeks of exposure, for all E_{app} , coating disbondment opening, and T_{wall} values simulated: (a) $T_{wall} = 25$ °C, (b) $T_{wall} = 50$ °C

With increased exposure time, the x position of first metal loss and d_{defect_max} move closer to the disbondment opening in all simulations (Figure 9-9a and Figure 9-9b). The confidence interval for all the data points in Figure 9-9 and Figure 9-10 illustrate the effect of coarsening and refinement of the normal mesh resolution. The defect length (l_{defect}) is also increased through extension of the corrosion to deeper x coordinates within the disbondment. This is shown only for 30 weeks and 150 weeks exposure times in Figure 9-9, whereas the remaining times in between show the x coordinates of d_{defect_max} for each condition. Confidence intervals represent the range of results obtained from different mesh resolutions. Higher E_{app} and a larger w dimension shortens l_{defect} and pushes the x location of d_{defect_max} further into the disbondment for all simulated conditions; both findings are an expected consequence of more CP reach and strength. Similarly, the leftward movement of d_{defect_max} and the growth of l_{defect} with time are the direct result of weaker CP levels due to the increased distance travelled in reaching the deepening defect surface. When the σ of the electrolyte increases with temperature, the x locations of first metal removal and d_{defect_max} are shifted further into the disbondment and l_{defect} becomes larger. This is although the depth of the overall corrosion defect and d_{defect_max} increases due to faster anodic kinetics with temperature.

Figure 9-10a and Figure 9-10b show the transient growth in d_{defect_max} for all the environments simulated during 150 weeks, with confidence intervals illustrating the change in results for different mesh resolutions. The numerical results are listed for 50 and 150 weeks in Table E-4 in Appendix E. The growth in d_{defect_max} is linear for all the conditions simulated, with 50 °C depths being slightly greater than the 25 °C counterparts. This is attributed to faster reaction kinetics with temperature. With an i_a of $\sim 10^{-4}$ A/cm² at the $E_s(x)$ and pH conditions present at the coordinates of d_{defect_max} , R_{steel} in {E-E.10} = ~ 1 mmpy using an equivalent (A_w/n) ratio to account for the alloying of X100 [124] (calculated previously as 27.66 g/mol [74]) and a density ρ_{Fe} of 7.75 g/cm³ for the material. Based on this calculation, the maximum penetration

rates of ~3 mm in 3 years simulated by the model are valid in comparison with experimental results.

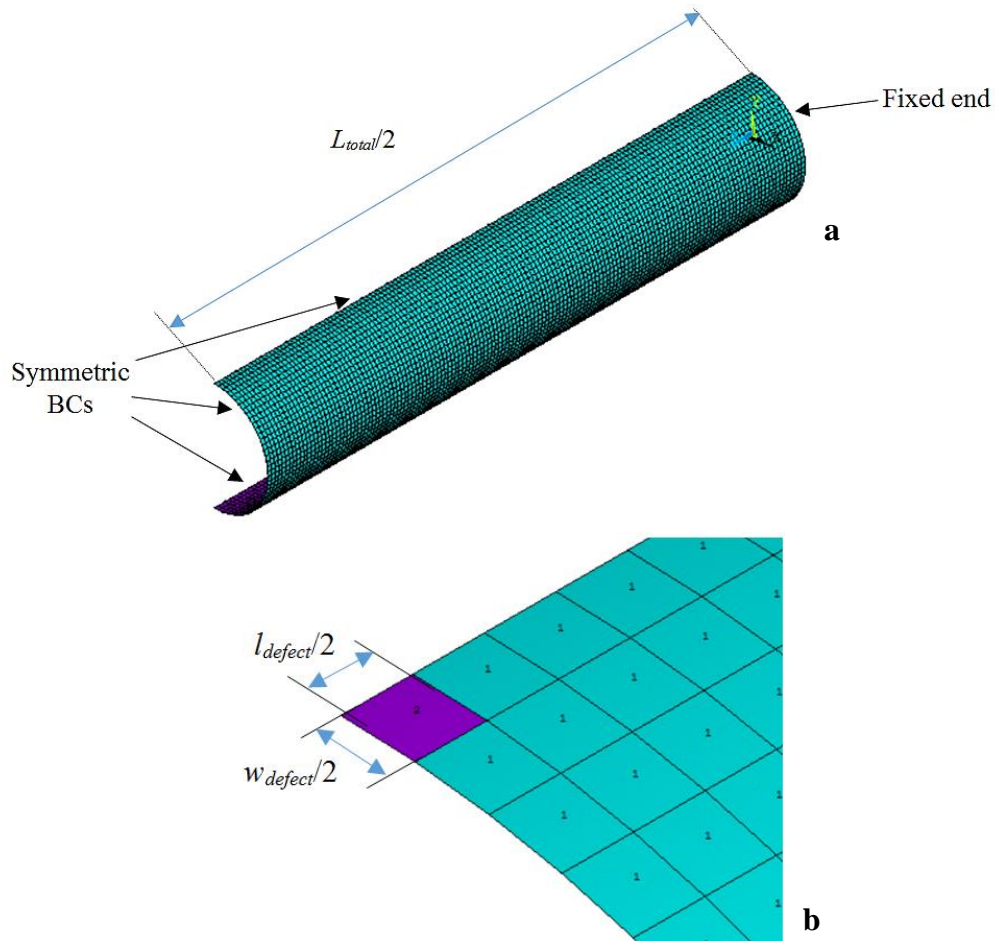


Figure 9-11: 3D representation of: (a) intact pipe FEM with shell elements; (b) corroded pipe section used to simulate structural integrity based on the defect dimensions resulting from the corrosion module

Also in Figure 9-10a and Figure 9-10b, the order of depth severity follows the rational trend of more CP reach and strength with greater E_{app} and larger w . The results, further observed in Table E-4, reveal the stronger influence of E_{app} on limiting the corrosion. With the values considered for these parameters here, a lower E_{app} is more detrimental than a larger w . The findings also highlight the consequential impact of seemingly small changes in system geometry and initial conditions on final corrosion defect size and shape. The difference between the smallest and largest d_{defect_max} is ~30% within 3 years. This is a significant change in wall

thickness during a time frame considered to be relatively short for large pipeline infrastructure. This gap continues to widen with more exposure time and has strong implications on structural integrity. Using the mechanical properties for X100 steel shown in Table E-5 in Appendix E, a pipeline diameter of $D = 0.2$ m, a total length for the analyzed section of $L_{total} = 2$ m, and a wall thickness of $t = 0.02$ m, the burst pressure (P_b) of the pipeline section in Figure 9-11 is simulated for the 3 year defect size dimensions of Table E-4. The width of the defect in the circumferential pipeline direction is not simulated in the corrosion module, hence it is kept as a constant 0.016 m in all cases. Circumferential width of corrosion defects has been shown to have a minor influence on P_b , which does increase with the growth of its ratio over l_{defect} but is always less influence than the influence of d_{defect_max} [146], [148], [151]. A FEM using shell elements is used to conduct this structural analysis, and case symmetry is exploited to minimize computational power and solving time through using a quarter pipeline section as seen in Figure 9-11. The P_b results from the shell model are divided by corresponding burst pressure for intact (i.e. uncorroded) pipeline denoted P_{bi} , which are calculated through {E-9.18} from the established ASME B31G code, where σ_y is the pipeline material's yield stress at 0.5% offset strain, t is the wall thickness, and D is the outer diameter ($D = 2R$, R : outer radius) [305], [306]:

$$P_{bi} = (1.1\sigma_y \cdot 2t)/D \quad \{\mathbf{E-9.18}\}$$

The resulting ratio values seen in Table 9-7 are compared to an empirical ratio developed by Netto et al. [146] based on detailed experimental and numerical results ({E-2.7} in section 2.4.2, reproduced here as {E-9.19} with the same parameter denotations). This formulation correlates well with the experimental test results in [146], and confirms conservatism of previous B31G and DNV codes as illustrated previously in Figure 2-13 of the literature review.

$$\frac{P_b}{P_{bi}} = 1 - 0.9435 \left(\frac{d}{t}\right)^{1.6} \left(\frac{l}{D}\right)^{0.4};$$

$$\frac{c}{D} \geq 0.0785, 0.1 \leq \frac{d}{t} \leq 0.8, \text{ and } \frac{l}{D} \leq 1.5 \quad \{\mathbf{E-9.19}\}$$

As seen in Table 9-7, the stress analysis results from the shell FEM yield values within approximately 6% of the experimentally validated formulation. The structural integrity of the pipeline simulated in this analysis, measured by its burst pressure, is diminished by approximately 7% - 8% after 3 years of an external coating disbondment with the E_{app} , w , and T_{wall} combinations shown in Table E-4. This brief synopsis of the stress analysis module of the mm-model serves to show its practical usability in conjunction with corrosion module, and the validity of its results compared to well-documented empirical structural integrity formulations. However, further discussions of this stress analysis module in the mm-model and the results obtained therein are beyond the scope of this thesis.

Table 9-7: Comparison of P_b/P_{bi} ratio results obtained from {E-9.19} versus those from the shell element FEM of Figure 9-11, using corrosion defect values simulated from the corrosion module of the mm-model

d_{defect_max} [mm]	l_{defect} [mm]	P_b/P_{bi} {E-9.19}	P_b/P_{bi} (Shell element FEM of Figure 9-11)
3	13.5	0.9850	0.9220
2.9	14.4	0.9847	0.9201
2.4	13.3	0.9896	0.9368
2.1	14.7	0.9913	0.9307
3.3	14.9	0.9820	0.9095
3.2	15.5	0.9826	0.9097
2.7	14.8	0.9869	0.9245
2.3	15.2	0.9898	0.9334

9.5 Model convergence through mesh sensitivity analysis

To confirm that the mesh resolutions used to obtain the results discussed above are appropriate, simulations for all conditions are repeated with the coarser and finer meshes described in Table 4-2 and Table E-1 for the m-model and mm-model, respectively. In the mesh sensitivity study conducted for the m-model, stable convergence of all parameters is found as shown in Figure 9-12 for i_{O_2} and i_{H_2} results at $T_{wall} = 323$ K (50 °C), $\theta = 0^\circ$, and $\psi = 0.2$ or 0.3 (C_{O_2} , E_{Fe} , and i_{Fe} are not shown). Other ψ , θ , and temperatures follow the same convergence trend. Both i_c values in Figure 9-12 increase by upwards of 1×10^{-5} A/cm² between extra coarse and extra fine meshes in peat, whereas the change is slightly less for sand and clay structures. All

profiles reach a nearly horizontal plateau at finer resolutions, indicating close proximity to the theoretical, most accurate solution. Convergence to this solution occurs at a high rate initially, then gradually asymptotes at finer resolutions in a manner characteristic to well-discretized finite element models [307]. Deviance of the normal mesh from the horizontal asymptote (i.e. $\% \Delta$ in Figure 9-12) is less than 5% for most cases, representing an acceptable 95% confidence for the simulation results. Thus, reduced solution times and computing resources required to solve the normal mesh resolution vs. the extra fine mesh resolution do not come at a significant expense of solution accuracy.

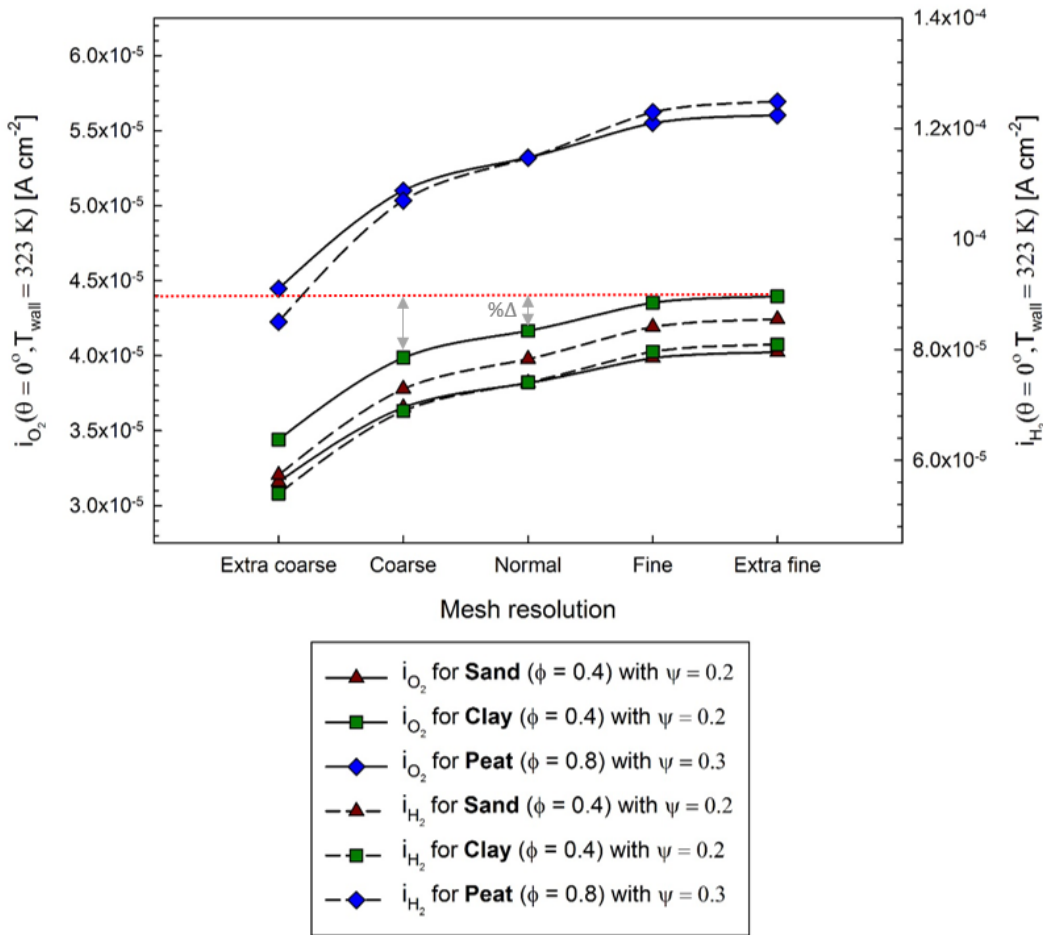


Figure 9-12: Convergence profiles for i_{O_2} and i_{H_2} results (at $T_{wall} = 323$ K, $\theta = 0^\circ$, and $\psi = 0.2$ or 0.3) using extra coarse to extra fine mesh resolutions in m-model

Similarly for the mm-model simulations, to verify the suitability of the resolutions used a convergence study is conducted for average E_s values of the entire exposed surface at 25 °C

$(E_{s_average}(25\text{ °C}) = E_{app} - \sum_i^L \varphi(x_i, 25\text{ °C}))$, in each E_{app} , w , and mesh resolution combination. Stable convergence of all results is seen throughout (Figure E-3 in Appendix E), characterized by a decreasing slope at finer mesh resolutions. Deviation of the coarse mesh results ($\Delta E_{s_average(C-F)}$) and normal mesh results ($\Delta E_{s_average(N-F)}$) from the fine mesh results is by approximately 1.25% and 5%, respectively. Considering that the most accurate solution is theoretically obtained at a point where mesh resolution refinement induces negligible change on the simulation results, the accuracies of the coarse and normal mesh resolution simulations by the mm-model are above 90% and 95%, respectively. Based on the rate of $\Delta E_{s_average}$ decline shown in Figure E-3, values of $\Delta E_{s_average} < 1\%$ are certainly anticipated at extra fine resolutions containing maximum element sizes on the order of 10^{-5} m, both in the electrolyte region and at the exposed steel surface. User discretion is required based on the level of accuracy needed and the computing power available; nevertheless, it is shown here that errors $< 1\%$ are achievable and model convergence is upheld within a wide range of practical mesh resolutions.

9.6 Summary

In this chapter, the external corrosion of buried steel pipeline sections at a coating breakdown site is simulated using meter-scale and millimeter-scale FEM, developed using both theoretical and experimental inputs and governing equations for the modelled phenomena. In the steady-state m-model, soils of different physicochemistry and aeration are assessed and the governing behaviors of interrelated heat transfer, CP, O₂ diffusion, and reaction kinetics effects are simulated. Laboratory corrosion experiments conducted on a X100 pipeline steel specimen reveal intricate temperature- and cathodic E -dependent behaviors where combined diffusion-activation control of corrosion processes is present. Integration of these experimental findings in the formulations of the m-model significantly changes simulation results; uncoupled simulations which use generic parameters yield conservative results compared to their coupled counterparts which use experimentally-derived formulations. Corrosion increases in dry and cold soils at sites

farther away from CP anodes due to a combination of CP deficiency, enhanced gas transport, and accelerated reaction kinetics. Nonetheless, for the common CP and pipeline system dimensions modelled, corrosion rates at the relatively large coating failure site are successfully suppressed by CP currents to below 1 mpy in most conditions. When combined with a higher moisture content to fill the pores, higher air porosity soil structures increase conductivity to allow better CP protection of exposed surfaces. The m-model is used in this chapter to determine appropriate anode placements and applied E to maximize efficiency and evade CP overprotection, highlighting the importance of the standard $-0.85 \text{ V}_{\text{Cu-CuSO}_4}$ NACE CP design criterion. These forms of practical analyses can be extended rapidly to other customizable environments and geometries, a feature which signifies the practical benefits which the developed model can provide operators and designers.

For the smaller scale of the coating disbondment and trapped water region, an integrative numerical simulation approach for pipeline integrity analysis is also presented in this chapter. This is achieved through the combination of a transient corrosion FEM module with a shell-element stress analysis in a structural FEM module. In the former, potential distributions in the trapped water existing beneath pipeline coating disbondments are modelled in conjunction with reaction kinetics on the corroding exposed steel surface using a moving boundary mesh. Temperature dependencies (25 & 50 °C) of reaction kinetics do not greatly affect final corrosion defect geometries after the 3 year simulation period. Conversely, CP levels and pH dependencies within the nn-pH range (6.7 - 8.5) strongly govern depth profiles caused by corrosion, reaching a maximum of ~3 mm into the pipeline wall. A 0.25 V amplification of CP potential combined with a 0.5 mm widening in disbondment opening size reduces defect penetration by almost 30%. Resulting corrosion defect geometries are imported into the structural analysis module stress examinations and burst pressure evaluations. Burst pressure values yielded by the stress analysis module are within approximately 6% of an experimentally validated formulation in the literature. Consequently, the structural integrity of the pipeline simulated in this chapter, measured by its

burst pressure, is diminished by approximately 7% - 8% after 3 years of an external coating disbondment with the CP, disbondment geometries, and physicochemical parameter values (e.g. temperature) used. The simulation results compare favorably to well-documented empirical structural integrity formulations.

10. Conclusions

10.1 Key contributions and broad implications

The novel environmental, surface/interfacial, hydrogen-related, and numerical modelling aspects of HSLA steel corrosion in nn-pH soil environments presented in this thesis contribute to a more complete understanding of corrosion mechanisms therein. The investigated material throughout this thesis is API X100 steel; being one of the newer alloys used in oil and gas transmission pipelines, its examination to better comprehend corrosion mechanisms which are not completely grasped until now adds further value to the findings. Overall, the contributions and broader implications to the fields of corrosion science and pipeline integrity made by the results of this work can be summarized in the following:

1. Throughout this thesis, it has been repeatedly shown that variations *within* the nn-pH range of electrolytes relevant to the external corrosion and SCC of pipelines greatly control the corrosion, passivation, adsorption, diffusion, and inhibition of exposed steel sections at coating failures. Judging from the use of a single pH, %CO₂, and ionic constituent electrolyte to simulate such environments in previous works, these consequential variations are largely ignored in such studies although they should warrant much more detailed attention.

Implications: The nn-pH environment range is itself a broad categorization which includes at least three “sub-ranges” with different corrosion behaviors in each. This thesis lays the groundwork for understanding the fundamental electrochemical processes occurring in each of these sub-ranges. These processes govern the overall behavior of the corroded pipeline structure, specifically with respect to its mechanical failure mechanism. Future works on nn-pH external pipeline corrosion should therefore completely shun the notion of a *single* simulated trapped water environment, and rather embrace the more accurate and representative concept of the *dynamic* concentration cell environment.

2. The results in chapters 5 - 7 attest that although the development of strongly passive corrosion products is unlikely in practical nn-pH electrolytes, weak passivation and passive-like corrosion products form in environments well within the nn-pH range. These products need not be created by $[\text{HCO}_3^-]$ greater than the standard level yielding a pH = 6.7 (i.e. 5.75×10^{-3} M), as confirmed by the results of experiments in dilute HCO_3^- , mildly alkaline environments with 0% CO_2 or with 5 ppm O_2 . Experiments reveal that both the pH of the environment and the synergistic effect of Cl^- and SO_4^{2-} are critical in spurring $\text{Fe}(\text{OH})_2$, FeCO_3 , and even $\text{Fe}_3\text{O}_4/\gamma\text{-Fe}_2\text{O}_3$ products in the presence of only trace $[\text{O}_2] < 1$ ppm.

Implications: Previous considerations of the nn-pH corrosion and SCC mechanism as being entirely uninfluenced by corrosion product of any passivation strength are incomplete and lacking. In fact, the nn-pH corrosion and SCC mechanism is influenced by the formation of weak and unstable passivation product(s), contributing to the distinctive distribution of corrosion defect severity beneath disbonded coatings.

3. The experimental results in chapter 7 and the modelling results in chapter 9 strongly indicate that the diffusivity of O_2 in both the local nn-pH electrolyte underneath disbonded coatings and the bulk external electrolyte of the soil controls the corrosion evolution of buried pipeline steels in O_2 -containing environments. This thesis has also provided the preliminary groundwork for the use of O_2 -scavenger treatments in eliminating O_2 -driven corrosion through cathodic and anodic inhibitor mechanisms, the latter of which involves the formation of a protective passive film on the steel surface.

Implications: In addition to factors like temperature and soil moisture, the porosity of either surface layers forming on the exposed steel or the bulk soil structure can be used to determine the severity and evolution of the external corrosion of buried pipelines. The porosities of corrosion products do not only govern the corrosion rate of the steel

substrate, but they also determine which compounds form and how the surface evolves over time. This finding has been largely overlooked in most studies prior to this work.

4. The results of experiments on hydrogen-related processes in chapter 8 further confirm the implication mentioned in point 1; that is, “sub-ranges” in the overall nn-pH range yield different redox conditions and corrosion behaviors. With regards to hydrogen and cathodic processes, this is shown to be differences in the specific involvement of H_2CO_3 , H^+ , H_2O , HCO_3^- , or CO_3^{2-} in hydrogen evolution kinetics at different pH and cathodic potential levels arising from CP shielding. Also, this thesis is the first to identify the diffusible hydrogen concentration in the X100 steel alloy at E -pH levels relevant to the nn-pH external corrosion and SCC phenomena.

Implications: Hydrogen is shown to have a strong contributing role in the transgranular SCC mechanism of pipeline steels, including X100 in environments relevant to those encountered in service. Sub-surface hydrogen concentrations in corroding X100 pipeline steel do not decay to zero even if no CP is present (i.e. the steel is freely corroding or at OCP). Based on previously established critical hydrogen concentrations which cause embrittlement of the X100 alloy, excessive applied CP voltages or improperly designed CP systems (such as incorrect anode placement) can indeed cause a significant loss of toughness in modern pipeline structures made of this material.

5. The meter-scale model and simulations in chapter 9 are the first to incorporate documented soil heat transfer, O_2 diffusion, and CP behaviors with experiment-based corrosion reaction kinetics in one integrated package. The significant improvement of simulation accuracy and validity, as consistently revealed in the “uncoupled” vs. “coupled” results, is an important contribution in the field of pipeline corrosion modelling.

Implications: Accurate simulation of external pipeline corrosion in a wide range of soil, environment, climatic, dimensional, CP, and pipeline system parameters is possible with

an experimentally-validated Finite Element Model. Without this intrinsic validation provided by experimentally-proven governing correlations and data, simulation results are largely inadequate and are most likely useless in any practical sense. Thus, it is suggested that the development of corrosion or pipeline models always be founded on correlations and results extracted from laboratory experiments or field data to be worthy. In this respect, it is important to remember the words of the renowned statistician George Box regarding modelling: “essentially, all models are wrong, but some are useful”!

6. The millimeter-scale model in chapter 9 is the first to integrate an experiment-based corrosion model with structural analysis to evaluate pipeline integrity and residual strength of corroded underground pipelines. In contrast, other structural models rely on generic or assumed values for external corrosion defect dimensions. Results of the corrosion module of this model corroborate the existence of subsections underneath the disbondment with combinations of pH and CP reach which yield non-uniform corrosion defect shapes.

Implications: The accurate transient simulation of corrosion defect growth beneath disbondments and its time-dependent effect on pipeline integrity is possible with Finite Element Modelling. With further development of the model presented in this work, it can eventually become a specialized tool for the complete corrosion and structural analysis of critical buried pipeline sections. An accurate predictive analytics software like this is needed for pipeline corrosion integrity management (PCIM) and can hence be very valuable to pipeline operators.

10.2 Summary of important technical findings

The goal of this work was to contribute to a comprehensive understanding and modelling capability of the corrosion of X100 pipeline steel in nn-pH soil environments. The contributions and overall implications of this work have been presented in the previous section. The results of the laboratory experiments and numerical simulations of this work, presented in chapter 5 through chapter 9, elucidate the criticality of environmental and surface conditions on the external corrosion of X100 steel and the subsequent presence and properties of passive layers formed. This section lists the important technical findings from experiments, analysis, and modelling of fundamental corrosion processes occurring across the full nn-pH range of HCO_3^- electrolytes:

- In O_2 -free environments and where CP is completely shielded from the metal surface, the corrosion of X100 decreases linearly with pH at all temperatures if the $[\text{HCO}_3^-]$ in the environment is not greater than $5.75 \times 10^{-3} \text{ M}$ (i.e. the $[\text{HCO}_3^-]$ in standard NS4 solution).
 - When pH increase is created by decreasing $\% \text{CO}_2$, the overall trend in behavior implies increased corrosion at lower pH due to accelerated hydrogen evolution cathodic reaction(s) *not involving* HCO_3^- and CO_3^{2-} species. Cathodic polarization studies indicate that at OCP, hydrogen evolution due to direct water reduction is the dominant reaction in O_2 -free and CO_3^{2-} -free solutions
- Conversely, in O_2 -free and CP-shielded environments, the corrosion of X100 increases with increased $[\text{HCO}_3^-] > 5.75 \times 10^{-3} \text{ M}$, even with a corresponding increase in pH.
 - Mildly alkaline HCO_3^- -rich environments, specifically those with $\text{pH} > 7.6$, manifest an opposite trend of increased corrosion rate with alkalinity due to accelerated hydrogen evolution cathodic reaction(s) *involving* HCO_3^- and possibly CO_3^{2-} at even higher pH. Cathodic polarization studies indicate that at potentials less than OCP, hydrogen evolution due to HCO_3^- discharge is thermodynamically inevitable and gradually dominates the other cathodic reactions which occur at OCP.

- In O₂-free environments, passive or passive-like corrosion products only form in solutions with [HCO₃⁻] > 5.75 x 10⁻³ M, *except* for mildly alkaline 0% CO₂ situations. In these situations, increased [OH⁻] creates a weak Fe(OH)₂ film which can easily break down with small changes in potential or solution constituents, specifically the increase of Cl⁻ and SO₄²⁻ concentrations in the groundwater. Experiments also show that in dilute HCO₃⁻ nn-pH electrolytes, the formation of FeCO₃ or Fe(OH)₂ likely does not occur in single reaction steps through the complexing of Fe²⁺ with CO₃²⁻ or OH⁻. Rather, the adsorption of HCO₃⁻ and OH⁻ and the formation of pre-passive complexes are necessary prior to the formation of FeCO₃ or Fe(OH)₂. This finding clarifies the mechanism behind corrosion rate changes which are observed in the presence of Cl⁻, SO₄²⁻, or NO₃⁻ in groundwater or trapped water electrolytes.
- Potentiodynamic polarization results coupled with chemical characterization analysis indicate that at medium range potentials, iron carbonates form in solutions with a pH ≥ 7.53, and iron oxides of different phases form in solutions with a pH ≥ 7.78 under the influence of Cl⁻/SO₄²⁻.
- The synergistic effect of Cl⁻ and SO₄²⁻ previously identified in the literature is confirmed, even in tests conducted at OCP. This means that the severity of X100 corrosion in nn-pH electrolytes is significantly higher in mixed anion solutions containing combinations of Cl⁻, SO₄²⁻, NO₃⁻, and/or HCO₃⁻ than it is in solutions containing equivalent concentrations of any of these anions individually. Moreover, passive layer breakdown and Fe₃O₄/γ-Fe₂O₃ formation over FeCO₃ are found to be highly dependent on the presence of Cl⁻ and SO₄²⁻, as have been observed clearly with SEM.
- Electrochemical processes on X100 in O₂-free environments and where CP is completely shielded from the metal surface can be classified into three categories based on subsets of the nn-pH range:

- **Acidic solution of pH < 6:** adsorptive and/or diffusive effects outside the capacitive double-layer are essentially absent. Passivation of the corroding steel surface is unlikely and corrosion rate is the most severe.
- **6.5 ≤ pH < 7.7:** adsorption processes appear, although their dominance decreases with the presence of Cl⁻ and/or SO₄²⁻. Passivation of the corroding steel surface is likely over time, hence reducing the severity of the metal's corrosion rate.
- **Alkaline solutions of pH ≥ 7.7:** mass-transfer behavior manifests in the interfacial processes, and the diffusion of complex ions controls the corrosion rate of the X100 steel. Unless the [HCO₃⁻] > 5.75 × 10⁻³ M, the corrosion rate of X100 is mild in comparison with the other pH sub-ranges.
- In environments conducive to the development of passive corrosion products, pre-passive, active-passive transition, and passive layer breakdown potential regions exhibit different adsorption and diffusion behaviors. Dynamic EIS in the chronological order of these potential regions quantifies the occurrence of these auxiliary electrochemical processes and specifically identifies the role of Cl⁻/SO₄²⁻ in increasing corrosion rate, decreasing pre-passive diffusion, and decreasing passive layer protection.
- The protectiveness of passive layers, when present, improves in colder, more alkaline, and more HCO₃⁻-rich environments. Dependencies on [HCO₃⁻] and temperatures are further supported by Mott-Schottky tests of semiconductive properties, which identify: increased donor densities, increased flat-band potentials, and decreased space-charge layer thicknesses with pH, [HCO₃⁻], and colder temperatures.
- Tubercles of FeOOH (both γ and α phases) form within 24 h in all nn-pH HCO₃⁻-based environments containing [O₂] > 5 ppm, with markedly higher porosities in conditions with lower dissolved [O₂]. Fe₃O₄, FeCO₃, and Fe₂O₃ are also identified in the corrosion product, the latter forming almost exclusively in ~5 ppm O₂ conditions which develop

- tubercles with noticeably higher porosities. Lower diffusivity of O_2 in the more compact tubercles formed in 20 ppm O_2 conditions is detected by EIS modelling results.
- In cases where it forms, the insulating properties of Fe_2O_3 causes a sharp decrease in corrosion rate after around 7 h immersion, which otherwise continually increases due to enhanced O_2 reduction kinetics occurring preferentially on Fe_3O_4 beneath the γ/α - $FeOOH$ tubercle.
 - N_2H_4 treatments in 0.5 ppm – 1 ppm concentrations virtually eliminate the formation of oxides and oxyhydroxides in O_2 -containing nn-pH HCO_3^- environments. N_2H_4 treatments in these concentrations shifts the corrosion rate of X100 to values even less than those exhibited in the standard 5% CO_2 deaerated NS4 environment of pH 6.7, through a combined anodic- and cathodic-type inhibition. Increasing the concentration of N_2H_4 treatment always improves the creation of a weak passivation effect appearing at low anodic polarizations, effectively inhibiting the corrosion of X100 in nn-pH environments by 18%-68%.
 - Hydrogen diffusivity in X100 steel is approximately $4.4 \times 10^{-7} \text{ cm}^2/\text{s}$. In completely CP-shielded conditions a measurable amount of diffusible hydrogen of approximately 1 atomic ppm is detected in the alloy. This hydrogen concentration increases at the more negative applied potentials of the partially-shielded or unshielded CP regions, and with higher % CO_2 in the local electrolyte environment. Results from hydrogen generation, uptake, and diffusion experiments support the proposed role of hydrogen embrittlement in the transgranular SCC mechanism of pipeline steels exposed to dilute HCO_3^- environments of nn-pH.
 - Using a Finite Element Model founded on the results of laboratory experiments, the corrosion rate of X100 at a 90° coating failure site is suppressed by CP to $< 1 \text{ mpy}$ in practical soil environments, for the specific CP and pipeline system dimensions

modelled. Simulations reveal that CP anodes need not be placed closer than 1.5 m away from buried pipelines, for most soil environments expected to be encountered in practice. Also, simulations show that achieving the standard $-0.85 \text{ V}_{\text{Cu-CuSO}_4}$ NACE CP design criterion is crucial, whereas the -300 mV shift criterion mostly results in overprotection and unwanted hydrogen evolution.

- Using a millimeter-scale Finite Element Model, it is found that underneath a disbonded coating CP levels and pH dependencies within the nn-pH range strongly govern depth profiles caused by corrosion, reaching a maximum of $\sim 3 \text{ mm}$ into the pipeline wall. A 0.25 V amplification of CP potential combined with a 0.5 mm widening in disbondment opening size reduces defect penetration by almost 30%.
- Numerical stress analysis of external defect dimensions generated by the corrosion models developed in this work reveal that the structural integrity of a typical transmission pipeline, measured by its burst pressure, is diminished by approximately 7% - 8% after 3 years of a typical external coating disbondment. These simulations use common dimensions, environments, and CP parameter inputs, and results are validated with empirical structural integrity equations.

10.3 Suggestions for future work

The external corrosion of pipeline steels is a complex and multi-faceted process which requires further investigation and research to understand and control. The following points are suggested as directions and areas for future research and development:

- This dissertation explored the corrosion behavior of API X100 pipeline steel. The corrosion of newer API X120 steel and the influence of microstructural differences arising from heat-treatments and welding would be highly beneficial, especially since it pertains to subsequent cracking phenomena.
- As the technology becomes more readily available, the use of localized electrochemical techniques such as Scanning Electrochemical Microscopy (SECM), Localized Electrochemical Impedance Spectroscopy (LEIS), and the Scanning Vibrating Electrode Technique (SVET) all provide avenues to study corrosion behaviors of CP-shielded situations under coating disbondments *in-situ*, at a greater level of detail. This requires the development of a new experiment apparatus which can in some way allow the miniature probe to effectively avoid the barrier of the disbonded coating while measuring the ongoing corrosion underneath.
- The temperatures investigated in this work were all ≥ 25 °C. Although the surface of buried pipelines (and therefore the corrosive electrolyte in contact with it) are normally not below 25 °C, the influence of cold and freezing temperatures (< 10 °C) on gas diffusion and CP at coordinates further away from the pipeline surface will be important. This direction for future research is especially relevant to pipeline infrastructure in Canada and other cold climate regions.
- The study of hydrogen generation, ingress, and diffusion in X100 presented in this thesis revealed useful information. Likewise, further investigation of the subsequent hydrogen-induced cracking and hydrogen embrittlement behaviors in similar simulated conditions

using Slow Strain Rate Testing (SSRT) would be beneficial. Based on the higher susceptibility of stronger alloys to hydrogen-related failures, these studies should be extended to API X120 and specimen of different microstructures arising from heat-treatment and welding processes.

- With regards to the models developed in this work, a highly beneficial next step would be to integrate all the modules to create a large multi-scale simulation tool for buried pipeline corrosion. The ultimate goal of this multi-scale package would be to act as a single-step tool which can take macro-scale environmental, soil, and climatic data as inputs, then without further user interaction yield accurate structural integrity and residual strength predictions for the system under consideration (i.e. pipeline material, operating pressures, pipeline age, etc.).
- Numerous individual aspects of the models presented in this thesis could also be further developed, including: (a) the coalescence of multiple defects/cracks of different quantities and distributions; (b) the influence of cyclic and shock loading on the structural integrity of the pipeline; (c) the interference of stray currents from other electrified infrastructure with CP; (d) the penetration of CP current through coating disbondments; (e) the gas diffusion/CP current behaviors in frozen soils, thawed soils, and/or permafrost; and (f) the influence of corrosion product formations on the metal surface and the aging of CP anodes in long-term simulations.

References

- [1] CEPA, “Pipeline Incidents,” 2014. [Online]. Available: <http://www.cepa.com/library/publications>. [Accessed: 03-Sep-2016].
- [2] N. E. B. Government of Canada, “NEB - Safety - Pipeline Ruptures,” 10-Aug-2007. [Online]. Available: <http://www.neb-one.gc.ca/clf-nsi/rsftyndthnvrnmnt/sfty/pplnrptrs/pplnrptrs-eng.html>. [Accessed: 18-Feb-2014].
- [3] United States Central Intelligence Agency, *The CIA World Factbook 2014*. New York: Skyhorse Publishing, 2013.
- [4] PHMSA, “PHMSA - Data & Statistics,” 2014. [Online]. Available: <http://www.phmsa.dot.gov/resources/data-stats>. [Accessed: 18-Feb-2014].
- [5] R. J. Eiber and D. J. Jones, *An Analysis of Reportable Incidents for Natural Gas Transmission and Gathering Lines, June 1984 Through 1990*. Columbus, OH: Pipeline Research Committee, 1992.
- [6] J. S. Mandke, “Corrosion causes most pipeline failures in Gulf of Mexico,” *Oil Gas J.*, vol. 88:44, no. 44, Oct. 1990.
- [7] H. C. ASM International, *Properties and selection: irons, steels, and high-performance alloys*. Metals Park, Ohio: American Society for Metals, 1995.
- [8] W. K. Kim, “HSLA steel development,” Pohang University of Science and Technology, Pohang, South Korea, 2010.
- [9] M. Mohitpour, H. Golshan, and A. Murray, *Pipeline Design & Construction: A Practical Approach*, Revised edition. New York: ASME, 2003.
- [10] H. Asahi, T. Hara, E. Tsuru, H. Morimoto, Y. Terada, M. Sugiyama, M. Murata, N. Doi, N. Ayukawa, and H. Akasaki, “X120 UOE Linepipe With Improved Properties and Varied Sizes,” *Proceedings of the 2006 6th ASME International Pipeline Conference*, Paper No. IPC2006-10087, pp. 83–87, Calgary, Alberta, Canada, September 25–29, 2006.
- [11] D. M. Ortega-Toledo, J. G. Gonzalez-Rodriguez, M. Casales, L. Martinez, and A. Martinez-Villafañe, “Co2 corrosion inhibition of X-120 pipeline steel by a modified imidazoline under flow conditions,” *Corros. Sci.*, vol. 53, no. 11, pp. 3780–3787, Nov. 2011.
- [12] C. I. Ossai, B. Boswell, and I. J. Davies, “Pipeline failures in corrosive environments – A conceptual analysis of trends and effects,” *Eng. Fail. Anal.*, vol. 53, pp. 36–58, Jul. 2015.
- [13] P. W. and G. S. C. Government of Canada, “Public Inquiry Concerning Stress Corrosion Cracking on Canadian Oil and Gas Pipelines: NE23-58/1996E-PDF - Government of Canada Publications,” 01-Jul-2002. [Online]. Available: <http://publications.gc.ca/site/eng/418383/publication.html>. [Accessed: 18-Oct-2013].
- [14] Y. F. Cheng, *Stress Corrosion Cracking of Pipelines*. Hoboken, New Jersey: Wiley, 2013.
- [15] B. Y. Fang, A. Atrens, J. Q. Wang, E. H. Han, Z. Y. Zhu, and W. Ke, “Review of stress corrosion cracking of pipeline steels in ‘low’ and ‘high’ pH solutions,” *J. Mater. Sci.*, vol. 38, no. 1, pp. 127–132, Jan. 2003.

- [16] B. Delanty and J. O’Beirne, “Major Field Study Compares Pipeline SCC with Coatings,” *Oil Gas J. U. S.*, vol. 90:24, Jun. 1992.
- [17] J. M. Sutcliffe, R. R. Fessler, W. K. Boyd, and R. N. Parkins, “Stress Corrosion Cracking of Carbon Steel in Carbonate Solutions,” *Corrosion*, vol. 28, no. 8, pp. 313–320, Aug. 1972.
- [18] L. Yan, R. Worthingham, F. King, and J. Been, “Factors Affecting the Generation of High-pH Environments Required for Stress Corrosion Cracking (SCC),” *presented at the 2012 9th International Pipeline Conference (IPC)*, Calgary, Canada, 2012, pp. 511–524.
- [19] Y. F. Cheng, “Fundamentals of hydrogen evolution reaction and its implications on near-neutral pH stress corrosion cracking of pipelines,” *Electrochimica Acta*, vol. 52, no. 7, pp. 2661–2667, Feb. 2007.
- [20] W. Chen, R. Kania, R. Worthingham, and G. V. Boven, “Transgranular crack growth in the pipeline steels exposed to near-neutral pH soil aqueous solutions: The role of hydrogen,” *Acta Mater.*, vol. 57, no. 20, pp. 6200–6214, Dec. 2009.
- [21] R. N. Parkins, W. K. Blanchard, and B. S. Delanty, “Transgranular Stress Corrosion Cracking of High-Pressure Pipelines in Contact with Solutions of Near Neutral pH,” *Corrosion*, vol. 50, no. 5, pp. 394–408, May 1994.
- [22] H. B. Xue and Y. F. Cheng, “Photo-electrochemical studies of the local dissolution of a hydrogen-charged X80 steel at crack-tip in a near-neutral pH solution,” *Electrochimica Acta*, vol. 55, no. 20, pp. 5670–5676, Aug. 2010.
- [23] C. Zhang and Y.-F. Cheng, “Synergistic effects of hydrogen and stress on corrosion of X100 pipeline steel in a near-neutral pH solution,” *J. Mater. Eng. Perform.*, vol. 19, no. 9, pp. 1284–1289, 2010.
- [24] W. Chen, F. King, T. R. Jack, and M. J. Wilmott, “Environmental aspects of near-neutral pH stress corrosion cracking of pipeline steel,” *Metall. Mater. Trans. A*, vol. 33, no. 5, pp. 1429–1436, May 2002.
- [25] A. Eslami, B. Fang, R. Kania, B. Worthingham, J. Been, R. Eadie, and W. Chen, “Stress corrosion cracking initiation under the disbonded coating of pipeline steel in near-neutral pH environment,” *Corros. Sci.*, vol. 52, no. 11, pp. 3750–3756, Nov. 2010.
- [26] A. Eslami, R. Kania, B. Worthingham, G. V. Boven, R. Eadie, and W. Chen, “Effect of CO₂ and R-ratio on near-neutral pH stress corrosion cracking initiation under a disbonded coating of pipeline steel,” *Corros. Sci.*, vol. 53, no. 6, pp. 2318–2327, Jun. 2011.
- [27] A. Eslami, R. Kania, B. Worthingham, G. V. Boven, R. Eadie, and W. Chen, “Corrosion of X-65 Pipeline Steel Under a Simulated Cathodic Protection Shielding Coating Disbondment,” *Corrosion*, vol. 69, no. 11, pp. 1103–1110, Jul. 2013.
- [28] W. Chen, F. King, and E. Vokes, “Characteristics of Near-Neutral-pH Stress Corrosion Cracks in an X-65 Pipeline,” *Corrosion*, vol. 58, no. 3, pp. 267–275, Mar. 2002.
- [29] Y.-S. Choi, J.-J. Shim, and J.-G. Kim, “Corrosion behavior of low alloy steels containing Cr, Co and W in synthetic potable water,” *Mater. Sci. Eng. A*, vol. 385, no. 1–2, pp. 148–156, Nov. 2004.

- [30] T. S. Rao, T. N. Sairam, B. Viswanathan, and K. V. K. Nair, "Carbon steel corrosion by iron oxidising and sulphate reducing bacteria in a freshwater cooling system," *Corros. Sci.*, vol. 42, no. 8, pp. 1417–1431, Aug. 2000.
- [31] D.-T. Chin and G. M. Sabde, "Modeling Transport Process and Current Distribution in a Cathodically Protected Crevice," *Corrosion*, vol. 56, no. 8, pp. 783–793, Aug. 2000.
- [32] V. K. Gouda, "Corrosion and Corrosion Inhibition of Reinforcing Steel: I. Immersed in Alkaline Solutions," *Br. Corros. J.*, vol. 5, no. 5, pp. 198–203, Sep. 1970.
- [33] E. B. Muehlenkamp, M. D. Koretsky, and J. C. Westall, "Effect of Moisture on the Spatial Uniformity of Cathodic Protection of Steel in Reinforced Concrete," *Corrosion*, vol. 61, no. 6, pp. 519–533, Jun. 2005.
- [34] I. S. Cole and D. Marney, "The science of pipe corrosion: A review of the literature on the corrosion of ferrous metals in soils," *Corros. Sci.*, vol. 56, pp. 5–16, Mar. 2012.
- [35] R. W. Revie, *Oil and Gas Pipelines: Integrity and Safety Handbook*. John Wiley & Sons, 2015.
- [36] C. De Waard and D. E. Milliams, "Carbonic Acid Corrosion of Steel," *Corrosion*, vol. 31, no. 5, pp. 177–181, May 1975.
- [37] R. Chu, W. Chen, S.-H. Wang, F. King, T. R. Jack, and R. R. Fessler, "Microstructure Dependence of Stress Corrosion Cracking Initiation in X-65 Pipeline Steel Exposed to a Near-Neutral pH Soil Environment," *Corrosion*, vol. 60, no. 3, pp. 275–283, Mar. 2004.
- [38] F. Gan, Z.-W. Sun, G. Sabde, and D.-T. Chin, "Cathodic Protection to Mitigate External Corrosion of Underground Steel Pipe Beneath Disbonded Coating," *Corrosion*, vol. 50, no. 10, pp. 804–816, Oct. 1994.
- [39] B. W. A. Sherar, P. G. Keech, and D. W. Shoesmith, "Carbon steel corrosion under anaerobic–aerobic cycling conditions in near-neutral pH saline solutions. Part 2: Corrosion mechanism," *Corros. Sci.*, vol. 53, no. 11, pp. 3643–3650, Nov. 2011.
- [40] B. W. A. Sherar, P. G. Keech, and D. W. Shoesmith, "Carbon steel corrosion under anaerobic–aerobic cycling conditions in near-neutral pH saline solutions – Part 1: Long term corrosion behaviour," *Corros. Sci.*, vol. 53, no. 11, pp. 3636–3642, Nov. 2011.
- [41] G. Z. Meng, C. Zhang, and Y. F. Cheng, "Effects of corrosion product deposit on the subsequent cathodic and anodic reactions of X-70 steel in near-neutral pH solution," *Corros. Sci.*, vol. 50, no. 11, pp. 3116–3122, Nov. 2008.
- [42] A. Benmoussa, M. Hadjel, and M. Traisnel, "Corrosion behavior of API 5L X-60 pipeline steel exposed to near-neutral pH soil simulating solution," *Mater. Corros.*, vol. 57, no. 10, pp. 771–777, Oct. 2006.
- [43] K. Belmokre, N. Azzouz, F. Kermiche, M. Wery, and J. Pagetti, "Corrosion study of carbon steel protected by a primer, by electrochemical impedance spectroscopy (EIS) in 3 %NaCl medium and in a soil simulating solution," *Mater. Corros.*, vol. 49, no. 2, pp. 108–113, Feb. 1998.

- [44] K. Kasahara and F. Kajiyama, "Determination of Underground Corrosion Rates from Polarization Resistance Measurements," *Corrosion*, vol. 39, no. 12, pp. 475–480, Dec. 1983.
- [45] X. H. Nie, X. G. Li, C. W. Du, and Y. F. Cheng, "Temperature dependence of the electrochemical corrosion characteristics of carbon steel in a salty soil," *J. Appl. Electrochem.*, vol. 39, no. 2, pp. 277–282, Oct. 2008.
- [46] J. R. Scully and K. J. Bundy, "Electrochemical methods for measurement of steel pipe corrosion rates in soil," *Mater. Perform.*, vol. 24, no. 4, pp. 18–25, 1985.
- [47] Y. H. Wu, T. M. Liu, C. Sun, J. Xu, and C. K. Yu, "Effects of simulated acid rain on corrosion behaviour of Q235 steel in acidic soil," *Corros. Eng. Sci. Technol.*, vol. 45, no. 2, pp. 136–141, Apr. 2010.
- [48] T. M. Liu, Y. H. Wu, S. X. Luo, and C. Sun, "Effect of soil compositions on the electrochemical corrosion behavior of carbon steel in simulated soil solution. Einfluss der Erdbodenzusammensetzung auf das elektrochemische Verhalten von Kohlenstoffstählen in simulierten Erdbodenlösungen," *Mater. Werkst.*, vol. 41, no. 4, pp. 228–233, Apr. 2010.
- [49] B. Fang, E.-H. Han, J. Wang, and W. Ke, "Mechanical and Environmental Influences on Stress Corrosion Cracking of an X-70 Pipeline Steel in Dilute Near-Neutral pH Solutions," *Corrosion*, vol. 63, no. 5, pp. 419–432, May 2007.
- [50] B. Gu, W. Z. Yu, J. L. Luo, and X. Mao, "Transgranular Stress Corrosion Cracking of X-80 and X-52 Pipeline Steels in Dilute Aqueous Solution with Near-Neutral pH," *Corrosion*, vol. 55, no. 3, pp. 312–318, Mar. 1999.
- [51] P. Liang, X. Li, C. Du, and X. Chen, "Stress corrosion cracking of X80 pipeline steel in simulated alkaline soil solution," *Mater. Des.*, vol. 30, no. 5, pp. 1712–1717, May 2009.
- [52] J.-J. Park, S.-I. Pyun, K.-H. Na, S.-M. Lee, and Y.-T. Kho, "Effect of Passivity of the Oxide Film on Low-pH Stress Corrosion Cracking of API 5L X-65 Pipeline Steel in Bicarbonate Solution," *Corrosion*, vol. 58, no. 4, pp. 329–336, Apr. 2002.
- [53] B. Bedairi, D. Cronin, A. Hosseini, and A. Plumtree, "Failure prediction for Crack-in-Corrosion defects in natural gas transmission pipelines," *Int. J. Press. Vessels Pip.*, vol. 96–97, pp. 90–99, Aug. 2012.
- [54] G. Pluvinage, *Fracture and Fatigue Emanating from Stress Concentrators*, 2003 edition. Dordrecht ; Boston: Springer, 2003.
- [55] G. S. Frankel, "Pitting Corrosion of Metals A Review of the Critical Factors," *J. Electrochem. Soc.*, vol. 145, no. 6, pp. 2186–2198, Jun. 1998.
- [56] F. F. Eliyan, E.-S. Mahdi, and A. Alfantazi, "Electrochemical evaluation of the corrosion behaviour of API-X100 pipeline steel in aerated bicarbonate solutions," *Corros. Sci.*, vol. 58, pp. 181–191, May 2012.
- [57] F. B. Mansfeld, *Corrosion Mechanisms*, 1 edition. New York: CRC Press, 1986.
- [58] X. Zhang, W. Xu, D. W. Shoesmith, and J. C. Wren, "Kinetics of H₂O₂ reaction with oxide films on carbon steel," *Corros. Sci.*, vol. 49, no. 12, pp. 4553–4567, Dec. 2007.
- [59] V. A. Alves and C. M. A. Brett, "Characterisation of passive films formed on mild steels in bicarbonate solution by EIS," *Electrochimica Acta*, vol. 47, no. 13–14, pp. 2081–2091, May 2002.

- [60] M. Yan, J. Wang, E. Han, and W. Ke, "Local environment under simulated disbonded coating on steel pipelines in soil solution," *Corros. Sci.*, vol. 50, no. 5, pp. 1331–1339, May 2008.
- [61] L. J. Qiao, J. L. Luo, and X. Mao, "The role of hydrogen in the process of stress corrosion cracking of pipeline steels in dilute carbonate-bicarbonate solution," *J. Mater. Sci. Lett.*, vol. 16, no. 7, pp. 516–520, Apr. 1997.
- [62] X. C. Li, R. L. Eadie, and J. L. Luo, "Influence of plasticity on corrosion and stress corrosion cracking behaviour in near neutral pH environment," *Corros. Eng. Sci. Technol.*, vol. 43, no. 4, pp. 297–303, Dec. 2008.
- [63] Y. H. Wu, T. M. Liu, S. X. Luo, and C. Sun, "Corrosion characteristics of Q235 steel in simulated Yingtan soil solutions. Korrosionsverhalten von Q235 Stahl in simulierter Bodenlösung," *Mater. Werkst.*, vol. 41, no. 3, pp. 142–146, Mar. 2010.
- [64] B. R. Linter and G. T. Burstein, "Reactions of pipeline steels in carbon dioxide solutions," *Corros. Sci.*, vol. 41, no. 1, pp. 117–139, Jan. 1999.
- [65] D. H. Davies and G. T. Burstein, "The Effects of Bicarbonate on the Corrosion and Passivation of Iron," *Corrosion*, vol. 36, no. 8, pp. 416–422, Aug. 1980.
- [66] C. A. M. Ferreira, J. A. C. Ponciano, D. S. Vaitsman, and D. V. Pérez, "Evaluation of the corrosivity of the soil through its chemical composition," *Sci. Total Environ.*, vol. 388, no. 1–3, pp. 250–255, Dec. 2007.
- [67] M. Sancy, Y. Gourbeyre, E. M. M. Sutter, and B. Tribollet, "Mechanism of corrosion of cast iron covered by aged corrosion products: Application of electrochemical impedance spectrometry," *Corros. Sci.*, vol. 52, no. 4, pp. 1222–1227, Apr. 2010.
- [68] B. W. A. Sherar, P. G. Keech, Z. Qin, F. King, and D. W. Shoesmith, "Nominally Anaerobic Corrosion of Carbon Steel in Near-Neutral pH Saline Environments," *Corrosion*, vol. 66, no. 4, pp. 45001–45001–11, Apr. 2010.
- [69] N. Naing Aung and Y.-J. Tan, "A new method of studying buried steel corrosion and its inhibition using the wire beam electrode," *Corros. Sci.*, vol. 46, no. 12, pp. 3057–3067, Dec. 2004.
- [70] M. Norin and T.-G. Vinka, "Corrosion of carbon steel in filling material in an urban environment," *Mater. Corros.*, vol. 54, no. 9, pp. 641–651, Sep. 2003.
- [71] Z. Qin, B. Demko, J. Noel, D. Shoesmith, F. King, R. Worthingham, and K. Keith, "Localized Dissolution of Millscale-Covered Pipeline Steel Surfaces," *Corrosion*, vol. 60, no. 10, Oct. 2004.
- [72] S. J. Oh, D. C. Cook, and H. E. Townsend, "Atmospheric corrosion of different steels in marine, rural and industrial environments," *Corros. Sci.*, vol. 41, no. 9, pp. 1687–1702, Aug. 1999.
- [73] Y. Lu, J. Dong, and W. Ke, "Corrosion Evolution of Low Alloy Steel in Deaerated Bicarbonate Solutions," *J. Mater. Sci. Technol.*, vol. 31, no. 10, pp. 1047–1058, Oct. 2015.
- [74] I. M. Gadala and A. Alfantazi, "Low Alloy X100 Pipeline Steel Corrosion and Passivation Behavior in Bicarbonate-Based Solutions of pH 6.7 to 8.9 with Groundwater Anions: An Electrochemical Study," *Metall. Mater. Trans. A*, vol. 46, no. 7, pp. 3104–3116, Apr. 2015.
- [75] I. M. Gadala and A. Alfantazi, "A study of X100 pipeline steel passivation in mildly alkaline bicarbonate solutions using electrochemical impedance

- spectroscopy under potentiodynamic conditions and Mott–Schottky,” *Appl. Surf. Sci.*, vol. 357, Part A, pp. 356–368, Dec. 2015.
- [76] F. M. AlAbbas, C. Williamson, S. M. Bholá, J. R. Spear, D. L. Olson, B. Mishra, and A. E. Kakpovbia, “Influence of sulfate reducing bacterial biofilm on corrosion behavior of low-alloy, high-strength steel (API-5L X80),” *Int. Biodeterior. Biodegrad.*, vol. 78, pp. 34–42, Mar. 2013.
- [77] T. Nishimura, H. Katayama, K. Noda, and T. Kodama, “Effect of Co and Ni on the corrosion behavior of low alloy steels in wet/dry environments,” *Corros. Sci.*, vol. 42, no. 9, pp. 1611–1621, Sep. 2000.
- [78] X. Chen, J. Dong, E. Han, and W. Ke, “Effect of Ni on the ion-selectivity of rust layer on low alloy steel,” *Mater. Lett.*, vol. 61, no. 19–20, pp. 4050–4053, Aug. 2007.
- [79] G. A. Zhang and Y. F. Cheng, “Micro-electrochemical characterization and Mott–Schottky analysis of corrosion of welded X70 pipeline steel in carbonate/bicarbonate solution,” *Electrochimica Acta*, vol. 55, no. 1, pp. 316–324, Dec. 2009.
- [80] H. El Hajj, A. Abdelouas, Y. El Mendili, G. Karakurt, B. Grambow, and C. Martin, “Corrosion of carbon steel under sequential aerobic–anaerobic environmental conditions,” *Corros. Sci.*, vol. 76, pp. 432–440, Nov. 2013.
- [81] R. W. Revie, *Uhlig’s Corrosion Handbook*. Wiley, 2011.
- [82] B. W. A. Sherar, P. G. Keech, and D. W. Shoesmith, “Carbon steel corrosion under anaerobic–aerobic cycling conditions in near-neutral pH saline solutions – Part 1: Long term corrosion behaviour,” *Corros. Sci.*, vol. 53, no. 11, pp. 3636–3642, Nov. 2011.
- [83] J. J. Perdomo, M. E. Chabica, and I. Song, “Chemical and electrochemical conditions on steel under disbonded coatings: the effect of previously corroded surfaces and wet and dry cycles,” *Corros. Sci.*, vol. 43, no. 3, pp. 515–532, Mar. 2001.
- [84] H. S. Isaacs, “The localized breakdown and repair of passive surfaces during pitting,” *Corros. Sci.*, vol. 29, no. 2–3, pp. 313–323, 1989.
- [85] J. Capelle, J. Gilgert, I. Dmytrakh, and G. Pluvinage, “Sensitivity of pipelines with steel API X52 to hydrogen embrittlement,” *Int. J. Hydrog. Energy*, vol. 33, no. 24, pp. 7630–7641, Dec. 2008.
- [86] D. Hardie, E. A. Charles, and A. H. Lopez, “Hydrogen embrittlement of high strength pipeline steels,” *Corros. Sci.*, vol. 48, no. 12, pp. 4378–4385, Dec. 2006.
- [87] J. A. Beavers, “2013 Frank Newman Speller Award Lecture: Integrity Management of Natural Gas and Petroleum Pipelines Subject to Stress Corrosion Cracking,” *Corrosion*, vol. 70, no. 1, pp. 3–18, Jul. 2013.
- [88] R. N. Parkins and J. A. Beavers, “Some Effects of Strain Rate on the Transgranular Stress Corrosion Cracking of Ferritic Steels in Dilute Near-Neutral-pH Solutions,” *Corrosion*, vol. 59, no. 3, pp. 258–273, Mar. 2003.
- [89] W. Chen, “An Overview of Near-Neutral pH Stress Corrosion Cracking in Pipelines and Mitigation Strategies for Its Initiation and Growth,” *Corrosion*, vol. 72, no. 7, pp. 962–977, Apr. 2016.

- [90] A. Mustapha, E. A. Charles, and D. Hardie, "Evaluation of environment-assisted cracking susceptibility of a grade X100 pipeline steel," *Corros. Sci.*, vol. 54, pp. 5–9, Jan. 2012.
- [91] G. Gabetta, "Transgranular Stress Corrosion Cracking of Low-Alloy Steels in Diluted Solutions," *Corrosion*, vol. 53, no. 7, pp. 516–524, Jul. 1997.
- [92] M. Yunovich, Z. Xia, and Z. Szklarska-Smialowska, "Factors Influencing Stress Corrosion Cracking of Carbon Steel in Diluted Bicarbonate Environments," *Corrosion*, vol. 54, no. 2, pp. 155–161, Feb. 1998.
- [93] D. X. He, W. Chen, and J. L. Luo, "Effect of Cathodic Potential on Hydrogen Content in a Pipeline Steel Exposed to NS4 Near-Neutral pH Soil Solution," *Corrosion*, vol. 60, no. 8, pp. 778–786, Aug. 2004.
- [94] Y. F. Cheng, "Analysis of electrochemical hydrogen permeation through X-65 pipeline steel and its implications on pipeline stress corrosion cracking," *Int. J. Hydrog. Energy*, vol. 32, no. 9, pp. 1269–1276, Jun. 2007.
- [95] R. N. Parkins and S. Zhou, "The stress corrosion cracking of C-Mn steel in CO_2 - HCO_3^- - CO_3^{2-} solutions. II: Electrochemical and other data," *Corros. Sci.*, vol. 39, no. 1, pp. 175–191, Jan. 1997.
- [96] R. N. Parkins and S. Zhou, "The stress corrosion cracking of C-Mn steel in CO_2 - HCO_3^- - CO_3^{2-} solutions. I: Stress corrosion data," *Corros. Sci.*, vol. 39, no. 1, pp. 159–173, Jan. 1997.
- [97] X. Liu and X. Mao, "Electrochemical polarization and stress corrosion cracking behaviours of a pipeline steel in dilute bicarbonate solution with chloride ion," *Scr. Metall. Mater.*, vol. 33, no. 1, pp. 145–150, Jul. 1995.
- [98] J. Capelle, J. Gilgert, I. Dmytrakh, and G. Pluvinage, "The effect of hydrogen concentration on fracture of pipeline steels in presence of a notch," *Eng. Fract. Mech.*, vol. 78, no. 2, pp. 364–373, Jan. 2011.
- [99] L. Niu and Y. F. Cheng, "Corrosion behavior of X-70 pipe steel in near-neutral pH solution," *Appl. Surf. Sci.*, vol. 253, no. 21, pp. 8626–8631, Aug. 2007.
- [100] S. Nešić, "Key issues related to modelling of internal corrosion of oil and gas pipelines – A review," *Corros. Sci.*, vol. 49, no. 12, pp. 4308–4338, Dec. 2007.
- [101] C. de Waard, U. Lotz, and D. E. Milliams, "Predictive Model for CO_2 Corrosion Engineering in Wet Natural Gas Pipelines," *Corrosion*, vol. 47, no. 12, pp. 976–985, Dec. 1991.
- [102] M. Azuma, K. Hashimoto, M. Hiramoto, M. Watanabe, and T. Sakata, "Electrochemical Reduction of Carbon Dioxide on Various Metal Electrodes in Low-Temperature Aqueous KHCO_3 Media," *J. Electrochem. Soc.*, vol. 137, no. 6, pp. 1772–1778, Jun. 1990.
- [103] M. B. Kermani and A. Morshed, "Carbon Dioxide Corrosion in Oil and Gas Production—A Compendium," *Corrosion*, vol. 59, no. 8, pp. 659–683, Aug. 2003.
- [104] C. F. Dong, Z. Y. Liu, X. G. Li, and Y. F. Cheng, "Effects of hydrogen-charging on the susceptibility of X100 pipeline steel to hydrogen-induced cracking," *Int. J. Hydrog. Energy*, vol. 34, no. 24, pp. 9879–9884, Dec. 2009.
- [105] W. w. Gerberich, P. g. Marsh, and J. w. Hoehn, "Hydrogen Induced Cracking Mechanisms — Are There Critical Experiments?," in *Hydrogen Effects in*

- Materials*, A. W. Thompson and N. R. Moody, Eds. John Wiley & Sons, Inc., 1994, pp. 539–554.
- [106] D. Li, R. P. Gangloff, and J. R. Scully, “Hydrogen trap states in ultrahigh-strength AERMET 100 steel,” *Metall. Mater. Trans. A*, vol. 35, no. 3, pp. 849–864.
- [107] W. W. Gerberich, T. Llvne, X. F. Chen, and M. Kaczorowski, “Crack growth from internal hydrogen—temperature and microstructural effects in 4340 steel,” *Metall. Trans. A*, vol. 19, no. 5, pp. 1319–1334.
- [108] T. Y. Jin, Z. Y. Liu, and Y. F. Cheng, “Effect of non-metallic inclusions on hydrogen-induced cracking of API5L X100 steel,” *Int. J. Hydrog. Energy*, vol. 35, no. 15, pp. 8014–8021, Aug. 2010.
- [109] M. A. Arafin and J. A. Szpunar, “Effect of bainitic microstructure on the susceptibility of pipeline steels to hydrogen induced cracking,” *Mater. Sci. Eng. A*, vol. 528, no. 15, pp. 4927–4940, Jun. 2011.
- [110] H. Cialone and R. J. Asaro, “The role of hydrogen in the ductile fracture of plain carbon steels,” *Metall. Trans. A*, vol. 10, no. 3, pp. 367–375, Mar. 1979.
- [111] R. W. Stahle, J. Hochmann, R. D. McCright, J. E. Slater, and S. R. Shatynski, “Stress Corrosion Cracking and Hydrogen Embrittlement of Iron Base Alloys,” *J. Electrochem. Soc.*, vol. 126, no. 5, p. 215C–215C, May 1979.
- [112] A. Torres-Islas, V. M. Salinas-Bravo, J. L. Albarran, and J. G. Gonzalez-Rodriguez, “Effect of hydrogen on the mechanical properties of X-70 pipeline steel in diluted solutions at different heat treatments,” *Int. J. Hydrog. Energy*, vol. 30, no. 12, pp. 1317–1322, Sep. 2005.
- [113] M. Kimura, T. Kushida, K. Nose, S. Okano, S. Endo, and Y. Nishida, “Effects of Metallurgical Factors and Test Condition on Low-pH Type Stress Corrosion Cracking of Pipeline,” *ASME-Publ.-PVP*, vol. 380, pp. 265–272, 1998.
- [114] L. Birry and A. Lasia, “Studies of the Hydrogen Evolution Reaction on Raney Nickel—Molybdenum Electrodes,” *J. Appl. Electrochem.*, vol. 34, no. 7, pp. 735–749.
- [115] L. Chen and A. Lasia, “Study of the Kinetics of Hydrogen Evolution Reaction on Nickel-Zinc Alloy Electrodes,” *J. Electrochem. Soc.*, vol. 138, no. 11, pp. 3321–3328, Nov. 1991.
- [116] E. J. Kelly, “The Active Iron Electrode I. Iron Dissolution and Hydrogen Evolution Reactions in Acidic Sulfate Solutions,” *J. Electrochem. Soc.*, vol. 112, no. 2, pp. 124–131, Feb. 1965.
- [117] B. B. Rath and I. M. Bernstein, “The relation between grain-boundary orientation and intergranular cracking,” *Metall. Trans.*, vol. 2, no. 10, pp. 2845–2851, Oct. 1971.
- [118] L. C. de Abreu, P. J. Modenesi, and P. Villani-Marques, “Comparative study of methods for determining the diffusible hydrogen content in welds,” *Weld. Int.*, vol. 9, no. 1, pp. 26–31, 1995.
- [119] N. Parvathavarthini, S. Saroja, and R. K. Dayal, “Influence of microstructure on the hydrogen permeability of 9%Cr–1%Mo ferritic steel,” *J. Nucl. Mater.*, vol. 264, no. 1–2, pp. 35–47, Jan. 1999.
- [120] T. Kushida, K. Nose, H. Asahi, M. Kimura, Y. Yamane, S. Endo, and H. Kawano, “Effects of Metallurgical Factors and Test Conditions on Near Neutral pH SCC of Pipeline Steels,” *Corros. 2001*, Jan. 2001.

- [121] S. D. Liberto and G. Gabetta, "Stress corrosion cracking by anodic dissolution and hydrogen permeation in pipeline steels," *Mater. Sci.*, vol. 33, no. 4, pp. 411–420, Jul. 1997.
- [122] Y. Bai and Q. Bai, "Chapter 1 - Corrosion and Corroded Pipelines," in *Subsea Pipeline Integrity and Risk Management*, Y. B. Bai, Ed. Boston: Gulf Professional Publishing, 2014, pp. 3–25.
- [123] C. L. Durr and J. A. Beavers, "Techniques for Assessment of Soil Corrosivity," Dec. 1998.
- [124] D. A. Jones, *Principles and Prevention of Corrosion*, 2 edition. Upper Saddle River, NJ: Prentice Hall, 1995.
- [125] D. Rabirot, F. Dalard, J.-J. Rameau, J.-P. Caire, and S. Boyer, "Study of sacrificial anode cathodic protection of buried tanks: Numerical modelling," *J. Appl. Electrochem.*, vol. 29, no. 5, pp. 541–550, May 1999.
- [126] G. H. Booth, A. W. Cooper, P. M. Cooper, and D. S. Wakerley, "Criteria of Soil Aggressiveness Towards Buried Metals. I. Experimental Methods," *Br. Corros. J.*, vol. 2, no. 3, pp. 104–108, May 1967.
- [127] M. Tomlinson and J. Woodward, *Pile Design and Construction Practice, Sixth Edition*, 6 edition. Boca Raton: CRC Press, 2014.
- [128] M. Romanoff, *Underground corrosion*. U.S. Govt. Print. Off., 1957.
- [129] P. Miltiadou and L. C. Wrobel, "Optimization of Cathodic Protection Systems Using Boundary Elements and Genetic Algorithms," *Corrosion*, vol. 58, no. 11, pp. 912–921, Nov. 2002.
- [130] S. Martinez and I. Štern, "A mathematical model for the internal cathodic protection of cylindrical structures by wire anodes," *J. Appl. Electrochem.*, vol. 30, no. 9, pp. 1053–1060, Sep. 2000.
- [131] N. H. Abu-Hamdeh and R. C. Reeder, "Soil Thermal Conductivity Effects of Density, Moisture, Salt Concentration, and Organic Matter," *Soil Sci. Soc. Am. J.*, vol. 64, no. 4, p. 1285, 2000.
- [132] J. Putkonen, "Soil thermal properties and heat transfer processes near Ny-Alesund, northwestern Spitsbergen, Svalbard," *Polar Res.*, vol. 17, no. 2, pp. 165–179, Dec. 1998.
- [133] G. S. Campbell, J. D. J. Jungbauer, W. R. Bidlake, and R. D. Hungerford, "Predicting the effect of temperature on soil thermal conductivity," *Soil Sci.*, vol. 158, no. 5, pp. 307–313, Nov. 1994.
- [134] S. E. Allaire, J. A. Lafond, A. R. Cabral, and S. F. Lange, "Measurement of gas diffusion through soils: comparison of laboratory methods," *J. Environ. Monit. JEM*, vol. 10, no. 11, pp. 1326–1336, Nov. 2008.
- [135] A. Thorbjørn, P. Moldrup, H. Blendstrup, T. Komatsu, and D. E. Rolston, "A Gas Diffusivity Model Based on Air-, Solid-, and Water-Phase Resistance in Variably Saturated Soil," *Vadose Zone J.*, vol. 7, no. 4, p. 1276, 2008.
- [136] S.-H. Lai, J. M. Tiedje, and A. E. Erickson, "In situ Measurement of Gas Diffusion Coefficient in Soils¹," *Soil Sci. Soc. Am. J.*, vol. 40, no. 1, p. 3, 1976.
- [137] A. Stadler, S. Rudolph, M. Kupisch, M. Langensiepen, J. van der Kruk, and F. Ewert, "Quantifying the effects of soil variability on crop growth using apparent soil electrical conductivity measurements," *Eur. J. Agron.*, vol. 64, pp. 8–20, Mar. 2015.

- [138] D. P. Riemer and M. E. Orazem, "Application of Boundary Element Models to Predict Effectiveness of Coupons for Assessing Cathodic Protection of Buried Structures," *Corrosion*, vol. 56, no. 8, pp. 794–800, Aug. 2000.
- [139] J.-F. Yan, S. N. R. Pakalapati, T. V. Nguyen, R. E. White, and R. B. Griffin, "Mathematical Modeling of Cathodic Protection Using the Boundary Element Method with a Nonlinear Polarization Curve," *J. Electrochem. Soc.*, vol. 139, no. 7, pp. 1932–1936, Jul. 1992.
- [140] F. M. Song, D. W. Kirk, J. W. Graydon, and D. E. Cormack, "Predicting Carbon Dioxide Corrosion of Bare Steel under an Aqueous Boundary Layer," *Corrosion*, vol. 60, no. 8, pp. 736–748, Aug. 2004.
- [141] S. C. Kranc and A. A. Sagüés, "Detailed modeling of corrosion macrocells on steel reinforcing in concrete," *Corros. Sci.*, vol. 43, no. 7, pp. 1355–1372, Jul. 2001.
- [142] S. C. Kranc and A. A. Sagüés, "Computation of Reinforcing Steel Corrosion Distribution in Concrete Marine Bridge Substructures," *Corrosion*, vol. 50, no. 1, pp. 50–61, Jan. 1994.
- [143] M. D. Koretsky, F. Aboameri, and J. C. Westall, "Effect of Concrete Pore Saturation on Cathodic Protection of Steel-Reinforced Concrete Bridges," *Corrosion*, vol. 55, no. 1, pp. 52–64, Jan. 1999.
- [144] "ASME B31G Manual Determining Remaining Strength" [Online]. Available: <https://www.asme.org/products/codes-standards/b31g-2012-manual-determining-remaining-strength>. [Accessed: 14-Feb-2014].
- [145] J. F. Kiefner and P. H. Vieth, "New method corrects criterion for evaluating corroded pipe," *Oil Gas J.*, vol. 88, no. 32, Aug. 1990.
- [146] T. A. Netto, U. S. Ferraz, and S. F. Estefen, "The effect of corrosion defects on the burst pressure of pipelines," *J. Constr. Steel Res.*, vol. 61, no. 8, pp. 1185–1204, Aug. 2005.
- [147] M. S. G. Chiodo and C. Ruggieri, "Failure assessments of corroded pipelines with axial defects using stress-based criteria: Numerical studies and verification analyses," *Int. J. Press. Vessels Pip.*, vol. 86, no. 2–3, pp. 164–176, Feb. 2009.
- [148] G. Fekete and L. Varga, "The effect of the width to length ratios of corrosion defects on the burst pressures of transmission pipelines," *Eng. Fail. Anal.*, vol. 21, pp. 21–30, Apr. 2012.
- [149] F. Dotta and C. Ruggieri, "Structural integrity assessments of high pressure pipelines with axial flaws using a micromechanics model," *Int. J. Press. Vessels Pip.*, vol. 81, no. 9, pp. 761–770, Sep. 2004.
- [150] H. Adib, S. Jallouf, C. Schmitt, A. Carmasol, and G. Pluvinage, "Evaluation of the effect of corrosion defects on the structural integrity of X52 gas pipelines using the SINTAP procedure and notch theory," *Int. J. Press. Vessels Pip.*, vol. 84, no. 3, pp. 123–131, Mar. 2007.
- [151] J. B. Choi, B. K. Goo, J. C. Kim, Y. J. Kim, and W. S. Kim, "Development of limit load solutions for corroded gas pipelines," *Int. J. Press. Vessels Pip.*, vol. 80, no. 2, pp. 121–128, Feb. 2003.
- [152] L. Y. Xu and Y. F. Cheng, "Reliability and failure pressure prediction of various grades of pipeline steel in the presence of corrosion defects and pre-strain," *Int. J. Press. Vessels Pip.*, vol. 89, pp. 75–84, Jan. 2012.

- [153] A. Hosseini, D. Cronin, A. Plumtree, and R. Kania, "Experimental Testing and Evaluation of Crack Defects in Line Pipe," *Proceedings of the 2010 8th ASME International Pipeline Conference*, IPC2010-31158, pp. 275–285, Calgary, Alberta, Canada, September 27 – October 1, 2010.
- [154] G01 Committee, "Practice for Evaluation of Hydrogen Uptake, Permeation, and Transport in Metals by an Electrochemical Technique," ASTM International, 2011.
- [155] M. a. V. Devanathan and Z. Stachurski, "The Adsorption and Diffusion of Electrolytic Hydrogen in Palladium," *Proc. R. Soc. Lond. Math. Phys. Eng. Sci.*, vol. 270, no. 1340, pp. 90–102, Oct. 1962.
- [156] F. S. LePera, "Improved etching technique for the determination of percent martensite in high-strength dual-phase steels," *Metallography*, vol. 12, no. 3, pp. 263–268, Sep. 1979.
- [157] M. Olasolo, P. Uranga, J. M. Rodriguez-Ibabe, and B. López, "Effect of austenite microstructure and cooling rate on transformation characteristics in a low carbon Nb–V microalloyed steel," *Mater. Sci. Eng. A*, vol. 528, no. 6, pp. 2559–2569, Mar. 2011.
- [158] F. Mohammadi, F. F. Eliyan, and A. Alfantazi, "Corrosion of simulated weld HAZ of API X-80 pipeline steel," *Corros. Sci.*, vol. 63, pp. 323–333, Oct. 2012.
- [159] G01 Committee, "Practice for Preparing, Cleaning, and Evaluating Corrosion Test Specimens," ASTM International, 2011.
- [160] J. R. Scully and P. J. Moran, "The Influence of Strain on Hydrogen Entry and Transport in a High Strength Steel in Sodium Chloride Solution," *J. Electrochem. Soc.*, vol. 135, no. 6, pp. 1337–1348, Jun. 1988.
- [161] H. M. Ha, J.-H. Ai, and J. R. Scully, "Effects of Prior Cold Work on Hydrogen Trapping and Diffusion in API X-70 Line Pipe Steel During Electrochemical Charging," *Corrosion*, vol. 70, no. 2, pp. 166–184, Aug. 2013.
- [162] G. Z. Meng, C. Zhang, and Y. F. Cheng, "Effects of corrosion product deposit on the subsequent cathodic and anodic reactions of X-70 steel in near-neutral pH solution," *Corros. Sci.*, vol. 50, no. 11, pp. 3116–3122, Nov. 2008.
- [163] G01 Committee, "Reference Test Method for Making Potentiodynamic Anodic Polarization Measurements," ASTM International, 2014.
- [164] J. Zhou, X. Li, C. Du, Y. Pan, T. Li, and Q. Liu, "Passivation process of X80 pipeline steel in bicarbonate solutions," *Int. J. Miner. Metall. Mater.*, vol. 18, no. 2, pp. 178–185, Apr. 2011.
- [165] G01 Committee, "Test Method for Conducting Potentiodynamic Polarization Resistance Measurements," ASTM International, 1900.
- [166] C. Zhang and Y. F. Cheng, "Corrosion of Welded X100 Pipeline Steel in a Near-Neutral pH Solution," *J. Mater. Eng. Perform.*, vol. 19, no. 6, pp. 834–840, Aug. 2010.
- [167] K. Darowicki, S. Krakowiak, and P. Ślepski, "Evaluation of pitting corrosion by means of dynamic electrochemical impedance spectroscopy," *Electrochimica Acta*, vol. 49, no. 17–18, pp. 2909–2918, Jul. 2004.
- [168] K. Darowicki, "Theoretical description of the measuring method of instantaneous impedance spectra," *J. Electroanal. Chem.*, vol. 486, no. 2, pp. 101–105, May 2000.

- [169] N. Boes and H. Züchner, "Electrochemical methods for studying diffusion, permeation and solubility of hydrogen in metals," *J. Common Met.*, vol. 49, pp. 223–240, Sep. 1976.
- [170] Gulf Interstate Engineering, *Temporary Right-of-Way Width Requirements for Pipeline Construction*. Houston, TX: INGAA Foundation, 1998.
- [171] B. T. Lu, J. L. Luo, and P. R. Norton, "Environmentally assisted cracking mechanism of pipeline steel in near-neutral pH groundwater," *Corros. Sci.*, vol. 52, no. 5, pp. 1787–1795, May 2010.
- [172] I. M. Gadala and A. Alfantazi, "Electrochemical behavior of API-X100 pipeline steel in NS4, near-neutral, and mildly alkaline pH simulated soil solutions," *Corros. Sci.*, vol. 82, pp. 45–57, May 2014.
- [173] J.-B. Li and J.-E. Zuo, "Influences of temperature and pH value on the corrosion behaviors of X80 pipeline steel in carbonate/bicarbonate buffer solution.," *Chin. J. Chem.*, vol. 26, no. 10, pp. 1799–1805, 2008.
- [174] Y. M. Zeng, J. L. Luo, and P. R. Norton, "Initiation and propagation of pitting and crevice corrosion of hydrogen-containing passive films on X70 micro-alloyed steel," *Electrochimica Acta*, vol. 49, no. 5, pp. 703–714, Feb. 2004.
- [175] Z. Lu, C. Huang, D. Huang, and W. Yang, "Effects of a magnetic field on the anodic dissolution, passivation and transpassivation behaviour of iron in weakly alkaline solutions with or without halides," *Corros. Sci.*, vol. 48, no. 10, pp. 3049–3077, Oct. 2006.
- [176] J. Xie, C. Foy, R. Worthingham, and M. Piazza, "Environmental effects on the susceptibility and crack growth of near neutral pH stress corrosion cracking," *Proceedings of NACE Corrosion 2010*, 2010.
- [177] L. Zhang, X. G. Li, C. W. Du, and Y. F. Cheng, "Corrosion and Stress Corrosion Cracking Behavior of X70 Pipeline Steel in a CO₂-Containing Solution," *J. Mater. Eng. Perform.*, vol. 18, no. 3, pp. 319–323, Apr. 2009.
- [178] E. B. Castro and J. R. Vilche, "Electrooxidation/electroreduction processes at composite iron hydroxide layers in carbonate-bicarbonate buffers," *J. Appl. Electrochem.*, vol. 21, no. 6, pp. 543–551, Jun. 1991.
- [179] E. B. Castro, C. R. Valentini, C. A. Moina, J. R. Vilche, and A. J. Arvia, "The influence of ionic composition on the electrodisolution and passivation of iron electrodes in potassium carbonate-bicarbonate solutions in the 8.4–10.5 pH range at 25°C," *Corros. Sci.*, vol. 26, no. 10, pp. 781–793, 1986.
- [180] L. S. Moiseeva, "Carbon dioxide corrosion of oil and gas field equipment," *Prot. Met.*, vol. 41, no. 1, pp. 76–83, Jan. 2005.
- [181] X. Mao, X. Liu, and R. W. Revie, "Pitting Corrosion of Pipeline Steel in Dilute Bicarbonate Solution with Chloride Ions," *Corrosion*, vol. 50, no. 9, pp. 651–657, Sep. 1994.
- [182] J. Zhou, X. Li, C. Du, Y. Pan, T. Li, and Q. Liu, "Passivation process of X80 pipeline steel in bicarbonate solutions," *Int. J. Miner. Metall. Mater.*, vol. 18, no. 2, pp. 178–185, Apr. 2011.
- [183] M. M. El-Naggar, "Effects of Cl⁻, NO₃⁻ and SO₄²⁻ anions on the anodic behavior of carbon steel in deaerated 0.50 M NaHCO₃ solutions," *Appl. Surf. Sci.*, vol. 252, no. 18, pp. 6179–6194, Jul. 2006.

- [184] J. Jelinek and P. Neufeld, "Temperature effect on pitting corrosion of mild steel in de-aerated sodium bicarbonate-chloride solutions," *Corros. Sci.*, vol. 20, no. 4, pp. 489–496, 1980.
- [185] B. Beverskog and I. Puigdomenech, "Revised pourbaix diagrams for iron at 25–300 °C," *Corros. Sci.*, vol. 38, no. 12, pp. 2121–2135, Dec. 1996.
- [186] S. I. Hirnyi, "Anodic Hydrogenation of Iron in a Carbonate–Bicarbonate Solution," *Mater. Sci.*, vol. 37, no. 3, pp. 491–498, May 2001.
- [187] F. F. Eliyan and A. Alfantazi, "Corrosion of the Heat-Affected Zones (HAZs) of API-X100 pipeline steel in dilute bicarbonate solutions at 90 °C – An electrochemical evaluation," *Corros. Sci.*, vol. 74, pp. 297–307, Sep. 2013.
- [188] C. M. Rangel, R. A. Leitão, and I. T. Fonseca, "Voltammetric studies of the transpassive dissolution of mild steel in carbonate/bicarbonate solutions," *Electrochimica Acta*, vol. 34, no. 2, pp. 255–263, Feb. 1989.
- [189] S. Simard, M. Drogowska, H. Me´nard, and L. Brossard, "Electrochemical behaviour of 1024 mild steel in slightly alkaline bicarbonate solutions," *J. Appl. Electrochem.*, vol. 27, no. 3, pp. 317–324, Mar. 1997.
- [190] P. Bénézech, J. L. Dandurand, and J. C. Harrichoury, "Solubility product of siderite (FeCO₃) as a function of temperature (25–250 °C)," *Chem. Geol.*, vol. 265, no. 1–2, pp. 3–12, Jul. 2009.
- [191] M. M. El-Naggar, "Cyclic Voltammetric Studies of Carbon Steel in Deaerated NaHCO₃ Solution," *J. Appl. Electrochem.*, vol. 34, no. 9, pp. 911–918, Sep. 2004.
- [192] V. A. Alves and C. M. A. Brett, "Influence of alloying on the passive behaviour of steels in bicarbonate medium," *Corros. Sci.*, vol. 44, no. 9, pp. 1949–1965, Sep. 2002.
- [193] B. W. A. Sherar, P. G. Keech, and D. W. Shoesmith, "Carbon steel corrosion under anaerobic–aerobic cycling conditions in near-neutral pH saline solutions. Part 2: Corrosion mechanism," *Corros. Sci.*, vol. 53, no. 11, pp. 3643–3650, Nov. 2011.
- [194] M. Honarvar Nazari, S. R. Allahkaram, and M. B. Kermani, "The effects of temperature and pH on the characteristics of corrosion product in CO₂ corrosion of grade X70 steel," *Mater. Des.*, vol. 31, no. 7, pp. 3559–3563, Aug. 2010.
- [195] F. M. Al-Kharafi, B. G. Ateya, and R. M. Abdallah, "Electrochemical behaviour of low carbon steel in concentrated carbonate chloride brines," *J. Appl. Electrochem.*, vol. 32, no. 12, pp. 1363–1370, Dec. 2002.
- [196] F. Farelas, M. Galicia, B. Brown, S. Nesic, and H. Castaneda, "Evolution of dissolution processes at the interface of carbon steel corroding in a CO₂ environment studied by EIS," *Corros. Sci.*, vol. 52, no. 2, pp. 509–517, Feb. 2010.
- [197] G. J. Brug, A. L. G. van den Eeden, M. Sluyters-Rehbach, and J. H. Sluyters, "The analysis of electrode impedances complicated by the presence of a constant phase element," *J. Electroanal. Chem. Interfacial Electrochem.*, vol. 176, no. 1–2, pp. 275–295, Sep. 1984.
- [198] S. L. Wu, Z. D. Cui, G. X. Zhao, M. L. Yan, S. L. Zhu, and X. J. Yang, "EIS study of the surface film on the surface of carbon steel from supercritical carbon dioxide corrosion," *Appl. Surf. Sci.*, vol. 228, no. 1–4, pp. 17–25, Apr. 2004.

- [199] G. Zhao, X. Lu, J. Xiang, and Y. Han, "Formation Characteristic of CO₂ Corrosion Product Layer of P110 Steel Investigated by SEM and Electrochemical Techniques," *J. Iron Steel Res. Int.*, vol. 16, no. 4, pp. 89–94, Jul. 2009.
- [200] M. Ergun and A. Y. Turan, "Pitting potential and protection potential of carbon steel for chloride ion and the effectiveness of different inhibiting anions," *Corros. Sci.*, vol. 32, no. 10, pp. 1137–1142, 1991.
- [201] Y. F. Cheng, *Stress Corrosion Cracking of Pipelines*. Wiley, 2013.
- [202] M. M. El-Naggar, "Effects of Cl⁻, NO₃⁻ and SO₄²⁻ anions on the anodic behavior of carbon steel in deaerated 0.50 M NaHCO₃ solutions," *Appl. Surf. Sci.*, vol. 252, no. 18, pp. 6179–6194, Jul. 2006.
- [203] J. W. Schultze and M. M. Lohrengel, "Stability, reactivity and breakdown of passive films. Problems of recent and future research," *Electrochimica Acta*, vol. 45, no. 15–16, pp. 2499–2513, May 2000.
- [204] Y. F. Cheng and J. L. Luo, "Electronic structure and pitting susceptibility of passive film on carbon steel," *Electrochimica Acta*, vol. 44, no. 17, pp. 2947–2957, Apr. 1999.
- [205] R. D. Gryse, W. P. Gomes, F. Cardon, and J. Vennik, "On the Interpretation of Mott-Schottky Plots Determined at Semiconductor/Electrolyte Systems," *J. Electrochem. Soc.*, vol. 122, no. 5, pp. 711–712, May 1975.
- [206] G. Nogami, "Some Aspects of Large Frequency Dispersion of Mott-Schottky Plots in TiO₂ Electrodes," *J. Electrochem. Soc.*, vol. 132, no. 1, pp. 76–81, Jan. 1985.
- [207] G. S. Popkurov, "Fast time-resolved electrochemical impedance spectroscopy for investigations under nonstationary conditions," *Electrochimica Acta*, vol. 41, no. 7–8, pp. 1023–1027, May 1996.
- [208] G. Zhao, X. Lu, J. Xiang, and Y. Han, "Formation Characteristic of CO₂ Corrosion Product Layer of P110 Steel Investigated by SEM and Electrochemical Techniques," *J. Iron Steel Res. Int.*, vol. 16, no. 4, pp. 89–94, Jul. 2009.
- [209] S. F. Mertens, C. Xhoffer, B. C. De Cooman, and E. Temmerman, "Short-Term Deterioration of Polymer-Coated 55% Al-Zn — Part 1: Behavior of Thin Polymer Films," *Corrosion*, vol. 53, no. 5, pp. 381–388, May 1997.
- [210] K. Y. Foo and B. H. Hameed, "Insights into the modeling of adsorption isotherm systems," *Chem. Eng. J.*, vol. 156, no. 1, pp. 2–10, Jan. 2010.
- [211] H. Ma, X. Cheng, S. Chen, C. Wang, J. Zhang, and H. Yang, "An ac impedance study of the anodic dissolution of iron in sulfuric acid solutions containing hydrogen sulfide," *J. Electroanal. Chem.*, vol. 451, no. 1–2, pp. 11–17, Jul. 1998.
- [212] D. H. Davies and G. T. Burstein, "The Effects of Bicarbonate on the Corrosion and Passivation of Iron," *Corrosion*, vol. 36, no. 8, pp. 416–422, Aug. 1980.
- [213] Y. Chen and W. Jepson, "EIS measurement for corrosion monitoring under multiphase flow conditions," *Electrochimica Acta*, vol. 44, no. 24, pp. 4453–4464, Jul. 1999.
- [214] F. F. Eliyan, E.-S. Mahdi, and A. Alfantazi, "Electrochemical evaluation of the corrosion behaviour of API-X100 pipeline steel in aerated bicarbonate solutions," *Corros. Sci.*, vol. 58, pp. 181–191, May 2012.
- [215] C. T. Lee, Z. Qin, M. Odziemkowski, and D. W. Shoesmith, "The influence of groundwater anions on the impedance behaviour of carbon steel corroding under

- anoxic conditions,” *Electrochimica Acta*, vol. 51, no. 8–9, pp. 1558–1568, Jan. 2006.
- [216] J. E. B. Randles, “Kinetics of rapid electrode reactions,” *Discuss. Faraday Soc.*, vol. 1, no. 0, pp. 11–19, Jan. 1947.
- [217] L. Niu and Y. F. Cheng, “Corrosion behavior of X-70 pipe steel in near-neutral pH solution,” *Appl. Surf. Sci.*, vol. 253, no. 21, pp. 8626–8631, Aug. 2007.
- [218] X. Mao, X. Liu, and R. W. Revie, “Pitting Corrosion of Pipeline Steel in Dilute Bicarbonate Solution with Chloride Ions,” *Corrosion*, vol. 50, no. 9, pp. 651–657, Sep. 1994.
- [219] L. J. Mu and W. Z. Zhao, “Investigation on carbon dioxide corrosion behaviour of HP13Cr110 stainless steel in simulated stratum water,” *Corros. Sci.*, vol. 52, no. 1, pp. 82–89, Jan. 2010.
- [220] P. Bénézech, J. L. Dandurand, and J. C. Harrichoury, “Solubility product of siderite (FeCO_3) as a function of temperature (25–250 °C),” *Chem. Geol.*, vol. 265, no. 1–2, pp. 3–12, Jul. 2009.
- [221] J. F. Dewald, “The charge distribution at the zinc oxide-electrolyte interface,” *J. Phys. Chem. Solids*, vol. 14, pp. 155–161, Jul. 1960.
- [222] G. Nogami, “Some Aspects of Large Frequency Dispersion of Mott-Schottky Plots in TiO_2 Electrodes,” *J. Electrochem. Soc.*, vol. 132, no. 1, pp. 76–81, Jan. 1985.
- [223] J. Schoonman, K. Vos, and G. Blasse, “Donor Densities in TiO_2 Photoelectrodes,” *J. Electrochem. Soc.*, vol. 128, no. 5, pp. 1154–1157, May 1981.
- [224] D. G. Li, Y. R. Feng, Z. Q. Bai, J. W. Zhu, and M. S. Zheng, “Influence of temperature, chloride ions and chromium element on the electronic property of passive film formed on carbon steel in bicarbonate/carbonate buffer solution,” *Electrochimica Acta*, vol. 52, no. 28, pp. 7877–7884, Nov. 2007.
- [225] B. Beverskog and I. Puigdomenech, “Revised pourbaix diagrams for iron at 25–300 °C,” *Corros. Sci.*, vol. 38, no. 12, pp. 2121–2135, Dec. 1996.
- [226] Z. Lu, C. Huang, D. Huang, and W. Yang, “Effects of a magnetic field on the anodic dissolution, passivation and transpassivation behaviour of iron in weakly alkaline solutions with or without halides,” *Corros. Sci.*, vol. 48, no. 10, pp. 3049–3077, Oct. 2006.
- [227] W. Xu, K. Daub, X. Zhang, J. J. Noel, D. W. Shoesmith, and J. C. Wren, “Oxide formation and conversion on carbon steel in mildly basic solutions,” *Electrochimica Acta*, vol. 54, no. 24, pp. 5727–5738, Oct. 2009.
- [228] X.-P. Guo, Y. Tomoe, H. Imaizumi, and K. Katoh, “The electrochemical behavior and impedance characteristics of the passive film on carbon steel in nitric acid solutions,” *J. Electroanal. Chem.*, vol. 445, no. 1–2, pp. 95–103, Mar. 1998.
- [229] B. W. A. Sherar, P. G. Keech, and D. W. Shoesmith, “The effect of sulfide on the aerobic corrosion of carbon steel in near-neutral pH saline solutions,” *Corros. Sci.*, vol. 66, pp. 256–262, Jan. 2013.
- [230] I. B. Butler, M. A. A. Schoonen, and D. T. Rickard, “Removal of dissolved oxygen from water: A comparison of four common techniques,” *Talanta*, vol. 41, no. 2, pp. 211–215, Feb. 1994.

- [231] F. Farahbod, "Investigations to find appropriate range of pH and a new replacement for hydrazine to protect corrosion in steam-tanks of petrochemical industries," *Eng. Fail. Anal.*, vol. 22, pp. 38–49, Jun. 2012.
- [232] A. M. Shams el din and R. A. Arain, "The kinetics of oxygen scavenging by catalysed hydrazine," *Corros. Sci.*, vol. 29, no. 4, pp. 445–453, 1989.
- [233] J. C. Fanning, "The chemical reduction of nitrate in aqueous solution," *Coord. Chem. Rev.*, vol. 199, no. 1, pp. 159–179, Apr. 2000.
- [234] I. M. Gadala and A. Alfantazi, "Bicarbonate, Temperature, and pH Influences on the Passivation of API-X100 Pipeline Steel in Simulated Groundwater Solutions," *Proceedings of the 2014 10th International Pipeline Conference*, Paper No. IPC2014-33180, p. V002T06A072, Calgary, Alberta, Canada, September 29 – October 3, 2014.
- [235] K. -Lal, P. S. Minhas, and R. K. Yadav, "Long-term impact of wastewater irrigation and nutrient rates II. Nutrient balance, nitrate leaching and soil properties under peri-urban cropping systems," *Agric. Water Manag.*, vol. 156, pp. 110–117, Jul. 2015.
- [236] Z. Wang, Y. Miao, and S. Li, "Effect of ammonium and nitrate nitrogen fertilizers on wheat yield in relation to accumulated nitrate at different depths of soil in drylands of China," *Field Crops Res.*, vol. 183, pp. 211–224, Nov. 2015.
- [237] J. Guo, S. Yang, C. Shang, Y. Wang, and X. He, "Influence of carbon content and microstructure on corrosion behaviour of low alloy steels in a Cl⁻ containing environment," *Corros. Sci.*, vol. 51, no. 2, pp. 242–251, Feb. 2009.
- [238] S. Bordbar, M. Alizadeh, and S. H. Hashemi, "Effects of microstructure alteration on corrosion behavior of welded joint in API X70 pipeline steel," *Mater. Des.*, vol. 45, pp. 597–604, Mar. 2013.
- [239] G. A. Zhang and Y. F. Cheng, "Micro-electrochemical characterization of corrosion of welded X70 pipeline steel in near-neutral pH solution," *Corros. Sci.*, vol. 51, no. 8, pp. 1714–1724, Aug. 2009.
- [240] F. King and T. R. Jack, "Role of Redox and Corrosion Potentials in the Corrosion of Line Pipe Steel," Pipeline Research Council International, PR-261-9711, Sep. 2001.
- [241] V. E. P. Perez and A. Alfantazi, "Effects of Oxygen and Sulfate Concentrations on the Corrosion Behavior of Zinc in NaCl Solutions," *Corrosion*, vol. 68, no. 3, pp. 35005–1, Mar. 2012.
- [242] B. Debelius, A. Gómez-Parra, and J. M. Forja, "Oxygen solubility in evaporated seawater as a function of temperature and salinity," *Hydrobiologia*, vol. 632, no. 1, pp. 157–165, Jun. 2009.
- [243] E. McCafferty, "Validation of corrosion rates measured by the Tafel extrapolation method," *Corros. Sci.*, vol. 47, no. 12, pp. 3202–3215, Dec. 2005.
- [244] E. E. Stansbury and R. A. Buchanan, *Fundamentals of Electrochemical Corrosion*. ASM International, 2000.
- [245] H. M. Ha, I. M. Gadala, and A. Alfantazi, "Hydrogen Evolution and Absorption in an API X100 Line Pipe Steel Exposed to Near-Neutral pH Solutions," *Electrochimica Acta*, vol. 204, pp. 18–30, Jun. 2016.

- [246] A. P. Grosvenor, B. A. Kobe, M. C. Biesinger, and N. S. McIntyre, "Investigation of multiplet splitting of Fe 2p XPS spectra and bonding in iron compounds," *Surf. Interface Anal.*, vol. 36, no. 12, pp. 1564–1574, Dec. 2004.
- [247] R. P. Gupta and S. K. Sen, "Calculation of multiplet structure of core p-vacancy levels," *Phys. Rev. B*, vol. 10, no. 1, pp. 71–77, Jul. 1974.
- [248] N. S. McIntyre and D. G. Zetaruk, "X-ray photoelectron spectroscopic studies of iron oxides," *Anal. Chem.*, vol. 49, no. 11, pp. 1521–1529, Sep. 1977.
- [249] M. A. Legodi and D. de Waal, "The preparation of magnetite, goethite, hematite and maghemite of pigment quality from mill scale iron waste," *Dyes Pigments*, vol. 74, no. 1, pp. 161–168, 2007.
- [250] J.-E. Hiller, "Phasenumwandlungen im Rost," *Mater. Corros.*, vol. 17, no. 11, pp. 943–951, Nov. 1966.
- [251] M. Honarvar Nazari, S. R. Allahkaram, and M. B. Kermani, "The effects of temperature and pH on the characteristics of corrosion product in CO₂ corrosion of grade X70 steel," *Mater. Des.*, vol. 31, no. 7, pp. 3559–3563, Aug. 2010.
- [252] A. Pineau, N. Kanari, and I. Gaballah, "Kinetics of reduction of iron oxides by H₂: Part I: Low temperature reduction of hematite," *Thermochim. Acta*, vol. 447, no. 1, pp. 89–100, Aug. 2006.
- [253] T. Jack R., M. Wilmott J., R. Sutherby L., and R. Worthingham G., "External corrosion of line pipe -- A summary of research activities," *Mater. Perform.*, vol. 35, no. 3, pp. 18–24, 1996.
- [254] W. Han, G. Yu, Z. Wang, and J. Wang, "Characterisation of initial atmospheric corrosion carbon steels by field exposure and laboratory simulation," *Corros. Sci.*, vol. 49, no. 7, pp. 2920–2935, Jul. 2007.
- [255] M. Stratmann and J. Müller, "The mechanism of the oxygen reduction on rust-covered metal substrates," *Corros. Sci.*, vol. 36, no. 2, pp. 327–359, Feb. 1994.
- [256] Y. H. Huang and T. C. Zhang, "Reduction of nitrobenzene and formation of corrosion coatings in zerovalent iron systems," *Water Res.*, vol. 40, no. 16, pp. 3075–3082, Sep. 2006.
- [257] K. Ritter, M. S. Odziemkowski, R. Simpgraga, R. W. Gillham, and D. E. Irish, "An in situ study of the effect of nitrate on the reduction of trichloroethylene by granular iron," *J. Contam. Hydrol.*, vol. 65, no. 1–2, pp. 121–136, Aug. 2003.
- [258] Y. Tamaura, K. Ito, and T. Katsura, "Transformation of γ -FeO(OH) to Fe₃O₄ by adsorption of iron(II) ion on γ -FeO(OH)," *J. Chem. Soc. Dalton Trans.*, no. 2, pp. 189–194, Jan. 1983.
- [259] R. M. Cornell and U. Schwertmann, *The Iron Oxides: Structure, Properties, Reactions, Occurrences and Uses*, 2nd, Completely Revised and Extended Edition edition ed. Weinheim: Wiley-VCH, 2003.
- [260] D. H. Everett, "Thermodynamics of adsorption from solution. Part 1.— Perfect systems," *Trans. Faraday Soc.*, vol. 60, no. 0, pp. 1803–1813, Jan. 1964.
- [261] C. Dong, K. Xiao, Z. Liu, W. Yang, and X. Li, "Hydrogen induced cracking of X80 pipeline steel," *Int. J. Miner. Metall. Mater.*, vol. 17, no. 5, pp. 579–586, Oct. 2010.
- [262] C. F. Dong, X. G. Li, Z. Y. Liu, and Y. R. Zhang, "Hydrogen-induced cracking and healing behaviour of X70 steel," *J. Alloys Compd.*, vol. 484, no. 1–2, pp. 966–972, Sep. 2009.

- [263] C. Manfredi and J. L. Otegui, "Failures by SCC in buried pipelines," *Eng. Fail. Anal.*, vol. 9, no. 5, pp. 495–509, Oct. 2002.
- [264] R. B. Rebak, Z. Xia, R. Safruddin, and Z. Szklarska-Smialowska, "Effect of Solution Composition and Electrochemical Potential on Stress Corrosion Cracking of X-52 Pipeline Steel," *Corrosion*, vol. 52, no. 5, pp. 396–405, May 1996.
- [265] E. A. Charles and R. N. Parkins, "Generation of Stress Corrosion Cracking Environments at Pipeline Surfaces," *Corrosion*, vol. 51, no. 7, pp. 518–527, Jul. 1995.
- [266] R. N. Parkins, "A Review of Stress Corrosion Cracking of High Pressure Gas Pipelines," *Presented at the Corrosion 2000*, 2000.
- [267] A. Q. Fu and Y. F. Cheng, "Electrochemical polarization behavior of X70 steel in thin carbonate/bicarbonate solution layers trapped under a disbanded coating and its implication on pipeline SCC," *Corros. Sci.*, vol. 52, no. 7, pp. 2511–2518, Jul. 2010.
- [268] S. Nestic, J. Postlethwaite, and S. Olsen, "An Electrochemical Model for Prediction of Corrosion of Mild Steel in Aqueous Carbon Dioxide Solutions," *Corrosion*, vol. 52, no. 4, pp. 280–294, Apr. 1996.
- [269] B. Mishra, S. Al-Hassan, D. L. Olson, and M. M. Salama, "Development of a Predictive Model for Activation-Controlled Corrosion of Steel in Solutions Containing Carbon Dioxide," *Corrosion*, vol. 53, no. 11, pp. 852–859, Nov. 1997.
- [270] J. McBreen, L. Nonis, and W. Beck, "A Method for Determination of the Permeation Rate of Hydrogen Through Metal Membranes," *J. Electrochem. Soc.*, vol. 113, no. 11, pp. 1218–1222, Nov. 1966.
- [271] H. M. Ha and J. H. Payer, "Devitrification of Fe-Based Amorphous Metal SAM 1651: A Structural and Compositional Study," *Metall. Mater. Trans. A*, vol. 40, no. 11, pp. 2519–2529, Oct. 2009.
- [272] J. Kittel, F. Ropital, and J. Pellier, "Effect of Membrane Thickness on Hydrogen Permeation in Steels During Wet Hydrogen Sulfide Exposure," *Corrosion*, vol. 64, no. 10, pp. 788–799, Oct. 2008.
- [273] W. Stumm, "Calcium Carbonate Deposition at Iron Surfaces," *J. Am. Water Works Assoc.*, vol. 48, no. 3, pp. 300–310, 1956.
- [274] S. L. Wolfson and W. H. Hartt, "An Initial Investigation of Calcareous Deposits upon Cathodic Steel Surfaces in Sea Water," *Corrosion*, vol. 37, no. 2, pp. 70–76, Feb. 1981.
- [275] W. H. Hartt, C. H. Culberson, and S. W. Smith, "Calcareous Deposits on Metal Surfaces in Seawater—A Critical Review," *Corrosion*, vol. 40, no. 11, pp. 609–618, Nov. 1984.
- [276] W. M. Haynes, Ed., *CRC Handbook of Chemistry and Physics, 95th Edition*, 95 edition. CRC Press, 2014.
- [277] "ChemEngineering - Henry's Law." [Online]. Available: <https://chemengineering.wikispaces.com/Henry%27s+Law>. [Accessed: 25-Dec-2016].
- [278] F. Smith, Francis L Smith, and Allan H Harvey, "Avoid Common Pitfalls When Using Henry's Law," *Chem. Eng. Prog.*, vol. 103, no. 9, p. 33, Sep. 2007.

- [279] H. S. Harned and S. R. Scholes, "The Ionization Constant of HCO_3^- from 0 to 50° C," *J. Am. Chem. Soc.*, vol. 63, no. 6, pp. 1706–1709, Jun. 1941.
- [280] F. J. Millero, D. Pierrot, K. Lee, R. Wanninkhof, R. Feely, C. L. Sabine, R. M. Key, and T. Takahashi, "Dissociation constants for carbonic acid determined from field measurements," *Deep Sea Res. Part Oceanogr. Res. Pap.*, vol. 49, no. 10, pp. 1705–1723, Oct. 2002.
- [281] R. N. Roy, L. N. Roy, K. M. Vogel, C. Porter-Moore, T. Pearson, C. E. Good, F. J. Millero, and D. M. Campbell, "The dissociation constants of carbonic acid in seawater at salinities 5 to 45 and temperatures 0 to 45 °C," *Mar. Chem.*, vol. 44, no. 2, pp. 249–267, Dec. 1993.
- [282] M. Nordsveen, S. Nešić, R. Nyborg, and A. Stangeland, "A Mechanistic Model for Carbon Dioxide Corrosion of Mild Steel in the Presence of Protective Iron Carbonate Films—Part 1: Theory and Verification," *Corrosion*, vol. 59, no. 5, pp. 443–456, May 2003.
- [283] M. Cabrini, S. Lorenzi, P. Marcassoli, and T. Pastore, "Hydrogen embrittlement behavior of HSLA line pipe steel under cathodic protection," *Corros. Rev.*, vol. 29, no. 5–6, pp. 261–274, 2011.
- [284] A. Contreras, A. Albitar, M. Salazar, and R. Pérez, "Slow strain rate corrosion and fracture characteristics of X-52 and X-70 pipeline steels," *Mater. Sci. Eng. A*, vol. 407, no. 1–2, pp. 45–52, Oct. 2005.
- [285] S. U. Koh, H. G. Jung, K. B. Kang, G. T. Park, and K. Y. Kim, "Effect of Microstructure on Hydrogen-Induced Cracking of Linepipe Steels," *Corrosion*, vol. 64, no. 7, pp. 574–585, Jul. 2008.
- [286] S. U. Koh, B. Y. Yang, and K. Y. Kim, "Effect of Alloying Elements on the Susceptibility to Sulfide Stress Cracking of Line Pipe Steels," *Corrosion*, vol. 60, no. 3, pp. 262–274, Mar. 2004.
- [287] S. U. Koh, J. S. Kim, B. Y. Yang, and K. Y. Kim, "Effect of Line Pipe Steel Microstructure on Susceptibility to Sulfide Stress Cracking," *Corrosion*, vol. 60, no. 3, pp. 244–253, Mar. 2004.
- [288] P. Liang, C. Du, X. Li, X. Chen, and Z. Liang, "Effect of hydrogen on the stress corrosion cracking behavior of X80 pipeline steel in Ku'erle soil simulated solution," *Int. J. Miner. Metall. Mater.*, vol. 16, no. 4, pp. 407–413, Aug. 2009.
- [289] C. E. Zambra and N. O. Moraga, "Heat and mass transfer in landfills: Simulation of the pile self-heating and of the soil contamination," *Int. J. Heat Mass Transf.*, vol. 66, pp. 324–333, Nov. 2013.
- [290] I. M. Gadala, M. Abdel Wahab, and A. Alfantazi, "Numerical simulations of soil physicochemistry and aeration influences on the external corrosion and cathodic protection design of buried pipeline steels," *Mater. Des.*, vol. 97, pp. 287–299, May 2016.
- [291] W. R. V. Wijk, *Physics of Plant Environment*, First edition. John Wiley & Sons, 1963.
- [292] D. Hillel, *Environmental Soil Physics: Fundamentals, Applications, and Environmental Considerations*, 1st edition. San Diego, CA: Academic Press, 1998.
- [293] J. Bornstein and M. McGuirk, "Modifications to a soil oxygen diffusion ratemeter," *Soil Sci.*, vol. 126, no. 5, pp. 280–284, Nov. 1978.

- [294] A. Eslami, B. Fang, R. Kania, B. Worthingham, J. Been, R. Eadie, W. Chen, “Stress corrosion cracking initiation under the disbanded coating of pipeline steel in near-neutral pH environment,” *Corros. Sci.*, vol. 52, no. 11, pp. 3750–3756, Nov. 2010.
- [295] J. R. Davis, Ed., *Corrosion: Understanding the Basics*. Materials Park, Ohio: ASM Intl, 2000.
- [296] M. Stern and A. L. Geary, “Electrochemical Polarization I. A Theoretical Analysis of the Shape of Polarization Curves,” *J. Electrochem. Soc.*, vol. 104, no. 1, pp. 56–63, Jan. 1957.
- [297] NACE, *Control of External Corrosion on Underground or Submerged Metallic Piping Systems*, [NACE SP-0169-13 Standard]. NACE International, 2013.
- [298] R. W. Revie, *Uhlig’s Corrosion Handbook*. John Wiley & Sons, 2011.
- [299] H. M. Ha, J.-H. Ai, and J. R. Scully, “Effects of Prior Cold Work on Hydrogen Trapping and Diffusion in API X-70 Line Pipe Steel During Electrochemical Charging,” *Corrosion*, vol. 70, no. 2, pp. 166–184, Aug. 2013.
- [300] C. Smith, *Coatings for Corrosion Protection: Offshore Oil and Gas Operation Facilities, Marine Pipeline and Ship Structures, April 14-16, 2004, Biloxi, Mississippi*. U.S. Department of Commerce, Technology Administration, National Institute of Standards and Technology, 2005.
- [301] W. von Baeckmann, W. Schwenk, and W. Prinz, *Handbook of Cathodic Corrosion Protection*. Gulf Professional Publishing, 1997.
- [302] NACE, *Control of External Corrosion on Underground or Submerged Metallic Piping Systems* [NACE SP-0169-96 Standard]. NACE International, 1996.
- [303] B. Gummow, “Corrosion Control of Iron and Steel Water Piping - A Historical Perspective,” *Presented at the NACE Northern Area Eastern Conference*, Quebec City, Canada, 2002.
- [304] S. Nešić and K.-L. J. Lee, “A Mechanistic Model for Carbon Dioxide Corrosion of Mild Steel in the Presence of Protective Iron Carbonate Films—Part 3: Film Growth Model,” *Corrosion*, vol. 59, no. 7, pp. 616–628, Jul. 2003.
- [305] A. P. Teixeira, C. Guedes Soares, T. A. Netto, and S. F. Estefen, “Reliability of pipelines with corrosion defects,” *Int. J. Press. Vessels Pip.*, vol. 85, no. 4, pp. 228–237, Apr. 2008.
- [306] ASME, “Manual for determining the remaining strength of corroded pipelines (supplement to ANSI/ASME B31 code for pressure piping),” 2012.
- [307] S. Natarajan, E. T. Ooi, I. Chiong, and C. Song, “Convergence and accuracy of displacement based finite element formulations over arbitrary polygons: Laplace interpolants, strain smoothing and scaled boundary polygon formulation,” *Finite Elem. Anal. Des.*, vol. 85, pp. 101–122, Aug. 2014.
- [308] M. Pourbaix, *Atlas of electrochemical equilibria in aqueous solutions*. National Association of Corrosion Engineers, 1974.

Appendices

Appendix A: supplementary figures for chapter 5

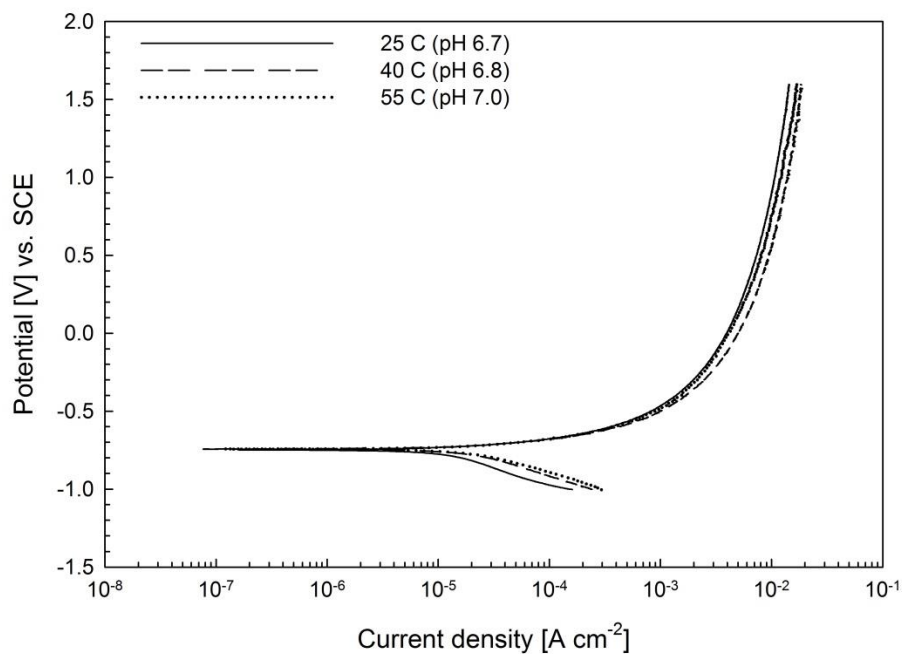


Figure A-1: PDP in 5% CO₂/95% N₂ purged NS4 at 25, 40, and 55 °C (pH 6.7, 6.8, and 7.0, respectively)

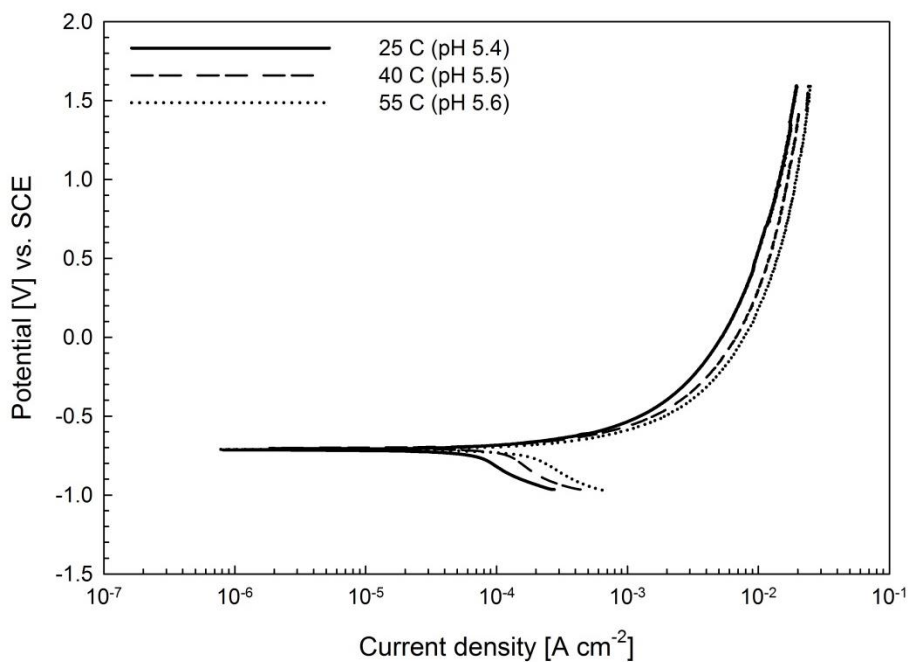


Figure A-2: 100% CO₂ purged NS4 at 25, 40, and 55 °C (pH 5.4, 5.5, and 5.6, respectively)

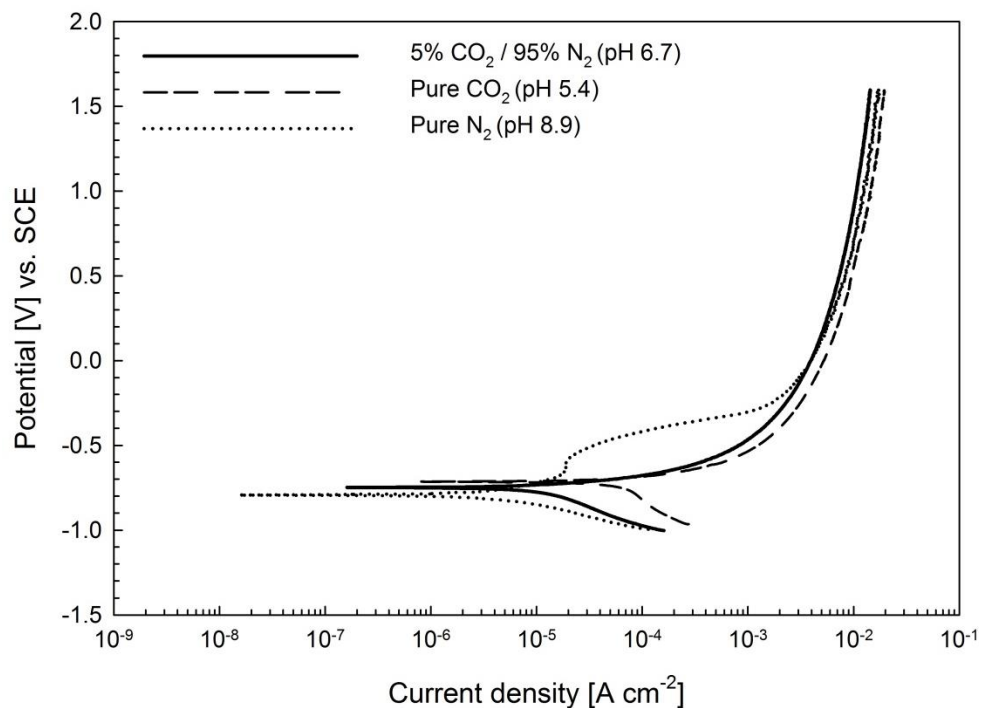


Figure A-3: NS4 at 25 °C with 5% CO₂/95% N₂, 100% CO₂, and 100% N₂ purging gas (pH 6.7, 5.4, and 8.9, respectively)

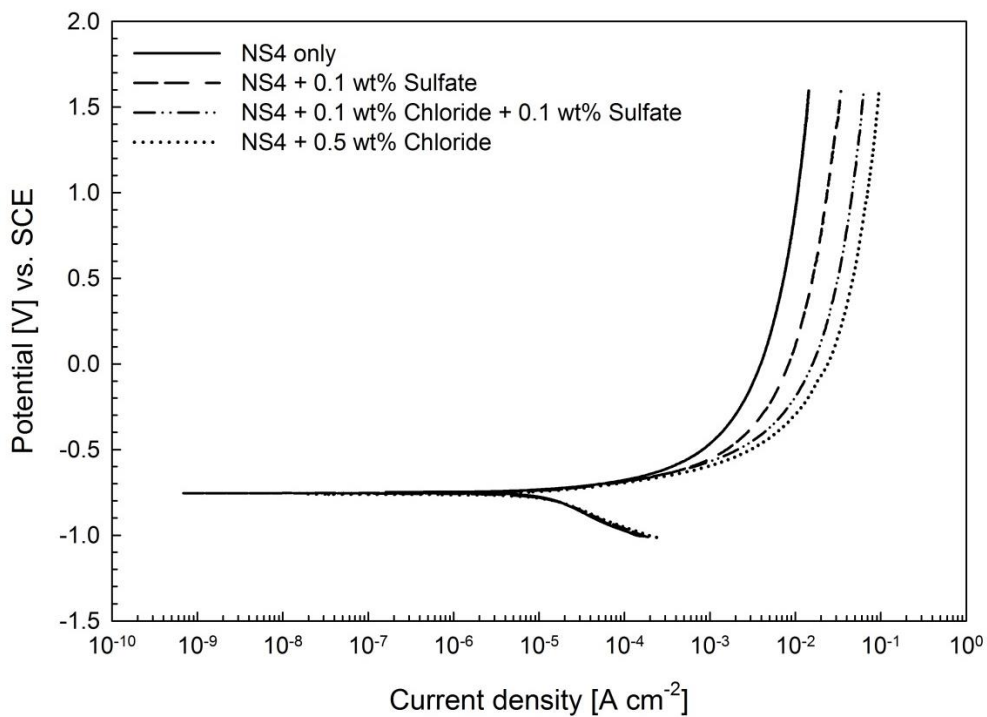


Figure A-4: 5% CO₂/95% N₂ purged NS4 at 25 °C with various Cl⁻ and/or SO₄²⁻ ion concentrations (pH 6.7)

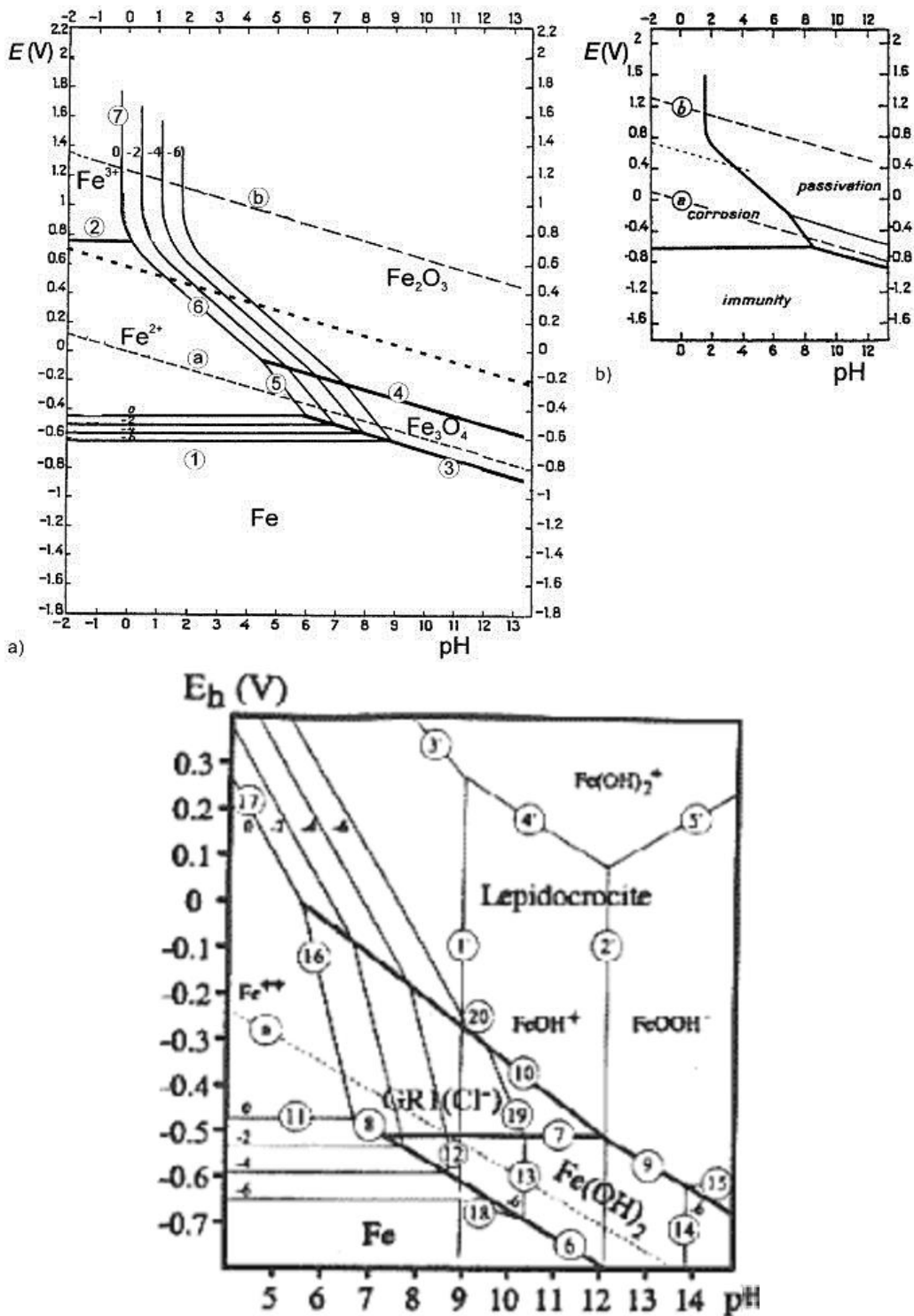


Figure A-5: (top-left) E -pH diagram for Fe in water; (top-right) Simplified E -pH diagram for Fe in water indicating the domains of immunity, corrosion, and passivity, including the experimental passivation potential as a central dashed line; (bottom) E -pH diagram of Fe in water with the presence of chlorides, where GR1(Cl⁻) is chloride green rust ($[\text{Fe}^{2+}_3\text{Fe}^{3+}(\text{HO})_8]^+ \cdot [\text{Cl}^- \cdot n\text{H}_2\text{O}]^-$) [308]

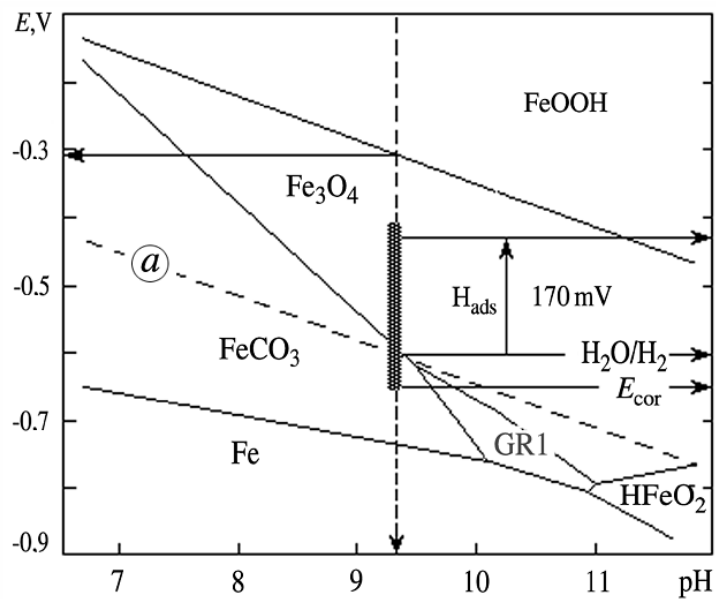


Figure A-6: E - pH diagram for the $Fe-HCO_3^- - CO_3^{2-} - H_2O$ system at around $50\text{ }^\circ\text{C}$, where GR1 is carbonate green rust ($[Fe^{2+}_4Fe^{3+}_2(OH^-)_{12}]^{2+} \cdot [CO_3^{2-} \cdot 2H_2O]^{2-}$) [186]

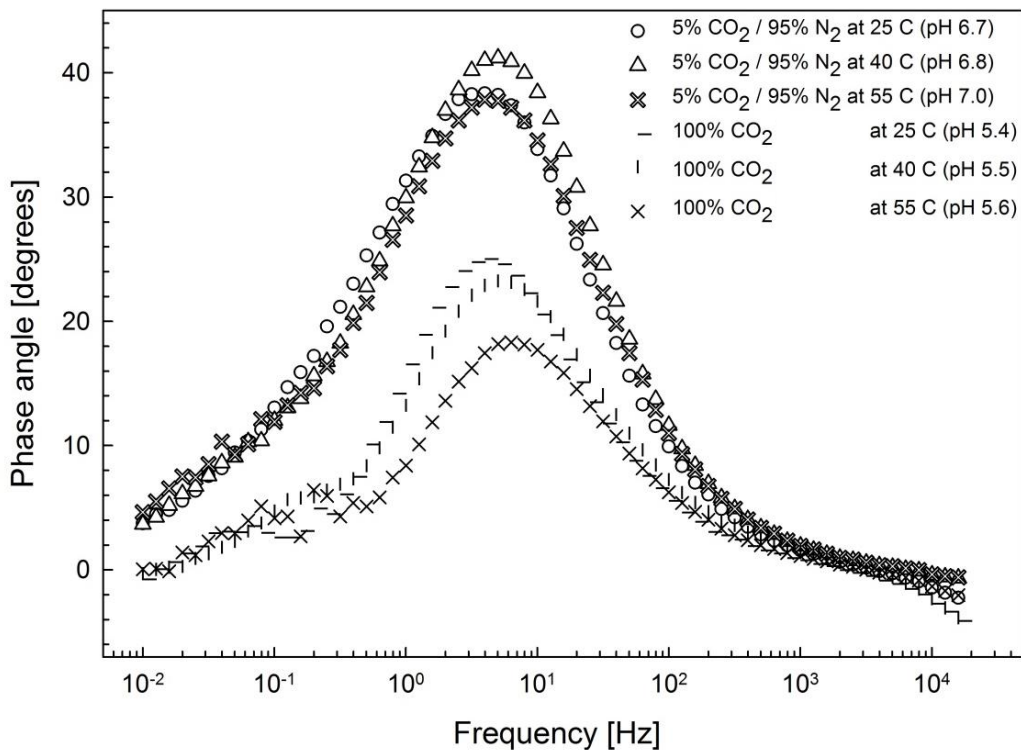


Figure A-7: Bode θ_{EIS} for NS4 solution at 25 , 40 , and $55\text{ }^\circ\text{C}$ purged with 5% $CO_2/95\%$ N_2 (pH 6.7 , 6.8 , and 7.0 , respectively) or 100% CO_2 (pH 5.4 , 5.5 , and 5.6 , respectively)

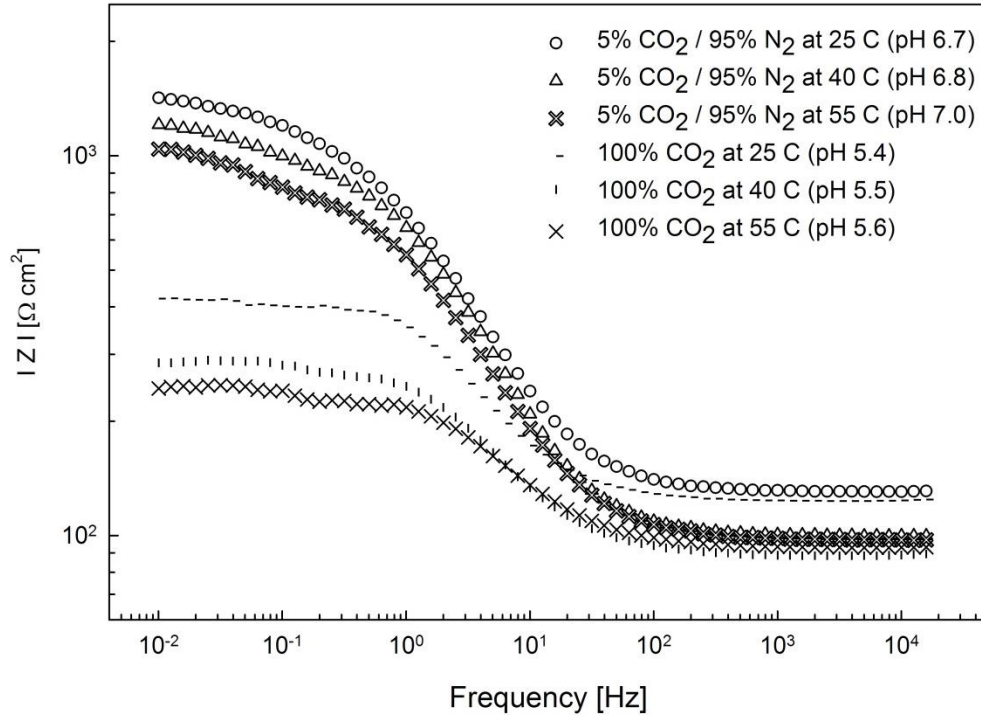


Figure A-8: Bode $|Z|$ for NS4 solution at 25, 40, and 55 °C purged with 5% CO₂/95% N₂ (pH 6.7, 6.8, and 7.0, respectively) or 100% CO₂ (pH 5.4, 5.5, and 5.6, respectively)

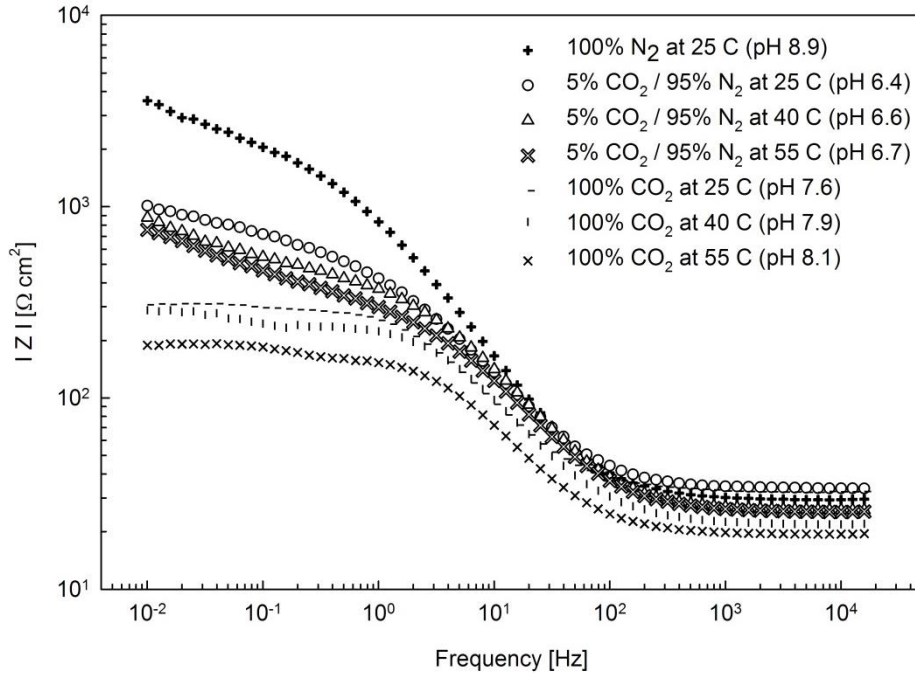


Figure A-9: Bode $|Z|$ for NS4 + 10x HCO₃⁻ solution at 25 °C purged with 100% N₂ (pH 8.9), and at 25, 40, and 55 °C purged with 100% CO₂ (pH 6.4, 6.6, and 6.7, respectively), and 5% CO₂/95% N₂ (pH 7.6, 7.9, and 8.1, respectively)

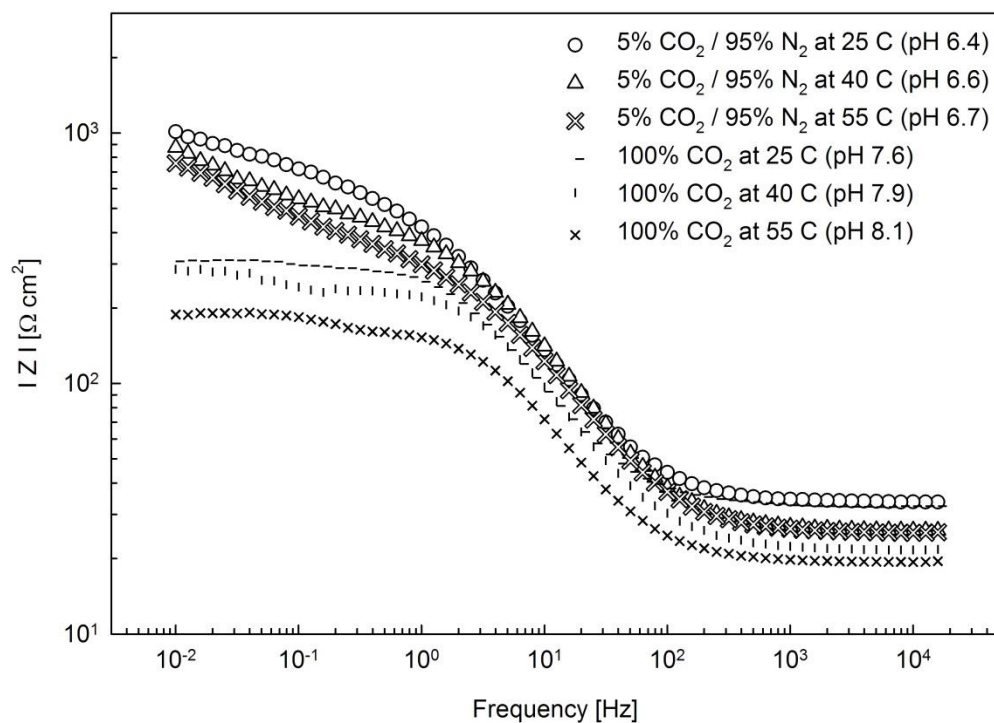


Figure A-10: Enlarged Bode $|Z|$ for NS4 + 10x HCO_3^- solution at 25, 40, and 55 °C purged with 100% CO_2 (pH 6.4, 6.6, and 6.7, respectively), and 5% $\text{CO}_2/95\% \text{N}_2$ (pH 7.6, 7.9, and 8.1, respectively)

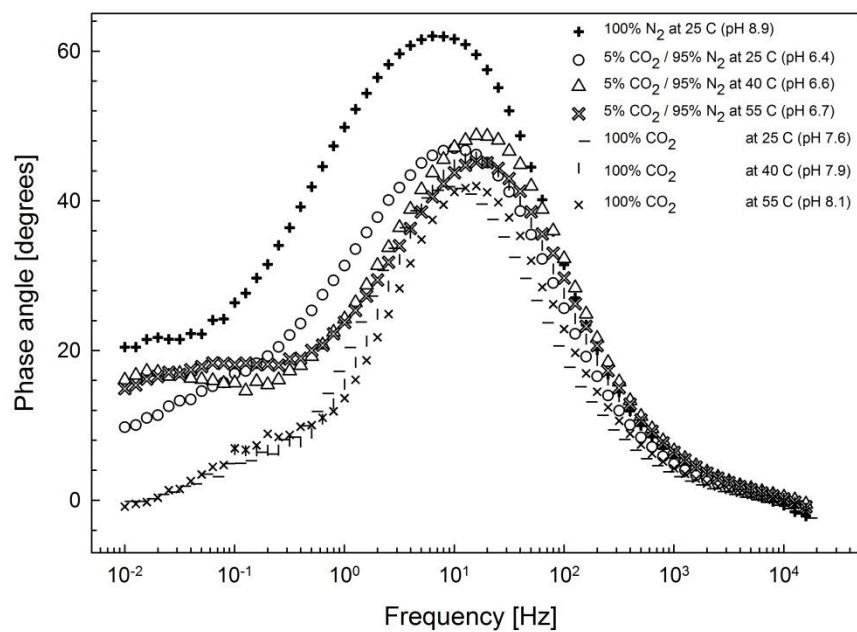


Figure A-11: Bode θ_{EIS} for NS4 + 10x HCO_3^- solution at 25 °C purged with 100% N_2 (pH 8.9), and at 25, 40, and 55 °C purged with 100% CO_2 (pH 6.4, 6.6, and 6.7, respectively), and 5% $\text{CO}_2/95\% \text{N}_2$ (pH 7.6, 7.9, and 8.1, respectively)

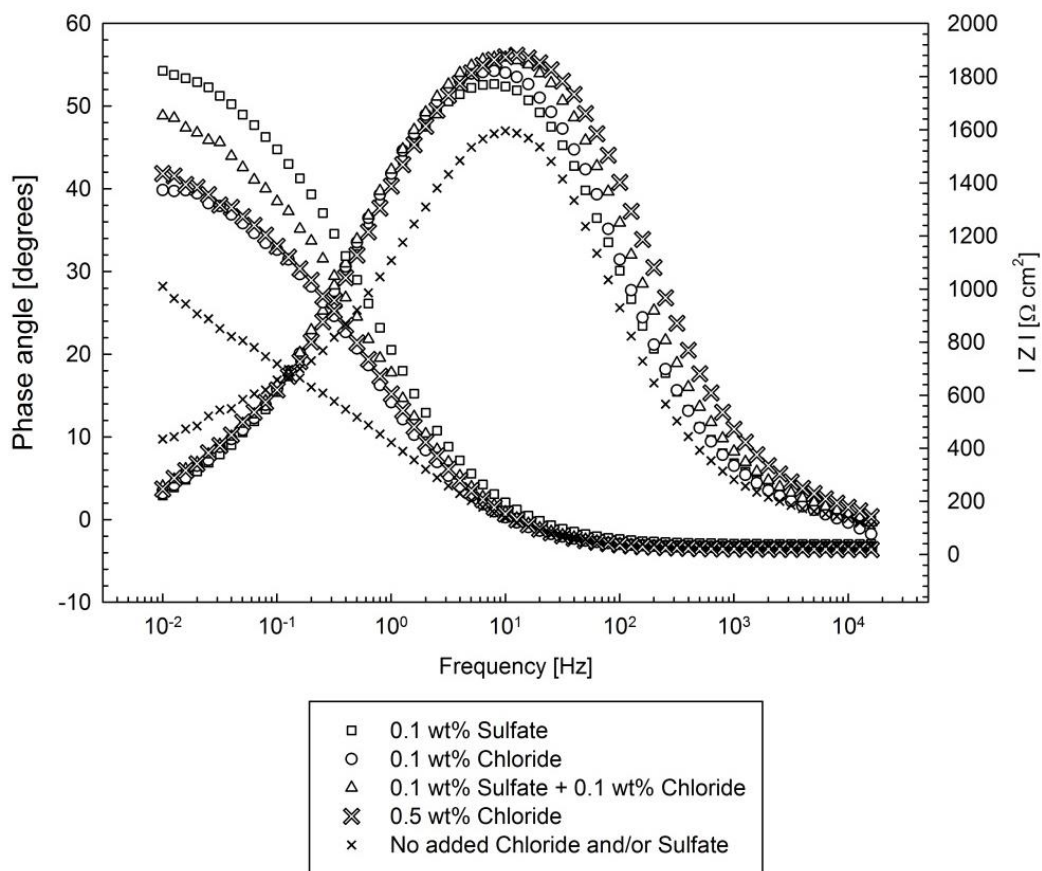


Figure A-12: Bode $|Z|$ and θ_{EIS} plots for NS4 + 10x HCO_3^- solutions with added Cl^- and/or SO_4^{2-} at 25 °C, purged with 5% CO_2 /95% N_2 (pH 7.6)

Appendix B: supplementary figures for chapter 6

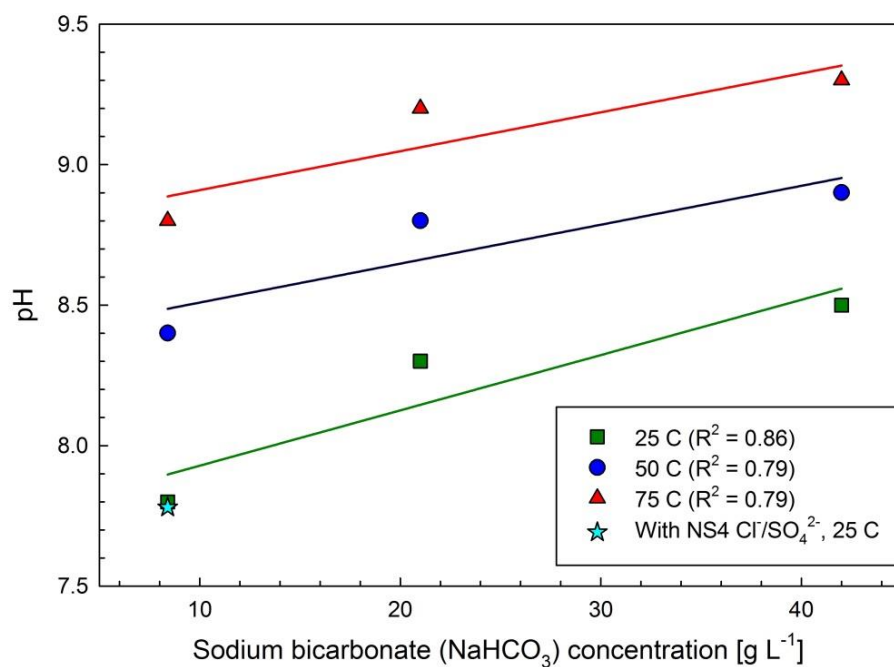


Figure B-1: Solution $[\text{NaHCO}_3]$, pH, and temperature relationships of test conditions in chapter 6

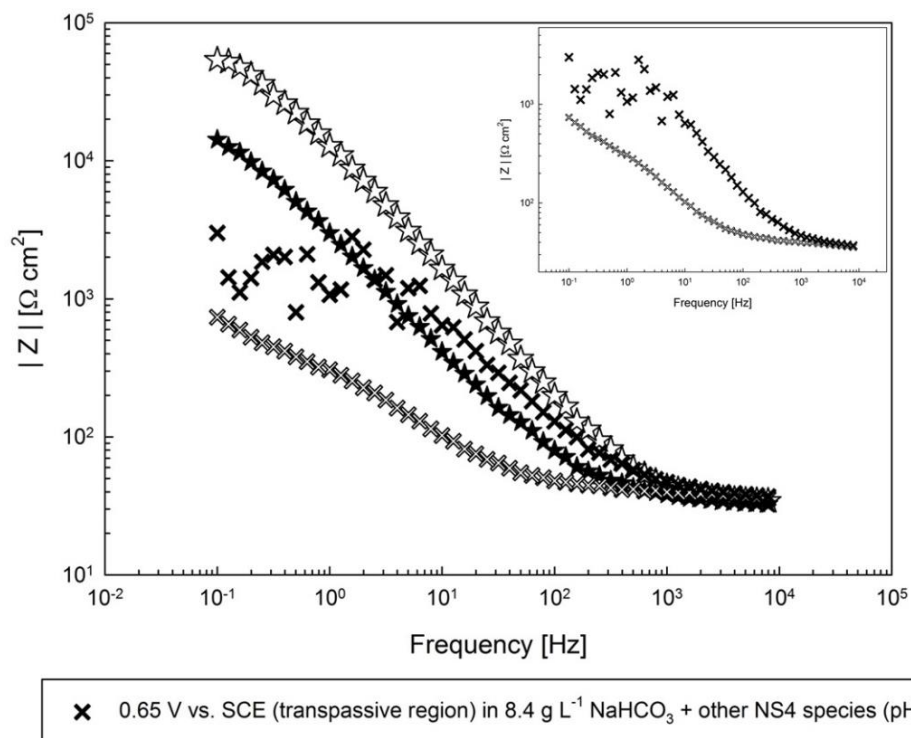


Figure B-2: $|Z|$ vs. frequency in the $E > 0 V_{\text{SCE}}$ region (see Figure 6-5a for legend of star data points)

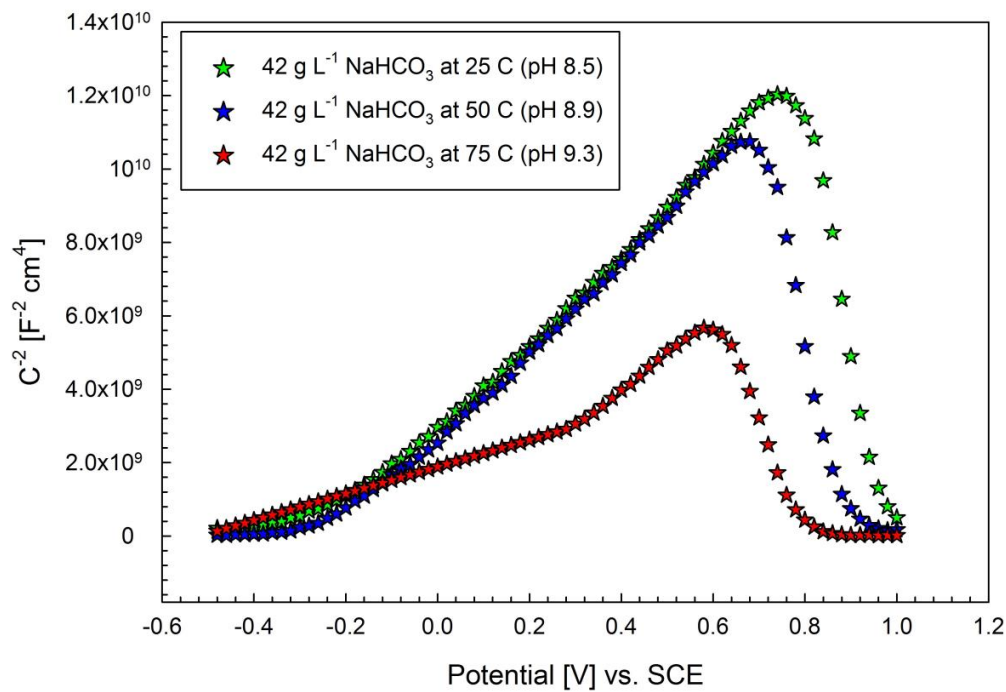


Figure B-3: Mott-Schottky plots at 1 kHz between $-0.5 \text{ V}_{\text{SCE}}$ and 1 V_{SCE} after 1 h of anodizing in 0.5 M NaHCO_3 at 25, 50, and 75 °C (pH 8.5, 8.9, and 9.3, respectively)

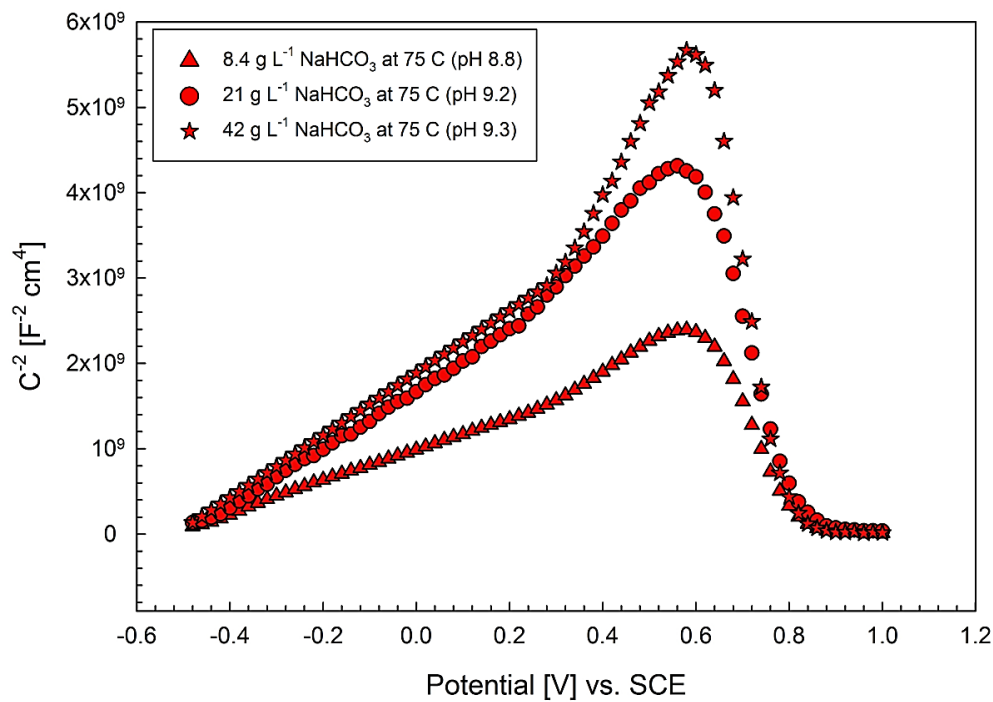


Figure B-4: Mott-Schottky plots at 1 kHz between $-0.5 \text{ V}_{\text{SCE}}$ and 1 V_{SCE} after 1 h of anodizing in 0.1 , 0.25 , or 0.5 M NaHCO_3 at 75 °C (pH 8.8, 9.2, and 9.3, respectively)

Appendix C: supplementary figures and tables for chapter 7

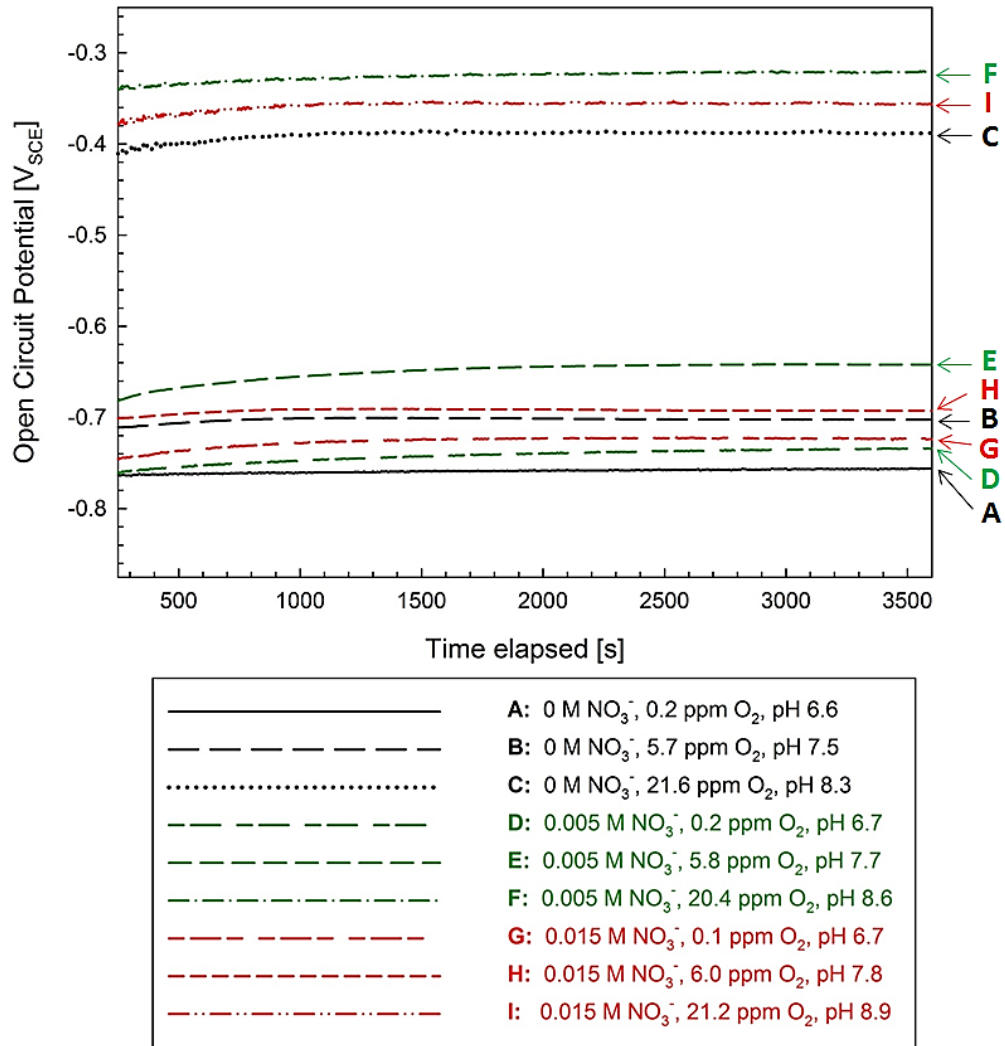


Figure C-1: Full spectrum OCP profiles showing stability approaching 1 h, in all conditions of Table 7-1

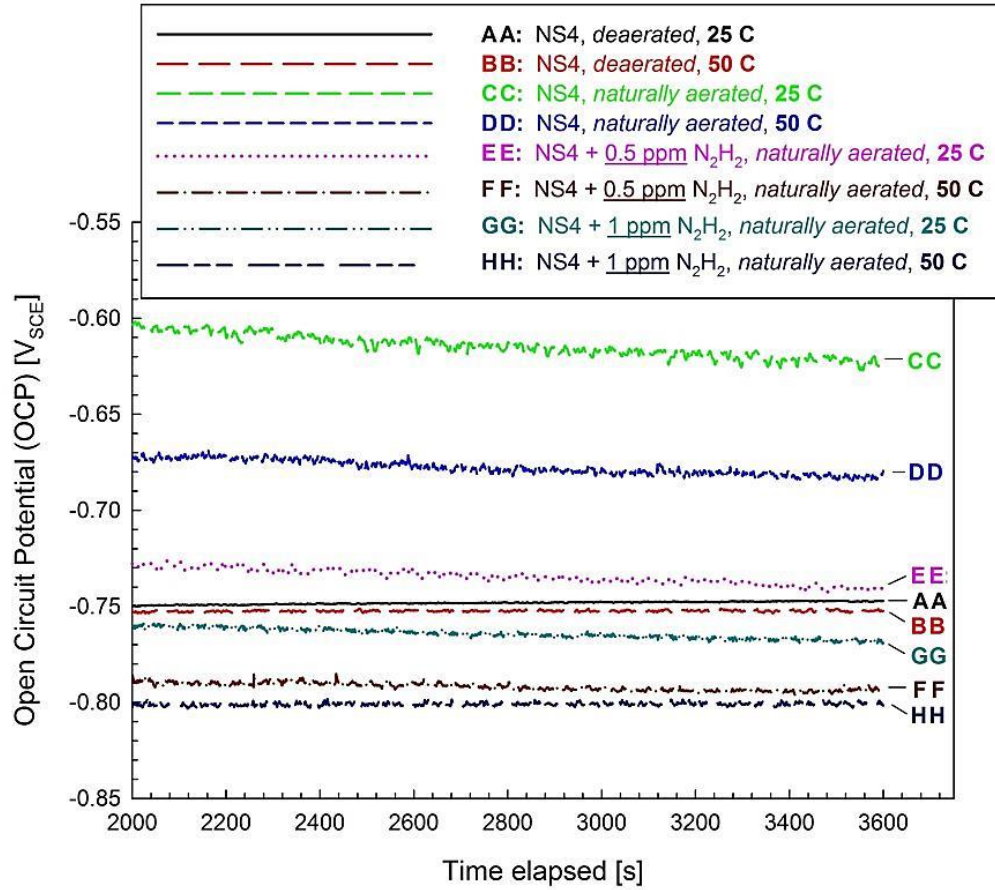


Figure C-2: OCP transients approaching 1 h of immersion in all test environments of Table 7-2

Table C-1: Corrosion parameters obtained from Tafel extrapolation of deaerated PDP results of three NO_3^- concentrations

Environment	NO_3^- [M]	Dissolved O_2 [ppm]	β_a [mV/decade]	β_c [mV/decade]	i_{corr} [$\mu\text{A}/\text{cm}^2$]
A	0	0.2	75	251	10.5
D	0.005	0.2	56	258	13.8
G	0.015	0.1	48	193	14.8

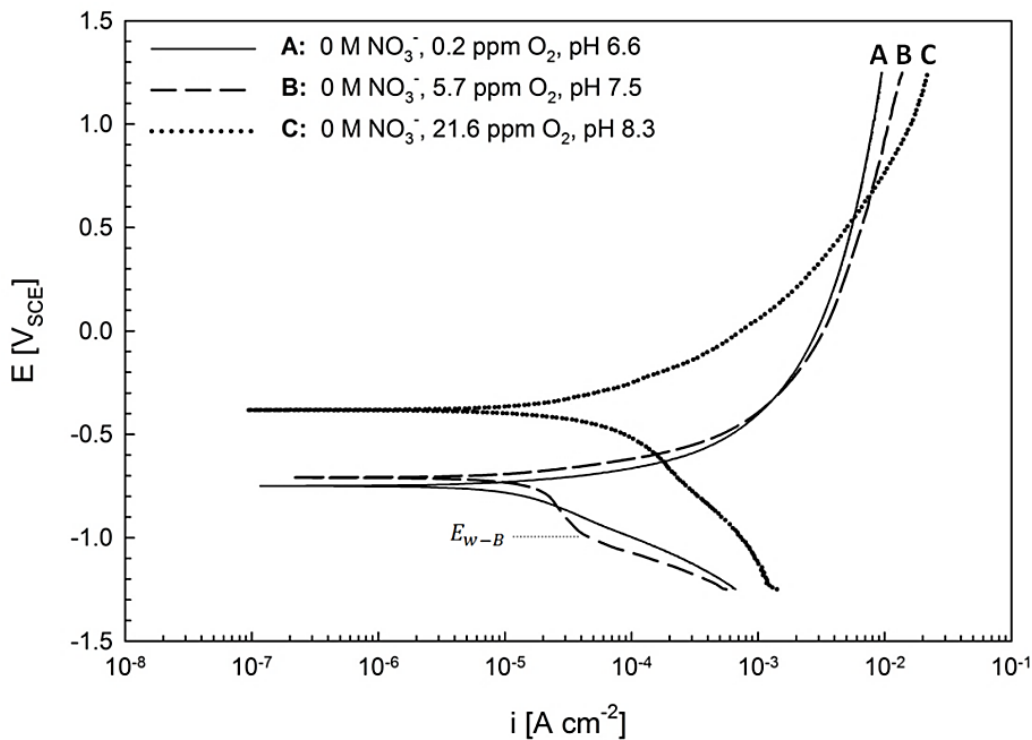


Figure C-3: PDP in 0 ppm, 6 ppm, and 20 ppm O_2 in NO_3^- -free solutions

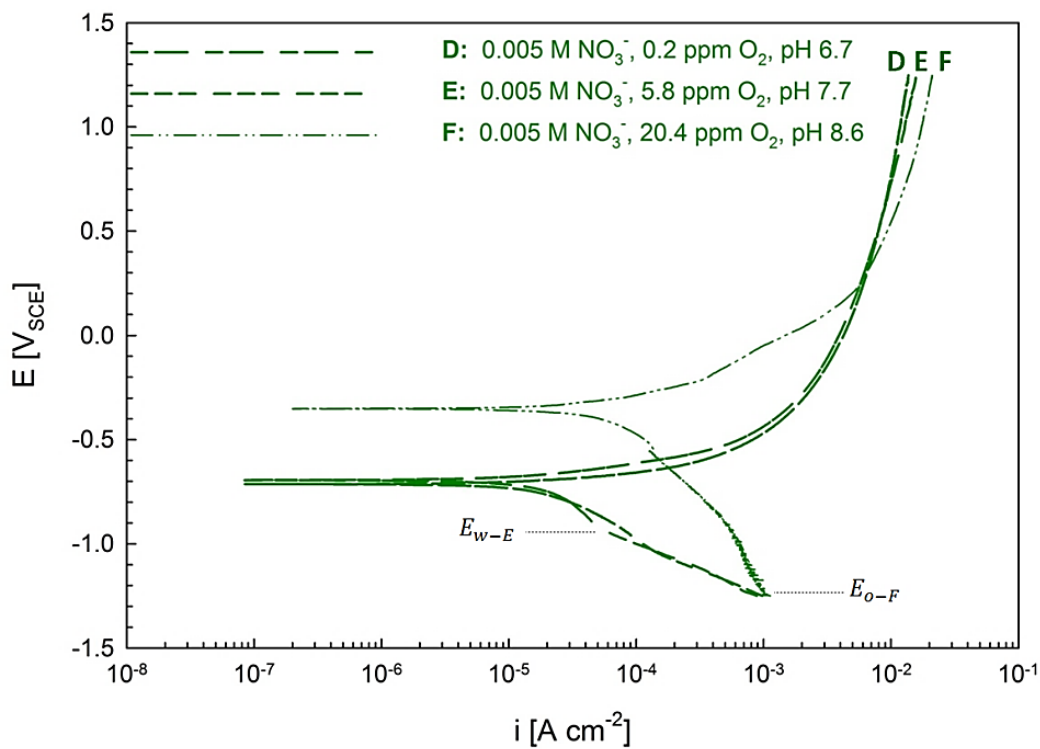


Figure C-4: PDP in 0 ppm, 6 ppm, and 20 ppm O_2 solutions with 0.005 M added NO_3^-

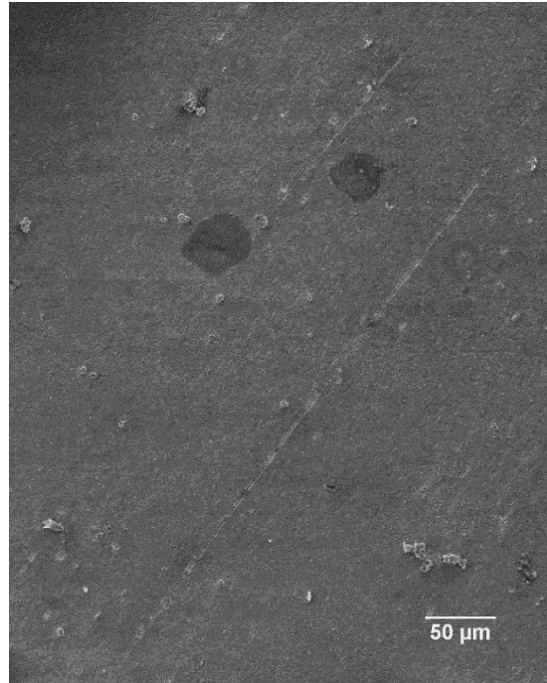


Figure C-5: SEM images of steel specimen surface following immersion in NS4 solution deaerated with 5% CO₂/95% N₂ and containing 0.015 M NO₃⁻ (0.1 ppm O₂, pH 6.7)

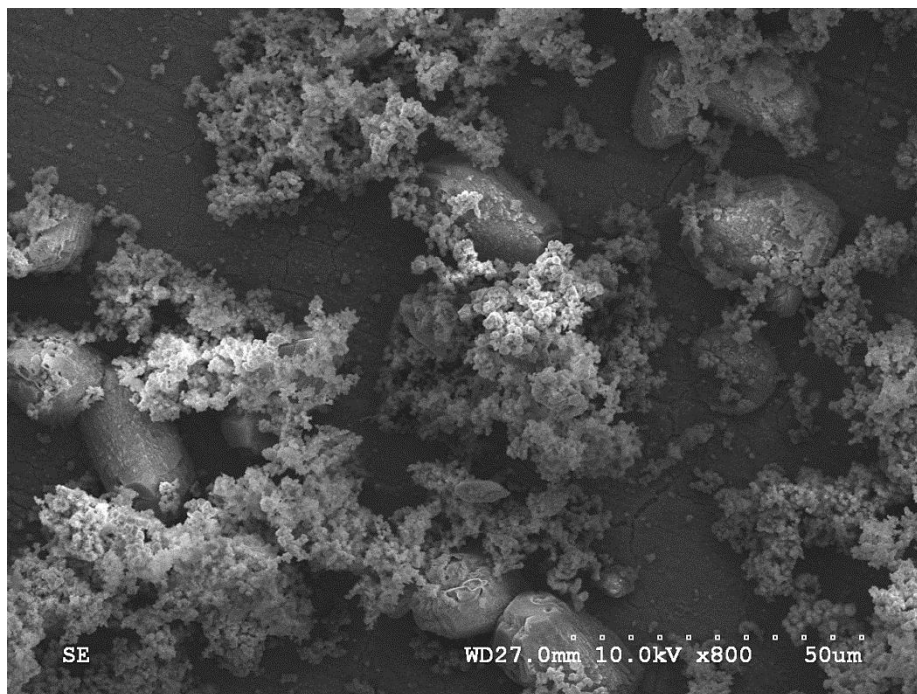


Figure C-6: Different corrosion product formations and steel substrate at the edge of the tubercle formed in solution containing 6.0 ppm O₂ (pH 7.8) and 0.015 M NO₃⁻

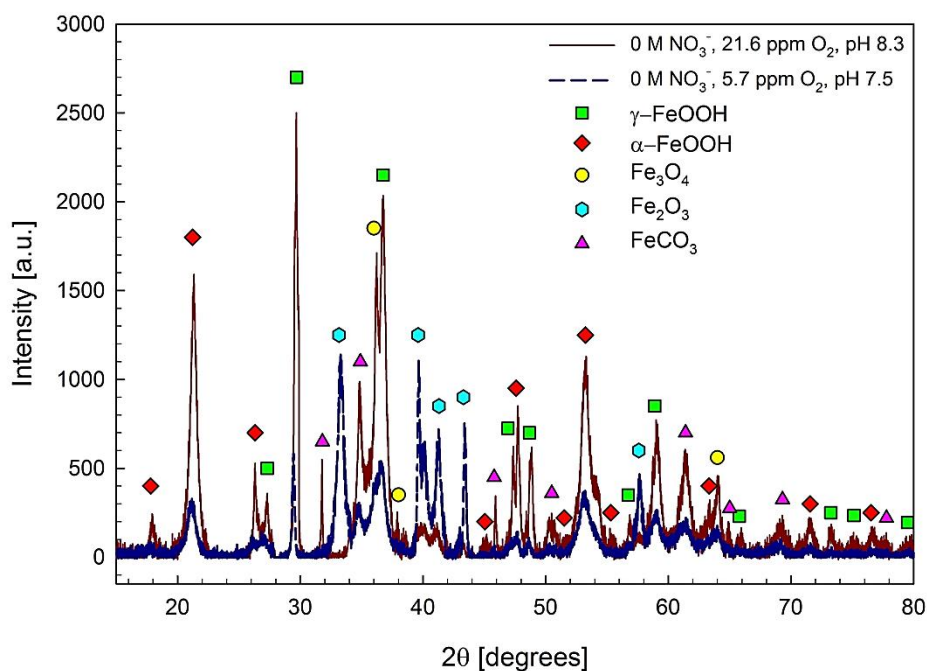


Figure C-7: Ex-situ XRD spectra of specimen immersed in 6 ppm and 20 ppm O₂ solutions free of NO₃⁻

Table C-2: Fitting results for linear and nonlinear regressions of final OCP values at 1 h and 24 h (Figure 7-1), valid for [O₂] values between 0 and 20 ppm

Immersion time [h]	NO ₃ ⁻ [M]	Linear fit:			Nonlinear fit:			
		$E = A_1 \cdot [O_2] - A_2$			$E = B_1 \cdot [O_2]^2 + B_2 \cdot [O_2] - B_3$			
		A_1	A_2	R^2	B_1	B_2	B_3	R^2
1	0	1.8×10^{-2}	0.78	0.98	5.0×10^{-4}	7.0×10^{-3}	0.76	1
1	0.005	2.1×10^{-2}	0.75	0.99	3.0×10^{-4}	1.5×10^{-2}	0.74	1
1	0.015	1.8×10^{-2}	0.76	0.96	8.0×10^{-4}	5.0×10^{-4}	0.72	1
24	0	7.8×10^{-3}	0.73	0.91	-5.0×10^{-4}	2.0×10^{-2}	0.76	1
24	0.005	7.7×10^{-3}	0.71	0.95	-4.0×10^{-4}	1.7×10^{-2}	0.72	1
24	0.015	7.5×10^{-3}	0.69	0.96	-3.0×10^{-4}	1.5×10^{-2}	0.70	1

Table C-3: EIS component values for deaerated 0.2 ppm O₂ solution (pH 6.7, 0.005 M NO₃⁻) at 2, 8, 16, and 24 h immersion

Components	2 h	8 h	16 h	24 h
R_s [Ω cm ²]	196	197	199	192
Q_{dl} [Ω^{-1} s ⁿ]	<i>2.4 x 10⁻⁴</i>	<i>2.3 x 10⁻⁴</i>	<i>1.7 x 10⁻⁴</i>	<i>1.9 x 10⁻⁴</i>
n_{dl}	0.81	0.83	0.90	0.93
${}^{\S}C_{dl}$ [F cm ⁻²]	<i>2.1 x 10⁻⁴</i>	<i>2.2 x 10⁻⁴</i>	<i>1.7 x 10⁻⁴</i>	<i>1.9 x 10⁻⁴</i>
R_{ct} [Ω cm ²]	1859	1923	1776	1895
Q_a [Ω^{-1} s ⁿ]	<i>1.1 x 10⁻²</i>	<i>1.0 x 10⁻²</i>	<i>1.0 x 10⁻²</i>	<i>9.3 x 10⁻³</i>
n_a	0.93	1	0.86	0.87
${}^{\S}C_a$ [F cm ⁻²]	<i>1.0 x 10⁻²</i>	<i>1.0 x 10⁻²</i>	<i>9.9 x 10⁻³</i>	<i>9.5 x 10⁻³</i>
R_a [Ω cm ²]	166	201	227	280
χ^2	1.7 x 10⁻⁴	1.8 x 10⁻⁴	1.3 x 10⁻⁴	1.5 x 10⁻⁴
% error in fit	< 1.3	< 1.3	< 1.1	< 1.2

[§]: post-processed parameters, results of which are italicized

Table C-4: EIS component values for 5.8 ppm O₂ solution (pH 7.7, 0.005 M NO₃⁻) at 2, 8, 16, and 24 h immersion

Components	2 h	8 h	16 h	24 h
R_s [Ω cm ²]	144	140	150	155
Q_{dl} [Ω^{-1} s ⁿ]	<i>4.4 x 10⁻³</i>	<i>5.9 x 10⁻³</i>	<i>4.9 x 10⁻³</i>	<i>3.9 x 10⁻³</i>
n_{dl}	0.84	0.83	0.84	0.92
${}^{\S}C_{dl}$ [F cm ⁻²]	<i>5.1 x 10⁻³</i>	<i>7.2 x 10⁻³</i>	<i>5.9 x 10⁻³</i>	<i>4.3 x 10⁻³</i>
R_{ct} [Ω cm ²]	1195	1019	1183	1307
Q_{sl} [Ω^{-1} s ⁿ]	<i>6.2 x 10⁻⁴</i>	<i>5.7 x 10⁻⁴</i>	<i>4.9 x 10⁻⁴</i>	<i>1.1 x 10⁻⁴</i>
n_{sl}	0.80	1	1	0.87
${}^{\S}C_{sl}$ [F cm ⁻²]	<i>6.9 x 10⁻⁴</i>	<i>5.7 x 10⁻⁴</i>	<i>4.9 x 10⁻⁴</i>	<i>1.3 x 10⁻⁴</i>
R_{sl} [Ω cm ²]	425	451	502	532
W [Ω cm ²]	41.2	39.5	35.7	18.8
χ^2	2.1 x 10⁻⁵	2.9 x 10⁻⁵	5.4 x 10⁻⁵	2.9 x 10⁻⁴
% error in fit	< 0.5	< 0.5	< 0.7	< 1.7

Table C-5: EIS component values for 20.4 ppm O₂ solution (pH 8.6, 0.005 M NO₃⁻) at 2, 8, 16, and 24 h immersion

Components	2 h	8 h	16 h	24 h
R_s [Ω cm²]	156	160	161	162
Q_{dl} [Ω^{-1} s^{<i>n</i>}]	4.1×10^{-3}	9.9×10^{-3}	1.3×10^{-2}	1.9×10^{-2}
n_{dl}	0.8726	0.8578	0.8176	0.7548
${}^sC_{dl}$ [F cm²]	3.3×10^{-3}	7.6×10^{-3}	8.5×10^{-3}	1.0×10^{-2}
R_{ct} [Ω cm²]	1150	396	129	79
Q_{sl} [Ω^{-1} s^{<i>n</i>}]	7.8×10^{-4}	3.4×10^{-4}	2.4×10^{-4}	3.4×10^{-3}
n_{sl}	0.86	0.87	0.88	0.84
${}^sC_{sl}$ [F cm²]	6.1×10^{-4}	2.7×10^{-4}	1.8×10^{-4}	2.3×10^{-3}
R_{sl} [Ω cm²]	589	610	620	369
W [Ω cm²]	50.0	31.3	24.2	14.2
χ^2	1.5×10^{-4}	1.1×10^{-4}	4.0×10^{-5}	5.4×10^{-5}
% error in fit	< 1.2	< 1.1	< 0.6	< 0.7

Appendix D: supplementary tables and figures for chapter 8

Table D-1: Test conditions and the measured natural pH of the test solutions in chapter 8

Solution	Purging gas	Temperature (°C)	Measured natural pH
NS4	Open air	20	8.8
	99.99% N ₂	20, 40, 60	8.4, 7.9, 8.1
	99.99% CO ₂	20, 40, 60	5.7, 4.7, 4.7
	5% CO ₂ + 95% N ₂	20	6.5
NS4 + 4.83 g/L NaHCO ₃	Open air	20	8.8
	99.99% N ₂	20, 40, 60	8.4, 7.4, 7.8
	99.99% CO ₂	20, 40, 60	6.5, 5.2, 5.1
	5% CO ₂ + 95% N ₂	20	7.4
NS4 + 1.81 g/L CaCl ₂ ·2H ₂ O	Open air	20	8.8
	99.99% N ₂	20	8.0
	99.99% CO ₂	20	5.2
	5% CO ₂ + 95% N ₂	20	6.2
NS4 + 1.22 g/L KCl	Open air	20	8.8
	99.99% N ₂	20	8.5
	99.99% CO ₂	20	5.4
NS4 + 1.31 g/L MgSO ₄ ·7H ₂ O	Open air	20	8.8
	99.99% N ₂	20	8
	99.99% CO ₂	20	5.2
NS4	99.99% N ₂	20	6.5*
	99.99% CO ₂	20	6.5*
NS4 + 4.83 g/L NaHCO ₃	99.99% N ₂	20	8.4*

* pH adjusted by adding either 1 M HCl or 1 M NaOH.

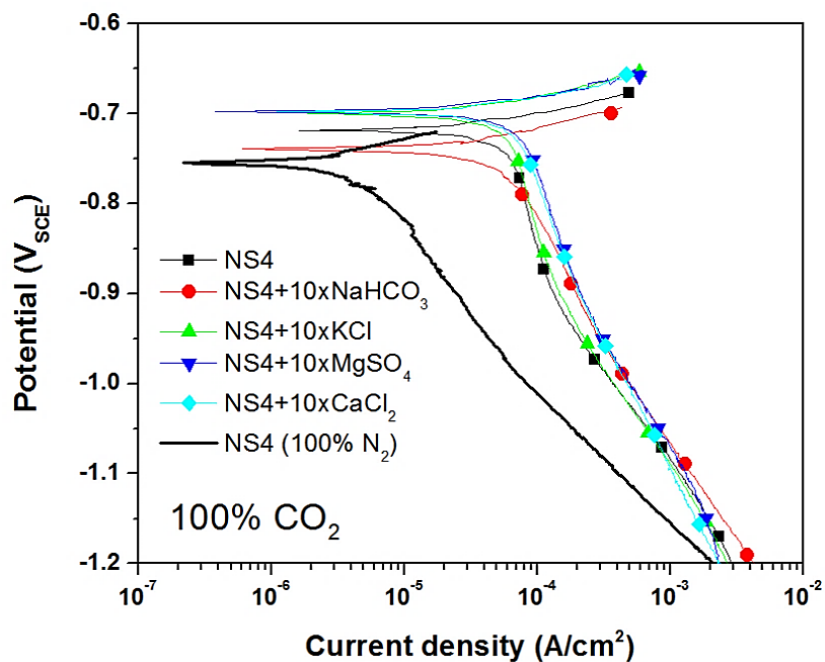


Figure D-1: Cathodic polarization curves of X100 steel in 100% CO₂ NS4 and modified NS4 solutions at 20 °C

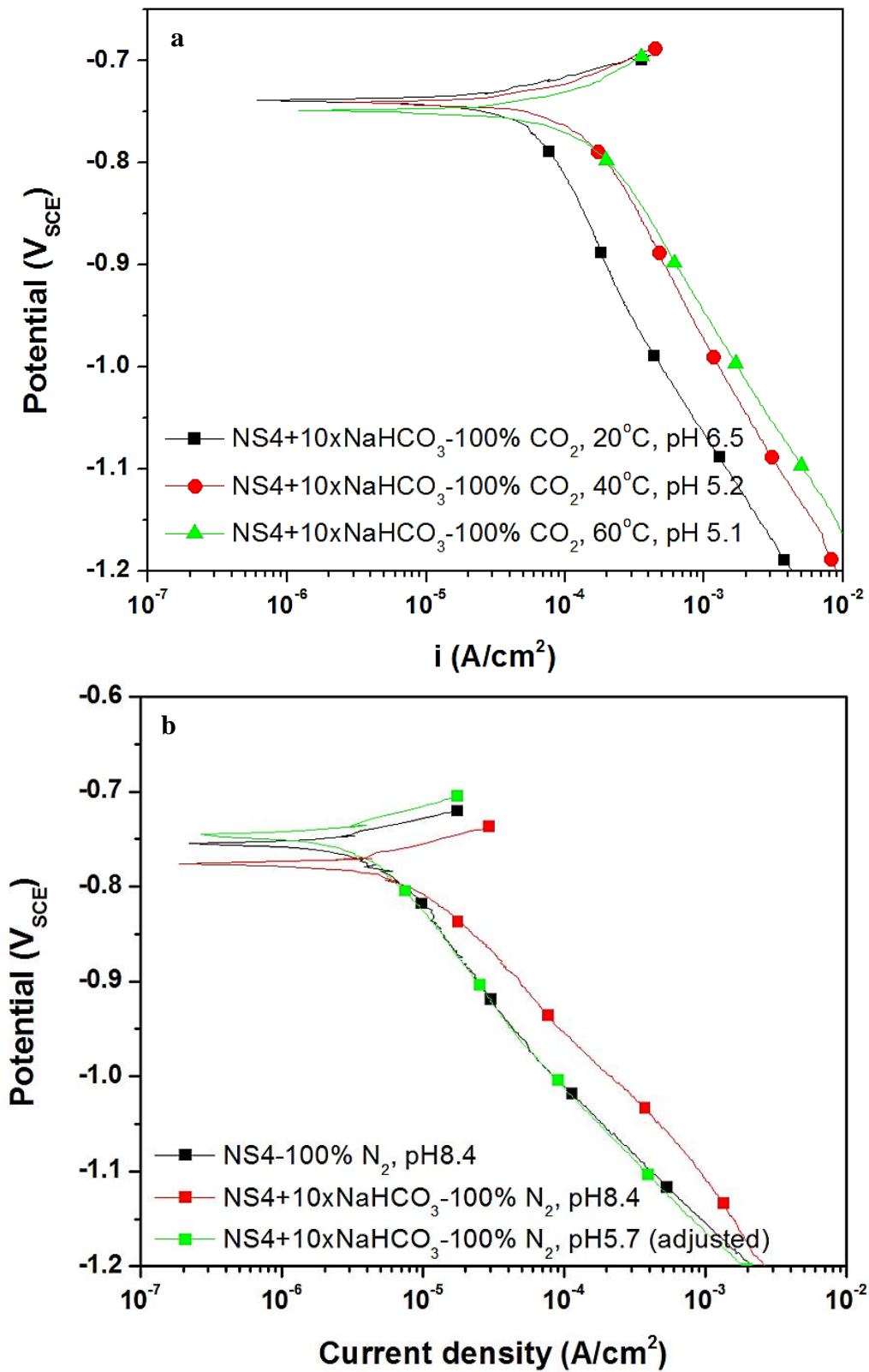


Figure D-2: Cathodic polarization curves of X100 steel in: (a) 100% CO₂ NaHCO₃-added NS4 solution at 20, 40, and 60 °C, natural pHs; (b) NaHCO₃-added NS4 solution with adjusted pH at 20°C

Table D-2: Some forms of Henry's law and values of Henry's constant for various gases in water at 298 K [277], [278]

equation:	$k_{H,pc} = \frac{p_{gas}}{c_{aq}}$	$k_{H,cp} = \frac{c_{aq}}{p_{gas}}$	$k_{H,px} = \frac{p_{gas}}{x_{aq}}$	$k_{H,cc} = \frac{c_{aq}}{c_{gas}}$
dimension:	$\left[\frac{L_{soln} \cdot atm}{mol_{gas}} \right]$	$\left[\frac{mol_{gas}}{L_{soln} \cdot atm} \right]$	$\left[\frac{atm \cdot mol_{soln}}{mol_{gas}} \right]$	dimensionless
O ₂	769.23	1.3 E-3	4.259 E4	3.180 E-2
H ₂	1282.05	7.8 E-4	7.099 E4	1.907 E-2
CO ₂	29.41	3.4 E-2	0.163 E4	0.8317
N ₂	1639.34	6.1 E-4	9.077 E4	1.492 E-2
He	2702.7	3.7 E-4	14.97 E4	9.051 E-3
Ne	2222.22	4.5 E-4	12.30 E4	1.101 E-2
Ar	714.28	1.4 E-3	3.955 E4	3.425 E-2
CO	1052.63	9.5 E-4	5.828 E4	2.324 E-2

Where:

c_{aq} = moles of gas per liter of solution

L_{soln} = liters of solution

p_{gas} = partial pressure above the solution, in atmospheres of absolute pressure

x_{aq} = mole fraction of gas in solution / moles of gas per mole of water

atm = atmospheres of absolute pressure

Appendix E: supplementary tables and figures for chapter 9

Table E-1 (for mm-model): Maximum element size, minimum element size, and maximum element growth rate for coarse to fine mesh resolutions, within the electrolyte domain vs. at the exposed steel surface in Figure 4-5

Mesh parameters		Mesh resolution		
		Coarse	Normal	Fine
In electrolyte	Maximum/minimum element size	7.6 x 10 ⁻³ m / 1.2 x 10 ⁻³ m	1.5 x 10 ⁻³ m / 6.9 x 10 ⁻⁶ m	4.6 x 10 ⁻⁴ m / 1.7 x 10 ⁻⁶ m
	Maximum element growth rate	2.0 m	1.30 m	1.20 m
At exposed steel surface	Maximum/minimum element size	4.6 x 10 ⁻³ m / 3.7 x 10 ⁻⁴ m	1.2 x 10 ⁻³ m / 6.9 x 10 ⁻⁶ m	2.3 x 10 ⁻⁴ m / 4.6 x 10 ⁻⁷ m
	Maximum element growth rate	1.8 m	1.30 m	1.10 m

Table E-2 (for m-model): Thermal conductivity and volumetric heat capacity parameters for the soil structure and ψ combinations simulated

Soil type	Porosity (ϕ)	Volumetric wetness (ψ)	Thermal conductivity (λ) [W m ⁻¹ K ⁻¹]	Volumetric heat capacity (C_v) [J m ⁻³ K ⁻¹]
Sand	0.40	0.10	1.34*	12.57*
		0.20	1.76	20.95
		0.30	2.18	29.33
Clay	0.40	0.10	0.75*	12.57*
		0.20	1.17	20.95
		0.30	1.59	29.33
Peat	0.80	0.30	0.19*	23.05*
		0.40	0.29	31.43
		0.50	0.40*	39.81*
		0.60	0.50	48.19

*: interpolated or extrapolated values

Table E-3 (for mm-model): List of current, potential, current balance, reaction kinetics (extracted from polarization plots), and regression fit equations governing corrosion simulations, with corresponding numbers, details, and conditions

Number	Equation	Details or Conditions
Current (Ohm's Law)		
{E-E.1}	$\mathbf{i}_l = -\sigma_i \nabla \varphi_i$	$\nabla \cdot \mathbf{i}_l = Q_l$
{E-E.2}	$-\sigma_i \nabla \varphi_i \cdot \vec{n} = 0$	\vec{n} is a unit vector normal to the surface
Potential and current balances		
{E-E.3}	$E_{bulk} - \Delta\varphi - E_s(x) + E_{app} = 0$	$\Delta\varphi = \varphi(x) - \varphi _{bulk}$
{E-E.4}	$E_s(x) = E_{app} - \varphi(x) + E_{bulk}$	/
{E-E.5}†	$i_{total}(x, T_{wall}) = i_a(x, T_{wall}) - i_c(x, T_{wall}) = (-\sigma \nabla \varphi \cdot \vec{n}) _{x, T_{wall}}$	i_c from {E-E.6} $i_a(E_s(x) < OCP_j)$ from {E-E.7}
Reaction kinetics (extracted from polarization plots)		
{E-E.6}†	$i_c = \left(\frac{x}{L}\right) \cdot \left\{ e^{\left(\frac{E_s(x) + C_1(T_{wall}, 5\%CO_2)}{C_2(T_{wall}, 5\%CO_2)}\right)} - e^{\left(\frac{E_s(x) + C_1(25^\circ C, 0\%CO_2)}{C_2(25^\circ C, 0\%CO_2)}\right)} \right\} + e^{\left(\frac{E_s(x) + C_1(25^\circ C, 0\%CO_2)}{C_2(25^\circ C, 0\%CO_2)}\right)}$	C_1 and C_2 values from Table 9-6
{E-E.7}†	$i_a(E_s(x) < OCP_j) = \left(\frac{x}{L}\right) \cdot \left\{ i_a^\circ(T_{wall}, 5\%CO_2) \cdot e^{\left\{\frac{2.3 \cdot \eta_s(E_s(x), T_{wall})}{\beta_a(T_{wall}, 5\%CO_2)}\right\}} - i_a^\circ(25^\circ C, 0\%CO_2) \cdot e^{\left\{\frac{2.3 \cdot \eta_s(E_s(x), 25^\circ C)}{\beta_a(25^\circ C, 0\%CO_2)}\right\}} \right\} + e^{\left(\frac{E_s(x) + C_1(25^\circ C, 0\%CO_2)}{C_2(25^\circ C, 0\%CO_2)}\right)}$	Only for $(E_s(x) < OCP_j)$
{E-E.8}	$\eta_s(x) = E_s(x) - E_s^{eq}(T_{wall})$	/
{E-E.9}	$E_s^{eq}(T_{wall}) = E_s^{eq, std} + \frac{RT_{wall}}{n_a F} \ln([Fe^{2+}])$	/
{E-E.10}	$R_{steel}(x, T_{wall}, \%CO_2) \propto \frac{i_a \cdot A_W}{n \rho_{Fe}}$	$\left(\frac{A_W}{n_i}\right)_{equivalent}$ for X100 from [74]
{E-E.11}	$i_a^\circ(T_{wall}, \%CO_2) = \left(\frac{\partial E_{LPR_{25^\circ C - 5\%CO_2}}}{\partial i_{LPR_{25^\circ C - 5\%CO_2}}}\right) / \left(\frac{\partial E_{LPR_{T_{wall} - \%CO_2}}}{\partial i_{LPR_{T_{wall} - \%CO_2}}}\right) \cdot i_a^{ref}$	/
{E-E.12}	$\beta_a(T_{wall}, \%CO_2) = \left(\frac{\partial E_{LPR_{T_{wall} - \%CO_2}}}{\partial i_{LPR_{T_{wall} - \%CO_2}}}\right) / \left(\frac{\partial E_{LPR_{25^\circ C - 5\%CO_2}}}{\partial i_{LPR_{25^\circ C - 5\%CO_2}}}\right) \cdot \beta_a^{std}$	/
Regression fit		
{E-E.13}	$\chi^2 = \sum_{j=1}^n \{w_j i_{c-j} - \overline{I_{c-j}}(x)\}^2$	/

†: the convention for current density ensures that cathodic current density always has an opposite sign to that of anodic current density

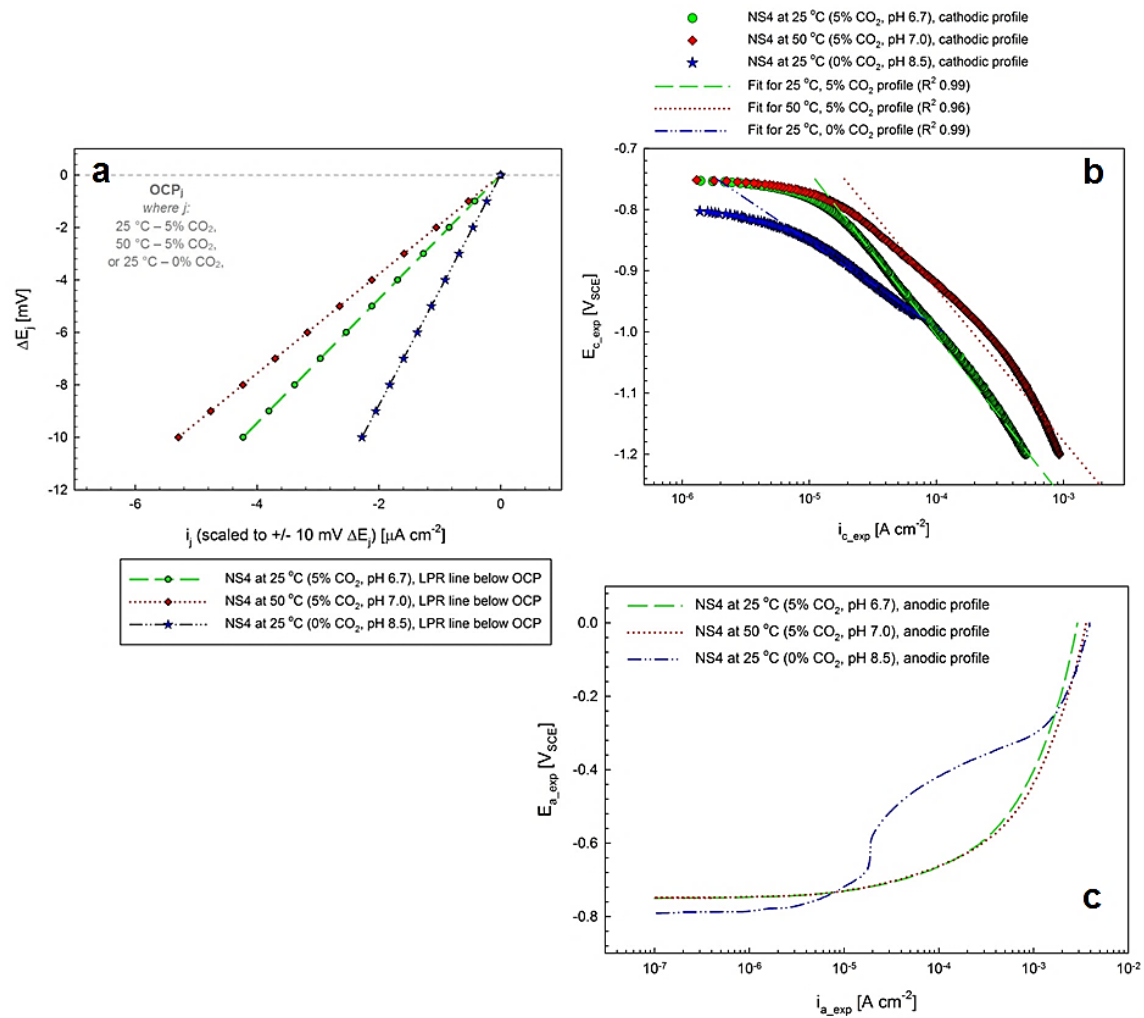


Figure E-1 (for mm-model): Polarization profiles of X100 specimen immersed in different temperature and %CO₂ environments, obtained through electrochemical corrosion experiments: (a) LPR fitting results at $E < OCP$; (b) cathodic regime of PDP results, with regression fits; and (c) anodic regime of PDP results

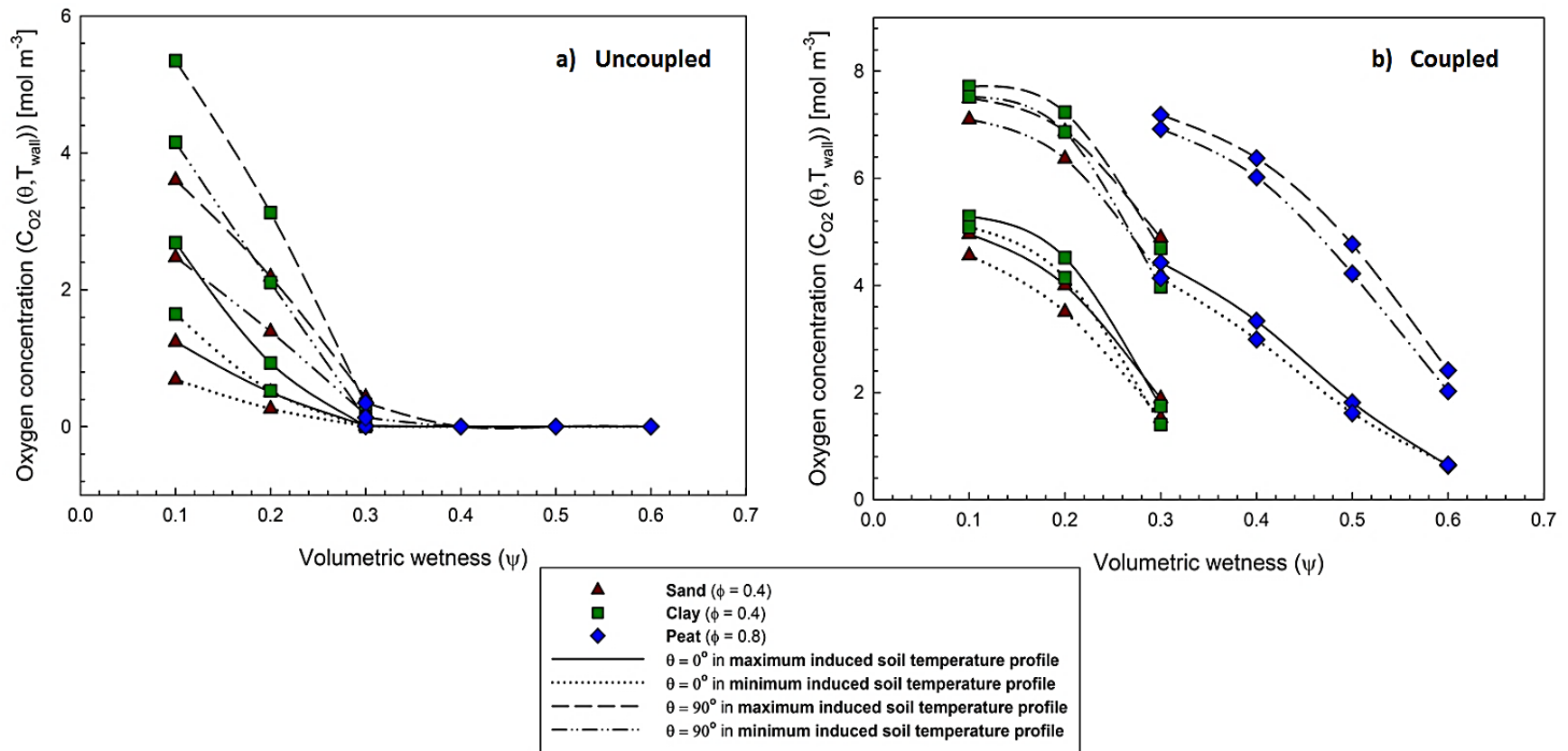


Figure E-2 (for m-model): C_{O_2} evaluated at $\theta = 0^\circ$ and $\theta = 90^\circ$ in minimum and maximum induced temperature profiles, different soil structures, and ψ using: (a) uncoupled governing equations; and (b) coupled governing equations

Table E-4 (for mm-model): Maximum radial depth (d_{defect_max}) and longitudinal length (l_{defect}) dimensions [mm] of corrosion defects at 1 and 3 year time stages for all temperatures (T_{wall}), applied potentials (E_{app}), and coating disbondment opening sizes (w) simulated

E_{app} [V _{SCE}]	w [mm]	T_{wall} [°C]	d_{defect_max} [mm]		l_{defect} [mm]	
			~50 weeks	~150 weeks	~50 weeks	~150 weeks
			(~1 year)	(~3 years)	(~1 year)	(~3 years)
-0.75	0.5	25	-1.0	-3.0	9.7	13.5
-0.75	1	25	-1.0	-2.9	10.9	14.4
-1	0.5	25	-0.9	-2.4	9.2	13.3
-1	1	25	-0.8	-2.1	11.8	14.7
-0.75	0.5	50	-1.2	-3.3	10.3	14.9
-0.75	1	50	-1.1	-3.2	12.5	15.5
-1	0.5	50	-0.9	-2.7	10.5	14.8
-1	1	50	-0.8	-2.3	12.8	15.2

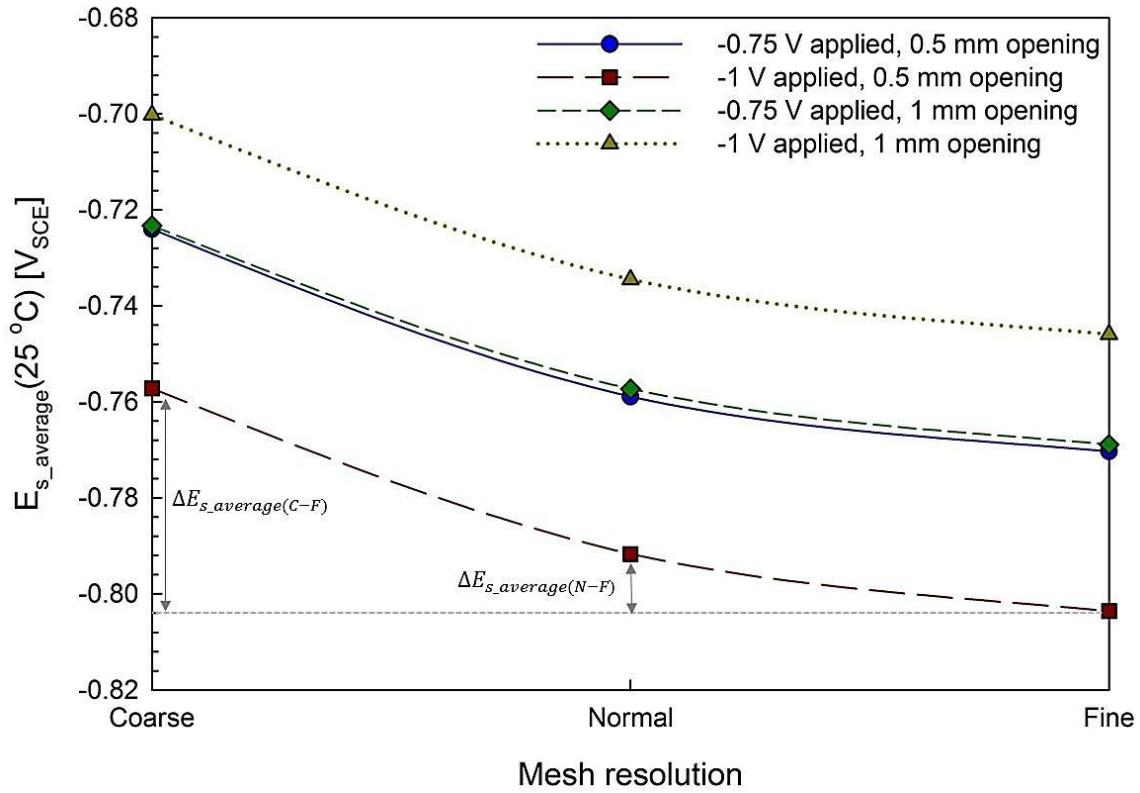


Figure E-3 (for mm-model): Convergence profiles of interfacial surface-electrolyte potential parameter (E_s) averaged over full length of exposed steel surface ($E_{s_average}$), for coarse, normal, and fine mesh resolutions

Table E-5: Mechanical properties of various grades of HSLA pipeline steels [152]

Mechanics properties	X65 steel	X80 steel	X100 steel
Young's modulus (MPa)	207000	207000	207000
Poisson's ratio	0.3	0.3	0.3
SMYS (MPa)	456	646	802
SMTS (MPa)	570	760	891
Yield/Tensile strength (Y/T)	0.80	0.85	0.90